RĒZEKNES TEHNOLOĢIJU AKADĒMIJA
Inženieru fakultāte

REZEKNE ACADEMY OF TECHNOLOGIES
Faculty of Engineering

VIDE. TEHNOLOĢIJA. RESURSI

XIII starptautiskās zinātniski praktiskās konferences materiāli
2021.gada 17.-18.jūnijs

3.SĒJUMS

ENVIRONMENT. TECHNOLOGY. RESOURCES

Proceedings of the 13th International Scientific and Practical Conference
June 17th – 18th, 2021

Volume III

Rēzekne
2021

VIDE. TEHNOLOĢIJA. RESURSI. 13.starptautiskās zinātniski praktiskās konferences materiāli. 2021. gada 17.-18. jūnijs. *3.sējums.* Rēzekne: Rēzeknes Tehnoloģiju akadēmija, 2021. 386 lpp.

ENVIRONMENT. TECHNOLOGY. RESOURCES. Proceedings of the 13th International Scientific and Practical Conference on June 17-18, 2021. *Volume III,* Rezekne: Rezekne Academy of Technologies, 2021. pp. 386.

Rekomendējusi publicēšanai Rēzeknes Tehnoloģiju akadēmijas Zinātnes padome 2021. gada 25. maijā.
Recommended for publication by the Scientific Council of Rezekne Academy of Technologies on May, 25 th, 2021.

NATIONAL DEVELOPMENT PLAN 2020
EUROPEAN UNION
European Regional Development Fund
INVESTING IN YOUR FUTURE

ERDF co-funded project "Funding of international projects in research and innovation at Rezekne Academy of Technologies" No. 1.1.1.5/18/I/012

13.starptautiskās zinātniski praktiskās konferences "Vide. Tehnoloģija. Resursi" materiālu trijos sējumos ir pārstāvēti jaunākie pēdējo divu gadu pētījumi vides inženierzinātnē, vides un dabas aizsardzībā, ilgtspējīgā lauksaimniecībā, enerģētikā, materiālzinātnē, mehānikā, metālapstrādē, lāzeru tehnoloģijās, matemātiskajā modelēšanā, elektrotehnikā, vides ekonomikā un vadībā, informācijas tehnoloģijās un sociotehnisko sistēmu modelēšanā, vides izglītībā un ilgtspējīgas attīstības procesos. Krājumā pārstāvēto pētījumu joma ir daudzpusīga un starpdisciplināra, balstīta uz starptautisko zinātnieku kolektīvu sasniegumu rezultātiem. Konferences materiālos iekļauti 157 zinātniskie raksti, kuru autori pārstāv 14 valstis.

Proceedings of the 13th International Scientific and Practical Conference "Environment. Technology. Resources" include studies of the last two years in fields of engineering, environmental and nature protection, sustainable agriculture, energy, material science, mechanics, metalworking, laser technologies, mathematical modelling, electrical engineering, environmental economics and management, information technologies and sociotechnical systems modelling, environmental education and sustainable development. The research area presented in the proceedings is comprehensive and cross disciplinary-based, on advances of international researchers. The proceedings comprise 157 scientific papers from 14 countries.

Online ISSN 2256-070X
Published by Rezekne Academy of Technologies, 2021

Scientific Committee Chairman

Dr.sc.ing. Edmunds Teirumnieks, Rezekne Academy of Technologies, Latvia

Scientific Committee Co-Chairmen

Dr. Walter Leal, Hamburg University of Applied Sciences, Germany, Manchester Metropolitan University, United Kingdom
Dr.sc.ing. Andris Martinovs, Rezekne Academy of Technologies, Latvia
Dr.sc.ing. Artis Teilāns, Rezekne Academy of Technologies, Latvia

Scientific Committee

PhD Andres Annuk, Estonian University of Life Sciences, Estonia
Dr. Dragen Antic, University of Nis, Serbia
Dr.oec. Dzintra Atstāja, BA School of Business and Finance, Latvia
DSc. Hristo Ivanov Beloev, Angel Kanchev University of Ruse, Bulgaria
PhD Plamen Bogdanov, Vasil Levski National Military University, Bulgaria
Dr.sc.ing. Jurijs Cizovs, Riga Technical University, Latvia
PhD Lubomir Dimitrov, Tehnical University of Sofia, Bulgaria
Dr.-Ing. Horst Exner, Mittweida University of Applied Sciences, Germany
Prof. Gian Luca Foresti, Udine University, Italy
PhD Gilberto Marzano, President of Ecoistituto Udine, Italy
PhD Vladimir Golenkov, Belarusian State University of Informatics and Radioelectronics, Belarus
Dr. Ants Kallaste, Tallinn University of Technology, Estonia
PhD Tsanko Karadzhov, Technical University of Gabrovo, Bulgaria
Dr. Vasily Karasev, Russian Academy of Sciences, Russian Federation
PhD Veiko Karu, Tallinn University of Technology, Estonia
Dipl.-Kfm. Lars Kempt, Chemnitz University of Technology, Germany
Dr. Linas Kliucininkas, Kaunas University of Technology, Lithuania
PhD Egons Lavendelis, Riga Technical University, Latvia
Dr.sc.ing. Lyubomir Lazov, Rezekne Academy of Technologies, Latvia
PhD Cristian-Emil Moldoveanu, Military Technical Academy "Ferdinand I", Romania
PhD Nikolay Nedyalkov, Bulgarian Academy of Sciences, Bulgaria
Dr.geogr. Oļģerts Nikodemus, University of Latvia, Latvia
Dr. Vlastimir Nikolic, University of Nis, Serbia
Dr. Nenad Pavlovič, University of Nis, Serbia
Dr. Svetlana Polukoshko, Ventspils University College, Engineering Research Institute "VSRC", Latvia
PhD Leonardo Quattrocchi, Confindustria, LUISS Business School, Italy
PhD Gabriel Raducanu, Air Force Academy Henri Coanda, Romania
Vilnis Rantins, Chairman of the Management Board of the Association of Mechanical Engineering and Metalworking Industries, Latvia
Dr. Anton Rassolkin, Tallinn University of Technology, Estonia
Dr.sc.ing. Andrejs Romanovs, IEEE Latvia Section, Riga Technical University, Latvia
Dr.habil.phys. Vladimir Solovyev, Pskov State University, Russian Federation
PhD Chrysostomos Stylios, Technological Educational Institute of Epirus, Greece
PhD Arita Takahashi, Riga Technical University, Latvia
Dr.sc.ing. Victor Tatarinov, Geophysical Centre of the Russian Academy of Sciences, Russian Federation
Dr.-Ing. Josef Timmerberg, Jade University of Applied Sciences, Germany
Dr. Toomas Vaimann, Tallinn University of Technology, Estonia
Dr.habil.sc.ing Janis Viba, Riga Technical University, Latvia
PhD Constantin-Iulian Vizitiu, Militar Technical Academy "Ferdinand I", Romania

Organizing Committee Chairman

Dr.habil.geol. Gotfrīds Noviks, Rezekne Academy of Technologies, Latvia

Organizing Commitee

Dr.sc.ing. Egils Ginters, Riga Tehnical University, Latvia
Dr.sc.ing. Pēteris Grabusts, Rezekne Academy of Technologies, Latvia
DSc. Dimitar Grekov, Agricultural University, Bulgaria
PhD Aleksandrs Gorbunovs, Riga Technical University, Latvia
PhD Krzysztof Krakowski, War studies University, Poland
Dr.sc.ing. Ēriks Kronbergs, University of Latvia, Latvia
Dr.sc.ing. Sergejs Kodors, Rezekne Academy of Technologies, Latvia
Dr.habil.sc.ing. Egons Lavendelis, Riga Technical University, Latvia
Dr.sc.ing. Lyubomir Lazov, Rezekne Academy of Technologies, Latvia
PhD Lienīte Litavniece, Rezekne Tecnologies Academy, Latvia
PhD Līga Mazure, Rezekne Academy of Technologies, Latvia
PhD Magdalena Mitkova, Prof. Assen Zlatarov University Burgas, Bulgaria
PhD Valyo Nikolov, Technical University of Sofia, Plovdiv Branch, Bulgaria
Dr.sc.ing. Imants Nulle, Latvia University of Life Sciences and Technologies, Latvia
Dr.geol. Janis Prols, United Nations Development Programme, Kazakhstan
PhD Leonardo Quattrocchi, Confindustria, LUISS Business School, Italy
Dr.geol. Valdis Segliņš, University of Latvia, Latvia
Dr.biol. Artūrs Škute, Daugavpils University, Latvia

Reviewers

PhD Nikolaj Angelov, Technical University of Gabrovo, Bulgaria
Dr.oec. Dzintra Atstāja, BA School of Business and Finance, Latvia
Dr.sc.ing. Anita Avišāne, Riga Technical University, Latvia
PhD Ivaylo Balchev, Rezekne Academy of Technologies, Latvia
PhD Jānis Bičevskis, University of Latvia, Latvia
Dr. Rene Brunsch, Apromace data systems GmbH, Germany
Dr.sc.ing. Edgars Čubars, Rezekne Academy of Technologies, Latvia
PhD Dimitar Diakov, Technical University of Sofia, Bulgaria
PhD Dimitar Dichev, Technical University of Gabrovo, Bulgaria
PhD Sandra Ezmale, Rezekne Academy of Technologies, Latvia
Dr.sc.ing. Egils Ginters, Riga Tehnical University, Latvia
PhD Jānis Grabis, Riga Technical University, Latvia
Dr.sc.ing. Pēteris Grabusts, Rezekne Academy of Technologies, Latvia
PhD Aleksandrs Gorbunovs, Riga Technical University, Latvia
Dr.oec. Elita Jermalajeva, Preili Municipality, Latvia
PhD Angelika Juško-Štekele, Rezekne Academy of Technologies, Latvia
Dr.sc.ing. Aivars Kaķītis, Latvia University of Life Sciences and Technologies, Latvia
Dr.paed. Ilmārs Kangro, Rezekne Academy of Technology, Latvia
Dr. paed. Janis Kapenieks, Riga Technical University, Latvia
PhD Atis Kapenieks, Riga Technical University, Latvia
Dr. Vasily Karasev, Russian Academy of Sciences, Russian Federation
PhD Tsanko Karadzhov, Technical University of Gabrovo, Bulgaria
Dr.geol. Andris Karpovičs, Rezekne Academy of Technologies, Latvia
Dr.sc.ing. Sergejs Kodors, Rezekne Academy of Technologies, Latvia
Dr.sc.ing. Ēriks Kronbergs, University of Latvia, Latvia
PhD Karīne Laganovska, Rezekne Academy of Technologies, Latvia
Dr.sc.ing. Lyubomir Lazov, Rezekne Academy of Technologies, Latvia

Dr. Walter Leal, Hamburg University of Applied Sciences, Germany, Manchester Metropolitan University, United Kingdom
PhD Angel Lengerov, Technical University of Plovdiv, Bulgaria
PhD Lienīte Litavniece, Rezekne Tecnologies Academy, Latvia
Dr.oec. Jelena Lonska, Rezekne Academy of Technologies, Latvia
PhD Gilberto Marzano, President of Ecoistituto Udine, Italy
PhD Arturs Medveckis, University of Liepaja, Latvia
PhD Jurijs Merkurjevs, Riga Technical University, Latvia
PhD Ziedonis Miklašēvičs, Rezekne Academy of Technologies, Latvia
PhD Nikolai Minkovski, University of Forestry, Bulgaria
PhD Sandra Murinska, Rezekne Academy of Technologies, Latvia
PhD Nikolay Nedyalkov, Bulgarian Academy of Sciences, Bulgaria
Dr.habil.geol. Gotfrīds Noviks, Rezekne Academy of Technologies, Latvia
Dr.chem. Sergejs Osipovs, Daugavpils University, Latvia
PhD Desislava Ivanova Petrova, Technical University of Gabrovo, Bulgaria
Dr.habil.sc.ing. Igor Plokhov, Pskov State University, Russian Federation
PhD Dimcho Pulov, Technical University of Gabrovo, Bulgaria
Dr. Anton Rassolkin, Tallinn University of Technology, Estonia
Dr.phys. Gita Rēvalde, Riga Technical University, Latvia
Dr.sc.ing. Igor Savraev, Pskov State University, Russian Federation
Dr.sc.ing. Andris Skromulis, Rezekne Academy of Technologies, Latvia
Dr.habil.phys. Vladimir Solovyev, Pskov State University, Russian Federation
Dr.geol. Juris Soms, Daugavpils University, Latvia
Dr.agr. Veneranda Stramkale, Institute of Agricultural Resources and Economics Latvia, Latvia
PhD Aina Strode, Rezekne Academy of Technologies, Latvia
PhD Gunars Strods, Rezekne Academy of Technologies, Latvia
PhD Arita Takahashi, Riga Technical University, Latvia
Dr.sc.ing. Edmunds Teirumnieks, Rezekne Academy of Technologies, Latvia
Dr.-Ing. Josef Timmerberg, Jade University of Applied Sciences, Germany
Dr.biol. Rasma Tretjakova, Rezekne Academy of Technologies, Latvia
PhD Dragomir Vassilev, Technical University of Gabrovo, Bulgaria
Dr.sc.ing. Imants Zarembo, Rezekne Academy of Technologies, Latvia
Dr. Mihails Zillbershmidt, Moscow State Mining University, Russian Federation
PhD Tsanka Zlateva-Petkova, Technical University of Gabrovo, Bulgaria
PhD Erika Zubule, Rezekne Academy of Technologies, Latvia
PhD Anda Zvaigzne, Rezekne Academy of technologies, Latvia

Secretariat Chairman

Mg.sc.chem. Ērika Teirumnieka, Rezekne Academy of Technologies, Latvia

Secretariat Members

Mg.sc.env. Sintija Augule, Rezekne Academy of Technologies, Latvia
Mg.sc.comp. Gundega Bēriņa, Rezekne Academy of Technologies, Latvia
Mg.sc.chem. Inese Bernāne, Rezekne Academy of Technologies, Latvia

III

ENGINEERING SCIENCES AND PRODUCTION TECHNOLOGIES

SATURS
CONTENTS

Engineering Sciences and Production Technologies

ENGINEERING SCIENCES AND PRODUCTION TECHNOLOGIES

Environment. Technology. Resources. Rezekne, Latvia
Proceedings of the 13th International Scientific and Practical Conference. Volume 3, 15-19

Influence of the Overlap Coefficient on the Contrast in Laser Marking of C110W Steel

Nikolay Angelov
Technical University of Gabrovo
Gabrovo, Bulgaria
angelov_np@abv.bg

Lyubomir Lazov
Rezekne Academy of Technology
Rezekne, Latvia
lyubomir.lazov@rta.lv

Edmunds Teirumnieks
Rezekne Academy of Technology,
Rezekne, Latvia
edmunds.teirumnieks@rta.lv

***Abstract* - The laser marking process by melting samples of C110W carbon tool steel was studied. The experiments were performed with a fiber laser and a CuBr laser. A field of squares is marked in a raster method for different values of the overlap coefficient and power density. The contrast of the marking is determined on each marked square. From the obtained experimental data, graphs of the dependence of the contrast on the overlap coefficient for three power densities were drawn. The obtained results for the two lasers are compared and the influence of the wavelength is indirectly analysed. The working intervals of the overlap coefficient for the studied power densities for the two lasers at which the optimal contrast in the processing zone is obtained are determined.**

Keywords* - *laser marking, fiber laser, CuBr laser, C110W steel, overlap coefficient, power density, contrast.

I. INTRODUCTION

Laser marking is a modern technology that is increasingly used in modern production in electronics, electrical engineering, mechanical engineering, medicine, and others. One of its main advantages is that it allows manufacturers to meet modern requirements for tracking and quality control of their products. Laser marking of serial numbers, matrix codes, barcodes, logos, tables, and other operational information is the main factor for proper optimization and monitoring of production processes [1 ÷ 3], [11 ÷ 17]. The wide penetration of laser marking technology in industrial production is primarily due to its special characteristics, such as non-contact during the process, which allows processing both ultra-hard materials for mechanical engineering and brittle and thin materials for microelectronics. The selectivity of the laser interaction with the material combined with the simultaneous ability to achieve heating, melting, and evaporation of the material in a very small area is another significant advantage of this innovative technology over other marking methods. The ability of modern laser scanners to control the movement of the laser beam in space at high speed and to position it with high accuracy is another important factor that has significantly contributed to the entry of this technology in the modern production of various types of products [4].

Laser marking is a complex technological process that depends on a number of factors that can be combined into three main groups [5, 6]. It can be noted that these factors in most cases are interrelated and have a complex effect on the specific technological process [7]. The article [8] with a nanosecond pulsed laser analyses the influence of the pulse tracking frequency and the distance between the processing lines when scanning titanium alloy substrates on the process of colour laser marking. The authors in [9] investigated the effect of a number of parameters of laser processing, such as power and fill factor of laser pulses on a certain working area when marking barcodes on the surfaces of aluminum alloys. The results show that the processing parameters significantly affect the surface roughness.

The study [10] demonstrated a processing technique related to the overlap of the laser pulses and the overlap between the scanning lines influencing the formation of specific microstructures on the surface of Ti6Al4V samples. The topology of processing in the process considered by the authors varies in a wide range between 40% and 90% and leads to a change in the density of the absorbed laser energy in the range from 0.49 J/cm^2 to

Online ISSN 2256-070X
https://doi.org/10.17770/etr2021vol3.6599

12.28 J/cm^2 and this in turn to optimization of the quality of the technological process.

The present study focuses on the analysis and the relationship between two technological factors, the overlap coefficient and the scan overlap coefficient, on the quality of the marking and in particular on the contrast in the processing area. Their influence has a direct impact on the linear density of the pulses entering at the processing area, as well as on the linear energy density and the effective energy for the realization of the specific technological process.

II. TOPOLOGY OF THE EXPERIMENTAL STUDY

The overlap coefficients k_{ov} of the laser pulses and the overlap coefficient k_s in the scanning process are complex factors that give us a relationship between the marking speed (factor related to the technological process), on the one hand, and the pulse repetition rate and laser power density in diameter. at the workplace (factors related to the parameters of the laser) on the other hand.

Considering that, the physical interaction of the laser radiation with the substance in the treatment area leading to heating, melting and evaporation is strongly influenced by the absorbed energy (effective energy for the specific technological process E_{eff}).

Considering that the linear energy density at laser action is the quantity defined by the absorbed energy per unit length in the laser marking area

$$E_\ell = \frac{AP}{v}\ , \tag{1}$$

where v is the marking speed, P is power and A is absorption capacity.

In the case of pulsed raster marking, as in our study, the overlap coefficient k_{ov} significantly affects the value of the linear pulse density of laser pulses entering the processing line

$$L_p = \frac{v}{v}\ , \tag{2}$$

where v is the frequency of pulse repetition.

In turn, the above two relations (1) and (2) have a significant influence on the effective absorbed energy of the laser radiation per unit area of the laser impact zone

$$E_{eff} = \frac{APv}{v^2} \tag{3}$$

and on the volume absorbed energy of the laser radiation

$$E_\rho = \frac{AP}{dv\delta}\ , \tag{4}$$

where δ is the penetration of laser radiation into the substance.

Taking into account all these interrelated relations between the physical quantities and the technological parameters of the processing of formulas (1) - (4) it is seen that the topology of the experiment is essential for the expected result of the processing.

The overlap coefficient k_{ov} of the laser radiation pulses is a complex factor that gives a relationship between the marking speed (factor related to the technological process) on the one hand and the frequency of pulse repetition and laser power density through the diameter of the working spot (factors related to the laser parameters) on the other hand. It is defined by the expression

$$k_{ov} = \frac{x}{d}.100\% = (1-\frac{\ell}{d}).100\%\ , \tag{5}$$

where d is the diameter of the working spot, x is the width of the overlapped part of two consecutive pulses of laser radiation, ℓ is the distance between two consecutive pulses (Fig. 1).

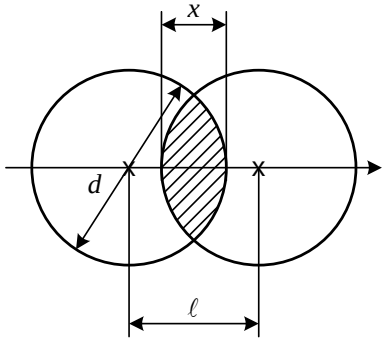

Fig. 1. Position of two consecutive pulses in the presence of overlap

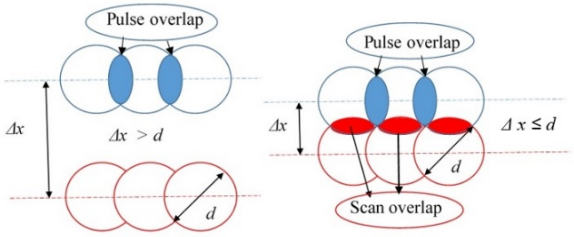

Fig. 2. Intervals of change of the scan overlap coefficient k_s

Taking into account that

$$\ell = \frac{v}{v} \tag{6}$$

where v is the marking speed and v is the frequency of pulse repetition, and replacing (2) in (1) is obtained

$$k_{ov} = (1-\frac{v}{vd}).100\% \tag{7}$$

The laser marking process also is affected on the scan overlap coefficient k_s. It depends on the diameter d of the working spot and the raster step Δx. The scan overlap coefficient is given by the formula

$$k_s = (1 - \frac{\Delta x}{d}).100\% \cdot \quad (8)$$

When the condition $\Delta x \leq d$ is fulfilled, it has positive values and is in the interval $k_s \in [0, 100]$ %. When the condition $\Delta x > d$ is fulfilled, it takes negative values. The limitation for raster marking is that the consecutive lines are at a smaller distance from the limiting ability of the human eye, i.e. $\Delta x \leq 70$ µm. In this case, the homogeneity of the marking is not disturbed.

It should be noted that there is a relationship between some of the considered physical quantities and technological parameters. For example, the overlap coefficient k_{ov} can be related to the linear pulse density L_p and the effective energy E_{eff} with the expressions

$$k_{ov} = (1 - \frac{1}{L_p d}).100\% \quad (9)$$

and $$k_{ov} = (1 - \frac{AP}{E_{eff} v d}).100\% \cdot \quad (10)$$

III. Experiments and Diskusions

The experiments refer to C110W carbon tool steel. It is widely used in industry. C110W steel is used for making hand taps, rasps, needle files, saws for woodworking, matrices for cold stamping. It is high carbon steel and has relatively high coefficients of thermal conductivity and diffusivity (see Table 1).

Table 1. Basic characteristics of the C110W carbon tool steel

Characteristic	**Value**
Coefficient of thermal conductivity k, W/(m.K)	45
Specific heat capacity c, J/(kg.K)	460
Density ρ, kg/m^3	7850
Coefficient of diffusivity a, m^2/s	1.25×10^{-5}

The experimental studies were performed with laser technological systems for marking with fiber laser and CuBr laser. Their main parameters are presented in Table 2.

Table 2 Some basic parameters of a laser technological system for marking with fiber laser Type Styles

Parameter	**Fiber laser**	**CuBr laser**
Wavelength λ, nm	1 064	511 & 578
Power P, W	20.0	10.0
Frequency ν, kHz	80	20
Pulse duration τ, ns	100	30
Pulse energy E_p, mJ	0.25	0.50
Pulse power P_p, kW	2.50	16.7
Quality of beam M2	< 1.1	< 1.7
Positioning accuracy, µm	2.5	2.5
Efficiency, %	40	10

The fiber laser is a modern laser emitting in the near infrared range. It works in pulse mode. It has extremely high beam quality, high efficiency. and cheap maintenance. The laser system has high precision and very good repeatability.

The CuBr laser emits in the visible range. It works in pulse mode. It is characterized by good beam quality and relatively good efficiency. The laser system has high precision and maintains stable parameters during operation.

During the experiments, the scan overlap coefficient k_s remained constant. Squares with a side of 5 mm were marked in a raster method way. The contrast was determined several times for each marked square. The contrast was measured according to the procedure described in [7]. The mean contrast value for each square was then obtained.

The experiments were conducted in two directions:

1. Investigation of the dependence of the contrast of the marking k^* on the overlap coefficient k_{ov} for fiber laser

A series of experiments was carried out in order to study the influence of the overlap coefficient kov on the contrast k^* of the marking. The overlap coefficient changes in the interval $k_{ov} \in [72.5 \div 95]$ % through 2.50 %. Experiments refer for three values of the power density: $q_{s1} = 1.24\times10^{10}$ W/m^2; $q_{s2} = 1.50\times10^{10}$ W/m^2 and $q_{s3} = 1.77\times10^{10}$ W/m^2. The parameters that are kept constant are given in Table 3. During the experiments, the scan overlap coefficient had value $k_s = -25$ %.

Table 3. Parameters that do not change during experiments

Parameter \ **Laser**	**Fiber**	**CuBr**
Pulse duration τ, ns	100	40
Diameter of working spot d, µm	40	30
Raster step Δx, µm	50	50
Number of repetition	1	1
Defocusing Δf, mm	0	0

The obtained experimental dependencies of the contrast k^* of the marking from the overlap coefficient kov are presented in graphical form in Fig. 3.

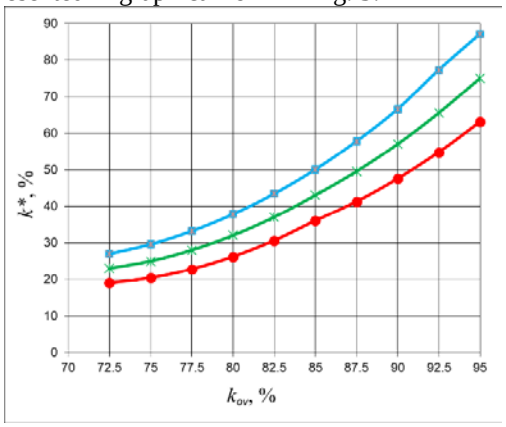

Figure 3. Dependence of the contrast on the overlap coefficient for marking with a fiber laser for power densities: red colour – $q_{s1} = 1.24\times10^{10}$ W/m^2; green colour – $q_{s2} = 1.50\times10^{10}$ W/m^2; blue colour – $q_{s3} = 1.77\times10^{10}$ W/m^2.

From the analysis of experimental results it sees that:

- With increasing the overlap coefficient results in a non-linear increase in contrast for all three power density. In the interval k_{ov} Є [80 ÷ 95] % the contrast k^* increases significantly faster versus the interval k_{ov} Є [72.5 ÷ 80] %;
- The rate of increase of the contrast k^* is given in the table below.

The rate of increase of the contrast k^*					
interval k_{ov} [**72.5 ÷ 80**] %			interval k_{ov} [**80 ÷ 95**] %		
q_{s1}	q_{s2}	q_{s3}	q_{s1}	q_{s2}	q_{s3}
0.96	**1.20**	**1.44**	**2.45**	**2.87**	**3.28**

The faster increase of the contrast in the interval k_{ov} Є [80 ÷ 95] % compared to the interval k_{ov} Є [72.5 ÷ 80] %kov is explained by the fact that with increasing the overlap coefficient the absorbency of the material in the impact zone also increases.

- The following working intervals were determined for the overlap coefficient k_{ov} .

for power density q_s, W/m^2	**the overlap coefficient k_{ov}**
1.24×10^{10}	91 % ÷ 95 %
1.50×10^{10}	87.5 % ÷ 95 %
1.77×10^{10}	85 % ÷ 95 %

These intervals refer to the visual perception of the marking, for which the contrast must be at least 50%.

2. *Investigation of the dependence of the contrast k* of the marking on the overlap coefficient k_{ov} for CuBr laser*

A number of experiments was carried out in order to study the influence of the overlap coefficient k_{ov} on the contrast k^* of the marking. The overlap coefficient changes in the interval k_{ov} Є [63.33 ÷ 93.33] % with step 3.33 %. The experiments were performed at three constant values of power density q_{s1} = 0.99×10^{10} W/m^2; q_{s2} = 1.20×10^{10} W/m^2 and q_{s3} = 1.42×10^{10} W/m^2. The parameters that are kept constant are given in Table 3. During the experiments, the scan overlap coefficient had value k_s = – 66.7 %

The obtained experimental dependencies of the contrast k^* of the marking from the overlap coefficient k_{ov} are presented in graphical form in Fig. 4. From the analysis of experimental results, it sees that:

- With increasing the overlap coefficient results in a non-linear increase in contrast for all three power density. In the interval k_{ov} Є [73.3 ÷ 93.3] % the contrast k^* increases significantly faster versus the interval k_{ov} Є [63.3 ÷ 73.3] %;

- When working with a CuBr laser, the optimal contrast of the marking is achieved with lower values of power density q_s and overlap coefficient than when marking with a fiber laser. It is explained that CuBr laser radiation (λ = 511nm & 578 nm) is better absorbed by the studied material than fiber laser radiation (λ = 1064 nm).

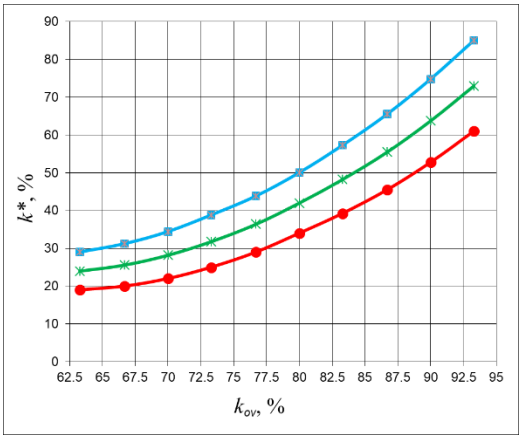

Figure 4. Dependence of the contrast on the overlap coefficient for marking with a CuBr laser for power densities: red colour – q_{s1} = 0.99×10^{10} W/m^2; green colour – q_{s2} = 1.20×10^{10} W/m^2; blue colour – q_{s3} = 1.42×10^{10} W/m^2.

- The rate of increase of the contrast k^* is given in the table below.

The rate of increase of the contrast k^*					
interval k_{ov} [**63.3 ÷ 73.3**] %			interval k_{ov} [**73.3 ÷ 93.3**] %		
q_{s1}	q_{s2}	q_{s3}	q_{s1}	q_{s2}	q_{s3}
0.60	**0.78**	**0.98**	**1.80**	**2.06**	**2.31**

Here again, the different rate of contrast increase is due to the dependence of the absorbency of the material on the overlap coefficient.

- The following working intervals were determined for the overlap coefficient k_{ov} for visual perception of the marking.

for power density q_s, W/m^2	**the overlap coefficient k_{ov}**
0.99×10^{10}	88.5 % ÷ 93.3 %
1.20×10^{10}	84 % ÷ 93.3 %
1.42×10^{10}	80 % ÷ 93.3 %

CONCLUSIONS

This study examines the effect of laser parameters on contrast in the area of marking. The processing field (squares) is marked using the raster method at different values of the overlap coefficient between the individual laser pulses and the overlap coefficient between the scanning lines. The research is related to optimizing the influence of the overlap coefficient on the marking process and more precisely on the contrast. The results and analyses of this study have a direct impact on the optimization and

quality of application of two-dimensional QR codes on C110W carbon tool steel surfaces with two types of lasers - fiber and CuBr.

REFERENCES

[1] Grigoryanc, A., Shiganov, I. & Misyurov, A., Technological processes of laser pro-cessing, Publ. MGTU N. Baumana, Moskow, 2006

[2] Lazov L. K., N. A. Petrov, Investigation of the Impact of the Number of Repetitions and Defocus on the Contrast of Laser Marking for Products Made of Tool Steel, Metalofizika I noveishie Tekhnologii, t.34, № 7, pp. 1003-1011, 2012, ISBN 1024-1809

[3] Sobotova, L., P. Demec, Laser Marking of Metal Materials, Modern Machinery Science Jounal, 808-812, 2015.

[4] E. Nikolidakis, I. Choreftakis, A. Antoniadis, Experimental Investigation of Stainless Steel SAE304 Laser Engraving Cutting Conditions, Machines, 6, 40; 1-8, 2018, DOI:10.3390/machines6030040

[5] Lazov L., N. Angelov, Basic factors determining quality of markings on metals and alloys. International Scientific Conference AMTECH - 2007, Gabrovo, Vol. I, 102-107, 2007

[6] Lazov L., A. Atanasov, N. Angelov, Investigation of the role of certain factors affecting the contrast in laser marking, Contemporary Materials, Vol. II−1, 13-17, 2011.

[7] Angelov, N., Optimization of the process of laser marking of samples of tool steel, dissertation for the degree of DOCTOR, TU - Gabrovo, 2011

[8] L. Chunling, L. Changhou, Laser-Induced Color Marking of Titanium Alloy, TELKOMNIKA, Vol.14, No.4, 1313-1320, 2016, ISSN: 1693-6930, DOI: 10.12928/TELKOMNIKA.v14i4.4177

[9] L. Jianmei, L. Changhou, W. Aiqun, W. Yusong, M. Zhuo, F. Xinxin, T. Liang, Experimental investigation and mathematical modeling of laser marking two-dimensional barcodes on surfaces of aluminum alloy, Journal of Manufacturing Processes 21, 141–152, 2016, DOI: https://doi.org/10.1016/j.jmapro.2015.12.007

[10] G. Schnell, U. Duenow, H. Seitz, Effect of Laser Pulse Overlap and Scanning Line Overlap on Femtosecond Laser-Structured Ti6Al4V Surfaces, Materials 2020, 13, 969; 1-15, DOI:10.3390/ma13040969

[11] Dolchinkov, N., Practical Research of Marking and Cutting of Textiles with Increased Resistance, Using CO2 Laser, Journal of Physics: Conference Series , Volume 1681, 2020 012014 IOP Publishing DOI:10.1088/1742-6596/1681/1/012014

[12] Kolev, I., T. Karadzhov, Classification, parameters, characteristics and application of matrix semiconductor photoconverters, 27th International Spring Seminar on Electronics Technology, vol. 3, 444-447, 2004, DOI: 10.1109/ISSE.2004.1490852

[13] Pencheva T., D. Pulov, B. Gyoch, M. Nenkov, Design of CCD Optical System for Thermal IR Spectral Region. In pr. 29-th International Spring Seminar fn Electronics Technology, St. Marienthal, Germany, Verlag Dr. Markus A. Detert, 413-418, 2006, ISBN 3-934142-23-0, DOI: 10.1109/ISSE.2006.365380

[14] Dolchinkov, N., Investigation of the State of the Radiation Control Systems and the Actions of the Competent Authorities and the Population in the Event of a Change in the Radiation Background in Bulgaria, International Conference KNOWLEDGE-BASED ORGANIZATION, Vol. XXIV No 3, 38-44, 2018, DOI: https://doi.org/10.1515/kbo-2018-0134

[15] Lazov L, N. Angelov, Physical model about laser impact on metals and alloys, Contemporary Materials, Vol. I−2, 124-128, 2010.

[16] Valiulin A., S. Gorniy,Y. Grechko, M. Patrov, K. Yudin, V. Yurevich, Laser marking of metals, Scientific and technical journal "Photonics",, №3, 16-22, 2007.

[17] Cvetanov, G., T. Karadzhov, R. Miteva, Determination of the elastic displacements in plain strained condition of involute cylindrical gears with asymmetric profile. *AIP Conference Proceedings*, Volume 2333, 2021, DOI: 10.1063/5.0042511

Environment. Technology. Resources. Rezekne, Latvia
Proceedings of the 13th International Scientific and Practical Conference. Volume 3, 20-24

Increasing the Effeciency of Laser Marking Ofaluminum Alloys by Double Writing of the Symbols

Atanas Atanasov
TU – Sofia, Plovdiv Branch
Plovdiv, Bulgaria
laser@gbg.bg

Angel Lengerov
TU – Sofia, Plovdiv Branch
Plovdiv, Bulgaria
anlengerov@abv.bg

***Abstract* - A comparison is made between samples marked by writing letters and symbols once, with these marked by twice but writing with two times greater velocity. As a consequence of the sharp decreasing of the main characteristic of the material –its reflective index, in the second case we received an enhancement of the effectiveness of the laser marking, decreasing energy use at the same time. Experimental studies have been carried out with a CuBr (copper bromide vapour) laser for specific mechanical engineering details.**

Keywords - double writing, aluminium, aluminium alloys, effectiveness, laser marking, copper bromide vapour laser.

I. INTRODUCTION

In recent years, the laser marking is widely used for a number of Aluminium devices and products – medical instruments, machine parts in aerospace, electronics and avionics, machine-building details, etc. [2, 4, 5] The requirements for the label regarding its quality, speed and efficiency of production [3] are constantly increasing. In order to meet all these challenges, it is necessary to carry out research, leading to the optimization and increasing the efficiency of the technological process of laser marking. The purpose of this report is to summarize and analyse the methods of laser marking by double or multiple writing and to show their capabilities. Specific examples for optimization of the laser marking process with various methods of industrial products are also shown, using a copper bromide vapor (CuBr) laser included in a MOPA (Master Oscillator Power Amplifier) system and optical galvo scanhead.

II. MATERIALS AND METHODS

In addition to the traditional laser marking, other marking methods have recently been applied, leading to a better design and aesthetics of the product - by double-writing the symbols, by hatching and by wobbling. The aim of the present research is to show the possibilities of these ways of marking and to determine some optimal intervals of the main parameters of the CuBr laser and the technological process for marking of aluminium details.

A. Marking by double-writing the symbols

This method of laser marking was proposed and discussed in [1]. For its realization it is necessary for the laser to have a power density around the threshold of destruction of the material. At the first writing along the contour, the reflection coefficient of the material in the impact zone decreases (due to the occurrence of structural changes or oxidation of the surface). Repeatedly passing the same contour absorbs a significantly larger part of the energy (~ up to 75 - 85%) compared to the first discharge. The energy absorbed by the heat source moving on the surface of the article is sufficient to form a contrast marking on it, and in some cases to form a channel with the required width b and depth h.

This method, compared to the traditional one-time pass, is realized with less energy due to the fact that the process itself is performed at twice the speed with the same quality of the marking. The use of modern scanners allows achieving marking speeds (relative displacement of the beam relative to the work surface) of the order of 3-4 mm/s.

B. Marking by hatching of the symbols

Shading at two different angles is used to increase the contrast and quality of the laser marking. Thus, in reflected light, a greater contrast of the treated surface is obtained as a result of the diffuse scattering of light by multiple reflection centres. Marking with very good

Online ISSN 2256-070X
https://doi.org/10.17770/etr2021vol3.6550

quality is obtained by writing strokes at angles 0º, 75º and 150º relative to a given axis of processing. In Fig. 1 is a photograph of such a CuBr MOPA laser marking on an aluminium plate (Al-1050) and Fig. 2 shows a photograph of the same marking taken under magnification using an "Optica B-150" metallographic microscope.

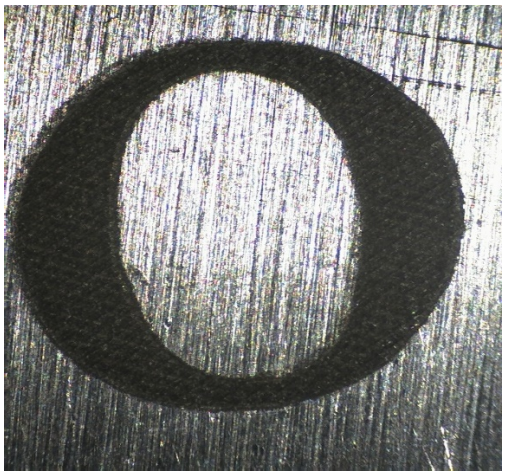

Fig. 1. CuBr MOPA laser marking on an aluminium plate.

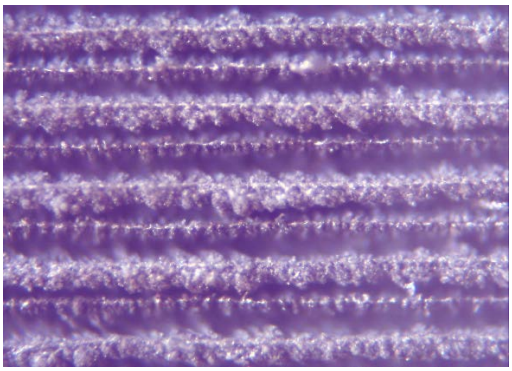

Fig. 2. Thesame marking taken under magnification using an optical microscope.

III. Experimental Set Up and Procedure

A series of experiments will be performed with a change in the marking speed and the number of repetitions on samples of Aluminum 1050. The obtained results will be analyzed, examining the change of the reflection coefficient and the change of the contrast of the processed samples depending on the variation of marking parameters.The experimental methods and testing of engraving of materials were prepared in laboratories of laser centre of Pulslight ltd. and Institute of Electronics, BAS-Sofia.

- Movement of the laser beam was achieved by an ARGES X-Y scanner (see device 2 on Fig.3).

- During the experiment the laser beam was focused perpendicular onto the sample surface with an F-Theta objective (see device 3 on Fig.3) (f=30 cm) because of that only one laser line was applicable. In the experiments we used the green laser line (511nm) because the focusing system was not achromatic. The focal spot after the scanner was 40 µm in diameter.

The control of the laser complex was achieved by a special Master Timing System (MTS). This PC controlled tool was aimed at synchronizing the work of the laser oscillator and the power amplifier. It also played the role of an optical shutter by controlling the delay time. PC also controlled the ARGES scanning system.

The laser engraving machine CBL-MOPA10 and software Arges InScript were used for the experimental testing of three types of materials at various parameters (Fig.3).

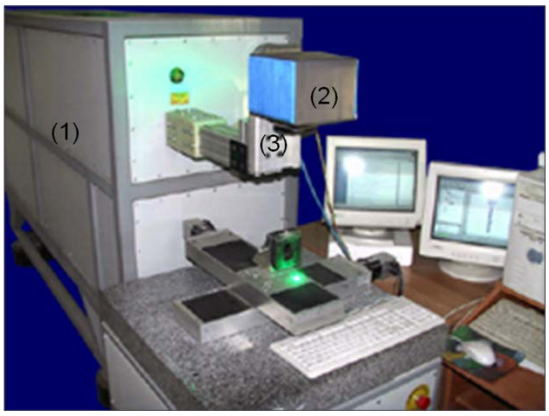

Fig. 3. The laser engraving machine CBL-MOPA10.

TABLE 1.TECHNICAL SPECIFICATION OF MOPA LASER SYSTEM

wavelength	510,6nm and 578,2nm (2:1)
Average power	10W
Pulse repetition rate	20 kHz – fundamental
Pulse energy	0.5 mJ
Beam diameter	20mm
Beam divergence	0.1 mrad
Quality of beam M^2	<1.5
Duration of pulse	30ns

During the proposal of the experiment we used the Arges InScript system to find right laser settings for tested materials. In the proposed experiment were chosen laser parameters and testing materials and suggested also the laser beam ways/run through the testing field and how the laser beam will run through the sample considering to the first setting. During the engraving by laser beam, the pattern of engraving determines:

- the angle of the incident beam at engraving is 90 degrees,

- number of repetitions–determined number of times the laser beam passes over a given quadrant,

- sample lines pitch 0.05 mm,

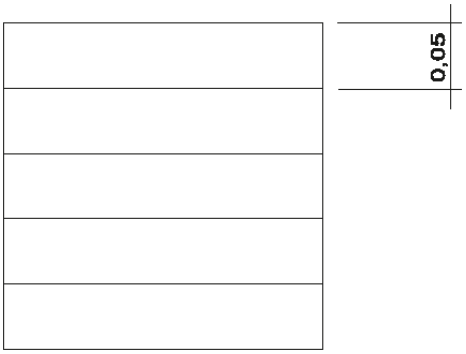

The track of pitch at the engraving Δ x=0.05mm

During the experiment was used material – aluminium 1050A, chemical properties are shown in the Table 2.

TABLE 2. CHEMICAL PROPERTIES OF ALUMINUM 1050A

Cu	max 0.05
Mn	max 0.05
Si	max 0.25
Fe	max 0.40
Mg	max 0.50
Zn	max 0.07
Ti	max 0.03
Al	max 99.5

TABLE 3. MECHANICAL AND PHYSICAL PROPERTIES OF ALUMINUM 1050A

Tensile Strength (MPa)	75
Proof Stress 0.2% (MPa)	35
Fatigue Strength 50 mil. cycles (MPa)	20
Hardness Vickers (HV)	22
Hardness Brinell	20
Elongation % 50mm	32
Density	2.79 Kg/m³
Melting Point	640 °C
Thermal Conductivity	121-193 W/m.K
Modulus of Elasticity	23.1 x10^-6 /K

• Format of Al samples for laser treating: 1x1cm² pieces, 2 mm thick

• We moved the laser beam to draw parallel lines with distances of 50 µm, almost equal to the laser spot size.

The treatment was done with 5 repetitions (A, B, C, D and E) and scanning beam velocities of 2, 5, 10, 20, 50,100, and 200 mm/s.

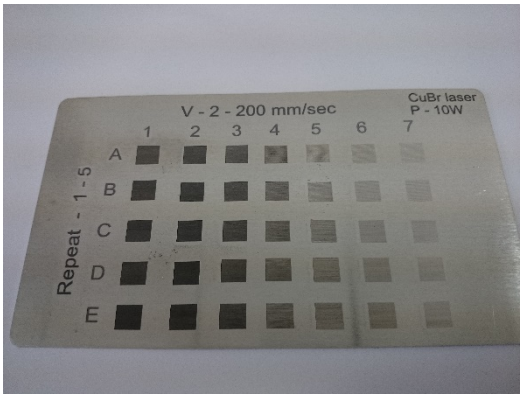

Fig. 4. The sample from Aluminum 1050A material with defined parameters.

A laser marked sample is created with a grid of 10x10 mm squares. Two technical parameters of laser system are varied within this grid, scanning speed (from 2 to 200 mm/s) and number of marking repetitions (from 1 to 5). The surface of Al sample with all squares is shown in figure 4. This figure shows how the surface contrast changes for each square in the matrix. An increase in contrast is observed with a decrease in scanning speed and increase of repetitions of laser marked lines.

IV. OTHER RESULTS AND DISCUSSION

With the help of the Image pro plus program we study the intensity of the reflected light at different parameters of laser processing. The ratio between treated and untreated surface in percent gives us an idea of the result obtained by changing the speed and number of repetitions on the treated aluminium substrate.

Definition of contrast in case of dark markings on a lighter background

$$k = \frac{J_f - J_x}{J_f}.100\% \quad (8),$$

where J_f is the intensity of the reflected light from the untreated surface of the sample (from the background), J_x is the intensity of the reflected light from the zone of influence on the sample.

In Fig.5, 6, 7 and 8 shows the graphical parameter "Ia" in percent's – intensity ratio of reflected light between the treated and untreated surface depending on the number of repetitions and scanning speed for aluminium A105. Intensity ratio is inversely proportional to the contrast of the laser marking. Therefore, a decrease in this indicator indicates the production of more contrast and quality marking. Repeated writing of the symbols results in about 25-30% lower reflected intensity obtained by marking compared to single marking. The result obtained is explained as follows. Because the speed of writing the symbols is twice as fast as writing them once, the falling energy in the impact zone is the same. However, the energy absorbed is different in the two ways of laser marking. In the case of a single mark, the

absorption capacity for the aluminium 1050 sample at this wavelength λ = 511 nm is A = 30%. With double marking at the first writing of the symbols the absorption capacity is the same, but at the second writing of the symbols it becomes A = 65%. The reason for the increase in the absorbency of this aluminium sample is that after the first writing of the symbols on the surface in the impact zone an oxide layer is formed and also increased roughness leading to diffuse reflection of light and more contrast marking.

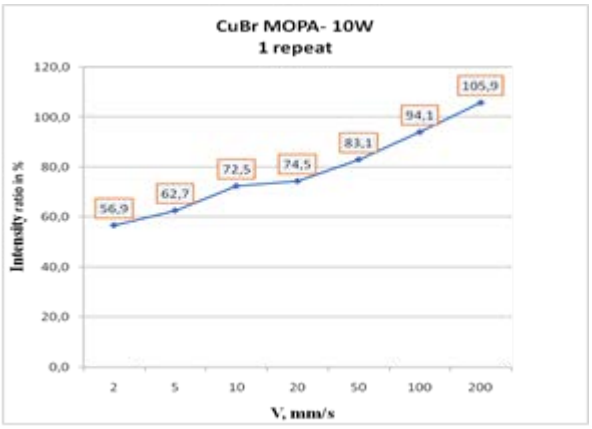

Fig. 5. Dependance of reflection of the light from scanning speed in case of 1 repeatition.

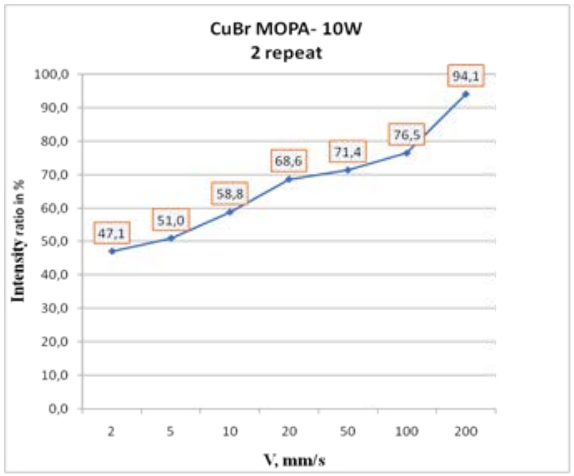

Fig. 6. Dependance of reflection of the light from scanning speed in case of 2 repetitions.

In FIG.7 and 8 shown the change in the intensity of the reflected light when marking an aluminium detail with a CuBr laser, power 10W, scanning speed respectively10 and 2 mm/s, repetitions from 1 to 5. We can see that at lower scanning speed obtain lower parameter of intensity, which means more contrast and quality marking.

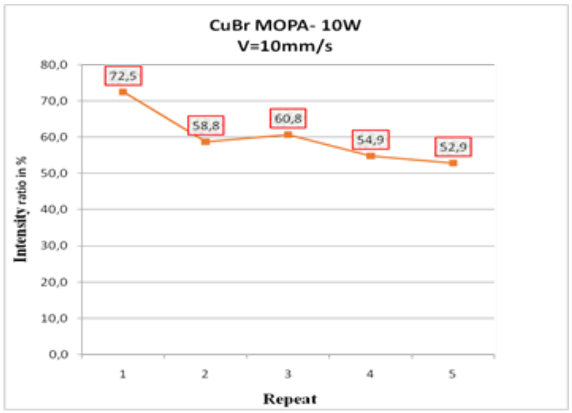

Fig. 7. Dependance of reflection of the light from repetitions in case of scannig speed 10 mm/s .

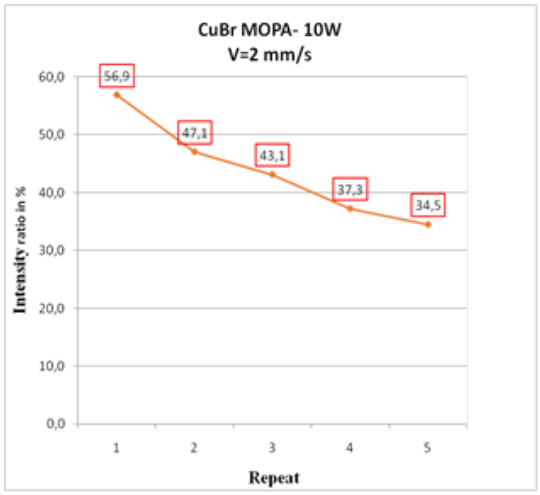

Fig. 8.

V. CONCLUSIONS

The optimization of the laser marking of Aluminum products requires for each specific case to determine the most appropriate way of marking with the optimal parameters of the laser and the technological process. It is of great importance for achieving high productivity with good quality laser marking.

Reducing the energy invested in production per unit of output, is great challenge in the modern industry. When characters are displayed twice (or repeatedly), in addition to improving efficiency marking through economy of energy, the possibilities of technical ecological system in terms of width and the depth of the marked symbols and the growth of marking at a specific denomination of laser power.

Achieving high quality brands is essential, but it must achieve an optimal ratio between durability and quality of markings on the one hand and its cost on the other.

REFERENCES

[1] Angelov N., L. Lazov, A. Atanasov Increasing the efficiency of laser marking of tool steel by double writing the symbols, International Scientific Conference UNITECH'08, Gabrovo, November 21-22, 2008

[2] Lazov L, Angelov N, Teirumnieks E, Teirumnieka E 2019 Proceedings of the 12th International Scientific and Practical Conf. 3 137-142

[3] Lazov L, Teirumnieks E, Angelov N, Teirumnieka E 2019 Proceedings of the 12th International Scientific and Practical Conf. 3 134-136

[4] Balchev I, Lazov L, Teirumnieks E 2019 Proceedings of the 12th International Scientific and Practical Conf. 3 13-17

[5] Lazov L, et al. 2015 Proceedings of the 10th International Scientific and Practical Conf. 1 108-115

[6] N.V. Sabotinov 1996 Pulsed Metal Vapour Lasers NATO ASI Series 1/5, Kluwer Academic Press. 113-124

[7] Sabotinov N, Bergmann H, Salimbeni R, Mizeraczyk J, Wallimann C, Kostadinov I 2002 Development of a System Based on a High Power and High Efficiency Copper Bromide Laser for Precision Materials Processing, Project NATO SfP – 972685 „NATO SfP – Copper Bromide Laser"

[8] Angelov N. Optimizaciya na procesa markirane s lazerno lichenie na obrazci ot instrumentalna stomana. Disertacionen trud za pridobivane na stepen doktor. TU-Gabrovo, 2011 (in Bulgarian)

Environment. Technology. Resources. Rezekne, Latvia
Proceedings of the 13th International Scientific and Practical Conference. Volume 3, 25-29

Comsol Simulation of Laser Welding of Aluminum

Ivaylo Balchev
Rezekne Academy of Technology
Rezekne, Latvia
Ivaylo.Balchev@rta.lv

Lyubomir Lazov
Rezekne Academy of Technology
Rezekne, Latvia
Lyubomir.Lazov@rta.lv

Nikolay Angelov
Technical University of Gabrovo
Gabrovo, Bulgaria
angelov_np@abv.bg

Erika Teirumnieka
Rezekne Academy of Technology,
Rezekne, Latvia
Erika.Teirumnieka@rta.lv

***Abstract* - This research includes a Comsol Mutiphysics model describing the temperature distribution on aluminum during the laser conductivity welding process. The influence of laser power and speed on the welding process is discussed and compared with experiments. Numerical simulations of laser welding process have been performed to determine the temperature fields of laser impact to samples of aluminum. Numerical calculations are made for fiber laser. The plots of the temperature dependence on the surface and in the depth of aluminum samples on the velocity are analyzed for several power densities for this laser.**

Keywords - laser welding, comsol multiphysics, aluminium, automotive industry, fibre laser

I. INTRODUCTION

The investigation of the temperature distribution in a material induced by laser radiation is very important for the optimization of different industrial laser material processing like cutting, drilling, marking, or welding.

Laser welding technology is popular in the automotive industry, where it is used in the production of a large number of parts due to its high welding speed, low energy input and the resulting low part distortion, ease of automation, and other benefits [1]. Meanwhile, aluminium is steadily growing in automotive use to lighten car components. It is considered “material of choice” to meet the challenge of reducing environmental footprints and improving fuel economy while still retaining the security of automobiles. Despite the good prospects, joining aluminium using this technique can be problematic at present in terms of weld quality.

Laser welding of light and high reflective metals such as aluminium is a very difficult technological process in particular, it requires extreme precision and selection of the correct laser source and technological parameters to ensure a quality welding seam. That is why it is necessary to use physical modelling and simulations as a powerful tool for clarifying the fundamental aspects of the laser welding process and for preliminary assessment and engineering forecasts of the emerging effects and for correct choice of the optimal working range of the technological parameters in the process of laser welding [2 - 5], [6 – 10], [14].

There are two types of heating modes, conduction and keyholes mode. They are used to describe the resulting melting of the metal during laser welding process. The power density applied to the welding area is the main difference between these two modes. Conduction welding takes place when the intensity is sufficient to cause meting but not sufficient to cause boiling [11 - 13].

In this article, a theoretical model describing the process of laser conduction welding of aluminum has been developed. The numerical simulation methods used in this research provide a good evaluation of both the optimum technical parameters, such as output laser power and speed of beam, as well as the dynamics of the process and the thermal isotherms in the processing area.

Online ISSN 2256-070X
https://doi.org/10.17770/etr2021vol3.6639

II. RESEARCH METHODOLOGY

In order to approximate the depth and width of a welding zone, a computer simulation of the laser welding process was conducted using the commercial finite element method (FEM) software package COMSOL Mutiphysics. The laser beam was simulated as a moving heat source whose profile was represented by vertical configuration of Hermite-Gaussian mode (TEM01). The simulation was performed for the purpose of moving the laser beam over the surface of the workpiece in a straight line. The heating due to laser is treated as a body heat source on the surface. The body heat load within the workpiece plate is given by the following expression:

$$Q(x,y,z) = Q_0(1-R_c)\frac{A_c}{\pi\sigma_x\sigma_y} e^{-\left[\frac{(x-x_0)^2}{2\sigma_x^2}+\frac{(y-y_0)^2}{2\sigma_y^2}\right]} . e^{-A_c z} \quad (1)$$

Q_0 is total input power, R_c – reflection coefficient, σ_x and σ_y are the standard deviation parameters which determine the beam width and astigmatism.

A. *Welding process thermal model*

The amount of energy that is absorbed from the target material is much lower than the amount of energy that transfers the laser beam as it is generated from the laser beam machine, due to reflection coefficient and energy losses that take place during the process. In order to examine welding process the schema of the heating process shown in Fig. 1. The target material is in liquid phase which means that the temperature is above the melting temperature but has not reached the evaporating temperature. The amount of the total power that is absorbed is calculated the same way as before using the reflectivity coefficient of the material at melting phase:

$$Q = Q_0(1-R_{melt}), \quad T_{melt} \le T < T_{evap} \quad (2)$$

where Q is the absorbed energy flux, Q_0 is the incidence laser beam heat flux, R_{melt} is the reflectivity of the target material at liquid phase, T_{melt} is the material melting temperature, and T_{evap} is the material evaporating temperature.

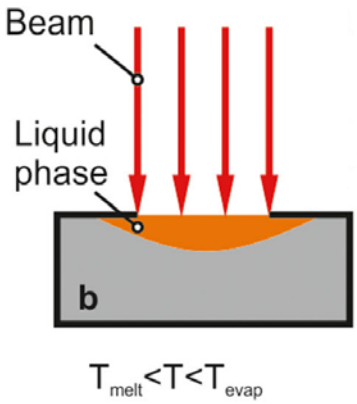

Fig. 1. Welding process thermal modelling

B. *Initial-boundary conditions and heat transfer model*

The top face of the 3D solid body used in the simulation was set to be the target face for the incidence laser beam pulses, and the geometry was set to be a rectangular block with dimensions WxDxH. The initial temperature of the solid body T_0 was set to be equal to the ambient temperature (T_0 = Tamb=20 ^{0}C) in terms of the initial and boundary conditions. The following version of the heat equation is used to model heat transfer in a solid body:

$$\rho C_p \frac{\partial T}{dt} + \nabla\vec{q} = Q, \quad \vec{q} = -k\nabla T \quad (2)$$

where ρ is the density of the material, C_p - heat capacity, k – thermal conductivity, Q is the heat source.

The focal spot of the laser radiation focuses on the surface of the body, so it is assumed that the heat source is on the surface.

A moving heat flux with a 2D Gaussian (4) density distribution is used as the laser beam. The expression for 2D Gaussian can easily be obtained as the product of 1D Gaussian (3) on the x and y axes

$$g_\sigma(x) = \frac{1}{\sqrt{2\pi}\sigma}\exp(-\frac{x^2}{2\sigma^2}) \quad (3)$$

$$G_\sigma(x,y) = g_\sigma(x).g_\sigma(y) = \frac{1}{\sqrt{2\pi\sigma^2}}\exp(-\frac{x^2+y^2}{2\sigma^2}) \quad (4)$$

TABLE 1. CHEMICAL COMPOSITIONS OF ALUMINUM ALLOYS

Element	Percent
Si	0.06
Fe	0.16
Cu	1.25
Mn	0.08
Mg	2.32
Zn	5.47
Cr	0.20
Ti	0.01
Ga	0.01
V	0.01
Al	90.41

The discretization of the sample was performed by triangular finite elements with maximum element size 0.6, minimum element size 0.1, maximum element growth rate 1.9 (Fig. 2).

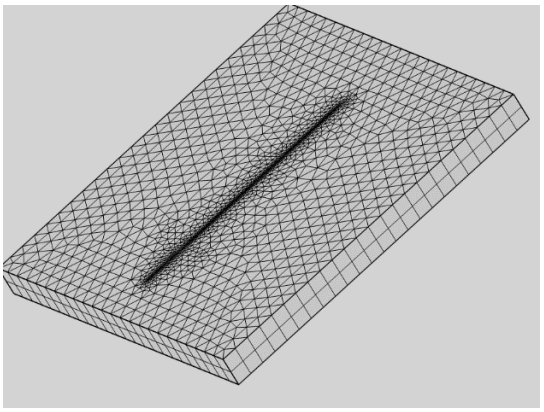

Fig. 2. Discretization of welded samples

The input data for numerical experiments is mentioned in Table 2.

TABLE 2. THERMAL AND PHYSICAL PROPERTIES OF THE ALUMIMUM 7075 –T6.

Properties	Value
Melting point T_m, ^{0}C	600
Boiling point T_v, ^{0}C	2450
Thermal conductivity coefficient k, W/(m.K)	150
Density ρ, kg/m^3	2800
Specific heat capacity c, J/(kg.K)	826
Thermal diffusivity coefficient a, m^2/s	23.4×10^{-6}

The numerical simulations of our study were divided into two main series:
The power is maintained at a constant value of 1500 watts, and the diameter of the focal spot on the surface is changed in the range from 0.75 to 1 mm and the welding speed in the range from 25 to 125 mm / s. In the second series of computer simulations, the power is fixed at 2500 watts, and the upper parameters of the laser radiation are changed at the same operating intervals.

III. RESULTS AND DISCUSSIUON

The Comsol Multiphysics software was used to conduct a number of numerical experiments. The speed of welding and the power of the laser were changed.

The Fig. 3 shows specific temperature distribution in the plane x and y, obtained from numerical calculations for the welding speed v = 25 mm/s and laser power 1500 W.

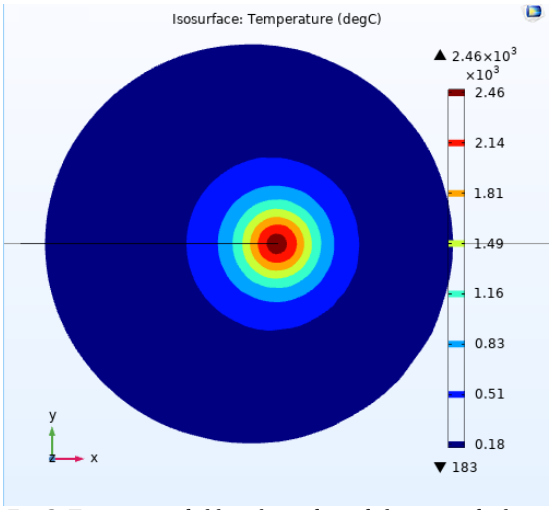

Fig. 3. Temperature field on the surface of aluminium for laser power P = 1.5 kW and speed v = 25 mm/s.

Fig. 4 and Fig. 5 shows graphs of the dependence of the depth of the welding pool on the speed for two diameters of the working spot d_1 = 0.75 mm and d_2 = 1.00 mm, respectively. The analysis of the results allows to draw the following conclusions:

- As the welding speed increases, the depth of the pool decreases non linearly for the four obtained graphic dependencies;
- The average rate of depth reduction
  for diameter d_1 = 0.75 mm is
  9.3 μm/(mm/s) for power P_1 = 1.5 kW;
  15.5 μm/(mm/s) for power P_2 = 2.5 kW;
  for diameter d_2 = 1.00 mm is
  8.0 μm/(mm/s) for power P_1 = 1.5 kW;
  11.1 μm/(mm/s) for power P_2 = 2.5 kW;
- The depth of the pool for diameter d_1 = 0.75 mm is about 40% greater than the depth of the pool for diameter d_2 = 1.00 mm.

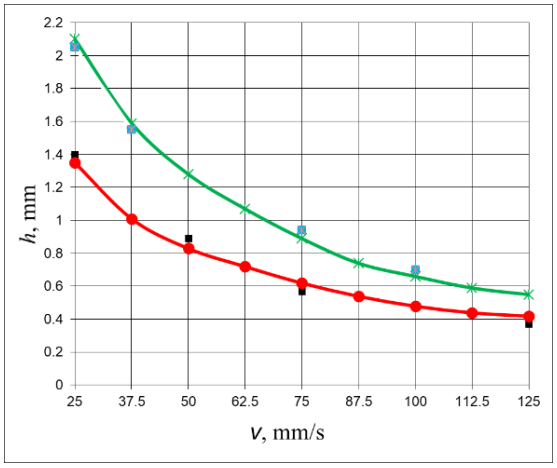

Fig. 4. Dependence of the depth h on the welding speed v for a diameter of the working spot d_1 = 0.75 mm and powers: P_1 = 1.5 kW (red colour), P_2 = 2.5 kW (green colour).

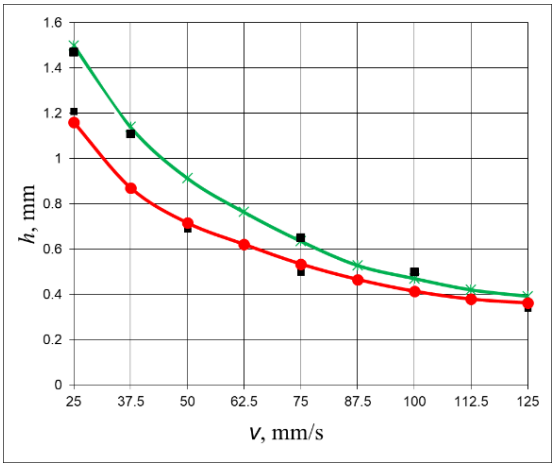

Fig. 5. Dependence of the depth h on the welding speed v for a diameter of the working spot d_2 = 1.00 mm and powers: P_1 = 1.5 kW (red colour), P_2 = 2.5 kW (green colour).

Fig. 6 presents graphs of the dependence of the depth h on the speed v for a power P_2 = 2.5 kW and diameters of the working spot d_1 = 0.75 mm and d_2 = 1.00 mm. The following conclusions can be drawn from them:

- As the welding speed increases, the depth of the bath decreases non linearly for both diameters. The curves for speed interval $v \in [25; 62.5]$ mm/s are steeper than the curves for speed interval $v \in [62.5; 125]$ mm/s;

- The depth of the pool varies from 0.67 mm to 2.10 mm for diameter d_1 = 0.75 mm and from 0.39 mm to 1.50 mm for diameter d_2 = 1.00 mm.

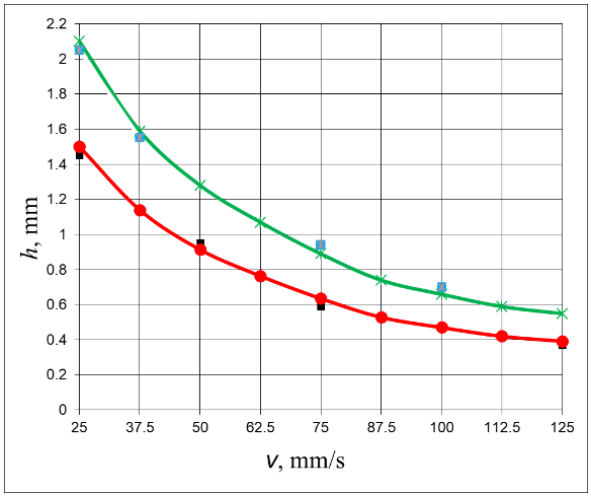

Fig. 6. Dependence of the depth h on the welding speed v for a power P_2 = 2.5 kW and diameters of the working spot: d_1 = 0.75mm (green colour); d_2 = 1.00 mm (red colour)

Fig. 7 and Fig. 8 shows graphs of the dependence of the width of the welding pool on the speed for two diameters of the working spot d_1 = 0.75 mm and d_2 = 1.00 mm, respectively. It follows from these graphs:

- As the welding speed increases, the depth of the pool decreases non linearly for all obtained graphic dependencies;
- The curves for speed interval $v \in [25; 62.5]$ mm/s are again steeper than the curves for speed interval $v \in [62.5; 125]$ mm/s;
- The average rate of width reduction
  for diameter d_1 = 0.75 mm is
  17.6 μm/(mm/s) for power P_1 = 1.5 kW;
  24.0 μm/(mm/s) for power P_2 = 2.5 kW;
  for diameter d_2 = 1.00 mm is
  20.5 μm/(mm/s) for power P_1 = 1.5 kW;
  29.5 μm/(mm/s) for power P_2 = 2.5 kW;
- The width of the pool for diameter d_2 = 1.00 mm is about 25-30% greater than the depth of the pool for diameter d_1 = 0.75 mm;
- The width of the pool for power P_2 = 2.5 kW is about 40% greater than the depth of the pool for P_1 = 1.5 kW for speed v = 25 mm/s and about 25% greater than the depth of the pool for P_1 = 1.5 kW for speed v = 125 mm/s.

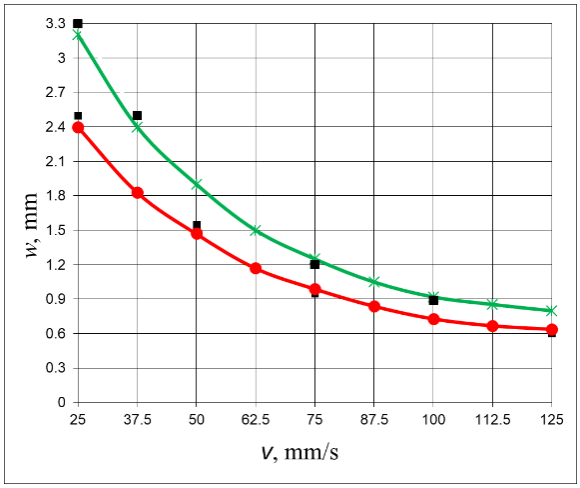

Fig. 7. Dependence of the width w on the welding speed v for a diameter of the working spot d_1 = 0.75 mm and laser power: P_1 = 1.5 kW (red colour) and P_2 = 2.5 kW (green colour).

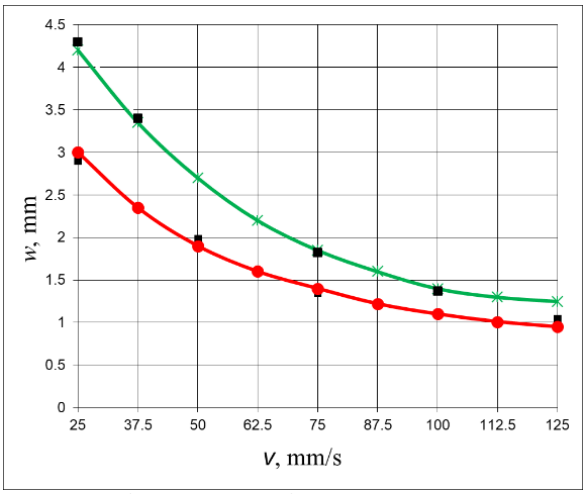

Fig. 8. Graphs of the dependence of the width w on the welding speed v for a diameter of the working spot d_2 = 1.00 mm and laser power: P_1 = 1.5 kW (red colour) and P_2 = 2.5 kW (green colour).

A good coherence of all experimental results with the results of numerical experiments is obtained.

IV. CONCLUSION

Our current study is an attempt to make little progress in the direction of optimization and implementation of model and simulation approaches in solving a specific technological process for laser welding of aluminium sheets. The study will help speed up the entry of laser technology and more accurate than that for welding in such industries as mechanical engineering, aerospace, automotive medicine, and others.

Due to their unique characteristics, laser welding is increasingly being used in industry today, especially for the production of value-added components that are difficult to produce using traditional welding methods.

Several synergistic factors will contribute to improving the quality and reliability of welds while reducing productivity and production costs.

These include continuous improvements in the use of appropriate software for modelling, simulations, and process optimization. The growing volume of research in this direction will ultimately contribute to the deeper penetration of laser technologies in the market of new innovative, highly productive, and energy-efficient technologies. Our model and numerical experiments with Comsol Multiphysics tools are a small step in the right direction.

ACKNOWLEDGEMENTS:

The authors gratefully acknowledge financial support by the European Regional Development Fund, Postdoctoral research aid Nr. 1.1.1.2/16/I/001 research application "Analysis of the parameters of the process of laser marking of new industrial materials for high-tech applications, Nr. 1.1.1.2/VIAA/3/19/474".

REFERENCES

[1] H. Zhao, D. R. White, and T. DebRoy, Current issues and problems in laser welding of automotive aluminium alloys. International Materials Reviews, 2013. 44(6): pp. 238-266.

[2] A. Haboudou, P. Peyre, A. Vannes and G. Peix, Reduction of porosity content generated during Nd:YAG laser welding of A356 and AA5083 aluminum alloys, Materials Science and Engineering: A, 363, 2003, pp. 40–52.

[3] J. Sánchez-Amaya, T. Delgado, L. González-Rovira and F. Botana, Laser welding of aluminum alloys 5083 and 6082 under conduction regime, Applied Surface Science, 255 (23), 2009, pp. 9512–9521.

[4] R. Ding, O. Ojo and M. Chaturvedi, Laser beam weld-metal microstructure in a yttrium modified directionally solidified Ni3Al-base alloy, Intermetallics, 15, 2007, pp. 1504–1510.

[5] N. Dolchinkov, Investigation of the State of the Radiation Control Systems and the Actions of the Competent Authorities and the Population in the Event of a Change in the Radiation Background in Bulgaria, International Conference KNOWLEDGE-BASED ORGANIZATION, Vol. XXIV No 3, 2018, pp. 38-44.

[6] J. Yan, X. Zeng, M. Gao, J. Lai and T. Lin, Effect of welding wires on microstructure and mechanical properties of 2A12 aluminum alloy in CO2 laser-MIG hybrid welding, Applied Surface Science, 255 (16), 2009, pp. 7307–7313.

[7] Y. Shi, F. Zhonga, X. Li, S. Gong, and L. Chen, Effect of laser beam welding on tear toughness of a 1420 aluminum alloy thin sheet, Materials Science and Engineering: A, 465, 2007, pp. 153–159.

[8] N. Abe, M. Tsukamoto, K. Maeda, K. Namba and J. Morimoto, Aluminum alloy welding by using a high power direct diode laser, Journal of Laser Applications, 18 (4), 2006, pp. 289–293.

[9] N. Dolchinkov, Practical Research of Marking and Cutting of Textiles with Increased Resistance, Using CO2 Laser, Journal of Physics: Conference Series , Volume 1681, 2020, 012014

[10] K. Howard, S. Lawson and Y. Zhou, Welding aluminum sheet using a highpower diode laser, Welding Journal 85 (5), 2006, pp. 101–110.

[11] L. Quintino, E. Assunção, 6 - Conduction laser welding, Editor(s): Seiji Katayama, In Woodhead Publishing Series in Electronic and Optical Materials, Handbook of Laser Welding Technologies, Woodhead Publishing, 2013, pp. 139-162.

[12] P. Narica, L. Lazov, A. Teilans, P.Grabusts, E. Teirumnieks and P. Cacivkins, Method for Color Laser Marking Process Optimization with the use of Genetic Algorithms. Environment. Technology. Resources. Proceedings of the 11th International Scientific and Practical Conference. Volume II. – Rezekne, 2017. – pp. 101. – 106. http://dx.doi.org/10.17770/etr2017vol2.2607

[13] L. Lazov, N. Angelov, E. Teirumnieks and E. Teirumnieka, Preliminary numerical analysis for the role of speed onto laser technological processes. Environment. Technology. Resources. Proceedings of the 12th International Scientific and Practical Conference. Volume III. – Rezekne, 2019. – pp. 137. – 142. http://dx.doi.org/10.17770/etr2019vol3.4154

[14] L. Lazov, E. Teirumnieks, I. Draganov and N. Angelov, Numerical modeling and simulation for laser beam welding of ultrafine-grained aluminium. Laser Physics 31 (6), 066001. https://doi.org/10.1088/1555-6611/abf5d3

Environment. Technology. Resources. Rezekne, Latvia
Proceedings of the 13th International Scientific and Practical Conference. Volume 3, 30-35

Experimental Study and Numerical Modelling for Flexural Capacity of FRC Structural Elements

1st Liva Luize Bleive
Ecological Construction Engineering Centre,
Institute of Building production,
Faculty of Civil Engineering
Riga Technical University
Riga, Latvia
liva.bleive@gmail.com

2nd Vitalijs Lusis
Institute of Mechanics and Mechanical Engineering,
Department of Theoretical Mechanics and
Strength of Material
Riga Technical University
Riga, Latvia
vitalijs.lusis@rtu.lv

***Abstract* - Concrete reinforced by short steel fibres is typical brittle matrix composite, in which fibres are impeding cracks growth, such way increasing material's tensile strength. The use of steel fibre reinforced concrete (SFRC) in structures with high physical and mechanical characteristics makes possible to reduce their weight and cost, to simplify their production technology, to reduce or eliminate reinforcement labour, at the same time increasing reliability and durability. Randomly distributed discontinuous fibres are bridging the crack's flanks providing material's "ductility"- like non-linear behaviour at cracking stage. The current study is focused on one formulation of a specific type of concrete matrix with added fibres and without fibres. Concrete cubes and prisms without fibres and having in every situation the same content of 60 mm long fibres were fabricated. Cubes (100×100×100 mm) were tested in compression and beams (100×100×400 mm prisms) were tested under four-point bending (4PBT). Fracture process (crack growth) in the material was modelled, based on experimental results (part of experimental data was used). Finite element method (FEM) using the *ANSYS* program analysis were realized modelling stress distributions in the broken beams with the goal to predict fracture process. Model's prediction was validated.**

Keywords - short steel fibre, concrete, bending, numerical modelling.

I. INTRODUCTION

Main used material in the construction sector is a reinforced concrete. It is used twice as much as all other building materials altogether [1]. At the same time reinforced concrete is changing [2], [3], steel in the reinforcing rebars is replacing by various materials as well as, in many situations, rebars are replaced by short fibers added to the concrete mix [4]–[7].

Nowadays, one of the main engineering challenges is to develop and introduce in the mass production efficient reinforcement material. An example is: innovative reinforcing composite fibre metal-crystal-polymer with protective properties from the electromagnetic field [8], [9]. Short fibres may be the main or the secondary reinforcement (in combination with rebars) bearing the bending moments and the shear stresses. We can mention investigations were a concrete matrix is successfully reinforced with various fibres, made out of various materials [10]–[13] and by different methods [13]–[19]. Homogenously mixed concrete with added short fibres is used widely for shrinkage crack arrest in combination with additional reinforcement [20]. A the same time fibers are improving resistance to cracking of the concrete structures [21]. One of the more important property of the Steel Fibre Reinforced Concrete (SFRC), with homogeneously distributed in the volume fibers, is its superior resistance to cracking and crack propagation [22]–[25].

The current study focused on mechanical properties investigation of a specific type of concrete matrix with added short steel fibres (60 mm), comparing results with the concrete without fibres. Cubes and beams were fabricated and tested, material fracture process was observed and then modelled, based on experimental results obtained in cubes compression tests and beams 4PBT. Model's predictions were validated by experimental data. Finite element method (FEM) using the *ANSYS* program analysis were realized modelling stress distributions in the broken beams with the goal to predict fracture process.

Online ISSN 2256-070X
https://doi.org/10.17770/etr2021vol3.6661

II. MATERIALS AND METHODS

A. Materials

Generally, concrete containing a hydraulic cement, water, fine and coarse aggregates and admixtures, such as fly ash, silica fume and nano-silica. When selecting raw materials to produce a concrete matrix, preference was given to locally available mineral materials and cement according to EN-206. The water to cement ratio was *W/C* = 0.3 and the amounts of ingredients were fixed and is tabulated in the table 1.

TABLE 1 DESIGNED CONCRETE MIX COMPOSITION AND USED COMPONENTS

Composition	**Weight, kg/m^3**
Portland cement CEM I 42.5N (*SCHWENK Latvia Ltd.*, Latvia)	490
Rubble 2/6 mm	650
Quartz Sand 0.4-1.2 mm (*Saulkalne*, Latvia)	417
Quartz Sand 0-1 mm (*Saulkalne*, Latvia)	277
Quartz Sand 0-0.4 mm (*Saulkalne*, Latvia)	92
Silica Fume, grade 920D (*Elkem*, Norway)	51
Fly Ash (*SCHWENK Ltd.*, Kozienice, Poland)	110
Tap water	202
Superplasticizer *"Sikament® 56"* (*Sika Baltic SIA*, Latvia)	10
Total	2300

Crimped steel fibres with shaped cross-section were used in this research. The figure 1. shows the geometry of steel fibre *Tabix+ 1/60*. Concentration of fibres in the concrete mix was 78 kg/m^3. The properties of the fibre were tabulated in the table below.

TABLE 2 SPECIFICATION OF THE STEEL FIBRES BY SUPPLIER'S DATA

Fibre Type	Length L_f, mm	Diameter d_f, mm	Density, kg/m^3	Tensile strength, N/mm^2	Modulus of elasticity, N/mm^2
Tabix+ 1/60 (*ArcelorMittal*, Luxembourg)	60	1	7900	1500	210000

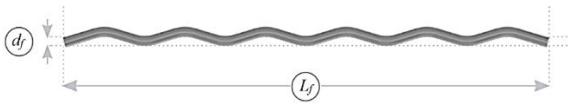

Fig. 1. Geometry of steel fibre Tabix+ 1/60, by supplier's data sheet.

B. Samples prepartion

Concrete mixing and casting details

The concrete mix with and without fibres was prepared for the study. The coarse aggregates, fine aggregates, cement, and silica fume were mixed first dry in a pan mixer. The superplasticizer was then mixed thoroughly with the water and added to the mixer. To obtain a fibre-reinforced concrete matrix, the fibres were dispersed by hand in the mixture to achieve a uniform distribution throughout the concrete. Fresh concrete mix was casted in steel moulds and compacted on a vibrating table.

Sample sizes

The samples were divided into Group A (5 beams without fibres) and Group B (5 beams with fibres). First, the concrete mix was casted into the prism's moulds of size 100×100×400 mm. The specimens were demoulded after 24 h and for maturing, were placed into a water tank until the time of testing. In the case of flexural tests, were used beam specimens (group A and B). Prisms were tested under bending till rupture and the averaged curves of these tests are reported in the load–deflection pictures (Fig. 7 and Fig. 8) and used for calculating the various parameters. After flexural strength tests were done, the non-cracked beam ends were cut into cubes of sizes 100×100×100 mm and then compressive strength tests were performed at 28 days from casting.

C. Expermental tests and results

Compressive testing procedure of concrete cubes

In the concrete design and quality control, concrete is classified by compressive strength. Many properties of a concrete, such as modulus of elasticity, tensile strength, permeability, etc., are believed to be dependent on the compressive strength and may therefore be deduced from the strength data. Though, the compressive strength cannot be utilised as a replacement for all properties, especially not for the increase of toughness observed in fibre-reinforced concrete. This means that for fibre-reinforced concrete some sort of toughness property is required, and that other test methods have to be utilized to characterise it [26]. Compressive Testing Procedure and strength of concrete cube the defining strength properties of these materials, be detected both by non-destructive methods [27]–[29] and by the classical destructive method in accordance with EN 12390-3. Standard compressive cube tests using 100×100×100 mm specimens were conducted to determine of the concrete compression strength including 14 specimen's data after 28 days.

A universal testing machine *Controls Automax 5* was used for testing the compressive strengths of cube specimens at 28th day from the casting moment. Load was applied in 0.25 kN steps for the period of 60s. The deflections were recorded with two *HBM WA20 LVDTs* sensors (*Spider8_1 CH 1* and *CH 2*) on to a computer connected through an electronic digital controller system.

Compressive strength of concrete cubes

Cubes in one formulation of a specific type of concrete matrix were tested. It was obtained that the compressive strength of the concrete cubes without fibres is 69.53 N/mm2 (concrete strength class C50/60 using correction factor 0.95 according to standard LVS 156-1 table 4). Compressive strength of the concrete cubes with steel fibres is 93.74 N/mm2 (concrete strength class C70/85 using correction factor 0.95 according to standard LVS 156-1 table 4). Using the test results stress (σ) and

strain (ε) values were calculated and stress-strain curves were generated.

Four-point bending test (4PBT) procedure

4PBT were performed after 28 days from the casting moment. Used *Controls Automax 5* 4PBT testing machines a test with constant bending moment by the application of load through upper and lower rollers as shown figure 4 according to standard EN 12390-5. Load was applied until the specimens breaks completely. To obtain the deflection of the beam, the frame with two *HBM WA10 LVDTs* sensors on its sides used for recording deformations in prisms during the tests were placed at centre of the span. The maximum load was sustained, the deflections were recorded and the flexural strength was calculated.

Four-point bending test results

Group A and Group B were experimentally tested in flexure under four-point bending conditions observing their load carrying capacity in the macro cracking stage. The maximum force in SFRC strength analysis is the post-cracking behaviour up on high strain levels. According to the testing results, specimens of Group B reached the highest load carrying capacity as they had the concentration of fibres in the prisms. Specimens of Group A showed lower load carrying capacity comparing to the specimens with fibres. Experimental average curves are given in Fig. 7 and Fig. 8. Using the test results stress (σ) and strain (ε) values were calculated and stress-strain curves were generated (Fig. 2 and Fig. 3).

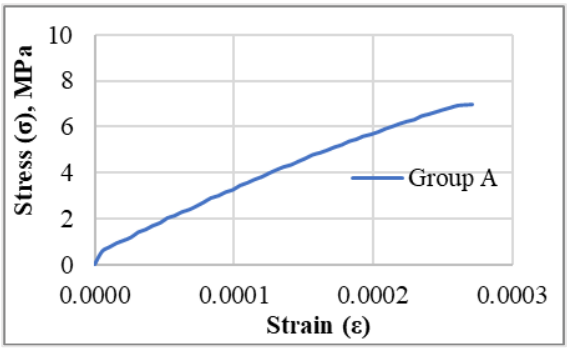

Fig. 2. 4PBT averaged experimental stress-strain curves of concrete for 28 days for Group A.

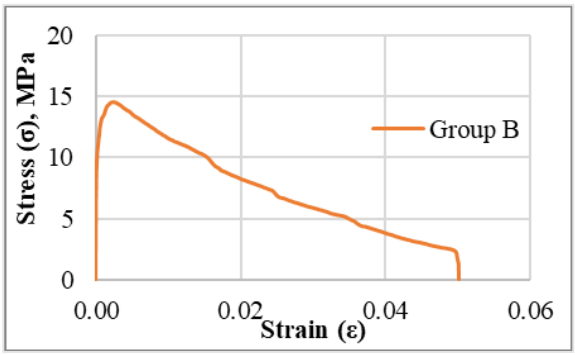

Fig. 3. 4PBT averaged experimental stress-strain curves of concrete for 28 days for Group B.

The presented results indicate that main contribution of steel fibres to a concrete. Fibers are working before and after matrix cracking. If a proper design is made, after the matrix cracking, randomly distributed, short fibres in the matrix arrests micro-cracks, bridge these cracks, undergo a pull-out process and are limiting cracks propagation [30], [31]. Steel fibres can increase significantly the bending and the shear resistance of concrete structural element. Specimens showed typical tri-linear variation in their load-deflection and load-crack mouth opening displacement curves under flexure.

D. Numerical modelling

Finite element (FE) analysis, allows to simulate the behaviour of reinforced concrete members with sufficient accuracy. A non-linear FE method is a numerical technique for obtaining approximate solutions to a wide variety of engineering problems. However, modelling of fibre-reinforced concrete is challenging as many parameters have to be taken into consideration to simulate the quasi brittle material behaviour of concrete accurately. [32]

In this study, FE modelling of beams with and without fibres is carried out using *ANSYS*, to simulate the behaviour of the control from linear through non-linear response and up to failure. One model of each group of samples were modelled in FEM software using *ANSYS*. A quarter of the full cube and beam was used for modelling by taking advantage of the symmetry of the sample, loading and boundary conditions (Fig. 5).

From the analyses the load deflection at mid span relationships until failure, and crack patterns that are obtained from numerical simulations were obtained and compared with the experimental results (Fig. 7 and Fig. 8). The load deflection plots obtained from numerical studies show good agreement with the experimental. The use of computer software to model these elements is much faster, and extremely cost-effective than make the real experiments.

SOLID65 element was used for modelling concrete material. The *SOLID65* element type available in *ANSYS* element library is a solid element with 8 nodes and has three translation degrees of freedom at each node. It can be used to model concrete with or without rebars and is capable of modelling cracking in tension, crushing in compression, plastic deformation and creep behaviour. *SOLID65* element requires linear isotropic and multilinear isotropic material properties to properly model concrete. [33]

Concrete material Elastic and Concrete material definitions were identified. In Elastic definition, the modulus of elasticity and *Poisson's* ratio were necessary. *Poisson's* ratio for concrete is assumed to be 0.2. The modulus of elasticity of concrete was determined by experiments. For Concrete definition, axial tension strength of concrete and shear transfer coefficients between crack surfaces for open and closed cracks were required. [33]

To facilitate the modelling process, it was assumed that the fibres in the element are divided into 3 equal parts in each of the 3 planes in the coordinate system. The volume ratio (0.01/3 = 0.00333) in each direction of the coordinate system was defined as the rebar volume divided by the total element volume. The orientation was defined by two angles (in degrees) from the element coordinate system. Material properties for the steel reinforcement for finite element modelling were taken as follows: E_s = 210 GPa and *Poisson's* ratio, ν = 0.3. [34].

Fibres in the specimens are random distributed across the volume. Fibre-reinforced concrete is considered as a "quasy" homogeneous material. Called "homogeneous" doesn't mean homogeneous in reality, because during filling the construction formwork (mix flowing process) fibres added to concrete mix blend are obtaining non-homogeneous distribution and orientations in to fresh mix concrete volume which inevitably affects the mechanical properties of FRC [35]–[39]. Despite the fact that the fibres are mixed randomly, to facilitate modelling, it was assumed that the fibres were mixed homogeneously.

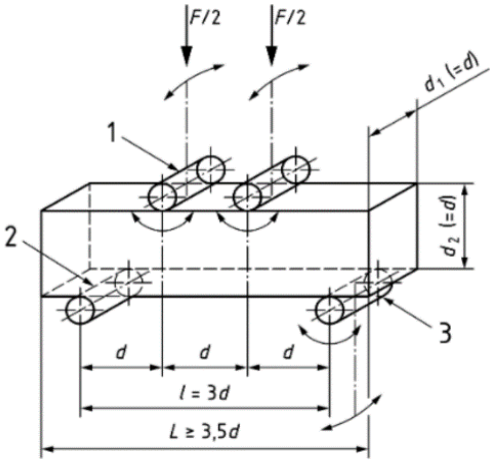

Fig. 4. Four-point bending test scheme (EN 12390-5) 1 – loading roller (capable of rotation and of being inclined); 2 – supporting roller; 3 – supporting roller (capable of rotation and of being inclined).

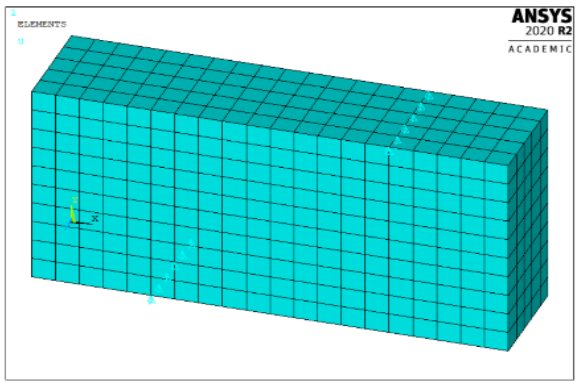

Fig. 5. Model of a quarter of the full beam in *ANSYS*.

Displacement in Y direction of the beam in *ANSYS* is shown in figure 6.

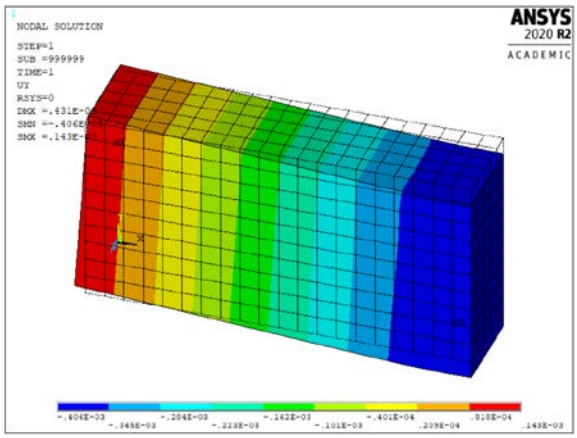

Fig. 6. Displacement in Y direction of the beam in ANSYS.

III. Results and Discussion

Averaged experimental load bearing curve comparison with numerical simulation results for prisms without fibres (Fig. 7) and with fibres (Fig. 8) were generated. The modelling results for Group A quit well approximate the data obtained experimentally, but to facilitate modelling the elastic properties of the concrete were not included, thereby a linear curve was obtained.

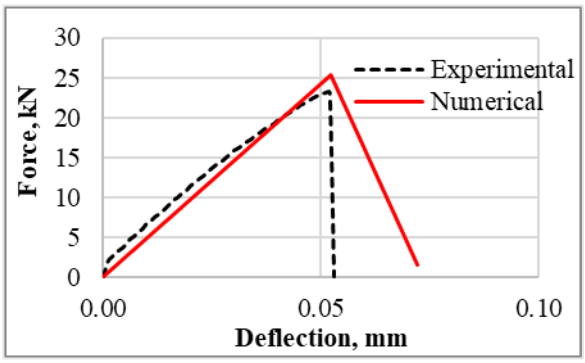

Fig. 7. Averaged experimental load bearing curve comparison with numerical simulation results for prisms without fibres (Group A).

Figure 8 shows that good agreement between experimental and modelling data is obtained: non-linear behaviour appears approximately at the load of 35 – 40 kN, and the load – bearing capacity of the prism is 49 kN. With the further loading, a drop of the force is observed in the experiments, since concrete due to cracking gradually goes out of loadbearing action, and the fibers take the load. Due to limitation of the applied FE model (the fibres in FE work only until the collapse of it), this phenomenon is not obtained numerically. By the same feature of the numerical model the drop of the force from 42 to 18 kN in the beginning of non-linear work of the prism could be explained.

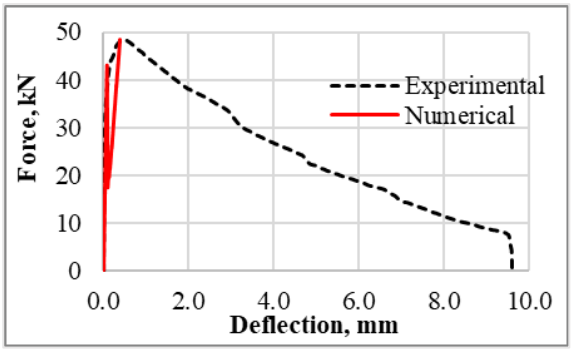

Fig. 8. Averaged experimental load bearing curve comparison with numerical simulation results for prisms with fibres (Group B).

IV. Conclusions

Modelling results agreement with experimental data is good in "general". The moderate disagreement in numerical values can have various reasons. Looking on data presented in Fig. 7 and Fig. 8 the possible reason for deviation from experimental data could also be because fibre orientation in the specimen contrary to modelling assumptions about random distribution across the volume and random distribution of orientation angles and the elastic properties of the concrete were not included in the model.

V. Acknowledgments

This work has been supported by the European Regional Development Fund within the Activity 1.1.1.2 "Post-doctoral Research Aid" of the Specific Aid Objective 1.1.1 "To increase the research and innovative capacity of scientific institutions of Latvia and the ability to attract external financing, investing in human resources and infrastructure" of the Operational Programme "Growth and Employment" (No.1.1.1.2/VIAA/2/18/324).

References

[1] C. R. Gagg, "Cement and concrete as an engineering material: An historic appraisal and case study analysis," *Eng. Fail. Anal.*, 2014, doi: 10.1016/j.engfailanal.2014.02.004.

[2] M. Corradi, "Concrete for the construction industry of tomorrow," in Measuring, Monitoring and Modeling Concrete Properties, 2007.

[3] G. Sahmenko et al., "The study of the combined effect of fly ash, silica fume, colloidal silica and superplasticizer on high performance cement composite applying mix optimization method," Mech. Compos. Mater., 2021. Submitted for publication.

[4] V. L. Kulakov, G. P. Terrasi, A. K. Arnautov, G. G. Portnov, and A. O. Kovalov, "Fastening of a High-Strength Composite Rod with a Splitted and Wedged End in a Potted Anchor 2. Finite-Element Analysis," Mech. Compos. Mater., vol. 50, no. 1, pp. 39–50, 2014, doi: 10.1007/s11029-014-9391-5.

[5] A. Kovalovs, P. Akishin, and A. Chate, "Detection Prestress Loss in Prestressed Concrete Slab using Modal Analysis," IOP Conf. Ser. Mater. Sci. Eng., vol. 471, p. 102015, Feb. 2019, doi: 10.1088/1757-899X/471/10/102015.

[6] S. Ramanathan, V. Benzecry, P. Suraneni, and A. Nanni, "Condition assessment of concrete and glass fiber reinforced polymer (GFRP) rebar after 18 years of service life," Case Stud. Constr. Mater., vol. 14, p. e00494, Jun. 2021, doi: 10.1016/j.cscm.2021.e00494.

[7] A. Kovalovs, S. Rucevskis, P. Akishin, and J. Kolupajevs, "Numerical Investigation on Detection of Prestress Losses in a Prestressed Concrete Slab by Modal Analysis," IOP Conf. Ser. Mater. Sci. Eng., vol. 251, p. 012090, Oct. 2017, doi: 10.1088/1757-899X/251/1/012090.

[8] I. Lasenko, S. Gaidukovs, and J. Rombovska, "Manufacturing of amber particles suitable for composite fibre melt spinning," Proc. Latv. Acad. Sci. Sect. B Nat. Exact, Appl. Sci., vol. 70, no. 2, pp. 51–57, 2016, doi: 10.1515/prolas-2016-0007.

[9] S. Gaidukovs, I. Lyashenko, J. Rombovska, and G. Gaidukova, "Application of amber filler for production of novel polyamide composite fiber," Text. Res. J., vol. 86, no. 20, pp. 2127–2139, Dec. 2016, doi: 10.1177/0040517515621130.

[10] I. Hussain, B. Ali, T. Akhtar, M. S. Jameel, and S. S. Raza, "Comparison of mechanical properties of concrete and design thickness of pavement with different types of fiber-reinforcements (steel, glass, and polypropylene)," Case Stud. Constr. Mater., vol. 13, p. e00429, Dec. 2020, doi: 10.1016/j.cscm.2020.e00429.

[11] A. Macanovskis, A. Lukasenoks, A. Krasnikovs, R. Stonys, and V. Lusis, "Composite Fibers in Concretes with Various Strengths," ACI Mater. J., vol. 115, no. 5, Sep. 2018, doi: 10.14359/51702343.

[12] A. Sarkar and M. Hajihosseini, "The effect of basalt fibre on the mechanical performance of concrete pavement," Road Mater. Pavement Des., vol. 21, no. 6, pp. 1726–1737, Aug. 2020, doi: 10.1080/14680629.2018.1561379.

[13] A. Macanovskis, A. Krasnikovs, O. Kononova, and A. Lukasenoks, "Mechanical Behavior of Polymeric Synthetic Fiber in the Concrete," Procedia Eng., vol. 172, pp. 673–680, 2017, doi: 10.1016/j.proeng.2017.02.079.

[14] B. Ali, L. A. Qureshi, and R. Kurda, "Environmental and economic benefits of steel, glass, and polypropylene fiber reinforced cement composite application in jointed plain concrete pavement," Compos. Commun., vol. 22, p. 100437, Dec. 2020, doi: 10.1016/j.coco.2020.100437.

[15] T. Kanda and V. C. Li, "Interface Property and Apparent Strength of High-Strength Hydrophilic Fiber in Cement Matrix," J. Mater. Civ. Eng., vol. 10, no. 1, pp. 5–13, Feb. 1998, doi: 10.1061/(ASCE)0899-1561(1998)10:1(5).

[16] A. Krasnikovs, O. Kononova, A. Machanovskis, V. Zaharevskis, P. Akishins, and S. Ruchevskis, "Characterization of mechanical properties by inverse technique for composite reinforced by knitted fabric. Part 2. Experimental evaluation of mechanical properties by frequency eigenvalues method," J. Vibroengineering, 2012.

[17] F. Benaoum, F. Khelil, and A. Benhamena, "Numerical analysis of reinforced concrete beams pre-cracked reinforced by composite materials," Frat. ed Integrita Strutt., vol. 14, no. 54, pp. 282–296, 2020, doi: 10.3221/IGF-ESIS.54.20.

[18] O. Kononova, A. Krasnikovs, G. Harjkova, and V. Lusis, "Numerical simulation of mechanical properties for composite reinforced by knitted fabric," in Ebook Congreso Mundial, 2014, vol. 5, pp. 2925–2932.

[19] A. Elbehiry, O. Elnawawy, M. Kassem, A. Zaher, and M. Mostafa, "FEM evaluation of reinforced concrete beams by hybrid and banana fiber bars (BFB)," Case Stud. Constr. Mater., vol. 14, p. e00479, Jun. 2021, doi: 10.1016/j.cscm.2020.e00479.

[20] N. Sohaib, R. Mamoon, S. G, and S. F, "Using Polypropylene Fibers in Concrete to achieve maximum strength," in Eighth International Conference On Advances in Civil and Structural Engineering - CSE 2018, Feb. 2018, pp. 37–42, doi: 10.15224/978-1-63248-145-0-36.

[21] P. K. Kolase and A. K. Desai, "Experimental study on monotonic and fatigue behaviour of polypropylene fibre-reinforced roller-compacted concrete with fly ash," Road Mater. Pavement Des., vol. 20, no. 5, pp. 1096–1113, Jul. 2019, doi: 10.1080/14680629.2018.1436466.

[22] T. S. Ng and T. S. H. Nyan, "Structural Application of Steel Fibres Reinforced Concrete With and Without Conventional Reinforcement," New Zeal. Concr. Ind., vol. 3101, no. 2006, 2017.

[23] V. Lusis et al., “Effect of short fibers orientation on mechanical properties of composite material–fiber reinforced concrete,” J. Civ. Eng. Manag., vol. 23, no. 8, pp. 1091–1099, Nov. 2017, doi: 10.3846/13923730.2017.1381643.

[24] A. Abolmaali, A. Mikhaylova, A. Wilson, and J. Lundy, “Performance of steel fiber-reinforced concrete pipes,” Transp. Res. Rec., vol. 1, no. 2313, pp. 168–177, 2012, doi: 10.3141/2313-18.

[25] V. Lusis and A. Krasnikovs, “Fiberconcrete with Non-Homogeneous Fibers Distribution,” Environ. Technol. Resour. Proc. Int. Sci. Pract. Conf., vol. 2, p. 67, Aug. 2013, doi: 10.17770/etr2013vol2.856.

[26] I. Löfgren, “Fibre-reinforced Concrete for Industrial Construction - a fracture mechanics approach to material testing and structural analysis,” Chalmers University of Technology, Göteborg, 2005.

[27] B. Ogunbayo and C. Aigbavboa, “Experimental Investigation of Concrete Block Walls Compressive Strength Using a Non-destructive Test,” 2021, pp. 393–397.

[28] A. Tatarinov, A. Shishkin, and V. Mironovs, “Correlation between ultrasound velocity, density and strength in metal-ceramic composites with added hollow spheres,” IOP Conf. Ser. Mater. Sci. Eng., vol. 660, p. 012040, Dec. 2019, doi: 10.1088/1757-899X/660/1/012040.

[29] V. Mironov, I. Pundiene, A. Tatarinov, and J. Baroninsh, “A Study of Metal-Cement Composites with Additives,” Constr. Sci., vol. 16, no. 1, Jan. 2014, doi: 10.1515/cons-2014-0008.

[30] N. Kurihara, M. Kunieda, T. Kamada, Y. Uchida, and K. Rokugo, “Tension softening diagrams and evaluation of properties of steel fiber reinforced concrete,” Eng. Fract. Mech., vol. 65, no. 2–3, pp. 235–245, Jan. 2000, doi: 10.1016/S0013-7944(99)00116-2.

[31] N. Banthia and Trottier J.F., “Concrete reinforced with deformed steel fibers .2. Toughness characterization,” ACI Mater. J., vol. 92, no. 2, pp. 146–154, 1995.

[32] N. K. Banjara and K. Ramanjaneyulu, “Experimental and numerical investigations on the performance evaluation of shear deficient and GFRP strengthened reinforced concrete beams,” Constr. Build. Mater., vol. 137, pp. 520–534, 2017, doi: 10.1016/j.conbuildmat.2017.01.089.

[33] Y. Dere and F. T. Dede, “Nonlinear finite element analysis of an R/C frame under lateral loading,” Math. Comput. Appl., vol. 16, no. 4, pp. 947–958, 2011, doi: 10.3390/mca16040947.

[34] M. Iqbal Khan and A. A. Abadel, “Numerical modeling of steel fiber-reinforced beam,” Appl. Mech. Mater., vol. 377, pp. 22–27, 2013, doi: 10.4028/www.scientific.net/AMM.377.22.

[35] H. Herrmann, O. Goidyk, and A. Braunbrück, “Influence of the Flow of Self-Compacting Steel Fiber Reinforced Concrete on the Fiber Orientations, a Report on Work in Progress,” in Part of the Advanced Structured Materials book series (STRUCTMAT, volume 95), Springer, Cham, 2019, pp. 97–110.

[36] H. Herrmann, O. Goidyk, H. Naar, T. Tuisk, and A. Braunbrück, “The influence of fibre orientation in self-compacting concrete on 4-point bending strength,” Proc. Est. Acad. Sci., vol. 68, no. 3, p. 337, 2019, doi: 10.3176/proc.2019.3.12.

[37] A. Krasnikovs, V. Zaharevskis, O. Kononova, V. Lusis, A. Galushchak, and E. Zaleskis, “Fiber Concrete Properties Control by Fibers Motion Investigation in Fresh Concrete During Casting,” in 8th Int. DAAAM Balt. Conf. "INDUSTRIAL Eng., 2012, pp. 657–662.

[38] C. Bao, J. H. Bi, D. Xu, J. Guan, and W. X. Cheng, “Numerical simulation of the distribution and orientation of steel fibres in SCC,” Mag. Concr. Res., vol. 72, no. 21, pp. 1102–1111, Nov. 2020, doi: 10.1680/jmacr.18.00432.

[39] H. Herrmann, A. Braunbrück, T. Tuisk, O. Goidyk, and H. Naar, “An Initial Report on the Effect of the Fiber Orientation on the Fracture Behavior of Steel Fiber Reinforced Self-Compacting Concrete,” in Advanced Structured Materials, 2019, pp. 33–50.

Environment. Technology. Resources. Rezekne, Latvia
Proceedings of the 13th International Scientific and Practical Conference. Volume 3, 36-39

Rigid Connection with Granite Chips in the Timber-Concrete Composite

Karina Buka-Vaivade
department of Structural Engineering
Riga Technical University
Riga, Latvia
Karina.Buka.Vaivade@gmail.com

Dmitrijs Serdjuks
department of Structural Engineering
Riga Technical University
Riga, Latvia
Dmitrijs.Serdjuks@rtu.lv

Andrejs Podkoritovs
department of Structural Engineering
Riga Technical University
Riga, Latvia
Andrejs.Podkoritovs@gmail.com

Leonids Pakrastins
department of Structural Engineering
Riga Technical University
Riga, Latvia
Leonids.Pakrastins@rtu.lv

Viktors Mironovs
department of Structural Engineering
Riga Technical University
Riga, Latvia
Viktors.Mironovs@rtu.lv

***Abstract* - Timber-concrete composite panels enables to combine advantages of pure timber and pure concrete panels in one structural member especially in the case, when the rigid timber-concrete connection is provided. The effectiveness of timber and concrete use and load-carrying capacity of the timber-concrete composite panels will grow in the case. The new concept of rigid timber to concrete connection was developed by the using of the granite chips as the keys to provide high quality of the glued connection. Behaviour of the timber-concrete composite panels were investigated by finite element method and laboratorian experiment. Three timber-concrete composite panels in combination with carbon fibre reinforced plastic composite tapes in the tension zone with the span 1.8 m were statically loaded till the failure by the scheme of three-point bending. One specimen was produced by dry method, by gluing together cross-laminated timber panel and prefabricated concrete panel. Timber-concrete connection of the other two specimens was provided by the granite chips, which were glued on the surface of the cross-laminated timber by epoxy, and then wet concrete was placed. Dimensions of the crushed granite pieces changes within the limits from 16 to 25 mm. The current study focuses on determining the effect of the use of granite chips for timber-concrete composite panels with adhesive connection between layers. The effect of the use of granite chips in rigid connection is determined by comparison of mid-span displacements and level of failure load of the two variants of the timber-concrete composite panels. Three-dimensional finite element models of timber-concrete composite with rigid connection was developed and validated by experiment data. Obtained results shown, that the use of the granite chips in rigid timber to concrete connection allow to make a quality rigid connection. Possibility to increase by 28% level of failure load of the timber-concrete composite panels by the adding of granite chips was stated. Maximal vertical mid-span displacements of the panels decrease about 3.8 times at the same time.**

Keywords* - *adhesive connection, bending test, carbon fibre reinforced plastic, finite element method, glued connection, rigid connection, timber-concrete composite, wood-concrete composite.

I. Introduction

Effectiveness of timber-concrete composite (TCC) structural members strongly dependent from the type of timber to concrete connection. Semi-rigid and rigid once are two types of timber to concrete connections in hybrid timber-concrete composite structural members, which are used now in the practice [1], [2]. Studies shows that the adhesive composite connection of the timber-concrete structural members is more effective in comparison with the semi-rigid one so as provides higher bending stiffness and leads to smaller deflections and a better structural members behaviour, including higher natural frequency, which is a very important characteristic of the floor structures [3] – [10].

Timber component in timber-concrete panels very often is presented by the cross-laminated timber (CLT). Cross-laminated timber is a renewable structural material, which possesses a decreased level of anisotropy in comparison with the solid and glued timber. CLT could be used for load-bearing walls and panels of multi-storey timber

Online ISSN 2256-070X
https://doi.org/10.17770/etr2021vol3.6552

buildings as well as the decking structures of pedestrian and road bridges [11].

Nowadays, two technologies to produce glued connection of the TCC are known [12]. "Dry" is the gluing of timber with a precast concrete slab; "wet" - is a technology when a fresh concrete is placed on a freshly applied layer of glue. Both techniques have high risk of forming a poor-quality rigid connection in TCC, and there are difficulties in controlling the quality of the glued connection. So, for popularization of the rigid connection in TCC it is necessary to offer more optimal connection production technology.

Providing of the rigid connection between CLT and concrete layers by gluing granite chips on the surface of the CLT panel probably enables to obtain timber-concrete composite structural member with increased stiffness [13] – [15]. So, the objective of current study is investigation of influence of the granite chips in the rigid timber to concrete connection on the behaviour of timber-concrete composite structural members subjected to flexure.

II. MATERIALS AND METHODS

A timber-concrete composite panel with CLT as timber component and additional strengthening by the carbon fibre reinforced plastic tape in the tension zone subjected to the three-point bending was considered as an object of this investigation. Influence of the granite chips in the rigid timber to concrete connection on the behaviour of hybrid timber-concrete composite structural members subjected to flexure was evaluated based on the laboratorian experiments and finite element method (FEM) analyses. Numerical model of TCC specimen (Fig.1.) was developed with structural analysis program RFEM. The solid finite elements were used for FEM model development. 3D orthotropic elastic material model was used for CLT elements, for carbon fibre reinforced plastic was used isotropic non-linear material model and 3D isotropic Mazars' damage material model was used with non-linear stress-strain diagram for concrete layer. For 3D numerical model of the TCC specimens contact solid between concrete and CLT layers is defined with full force transmission. Target length of FE equal to 0.02 m and 100 load increments was used for TCC model. The model of TCC was divided into the finite elements by the rectangular mesh.

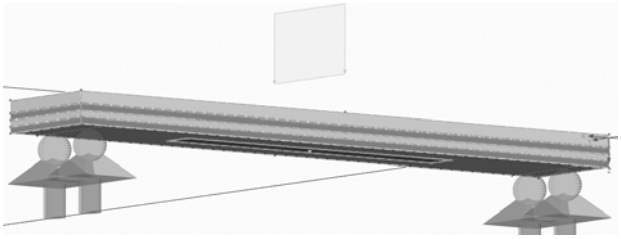

Fig. 1. FEM model of timber-concrete composite with carbon fibre reinforced plastic tape developed by the software RFEM.

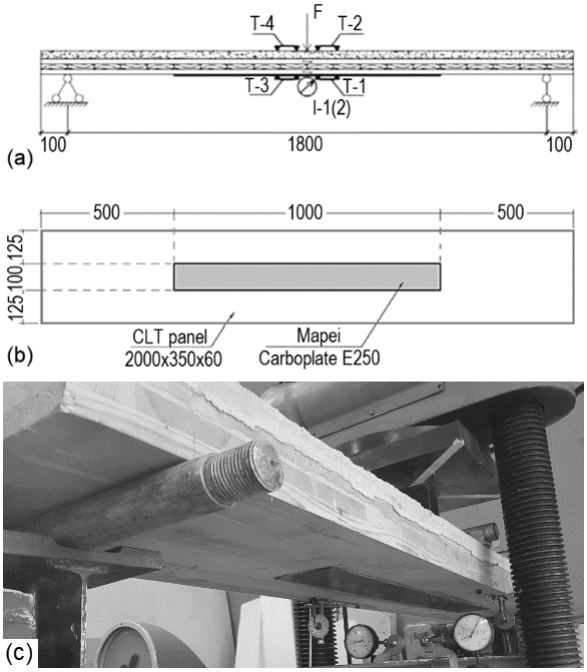

Fig. 2. TCC panel (a) design scheme; (b) placement of carbon fiber reinforced tape on its surface in the tensioned zone, (c) placement in testing machine.

The first laboratorian experiment was carried to investigate the behaviour of the timber-concrete composite produced by dry method [16]. Timber to concrete connection in TCC panels was provided by gluing CLT panel with prefabricated concrete panel by the epoxy Sicadur 330. Timber-concrete composite panels consist of the CLT components, which are strengthened by the carbon fibre reinforced plastic tape Mapei Carboplate E250 in the tensioned zone and with the layer of finishing mass Sacret BAM with thickness of 30 mm in compressed zone.

The cross-laminated timber base was formed by the three layers of strength class C24 timber boards. Thickness of each board layer is equal to 20 mm. Fibres of outer layers are oriented parallel to the longitudinal axis of the panels. The panels have length, width and thickness equal to 2000, 350 and 60 mm, correspondingly. The panels were produced by the Sconto enterprise, Ltd, Jelgava, Latvia.

The second laboratorian experiment was carried out to check influence of the granite chips in the rigid timber to concrete connection on the behaviour of timber-concrete composite panel. Two specimens with the same dimensions as the specimen from the first laboratorian experiment were prepared. Timber to concrete connection was provided by the granite chips with dimensions changing within the limits from 16 to 25 mm glued to the surface of CLT by the epoxy Sikadur 330 [17].

Design scheme of the laboratorian experiments and specimen placement in testing machine are shown on the Fig.2. Two groups of strain measuring devices and one group of deflectometers were used during the static loading of the timber-concrete composite. Strain measuring devices T-2 and T-4 were placed in compressed zone. Strain measuring devices T-1 and T-3 were placed in tensioned

zone on the surface of the cross-laminated timber. A group of the deflectometers I-1 and I-2 was placed in the middle of the span. Precision of the maximum vertical displacements and absolute deformations measurements was equal to 0.01.mm and 0.001 mm, correspondingly. All specimens were loaded until the failure to determine their level of failure load.

III. Results and Discussion

The load-displacement curves of the specimens of TCC subjected to the three-point bending are shown on the Fig.3. The dependences of TCC specimens were obtained by the experiment and developed 3D numerical model, for the TCC with granite chips there are shown curve with average values of two specimens.

As it can be seen from load-displacement curve of TCC specimen with glued connection with granite chips, the behaviour of the specimens is linear up to about 15 kN, then increasing of specimen's stiffness is observed. According to the laboratory test, mid-span displacement of the TCC specimen with granite chips at the load level equal to 15 kN is 3.18 mm, while the calculated by 3D non-linear numerical model corresponding displacement is 3.50 mm. 3D model produces little more conservative results of the behaviour of the TCC specimens with granite chips subjected to the three-point bending than data obtained by the experiment. The curve obtained with the 3D model very accurately describes the behaviour of the specimen with granite chips in the initial linear stage. It can be concluded, that developed model is safe for prediction of the behaviour of TCC with rigid connection provided by use of granite chips.

The behaviour of the TCC specimen produced by dry technic without gluing of granite chips on the surface of the CLT is completely different in comparison with TCC specimen where new concept of rigid connection with granite chips is used. According to the laboratory test, mid-span displacement of the TCC specimen without granite chips at the load level equal to 30 kN is 22.90 mm, for TCC specimen with granite chips value of mid-span displacements at the same load level was only 5.77 mm.

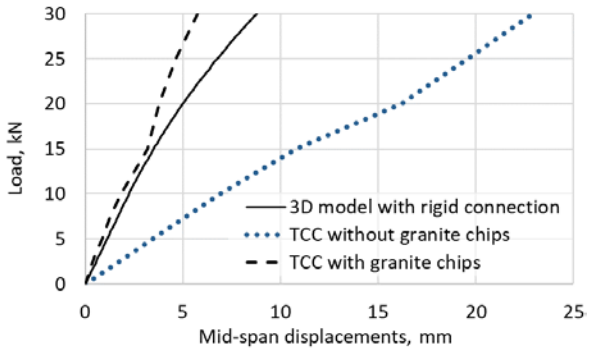

Fig. 3. Load-displacement curves for TCC specimens.

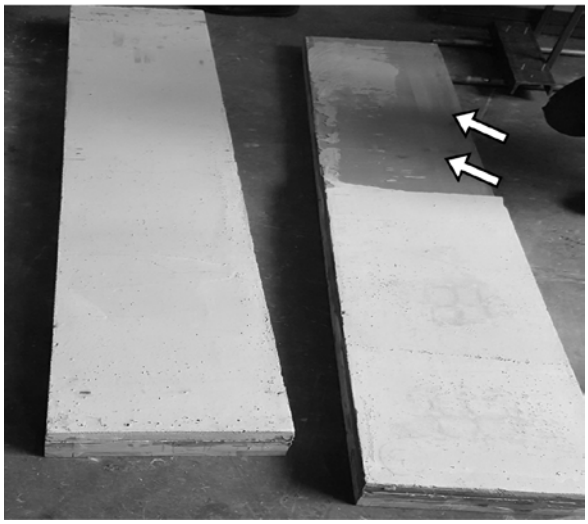

Fig. 4. Failure of the TCC specimen produced by dry technic without gluing of granite chips.

Results obtained by bending tests and FEM analyses show, that connection of the TCC specimen without granite chips is not rigid. The reason for this is the main problem of this type of connection, it is the difficulty to ensure complete and high-quality gluing of the layers. Splitting of the concrete layer from the CLT panel after collapse can be seen in Fig.4. It can be seen that a quality connection was formed only on about 40% of all connection surface. A similar result was obtained in testing of small-scale specimens. Fig. 5 shows the collapse scenes for small-scale TCC specimens with and without granite chips in the glued connection. In the TCC specimen without granite chips (Fig.5. (a)) splitting of the concrete layer takes place at the glued connection. In the case of the TCC specimen with the proposed connection concept with granite chips (Fig.5. (b)) it can be seen composite action of specimen and collapse on concrete layer.

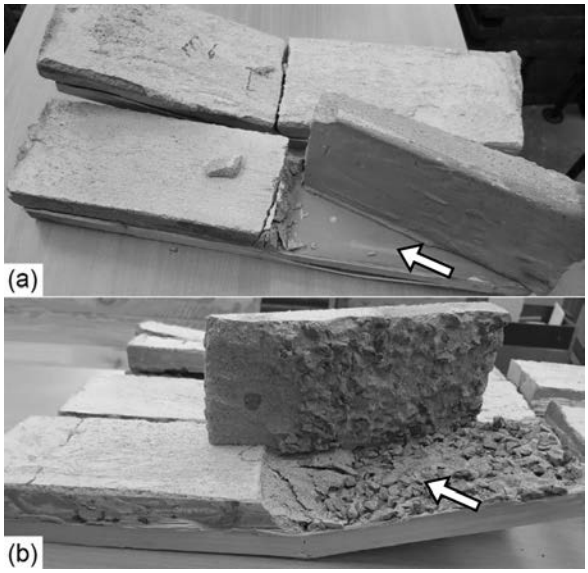

Fig. 5. Failure mode of the TCC small-scale specimens (a) without granite chips in glued connection, (b) with granite chips.

According to the laboratory tests, level of failure load for TCC specimen without use of granite chips with span 1.8 m in tree-point bending is equal to 32 kN. For TCC specimen with rigid connection provided by granite chips use the failure load equal to 41 kN was obtained.

IV. Conclusions

Results of the laboratory experiments shows that proposed concept of rigid adhesive connection with gluing of granite chips on the surface of timber layer in timber-concrete composite provides good connection quality and full composite action.

Developed 3D numerical model of timber-concrete composite member subjected to the flexure with rigid connection and full composite action with sufficient precision describes the behaviour of the TCC specimen where connection between layers was provided by gluing of granite chips on timber component surface and after that placing wet concrete layer. In this case, quality of the glued granite chips can be assessed visually but bonding between concrete matrix and granite chips as aggregates of concrete is developed naturally.

Based on the obtained data, an increase in stiffness of the TCC specimens with granite chips has been observed. On the load level of 30 kN 1.52 times less mid-span displacements of the TCC specimen with granite chips was obtained in comparison with displacement calculated by developed numerical model of timber-concrete composite with full composite action.

The difference in the failure load level between timber-concrete composite specimen with and without use of granite chips in connection between material layers obtained by experimental bending tests is about 28%. Timber-concrete composite with proposed connection technology picks up greater load level than TCC without granite chips in connection.

Possibility to increase by 28% level of failure load of the timber-concrete composite panels by the adding of granite chips was stated. Maximal vertical mid-span displacements of the panels decrease about 3.8 times at the same time.

At the load level equal to 30 kN by timber-concrete composite specimen with granite chips in timber to concrete connection it is possible to obtain at least 3.8 times less vertical mid-span displacements than by timber-concrete composite specimen without granite chips.

Acknowledgments

This research was supported by Riga Technical University's Doctoral Grant programme and Latvian Council of Science funded project “Method of correlation of coaxial accelerations in 6-D space for quality assessment of structural joints (COACCEL)” (Nr. lzp-2020/1-0240).

References

[1] T. Tannert, A. Gerber and T. Vallee, "Hybrid adhesively bonded timber-concrete-composite floors," International Journal of Adhesion and Adhesives, vol. 97, Nr. 102490, 2020. DOI: 10.1016/j.ijadhadh.2019.102490

[2] M. Fragiacomo, A. Gregori, J. Xue, C. Demartino and M. Toso, "Timber-concrete composite bridges: Three case studies," Journal of Traffic and Transportation Engineering (English Edition), vol. 5, pp. 429-438, 2018. DOI: 10.1016/j.jtte.2018.09.001

[3] J. Kanocz, V Bajzecerova and S. Steller, "Timber – concrete composite elements with various composite connections. Part 1: screwed connection," Wood Research, vol. 58, pp. 555–570, 2013.

[4] J. Kanocz and V Bajzecerova, "Timber – concrete composite elements with various composite connections. Part 3: adhesive connection," Wood Research, vol. 60, pp. 939–952, 2015.

[5] M. Brunner, M. Romer and M. Schnüriger, "Timber-concrete-composite with an adhesive connector (wet on wet process)," Materials and Structures/Materiaux et Constructions, vol. 40, pp. 119–126, 2007. DOI: 10.1617/s11527-006-9154-4

[6] J.H. Negrao, F.M. Oliveira and C.L. Oliveira, "Investigation on timber-concrete glued composites," In: 9th World Conference on Timber Engineering (WCTE 2006). Portland, Oregon, USA, 2006.

[7] M. Al Ali, V. Bajzecerova and V. Kvocak, "Design methods of timber-concrete composite ceiling structure," Magazine of Civil Engineering, vol. 73(5), pp. 88–95, 2017. DOI: 10.18720/MCE.73.8

[8] V. Mironovs, A. Tatarinov, and S. Gorbacova, "Expanding Application of Perforated Metal Materials," In: Construction and Architecture IOP Conference Series: Materials Science and Engineering, vol. 251(1), Nr. 012027, 2017. DOI: 10.1088/1757-899X/251/1/012027

[9] M. V. Gravit, D. Serdjuks, A. V. Bardin, V. Prusakov and K. Buka-Vaivade, "Fire design methods for structures with timber framework," Magazine of Civil Engineering, vol. 85, pp. 92-106, 2019. DOI: 10.18720/MCE.85.8

[10] M. N. Kirsanov, "Lower estimate of the fundamental frequency of natural oscillations of a truss with an arbitrary number of panels," Vestnik MGSU, vol. 14(7), pp. 844-851, 2019. DOI: 10.22227/1997-0935.2019.7.844-851

[11] K. Buka-Vaivade, D. Serdjuks, V. Goremikins, A. Vilguts and L Pakrastins, "Experimental verification of design procedure for elements from cross-laminated timber," Procedia Engineering, vol. 172, pp. 1212–1219, 2017. DOI: 10.1016/j.proeng.2017.02.142

[12] A. Dias, J. Schänzlin and P. Dietsch, "Design of timber-concrete composite structures", Aachen: Shaker Verlag GmbH, 2018.

[13] R. Vasiljevs, D. Serdjuks, K. Buka-Vaivade, A. Podkoritovs and N. Vatin, "Load-carrying capacity of timber-concrete composite panels," Magazine of Civil Engineering, vol. 93, pp. 60-70, 2020. DOI: 10.18720/MCE.93.6

[14] R. Vasiljevs, D. Serdjuks, J. Gerasimova, K. Buka-Vaivade and A. Orhun Erüz, "Behaviour of Timber-Concrete Joints in Hybrid Members Subjected to Flexure," IOP Conference Series: Materials Science and Engineering, vol. 660, Nr. 012050, 2019. DOI: 10.1088/1757-899X/660/1/012050

[15] A. Skincs, D. Serdjuks, K. Buka-Vaivade, V. Goremikins and A.Y. Mohamed, "Steel and composite tapes in timber to concrete joint," Lecture Notes in Civil Engineering, vol. 141, pp. 68–79, 2021.

[16] J. Gerasimova, "Testing of design method for hybrid elements subjected to flexure," M.S. thesis, Riga Technical university, Riga, Latvia, 2017.

[17] R. Vasiljevs, "Load-carrying Capacity Analyse for Hybrid Composite Member," M.S. thesis, Riga Technical university, Riga, Latvia, 2018

Environment. Technology. Resources. Rezekne, Latvia
Proceedings of the 13th International Scientific and Practical Conference. Volume 3, 40-44

Timber-Concrete Composite Ribbed Slabs with High-Performance Fibre-Concrete

Karina Buka-Vaivade
department of Structural Engineering
Riga Technical University
Riga, Latvia
Karina.Buka.Vaivade@gmail.com

Dmitrijs Serdjuks
department of Structural Engineering
Riga Technical University
Riga, Latvia
Dmitrijs.Serdjuks@rtu.lv

Janis Sliseris
department of Structural Engineering
Riga Technical University
Riga, Latvia
Janis.Sliseris@rtu.lv

Andrejs Podkoritovs
department of Structural Engineering
Riga Technical University
Riga, Latvia
Andrejs.Podkoritovs@gmail.com

Raimonds Ozolins
department of Structural Engineering
Riga Technical University
Riga, Latvia
Raimonds.Ozolins@rtu.lv

***Abstract* - Composite of such renewable material as timber and the most popular man-made material as concrete offers many benefits. Such of them are high load-bearing capacity with low dead load and increased structural bending stiffness. Higher specific strength of high-performance concrete in comparison with ordinary concrete ensures more efficient use of the material. Addition of fibres can reduce the fragility and autogenous shrinkage cracks of high-performance concrete and makes it possible to design thinner layers of concrete for timber-concrete composite structures. Ribbed slabs as solution for the floor slabs, allows to reduce material consumption and to integrate engineering communications into the structures. The current study focuses on determining the effect of the use of high-performance fibre reinforced concrete for timber-concrete composite ribbed slabs with adhesive connection between layers, as the most effective connection type for composite action. The effect of the use of high-performance fibre reinforced concrete is determined by comparison of mid-span displacements of the ribbed slabs numerical models. Three-dimensional finite element models of timber and ordinary concrete composite ribbed slab and high-performance fibre reinforced concrete with additional longitudinal reinforcement ribbed slab are validated by experiment data. Developed numerical models makes it possible to predict the dependence of applied load on mid-span displacement in three-point bending with sufficient precision. Obtained results showed, that replacement of ordinary concrete layer by high-performance fibre reinforced concrete in timber-concrete composite ribbed slab with adhesive connection up to 1.68 times decrease vertical mid-span displacements.**

Keywords - finite element method, high-performance fibre-reinforced concrete, ribbed slab, timber-concrete composite, wood-concrete composite.

I. Introduction

Timber is a renewable material what makes the significant advantage for it use in construction. Concrete is the most widely used man-made building material. Timber-concrete composite (TCC) structures can ensure more efficient use of resources and meet the growing demand for sustainable structures.

Combining such two materials as timber and concrete, can improve various classic disadvantages of wooden floors, such as dynamic reaction, bending stiffness, load-bearing capacity, sound insulation [1] – [3], structural fire safety - the effective cross-sectional area increases as timber member is subjected to the fire action from one side [4], [5], seismic performance [6] and heat mass. The natural frequency of the structure [7] is also important. Timber-concrete slabs allow to achieve such dynamic design parameters that ensure their safe operation for rhythmic activities [2].

As high-performance concrete is characterized by higher specific strength in comparison with ordinary strength concrete, its use in structures is more rational. Disperse reinforcement can reduce the fragility of high-performance concrete [8] – [10], which makes it possible to design thin layers and improve the fire safety of the material. The ribbed slabs allow to reduce material

Online ISSN 2256-070X
https://doi.org/10.17770/etr2021vol3.6551

consumption and the dead load of structures, as well as to integrate engineering communications into the structures.

Studies approve that the use of fibre-reinforced concrete in TCC structures with notch connections or shear mechanical connectors increases the shear strength of structure [11] – [13]. From the point of view of structure strength and stiffness, adhesive connections are the best solution that can ensure almost perfect performance of the composite material.

The structural solution offered by the composite of timber and high-performance fibre reinforced concrete (HPFRC) ribbed slabs is actual and complies with the principles of sustainable construction. So, the aim of this study is to determine the effect of using HPFRC instead of ordinary concrete (OC) layer in TCC ribbed slab with the adhesive connection between materials.

II. Materials and Methods

A ribbed slab subjected to the three-point bending was considered as an object of this investigation. Influence of HPFRC in TCC ribbed slab with rigid connection between materials layers on mid-span displacements was evaluated by finite element (FE) numerical model. All numerical models were developed with structural analysis program RFEM by solid elements. For timber-based elements 3D orthotropic elastic material model was used. For the concrete type elements 3D isotropic Mazars' damage material model was used with non-linear stress-strain diagrams. For 3D numerical model of the TCC specimens contact solid between concrete and plywood layers is defined with full force transmission. Target length of FE equal to 0.0075 m and 200 load increments was used for TCC model, 0.02 m and 100 was used for HPFRC ribbed slab model.

Two laboratorian experiments were carried out to validate the used numerical modelling procedure of TCC member and HPFRC material behaviour. The aim of the numerical modelling procedure validation is comparison of the specimen behaviour with actual operation and checking of developed model safety.

The first laboratorian experiment was necessary to validate TCC slab three-dimensional (3D) numerical model by small-scale specimens. The four specimens of TCC ribbed slabs were made with C24 strength class timber boards with dimensions 67x43 mm for slabs ribs, 30 mm OC layer with strength of C20/25 class and 9 mm plywood layer. PVA D3 was used for timber boards and plywood layer gluing. The adhesive connection between concrete and plywood layers are made by gluing 16-25 mm granite chips on plywood by epoxy Sikadur-31 CF [14], [15]. After that concrete layer was placing on granite chips. Total length of the specimens was 600 mm, with effective span 430 mm. Cross-section and design scheme of the timber-concrete ribbed slab specimen is shown in Fig.1.

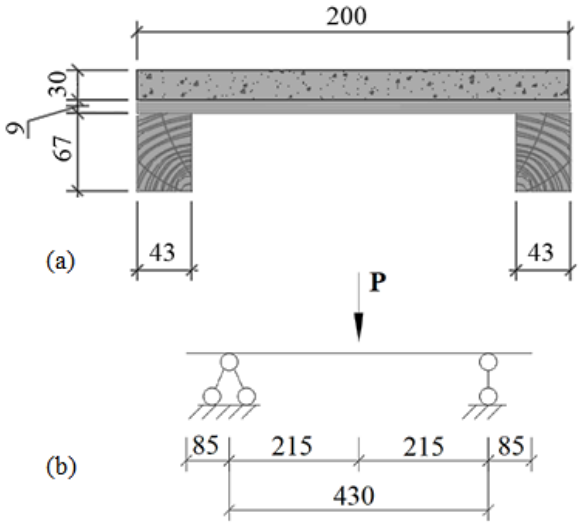

Fig. 1. TCC ribbed slab specimen (a) cross-section, (b) design scheme.

The second laboratorian experiment was necessary to determine the accuracy of prediction of high-performance fibre reinforced concrete ribbed slab non-linear behaviour by 3D numerical model within degradation of modulus of elasticity cause of cracking.

The specimen of HPFRC ribbed slab was free supported slab with span 1.23 m. The geometric dimensions and loading scheme of HPFRC specimen is shown in Fig.2. Each rib has B500 steel longitudinal bar with diameter of 6 mm. Polypropylene (PP) Strux 90/40 fibres in amount of 0.5% of the concrete volume were used. For 40 mm long fibres with an aspect ratio of 90, the tensile strength is 620 MPa, the modulus of elasticity - 9.5 GPa and the elongation - 10%. Compressive strength of cube specimen with dimensions 10x10x10 cm from high-performance synthetic macro fibres reinforced concrete, according to compressed cube tests, was determined as 92.5 MPa. The following parameters of HPFRC were used for calculations: 78 MPa compressive strength, 4.6 MPa tensile strength and 41 GPa modulus of elasticity.

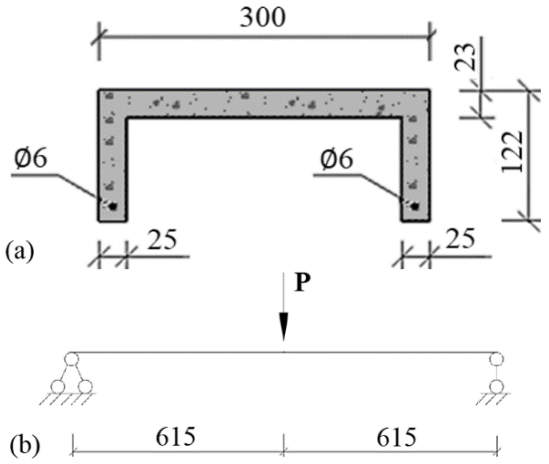

Fig. 2. HPFRC ribbed slab specimen (a) cross-section, (b) design scheme.

With the aim of determining the effect of the use of HPFRC in TCC ribbed slab 3D model with the same dimension as timber-concrete composite ribbed slab was developed by replacing ordinary concrete layer with HPFRC.

III. Results and Discussion

Load-displacement curves of TCC ribbed slab specimen in three-point loading, according to laboratory testing as average result of four specimens testing and numerical model calculations, are summarized in Fig.3. First cracks in timber was heard at load level equal about 25 kN, at load level about 55 kN the concrete layer cracked, average crashing load of the slabs was about 61.25 kN [16]. According to the results obtained (Fig.4.), distribution of maximal stresses calculated by 3D numerical model corresponds to the nature of the collapse of the TCC ribbed slab with ordinary concrete layer. As it can be seen from load-displacement curves of TCC ribbed slabs, linear elastic stage is until about 40 kN, after what elastic-plastic stage is started. According to the laboratory test, mid-span displacement of the TCC ribbed slab at the load level equal to 40 kN is 4.42 mm, while the calculated by 3D non-linear numerical model corresponding displacement is 4.81 mm.

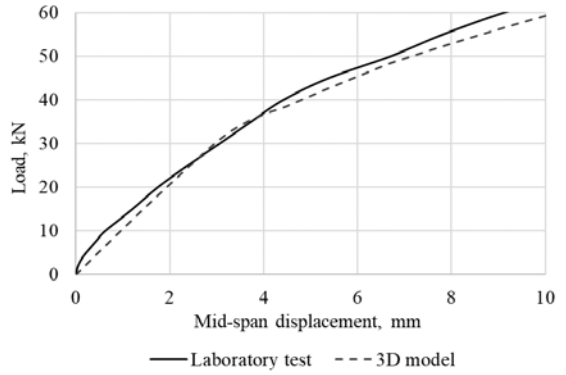

Fig. 3. Load-displacement curves for TCC ribbed slab specimen.

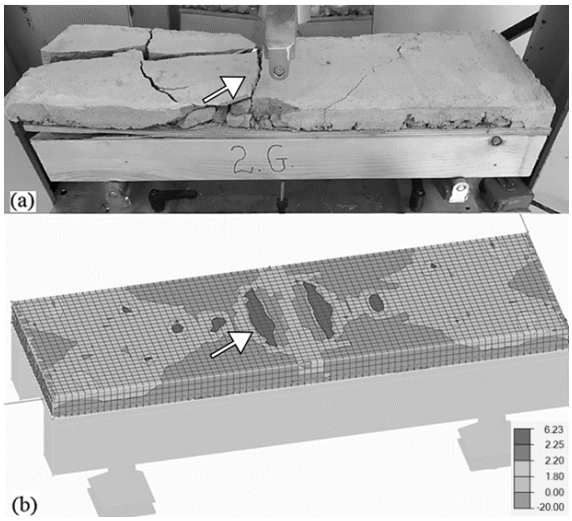

Fig. 4. OC layers of TCC ribbed slab (a) collapse and (b) corresponding stress distribution.

In elastic-plastic stage 3D model produces little more conservative results of the behaviour of the TCC ribbed slab subjected to the three-point bending than data obtained by the experiment. The curve obtained with the 3D model very accurately describes the behaviour of the specimen.

Load-displacement curves of HPFRC ribbed slab specimen in three-point loading, according to laboratory testing and numerical model calculations, are summarized in Fig.5. Experimental maximal load for ribbed slab was 15.42 kN with corresponding mid-span displacement 10.16 mm. Results obtained by numerical model showed, that starting with the load level of 14.65 kN with corresponding displacement 10.08 mm, load increasing by 1% increased displacements by 8.3-22%. The behaviour of the calculation model at the linear stage is identical to the actual operation of the HPFRC ribbed slab specimen. The linear stage of load-displacement curve is until about 4.28 kN with corresponding mid-span displacement equal to 0.34 mm, after what elastic-plastic stage is started. In elastic-plastic stage 3D model produces more conservative results of the behaviour of the HPFRC ribbed slab subjected to the three-point bending than data obtained by the experiment.

As it can be seen in Fig.6., distribution of maximal stresses calculated by 3D numerical model corresponds to the nature of the collapse of the HPFRC ribbed slab. It can be concluded, that developed model is safe for prediction of the behaviour of HPFRC material.

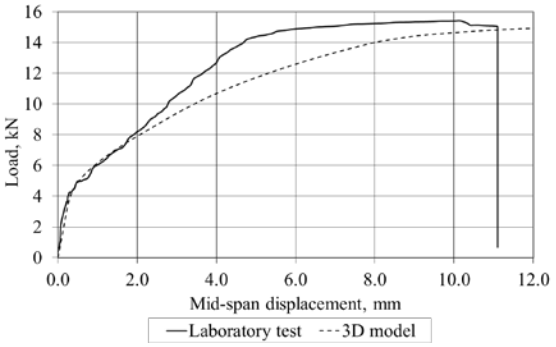

Fig. 5. Load-displacement curves for HPFRC ribbed slab specimen.

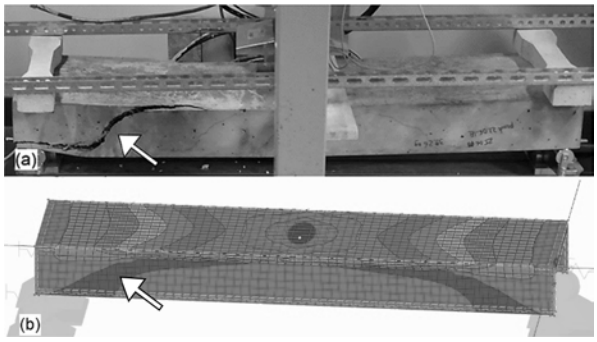

Fig. 6. HPFRC ribbed slab (a) collapse and (b) corresponding stress distribution.

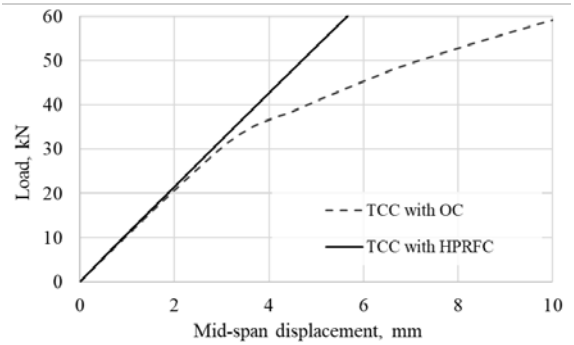

Fig. 7. Load-displacement curves for TCC ribbed slab specimens with OC or HPFRC obtained by numerical model.

The load-displacement curves of ribbed slab subjected to the three-point bending according to the developed 3D numerical models of TCC with OC and with HPFRC layer are enclosed in Fig.7.

As it can be seen from obtained curves, the character of the curves is the same up to about 22 kN. After these load level in the specimen with OC layer larger deformations begin to develop, but for specimen with HPFRC layer the dependence of the displacements on the load remains linear. So, on the 40 kN load level, displacement obtained by 3D numerical model with HPFRC layer equal to the 3.73 mm. At load level of 55 kN, when according laboratory test OC layer in TCC completely cracked, the mid-span displacement of the TCC ribbed slab with OC layer obtained by numerical model is 8.67 mm, but displacement of the TCC ribbed slab with HPFRC layer is only 5.15 mm.

On the load level of 61 kN maximal tension stresses obtained by 3D numerical model of the TCC ribbed slab with OC layer is up to 6.23 MPa, at a tensile strength of OC 2.2 MPa. At the same load level maximal tension stresses obtained by 3D numerical model of the TCC ribbed slab with HPFRC layer is up to 5.18 MPa, at a tensile strength of HPFRC 4.6 MPa.

IV. Conclusions

Numerical models of high-performance fibre reinforced concrete ribbed slabs and timber-concrete ribbed slabs with ordinary concrete layer were checked and showed adequate results. Developed models with sufficient precision describes the behaviour of the ribbed slabs subjected to the flexure. The difference in the mid-span displacement between calculated with developed numerical model and experimental results on the load level of linear-elastic stage is about 8.8% for the TCC ribbed slab with ordinary concrete layer. For high-performance fibre reinforced concrete ribbed slab almost identical mid-span displacements in the linear-elastic stage were obtained.

The use of high-performance fibre reinforced concrete instead ordinary concrete layer in timber-concrete ribbed slab increases energy absorption of the element. At the low load level to about 22 kN there is no difference in behaviour of the both specimens with different concrete layers. At the load level, which according to the experiment corresponds to the linear-elastic stage end with the HPFRC layer it is possible to obtain at least 1.18 times less displacements than with ordinary concrete, and for load level of 55 kN, which correspond to complete cracking of the ordinary concrete layer, according to the numerical models, with the HPFRC layer it is possible to obtain 1.68 times less displacements of the TCC ribbed slab than with ordinary concrete layer.

Results of tensile stresses obtained by numerical models shows, that the specimen of the TCC ribbed slab with OC layer completely cracked, because tensile stresses exceeding the tensile strength of ordinary concrete by 183%. At the same time, tensile stresses of the TCC ribbed slab with HPFRC layer exceeds the tensile strength by only 12.6%, what means, that cracking in this specimen are only in initial stage.

In future studies, it is planned to make specimens of TTC with the fibre reinforced concrete layer for laboratory testing to verify the results obtained by numerical modelling.

Acknowledgments

This research was supported by Riga Technical University's Doctoral Grant programme and Latvian Council of Science funded project “Method of correlation of coaxial accelerations in 6-D space for quality assessment of structural joints (COACCEL)” (Nr. lzp-2020/1-0240).

References

[1] J. Rodrigues, A. Dias and P. Providência, "Timber-concrete composite bridges: State-of-the-art review," BioResources, vol. 8, pp. 6630-6649, 2013. DOI: 10.15376/biores.8.4.6630-6649

[2] A. Dias, J. Skinner, K. Crews and T. Tannert, "Timber-concrete-composites increasing the use of timber in construction," European Journal of Wood and Wood Products, vol. 74, pp. 443–451, 2016. DOI: 10.1007/s00107-015-0975-0

[3] V. Bajzecerová, "Bending Stiffness of CLT-Concrete Composite Members - Comparison of Simplified Calculation Methods," Procedia Engineering, vol. 190, pp. 15-20, 2017. DOI: 10.1016/j.proeng.2017.05.301

[4] M. V. Gravit, D. Serdjuks, A. V. Bardin, V. Prusakov and K. Buka-Vaivade, "Fire design methods for structures with timber framework," Magazine of Civil Engineering, vol. 85, pp. 92-106, 2019. DOI: 10.18720/MCE.85.8

[5] J. Natterer, "A way to sustainable architecture by new technologies for engineered timber structures," Proceedings of the World Conference on Timber Engineering, 2004.

[6] P. Croce, M. Beconcini, P. Formichi, F. Landi and D. Cardella, "Fatigue behaviour of composite timber-concrete beams," Procedia Structural Integrity, vol. 11, pp. 363-370, 2018. DOI: 10.1016/j.prostr.2018.11.047

[7] M. N. Kirsanov, "Analytical assessment of the frequency of natural vibrations of a truss with an arbitrary number of panels," Structural Mechanics of Engineering Construc-tions and Buildings, vol. 16, pp. 351-360, 2020. DOI: 10.22363/1815-5235-2020-16-5-351-360

[8] K. Buka-Vaivade, J. Sliseris, D. Serdjuks, L. Pakrastins and N. I. Vatin, "Rational use of HPSFRC in multi-storey building, " Magazine of Civil Engineering, vol. 84, pp. 3–14, 2018. DOI: 10.18720/MCE.84.1

[9] K. Buka-Vaivade, J. Sliseris, D. Serdjuks, G. Sahmenko and L. Pakrastins, "Numerical Comparison of HPFRC and HPC Ribbed Slabs," IOP Conference Series: Materials Science and Engineering, vol. 660, Nr. 012054, 2019. DOI: 10.1088/1757-899X/660/1/012054

[10] J. Sliseris and K. Buka-Vaivade, "Numerical Modelling of High Strength Fibre-Concrete’s columns in Multi-Storey Building," IOP

Conference Series: Materials Science and Engineering, vol. 660, Nr. 012062, 2019. DOI: 10.1088/1757-899X/660/1/012062

[11] K. Holschemacher and H. Kieslich, "Recent developments in timber-concrete composite," CLEM+CIMAD 2017, 2017.

[12] S. Lamothe, L. Sorelli, P. Blanchet and P. Galimard, "Engineering ductile notch connections for composite floors made of laminated timber and high or ultra-high performance fiber reinforced concrete," Engineering Structures, vol. 211, Nr. 110415, 2020. DOI: 10.1016/j.engst

[13] K. Holschemacher, S. Klotz and D. Weisse, "Application of Steel Fibre Reinforced Concrete for Timber-Concrete Composite Constructions," Lacer, pp. 161-170, 2002.

[14] R. Vasiljevs, D. Serdjuks, J. Gerasimova, K. Buka-Vaivade and A. Orhun Erüz, "Behaviour of Timber-Concrete Joints in Hybrid Members Subjected to Flexure," IOP Conference Series: Materials Science and Engineering, vol. 660, Nr. 012050, 2019. DOI: 10.1088/1757-899X/660/1/012050

[15] R. Vasiljevs, D. Serdjuks, K. Buka-Vaivade, A. Podkoritovs and N. Vatin, "Load-carrying capacity of timber-concrete composite panels," Magazine of Civil Engineering, vol. 93, pp. 60-70, 2020. DOI: 10.18720/MCE.93.6

[16] V. Budovskis, "Analyse of load – currying capacity increase for timber subjected for flexure," M.S. thesis, Riga Technical university, Riga, Latvia, 2020.

Environment. Technology. Resources. Rezekne, Latvia
Proceedings of the 13th International Scientific and Practical Conference. Volume 3, 45-48

Experimental Determination of the Powder Quantity in the Ignition Cartridge for the Reusable Training-Practice Mortar Round for Firing on Short Distances

Conyu Conev
National Military University
Artillery, AD and CIS Faculty
Shumen, Bulgaria
coni19@abv.bg

Tsanko Karadzhov
Department of Mechanical and
Precision Engineering
Technical University of Gabrovo
Gabrovo, Bulgaria
karadjov_st@abv.bg

Abstract **- The article presents an experimental investigation for the powder quantity in the ignition cartridge for the reusable training-practice mortar round for firing on short distances, which is part of a training simulator for mortar crews. A formula for approximately calculating of the required amount of quantity of the gun powder in the ignition cartridge for many times used training-practice mine for shooting at a distance of 100 meters is presented in the article. The experimental investigation and the statistical hypothesis checking confirm that the formula can be used for practically determination of the required amount of charge in the ignition cartridge.**

Keywords - mortar, training-practice mortar round

I. INTRODUCTION

A tendency aimed towards the modernization of the Bulgarian Armed forces has been seen during the recent decades. The modernization of the armed forces however requires not only new equipment but also the implementation of modern means and methods for training military personnel and in military education institutions.

Part of these tools are the practical simulators. The most common disadvantage found in most practical simulators is the fact that they cannot simulate the full range of the crew's combat functions. In most cases they lack: the practical implementation of activities related to the preparation of ammunition at the fire position (installation of the fuze; setting the fuze function impact or delayed detonation etc.) and activities related to the loading and unloading of the mortar whether a misfire occurs. In addition, training equipment and simulators do not give an accurate notion for the psychological impact that affects the personnel during the use of real ammunition at the firing position and the additional stress accumulated during the firing.

One type of artillery system that is currently in service in the majority of armies are mortars.

In order for a high quality and effective practical, mortar training to be achieved, the development and implementation of a practical simulator is required. The created simulator must not only lower financial expenses but also guarantee a high level of immersion in real combat activities conducted on the firing position during live firing.

Based on the analysis conducted on developed practical simulators for the training of mortar crews in different countries the following basic requirements for the designed simulator can be identified:

- the construction of the simulator must include the basic components that are required for live-firing: mortar, training-practice mortar round, fuze and ignition cartridge;

- to enable the simulator to most accurately mimic the activities performed by the mortar crew during real combat operations;

- the training-practice mine must resemble, as much as possible, its combat counterpart in terms of appearance, weight and dimensions. The abovementioned criteria are

Online ISSN 2256-070X
https://doi.org/10.17770/etr2021vol3.6575

required in order for the round to provide better practical training and to create a true picture of the round's operation;

- the construction of the training-practice mortar round must have simple technological design that incorporates already manufactured elements from its combat counterpart;

- the training-imitational fuze must be able to mark the area where the round has made impact with the ground. The fuze must be unable to cause fire, but at the same time, must still be capable of clearly indicating the area where the round has made impact;

- the training-practice fuze must fiction reliably and have a simple design and reliable action;

- the construction of the training-practice fuze must incorporate a safety mechanism that does not allow detonation before the round is fired;

- the ignition cartridge must resemble the ignition cartridge used in the live round as much as possible in terms of appearance and dimensions;

- the maximum firing distance must be 100 m, allowing the system to be used on firing ranges and training grounds;

- the minimum firing distance must be 20 m, ensuring the safety of the mortar team.

In accordance with the above listed requirements a simulator designed for the training of mortar teams was developed. As one of the elements of the simulator is a reusable training-practice mortar round for short distance engagements.

Analytical calculations were carried out about the required initial velocity of the round and the amount of powder in the ignition cartridge in order for a maximum engagement distance of 100 m.

The next step is an experimental study of the fidelity of analytical models and the correct determination of the amount of powder in the ignition charge.

The analytically determined initial velocity of the round required for it to reach 100 m is 35 m/s.

For an approximate determination of the required amount of smokeless nitroglycerin, ballistic, strip gunpowder, brand NBL-11 (НБЛ – 11) in the ignition cartridge, formula 1 is used [2],[4]:

$$\omega = \sqrt[b]{\frac{V_0}{a}} \qquad (1)$$

where:

ω – mass of the smokeless powder in the ignition cartridge[g];

V_0 – the desired initial velocity for the training-practice mortar round required for maximum distance firing 100 m (the desired initial velocity has a value of 35 m/s) [m/s];

a – coefficient determined by the caliber and mass of the round (for the 82 mm training-practice mortar round the value of this coefficient is 20,601892) [2];

b – degree indicator (for the 82 mm training-practice mortar round the value of this coefficient is 0,60068571) [2].

$$\omega = \sqrt[b]{\frac{V_0}{a}} = \sqrt[0,6006]{\frac{35}{20,602}} = 2,4166$$

The required amount of gunpowder brand NBL-11 (НБЛ–11) calculated via (1) is calculated to be approximately 2,4 g.

Using the calculated amount of gunpowder the ignition cartridge are filled with 2,4 g of gunpowder brand NBL-11 (НБЛ – 11).

II. Experimental Study

2.1. Objective: experimentally determine the required amount of propelling charge required for the 82 mm reusable training-practice mortar in order for the round to reach 100 m.

2.2. Tasks:

- the amount of propelling charge required for reaching a distance of 100 m for the 82mm reusable training-practice mortar round for short distance engagements;

- determining the hit deviation ellipse for the 82 mm reusable training-practice mortar round at a distance of 100 m.

The experimental research was conducted on the artillery and small arms training site "Markovo".

Conditions under which the research was conducted:

- ambient temperature $19^{o} \pm 2^{o}$C; with a relative humidity of 65 ±5%;

- ignition charges were armed with 2,4 g smokeless nitroglycerin, ballistic, strip gunpowder, brand NBL-11 (НБЛ – 11);

- the temperature conditioning of the ignition charges is conducted inside the premises inside the premise of the armory in the cadet's battery at a constant temperature for the period of 24 hours before firing;

- the trial is conducted by firing from a single 82 mm mortar;

- firing is conducted at an elevation angle of 45^{0} for maximum firing distance.

2.3. Procedure for conducting the experimental study

A. Preparation of the weapon system and ammunition

Sequence of activities:

- the bore of the mortar is cleaned from lubricant, carbon and other contaminants before it is fired;

- the mortar is deployed in the firing position;

- the training practice mortar rounds are armed with the ignition cartridges and the charges for the imitational fuze;

- a mortar warm up shot is fired.

B. Carrying out the experimental shooting

The experimental shooting is carried out in the following sequence:

- 10 shots are fired sequentially with training practice mortar rounds;

- after each shot the area where the round has hit is determined and the distance between the hit and the muzzle of the mortar is measured.

2.4. Material supply.

The following material was used to carry out the experimental shootings:

- ignition charges armed with 2,4 g smokeless nitroglycerin, ballistic, strip gunpowder, brand NBL-11 (НБЛ – 11) – 10 (ten) pc.

- charges for the imitation fuze – 10 (ten) pc.

- training-practice mortar rounds – 10 (ten) pc.

- 82 mm mortar;

- tape measure – 25 m.

III. RESULTS FROM THE EXPERIMENTAL STUDY

The results gathered from the experimental study from firing the training-practice mortar rounds, armed with smokeless nitroglycerin, ballistic, strip gunpowder, brand NBL-11 (НБЛ – 11) in the ignition charge, fired from an elevation angle of 45° are presented in table 1.

TABLE 1 RESULTS FROM THE EXPERIMENTAL STUDY GATHERED FROM FIRING THE TRAINING-PRACTICE MORTAR ROUND ARMED WITH SMOKELESS NITROGLYCERIN, BALLISTIC, STRIP GUNPOWDER, BRAND NBL-11 (НБЛ – 11) IN THE IGNITION CHARGE, FIRED FROM AN ELEVATION ANGLE OF 45°

№ fired shot	*Elevation angle*	*Expected hit distance*	*Actual hit distance*	*Error*
	[deg]	[m]	[m]	[%]
1	45°	100	86	-24%
2	45°	100	90	-10%
3	45°	100	97	-3%
4	45°	100	106	+6%
5	45°	100	111	+11%
6	45°	100	115	+15%
7	45°	100	89	-11%
8	45°	100	92	-8%
9	45°	100	103	+3%
10	45°	100	105	+5%
Average hit and error values			99,4	9,6%

The average firing distance is 99,4 m, with an average error from the experimental study results from firing the training practice mortar-round armed with smokeless nitroglycerin, ballistic, strip gunpowder, brand NBL-11 (НБЛ – 11) in the ignition charge, fired from an elevation angle of 45° is 9,6% .

The big axis of the deviation ellipse is 29 m.

IV. STATISTICS HYPOTHESIS CHECKING

The statistics hypothesis can be checked by comparing of the dispersions of the experimental and analytical results [5] [6] [7]. The zero hypothesis is that the dispersion of data, received from the analytical model is commensurable with the dispersion of the experimental data [8].

Formula (2) can be used to check the statistics hypothesis [1]:

$$\chi_0^2 = \frac{SS}{\sigma_0^2} \qquad (2)$$

where:

$SS = \sum_{i=1}^{n}\left(y_{Ei} - \bar{y}_E \right)^2$ - corrected sum of the squares of the experimental investigation data;

$\sigma_0^2 = \frac{1}{n-1}\cdot\sum_{i=1}^{n}\left(y_i - \bar{y} \right)^2$ - dispersion of the analytical model data;

$\bar{y} = \frac{1}{n}\sum_{i=1}^{n} y_i$ - average analytical model data;

$\bar{y}_E = \frac{1}{n}\sum_{i=1}^{n} y_{Ei}$ - average experimental investigation data;

n - data number.

The zero hypothesis is rejected in cases, when $\chi_0^2 > \chi_{\alpha/2;n-1}^2$ or $\chi_0^2 < \chi_{1-\alpha/2;n-1}^2$ [1]. The values of $\chi_{\alpha/2;n-1}^2$ and $\chi_{1-\alpha/2;n-1}^2$ are tabu1lar [1].

The received results are presented in table 2.

TABLE 2 RESULTS OF ZERO HYPOTHESIS CHECKING

№	*α*	χ_0^2	$\chi^2_{(0,025;9)}$	$\chi^2_{(0,975;9)}$
1	0,05	12,24168	23,3366	4,40778

V. CONCLUSIONS

The results presented in table 2 show that the zero hypothesis can be accepted as true and the analytical model can be used for practical calculation of the quantity of powder placed in the ignition cartridge for the reusable training-practice mortar round for firing on short distances.

VI. REFERENCES

[1] D.K. Montgomeri, Planirovanie eksperimenta i analiz dannayh., Leningrad: Sudostroenie, 1980. pp 30 – 35.

[2] H.A. Hristov, Opredelyane na kolichestvoto barut na osnovniya zaryad pri svrah kasi distantsii na strelba s 82 mm batalyonen minomet., Sbornik nauchni trudove na NVU „V. Levski" Chast 1, 2010. Veliko Tarnovo. ISSN 1314-1953.

[3] H.A. Hristov, Ts.G. Tsonev, Uchebno-prakticheska mina za ogneva podgotovka na minohvargachnite razcheti., Godishnik 1/2013 na VA „G.S. Rakovski". Sofiya. ISSN 1312-2991.

[4] H.A. Hristov, Obobshten matematichen model na vrazkata nachalna skorost – energiya,. MATTEH 2012. Shumen. ISSN 1314-3921.

[5] D. Dichev, I. Zhelezarov, R. Dicheva, D. Diakov, H. Nikolova and G. Cvetanov, "Algorithm for estimation and correction of dynamic errors," in 30th International Scientific Symposium Metrology and Metrology Assurance, MMA 2020, Sozopol, Bulgaria, 2020. DOI: 10.1109/MMA49863.2020.9254261

[6] D. Dichev, H. Koev, T. Bakalova and P. Louda, "A model of the dynamic error as a measurement result of instruments defining the parameters of moving objects," Measurement Science Review, vol. 14, no. 4, pp. 183-189, 2014. DOI: 10.2478/msr-2014-0025

[7] D. Dichev, H. Koev, T. Bakalova and P. Louda, "A measuring method for gyro-free determination of the parameters of moving objects," Metrology and Measurement Systems, vol. 23, no. 1, pp. 107-118, 2016. DOI: 10.1515/mms-2016-0001

[8] L. Lazov, N. Angelov, E. Teirumnieks, Method for Preliminary Estimation of the Critical Power Density in Laser Technological Processes, Proceedings of the 12th International Scientific and Practical Conference, Rezekne, Latvia, 2019, Volume III, Pages 129-133, DOI: 10.17770/etr2019vol3.4140

Environment. Technology. Resources. Rezekne, Latvia
Proceedings of the 13th International Scientific and Practical Conference. Volume 3, 49-53

Geometric Synthesis of Involute Planetary Gears with Connected Gear Wheels of Type 2K-H

Genadi Cvetanov
Department of Mechanical and Precision Engineering
Technical University of Gabrovo
Gabrovo, Bulgaria
gencvet@tugab.bg

Tsanko Karadzhov
Department of Mechanical and Precision Engineering
Technical University of Gabrovo
Gabrovo, Bulgaria
karadjov_st@abv.bg

***Abstract* - Based on the basic law of flat interlocking, the paper considers a possibility of increasing the gear ratio of low module involute cylindrical planetary gears by using asymmetric tooth profile for the purposes of measuring devices. An example of the synthesis of such reduction gearing by optimal choice of asymmetry between the profiles and Possibility of generation III is presented. Also presented is a planar matching of the unconditional existence areas in the field of independent coefficients of instrument displacement by the straight optimization method and pre-set qualitative indicators of the gearing.**

Keywords* - *planetary involute cylindrical tooth gears, asymmetric profile

I. INTRODUCTION

With large gear ratios in precision engineering gears with combined gearing – internal and external are used. These are the epicyclical gear drives, of which the most widely spread is the kinematic scheme of 2K-H involute cylindrical gear with symmetrical tooth profile and different number of steps [1] [2] [3].

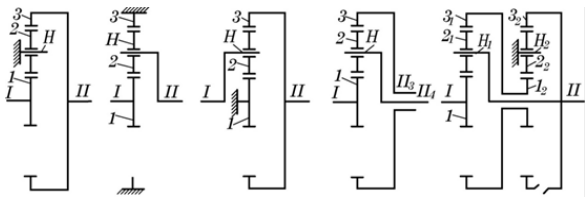

Fig. 1. Kinematic schemes of variants of gear 2K-H

According to fig. 1, five basic kinematic schemes of an epicyclical mechanism with geometrically connected gears are possible. Gear axes 1 and 3 coincide with the mutual geometric axis and are called basic units of the mechanism and the corresponding gears are called central. The gear ratio is the ratio of the angular velocities of the two units – 1 and 3. Gear 2 engaged with units 1 and 3 does not affect the gear ratio from shaft I to shaft II and is called a satellite wheel.

The carrier that carries the satellites can serve as the main unit and in fig. 1 it is denoted by the letter H. In this case the axis of gear 2 moves in space and the gear is called planetary. Gear mechanism in which at least one axis is mobile in space is called a planetary gear mechanism.

When the epicyclical gear mechanism has two degrees of freedom it is called "differential", and with one degree of freedom – "planetary". Combination of internal and external gearing in one gear mechanism has a number of advantages, some of which are:

- expanding the possibilities of planar gearing by possible choice of three coefficients of displacement and heights of the tooth profiles;
- increased load capacity of the gear at high torque;
- obtaining gears with larger gearing angles and higher frontal overlap coefficient than those realized only with external gearing at the same gear ratio;
- compactness of construction and manufacturability in the process of manufacturing the gear wheels.

II. EXPOSITION

Depending on the specific implementation 2K – H uniaxial gears can be with or without connected wheels [4] [5]:

$$m_{t_{1,2}} = \frac{z_2 \pm z_1}{\cos \alpha_{tw_{12}}} = m_{t_{3,4}} = \frac{z_4 \pm z_3}{\cos \alpha_{tw_{34}}}$$

Online ISSN 2256-070X
https://doi.org/10.17770/etr2021vol3.6643

$$m^*_{t_{1,2}} = \frac{z_2 \pm z_1}{\cos \alpha^*_{tw_{12}}} = m^*_{t_{3,4}} = \frac{z_4 \pm z_3}{\cos \alpha^*_{tw_{34}}} \quad (1)$$

where $m_{t1,2}$ and $m_{t3,4}$ are the front modules of the coupled gears;

z_1, z_2, z_3 and z_4 – the number of teeth of the gear wheels;

$\alpha_{tw1,2}$ and $\alpha_{tw3,4}$ – engagement angles between the coupled gear wheels for the "working part" of the tooth profile;

$\alpha^*_{tw1,2}$ and $\alpha^*_{tw3,4}$ – engagement angles between the coupled gear wheels for the "non-working part" of the tooth profile;

In case of an asymmetric tooth profile the engagement angles are determined depending on the type of formation and the following transcendental dependencies:

$$\begin{cases} inv\alpha_{tw_{1,2}} + inv\alpha^*_{tw_{1,2}} = \dfrac{2.(x_2 \pm x_1).(tg\alpha + tg\alpha^*)}{z_2 \pm z_1} + \\ \qquad + inv\alpha_t + inv\alpha^*_t \\ \dfrac{d_{tb_{1,2}}}{cos\ \alpha_{tw_{1,2}}} = \dfrac{d^*_{tb_{1,2}}}{cos\ \alpha^*_{tw_{1,2}}} \end{cases}$$

$$\begin{cases} inv\alpha_{tw_{3,4}} + inv\alpha^*_{tw_{3,4}} = \dfrac{2.(x_4 \pm x_3).(tg\alpha + tg\alpha^*)}{z_4 \pm z_3} + \\ \qquad + inv\alpha_t + inv\alpha^*_t \\ \dfrac{d_{tb_{3,4}}}{cos\ \alpha_{tw_{3,4}}} = \dfrac{d^*_{tb_{3,4}}}{cos\ \alpha^*_{tw_{3,4}}} \end{cases} \quad (2)$$

where $d_{tb1,2}$ and $d_{tb3,4}$ are the diameters of the main circles in the frontal section for the "working part" of the tooth profile;

$d^*_{tb1,2}$ and $d^*_{tb3,4}$ - diameters of the main circles in the frontal section for the "nonworking part" of the tooth profile;

x_1, x_2, x_3 and x_4 – the displacement coefficient of the tool for the respective gear wheels. The value of the displacement coefficient of the wheel with internal teeth is assumed to be the same as the displacement coefficient of the equivalent wheel with external teeth.

In this model of kinematic gears there is no restriction in the choice of instrument parameters and gearing module, which make the epicyclical mechanisms attractive for manufacturing when using a method other than standard one - filament erosion.

uniaxial 2K – H gears with connected wheels with asymmetric profile of the teeth (fig.2).

In this gear model the satellite wheel 2 is in external engagement with central wheel 1 and internal wheel 3. If the gear is driven by the central wheel clockwise, the engagement of wheel 1 and 2 is along the active length of the line $B_1^*B_2^*$ with profile angle $\alpha_w{}^*_{1\text{-}2}$.. At the same time the point of contact of wheels 2-3 is along the engagement line B_2B_3 with profile angle $\alpha_{w2\text{-}3}$

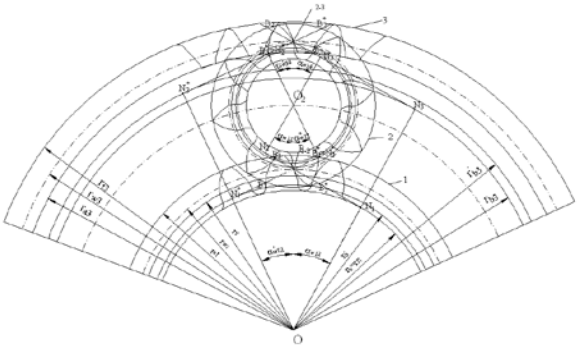

Fig. 2. Computational scheme of planetary gear with asymmetric profile of the teeth

Based on the basic law, the engagement angles for the two parts of the composite profile are determined:

$$\begin{cases} \text{inv}\alpha_{tw_{1,2}} + \text{inv}\alpha^*_{tw_{1,2}} = \dfrac{2.(x_2 + x_1).(\text{tg}\alpha + \text{tg}\alpha^*)}{z_2 + z_1} + \\ \qquad + \text{inv}\alpha_t + \text{inv}\alpha^*_t \\ \dfrac{d_{tb_{1,2}}}{\cos \alpha_{tw_{1,2}}} = \dfrac{d^*_{tb_{3,4}}}{\cos \alpha^*_{tw_{1,2}}} \end{cases}$$

$$\begin{cases} \text{inv}\alpha_{tw_{2,3}} + \text{inv}\alpha^*_{tw_{2,3}} = \dfrac{2.(x_3 - x_2).(\text{tg}\alpha + \text{tg}\alpha^*)}{z_3 - z_2} + \\ \qquad + \text{inv}\alpha_t + \text{inv}\alpha^*_t \\ \dfrac{d_{tb_{2,3}}}{\cos \alpha_{tw_{2,3}}} = \dfrac{d^*_{tb_{2,3}}}{\cos \alpha^*_{tw_{2,3}}} \end{cases} \quad (3)$$

In the case of asymmetric tooth profile it is necessary to take into account the driving unit because it affects the alignment condition [6] [7] [8]. The use of the standard dependency for symmetric profile is possible when the drive is performed by satellite wheel 2:

$$\begin{cases} \dfrac{\cos \alpha_{tw_{1,2}}}{\cos \alpha_{tw_{2,3}}} = \dfrac{z_1 + z_2}{z_3 - z_2} \\ \dfrac{\cos \alpha^*_{tw_{1,2}}}{\cos \alpha^*_{tw_{2,3}}} = \dfrac{z_1 + z_2}{z_3 - z_2} \end{cases}$$

$$\begin{cases} \dfrac{\cos \alpha^*_{tw_{1,2}}}{\cos \alpha_{tw_{2,3}}} = \dfrac{z_1 + z_2}{z_3 - z_2} \cdot \dfrac{\cos \alpha^*_t}{\cos \alpha_t} \\ \dfrac{\cos \alpha_{tw_{1,2}}}{\cos \alpha^*_{tw_{2,3}}} = \dfrac{z_1 + z_2}{z_3 - z_2} \cdot \dfrac{\cos \alpha_t}{\cos \alpha^*_t} \end{cases} \quad (4)$$

The quality indicators of the planetary gears with asymmetric profile depend on the parameters of the tool, its coefficient of displacement and the parameter q:

$$q = z_3 - z_2 - 2.z_1 \quad (5)$$

When selecting the number of teeth of the gear wheels, so that the parameter q has a value of zero the following correlations for the alignment condition of the gear are obtained:

$$\left|\begin{array}{l}\dfrac{\cos\alpha^{*}_{tw_{1,2}}}{\cos\alpha_{tw_{2,3}}}=\dfrac{\cos\alpha^{*}_{t}}{\cos\alpha_{t}}\\[2ex]\dfrac{\cos\alpha_{tw_{1,2}}}{\cos\alpha^{*}_{tw_{2,3}}}=\dfrac{\cos\alpha_{t}}{\cos\alpha^{*}_{t}}\end{array}\right. \qquad (6)$$

After determining the engagement angles for the two parts of the composite profile a method for calculating the vertex circle of the wheel is selected. Irrespective of the adopted method of making the wheels, the following correlation should always be observed:

$$d^{12}_{a2}=d^{23}_{a2} \qquad (7)$$

where d^{12}_{a2} is diameter of the vertex circle for wheel 2, but determined by external meshing with wheel 1;

d^{23}_{a2} - diameter of vertex circle for wheel 2, but determined by internal meshing with wheel 3;

With this method of forming the profile the radial clearance at external and internal meshing is kept constant, and the standard method of checking the qualitative indicators is fully applicable. The checking of the radial clearance ratio is performed only between the heel circle of the wheel with internal teeth and the vertex circle of the satellite (c_{23}). In the case of a negative value of the coefficient c_{23}, a tool for manufacturing the wheel with internal teeth with increased coefficient of the tooth height is selected.

Thus, the proposed approach for making the gear wheels with asymmetric profile has the following advantages:

- the teeth of the gear wheels have different heights at different displacement coefficients;
- the involute profile of the teeth with internal gearing is entirely used, achieving higher values of the frontal overlapping;
- for the wheels with external gearing a tool with standard heights is used;

The asymmetric profile of the teeth makes it possible to obtain an involute cylindrical gear which has a constant gear ratio, but has different quality indicators when reversing the movement direction [9] [10].

One of the quality indicators of particular interest is the coefficient of the pitch point displacement of gearing**δ**, because the asymmetry and its possibilities of generation make it possible to influence its value. This makes it possible to obtain gears with hitherto unknown quality indicators.

For the case of pitch point displacement Σ shown in fig. 3 a) and b), the displacement coefficients $\delta_{1,2}$ and $\delta^{*}_{1,2}$ are determined successively for the two parts of the tooth:

$$\left|\begin{array}{l}\delta_{1,2}=\cos\alpha_{t}\cdot\left[\dfrac{z_{1,2}\cdot\left(\mathrm{tg}\alpha_{ta_{1,2}}-\mathrm{tg}\alpha_{tw}\right)}{2}-\pi\right]\\[2ex]\delta^{*}_{1,2}=\cos\alpha^{*}_{t}\cdot\left[\dfrac{z_{1,2}\cdot\left(\mathrm{tg}\alpha^{*}_{ta_{1,2}}-\mathrm{tg}\alpha^{*}_{tw}\right)}{2}-\pi\right]\end{array}\right. \qquad (8)$$

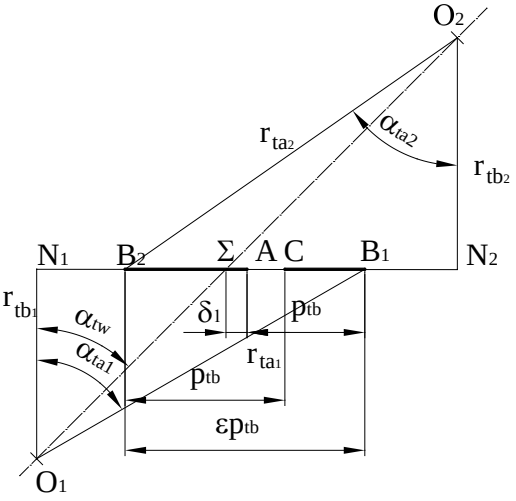

Fig. 3. a) at the base of the tooth of wheel – 1 and the head of the tooth of wheel - 2

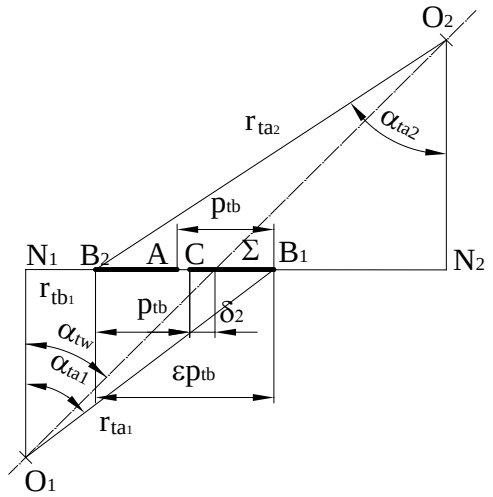

Fig. 3 b) at the base of the tooth of wheel – 2 and the head of the tooth of wheel – 1

The asymmetric tooth profile hasn't been considered in this respect, as well as the effects that can be achieved with it.

From fig 3 a) and b) and from dependency (8) it follows that the asymmetry of the profile leads to obtaining involute cylindrical gears that has "prediction „and "addiction" of the pitch point.

Therefore the asymmetry of the profile allows:

- to realize gears with different quality indicators when reversing movement direction;
- to achieve different load capacity of the gear wheels with and without revering the direction of movement;
- to design a gear that takes into account the stiffness of the meshing when reversing, and the actual frontal overlapping coefficient of the profiles;

The unconditional existence area makes possible the realization of one gear with preset extreme quality indicators in the field of different independent variables. For the purposes of this work, the following values of the quality indicators are accepted as limiting:

- $S^{\Sigma}_{ta1,2} = S_{ta1,2} = 0$ – thickness of the teeth on the vertex circles, determined by the milling method;
- $\varepsilon=1,0$ и $\varepsilon^*=1,0$ – frontal overlapping coefficients when reversing movement direction;
- $|\theta_a|=6,0$; $|\theta^*_a|=6,0$; $|\theta_e|=6,0$; $|\theta^*_e|=6,0$ – coefficient of specific sliding between the profiles;
- c=0 – radial clearance between the wheel and the gear;

The conditional area of existence determines a certain limit for the quality indicators, but only above a certain extreme value. Therefore, the unconditional area of existence contains in itself a number of conditional areas, offering the possibilities for realization of such gears.

In such a synthesis approach the displacement coefficient of the internal gear wheel (x_3) is obtained as a dependent variable:

$$x_3 = x_2 + \frac{\left(\text{inv}\alpha_{tw23} + \text{inv}\alpha^*_{tw23} - \text{inv}\alpha_t - \text{inv}\alpha^*_t\right)\left(z_3 - z_2\right)}{2.\left(\text{tg}\alpha + \text{tg}\alpha^*\right)} \quad (9)$$

To illustrate the unconditional areas of existence, consider a 2 K-H planetary gear with parameters: m=1mm, $\alpha=20°$, $\alpha^*=30°$, $h^*_a=1$, $h^*_f=1.25$, number of teeth of the gear wheels - $z_1=30$, $z_2=20$, $z_3=70$, angle of inclination of the teeth $\beta=0$ and open profile milling method, with and without reversing the direction of movement.

The geometric interpretation of contour lines with constant magnitude of the coefficient x_3 is inclined straights relative to the displacement coefficients x_1 and x_2 (fig. 4 and 5). The contour lines of constant coefficient x_3 coincide with contour lines of coefficient x_1 only in the case of symmetric profile.

The slope of the contour lines (isolines) x_3 is determined by the set asymmetry between the composite profiles. This allows the cross section of the spatial area of existence to be considered as a plane, where $x_3=x_1$ is satisfied along the ordinate of the unconditional area.

Fig 4 and 5 show the unconditional areas of existence of planetary gear depending on the drive mechanism. They are valid when involute corresponding to profile angle α_t is selected for working angle of the gear with external gearing.

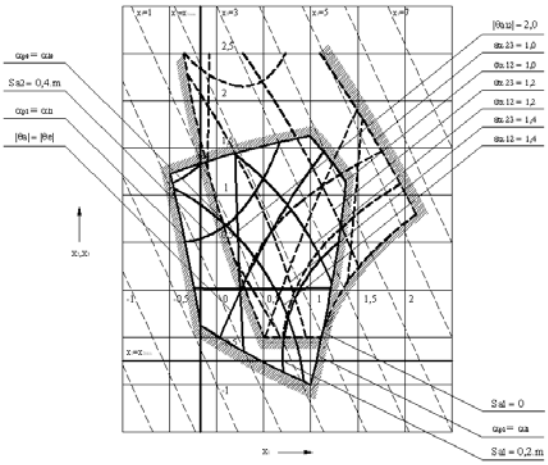

Fig. 4. Unconditional area of existence of a planetary gear with asymmetric profile of the teeth, driven by wheel 1 or 3

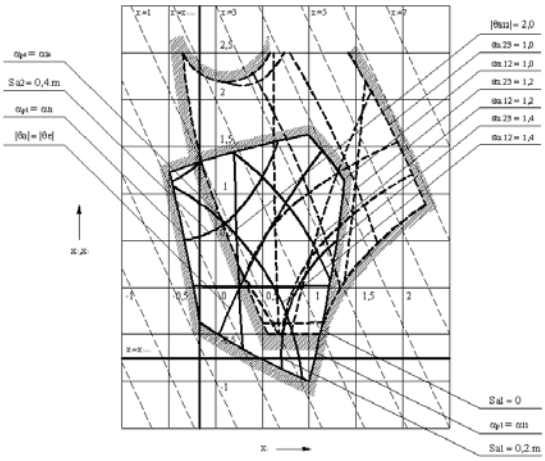

Fig. 5. Unconditional area of existence of a planetary gear with asymmetric tooth profile driven by satellite wheel 2

When reversing the direction of motion of the planetary mechanism, the areas of existence have another axiomatic form.

If we adopt the concept of “complex” unconditional area of existence in planetary gears with asymmetric tooth profile, we find that there are two such areas which depend on the driving mechanism. The two complex areas are a consistent combination of the qualitative indicators of engagement with and without reversing of the direction of movement.

Fig.6 shows a spatial solid model of 2K-H gear designed by CAD/CAM system of company “Autodesk-Inventor Professional”

Based on the presented geometric synthesis of planetary involute cylindrical gears with asymmetric tooth profile, it is possible to achieve large gear ratios. This is possible by reducing the number of teeth of the satellite wheel and selecting an appropriate asymmetry and drive of the gear mechanism.

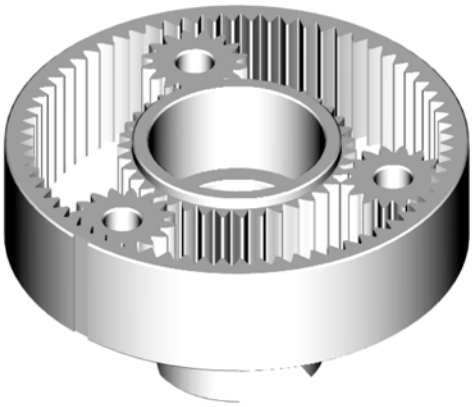

Fig. 6. Solid model of 2K-H gear with asymmetric tooth profile and geometrically connected gear wheels

III. CONCLUSION

The traditional approach in geometric synthesis of 2K-H gears with asymmetric tooth profile with and without connected gear wheels and combined gearing in different possibilities of generation is presented. Also presented is the necessary condition for alignment.

The main qualitative indicators are given and the pitch point displacement is defined for the different possibilities of generation, which allows the creation of sub-polar and post-polar gears with increased efficiency because these gears are used in measuring devices.

A field of the independent displacement coefficients of the initial contour is defined, which allows the spatial unconditional areas of existence of the 2K-H gear to be depicted as a plane.

IV. REFERENCES

[1] E. B. Vulgakov, Teoriya evolyventayh zubchatayh peredach, Moskva: Mashinostroenie, 1995.

[2] E. B. Vulgakov, Soosnaye zubchataye peredachi. Spravochnik, Moskva: Mashinostroenie, 1987.

[3] Spravochnik po geometricheskomu raschetu evolyventayh zubchatayh i chervyachnayh peredach, I. A. Bolotovskogo ed., Moskva: Mashinostroenie, 1986.

[4] S. Simeonov and G. Tsvetanov, "Theorem for reversing the direction of the involute cylindrical gears with asymmetric profile of teeth," *Mechanics of machines*, no. 63, 2005, ISSN 0861-9727

[5] S. Simeonov and G. Tsvetanov, "Theorem for reversing the direction of the involute cylindrical gears with asymmetric profile of teeth," *Proceedings of the Technical University of Gabrovo*, no. 32, 2005, ISSN 1310-6686

[6] D. Dichev, H. Koev, T. Bakalova and P. Louda, "A model of the dynamic error as a measurement result of instruments defining the parameters of moving objects," *Measurement Science Review*, vol. 14, no. 4, pp. 183-189, 2014, DOI: 10.2478/msr-2014-0025

[7] D. Dichev, H. Koev, T. Bakalova and P. Louda, "An algorithm for improving the accuracy of systems measuring parameters of moving objects," *Metrology and Measurement Systems*, vol. 23, no. 4, pp. 555-565, 2016, DOI: 10.1515/mms-2016-0041

[8] L. Lazov, E. Teirumnieks, N. Angelov and E. Teirumnieka, "Methodology for Automatic Determination of Contrast of Laser Marking for Different Materials," in *Proceedings of the 12th International Scientific and Practical Conference*, Rezekne Latvia, 2019, DOI: 10.17770/etr2019vol3.4143

[9] X. Zhao and A. Vacca, "Formulation and optimization of involute spur gear in external gear pump," *Mechanism and Machine Theory*, vol. 117, pp. 114-132, November 2017, DOI: 10.1016/j.mechmachtheory.2017.06.020

[10] C. G. Conev and K. S. Davidov, "Analytical Model For Approximately Calculating Of The Second Frequency Of Cross Vibrations For Complex Shape Barrel Of The Small ARM," in *The 21st International Conference The Knowledge – Based Organization*, Sibiu Romania, 2015, ISSN 1843-6722

Environment. Technology. Resources. Rezekne, Latvia
Proceedings of the 13th International Scientific and Practical Conference. Volume 3, 54-57

Consequences of the Basic Law of Flat Interlocking of Involute Cylindrical Gears

Genadi Cvetanov
Department of Mechanical and Precision Engineering
Technical University of Gabrovo
Gabrovo, Bulgaria
gencvet@tugab.bg

Tsanko Karadzhov
Department of Mechanical and Precision Engineering
Technical University of Gabrovo
Gabrovo, Bulgaria
karadjov_st@abv.bg

***Abstract* - Three consequences based on the basic law of the flat interlocking have been determined that allow the generation of asymmetric tooth profile on different poloidal circles. Gears with asymmetric profile are used in both mechanical engineering and measuring devices. Qualitative indicators of engagement that cannot be accomplished with a symmetric profile have been developed. A specific example of generation III has been presented. The qualitative indicators of engagement, which are invariant to the parameters of the tool, have been improved.**

Keywords - possibilities of generation, involute cylindrical gears, asymmetric profile

I. INTRODUCTION

The asymmetric profile of the teeth relates to the special gear transmissions in mechanical engineering for the following reasons:

- use of non-standard tool to produce the toothed wheels – by the method of centroid wrapping or copying in view of the lack of interference and clipping of the work piece [1] [4];
- a relatively small number of examples in literature for gears with asymmetric profile of the teeth [2] [3];
- a lack of systematic approach in considering the asymmetry of the tooth of the gear and the output contour [1] [2] [3] [4];
- adoption of asymmetric modification of the profile only for non-reversible gearings [2];
- adoption of asymmetric profile creates difficulties of computational nature in determining the parameters and the qualitative indicators of a gear transmission [3] [4];
- incomplete use of the accumulated stock of knowledge on the symmetrical profile of teeth that can with certain conditions be extrapolated onto the asymmetric profile.

II. EXPOSITION

Low-module gears are one of the main components in devices. The quality and reliability of these components determine the accurate and reliable operation of the whole device.

The specific requirements and conditions of operation have separated the small-module gears in a separate group for which the theoretical and experimental data obtained for large and medium module gears are not applicable.

The lack of sufficient information about the possibilities and accuracy in manufacturing gears with asymmetric tooth profile makes their implementation quite difficult.

In this regard, the investigation of small-module involute cylindrical gears with an asymmetric tooth profile is a pressing task of our industry.

Therefore, there is a need for development of a system for calculation of asymmetric profile without using special geometric parameters, which will allow for these gears to be widely used in mechanical and precision engineering [5] [6].

When the requirements for the gear cannot be satisfied by the symmetrical profile, asymmetric modification can be adopted and reversible or non-reversible gear with different from the hitherto known qualitative indicators can be obtained [7].

The basic law of the flat engagement in involute cylindrical gears with asymmetric profile is derived on the basis of the theorem for reversing the direction of the movement [6, 7] and allows deriving the following consequences:

Online ISSN 2256-070X
https://doi.org/10.17770/etr2021vol3.6576

Consequence I:Equal thickness of the teeth of the jointly working wheels of the gear along the poloid circle are obtained within one complete pitch angle ($2.\pi/z$) – Possibility I for generation.

This approach assumes that all variables are known in the following transcendental system:

$$\begin{cases} \text{inv}\alpha_{tw} + \text{inv}\alpha^*_{tw} = \dfrac{2.(x_2 \pm x_1).\left(\text{tg}\alpha + \text{tg}\alpha^*\right)}{z_2 \pm z_1} + \text{inv}\alpha_t + \text{inv}\alpha^*_t \\ \dfrac{d_{tb}}{\cos\alpha_{tw}} = \dfrac{d^*_{tb}}{\cos\alpha^*_{tw}} \end{cases} \quad (1)$$

where:

α_{tw} and α^*_{tw} are the angles of engagement in the front section;

α_t and α^*_t – profile angles of the tool in the front section;

x_1 and x_2 – coefficient of tool displacement for the gear wheels as the internal gearing is assumed to be the equivalent wheel with external teeth.

In this correlation the „+" sign refers to external gearing while „-„ sign refers to internal gearing.

It is solved with respect to the unknown angles of engagement α_{tw} and α^*_{tw}:

$$\alpha_{tw(n+1)} = \alpha_{tw(n)} - \frac{\text{inv}\alpha_{tw(n)} + \text{inv}\left(\arccos\left(\dfrac{\cos\alpha^*_t}{\cos\alpha_t}.\cos\alpha_{tw(n)}\right)\right)}{\text{tg}^2\alpha_{tw(n)} + \text{tg}^2\left(\arccos\left(\dfrac{\cos\alpha^*_t}{\cos\alpha_t}.\cos\alpha_{tw(n)}\right)\right)} +$$

$$+ \frac{\left\{\left[2.(x_2 \pm x_1).(\text{tg}\alpha + \text{tg}\alpha^*)/(z_2 \pm z_1)\right] + \text{inv}\alpha_t + \text{inv}\alpha^*_t\right\}}{\text{tg}^2\alpha_{tw(n)} + \text{tg}^2\left(\arccos\left(\dfrac{\cos\alpha^*_t}{\cos\alpha_t}.\cos\alpha_{tw(n)}\right)\right)} \quad (2)$$

What is important with this possibility of generation is that the sufficient condition for equality of inter axis distances is reduced to the following:

$$\frac{\cos\alpha_t}{\cos\alpha_{tw}} = \frac{\cos\alpha^*_t}{\cos\alpha^*_{tw}} \quad (3)$$

From correlation (3) it follows that this possibility of generation has the following disadvantages (fig.1):

- the profile angles of the tool α_t и α^*_t must be known in advance;
- when a large difference between the profile angles is used, the height of the tool is decreased;
- the full form of the transcendental system (1) is not used;

there is wide range of data about gears with symmetric profile, which cannot be extrapolated directly onto the asymmetric profile;

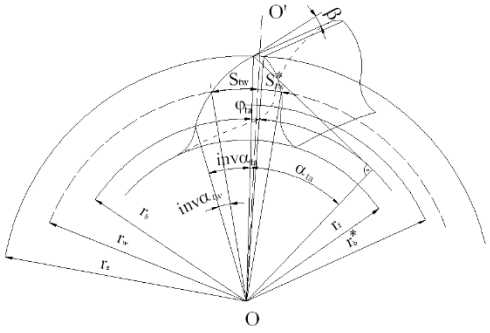

Fig. 1. General form of the tooth profile for possibility I of generation

All these disadvantages are eliminated by using a new option in the synthesis, which is determined by the following *Consequence II*: *The asymmetric gear profile can be implemented with a single tool by the method of centroid wrapping*.

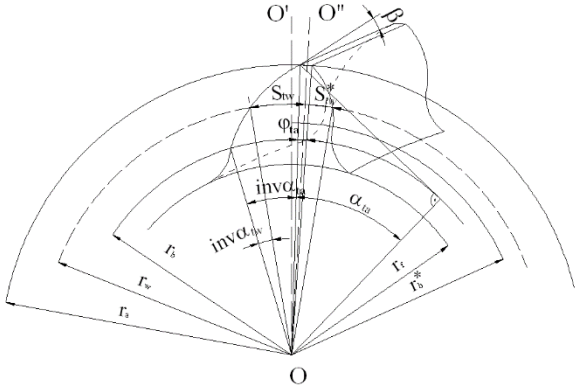

Fig. 2. Difference between the initial symmetry axis OO' and the new axis OO" for Possibility II of generation in the front section of the wheel

Based on consequence II of the basic law of engagement, two new approaches are offered for solving the transcendental system (1). For the geometrical interpretation of these two possibilities it is assumed that the full form of the transcendental system (1) is implemented, which implies that the asymmetry between the profiles is expressed by the basic circles and not only by the difference between the profile angles of the tool. This implies a difference in the "initially" accepted axis OO'. Fig. 2 shows the difference between the "initial" symmetry axis OO' and the "new" axis - OO" in the front section of the wheel. Hypothetically, we will assume that we can set the position of this new axis OO".

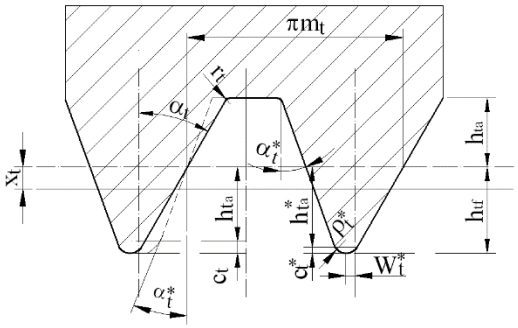

Fig. 3. Congruent output contour for possibility II of generation of asymmetric gear profile in the front section

It is assumed that the profile angles of the output contour α и α* in the normal cross-section (fig.3) are known in advance. Based on the transcendental system (1) the engagement angle α^*_{tw} is determined by the method of successive approximations [8], until the desired accuracy:

$$\alpha^*_{tw(n+1)} = \alpha^*_{tw(n)} - \frac{(z_2 \pm z_1).\left(inv\alpha_{tw} + inv\alpha^*_{tw(n)} - inv\alpha - inv\alpha^*\right)}{tg^2\alpha^*_{tw(n)}} + \frac{2.(x_2 \pm x_1).\left(tg\alpha + tg\alpha^*\right)}{tg^2\alpha^*_{tw(n)}} \quad (4)$$

The profile angle of the tool (α_t*) in the front section is determined by the sufficient condition of the basic law of engagement in asymmetric profile [9]. The general form of that other sequence of solving the system is:

$$\begin{cases} inv\alpha_{tw} = \dfrac{2.(x_2 \pm x_1).tg\alpha}{z_2 \pm z_1} + inv\alpha_t \\ \dfrac{d_{tb}}{\cos\alpha_{tw}} = \dfrac{d^*_{tb}}{\cos\alpha^*_{tw}} \\ inv\alpha^*_{tw} = \dfrac{2.(x_2 \pm x_1).\left(tg\alpha + tg\alpha^*\right)}{z_2 \pm z_1} + inv\alpha_t + inv\alpha^*_t - inv\alpha_{tw} \end{cases} \quad (5)$$

Apart from this variant of solution, the transcendental system (1) offers a third possibility for the same initial assumptions, but in a different sequence.

The engagement angle α^*_{tw} is determined based on the ratio of the main circles, which is known in advance:

$$\alpha^*_{tw} = \arccos\left(\frac{d^*_b}{d_b}\cos\alpha_{tw}\right) \quad (6)$$

The profile angle of the tool α^*_t, is determined depending on the correlation on slack-free gearing (1) as a dependent variable until the desired accuracy:

$$\alpha^*_{t(n+1)} = \alpha^*_{t(n)} - \frac{(z_2 \pm z_1).\left(inv\alpha_{tw} + inv\alpha^*_{tw} - inv\alpha_t - inv\alpha^*_{t(n)}\right)}{2.(x_2 \pm x_1).\cos^2\alpha^*_{(n)} + (z_2 \pm z_1).tg^2\alpha^*_{t(n)}} + \frac{2.(x_2 \pm x_1).\left(tg\alpha + tg\alpha^*_{(n)}\right)}{2.(x_2 \pm x_1).\cos^2\alpha^*_{(n)} + (z_2 \pm z_1).tg^2\alpha^*_{t(n)}} \quad (7)$$

The engagement angle α^*_{tw} relative to axis OO' is determined in accordance with correlation (3).

$$\begin{cases} inv\alpha_{tw} = \dfrac{2.(x_2 \pm x_1).tg\alpha}{z_2 \pm z_1} + inv\alpha_t \\ \cos\alpha^*_{tw} = \dfrac{d^*_{tb}}{d_{tb}}\cos\alpha_{tw} \\ inv\alpha^*_{tw} + inv\alpha_{tw} = \dfrac{2.(x_2 \pm x_1).\left(tg\alpha + tg\alpha^*\right)}{z_2 \pm z_1} + inv\alpha_t + inv\alpha^*_t \end{cases} \quad (8)$$

Based on this other sequence in solving transcendental correlation (3), the following Consequence III is reached: The synthesis of gears with asymmetric profile allows optimizing of the engagement of gears with symmetric profile [10].

Such optimization of the asymmetric profile based on the basic law of engagement has been implemented for output involute cylindrical gear with external engagement and the following parameters of the output contour: m=1mm, α=α*=20°, h^*_a=1, h^*_f=1,25, displacement of the contour $x_1=x_2$=0,5, number of teeth of wheel 1 of gear z_1=20, u=1.5, β=0 and an open profile milling method. The data about the main qualitative indicators and comparison with the output symmetric profile are given in table 1 [11].

As a basic parameter for the optimization (Table 1) the criterion of maximum front overlap ratio ε_α=max. One optimal variant has been determined without clipping at integer value of α*. This possibility of solving obtains increase of the front overlap ratio from ε_α=1,33 for symmetric profile up to ε^*_α=1,44 for asymmetric profile – possibility III.

This new optimization procedure, proposed for the first time by the authors, is graphically interpreted in the field of independent coefficients of displacement of the tool and is a two-dimensional representation of a spatial area. This is achieved through the new optimization procedure which allows a finite number of iterations to reach the required parameters of the output contour (fig.4).

This proposed new possibility III of generation has the following advantages:

- uses the available data for symmetric profile;
- allows synthesis of asymmetric profile, where the slack-free engagement is achieved relative to an axis different from the initial one;
- the limitation of the tool is eliminated, while the profile angle α* varies within the accepted proportionality between the two basic (generating) circles;

Gear	Angles of the contour for optimized profile	Thickness of the teeth along the top circles	Overlap ratio	Specific slipping
Symmetric	$\alpha^* = 20°$	$Sa_1 = 0,62$ $Sa_2 = 0,70$	$\varepsilon_\alpha = \varepsilon^*_\alpha = 1,33$	$\lvert\theta_a\rvert=1,21$ $\lvert\theta_e\rvert=1,17$
Asymmetric III	$\alpha^* = 15°$	$Sa_1 = 0,67$ $Sa_2 = 0,76$	$\varepsilon^*_\alpha=1,44$	$\lvert\theta^*_a\rvert=2,05$ $\lvert\theta^*_e\rvert=1,74$

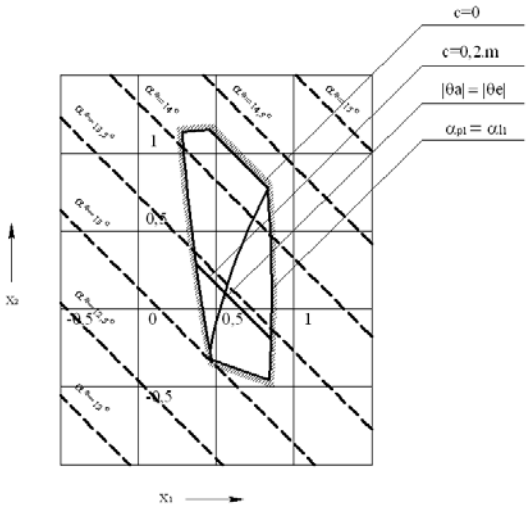

Fig. 4. Unconditional range of existence of involute cylindrical gear with asymmetry factor 1,0368 and guaranteed front overlap ratio ε_α>1,4 through the whole range

From correlation (5) and (8) it follows, that possibility III for synthesis does not change the necessary and sufficient condition but complements, those by setting them in the context of the Basic law of interlocking. Therefore, the involutes generated through possibility I are equidistant to those generated through possibility III. Compared to possibility I for synthesis, possibility III offers another sequence for solving the transcendental system (1), which is a conversion of the classic theory of tooth engagement and creation of new gears with hitherto unknown qualitative and strength parameters.

III. Conclusion

Three consequences of the basic law of gear interlocking have been defined and proved, which presupposes different possibilities of generation and geometric synthesis of involute gearing with asymmetric profile of the teeth with different starting poloids of the gear wheels, as well as various improved qualitative indicators of the tooth engagement which is impossible to achieve if the teeth have symmetric profile.

The existence of three possibilities of generation of asymmetric tooth profile was proven, providing different qualitative and strength parameters at equal initial variables of the synthesis, which has been shown by example of optimization of a gear with asymmetric profile of the teeth according to the criterion of maximum front overlap ratio εα=max.

A new optimization procedure has been obtained and geometrically presented, allowing geometric synthesis of involute cylindrical gears with symmetric and asymmetric profiles of the teeth according to pre-set qualitative indicators through Possibility III of generation, which provides equidistant profiles at variable parameters of the tool.

IV. References

[1] E. B. Vulgakov, Soosnyye zubchatyye peredachi – Spravochnik, Moskva: Mashinostroyeniye, 1987.

[2] E. B. Vulgakov, Teoriya evol'ventykh zubchatykh peredach, Moskva: Mashinostroyeniye, 1995.

[3] E. B. Vulgakov, Zubchatyye peredachi s uluchshennymi svoystvami – Obobshchennaya teoriya i proyektirovaniye, Moskva: Mashinostroyeniye, 1975.

[4] E. B. Vulgakov and V. M. Ananyev, "Avtomatizirovannoye proyektirovaniye soosnoy peredachi," *Vestnik mashinostroyeniya*, no. 5, 1986.

[5] D. Dichev, R. Miteva, I. Zhelezarov and D. Diakov, "A model of the dynamic error in the devices for measuring moving objects parameters," in *45th International Conference on Application of Mathematics in Engineering and Economics, AMEE 2019*, Sozopol, 2019, DOI: 10.1063/1.5133593

[6] D. Dichev, F. Kogia, H. Nikolova and D. Diakov, "A Mathematical Model of the Error of Measuring Instruments for Investigating the Dynamic Characteristics," *Journal of Engineering Science and Technology Review*, vol. 11, no. 6, pp. 14-19, 2018, DOI: 10.25103/jestr.116.03

[7] C. G. Conev and K. S. Davidov, "Investigation Of The Influence On Additional Mounted On Barrel Edge Concentrated Mass Over The Grouping Of Gunshot Hits In Single Shooting," in *21st International Conference The Knowledge – Based Organization*, Sibiu Romania, 2015, ISSN 1843-6722

[8] I. N. Bronshteyn and K. A. Semendyayev, Spravochnik po matematike dlya inzhenerov i uchashchikhsya VTUZOV, Moskva: Nauka, 1986.

[9] S. Simeonov and G. Tsvetanov, "Theorem for reversing the direction of the involute cylindrical gears with asymmetric profile of teeth," Gabrovo, 2005, ISSN 1310-6686

[10] S. Simeonov and G. Tsvetanov, "Theorem for reversing the direction of the involute cylindrical gears with asymmetric profile of teeth," *Mechanics of machines*, no. 63, 2005, ISSN 0861-9727

[11] L. Lazov, E. Teirumnieks, N. Angelov and E. Teirumnieka, "Methodology for Automatic Determination of Contrast of Laser Marking for Different Materials," in *Proceedings of the 12th International Scientific and Practical Conference*, Rezekne Latvia, 2019, DOI: 10.17770/etr2019vol3.4143

Environment. Technology. Resources. Rezekne, Latvia
Proceedingsofthe 13th InternationalScientificandPractical Conference. Volume 3, 58-61

Influence of Vehicle Suspension Parameters on its Braking Properties

Anna Dmitrieva
Institute of Engineering Sciences
Pskov State University
Pskov, Russia
anna-listratova@rambler.ru

Alexander Enaev
Institute of Engineering Sciences
Pskov State University
Pskov, Russia
enaa53@mail.ru

Vladimir Timofeev
Institute of Engineering Sciences
Pskov State University
Pskov, Russia
timofeev1097@yandex.ru

Evgeny Seleznev
Institute of Engineering Sciences
Pskov State University
Pskov, Russia
evgeniys84@yandex.ru

Tatyana Klets
Institute of Humanities and Linguistic Communications
Pskov State University
Pskov, Russia
kte63@yandex.ru

***Abstract* - The paper focuses on the study of the performance of elastic and damping parameters of the car suspension. The problem of arising vibrations of the sprung and unsprung vehicle masses on the braking process is considered. The article presents theoretical models of vehicle braking taking into account the oscillations of the vehicle's sprung masses. The research results will make it possible to establish the relationship between the suspension parameters and the estimated parameters of braking properties, to supplement the "driver - car - road" system, and also to more accurately assess the active safety of vehicles associated with braking dynamics.**

Keywords - car braking, mathematical model, sprung mass, vibrations.

I. INTRODUCTION

A car as a mechatronic object and a complex technical system has a number of operational properties, which, in the theory of car movement, are divided into two main groups - associated and not associated with the movement of the car. Also, in the classification of operational properties, there are those that affect the active and passive safety of the car [1]. According to the terminology, in the automotive industry, passive safety is a combination of properties that reduce the severity of the consequences of road accidents, and its main requirement is the design of the outer surfaces and elements of the car, in which the probability of damage to the driver and passengers by these elements in the event of a road traffic accident could be minimal [1], [2].

Active safety refers to properties designed to minimize the likelihood of a road traffic accident. Its provision is a priority task in the formation of road safety. Active safety includes several operational properties that allow you to confidently drive a car: accelerate and decelerate with the required intensity, as well as perform maneuvers required by the road situation. The most important are braking properties, and they account for 41.3% of the active safety of vehicles [2], [3].

The braking process of a car is dynamic and there are many factors affecting the braking performance, but in the theory of vehicle motion, the brake dynamics is considered under idealized conditions, corresponding to braking on a flat road. However, in the process of braking on an uneven road, under the influence of road irregularities, the car makes longitudinal and angular vibrations, which lead to a change in the indicators of the braking properties of the car.

II. VIBRATION SYSTEM OF THE CAR AND SUSPENSION PARAMETERS

The car is an oscillatory system that determines the smoothness of the vehicle and affects almost all performance properties.

To determine the effect of vibration of a car on braking properties, Fig. 1 shows a diagram of an oscillatory system, which is equivalent to a car when braking. The presented oscillatory system differs from the generally

Online ISSN 2256-070X
https://doi.org/10.17770/etr2021vol3.6593

accepted one in the theory of oscillations and smoothness of cars in that braking forces are applied in the contact of the wheels with the supporting surface, causing an inertial force applied at the center of gravity.

The designations on the diagram are generally accepted in the theory of oscillations [4], [5]: M - sprung mass of the vehicle; $c_{1,2}$ - reduced coefficient of normal suspension stiffness; $\eta_{1,2}$ - reduced coefficient of inelastic resistance of the suspension; $q_{1,2}(t)$ - the current values of the ordinates of the road surface micro-profile in the contact of the wheels in time; $z_{1,2}(t)$ - the values of the vertical displacements of the sprung masses; J_y – moment of inertia of the vehicle's sprung masses relative to the central transverse axis O; $P_{\tau 1,2}$ - braking forces applied in the contact of the wheels; $R_{z1,2}$ - normal reaction in the contact of the wheels with the supporting surface; F_j is the inertial force of the total mass of the vehicle during braking; $r_{1,2}$ - pair of forces equivalent to the moment of braking forces and inertial force; L - vehicle base; a, b - distance from the center of gravity to the vertical planes of the front and rear unsprung masses; h_0 is the height of the vehicle's center of gravity above the center line of the road support surface.

Indices 1 and 2 mark the parameters belonging to the front and rear suspensions, respectively.

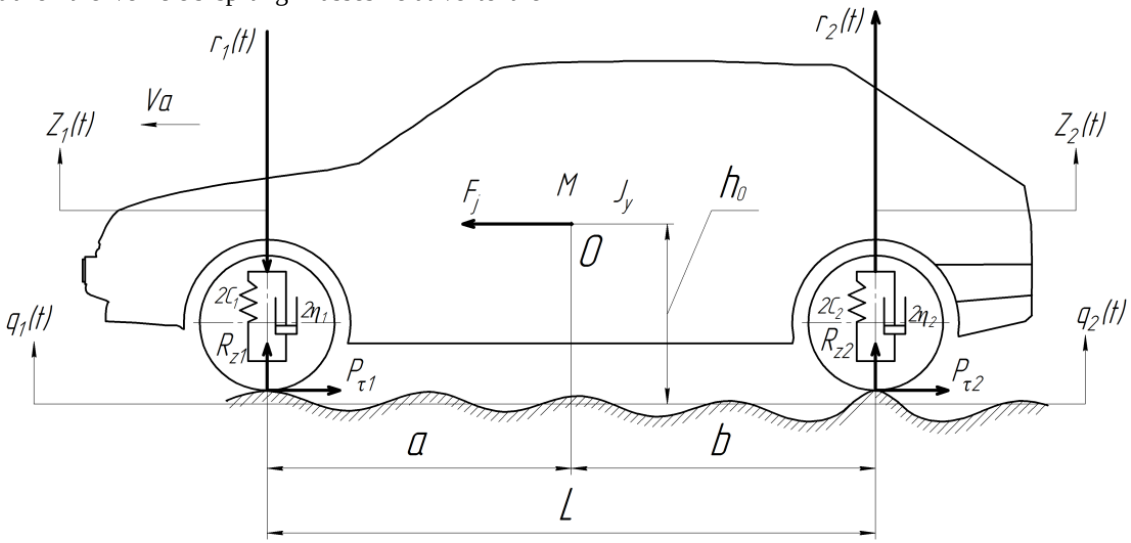

Fig. 1. Scheme of the oscillatory system, equivalent to the car when braking

This oscillatory system is simplified due to the fact that the vibrations of the sprung mass are dominant, and the influence of high-frequency vibrations of the unsprung masses with a relatively small amplitude can be neglected. Therefore, unsprung masses are excluded from consideration, and the reduced stiffness coefficients are introduced to take into account the elastic elements [4], [5]:

$$c_{1,2} = \frac{c_{p1,2}\, c_{t1,2}}{c_{p1,2}+c_{t1,2}}, \qquad (1)$$

Where $c_{s1,2}$ is the coefficient of normal stiffness of the suspension; $c_{t1,2}$ is the coefficient of normal stiffness of tires.

Combining in the same way the inelastic resistance of the suspension and tires and considering it proportional to the deformation rate, following the example of an already united elastic element, the damping properties of the above system (Fig. 1) will be estimated by the coefficient of inelastic resistance $\eta_{1.2}$.

The movement of the rear and front sprung masses of the vehicle during braking is described by the system of equations:

$$\begin{cases} M_1\ddot{z}_1 + \eta_1(\dot{z}_1 - \dot{q}_1) + c_1(z_1 - q_1) = -r_1 \\ M_2\ddot{z}_2 + \eta_2(\dot{z}_2 - \dot{q}_2) + c_2(z_2 - q_2) = r_2 \end{cases} \qquad (2)$$

These equations are simplified by introducing the well-known notation:

$$\frac{\eta_{1,2}}{M_{1,2}} = 2k_{1,2}, \frac{c_{1,2}}{M_{1,2}} = \omega^2{}_{1,2}, \qquad (3)$$

After substitution and elementary transformations, the differential equations take the following form:

$$\begin{cases} \ddot{z}_1 + 2k_1\dot{z}_1 + \omega^2{}_1 z_1 = \omega^2{}_1 q_1 + 2k_1 q_1 - \frac{\cdot}{M_1} r_1; \\ \ddot{z}_2 + 2k_2\dot{z}_2 + \omega^2{}_2 z_2 = \omega^2{}_2 q_2 + 2k_2 \dot{q}_2 - \frac{\cdot}{M_2} r_2; \end{cases} \qquad (4)$$

Forces equivalent to the moment of braking and inertial forces are described by the dependence [4]:

$$r_{1,2} = \pm\frac{h_u}{L}\varphi\begin{bmatrix} Mg\delta_0(t) + c_1(z_1 - g_1) + \\ +\eta_1(\dot{z}_1 - \dot{g}_1) + c_2(z_2 - g_2) + \\ +\eta_2(\dot{z}_2 - \dot{g}_2) \end{bmatrix} \qquad (5)$$

In equation (5), taking into account braking with full use of adhesion forces and instantaneous application of

braking forces $\delta_0(t)$, the unit Heaviside function is displayed, expressing a unit jump in the form:

$$\delta_0(t) = \begin{cases} 0 \; for \; t < 0, \\ \infty \; for \; t > 0. \end{cases} \quad (6)$$

The obtained equations reveal a significant feature of vehicle vibrations with full use of adhesion forces, namely, when braking forces are applied, a close interdependence of vertical vibrations of the front and rear sprung masses arises.

III. ESTIMATED PARAMETERS OF BRAKING PROPERTIES TAKING INTO ACCOUNT VIBRATIONS

When the vehicle's sprung masses oscillate, the vertical load, which is formed in the contact of the wheels with the road, also changes. When the vertical load changes, the braking forces also change, which leads to a deterioration in the braking dynamics of the vehicle.

The magnitude of the braking force Pτ1.2 in contact of the wheels with the road is determined as:

$$P_{\tau 1,2} = R_{z1,2}\varphi_x, \quad (7)$$

where$\varphi_x$is the coefficient of adhesion of the tires to the supporting surface.

The normal reaction in contact of the wheel with the road, taking into account the resulting vibrations, is determined:

$$R_{z1,2} = M_{1,2}(g \pm \ddot{z}_{1,2}), \quad (8)$$

where$g$— acceleration of gravity;$\ddot{z}_{1,2}$—acceleration of the front and rear sprung masses of the vehicle.

The amount of deceleration, taking into account the vibrations of the sprung masses, can be determined:

$$j = (g \pm \ddot{z}_0)\varphi_x, \quad (9)$$

where $\ddot{z}_0$ – vertical acceleration of the center of gravity of the sprung masses.

$$\ddot{z}_0 = \frac{\ddot{z}_2 a + \ddot{z}_1 b}{a+b} \quad (10)$$

The change in stopping distance when impacted by an uneven road can be seen through the loss of kinetic energy when driving.

The kinetic energy of a car moving in braking mode under the influence of road surface irregularities is spent on the work of friction in contact of the wheels with the road, on overcoming the horizontal component R_x, arising from the action of the normal reaction R_z, and on the excitation of vibrations of sprung and unsprung masses:

$$\frac{MV_a{}^2}{2} = S_t R_z \varphi_x \pm E_{Rx} + E_p, \quad (11)$$

where $\frac{MV_a{}^2}{2}$ – kinetic energy of a car moving in braking mode; V_a – travel speed; $S_t R_{z1.2}\varphi_x$ – friction work in contact of the wheels with the road; S_t – braking distances; E_{Rx} – energy consumption to overcome the horizontal component R_x; E_p – energy consumption for vibrations of sprung masses.

Energy costs to overcome the horizontal component R_x can be defined as [6]:

$$E_{Rx} \approx 0{,}063 \frac{c_{1.2}}{M} M\upsilon z_0^2, \quad (12)$$

where υ – disturbance frequency.

Disturbance frequency:

$$\upsilon = \frac{V_a}{l_н}, \quad (13)$$

where $l_н$ –irregularity length.

Energy consumption for vibrations of sprung masses:

$$E_p = P_p z_{0,} \quad (14)$$

where P_p – work spent on vibrations.

$$P_p = 0{,}392 q_0 \omega^2 M \quad (15)$$

where ω – frequency of natural vibrations.

$$\omega^2 = \frac{c}{M}. \quad (16)$$

Braking distances:

$$S_t = \frac{MV_a{}^2 - 2(E_p \pm E_{Rx})}{2R_{z1,2}\varphi_x}. \quad (17)$$

Deceleration time provided that the final speed is equal to zero:

$$t = \frac{2MV_a{}^2 - 2(E_p \pm E_{Rx})}{2V_a M(g \pm \ddot{z})\varphi_x}. \quad (18)$$

IV. THEORETICAL RESEARCH

For the theoretical study, a car was chosen, which is characterized by the following parameters:

- car base L = 2900 mm;

- distance from the center of mass of the vehicle to the front axle a = 1500 mm;

- distance from the center of mass of the vehicle to the rear axle b = 1400 mm;

- coefficient of normal suspension stiffness $c_{1,2}$ = 3 MN/m; $c_{1,2}$ = 6MN/m; $c_{1,2}$ = 9 MN/m; c_p = 12 MN/m;

- coefficient of normal stiffness of tires c_t = 1,3MN/m;

- vehicle center of mass h_0 = 750 mm;

- sprung vehicle weight M = 1700 kg.

The adhesion coefficient is taken to be φ_x = 0.7, unevenness height Q = 0,05 m.

As a disturbing external influence during braking, an impulse irregularity was chosen, the mathematical description of which is characterized by the function[7], [8]:

$$\begin{cases} q = 0, \text{ for } t < t1, t > t_2 \\ q = Q, \text{ for } t_1 \le t \le t_2 \end{cases} \quad (19)$$

where Q — unevenness height; t_2, t_1 — the travel time of the unevenness.

The variable parameter in the study by the mathematical model is the suspension stiffness coefficient, which for cars is in the range $c_{1,2}$ = 3 – 12 MN/m.

The solution of the system of equations (4), allows you to obtain the values of the acceleration of the sprung mass, which are used in formulas (7) - (18) to determine the estimated parameters of the braking properties.

The results of calculating the main values are presented in Table 1.

TABLE 1 - CALCULATION RESULTS

Nomination	**Coefficient of Normal Suspension Stiffness $c_{1,2}$, MN/m**			
	3	***6***	***9***	***12***
Reduced stiffness of the suspension *C*, МН/м	1,18	2,14	2,27	2,35
Moving the sprung mass *Z*, m	0,56	0,61	0,64	0,65
Acceleration of the sprung mass $\ddot{Z}$, mm/s^2	6,5	6,9	7,2	7,5
Braking distances S_t, m	6,56	7,43	8,26	9,3
Deceleration *j*, mm/s^2	2,010	1,766	1,584	1,402
Braking time *t*, s	2,38	2,71	3,01	3,4

For clarity, the calculated data plotted the dependence of the obtained values on the suspension stiffness coefficient (Fig. 2).

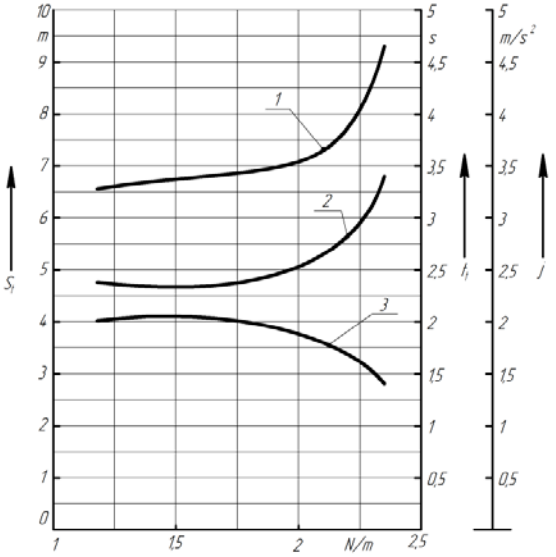

1 – braking distances 2 – braking time 3 - car deceleration

Fig. 2. Influence of the suspension stiffness coefficient on the estimated parameters of braking properties.

V. CONCLUSIONS

The carried out theoretical studies allow us to conclude that when braking on an uneven road with full use of adhesion forces, an increase in the coefficient of normal stiffness leads, as a consequence, to a change in the arising oscillations of the sprung masses of the vehicle, leading to an increase in the braking distance and braking time of the vehicle, and to a significant decrease in deceleration, which corresponds to deterioration of the braking dynamics of cars.

In addition, it should be noted that when braking on an uneven road, the braking properties are reduced, in contrast to braking on a flat road.

REFERENCES

[1] V.K.Vakhlamov, Automobiles: Operational properties. textbook for stud. higher studies. institutions. 3rd edition., P. M.: Publishing house. Center "Academy", 2007, 238 p.

[2] V.F.Yukhimenko and A.A. Yatsenko, Vehicle safety: study guide. Vladivostok: Publishing house of VSUES, 2009. 208 p.

[3] A.Sh. Khusainov, Passive safety of the car: a tutorial. Ulyanovsk: UlSTU, 2011, 89 p.

[4] A.A. Enaev, Fundamentals of the theory of vibrations of a car during braking and its applications. M.: Mechanical Engineering, 2002, 341 p.

[5] N. N.Yatsenko and A. A.Enaev, Oscillations of the car during braking. Irkutsk: Irkutsk University Publishing House, 1989, 248 p.

[6] N. Ya.Govorushchenko, Fundamentals of the theory of car exploitation. K .: Vischa school, 1971, 240 p.

[7] N.N. Yatsenko and O.K. Prutchikov, Smooth running of trucks. M.: Mechanical Engineering, 1969, 218 p.

[8] M. Ya. Pevzner and G. G.Gridasov, Oscillations of the car. M.: Machine building, 1979, 208 p.

Environment. Technology. Resources. Rezekne, Latvia
Proceedings of the 13th International Scientific and Practical Conference. Volume 3, 62-65

High Rigidity and Vibration Endurance Bar for Deep Holes

Evgenia Evgenieva
Departament of Engineering technologies and technosphere safety
Pskov State University
Pskov, Russia
Zhen_sheny@mail.ru

Igor Nikiforov
Departament of Engineering technologies and technosphere safety
Pskov State University
Pskov, Russia
Nikiforov.i.p@mail.ru

Pavel Maltsev
Departament of Engineering technologies and technosphere safety
Pskov State University
Pskov, Russia
Inertan@gmail.com

Sergei Dmitriev
Departament of Engineering technologies and technosphere safety
Pskov State University
Pskov, Russia
Dmitrievsi55@gmail.com

***Abstract* - Different constructions of bars are analyzed in the article, all of which are based on the idea of creating prestressed state in material. Improved construction of bar is proposed for equable spreading of elasticity zone along axis of boring bar.**

Keywords - Grinding, boring, rigidity, vibration endurance, stress, Hooke's law, dissipation.

I. INTRODUCTION

One of the problems which appear during boring and internal grinding of deep holes is a complexity of providing a required rigidity and vibration endurance of bar in the limited space. The problems appear during machining in conditions of reduced rigidity of manufacturing system. There are two basic ways to solve them: to increase rigidity and decline value of cutting force.

One of the best solutions of increasing rigidity and vibration endurance is making prestressed state in the bar material. The point of this method is mechanical influence on the bar material. As a result, crystal lattice of material is deformed and the distance between atoms decreases. This impaction takes place according to Hooke's law and doesn't lead to plastic deformation. In the same time, rigidity of bar goes up, vibration endurance and energy dissipation are improving and the logarithmic decrement of oscillations is increasing.

II. MATERIALS AND METHODS

There are many researchers about ways to increase rigidity and vibration endurance of bars by creating prestressed state their body [1-6].

One of the accomplished solutions is a boring bar for stepped deep holes in hardly processed parts, welded of different materials [1]. The bar has an expanding taper which is set in an empty body from the cutting insert side. The taper is connected with thread kernel which has a regulating nut with a thrust on the end of the body. The expanding taper is made of steel with a hardness <200 HB and empty body is made of steel with a hardness 350-370 HB. The bar is mounted in a turret CNC machine through a split bushing.

This construction provides even spread of stretched tension in a cross section body of the bar. Radial component of cutting force leads to bar bending, and in according to machining scheme, its direction is essentially permanent. It means that bending can be compensated more effectively.

Other known construction is low-vibration tool holder [2] (Fig. 1) with a tool holder base body 1 and a tensioning arrangement 2 which provides axial tensioning of the tool holder base body and which is simultaneously tensioned in a radially flexible way with respect to the tool holder base body.

Online ISSN 2256-070X
https://doi.org/10.17770/etr2021vol3.6522

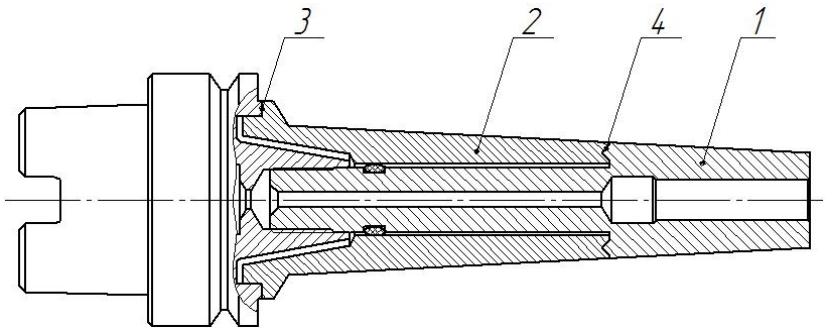

Fig. 1. Tool holder by RU 2400330.

This tool holder is less susceptible to vibration than previously known tool holders, which ensures better true running even during operation and in particular when heat-induced expansion of materials occurs, since the clamping arrangement which is integrated in the tool holder is continuously centered with respect to the tool holder base body. Furthermore, such a tool holder, in particular within a modular design, can be adapted very flexibly to different types of tools and workpiece machining processes. This holder has one or several formed seats 3 and 4 which interact during movable contact with one or several mating surfaces.

The most part of tensions made by such bar has axial direction and its construction is good for tools with constantly change directions of radial component of cutting force. Besides, location of formed seats and mating surfaces on the outer side of the bar leads to increased requirement of careful during using and storage.

Another construction of boring bar [3] consist of body 1 which face surface has a hole with sliders 2 to tune the damper, O-rings 3 and the absorber 4, relocatable by a diagonal tuner 5 (Fig. 2). The bar also has end plug 6 and cartridge 7 to mount the cutting insert. This construction provides protection of absorber 4 and O-rings 3, however, not good for rotatable bar because of imbalance which emerges in the presents of tuner 5 and its variable position. Besides rigidity increases on the limited length of the bar.

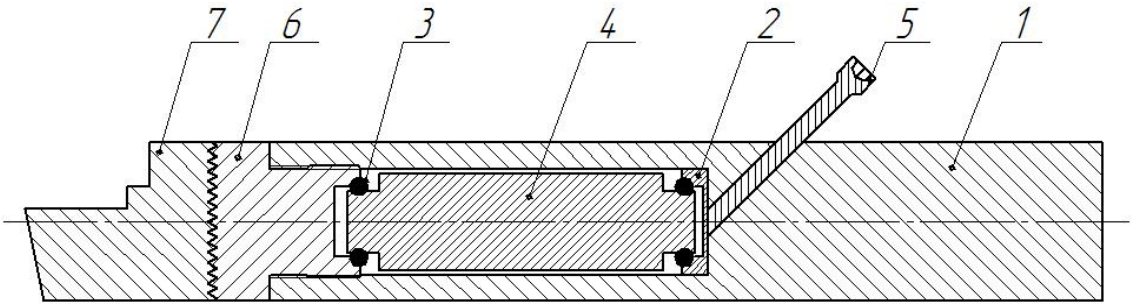

Fig. 2. Damper boring bar with inner absorber and tuner.

The enhanced version of previous construction is a boring bar with improved stiffness [4]. A tunable or tuned boring bar having increased stiffness is provided. Increasing the stiffness of the bar increases the natural frequency, thereby reducing directional deformation of the bar during use. The tunable boring bar includes a distal portion configured to support a tool, a proximal portion configured for attachment to a support structure of a metalworking machine, and a body, which is at least partially tubular, extending between the proximal portion and the distal portion. The tubular portion of the body has an elongated cylindrical cavity. The body of the boring bar includes a core layer 1 formed from a first material and a coating layer 2 formed from a second material (Fig. 3). The second material has a higher modulus of elasticity than the first material. In certain configurations, the coating layer is bonded to the core layer by cladding, welding, chemical adhesives, chemical vapor deposition, pulsated plasma diffusion, or combinations thereof.

This design provides an increase bar rigidity over the entire length of the body, a decrease imbalance due to a decrease length of the screw, but does not protect the outer layer of the coating from external factors.

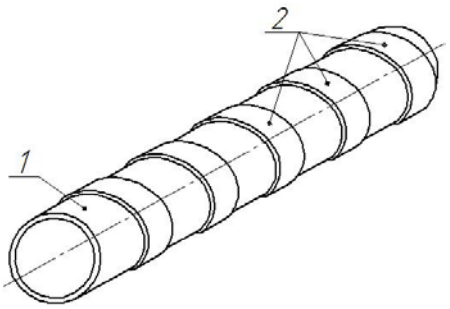

Fig. 3. Boring bar with improved stiffness by US 10040127.

III. Results and Discussion

A new bar with high rigidity and vibration endurance is developing now. It will provide an opportunity to solve mentioned problems of increasing spreading tension along the body length and decreasing interaction external influence on elements which are responsible for creating prestressed state in boring bars, tool bars, etc.

The base of the offered solution is another widely known tool for hardening processing inner cylindrical surfaces [5]. It is made in a shape of cylindrical shells 1 and 2, one of them has a collar at the end and another one has a flange (Fig. 4).

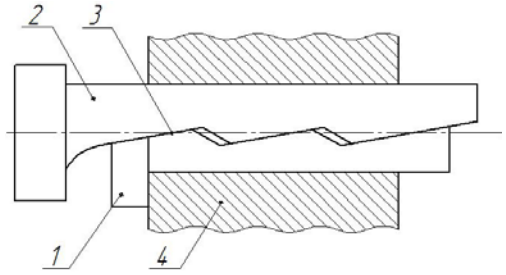

Fig. 4. Tool for hardening processing inner cylindrical surfaces by SU 854696.

Those shells have stepped bevels 3 forming wedge pairs. The angle of bevels to longitudinal axes of the shell and bar is bigger than the self-holding angle on 1-2 degrees. Bevels length and angle of their surface on the each step are equal. The amount and value of the steppes are defined by length of the hole, its diameter and condition of the bevels angle excess above the self-holding angle.

Radial force emerges during the axial moving those shells in the hole 4 and interacts on the walls of the hole. Accordingly, a new prestressed device could be got by placing such shells into the hole of the body.

This solution (Fig. 5) is based on construction tool bar using which has an empty body 1 with cylindrical hole which includes a system 2 for creating prestressed state in the bar. This system consists of movable 3 and unmovable 4 shells and a nut 5. Stepped bevels 6 are made on the both shells for forming wedge pairs. Unmovable shell 4 is fixed on the body and movable shell 3 has a thread journal 7 with a nut 5. The journal 7 partially located outside the body 1. The opposite end of the movable shell 3 has the mating surfaces and thread holes for tool 8 fixation. Plenty of bevels 6 will increase life time of the bar and provide equable spreading tensions along its length, while the body 1 will provide shells protection from external influence.

Partial location of thread journal 7 provides free nut 5 moving during creating prestressed state. To increase bar rigidity one end of the movable shell 3 can be provided by a collar 9 and between it and body end is located length compensator 10 such as set of rings. It will allow to get rid of axial tensions in the tool 8.

In the preferable construction value of the bevels angle to the body axis was not less than the angle of friction, which for steel shells is not less than 1°25'56" similarly metric taper. The maximum value for this angle is about 10° which fits for composite or polymer materials of shells.

The developing high rigidity and vibration endurance bar for deep holes has an empty (for instance, cylindrical or conical) body with cylindrical hole, which provides simplicity and high accuracy of machining. Unmovable shell of the system for creating prestressed state is fixed by radial screws which are located in the body walls. In the preferable construction the screws amount is equal the amount of bevels.

Shells are made of the same material (for instance, constructed or alloy steel) which is softer than material of the body, for example, due to different heat treatment or composition. The thread journal with a nut can include a device or material for providing self-locking anti-disassembly such as locknut, spring lock washer, etc.

Shells are made of a one blank for machining error decreasing. It can be provided by electrical-discharging cutting with subsequent finishing bevels for decreasing of resistance forces sliding. For the mentioned result lubricant or grease also can be inflicted on the out surface of movable shell and bevels.

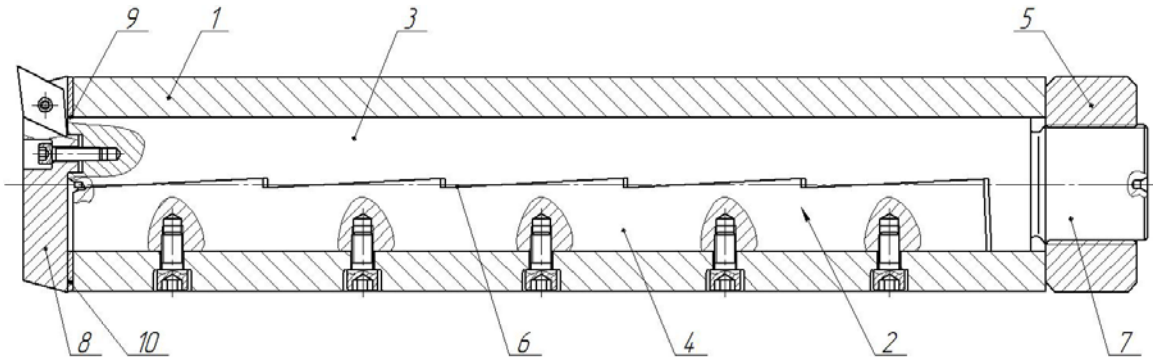

Fig. 5. Developing high rigidity and vibration endurance bar for deep holes.

The mounting shells surface can be located perpendicularly to direction of radial component of cutting force during using bar for the boring tool. It will have a positive influence due to compress tensions emerging in shells and sections A and B of the body wall (in according to Fig. 6) will partially compensate this component. At the same time, sections C and D of the body wall will have the respond stretching tensions and will not increase a moment, which is created by a tangential component of cutting force.

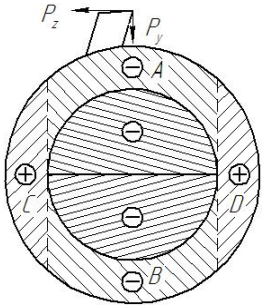

Fig. 6. Cross-section of the developing bar.

IV. CONCLUSIONS

The developing bar can be used in the serial production for edge and grinding of deep holes with different diameters.

REFERENCES

[1] V.V. Maksarov, D.F.Osminko and T.S.Golikov, "Bar for boring stepped deep holes in difficult-to-cut dissimilar welded workpieces," RU Patent 191536, August 12, 2019.

[2] F. Haimer, "Tool holder characterised by low vibration," RU Patent 2400330, October 20, 2009.

[3] A. Yadav, D. Talaviya, A. Bansal, and M. Law, "Design of Chatter-Resistant Damped Boring Bars Using a Receptance Coupling Approach," Journal of Manufacturing and Materials Processing, vol. 4, no. 2, p. 53, Jun. 2020 [Online]. Available: http://doi.org/10.3390/jmmp4020053.

[4] Ruy Frota de Souza Filho, "Boring bar with improved stiffness" US Patent 10040127, Mar 14, 2014.

[5] S.P. Krapivin, A.O. Reidman and E.T. Vasilevskyi, "Tool for hardening processing of internal cylindrical surfaces," SU Patent 854696, November 15, 1979.

[6] E. I. Yatsun, O.S. Zubkova, I.S. Karnaukhov, A. Gorchakov, "Anti-vibration tool holder," Modern materials, equipment and technologies, vol. 23, pp. 80-90, 2019.

Environment. Technology. Resources. Rezekne, Latvia
Proceedings of the 13th International Scientific and Practical Conference. Volume 3, 66-71

Synthesis of the Low-Frequency Vibration Exciter

Dmitriy Fedorov
Department of Electric Coupling and Automation Systems
Pskov State University
Pskov, Russia
dmitriy-fedorov-2012@mail.ru

Andrei Khitrov
Department of Electric Coupling and Automation Systems
Pskov State University
Pskov, Russia
khitrov.aa@gmail.com

Evgeniy Veselkov
Department of Electric Coupling and Automation Systems
Pskov State University
Pskov, Russia
wes_el@bk.ru

Yulia Domracheva
Department of Electric Coupling and Automation Systems
Pskov State University
Pskov, Russia
juli-politeh@yandex.ru

Oksana Kozyreva
Department of Electric Coupling and Automation Systems
Pskov State University
Pskov, Russia
ks_33n@mail.ru

***Abstract* - The article is devoted to synthesis of the low-frequency vibration exciter for checking of sensors of acceleration. In many areas of the modern equipment sensors of acceleration working in very low range of frequencies are widely used. For checking and graduation of such sensors the vibration exciter capable to provide rectilinear horizontal harmonic oscillations of the calibrated accelerometer in so low range of frequencies are required. Low frequencies of fluctuations cause the necessity of creation of big amplitudes of movements for ensuring the acceptable values of amplitudes of accelerations. The low-frequency electrodynamic vibration exciter with a magnetic suspension of mobile part which is a component of the National Standard of the vibration movement of the Russian Federation is so far created. However, development of the modern equipment demands expansion of frequency ranges to the area of ultralow frequencies. One of requirements shown to the vibration exciter working in the ultralow range of frequencies is increase in amplitude of horizontal movements of a mobile part as with small amplitudes the speed and acceleration of the harmonious law of the movements proportional according to the frequency of fluctuations and a square of this frequency, will have small amplitude values. One of problems of realization of a control system of the electric drive of the vibration exciter consists in that a mobile part possesses indifferent position of balance. The centre of fluctuations of a mobile part is not defined and can be in any point on magnetic conductor length. That fluctuations had the steady centre in an average point of a magnetic conductor without use of a mechanical spring, the drive is supplied with an additional control system of fluctuations, or a so-called electromagnetic spring.**

Keywords* - *vibration, vibration exciter, active magnetic suspension, digital control system, magnetization, electromagnetic drive.

I. INTRODUCTION

In many areas of the modern equipment (seismology, the space and aviation industry, high-powered power stations, construction of altitudinal objects, transport) sensors of acceleration (accelerometers) working in very low range of frequencies are widely used (0,01 … 5 Hz). For checking and graduation of such sensors the vibrating exciters capable to provide rectilinear horizontal harmonic oscillations of the calibrated accelerometer in so low range of frequencies are required.

Low frequencies of fluctuations cause the necessity of creation of big amplitudes of movements for ensuring the acceptable values of amplitudes of accelerations. The low-frequency electrodynamic vibrating [1] exciter with a magnetic suspension of mobile part [2] with a range of frequencies of 0,1 - 5 Hz and with an amplitude of fluctuations of 0,5 m which is a component of the National Standard of the vibration movement of the Russian Federation is so far created. However, development of the modern equipment demands expansion of frequency ranges to the area of ultralow frequencies to 0,01 Hz.

This article examines the method of determining the traction force of the vibrating exciter, the synthesis of the digital control system and the results of the experiment in physical modeling of the vibrating exciter.

Online ISSN 2256-070X
https://doi.org/10.17770/etr2021vol3.6526

II. MATERIALS AND METHODS

Driving part of the vibrating stand (fig. 1) consists of a magnetic conductor, four motionless coils of magnetization 1 and one mobile coil 2. The magnetic conductor consists of five horizontally located ferromagnetic cores of round cross section - three longitudinal 3 and two cross 4, connecting face surfaces of the longitudinal cores.

Coils of magnetization are put on cross cores, connected consistently, are powered a direct current I_1 from the power supply unit and create constant magnetic field on all length of a working air gap between central and side longitudinal cores. The mobile coil is put freely on the central longitudinal core. At power supply of the coil with the sinusoidal setting current it will be affected in the longitudinal direction by the harmonious force of electrodynamic influence.

The mobile coil together with the examinee accelerometer forms a mobile part of the vibrating stand which is supplied with system of an active magnetic suspension [3].

The active magnetic suspension, thanks to lack of lubricant and mechanical contact between mobile and motionless parts, allows to exclude influence of friction and dust on quality of working off of the setting signal.

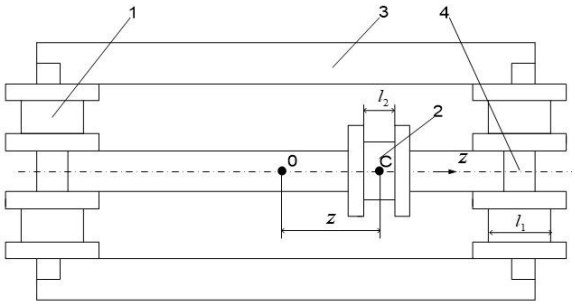

Fig. 1. System of the electrodynamic drive of a vibrating exciter.

To synthesize the parameters of a low-frequency vibration exciter, it is necessary to obtain an analytical expression for the traction force of the mobile part. Given the large linear size of the exciter, we scheme it as an electromagnetic system with distributed parameters.

Let z be the coordinate of the center of the moving coil, measured from the middle of the length of the magnetic circuit.

Having written down expression for magnetic energy [4] systems

$$w = \frac{1}{2}L_{11}i_1^2 + \frac{1}{2}L_{22}i_2^2 + L_{12}i_1i_2, \quad (1)$$

and taking the partial derivative of it with respect to the z coordinate, considering that self-inductances L_{11} and L_{22} do not depend on displacement, we arrive at an expression for the electromagnetic traction force of the form

$$P_{em} = \frac{\partial L_{12}}{\partial z} I_1 i_2(t), \quad (2)$$

where I1 is the current of the magnetizing coils (primary circuit); i2(t) - current of the moving coil (second circuit); L12 - coefficient of mutual inductance of these circuits.

The mutual inductance of the circuits can be defined as

$$L_{12} = L_{21} = {}^{\Psi_{21}}/_{I_1}, \quad (3)$$

where Ψ_{21} is the flux linkage of the flows of the coils of the first circuit with the turns w_2 of the second circuit.

It is supposed that the magnetic system is not saturated both linear and, therefore, the magnetic resistance of steel is constant. Therefore, we will use the principle of superposition. Proceeding from it, we decompose the magnetic system into two subsystems, one of which is powered by the left magnetizing coils, the other - by the right ones. We replace the magnetodriving force created by two coils of magnetization located on a cross core with one, located at the beginning of a longitudinal core.

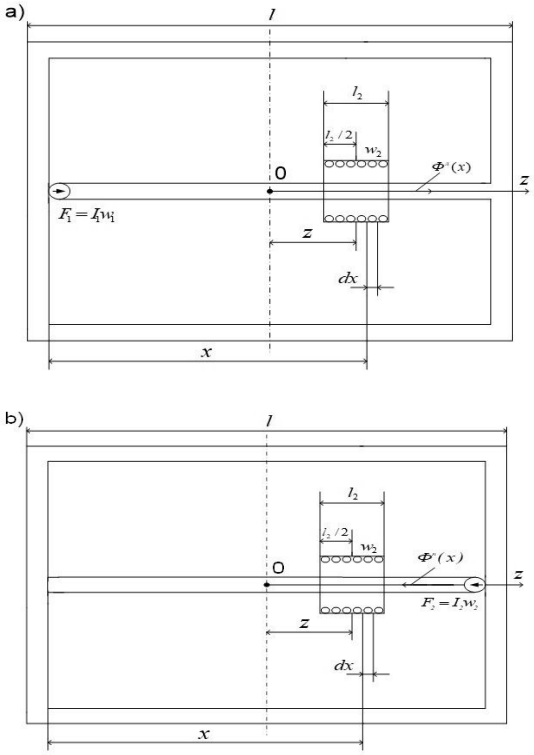

Fig. 2. Decomposition of the magnetic system into two subsystems powered by magnetizing coils a) left; b) right.

In the moving coil, we select an element with a length dx at a distance x from the left end of the longitudinal rods of the magnetic circuit. The element has the number of turns $dw = \frac{w_2}{l_2}dx$, where l_2 is the length of the winding of the moving coil.

In this case, it is obvious that the component of the magnetic induction in the direction of the z-axis is in the air $B_z^B = 0$, and only the radial component $B_r^B \neq 0$ is present. In addition, let the diameter l_1 of the magnetizing coils be

small in comparison with the length l of the magnetic circuit.

We consider that the left and right magnetizing coils create counter-directed magnetic fluxes.

Let's find the magnetic fluxes created by the left and right coils.

The considered magnetic system is the magnetic line with the distributed parameters consisting of the longitudinal and cross magnetic resistances distributed on length. In this case, longitudinal magnetic resistance is magnetic resistance of ferromagnetic cores (steel), and cross - magnetic resistance of an air gap between central and side cores. This magnetic line can be considered uniform, since all the longitudinal resistances of the sections of the cores of the same length are equal to each other, and the cross resistances of the sections of the line of the same length, due to the parallelism of the cores, are also equal to each other.

We will neglect the magnetic resistances of the end cores. The settlement scheme of the magnetic circuit for the case with left magnetizing coils is shown in Fig. 3. The diagram of the magnetic circuit for the case with the righ coils has a similar view.

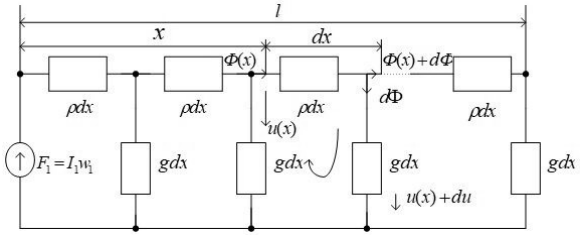

Fig. 3. The settlement scheme of the magnetic circuit for the case with left magnetizing coils.

On the provided scheme: dx - infinitesimal element of the line length; ρ - reduced longitudinal magnetic resistance per unit length of the magnetic circuit; g - reduced cross magnetic conductivity of a unit of line length; Φ(x) - magnetic flux; u(x) – magnetic voltage; $F(x) = I_1 w_1$ - magnetodriving force created by the left magnetizing coils.

From the scheme according to Kirchhoff's laws, we have the following equations:

$$-du/dx=\rho\Phi(x); \quad (4)$$

$$-d\Phi/dx=gu(x). \quad (5)$$

At the solution of the equations [5] it is necessary to set boundary conditions. They are known only for u and have an appearance $u=F_1$ at x=0; u=0 at x=l.

From the above, the following differential equation follows

$$\frac{d^2u}{dx^2} - a^2u = 0, \quad (6)$$

where $a = \sqrt{g\rho} = \frac{\sqrt{G^{\text{пр}}R^{\text{пр}}}}{l}$.

The solution of this equation is the expression

$$u^{л} = F_1[ch(ax) - cth(al) \cdot sh(ax)]. \quad (7)$$

Having made a number of substitutions, we obtain the following expression for the traction force of the electrodynamic vibration exciter:

$$P_{em} = \frac{\partial L_{12}}{\partial z} I_1 i_2(t) =$$

$$= \frac{F_1 F_2(t) g}{ch\left(\frac{al}{2}\right)}\left(1 + \frac{1}{2}a^2z^2\right). \quad (8)$$

From the obtained expression it follows that the traction force will be purely harmonic at $F_2(t) = w_2 I_2 \sin\omega t$, if $a = \sqrt{g\rho} = 0$. As at g=0 we have Рем=0, the necessary condition takes a form $\rho = 0$.

But, since even with small inductions $\rho \neq 0$, the presence of higher harmonics is inevitable in the expression for the force. They can be reduced by avoiding saturation of the steel. A recommendation has been developed to ensure a given permissible level of higher harmonics.

The synthesis of the parameters of the vibration exciter is carried out taking into account the expression for the traction force. Since when using the full number of turns of the coils with a decrease in the oscillation frequency, the currents in the coils decrease and take values of the same order of magnitude with the noise currents, it is necessary to increase the values of the currents in the windings.

This can be achieved by sectioning the windings of the moving and stationary coils, adjusting the number of turns in them with constant currents. The value of the currents can be set based on the maximum vibration frequency of the moving part, which will correspond to the maximum number of turns in the coils. The magnetodriving forces will be regulated with constant currents in windings. At a given frequency range change of traction effort by 400 times is observed. In this case, the number of turns of primary and secondary coils at the boundaries of the frequency range differ by 7,5 and 53 times respectively.

Next problem of synthesis of the low-frequency vibration exciter consists in that a mobile part possesses indifferent position of balance. The centre of fluctuations of a mobile part is not defined and can be in any point on magnetic conductor length. That fluctuations had the steady centre in an average point of a magnetic conductor without use of a mechanical spring, the drive is supplied with an additional control system of fluctuations, or a so-called electromagnetic spring.

In case of realization of control systems of the movement in analog execution, the regulator will have constant control (in sense of constancy of coefficients of strengthening of feedback). However, setup of the regulator has to change with change of frequency of fluctuations. As

the set range of working frequencies assumes change of frequency by 20 times, use of the analog regulator will be difficult. This circumstance caused transition to digital control [6] which advantage is flexibility.

The object of control is the moving part of the vibration exciter, which is a dynamic link, the input (control) variable of which is the current in the moving coil of the magnetic circuit, and the output (controlled) variable is the coordinate of the center C of the moving coil relative to the center of oscillations O. Considering that an active magnetic suspension is used the moving part of the vibration exciter, there is no friction force and the equation of the object has the form

$$m\ddot{x}(t) = F(t); \quad (9)$$

$$F(t) = hi_2(t), \quad (10)$$

where h - coefficient of transfer "current-force", depending on the current I1 in the magnetizing coils; m - the mass of the moving part.

The resulting discrete model of the control object in the form of difference equations:

$$y(k+1) = Ay(k) + Bi_2(k); \quad (11)$$

$$z(k) = Cy(k), \quad (12)$$

where $y(k) = \begin{matrix} z(k) \\ \dot{z}(k) \end{matrix}$; $y(k+1) = \begin{matrix} z(k+1) \\ \dot{z}(k+1) \end{matrix}$; $A = \begin{pmatrix} 1 & T_0 \\ 0 & 1 \end{pmatrix}$; $B = \begin{matrix} a\frac{T_0^2}{2} \\ aT_0 \end{matrix}$; $C = (1 \quad 0)$,

where k is an integer; T0- period of quantization of an ideal quantizer; a=h/m - coefficient.

The drive control system consists of a displacement sensor δ(z) of the movable part in the longitudinal direction from the center of vibrations and a regulator. The signal from the sensor is processed by the regulator, amplified and summed up with the reference current.

The signal from the displacement sensor goes to the input of the transducer located in the control unit. The differential displacement sensor, as one of the options, consists of two ferromagnetic coils moving together with the moving part of the vibration exciter along opposite sides of the tensioned electrical steel strip (Fig. 4).

This realization allows to achieve almost linear dependence of the measured voltage on the position of an object. Small nonlinearity, connected with inhomogeneity of material of the stretched tape, are eliminated by introducing second-order digital filter into the control system according to the control signal.

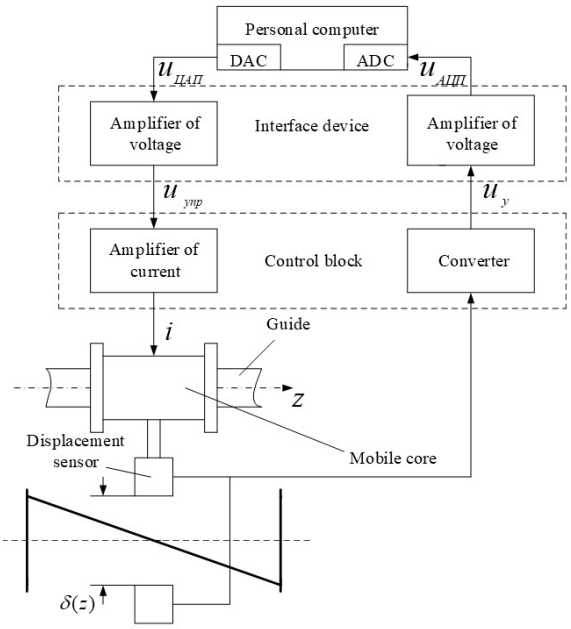

Fig. 4. Function chart of a control system.

The output voltage of the converter is proportional to the position of the moving part of the vibration exciter. This voltage through a matching amplifier located in the interface device is fed to the input of the analog-to-digital converter of the input-output board of the personal computer.

A personal computer acts as a control device and implements a digital controller for object control. The signal calculated by the regulator [7] is fed to the input of the digital-to-analog converter of the input-output board. The output voltage through the matching amplifier of the interface device is fed to the input of the current amplifier.

The current amplifier controls the current i2 of the moving coil of the vibration exciter in proportion to the voltage supplied to the input.

A filter can be added to the system output to smooth out micro current surges and acceleration.

III. RESULTS AND DISCUSSION

When carrying out measurements, the problem of experimental verification of the main theoretical relations obtained when solving the problem of synthesis of a low-frequency electrodynamic vibration exciter was solved.

Experimental studies were carried out on a model of a vibration exciter created at the Pskov State Polytechnic Institute

The model has the following parameters:

- amplitude of fluctuations at a frequency of 1Hz is equal to 0,125 m;

- the magnetic conductor is made of Steel 10, length of longitudinal cores of 0,66 m, cross cores 0,42 m, diameter of cores of 0,1 m, an air gap between longitudinal cores of 0,06 m;

- constant magnetic field in air gaps between longitudinal cores is created by means of four magnetizing coils, the 0,1 m coil radius, the 0,06 m coil length, a framework of the coil is made of textolite, thickness of walls of 5 mm, coils have on 530 turns of a copper wire diameter of 1,55 mm;

- the mobile coil has the 74 mm radius, a framework from textolite, the 0,05 m coil length, a gap between the coil and the central core of a magnetic conductor along which it moves of 8 mm, number of turns is 350, a winding is executed by an aluminum wire; diameter of a wire of 1 mm.

- the mobile coil has the electromagnetic suspension consisting of four linear active magnetic support moving along a cylindrical guide from Steel 3 diameter of 25 mm, and the linear active magnetic support limiting the rotary pendular movements in the direction;

To measure the traction force, a stop was installed on the central core of the magnetic circuit. When the currents of the moving and stationary coils interact, a force arises that presses the moving coil against the stop. A thread thrown over a block was attached to a moving coil; a cup with a weight was suspended from the second end of the thread.

If the current is gradually reduced from a certain maximum value (1,4A) to the value at which the coil will detach from the stop, then we can assume that $P_{em} = mg$, where m is the mass of the cup with the load. The traction force was measured by measuring the breakout force. I1=4A current was supplied to the stationary coils, and I2 current in the interval $(0{,}16 \div 1{,}4)$A to the moving one.

Thus, the dependence Рем(I2) was removed at fixed values of the z coordinate and current I1. The form of the function and the theoretical curve at z=125 mm and I1=4A are shown in Fig.5.

Fig.5 shows that the dependence is linear, while the calculated value of the traction force is 8-12% higher than the experimental one.

The reason for the discrepancy may be unaccounted for in the calculations such factors as the magnetic resistance of the joints of the longitudinal and transverse rods of the magnetic circuit; inhomogeneity of the magnetic properties of the material along the length of the rods; leakage fluxes of magnetizing coils.

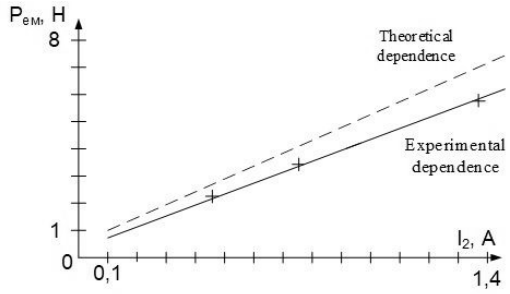

Fig. 5. Experimental and theoretical dependences of the traction force on the current of the moving coil.

In a similar way, the dependence Pem(z) was removed at fixed values of I1=4A and I2=0,4A. The form of the function and the theoretical curve are shown in Fig.6.

Fig.6 shows that the experimental dependence of the traction force on the coordinate has a parabolic form, which qualitatively confirms the theory. The theoretical curve shown in this figure corresponds to the second term in the expression for the thrust force. It follows from the comparison of the curves that the experimental dependence of the traction force on the coordinate is stronger than the theoretical one.

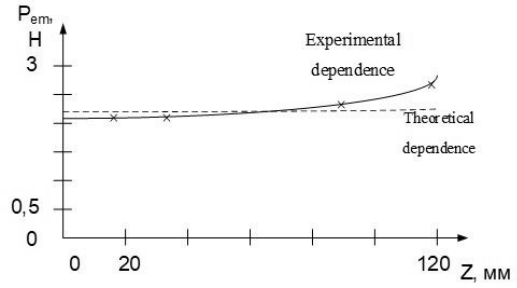

Fig. 6. Dependence of the traction force on the coordinate of the moving part.

For the given values of the currents I1=4A and I2=0,4A, the contribution of the second term according to the experiment is 19%, while according to the theoretical dependence at the same currents this contribution is 0.9%. Air gaps in joints of longitudinal and cross cores which were not considered when calculating a magnetic conductor are the reason of divergences. In addition, the magnitude of the traction force can be influenced by the inhomogeneity of the magnetic field in the working gap in the direction of the coordinate z where the moving coil moves.

The available equipment made it possible to perform harmonic analysis in amplitude and acceleration and measure the harmonic distortion, starting from 2 Hz. The measurements were carried out at a frequency of 2.05 Hz. The amplitude harmonic coefficient was found to be 0.2%, although spikes of up to 0.7% were occasionally observed. The acceleration harmonic coefficient did not exceed 1.7%.

IV. CONCLUSIONS

The article presents the main problems associated with the synthesis of a low-frequency vibration exciter. A method for determining the traction force of a low-frequency vibration exciter with an active magnetic suspension of the moving part is presented. The problem associated with the uncertainty of the position of the moving part of the vibration exciter is considered.

As a solution to this problem, a digital control system for a low-frequency vibration exciter has been proposed and implemented. The results of experimental studies on the physical model of the vibration exciter are presented. A comparative analysis of theoretical and experimental dependences is carried out. The results of the experiment

qualitatively and quantitatively confirm the theoretical researches.

The research results are implemented at the Mendeleev Research Institute.

V. ACKNOWLEGMENTS

This article is prepared with partial help of Yury Zhuravlev. We also thank the Pskov Polytechnic Institute, which provided an opportunity for experimental research. Special thanks to the Mendeleev Research Institute.

VI. REFERENCES

[1] M. D. Genkin, Electrodynamic vibrators. M.: Mechanical engineering, 1975. – 98 p.

[2] A. N. Gribov, Y. N. Zhuravlev, V. G. Matsevich. The vibrating stand of low-frequency vibration with an active magnetic suspension of a mobile part//Modern problems of improvement of measuring instruments of mechanical sizes. L.: Energoatomizdat, 1986. P. 77-82.

[3] Y. N. Zhuravlev, Active magnetic bearings: Theory, design, applications. SPb.: Polytechnics, 2003. – 206 p.

[4] D. B. Sivukhin, General course of physics. Vol. III. Electricity. - Prod. the 4th, stereotypic. M.: MIPT publishing house, 2004. - 656 p.

[5] B. K. Bul, fundamentals of theory and calculation of magnetic fields. M. – L.: Energy, 1964. – 464 p.

[6] B. Kuo, Theory and design of digital control systems. M.: Mechanical engineering, 1986. - 447 p.

[7] G. Olson, D. Piani, Digital systems of automation and management. SPb.: Nevsky publishing house dialect, 2001. – 557 p.

Environment. Technology. Resources. Rezekne, Latvia
Proceedings of the 13th International Scientific and Practical Conference. Volume 3, 72-77

Plain and PVA Fibre-Reinforced Geopolymer Compact Tension Specimen Critical Area Surface Composition Assessment

Rihards Gailitis
Faculty of Civil Engineering
Riga Technical University
Riga, Latvia
rihards.gailitis@edu.rtu.lv

Andina Sprince
Faculty of Civil Engineering
Riga Technical University
Riga, Latvia
andina.sprince@rtu.lv

Leonids Pakrastins
Faculty of Civil Engineering
Riga Technical University
Riga, Latvia
leonids.pakrastins@rtu.lv

Patrycja Bazan
Faculty of Materials Science and Physics
Cracow University of Technology
Krakow, Poland
patrycja.bazan@pk.edu.pl

Kinga Korniejenko
Faculty of Materials Science and Physics
Cracow University of Technology
Krakow, Poland
kkorniej@gmail.com

***Abstract* - For more than 40 years, low calcium alkali-activated cement composite, or in other words, geopolymer, has been around. In recent years there has been increased interest in this material and its properties. It is mainly due to the claim that geopolymer is the cement of the future. This claim is based on environmental factors. For instance, the CO_2 emissions for geopolymer binder can be up to 6 less than for Portland cement binder. Most of the researches regarding geopolymer composite properties examine only mechanical and long-term properties in compression. There has been a lack of long-term tests in tension due to difficulties in performing them. As the tensile stresses are an essential part of structure assessment, it is necessary to evaluate new material properties as thoroughly as possible. Due to the nature of geopolymer specimen hardening (polymerisation), there is a difference in modulus of elasticity development and shrinkage caused by binding that could have factors that regular Portland cement specimens do not.**

This article aims to evaluate the surface composition of plain and 1% PVA reinforced geopolymer compact tension specimens that have been subjected to creep and shrinkage tests. Specimen cross-section images were acquired using the scanning electron microscope (SEM). Using the quantitative image analysis method, amounts of cross-section composition elements are determined. Furthermore, the amount of cracks is determined and compared between plain and PVA fiber-reinforced specimens.

It has been determined that even though 1% of PVA fibre-reinforced specimens have lower tensile strength, their creep and shrinkage strains are lower, and the number of microcracks at the notch base of the specimen. Still, it has to be acknowledged that the amount of air voids in all analysed specimens is relatively high.

Keywords* - *Geopolymer composite, long-term properties, creep, shrinkage, quantitative image analysis

I. Introduction

Alkali-activated materials have been known as an alternative binder to ordinary Portland cement (OPC) mainly due to environmental reasons. Year by year, cement consumption goes up and now is responsible for more than 1.5 billion tonnes of CO_2 emission annually or, in other words, 5 to 8% of global CO_2 emissions. This due to limestone decomposition to generate reactive calcium silicate and aluminate phases [1]–[4]. By using alkali-activated materials, environmental benefits are gained in two ways. One is waste material stockpile reduction because, in alkali-activated material, such materials are used like fly ash, blast furnace slag, etc., as a part of the binder. The second way is by using these industrial waste materials as binder components, the necessity for OPC is reduced, and therefore, the CO2 is reduced. It has been estimated that by replacing OPC as a binder altogether with a geopolymer matrix, the emitted CO_2 level can be reduced

Online ISSN 2256-070X
https://doi.org/10.17770/etr2021vol3.6569

up to 46% [5], [6]. The negative aspect of binder change from OPC to geopolymer shows in cost increase, approximately up to 39% [7].

Alkali-activated blast furnace slag cement types have been studied since the 1930s, but research in alkali-activated composites and geopolymers has increased significantly since the 1980s [1]. Geopolymer is a low calcium alkali-activated binder formed because of silicon and aluminium reactions activated by hydroxide silicates from sodium and potassium hydroxide solutions [7], [8]. The main issue regarding the wide usage of geopolymer composites in construction is mainly because there is a need for increased temperature for proper binder hardening. In fact, for sufficient polymerisation, composite has to be subjected to temperature from 40 to 100°C (depending on fly ash or slag type and alkali activator) and heated in this temperature from 12 to 48 hours and more, therefore, preventing any on-site construction works [9].

Geopolymer composites have similar compressive strength to OPC-based composites. The difference between geopolymer and OPC composites is that geopolymer composites will achieve 85% of their final compressive strength in the first 48 hours [10]. Long-term property geopolymer composites have 78% less shrinkage and 50% less creep strains than foamed OPC-based composite and a bit larger creep and shrinkage strains than OPC composite [11].

Creep and shrinkage are very well-known phenomenon for cement and similar binder-based composites. These phenomenons may influence the lifetime of structures. Most creep and shrinkage happen in the first ten years of the composite's lifetime. Cement and cement-like materials are considered to have insufficient tensile strain capacity and low tensile strength. Consequently, they are brittle and susceptible to cracking. As performing creep test in tension is quite difficult and there are differences in creep and shrinkage mechanisms in compression and tension, it is necessary not only to develop and carry out these kinds of tests but also to determine factors that are influencing long-term properties in tension [12]–[16].

This article focuses on determining the differences in compact tension (CT) specimen polished section sample surface compositions after creep and shrinkage tests. The polished section's specific zone is marked. The images taken and quantitively analysed to determine whether the 1% PVA fibre reinforcement incorporation has a significant effect on sample microstructure and, therefore, influence long-term properties.

II. Materials and Methods

For long-term tests, two types of geopolymer composites were prepared. Geopolymer specimen matrixes were based on fly ash sourced from the power plant based in Skawina city (Poland). The fly ash contains spherical aluminosilicate particles and contains oxides such as SiO2 (47.81%), Al2O3 (22.80%). The high value of SiO2 and Al2O3 allows polymerisation [17].

Geopolymer specimens were prepared using sodium promoter, fly ash, and sand (sand and fly ash ratio – 1:1). The geopolymer activation process has been made by 10M NaOH solution and the sodium silicate solution (at a rate of 1:2.5). The technical NaOH in flake form and tap water with sodium silicate R–145 solution is used to make the composite solution. The alkaline solution was prepared by pouring sodium silicate and water over solid sodium hydroxide into sodium silicate and water aqueous solution. The solution was mixed, and the temperature was stabilised. The fly ash, sand, and alkaline solution were mixed for about 15 minutes using a low-speed mixing machine (to achieve homogenous paste). Then the geopolymers were poured into the plastic moulds, as is shown in Fig.1. The specimens were hand-formed, and then the air bubbles were removed by vibrating the mass. Moulds were heated in the laboratory dryer for 24h at 75 °C. Then, the specimens were unmolded. All the geopolymer specimen preparation was done at Cracow University of Technology (CUT), Poland.

The mixes were moulded into cube moulds 150x150x150mm. The mixing procedure is shown in Fig. 1.

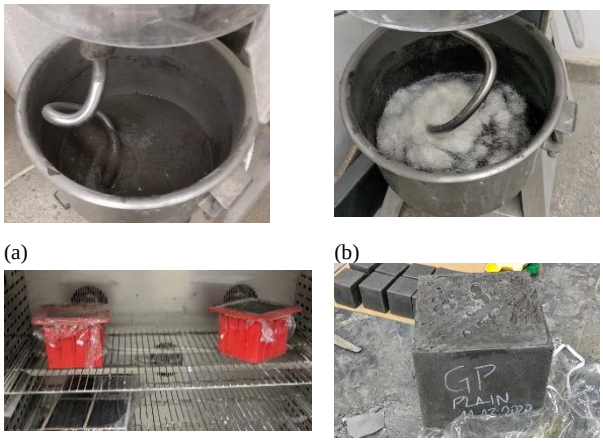

Fig. 1. Plain (a) and fibre-reinforced (b) geopolymer composite mixing and moulding (c, d) process, CUT lab

For long-term testing purposes, each of the cubes was cut to the tile-shaped CT specimens with a thickness of 15mm. Each of the tile-shaped specimens had grip 20mm holes drilled, and 2mm notch sawed according to ASTM E647 [18]. The rules of ASTM E647 for specimens preparation, please see Fig. 2 (b). The actual prepared CT dimensions are shown in Fig. 2 (a).

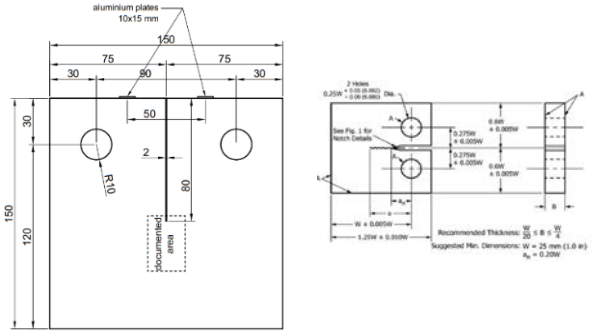

(a) (b)

Fig. 2. Geometry of the Compact Tension (CT) specimen [18], [19]

Compact tension specimens for the creep test were loaded with 20% of their tensile strength, and shrinkage specimens were kept in the same environment as the creep specimens (*without loading). Strain readings were done simultaneously for both tests. Tests were carried out for 91 days.

When long-term testing was done, each of the CT specimens had their notch base area drilled out. In Fig. 3 (a,b,c) drilling process is shown.

(a) (b) (c)

Fig. 3. CT specimen notch base sample drilling process, RTU lab

When areas for polished section samples were drilled out, they were ground and polished with various compounds at various speeds and durations. The polishing and grinding are done with Mecatech 334 automatic single station polishing machine. The polishing sequence is shown in Table 1.

TABLE 1 SAMPLE SURFACE POLISHING SEQUENCE

Polishing stage number	Polishing compound (sandpaper or paste grade) type	Polishing cycle time, minutes	Compression force to sample polishing surface, daN
1.	P180	2	2.5
2.	P320	2	2.5
3.	P600	2	2.5
4.	P1000	2	2.5
5.	P1200	2	2.5
6.	3µm	4	2.5

The polishing procedure is shown in Fig.4 (a,b).

(a) (b)

Fig. 4. Notch base samples grinding (a) and polishing (b) process, RTU lab

After grinding and polishing, samples are dried in the chamber at 40°C for 48 hours to release all the excess moisture from grinding. When samples are dried, they are placed in zip-lock bags together with silica gel so that samples stay dried for longer.

At the beginning of the samples' SEM microanalysis, the samples are covered with gold (Fig. 5 (a)). After the sample covering the specific zone on it is marked, the specific area's tracing on the polished section would be done more precisely (Fig. 5 (b)).

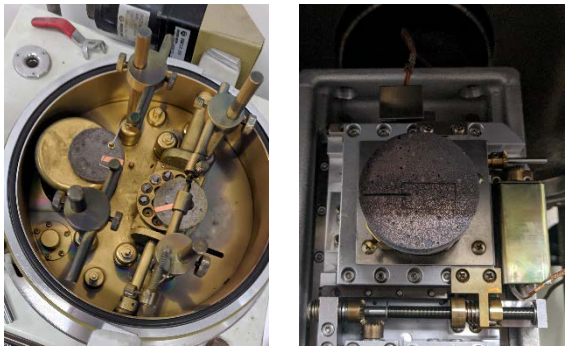

(a) (b)

Fig. 5. CT specimen polished section sample covering with gold (a) and placement in SEM vacuum chamber (b), CUT lab

The marked zone on the sample in Fig. 5(b) is 10 x 20 mm. SEM microanalysis is done in JEOL JSM-820. Achieved images are compiled and divided into layers and analysed using Adobe Photoshop CC. Dividing into layers is based on the partition type visible within the analysed cross-section. Division layers are matrix, filler, air-voids, and reinforcement. For each specific layer, an RGB tone is allocated. The process is shown in Fig. 6(a,b,c,d).

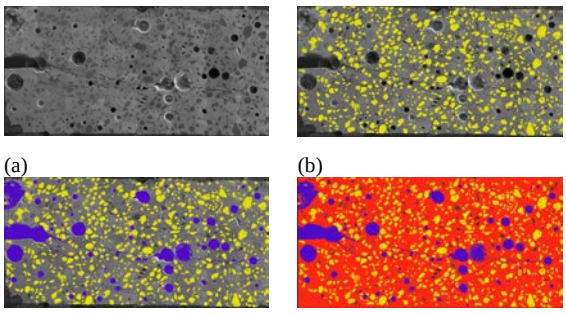

(a) (b) (c) (d)

Fig. 6. Image dividing sequence into layers

When the image dividing and RGB tone selection were made, the amount of specific RGB pixels was counted. This way, the composition amount of the studied cross-section was acquired.

III. Results and Discussion

The tensile strength of the CT specimens at the beginning of the long-term tests is compiled in Table 2.

TABLE 2 TENSILE STRENGTH OF CT SPECIMENS

Mix type	Ultimate tensile load value, average (kN)	Average tensile strength, MPa
Plain geopolymer composite	0.2767	5.1326
Geopolymer composite with 1% PVA	0.2667	4.9471

When the tensile strength values are determined, then load for the creep test is calculated. Creep and shrinkage tests are carried out for 91 days. The creep and shrinkage curves are shown in Fig.7.

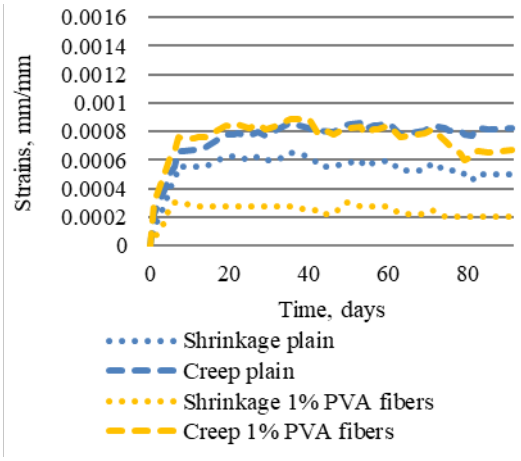

Fig. 7. Plain and fibre-reinforced geopolymer composite CT specimen creep and shrinkage strains

From Fig. 7, it is apparent that 1% PVA fibre incorporation into geopolymer composite does not bear any significant improvements in creep properties. The creep curves for plain and reinforced specimens are the same. As for the shrinkage strain curves, there is a significant difference between plain and fibre-reinforced specimens. The difference here is, on average, a 54.21% decrease in shrinkage strains for reinforced specimens in contrast to plain specimens.

Also, it is visible in Fig.7 that reinforced specimens have a significant reduction on day 70th. This leads to thinking that something has happened to one or more specimens that could have caused this reduction in strains and loss of load-bearing capability. To further elaborate on this decrease in strains, the quantitative surface composition analysis is done for the notch-based polished sections. The results of the analysis are compiled in Table 3.

TABLE 3 CROSS-SECTION COMPOSITION OF CT SPECIMENS

Test type	Mix type	Matrix amount, %	Filler amount, %	Air void amount, %	Fiber amount, %
Shrinkage	Plain	75.48	16.93	7.59	-
	Fibre-reinforced	75.75	14.07	9.47	0.71
Creep	Plain	77.39	15.60	7.01	-
	Fibre-reinforced	74.98	14.58	9.51	0.93

As shown in Table 3, the reinforced samples show higher amounts of air voids than plain samples. On average, the increase is 19.85% and 26.29% for reinforced shrinkage and creep specimens, respectively. Further analysing results, there are differences between plain and reinforced samples. For instance, plain samples that have been subjected to load (samples from creep specimens) show a lower amount of air voids than those that have not been subjected to any load. The decrease to loaded specimens on average is 7.64%. The same is not happening with fibre-reinforced samples. There is a slight visible increase of 0.42% in air void amount for loaded samples for them. This amount is negligible and leads to thinking that even specimens are tested only in tension; there is still some compression happening to specimens. As these compression strains are quite low, the fibre reinforcement does not allow compression effects to occur in the cross-section.

At the microanalysis, it was also discovered that fibre-reinforced samples have a significantly higher amount of micro-cracks that had developed a macro crack that would explain the creep curve drop in one polished section case Fig. 7 on day 70th. In Fig. 8 (a,b), the actual image is shown.

In Fig. 8 (b), there is directly visible one main crack that starts at the CT specimen base and goes throughout the sample.

Further analysing the surface microanalysis results in Table 3 shows a common trend that all of the reinforced samples have lower filler amounts than plain samples. The filler amount is relatively stable in context whether samples have or have not been subjected to any load. The difference between shrinkage and creep samples for reinforced samples is 3.51%, and for plain samples, 7.86%.

The matrix amount of all the samples is similar to all other entity amounts.

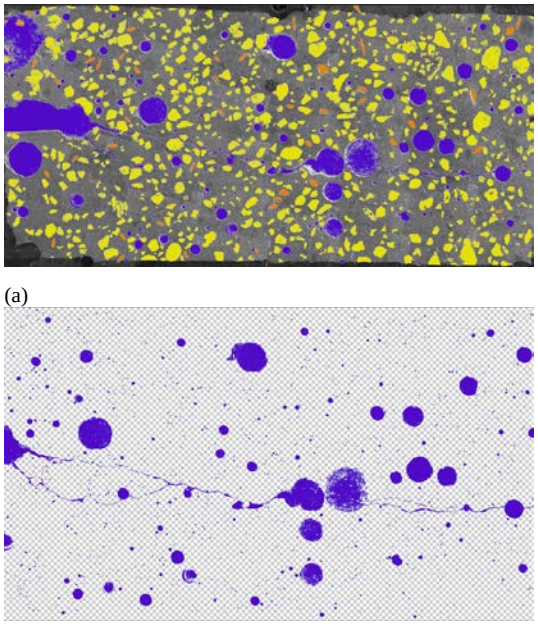

(a)

(b)

Fig. 8. Fibre-reinforced CT specimen notch base sample air void, reinforcement, filler placement (a), and air void/crack placement (b) in polished section

IV. Conclusions

Such conclusions can be drawn from the results:

1. The air inclusion amount for the fibre-reinforced samples is significantly higher and is not influenced by tension strains. It is 19.85 and 26.29% higher than plain shrinkage and creep samples correspondingly.
2. Increased air void amount and low amounts of fibre reinforcement increase the possibility of sample cracking and load-bearing capability loss. Fibre-reinforced specimens show 3.7% lower tensile strength and structural imperfections due to the small fibre reinforcement amount.
3. Reinforced samples show lower amounts of filler in them. In contrast to plain specimens, the filler amount for reinforced shrinkage and creep samples is 3.51% and 7.86%, respectively.
4. Fibre reinforcement does not significantly affect creep properties in tension but affects shrinkage strain reduction. On average, shrinkage strains are 54.21% lower for fibre-reinforced specimens than plain geopolymer CT specimens.

V. Acknowledgements

This work has been supported by the European Regional Development Fund within the Activity 1.1.1.2 "Post-doctoral Research Aid" of the Specific Aid Objective 1.1.1 "To increase the research and innovative capacity of scientific institutions of Latvia and the ability to attract external financing, investing in human resources and infrastructure" of the Operational Programme "Growth and Employment" (No.1.1.1.2/VIAA/3/19/401).

This publication was supported by Riga Technical University's Doctoral Grant programme.

References

[1] N. Alharbi, B. Varela, and R. Hailstone, “Alkali-activated slag characterization by scanning electron microscopy , X- ray microanalysis and nuclear magnetic resonance spectroscopy,” Mater. Charact., vol. 168, no. July, p. 110504, 2020, doi: 10.1016/j.matchar.2020.110504.

[2] C. Shi, A. F. Jiménez, and A. Palomo, “New cements for the 21st century: The pursuit of an alternative to Portland cement,” Cem. Concr. Res., vol. 41, no. 7, pp. 750–763, 2011, doi: 10.1016/j.cemconres.2011.03.016.

[3] W. Tu, Y. Zhu, G. Fang, X. Wang, and M. Zhang, “Internal curing of alkali-activated fly ash-slag pastes using superabsorbent polymer,” Cem. Concr. Res., vol. 116, no. December 2018, pp. 179–190, 2019, doi: 10.1016/j.cemconres.2018.11.018.

[4] K. Kermeli et al., “The scope for better industry representation in long-term energy models: Modeling the cement industry,” Appl. Energy, vol. 240, no. March 2018, pp. 964–985, 2019, doi: 10.1016/j.apenergy.2019.01.252.

[5] L. Sele, D. Bajare, G. Bumanis, and L. Dembovska, “Alkali Activated Binders Based on Metakaolin,” vol. 1, pp. 200–204, 2015, doi: 10.17770/etr2015vol1.204.

[6] A. M. Rashad and G. M. F. Essa, “Effect of ceramic waste powder on alkali-activated slag pastes cured in hot weather after exposure to elevated temperature,” Cem. Concr. Compos., vol. 111, no. September 2019, p. 103617, 2020, doi: 10.1016/j.cemconcomp.2020.103617.

[7] E. Linul et al., “Quasi-Static Mechanical Characterization of Lightweight Fly Ash-Based Geopolymer Foams,” IOP Conf. Ser. Mater. Sci. Eng., vol. 416, no. 1, 2018, doi: 10.1088/1757-899X/416/1/012102.

[8] S. Yan et al., “Effects of high-temperature heat treatment on the microstructure and mechanical performance of hybrid C f -SiC f -(Al 2 O 3p) reinforced geopolymer composites,” Compos. Part B Eng., vol. 114, pp. 289–298, 2017, doi: 10.1016/j.compositesb.2017.02.011.

[9] S. H. Kang, Y. Jeong, M. O. Kim, and J. Moon, “Pozzolanic reaction on alkali-activated Class F fly ash for ambient condition curable structural materials,” Constr. Build. Mater., vol. 218, pp. 235–244, 2019, doi: 10.1016/j.conbuildmat.2019.05.129.

[10] L. N. Assi, K. Carter, E. Deaver, and P. Ziehl, “Review of availability of source materials for geopolymer/sustainable concrete,” J. Clean. Prod., vol. 263, p. 121477, 2020, doi: 10.1016/j.jclepro.2020.121477.

[11] M. Amran et al., “Fibre-reinforced foamed concretes: A review,” Materials (Basel)., vol. 13, no. 19, pp. 1–36, 2020, doi: 10.3390/ma13194323.

[12] M. Nastic, E. C. Bentz, O. Kwon, V. Papanikolaou, and J. Tcherner, “Shrinkage and creep strains of concrete exposed to low relative humidity and high temperature environments,” Nucl. Eng. Des., vol. 352, no. June, p. 110154, 2019, doi: 10.1016/j.nucengdes.2019.110154.

[13] I. Boumakis, G. Di Luzio, M. Marcon, J. Vorel, and R. Wan-Wendner, “Discrete element framework for modeling tertiary creep of concrete in tension and compression,” Eng. Fract. Mech., vol. 200, no. July, pp. 263–282, 2018, doi: 10.1016/j.engfracmech.2018.07.006.

[14] P. Rossi, J. L. Tailhan, and F. Le Maou, “Comparison of concrete creep in tension and in compression: Influence of concrete age at loading and drying conditions,” Cem. Concr. Res., vol. 51, pp. 78–84, 2013, doi: 10.1016/j.cemconres.2013.04.001.

[15] N. Ranaivomanana, S. Multon, and A. Turatsinze, “Basic creep of concrete under compression, tension and bending,” Constr. Build.

Mater., vol. 38, pp. 173–180, 2013, doi: 10.1016/j.conbuildmat.2012.08.024.

[16] Z. Q. Cheng, R. Zhao, Y. Yuan, F. Li, A. Castel, and T. Xu, "Ageing coefficient for early age tensile creep of blended slag and low calcium fly ash geopolymer concrete," Constr. Build. Mater., vol. 262, p. 119855, 2020, doi: 10.1016/j.conbuildmat.2020.119855.

[17] K. Korniejenko, M. Łach, M. Hebdowska-Krupa, and J. Mikuła, "The mechanical properties of flax and hemp fibres reinforced geopolymer composites," IOP Conf. Ser. Mater. Sci. Eng., vol. 379, no. 1, 2018, doi: 10.1088/1757-899X/379/1/012023.

[18] ASTM, "E647 - Standard Test Method for Measurement of Fatigue Crack Growth Rates," ASTM B. Stand., vol. 03, no. July, pp. 1–49, 2016, doi: 10.1520/E0647-15E01.2.

[19] A. Sprince, L. Pakrastinsh, B. Baskers, and L. Gaile, "Crack development research in extra fine aggregate cement composites," Vide. Tehnol. Resur. - Environ. Technol. Resour., vol. 1, pp. 205–208, 2015, doi: 10.17770/etr2015vol1.199.

Environment. Technology. Resources. Rezekne, Latvia
Proceedings of the 13th International Scientific and Practical Conference. Volume 3, 78-83

Methods for Obtaining Silver Nanoparticles - a Review

M.E. Ing. Risham Singh Ghalot
Engineering Faculty
Rezekne Academy of Technology
Rezekne, Latvia
singhrisham93@gmail.com

Dr. Sc. Ing. Lyubomir Lazov, Prof.
Engineering Faculty
Rezekne Academy of Technology
Rezekne, Latvia
Lyubomir.Lazov@rta.lv

Abstract **- Silver has been part of active medical use for treatment and disinfection from ages, even in the present times. Particularly relevant today is the question of the effect of silver nanoparticles on bacteria and viruses, including against COVID-19. The study reviews distinct methods for producing silver nanoparticles. The comparison and preferences of different methods based on their classification and features are reviewed. The main goal of this study is to reveal the top-notch method and their benefits and prospects of the possibilities of the method - laser ablation, as a cost-effective and environment friendly technology for generating silver nanoparticles in an aqueous environment. The method of Pulsed Laser Ablation in Liquid for obtaining nanoparticles is explained in detail. The paper is divided into several main parts, starting with a briefing on silver and its nanoparticles and is followed by various methods for their production.**

Keywords - Silver Nanoparticles, Laser Ablation, Material Processing, Nanoparticles, Pulsed Laser Ablation in Liquid.

1. SILVER NANOPARTICLES

Silver (Ag) is the remarkably vital antimicrobial agent usable before the introduction of antibiotics. [1] Silver Nanoparticles (Ag NPs) are nanoparticles (NPs) of Ag produced via nanotechnology of size varying between 1 – 100 nm in any dimension. [2] Ag NPs have been the research theme from the past several decades because of size, shape, antimicrobial effects, chemical stability, catalytic activity high conductivity, and other extraordinary characteristics. Several techniques for obtaining Ag NPs have been priorly researched such as laser ablation, gamma irradiation, electron irradiation, chemical reduction, photochemical methods, microwave processing, and synthetic biological methods. [3]

Nanotechnology is an essential field of present-day research dealing in design, synthesis, and administrating particle structures ranging, approximately, 1-100 nm. NPs have several applications in fields of medication, cosmetics, Eatables, substantial well-being, optics, biomedical sciences, chemical & space industries, electronics and many more. Synthesised Ag NPs are used for various pharmaceutical applications. Few are mentioned below: [3] [4]

- The remedy of ulcerative colitis & acne
- Remedy of dermatitis
- Inhibition of HIV-1 replication
- Molecular imaging of cancer cells
- Disclosure of viral structures (SERS & Ag nanorods)
- Antimicrobial effects against infectious organisms
- Varnishing of surgical mesh for pelvic reconstruction
- Varnishing of breathing mask patent (used in COVID-19 pandemic)

Online ISSN 2256-070X
https://doi.org/10.17770/etr2021vol3.6618

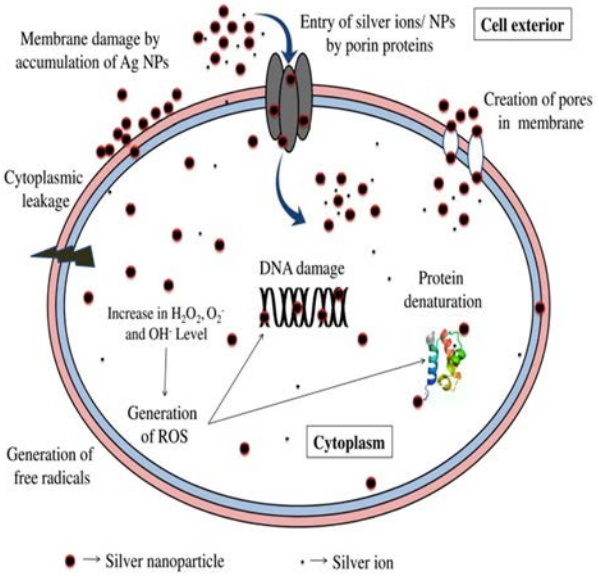

Figure 1: Bio-mechanism of antibacterial action of silver nanoparticles and silver ions [5]

Depending on reducing sources and mechanism, there are three prime methods to formulate Ag NPs. Physical processes usually operate with laser impulse energy to reduce Ag from volume to atoms and ions. Whereas, chemical and biological methods utilise reducing synthetic and organic agents, respectively, to reduce Ag ions from their harbinger into metallic Ag atoms. [6]

2. FACTS ABOUT SILVER AND AG NPS

Over the centuries, because of alteration in nomenclature, the complexity has remained among scientists, that the use of Ag, commercially, is accessible for over 100 years and are used as wound remedy, conductive/antistatic composites, catalysts, as a biocide, and many more is undeniable. The use of nanoscale Ag has a protracted, distinct, and complexed past, that is why recently, an exceptional study of AgNPs nomenclature has been conducted approximately over the past 120 years, which did not use "nano" classification. [7]

A. FACTS [7] [1]

- In 702–705, Gabor listed the demand for silver nitrate being used as a medical agent, for the first time.
- In 980 A.D. the Persian physicist-Avicenna registered silver filings as a blood purifier, which countered the heart palpitations and offensive breath.
- In 1520, Paracelsus introduced a treatment, which is in use until present, used silver internally and applied silver nitrate as a caustic for the treatment of wounds.
- In 1614, Angelo Sala gave silver nitrate internally as a counterirritant, as a purgative, and for the treatment of brain infections.
- In 1889, M. C. Lea reported the fusion of a citrate-stabilized silver colloid and the obtained size for the particles was between 7 - 9 nm.
- At present, every year, an estimate of about 320 tons of nano-silver is manufactured and used universally.

3. METHODS FOR PROCESSING AG NPS

The synthesis of Ag NPs has been examined extensively and, over the years, several procedures have been offered for the processing. [8] Under two important techniques, NP Production is classified (figure 2):

- Top-down Approach: - In this, an external force applies to a solid bulk that guides it to breaking it into nanostructures.
- Bottom-up Approach: - It begins at the atomic scale & produces the NPs, till the required size & shape is obtained. [9]

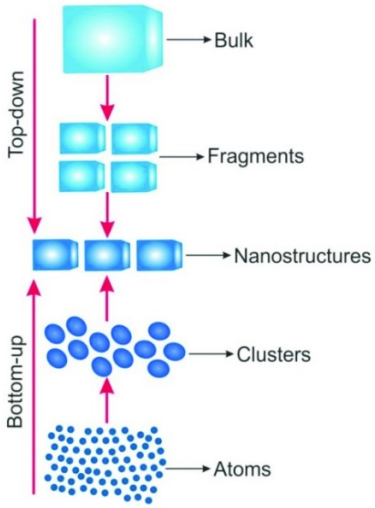

Figure 2: Schematic representation of 'top-down' and 'bottom-up' approaches for the synthesis of nanoscale materials. [10]

Different methods to synthesise Ag NPs; such are Physical, Chemical, and Biological Methods are explained below:

A. PHYSICAL METHODS

Having non-synthetic liquids in the groomed thin films and the NPs distribution having consistency are some of the advantages of physically synthesised NPs as compared to that of chemical methods. [3] These can be categorised into different types of processes such as [8]

- Arc Discharge - The original element is vaporized via an arc discharge between electrodes pursued by condensation, nucleation, and production of NPs. [11]
- High-Pressure Magneton Sputtering - It is a bottom-up mechanism & dwells in condensation of a super-saturated vapour in a flow of cold inert gas and this vapour atmosphere is procured by various methods as

thermal evaporation, laser ablation, magnetron plasma sputtering, etc. [12]

- Laser Ablation - The process separated the layers from solid bulk materials by utilising a laser beam for utmost accuracy. The laser beam irradiates the top layer, concluding that it has been disclosed to laser beam radioactivity. [13]

B. CHEMICAL METHODS

The synthetic procedure became famous via several works by John Turkevich in the 1950s, a professor of chemistry in Princeton and a pioneer in the field of catalysis. The synthetic reduction by organic and inorganic reducing agents is the most appropriate and suggested method for generating the Ag NPs. Various reducing agents such as sodium citrate, ascorbate, elemental hydrogen, polyol process, are commonly used for silver ions (Ag^+) reduction in all kind of solutions, whether it is liquid or non-liquid. These agents dwindle Ag^+ and manage the formation of silver (Ag^0). [14] Protective agents are a priority to be used to stabilise the breaking-up NPs during metal NPs preparation and secure them from being consumed or bind onto NPs surfaces, escaping their aggregation. [15] The presence of surface-active agents like acids, amines or alcohol, comprising functionalities for cooperation with particle skin can stabilise the growth of particle, and conserve particles from sedimentation, accumulation, or losing surface properties. [3] The chemical methods can be differentiated into various types also: [16] [8]

- Photochemical – It involves Ultraviolet irradiation of the solid forerunner solution in an electron-contributing reagent. With this method, NPs are produced under solid-state status & at low temperatures. [17]
- Microemulsion – It is thermodynamically balanced colloidal diffusion of water in oil or vice-versa, balanced by a surfactant. Ultralow interfacial tension, large interfacial area, and being thermodynamically stable and monodispersed NPs, are the advantages of this method. [18]
- Hydrothermal - It is a solution reaction-based approach and can produce NPs in a room- to a very high- temperature. [19]
- Chemical Reduction - A prevailing synthesis method of Ag NPs, by organic & inorganic reducing agents such as sodium citrate, ascorbate, sodium borohydride ($NaBH_4$), elemental hydrogen, N-dimethylformamide (DMF), & poly (ethylene glycol)-block copolymers are used for Ag^+ ions reduction. [3]
- Electrochemical Mechanism - A traditional method, utilizing a two-electrode system for the electrochemical synthesis. It has advantages over other bottom-up approaches (purity of NPs). [20]

C. BIOLOGICAL METHODS

The concept of Green synthesis comprises polysaccharides, organic and irradiation mechanisms, which have preferences over traditional methods requiring synthetic agents associated with substantial harms. [21] It has been gaining interest because this process uses organic agents such as bacteria, fungi, yeast, and plant, making it a simple, cost-effective, and eco-friendly mechanism. It has a regular chemical reduction, with the reducing agent as natural agents. [8] Ag NPs can be natural synthesised (a.k.a. green synthesis) with the help of:

- Bacteria – It has great abilities to diminish heavy metal ions & is the most prescribed for manufacturing NP. E.g.: Pseudomonas stutzeri and Pseudomonas aeruginosa. [22]
- Plants - Plant crude extract consists of metabolites, which are highly important for the reduction of ionic into bulk metallic NPs production. E.g.: Acalypha indica, Alternanthera sessilis. [23]
- Fungi - These are interesting reducing agents for the biosynthesis of Ag NPs as they offer high tolerance to metals and are handled easily. The extraction of extracellular proteins from fungi contributes to the stability of the NPs. E.g.: Fusarium oxysporum. [24]
- Algae - These are uni- or multi- cellular organisms residing in the distinct surrounding. Synthesis at low temperature with higher energy efficiency, less toxicity, & the risk to the environment, are some of its advantages. E.g.: Chlorella vulgaris, Spirulina platensis. [25]

4. COMPARISON

From all the above-mentioned methods, the mechanisms for generating Ag NPs, Physical Methods can be preferred as a top-notch method after tabular comparison with other mechanisms, see table 1.

TABLE 1: COMPARISON BETWEEN VARIOUS MECHANISMS FOR THE SYNTHESIS OF SILVER NANOPARTICLES [8]

METHOD ⇨ / FEATURES ⇩	**PHYSICAL**	**CHEMICAL**	**BIO**
Type of Method	Green	Non-Green	Green
Environment Friendly	Yes	No	Yes
Hazardous Liquids	None	Yes	None
Time consumed	Timesaving	Long time	Long time
Synthesised using	Laser Ablation	Reducing agents	Bacteria, Fungi, etc
Resulted NPs	Pure and Uncontaminated	Chemically Uncontaminated	Organically Uncontaminated

5. TOP-NOTCH PREFERRED METHODS

Pulsed Laser Ablation in Liquid (PLAL) under physical methods has the top-notch priority for synthesising Ag NPs of metallic bulk in liquid because it is a green method and consumes the lowest time & finances as compared to

traditional mechanisms. [26] [27] It is also introduced as a bottom-up process because of nucleation, advancement, & gathering of clusters. With the interaction of ultrashort laser pulses (10^{-13} - 10^{-8} s), the generation of nanostructures from the solid bulk material substrate, is defined as laser ablation. Materials can be ablated in a vacuum, gas, or liquid mediums. [9] [28] [29] [40]

Moreover, the Ag NPs produced by laser ablation have rare properties as they are pure and uncontaminated metal colloids. The obtained efficiency and the characteristics of Ag NPs generated are based on several specifications, including the laser's wavelength (λ), pulse duration and ablation time operating on the marker. [30] [31] This method is of high-quality and highly preferred because it produces metal colloids without any synthetic or organic assistance. Crucial specifications such as laser wavelength (λ), pulse duration, & the interaction of individual NP with a laser beam inside the liquid, influences the characteristics of NPs obtained in the liquid solution. NPs size distribution in aqueous solution is controlled either by spatial profiling of laser beam intensity or fine balancing of λ. [32] Some of the important parameters are briefed below:

a) Pulse Duration: PLAL is used for the generation of NP with pulse duration varying from Femto- to nano-seconds. NPs produced by PLAL, originate due to sputtering of the molten layer by the recoil pressure of the liquid around the targeted element. The temperature "T" of the laser spot is expressed by the Simple heat balancing equation, i.e.:

$$T \approx \frac{Aj}{c\rho h} \quad (1)$$

Here, **A** - absorptivity of the targeted material (**A** $= 1 -$ R) [**R** - reflectivity coefficient]

c - heat capacity of the targeted material,

ρ - density of the target material,

h - heat diffusion length inside the targeted material,

The heat diffusion length "h" dependent on the heat diffusivity of the targeted element, expressed as:

$$h \propto \sqrt{at_p} \quad (2)$$

wherein, a $= \frac{k}{c}$, [k - heat conduction coefficient of the target, & "t_p" - laser pulse duration].

Larger the t_p, thicker is the layer of the solid bulk which is fiery by absorbed laser energy. Also, for heating & evaporation of a liquid adjacent to the laser spot, an amount of energy is consumed which is as small as to be neglected in comparison to the one absorbed because of lower thermal conductivity of liquids. [32]

b) Laser Wavelength: Any available wavelength is relevant when PLAL is considered. Undoubtedly, produced NPs can absorb laser radiation. Most of the NPs absorb in UV range because of which the use of excimer UV lasers is least preferred. [32]

c) Repetition Rate: With each laser beam pulse (absorbed laser energy can melt the material), NPs are thrown out from the solid target. Therefore, the production of NPs is higher, provided the repetition rate of laser pulses is higher too. [32]

In the PLAL method, laser radiation is focused onto a solid target immersed in a liquid. It is assumed that the liquid is transparent at the laser wavelength, otherwise, the focalization of the beam would be problematic due to absorption of laser radiation in it. The simplest way is working with the free surface of the liquid, which allows avoiding additional reflection at the interface "covering glass/air". However, the use of volatile liquids, such as acetone, ethanol, etc., requires covering the liquid with a window that is transparent at the laser wavelength. [32]

The process of laser ablation works when - nanostructures of noble metal are produced by pulsed laser ablation in liquid, see figure 1. [33] In the process, a metallic Ag target is placed in distilled water under a pulsed laser and is synthesised by the laser ablation. Various lasers can be used in the process such as Solid, Gas or chemical lasers of several wavelengths varying from picosecond to femtosecond. Laser ablated NPs have unique properties and are non-reproducible by any existing methods. [34]

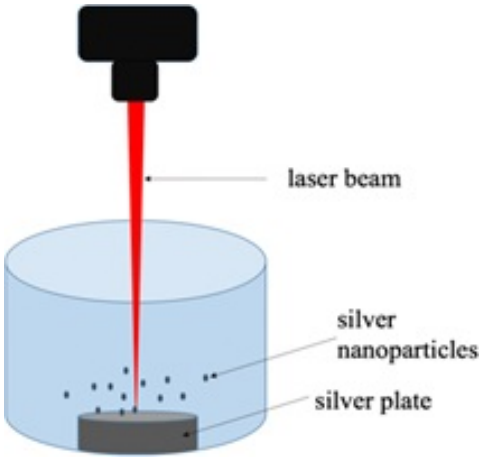

Figure 3: Systematic showing the working of the laser ablation process for producing silver nanoparticles [6]

To generate Ag NPs out of a metallic silver target through laser ablation, high-power pulsed lasers are required. Eventually, the ablation process relies on the physical features of the element used. The ablation rate is affected by several laser specifications including wavelength (λ), fluence, pulse duration, repetition rate, the light absorption efficiency of the marked material, transmission, and chemical composition of the liquid. These laser parameters can be used to tune several NP features, such as size, shape, surface properties, aggregation state, solubility, structure, and chemical composition, see table 2. [8]

TABLE 2: COMPARISON OF DIFFERENT PARAMETERS FOR PREPARING SILVER NANOPARTICLES VIA LASER ABLATION. [35] [36] [37]

Wavelength (λ)	532 nm	800 nm	1064 nm
Laser	Nd: YAG (ns)	Ti: Sapphire (fs)	Nd: YAG (ns)
Mean Diameter	2-3 nm	400 nm	2-5 nm
Absorbance	0.28	> 0.05	< 0.1
Quantity	170 ml (pure water)	5 ml (deionised water)	25 ml (pure water)

When compared, the formation efficiency and the size of colloidal pieces, was greater than those generated by a nanosecond laser. The nanosecond pulses have higher formation efficiency as of the femtosecond pulses. And the produced colloids by nanosecond pulses are more scattered than that of femtosecond pulses. Moreover, it was discovered that the ablation performance for femtosecond ablation in distilled water was diminishing than that in the air. In contrast, in the case of nanosecond pulses, the ablation energy was similar in both liquid and air. It was noted that self-absorption efficiency of Ag is superior at lower wavelengths than that of higher wavelengths, which concludes that the ablation energy with shorter-wavelength laser is lessened than that of a longer-wavelength laser. [35] [38] [41] [42]

SUMMARY

As Ag NPs possess unique properties, they are usable in various fields of science and technology, such as medicine, ecology, food industry, pharmacy, biotechnology, microelectronics, physics, and others. This is because Ag NPs are chemically stable and antimicrobial agents have a significant protective effect against microbial pathogens. Also, Ag NPs are not toxic to the human body in low concentrations. This makes them an integral part of the composition of various products with antimicrobial action.

These characteristics necessitated the active search and development of new technologies to produce Ag NPs with different shapes and sizes. Various teams from leading research laboratories study and improve the mechanisms of Ag NPs extraction, using chemical / synthetic reduction, laser ablation, electron beam exposure, concentrated microwave exposure, and many more.

Bio methods for NP synthesis have new possibilities for using organic and stabilizing agents. The proposal to use bio-organisms to extract NPs can contribute to the ecological purity of the environment. The biological activity of Ag NPs depends on factors including surface chemistry and morphology, size, shape, coating agent, NP agglomeration and dissolution rate, particle reactivity in solution, and ion release efficiency.

The flexibility of the chemical methods of Ag NPs and the rapid incorporation of Ag NPs into individual environments have motivated researchers to continue to study the mechanistic aspects of the antimicrobial, antiviral and anti-inflammatory effects of these NPs. This is achieved mainly through studies leading to a change in the form, size of Ag NPs by changing the reaction conditions, as well as the reagents and stabilizers used.

The laser ablation method to generate pure and uncontaminated metal NPs with unique properties, without the use of chemicals - organic or inorganic agents, has an exceptional environmental effect. In this method, laser parameters such as wavelength (λ) and laser intensity turn out to be the most characteristic responsible for NP production, for example, green lasers show higher formation efficiency than infrared lasers, and nanosecond pulses of the laser cause a strong thermal effect.

REFERENCES

[1] J. W. Alexander, “History of the Medical Use of Silver,” *SURGICAL INFECTIONS*, vol. 10 (3), 2009.

[2] V. D. L. I. A. v. B. A. Graf Christina, “A General Method To Coat Colloidal Particles with Silica,” *Langmuir*, vol. 19 (17), pp. 6693–6700, 11 July 2003.

[3] K. H. M. S. Z. B. Iravani S, “ Synthesis of silver nanoparticles: chemical, physical and biological methods,” *Research in Pharmaceutical Sciences*, vol. 9, pp. 385–406, 2014.

[4] S. S., *Biosynthesis and immobilization of nanoparticles and their applications*, University of pune, 2005, pp. 1–57.

[5] G. R. P. J. Pareek V., “Do physico-chemical properties of silver nanoparticles decide their interaction with biological media and bactericidal action? A review.,” *Mater. Sci. Eng. C.*, vol. 90, pp. 739–749, 2018.

[6] Y. T. &. B. V. Shu Zhang, “A Review on Preparation and Applications of Silver-Containing Nanofibers,” *Nanoscale Research Letters*, vol. 80, 09 February 2016.

[7] H. F. K. a. M. H. Bernd Nowack, “120 Years of Nanosilver History: Implications for Policy Makers,” *Environ. Sci. Technol.*, vol. 45(4), pp. 1177–1183, 10 January 2011.

[8] M. I. A. V. M. C. R. A. P. A. A. P. M. L. G. P. a. N. C. Maria Chiara Sportelli, “The Pros and Cons of the Use of Laser Ablation Synthesis for the Production of Silver Nano-Antimicrobials,” *Antibiotics (Basel)*, vol. 7, 28 July 2018.

[9] B. B. B. C. R. e. Manish Kothakonda, “Core-Shell Nanoparticles for Energy Storage Applications,” in *Pulsed Laser Ablation: Advances and Applications in Nanoparticles and Nanostructuring Thin Films*, Pan Stanford Publishing Pte. Ltd., 2018, pp. 277-316.

[10] M. P. B. V. S. e. Vardan Galstyan, “Metal Oxide Nanostructures in Food Applications: Quality Control and Packaging,” *Chemosensors*, vol. 6, no. 2, 14 April 2018.

[11] A. M.A.Virji, “8.06 - A Review of Engineered Nanomaterial Manufacturing Processes and Associated Exposures,” *Comprehensive Materials Processing*, vol. 8, pp. 103-125, 16 April 2014.

[12] L. G. C. E. M. e. Tomy Acsente, Tungsten Nanoparticles Produced by Magnetron Sputtering Gas Aggregation: Process Characterization and Particle Properties, London: IntechOpen, 2020.

[13] SPI LASERS LIMITED, [Online]. Available: https://www.spilasers.com/application-ablation/what-is-laser-ablation/.

[14] R. W. G. L. B. H. M. a. D. M. Getahun Merga, "Redox Catalysis on "Naked" Silver Nanoparticles," *J. Phys. Chem. C*, vol. 111, pp. 12220–12226, 2007.

[15] U. D. Z. D. Z. A. Oliveira M, " Influence of synthetic parameters on the size, structure, and stability of dodecanethiol-stabilized silver nanoparticles," *J Colloid Interface Sci.*, vol. 292, pp. 429–435, 2005.

[16] J. Y. Song and B. S. Kim, "Rapid biological synthesis of silver nanoparticles using plant leaf extracts," *Bioprocess and Biosystems Engineering*, vol. 32, pp. 79-84, 26 04 2008.

[17] J. G. L. S.-Z. Qiao, "Chapter 21 - Synthetic Chemistry of Nanomaterials," in *Modern Inorganic Synthetic Chemistry (Second Edition)*, Elsevier B.V., 2017, pp. 613-640.

[18] A. A. S. C. P. Suk Fun Chin, "Size Controlled Synthesis of Starch Nanoparticles by a Microemulsion Method," *Journal of Nanomaterials*, vol. 2014.

[19] A. H. J. Z. Y. X. C. M. L. Yong X. Gan, "Hydrothermal Synthesis of Nanomaterials," *Journal of Nanomaterials*, vol. 2020.

[20] S. B. S. A. R. Singaravelan, "Electrochemical synthesis, characterisation and phytogenic properties of silver nanoparticles," *Applied Nanoscience*, vol. 5, no. 8, pp. 983–991, 18 January 2015.

[21] A. M. Hussein, *Synthesis of silver nanoparticles*, Mansoura University, 2016.

[22] S. Iravani, "Bacteria in Nanoparticle Synthesis: Current Status and Future Prospects," vol. 2014.

[23] M. M. G. P. M. N. G. Palaniselvam Kuppusamy, "Biosynthesis of metallic nanoparticles using plant derivatives and their new avenues in pharmacological applications – An updated report," *Saudi Pharmaceutical Journal*, vol. 24, no. 4, pp. 473-484, July 2016.

[24] R. d. L. Mariana Guilger-Casagrande, "Synthesis of Silver Nanoparticles Mediated by Fungi: A Review," *Bioeng. Biotechnol*, vol. 7, 22 October 2019.

[25] S. V. M. A. e. Felix LewisOscar, Algal Nanoparticles: Synthesis and Biotechnological Potentials, London: IntechOpen, 2016.

[26] K. J. T. Y. K. T. S. H. Mafune F, "Structure and stability of silver nanoparticles in aqueous solution produced by laser ablation," *J Phys Chem B.*, vol. 104, pp. 8333–8337, 2000.

[27] S. A. V. V. S. G. B.-V. F. Dolgaev SI, "Nanoparticles produced by laser ablation of solids in liquid environment," *Appl Surf Sci.*, vol. 186, pp. 546–551, 2002.

[28] a. M. M. Amendola V., "Laser ablation synthesis in solution and size manipulation of noble metal nanoparticles," *Phys. Chem. Chem. Phys.*, vol. 11, pp. 3805–3821, 2009.

[29] F. M. a. M. T. Sakamoto M., "Light as a construction tool of metal nanoparticles: synthesis and mechanism," *j. Photochem. Photobiol. C*, vol. 10, no. 1, pp. 33–56, 2009.

[30] N. N. Kawasaki M, "1064-nm laser fragmentation of thin Au and Ag flakes in acetone for highly productive pathway to stable metal nanoparticles," *Appl Surf Sci.*, vol. 253, pp. 2208–2216, 2006.

[31] B. C. N. B. E.-S. M. Link S, "Laser-Induced shape changes of colloidal gold nanorods using femtosecond and nanosecond laser pulses.," *J Phys Chem B.*, vol. 104, pp. 6152–6163, 2000.

[32] G. A. Shafeev, "FORMATION OF NANOPARTICLES UNDER LASER ABLATION OF SOLIDS IN LIQUIDS," in *Laser Ablation: Effects and Applications*, New York, Nova Science Publishers, Inc., 2011, pp. 191-226.

[33] I. I. B. N. N. N. I. K. K. D. B. K. G. B. A. A. S. Nikolov, "Influence of the laser pulse repetition rate and scanning speed on the morphology of Ag nanostructures fabricated by pulsed laser ablation of solid target in water," *Applied Physics : A Material science and processing*, vol. 123, 27 October 2017.

[34] M. A. M. F. A. a. S. A. R. Amir Reza Sadrolhosseini, "Laser Ablation Technique for Synthesis of Metal Nanoparticle in Liquid," in *Laser Technology and its Applications*, 2018.

[35] K. I. N. W. M. T. Takeshi Tsujia, "Preparation of silver nanoparticles by laser ablation in solution: influence of laser wavelength on particle size," *Applied Surface Science*, Vols. 202 (1-2), pp. 80–85, December 2002.

[36] B. S. H. A. K. Mohammad Zamakhsari Alhami, "Synthesis of silver nanoparticles using laser ablation Method utilizing Nd:YAG Laser," *AIP Conference Proceedings*, vol. 2202, no. 1, 27 December 2019.

[37] K. S. M. Y. e. Alexander Pyatenko, "Synthesis of silver nanoparticlesby laser ablation in pure water," *Applied Physics A*, vol. 79, no. 4, pp. 803-806, September 2004.

[38] K. T. T. M. Tsuji T, "Preparation of nano-size particle of silver with femtosecond laser ablation in water.," *Applied Surface Science*, vol. 206, pp. 314–320, 2003.

[39] P. Singh Beer Pal, *TOP-DOWN AND BOTTOM-UP APPROACHES FOR SYNTHESIS OF NANOMATERIALS.*

[40] E. Teirumnieks, I. Balchev, R.S. Ghalot, and L. Lazov, "Antibacterial and anti-viral effects of silver nanoparticles in medicine against COVID-19 - A review". Laser Physics 31 (1), 013001. https://doi.org/10.1088/1555-6611/abc873

[41] L. Lazov, N. Angelov, E. Teirumnieks and E. Teirumnieka, "Preliminary numerical analysis for the role of speed onto laser technological processes". Environment. Technology. Resources. Proceedings of the 12th International Scientific and Practical Conference. Volume III. – Rezekne, 2019. – pp. 137. – 142. http://dx.doi.org/10.17770/etr2019vol3.4154

[42] P. Narica, L. Lazov, A. Teilans, P.Grabusts, E. Teirumnieks and P. Cacivkins, "Method for Color Laser Marking Process Optimization with the use of Genetic Algorithms". Environment. Technology. Resources. Proceedings of the 11th International Scientific and Practical Conference. Volume II. – Rezekne, 2017. – pp. 101. – 106. http://dx.doi.org/10.17770/etr2017vol2.2607

Environment. Technology. Resources. Rezekne, Latvia
Proceedings of the 13th International Scientific and Practical Conference. Volume 3, 84-88

Features of the Work of Industrial Fences in the Conditions of the Far North and Analysis of Technologies for Strengthening Existing

Alexander Grigoriev
Institute of Engineering Sciences
Pskov State University
Pskov, Russia
grigorevalexandr@mail.ru

Alexander Rytvin
Institute of Engineering Sciences
Pskov State University
Pskov, Russia
ry.work@mail.ru

Melkov Boris
Institute of Engineering Sciences
Pskov State University
Pskov, Russia
bormssp@bk.ru

Nadezhda Dmitrieva
Institute of Engineering Sciences
Pskov State University
Pskov, Russia
tom-cat28@ya.ru

Elena Strelnikova
Institute of Engineering Sciences
Pskov State University
Pskov, Russia
strelnikova-l64@mail.ru

Abstract **- The paper focuses on the work of steel industrial fences in the conditions of the Far North, based on the results of the actual impact of snow masses. A computational model is developed for estimating the resulting stresses in the structure. Methods for assessing the impact of snow masses are proposed. The technologies of strengthening the existing fences are analyzed.**

Keywords **- industrial fences, snow loads, technology of reinforcement of industrial fences**

I. INTRODUCTION

The article describes the features of the work of industrial fences of the Glitter3d type, produced in the form of a welded grating made of a steel bar with a diameter of 3-5 mm with a polymer shell. Fences of this type are used everywhere for the construction of fences of various objects. The peculiarity of this fence is the ability to maintain visual transparency without losing its main functional purpose. Such fences can be used for fencing school yards, warehouses, military and industrial facilities. They are often installed on the borders of land plots of railway stations and bus stations, sports grounds and house territories, parks, gardens, squares. This type of fencing is particularly widely used in the construction of protective fences of protected areas and objects. Due to the transparency, grating fences ensure timely detection of the intruder near the protected object.

The use of industrial fences is now widespread on the territory of the Russian Federation. Fences are widely used in various climatic latitudes. However, when using industrial fences in latitudes with a high height of snow cover, frequent destruction of the grids of this fence was repeatedly noted.

In 2019, the authors of the article conducted a technical survey of more than 30 kilometers of such a fence located in the area of the Kola Peninsula, near the city of Murmansk. During the survey, numerous damage to the grating nets was revealed. Due to the large length of the fence examined, it became possible to systematize the defects and damages that occur in them in the conditions of the Far North.

II. CLIMATIC CONDITIONS

The climate of the area where the survey of fences was carried out is formed under the influence of Arctic and warm Atlantic air masses.

Natural and climatic conditions are characterized by long and cold winters with strong winds, a lack of natural light and ultraviolet radiation, the spread of permafrost, and high humidity. Murmansk belongs to the Atlantic-Arctic zone of temperate climate with a predominance of warm air flows from the North Atlantic and cold air flows from the Atlantic sector of the Arctic, which is characterized by an increase in the frequency of cyclones in the cold season and anticyclones in the warm season.

Online ISSN 2256-070X
https://doi.org/10.17770/etr2021vol3.6583

The proximity of the warm Gulf Stream causes abnormally high winter air temperatures here, large temperature differences between the Barents Sea and the mainland in the summer and winter months – large temperature variability when the wind direction changes.

According to the schematic map of climate zoning (SP 131.13330.2012), the construction area belongs to the construction and climate zone IIA. According to the schematic map of the zoning of the northern construction and climate zone (SP 131.13330.2012, fig. A2) the territory is characterized by the least severe conditions.

The average temperature of the coldest winter months (January, February) is - 9 ° C on the coast of the Kola Bay. The average temperature of the warmest month (July) ranges from +10 ° C to +14 ° C. The duration of the frost-free period on the coasts exceeds 100 days, in other areas it ranges from 50 to 100 days.

Murmansk completely belongs to the area of excessive moisture. The annual precipitation reaches 600-700 mm (on the coast of the Kola Bay). The height of the snow cover varies from 80 cm in the south to 40 cm or less on the coast of the Kola Bay, where the snow is blown away by the wind.

Frequent snowstorms are typical for the city of Murmansk. The largest number of them falls on the period from January to March.

The Polar night lasts from December 2 to January 12, and December 22 is its peak. In the period from May 22 to July 22, the sun does not go below the horizon, the polar day comes.

Storms are most frequent (the average annual number of days – 70 - 90) from October to March, fog and precipitation - in July - August. Poor visibility (less than 1 mile) can be observed throughout the year, its frequency is 5-15%.

Frequent and abrupt changes in weather conditions sometimes lead to heavy snowfall with the formation of snow drifts on the roads (with an average daily precipitation rate of about 40 cm), storm winds (with a wind force of 25 m/s. and more), severe frosts (with a temperature of-25-30 ° C), ice on the roads, icing of power lines.

In accordance with SP 20.13330.2016 “Loads and impacts. Updated version of SNiP 2.01.07-85,*” the territory belongs to:

- to the IV wind region, the standard wind pressure is 0.48 kPa (48 kgf/m2);
- to the II district by the thickness of the ice wall, the thickness of the ice wall is 5 mm;
- by the weight of the snow cover to the V district with the calculated value of the weight of the snow cover-350 kgf/m2.

According to SP 14.13330.2018 and OSR-97, the seismicity of the area is 6 points.

According to V. Demin and F. Romanenko, the climate has been warming recently, but precipitation is also increasing [1] – [4].

III. RESULTS OF THE FENCE SURVEY AND DAMAGE CLASSIFICATION

The fence is a metal grating welded at the crosshairs of the rods. The rods are coated with a polymer shell or paint. The supporting elements are metal racks with a cross section of 50x50x2 or 80x80x2 millimeters.

The appearance of the section is shown in Fig. 1. The main damage to the sections is structured according to the frequency of their occurrence and is shown in the following figures:

Fig. 1. View of an undamaged grating fence.

Fig. 2. Destruction of the panel near to the support.

Fig. 3. Destruction of the panel near to the support.

Fig. 4. Destruction of the panel between the supports.

The most common defect of the panels is the destruction of the welded joints near the supports with the bending of the panels. Next in frequency is damage with the grid bending out of the plane. There are also such destructions as a cut of bolts of fastenings, loss of stability of support posts, but all these damages make no more than 10 percent, and are manifested together with damage to welded joints near supports with bending of panels. Damage to the panels is significant for the fence as a whole. To determine the causes of destruction, it is necessary to analyze the causes that led to the occurrence of these damages.

IV. ANALYSIS OF THE CAUSES OF DEFECTS

After analyzing the nature of the damage to the fences, taking into account their localization along its length, the complex terrain where the fences are located, and the difficult climatic and meteorological conditions of the construction area, it can be concluded that all the above-mentioned defects appeared due to the impact on the fence of increased snow deposits that occur around it and which, apparently, are characteristic of this type of terrain. In accordance with SP 20.13330.2016 “Loads and impacts. Updated version of SNiP 2.01.07-85,*” construction territory refers to:

- to the IV wind region, the standard wind pressure - 48 kgf/m2;
- to the II district by the thickness of the ice wall; the thickness of the ice wall is 5 mm;
- to the V snow area, the estimated weight of the snow cover is 350 kgf/m2.

The estimated value of the snow cover weight according to the normative data for this area is only 350 kgf/m2 (250 kgf/m2 is the normative value), but it is obvious that the actual snow loads in the area where the fences are located are much higher.

Snowfall and snowstorms in winter due to the difficult terrain lead to increased snow deposits, especially at the foot of the slopes, in the lowlands and in the beds of streams, forming snow drift of different heights and different lengths.

In order to analyze what happens in the winter period with the built fence, we will use information taken from open sources, including data from manufacturers of similar fence systems.

Let us consider the freely available photos taken in the winter of 2016-2017 clearly illustrating the amount of snow deposits (Fig. 5).

On the one hand, fences can be completely covered with snow at its entire height. The thickness of the snow cover in this case can reach 2-2.5 m, and in the presence of a protective safety barrier and large values. The density and thickness of the snow layer is such that it can withstand the weight of a person (Fig. 5).

Fig. 5. The height of the snow next to the fence.

Fig. 6. Snow cover height.

On the other hand, in winter, the elements of fences become icy, snow freezes on them, gradually turning the mesh panel into a vertical surface that is almost impervious to wind and snow. In this state, the fences practically begin to perform a snow-retaining function, for which they were not designed.

Fig. 7. Snow cover height.

Snowfalls and blizzards lead to increased snow deposits at the icy fences, forming snow drifts – snow bags. The height of snow bags can reach values commensurate with the height of the fence. At the same time, the snow bag is formed in two directions, but on the windward side its value is greater.

Snow deposits are formed in layers. With temperature changes and wind action, the snow gradually cures and increases its density. In the lower layers, during thaws, meltwater can appear, which, when absorbed into the snow, significantly increase its mass, and when frozen, the snow mass saturated with water can turn into ice.

Next, we will show how much the value of the snow load can differ from the standard value for the V snow area during the formation of snow drifts.

Let us estimate the amount of snow load on the earth's surface from the accumulated snow cover with a thickness of 2-2.5 m.

According to clause 5.3 of GOST R 53613-2009 “The impact of natural external conditions on technical products. General characteristics. Precipitation and wind”, the density of the accumulated snow varies from 200 to 400 kg/m3.

Then the snow load from the snow cover with a capacity of 2 - 2.5 m on the ground surface will be:

$2 \cdot 200 = 400$ kg/m^2; $2 \cdot 400 = 800$ kg/m^2;
$2.5 \cdot 200 = 500$ kg/m^2; $2.5 \cdot 400 = 1000$ kg/m^2,

400 - 1000 kg/m^2, which is 1.6 - 4 times higher than the standard value for the V snow area of 250 kg/m^2.

Let us estimate the amount of snow load when a snow bag is formed at a fence with a height of 2 m and 2.5 m.

The assessment is performed using the program of the WEST engineering and calculation complex “SCAD OFFICE” in accordance with the requirements of clause 10 of SP 20.13330.2016 “Loads and impacts. Updated version of SNiP 2.01.07-85*”. According to the results of the calculation, it turns out that the snow load in the area of the formation of a snowbank at the fence exceeds the standard value for the V snow area equal to 250 kg/m^2 by 1.3 - 1.6 times (Fig. 8).

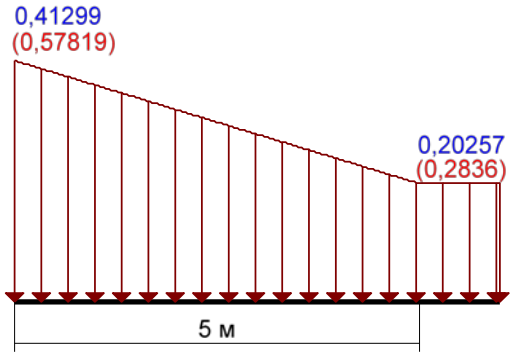

Fig 8. Calculation result snow load.

Snow and ice masses formed at the panels in winter, when freezing and subsequent thawing leads to deformation of the panels and further to their damage in the form of destruction of welded joints between the grid rods. When the welded joints between the mesh rods are destroyed, the rigidity of the panel decreases, causing even greater deformations, which in turn lead to even greater damage to it. Eventually, the panel breaks out of the mounts on the racks.

Freezing and subsequent melting of snow and ice masses also leads to damage to the fence elements.

Damage to panels and elements of protective barriers can occur both during one winter period (for one year), and gradually over several years. Since damage to fences leads to violations of the protective perimeter and to expensive repairs to replace fences, it is necessary to develop measures for the construction of fences that resist such snow loads [4] – [5]. Fences of this type are used throughout the Russian Federation and it should be noted that the fences which are regularly cleaned of snow do not experience such damage.

V. MEASURES THAT INCREASE THE OPERATIONAL PROPERTIES OF FENCES

To reduce the impact of meteorological influences (primarily snow) on the elements of fences, two groups of measures can be distinguished: constructive and operational.

Structural measures (for strengthening fences) should include the installation of 2 - 3 horizontal elements between the posts at a height – crossbars made of bent or closed galvanized profiles, to which additional fastening of the panels is carried out with retainers.

An example of a reinforced similar fence and its elements are shown in Fig. 9 and 10 (technical solution of JSC "CeSIS NIKIRET», http://www.cesis.ru/zagrazhdenie-maxaon-arktika).

Fig. 9. An example of a reinforced similar fence, an additional stiffener, a reinforced tip (taken from the site http://www.cesis.ru)

Fig. 10. Additional stiffener (taken from the site http://www.cesis.ru)

Operational measures should include:

- regular snow removal between the fences and in front of them, thereby preventing the accumulation of snow masses and the formation of huge snow drifts at the fences;
- cleaning of fence panels from frozen snow.

Snow removal is also recommended during the construction period.

VI. CONCLUSION

According to the results of the study of the grating fences features in the conditions of the Far North, it was determined that the existing technology of the device of fences needs to be improved. Fences around which snow removal will be periodically carried out do not need to be finalized. For the rest of the installed or projected fences of this type, it is recommended that the fences be made with additional horizontal elements that ensure the rigidity of the panels.

When using horizontal crossbars between the risers, a structure is formed in which the panels cease to be load-bearing elements and perform only an enclosing function.

In conclusion, it should be noted that the existing standards of the Russian Federation do not have instructions for determining the snow load on such panels, which makes it difficult to calculate such structures. According to the results of the inspection of the actually mounted panels, it was determined that the fence panels work as beams taking on the snow load. The deformation and destruction of the panels look like a beam with a rigid pinching on the supports.

Based on the results of this work, it is recommended to conduct experiments with a real assessment of the snow load on the fence panel. According to the results of the survey, it was determined that a significant part of the snow load can be transmitted directly to the fence panels, and not to the ground surface.

REFERENCES

[1] F. Romanenko, "Geomorphological processes in the mountains of the Kola Peninsula and climate change," Bulletin of Moscow University, Moscow, № 5, pp. 78-86, 2016. (in Russian)

[2] V. Diomin, A. Antsiferova, and O. Mokrotovarova, "Changes of the air temperature in Murmansk since the 19th century," Bulletin of Kola Scientific Center RAN, Murmansk, № 1, pp. 113-125, 2015. (in Russian)

[3] A. Fedyaev, "Development of methods for calculating the probabilistic characteristics of snow loads for assessing the reliability of building structures," Bulletin of Scientific Conferences, Tambov, № 12-2, pp. 106-108, 2016. (in Russian)

[4] A. Chapligin and N. Fedorov, "Protective fences. Problems and prospects of application," Security Algorithm, Saint Petersburg, № 4, pp. 50-53, 2016. (in Russian)

[5] I. Vasilyev, "Modular temporary fencing and stationary objects," Oil and Gas Exposition, Penza, № 4, p. 82, 2014. (in Russian)

[6] N. Kazakov, A. Muzichenko, E. Kazakova, I. Kononov, and V. Pavlov "The structure and texture of the snow mass on the Kola Peninsula," Snow Physics, Chemistry, and Mechanics, Yuzhno-Sakhalinsk, part 1, pp. 58-63, 2017. (in Russian)

[7] SP 20.13330.2016 "Loads and impacts. Updated version of SNiP 2.01.07-85* (with Amendments N 1, 2)"

[8] SP 131.13330.2018 "SNiP 23-01-99* Construction Climatology"

[9] GOST R 57278-2016 "Protective fences. Classification. General provisions"

[10] GOST R 53613-2009. "The impact of natural external conditions on technical products. General characteristics. Precipitation and wind"

[11] SP 16.13330.2017 "Steel structures. Updated version of SNiP II-23-81*" (as amended, with Amendments N 1, 2)

[12] T. Ohlopkova, G. Guryanov, A. Plotnikov, "Construction and design of buildings and structures in permafrost conditions," Engineering Bulletin of the Don, №4, 2018. (in Russian)

[13] M. Kasperski, "A consistent approach for estimating the design value of the snow load on the ground from confined ensembles," in Proc. of 7th Int. Conf. on Snow Engineering, 2012, Fukui, Japan.

[14] M. Kovalev, "New Fensys developments for GAZPROM Group facilities," Oil and Gas Exposition, p. 73, 2013. (in Russian).

Environment. Technology. Resources. Rezekne, Latvia
Proceedings of the 13th International Scientific and Practical Conference. Volume 3, 89-94

Cleaning of Ceramic Ultrafiltration Membranes After Filtration of Hay Hydrolysate

Kamila Gruskevica
Water Research and Environmental Biotechnology Laboratory
Riga Technical University
Riga, Latvia
kamila.gruskevica@rtu.lv

Matrins Strods
Water Research and Environmental Biotechnology Laboratory
Riga Technical University
Riga, Latvia
martins.strods_4@rtu.lv

Janis Rubulis
Water Research and Environmental Biotechnology Laboratory
Riga Technical University
Riga, Latvia
janis.rubulis@rtu.lv

Linda Mezule
Water Research and Environmental Biotechnology Laboratory
Riga Technical University
Riga, Latvia
linda.mezule@rtu.lv

***Abstract* - Hydrolysis of the lignocellulosic biomass results in the release of high-value chemicals that during industrial processing can be recovered with membrane technologies. To maintain an effective performance of the membranes used in the technological processing of biomass, their regular cleaning is essential. Although several guidelines may be found for membrane cleaning in the cases of organic fouling, the data for cleaning membranes fouled by hydrolyzed lignocellulosic biomass is limited. Current research is aimed to evaluate physical (air backpulse) and common cheap chemical membrane cleaning methods. The results showed that air backpulse alone had a minor (9%) effect on the membrane cleaning. The alternation of NaOH (1 %) solution with the NaClO (200 mg/L of Free chlorine) was the most effective approach for membrane cleaning. The cleaning effectiveness was 95.1 % for 50 nm membrane and 89 % for 200 nm membrane, indicating that membranes used for hydrolyzed lignocellulosic biomass filtration can be effectively cleaned using affordable and accessible chemicals.**

Keywords* - *ceramic membranes, cleaning, fouling, lignocellulosic biomass

I. Introduction

Lignocellulosic biomass is abundant on Earth with an annual global production of about 181.5 billion tonnes. Around 7 billion tonnes are used as fodder or for energetic and material purposes and about 3.5 billion tonnes are produced as agricultural residues without any further use [1]. At the same time, lignocellulosic raw materials and bio-based primary products can be converted into high-value chemicals, e.g., biofuels, furfural, carbohydrates [2]. Traditionally, the conversion is one-way subsequent pre-treatment, hydrolysis, fermentation, and product extraction. To facilitate product concentration, purification, and resource recovery, the introduction of membranes in the process stream has been recognized and tested in the treatment of lignocellulosic biomass after enzymatic hydrolysis [3]. Despite the high potential of membrane technologies, their efficiency is highly dependent on the properties of the liquid to be treated and membrane material.

Ceramic ultrafiltration membranes in comparison to polymeric membranes possess several advantages, including toleration to high temperatures and harsh chemical conditions, and a lifespan of 10-20 years [4], [5]. Therefore, ceramic membranes are widely used in food production, pharmaceutical, bioenergy, and other industries. At the same time, membrane operation is cumbersome, especially when fouling is tackled, since it reduces membrane performance efficiency by flux decline (in constant transmembrane pressure (TMP) systems) or increases TMP in constant flux systems. To maintain the membrane performance at a satisfactory level, regular membrane cleaning should be performed [6]. Cleaning procedures are commonly divided into physical (non-reagent) and chemical. While every physical cleaning method has different parameters affecting efficiency, chemical cleaning depends on four basic parameters: flow, reagent concentration, temperature, and contact time [7]. In

Online ISSN 2256-070X
https://doi.org/10.17770/etr2021vol3.6579

the food industry, where organic compounds are the main foulants, it is considered that the cleaning should be performed at the same temperature as the filtration [7], to avoid protein crosslinking and denaturation [8]. The selection of the most appropriate cleaning agent and its concentration is crucial to avoid unwanted chemical reactions, damage of the membrane, or worsen contamination. Similarly, as in the food industry, the same issues have also been observed in the treatment of hydrolyzed biomass, where the solution contains lignocellulosic residue, released carbohydrates, and proteins, if enzymatic hydrolysis is performed [3]. All of these tend to foul the membranes.

To remove the organic foulants, alkaline reagents are the most widespread, since alkalis dissolve organic compounds, saponificate fats, and oils, and hydrolyze proteins [9], [10]. Nevertheless, the longevity of the cleaning procedure should be carefully evaluated to perform effective cleaning from one side, and not to terminate the production process for too long on the other. Although, general guidelines can be found on the cleaning of membranes fouled with different types of contaminants, every case must be evaluated individually. There are detailed recommendations available for various fields of the food industry [7], however, cleaning protocols for membranes applied in the treatment of hydrolyzed lignocellulosic biomass have not been reported or the data is limited. Within this study, the selection of the most appropriate treatment protocol for cleaning of ceramic ultrafiltration membranes after the filtration of hay hydrolysate was performed. To mimic industrial production, a laboratory pilot scale membrane system was used for the studies. Permeate flux was selected as the representative parameter to characterize membrane fouling. The general acceptance, that the lower the flux, the bigger the fouling was used to estimate the efficiency of the cleaning procedure.

II. Materials and Methods

A. Experimental Setup

Filtration experiments and cleaning procedures were performed in a pilot-scale system (JWCMF – C.2, Jiangsu Jiuwu Hitech Co, China) equipped with a 30L AISI 316 tank with a water jacket for temperature control. The filtration setup (Fig. 1) was designed for constant flux filtration experiments with an air backpulse option. The constant feed flow was supplied by pump 4 (Grudfoss, CM5-4 A-R-GE-AQQE F-A-A-N) and regulation valves 5 and 12. Air backpulse was driven by the air compressor 21, solenoid valves 15; 19; 20, and a programmable logic controller for permeate flow, air intake, and air exhaust time control. Two mechanical pressure meters (8, 11) were used for the pressure measurement in feed flow and retentate flow. Flow meters were used to measure the flow of permeate (16) and retentate (13). The temperature was recorded using an electronic thermometer (6).

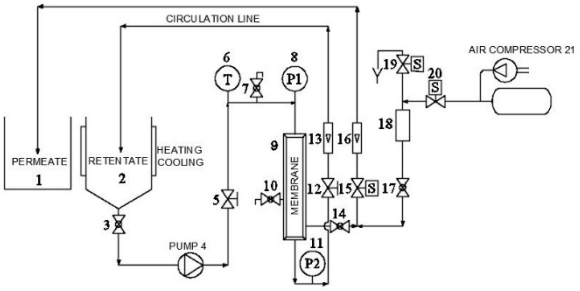

Fig. 1. Experimental filtration system with 30 L tank and 0.24 m2 membrane filtration area.

B. Membranes

Two tubular ceramic membranes from Jiangsu Jiuwu Hitech Co (Jiangsu, China) with a pore size of 50 and 200 nm were used for filtration. Both membranes were made of TiO_2 filtering layer on α-alumina support with 19 parallel feed flow channels, an outer diameter of 25.4 mm, and a total length of 1016 mm. The inner diameter of the feed flow channels was 3.3 mm, the membrane area 0.24 $m^{2,}$ and the porosity 35 %. The hydraulic resistance for 50 and 200 nm membranes was calculated from the deionized water flux to 4.8 * 10^{-3} and 3.9 * 10^{-3} bar m^2 hl^{-1}, respectively. The cross-flow velocity during filtration was 0.87 ms^{-1}.

C. Hydrolysate Preparation and Filtration

Dried hay from semi-natural grasslands was used as a source material for hydrolysate production. The biomass was milled (Retsch SM100, Haan, Germany) to obtain particle size ~ 1 mm. Then, the biomass (3% w/v in nanofiltered water) was thermally pre-treated/hydrolyzed (121°C, 1 bar for 5 minutes) in a 30 l AISI 316 reactor equipped with a mixer. Further, the hay solution was cooled to 30 °C and passed through the microfilter with a pore size of 1 μm (Geyser, Russia) to remove major suspended solids able to block the ceramic membrane and the peristaltic pump. All tests were performed using 15 l of hydrolysed hay solution at 30°C that is the reported optimum concentration for biomass hydrolysis in the given reactor system [11].

Transmembrane pressure (TMP) was calculated according to (1) :

$$TMP = \frac{P_1+P_2}{2} \quad (1)$$

where: – P_1 feed pressure, MPa; P_2 – retentate pressure, MPa;

After each filtration test, the membranes were cleaned using selected chemicals.

D. Biomass granulometric composition

To analyze biomass particle size and evaluate the efficiency of microfiltration, the granulometric composition of the biomass collected from the microfilter was determined with the vibration separator Controls D 407 (Newzeland) and different sieve sizes (<63, 63, 125, 250, 500, 1000).

E. Physical Membrane Cleaning

During air-water backpulse cleaning, the air was supplied by the compressor through valve 7 (Fig. 1). The air compressor pressure was set to 3 bar. The backpulsing was performed for 5 sec. every 5 mins. The air exhaust time was 8 mins.

F. Chemical Membrane Cleaning

The cleaning of membranes was performed according to the scheme in Table 1 at TMP of 0.5 bar and included 8 different test setups at a constant temperature regime. Before each chemical cleaning procedure, an initial rinse of the fouled membrane and the filtration system with deionized water at room temperature and a TMP of 0.5 bar was performed for 3 min. After the rinse, permeate flux (Q_b) with deionized water at 25°C and average TMP of 2.5 bar was measured. The second rinse (0.5 bar TMP) was performed with deionized water to remove chemical cleaning agents after the cleaning. Finally, permeate flux (Q_a) was measured with deionized water at temperature 25°C and TMP average 2.5 bar.

G. Cleaning Efficiency Calculations

Before every filtration experiment, the initial water flux of the clean membrane was measured using deionized water. The cleaning efficiency was evaluated as permeate flux recovery. The final flux recovery was based on the measurements of deionized water permeate flux through the cleaned membrane. Cleaning efficiency (%) was calculated according to (2)

$$F = \frac{Q_b - Q_a}{Q_b} \times 100 \qquad (2)$$

where: Q_a – deionized water permeate flux after cleaning, l/h; Q_b – deionized water permeate flux before cleaning, l/h.

TABLE 1 TESTED CLEANING APPROACHES FOR 50 AND 200 NM CERAMIC MEMBRANES

Test	Membrane pore size, nm	Cleaning agents	Agent concentration, %	Cleaning time, min	Temperature, °C
1	50	HNO_3	1	30	50
2	50	NaOH	1	30	60
3	50	backpulse	-	30	30
4	50	NaOCl	0.023	30	30
5	50	backpulse and NaOH	1	30 + 30	30 and 50
6	50	NaOH and NaOCl	1 and 0.02	30 + 30	50 and 30
7	200	NaOH and NaOCl	1 and 0.02	30 + 30	50 and 30
8	200	NaOCl and NaOH	0.02 and 1	30 + 30	30 and 50

III. RESULTS AND DISCUSSION

The initial permeability of the two membranes (50 nm and 200 nm) was determined before the experiments by linear regression of the deionized water flux (J) against the TMP (Fig.2).

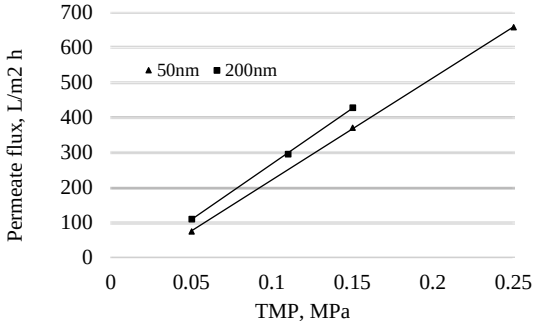

Fig. 2. Water flux against transmembrane pressure for the 50 nm (▲) and 200 nm (■) membranes at 25°C.

As expected, the permeate flux (J) of deionized water for clean membranes was higher for 200 nm membrane if compared to 50 nm membrane. The estimated maximal permeate flux in the pilot system was 1250 m^2 hl^{-1} for 50 nm membrane and 1653 m^2 hl^{-1} for 200 nm membrane.

A. Biomass and hydrolyzate characterization

The estimated granulometric composition revealed that the particles are distributed within the whole range of used sieves. The highest fraction attributed to 125 and 250 μm sizes (Table 2). The fractions were acceptable for further filtration tests.

The estimated physical parameters of the hay hydrolysate (186 NTU turbidity, pH 5.1 – 5.5, conductivity 1850 μS/cm and zeta-potential of 17.5±4.5 mV) were representative of both thermally treated/hydrolyzed biomass and organic filtrates [12].

TABLE 2 GRANULOMETRIC COMPOSITION OF LIGNOCELLULOSIC BIOMASS

Sieve eye size, μm	Amount, %
1000	21,8
500	10,6
250	24,7
125	25,7
63	10,7
< 63	6,5

B. Permeate Flux

Two different stages concerning the permeate flux were distinguished in the thermally hydrolysed hay filtration process. In the first stage, permeate flux decreased significantly (from 28 hl^{-1} to 10 hl^{-1}). This stage lasted approximately 15 minutes for both selected membranes. Then the permeate flux reached a steady-state and remained constant (Fig. 3). The calculated trendlines of the permeate flux decrease were similar when compared with

other studies utilizing 50 and 200 nm ceramic membranes [13], [14].

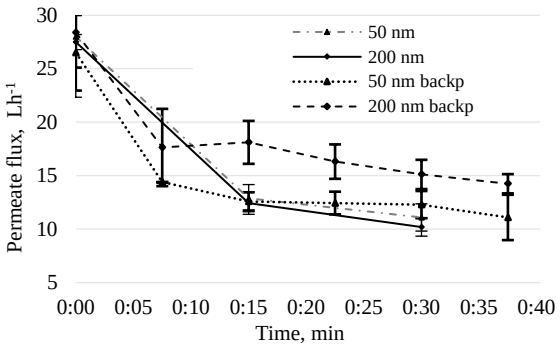

Fig. 3. The permeate flux of thermally hydrolyzed hay solution at 30°C with and without air backpulse for 50 nm and 200 nm ceramic membranes (t=2.02, P=0.05).

To enhance permeation flux, permeate or water can be used for membrane backwashing [15]. Alternatively, air backpulsing can be used [16]. In this study, backpulsing was used to enhance permeation during the hay hydrolysate filtration. The results showed a positive effect of air backpulsing only for a 200 nm membrane. And no effect for the 50 nm membrane. The 200 nm membrane air backpulsing could withstand permeate flux near 15 hl^{-1} for 37 mins (until the full volume of thermally hydrolyzed hay was filtered) (Figure 3).

Similar results for the positive effect of air backpulsing for larger pore size membranes were obtained by [17] for synthetic leather industry wastewater and [18] for raw sugar cane juice filtration. The authors of both studies indicated no positive effect for 20 and 50 nm membranes. Thus, the results of the current study with lignocellulosic hydrolysate complement other findings where air backpulsing is useful for ceramic membranes of microfiltration range/or some loose ultrafiltration range (100-200 nm).

Furthermore, air backpulsing shortened the first phase of intensive flux decline from 15 minutes to 7 minutes. This phenomenon could be attributed to a small-size particle layer disruption and resuspension, leading to more intensive flux decline and faster stable phase onset.

C. Cleaning of Membranes

All of the thermally hydrolysed hay filtration experiments were followed by cleaning methods (Table 1). First, the efficiency of single-step cleaning methods (Test 1-4, Table 1) for a 50 nm membrane was evaluated (Fig. 4). Assessment of HNO_3 (1%) acid solution resulted in no positive effect on the membrane cleaning. This phenomenon may be attributed to the fact that the filtered solution of hydrolysed hay is of organic origin, whereas acids are effective for dissolving inorganic contaminants like metal oxides [8],[19]. The results were therefore excluded from the graphs. NaOH (1%) solution resulted in a 46.2% increase of permeate flux in 30 mins showing the best results obtained by single-step cleaning technique (Fig. 4).

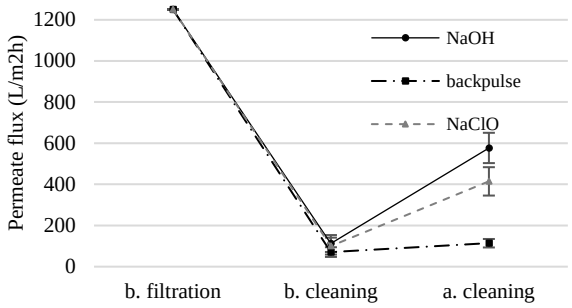

Fig. 4. The permeate flux for 50 nm membrane before filtration ("b. filtration"), after the filtration of thermally hydrolyzed hay solution ("b. cleaning"), and after the cleaning ("a. cleaning").

The Zeta potential of the filtering solution was 17.5±4.5 mV, meaning that the solution was in the unstable region, and particle aggregation and sedimentation could take place on the membrane surface [20]. In this case, it can be beneficial to raise the pH by adding alkali, promoting particle desorption from the membrane surface. The common concentrations of alkalis in these systems are in the range of 0.5 – 2% w/v [8].

Water + air backpulse showed minimal (9%) effect on the cleaning of 50 nm membrane, probably because residual hay particles present in the hydrolysate were much bigger in size than membrane pores. Furthermore, the size of air bubbles generated by the compressor was two orders of magnitude larger than the size of membrane pores, thus, air bubbles could not enter and clean the pores. Thus, air-based hydraulic cleaning techniques are unsuitable for microfiltration membranes [21], [22].

Application of NaOCl solution containing 200 mg/L of free chlorine (shock chlorination technique) resulted in 33.2% cleaning efficiency.

Since single-step cleaning approaches showed only modest results, two-step cleaning approaches were tested (Tests 5-6 in Table 1) to evaluate the potential use of apparently different chemicals in a single set-up.

The combination of air backpulse and NaOH resulted in 21% cleaning efficiency (Fig. 5),

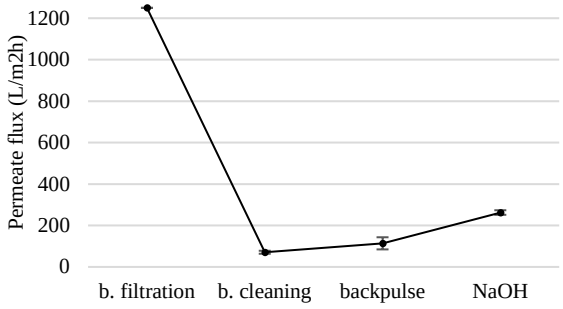

Fig. 5. The permeate flux for 50 nm membrane before filtration, after the filtration of thermally hydrolyzed hay solution, and after the cleaning with air-water backpulse and 1% NaOH solution. b.-before, a.-after.

which is low considering that in single-step cleaning approach with NaOH efficiency was 46.2%. Probably

backpulse disturbed debris layer presented in the pilot system walls, resulting in secondary contamination and decreased NaOH efficiency.

Subsequent use of NaOH and NaClO showed the best performance resulting in 95.1 % cleaning efficiency (Fig. 6).

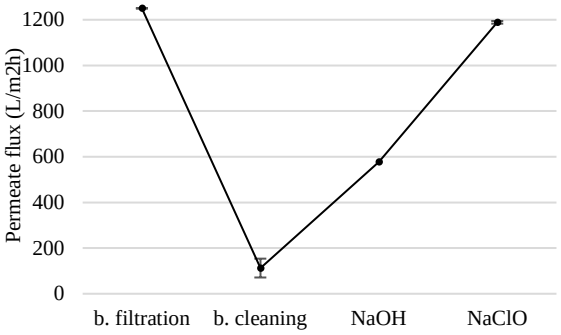

Fig. 6. The permeate flux for 50 nm membrane before filtration, after the filtration of thermally hydrolyzed hay solution, and after the sequencing cleaning with 1% NaOH solution and 0.023% NaClO solution. b.-before, a.-after.

Such consecutive use of alkali and active chlorine has been also shown to be effective for removing biofilms from pipe walls and killing *Bacillus* spores in a bulk [23]. After successful selection of the treatment approach, filtration of hydrolysed hay was validated for the 200 nm membrane. The results demonstrated 89 % efficiency for the consecutive use of NaOH and NaClO (Fig. 7), meaning that the method is equally effective for different size ultrafiltration membranes.

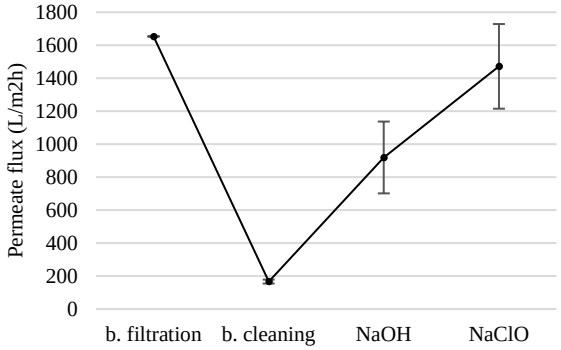

Fig. 7. The permeate flux for 200 nm membrane before filtration, after the filtration of thermally hydrolyzed hay solution, and after the sequencing cleaning with 1% NaOH solution 0.023% NaClO solution. b.-before, a.-after.

To demonstrate the efficiency of the selected step-wise treatment, NaOH and NaClO application was inversed. As expected, the two-step protocol resulted in a mere 46 % cleaning efficiency (Fig. 8), which was lower than using the opposite sequence of reagents.

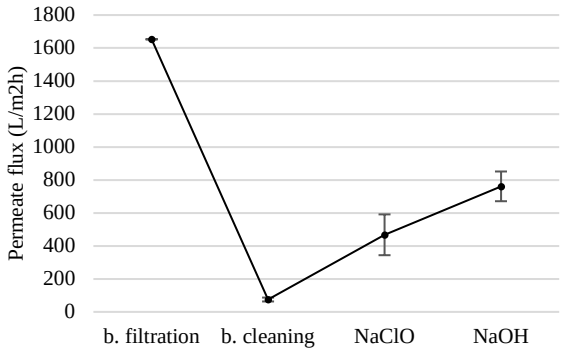

Fig. 8. The permeate flux for 200 nm membrane before filtration, after the filtration of thermally hydrolyzed hay solution, and after the sequencing cleaning with 0.023% NaClO solution and 1% NaOH solution. b.-before, a.-after.

This phenomenon may be attributed to the fact that NaOH loosens deposits on the membrane surface and disperse them, while NaClO promotes a gel layer on the membrane surface to decompose by oxidation and then fall off. The cleaning process is not as effective if active chlorine cannot penetrate the gel layer and effective reaction occurs only with loose particles. Thus, the sequence of the reagents is of big importance.

IV. Conclusions

Multiple physical and chemical methods have been tested to clean ceramic membranes after the filtration of hydrolyzed lignocellulosic biomass to extract fermentable carbohydrates. The results showed that single-step treatment does not provide efficient cleaning and result in less than 50 % cleaning efficiency. Alternation of NaOH (1 %) solution with the NaClO (0.023%) was the most effective approach for membrane cleaning resulting in 95.1 % for 50 nm membrane and 89 % cleaning efficiency for 200 nm membrane. Thus, membranes used industrial production of fermentable carbohydrates from hydrolyzed lignocellulosic biomass can be effectively and quickly cleaned with conventional inexpensive chemicals.

Acknowledgment

The work has been funded by ERDF Project “Zero-to-low-waste technology for simultaneous production of liquid biofuel and biogas from biomass”, No. 1.1.1.1/18/A075.

References

[1] N. Dahmen, I. Lewandowski, S. Zibek, and A. Weidtmann, “Integrated lignocellulosic value chains in a growing bioeconomy: Status quo and perspectives,” *GCB Bioenergy*, vol. 11, no. 1, pp. 107–117, 2019.

[2] O. Rosales-Calderon and V. Arantes, *A review on commercial-scale high-value products that can be produced alongside cellulosic ethanol*, vol. 12, no. 1. BioMed Central, 2019.

[3] A. R. P. P. Weerasuriya Arachchige, L. Mezule, and T. Juhna, “Separation of reducing sugars from lignocellulosic hydrolysate: Membrane experiments & system dynamic modelling,” *Agron. Res.*, vol. 18, no. Special Issue 1, pp. 1099–1106, 2020.

[4] R. J. Ciora and P. K. T. Liu, “Ceramic membranes for environmental related applications,” *Fluid - Part. Sep. J.*, vol. 15,

no. 1, pp. 51–60, 2003.

[5] S. Luque, D. Gomez, and J. R. Alvarez, "Industrial Applications of Porous Ceramic Membranes (Pressure-Driven Processes)," in *Membrane Science and Technology*, vol. 13, Elsevier, 2008, pp. 177–216.

[6] W. Li *et al.*, "Ceramic membrane fouling and cleaning during ultrafiltration of limed sugarcane juice," *Sep. Purif. Technol.*, vol. 190, no. July 2017, pp. 9–24, 2018.

[7] Tetra Pak Processing Systems, *Cleaning in place – a guide to cleaning technology in the food processing industry*, no. Technology, Engineering, Agriculture. Tetra Pack Processing Systems, 2015.

[8] H. Li and V. Chen, "Membrane Fouling and Cleaning in Food and Bioprocessing," in *Membrane Technology*, First Edit., no. July, Elsevier Ltd, 2010, pp. 213–254.

[9] D. C. Olk *et al.*, "Environmental and Agricultural Relevance of Humic Fractions Extracted by Alkali from Soils and Natural Waters," *J. Environ. Qual.*, vol. 48, no. 2, pp. 217–232, 2019.

[10] H. Li, "Cleaning Cycle of Fouled Membranes," in *Encyclopedia of Membranes*, E. Drioli and L. Giorno, Eds. Berlin, Heidelberg: Springer Berlin Heidelberg, 2016, pp. 412–416.

[11] L. Mezule and A. Civzele, "Bioprospecting white-rot basidiomycete irpex lacteus for improved extraction of lignocellulose-degrading enzymes and their further application," *J. Fungi*, vol. 6, no. 4, pp. 1–10, 2020.

[12] L. De Angelis and M. M. F. De Cortalezzi, "Ceramic membrane filtration of organic compounds: Effect of concentration, pH, and mixtures interactions on fouling," *Sep. Purif. Technol.*, vol. 118, pp. 762–775, 2013.

[13] S. Popović, S. Milanović, M. Iličić, M. Djurić, and M. Tekić, "Flux recovery of tubular ceramic membranes fouled with whey proteins," *Desalination*, vol. 249, no. 1, pp. 293–300, 2009.

[14] R. Pérez-Gálvez, E. M. Guadix, J. Berg, and A. Guadix, "Operation and cleaning of ceramic membranes for the filtration of fish press liquor," *J. Memb. Sci.*, vol. 384, no. November, pp. 142–148, 2011.

[15] R. Shang *et al.*, "Hydraulically irreversible fouling on ceramic MF/UF membranes: Comparison of fouling indices, foulant composition and irreversible pore narrowing," *Sep. Purif. Technol.*, vol. 147, pp. 303–310, 2015.

[16] S. Mozia, K. Szymański, B. Michalkiewicz, B. Tryba, M. Toyoda, and A. W. Morawski, "Effect of process parameters on fouling and stability of MF/UF TiO2 membranes in a photocatalytic membrane reactor," *Sep. Purif. Technol.*, vol. 142, pp. 137–148, 2015.

[17] Q. Zhang *et al.*, "Performance study of ZrO2 ceramic micro-filtration membranes used in pretreatment of DMF wastewater," *Desalination*, vol. 346, pp. 1–8, 2014.

[18] V. Jegatheesan, D. D. Phong, L. Shu, and R. Ben Aim, "Performance of ceramic micro- and ultrafiltration membranes treating limed and partially clarified sugar cane juice," *J. Memb. Sci.*, vol. 327, no. 1–2, pp. 69–77, 2009.

[19] C. V. Vedavyasan, *Encyclopedia of Membranes*, no. i. Springer, Berlin, Heidelberg, 2016.

[20] "Zeta potential: An Introduction in 30 minutes," 2011.

[21] X. Shi, G. Tal, N. P. Hankins, and V. Gitis, "Fouling and cleaning of ultrafiltration membranes: A review," *J. Water Process Eng.*, vol. 1, pp. 121–138, 2014.

[22] D. Kuzmenko, E. Arkhangelsky, S. Belfer, V. Freger, and V. Gitis, "Chemical cleaning of UF membranes fouled by BSA," *Desalination*, vol. 179, no. 1-3 SPEC. ISS., pp. 323–333, 2005.

[23] K. Gruskevica, "Decontamination of water supply systems after deliberate pollution," 2015.

Environment. Technology. Resources. Rezekne, Latvia
Proceedings of the 13th International Scientific and Practical Conference. Volume 3, 95-103

3D Mathematical Model Characterizing the Dynamics of the Temperature Field of a Wall Structure with a Double-sided Facing from a Sapropel-hemp Composite Material

Sharif E. Guseynov
Faculty of Science and Engineering
Liepaja University
Liepaja, Latvia
sh.e.guseinov@inbox.lv

Janis S. Rimshans
Institute of Science and Innovative Technologies
Liepaja University
Liepaja, Latvia
no email address

Jekaterina V. Aleksejeva
Institute of Science and Innovative Technologies
Liepaja University
Liepaja, Latvia
Riga Secondary School 34
Riga, Latvia
jekaterina.v.aleksejeva@gmail.com

Aleksandrs Bereznojs
ISMA University of Applied Sciences
Riga, Latvia
alexander.v.berezhnoy@gmail.com

Stanislavs Pleiksnis
Faculty of Engineering
Rezekne Academy of Technologies
Rezekne, Latvia
stanislavs.pleiksnis@inbox.lv

***Abstract* - In this paper, a 3D mathematical model is proposed to determine the dynamics of the temperature field in a three-layer composite sapropel-hemp slab. The proposed model consists of a system of three initial-boundary value problems with respect to the temperature function for each layer, respectively, and one initial-boundary value problem with respect to the unknown velocity of heat propagation along the thickness dimension of the composite sapropel-hemp slab.**

Keywords* - *Composite sapropel-hemp slab, temperature field, mathematical model

I. Introduction

One of the main ways to study the dynamics of the temperature field in multilayer building structures is the apparatus of the thermal conductivity theory, where the hypothesis of a continuous medium is used in modelling, which leads to obtaining linear and nonlinear differential equations: therefore, there appears smoothness requirement both in time and by spatial variables [1]-[3] related to the functions characterizing the properties and states of the components of the medium.

The main goal of such studies is to find the temperature field inside a composite body under known initial and boundary conditions [4]. In this paper, we consider the problem of determining the temperature field in a three-layer composite slab of the parallelepiped shape, where the outer layers (fireproof facing) are bonded with hemp and sapropel mineralized fill. Since sapropel consists mainly of organic substances (ash content of organo-mineral sapropel varies within 25÷50%, mineral-organic – 50-70%, mineralized – 70÷85%, organic – about 30%), then over time, the temperature state of the sapropel-hemp slab will significantly depend, in addition to its heat exchange with the environment, also on the processes of heat release/heat absorption by the volume of the slab, happening due to various reasons (it must be taken into account that the viscosity of the sapropel can reduce gas exchange): for example, resulting in exothermic/endothermic chemical reactions [5]; the energy of radiation penetrating into the volume of the slab through the deformed facing [3],[6],[7]; etc. Consequently, inside the sapropel-hemp slab, internal sources of thermal energy are formed, which can have various types of dependences both on time and spatial variables, as well as on the temperature itself: for example,

Online ISSN 2256-070X
https://doi.org/10.17770/etr2021vol3.6648

if the energy release in the inner layer of a sapropel-hemp slab is caused by chemical reactions, which rate is described by the Arrhenius equation, then the dependency of the volumetric power of energy release on temperature has a reverse exponential character [5],[8].

In this work, a 3D mathematical model is proposed that describes dynamics of the temperature field in the studied sapropel-hemp slab. In the proposed mathematical model, due to the specifics of the material of the inner layer – sapropel-hemp material, it is assumed that, firstly, the temperature conductivity coefficient is a given step function along the vertical axis directed along the thickness dimension of the sapropel-hemp slab, and secondly, the velocity of heat propagation, along with the thermal field, is also considered to be the required function.

II. Restrictive Assumptions, and Construction of Mathematical Model for Temperature Field

Before proceeding to the description of the mathematical model, let us choose the Cartesian coordinate system so that the positive semiaxis of the vertical axis OX_3, characterizing the thickness of the considered sapropel-hemp slab is directed from the outer facing of the slab to the inner side.

Fig. 1 schematically depicts the studied composite sapropel-hemp slab having the size (length, width, height/thickness, respectively) with a double-sided fireproof facing: the outer facing $P^{0,0,0}_{L_1,L_2,L_3}$, where $P^{a_1,a_2,\ldots,a_n}_{b_1,b_2,\cdots,b_n} \overset{def}{\equiv} \left\{x \in \mathbb{R}^n : x_i \in [a_i,b_i],\ i=\overline{1,n}\right\}$, has a height l_1; the inner fireproof facing P_{x_1,x_2,L_3} has a height $L_3 - l_2$; the sapropel-hemp component (i.e. the second/inner layer) of the composite slab has a height $l_2 - l_1$.

Now we can proceed to the construction of a mathematical model for the dynamics of the temperature field of the considered sapropel-hemp slab, having previously listed its physical and mathematical peculiarities and the necessary mathematical assumptions arising from these aspects [9]-[12]. Due to the fact that the considered composite slab is a solid non-periodic heterogeneous medium, the following three circumstances will be present in the constructed 3D mathematical model of the temperature field dynamics [8], [13]-[19]:

First, it cannot be assumed that the velocity of heat propagation is a priori given. Obviously, this circumstance also gives rise to the necessity of constructing a mathematical model to determine the unknown heat propagation velocity. Consequently, there is a need to construct a complete mathematical model consisting of two interconnected equations with the corresponding initial and boundary conditions: in the first equation with respect to the desired unsteady temperature field $T(x,t)$, there is a vector function

$$\vec{\vartheta} \overset{def}{\equiv} \vec{\vartheta}(x,t) = \left(\vartheta_{x_1}, \vartheta_{x_2}, \vartheta_{x_3}\right)^T (x,t),$$

describing the velocity of heat propagation in directions OX_1, OX_2, OX_3, and the second equation is an equation relating to this unknown velocity.

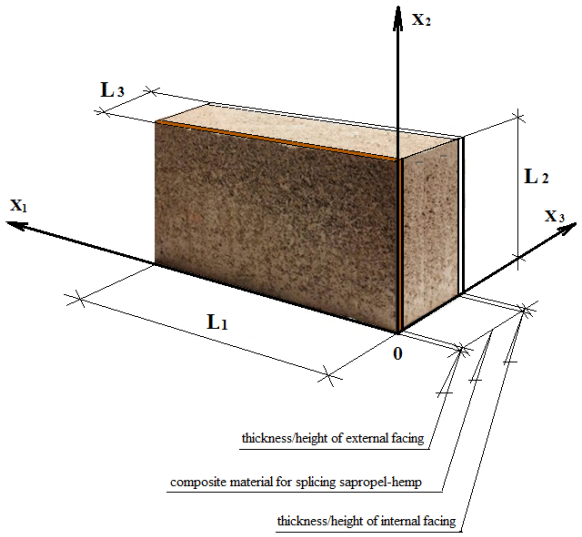

Fig. 1. Composite sapropel-hemp slab.

Second, the coefficient of temperature conductivity $\alpha(\vec{\vartheta}_T)$ can be considered a step function along the vertical axis OX_3 (i.e. relating to the layers). This circumstance, together with the assumption about the insignificance of thermal perturbations [13] in directions OX_1 and OX_2, allows to construct a one-dimensional by the spatial variable (i.e. in the vertical component) nonlinear inhomogeneous equation with respect to the heat propagation averaged over directions OX_1 and OX_2 vector velocity in a composite sapropel-hemp slab, i.e. with respect to scalar function $\vartheta_{x_3}(x,t)$.

Third, due to the fact that the first and third layers interacting with the environment (i.e. facing – outer layers) of the considered composite slab are made of homogeneous fireproof materials (for example, made of clay; of mineral fibres; etc., moreover, it is not necessary that both facings are made of the same fireproof material), and the second layer (inner layer) is its sapropel-hemp component (solid non-periodic heterogeneous medium), then from a mathematical point of view the heating processes on the first and third layers should proceed with the heat flux relaxation mode [17]-[19].

Taking into account the corresponding basic fundamental laws of physics – the laws of molecular diffusion and the laws of heat transfer in solid non-periodic heterogeneous media [13]-[15], [20], – taking into account the above listed three circumstances, we will have the following mathematical model: for $\forall t \geq 0$ it is required to determine the temperature field

$$T(x,t)=\begin{cases}T^{\{1\}}(x,t), x\in P^{0,0,0}_{L_1,L_2,l_1},\\ T^{\{2\}}(x,t), x\in P^{0,0,l_1}_{L_1,L_2,l_2},\\ T^{\{3\}}(x,t), x\in P^{0,0,l_2}_{L_1,L_2,L_3},\end{cases} \quad (1)$$

at any point $x\in P^{0,0,0}_{L_1,L_2,L_3}$ of the composite sapropel-hemp slab from

– a heterogeneous partial differential equation:

$$\frac{\partial T^{\{1\}}(x,t)}{\partial t}+R_1\frac{\partial^2 T^{\{1\}}(x,t)}{\partial t^2}-T_{\text{external}}(x,t) = div\left(\alpha\left(\vec{\vartheta}\right)\overrightarrow{grad}\,T^{\{1\}}(x,t)\right), x\in \text{int}\,P^{0,0,0}_{L_1,L_2,l_1}; \quad (2)$$

– two initial conditions:

$$T^{\{1\}}(x,t)\Big|_{t=0}=T_0^{\{1\}}(x),\ x\in P^{0,0,0}_{L_1,L_2,l_1}; \quad (3)$$

$$\left.\frac{\partial T^{\{1\}}(x,t)}{\partial t}\right|_{t=0}=T_1^{\{1\}}(x), x\in P^{0,0,0}_{L_1,L_2,l_1}; \quad (4)$$

– six boundary conditions:

- Neumann homogeneous boundary condition at the right end of the outer facing:

$$\frac{\partial T^{\{1\}}(x,t)}{\partial x_1}=0, x\in P^{0,0,0}_{0,L_2,l_1}(x_2,x_3), \quad (5)$$

- Neumann homogeneous boundary condition at the left end of the outer facing:

$$\frac{\partial T^{\{1\}}(x,t)}{\partial x_1}=0, x\in P^{L_1-0,0,0}_{L_1,L_2,l_1} \quad (6)$$

- Neumann homogeneous boundary condition at the underside of the outer facing:

$$\frac{\partial T^{\{1\}}(x,t)}{\partial x_2}=0, x\in P^{0,0,0}_{L_1,0,l_1}, \quad (7)$$

- Neumann homogeneous boundary condition at the upper side of the outer facing:

$$\frac{\partial T^{\{1\}}(x,t)}{\partial x_2}=0, x\in P^{0,L_2-0,0}_{L_1,L_2,l_1}, \quad (8)$$

- Robin boundary condition at the outer surface of the outer facing:

$$-\chi\left(\vec{\vartheta}\right)\frac{\partial T^{\{1\}}(x,t)}{\partial x_3}+\beta_1^{m_1}\left\{T^{\{1\}}(x,t)+\theta_{\text{external}}(t)\right\}^{m_1}=0, x\in P^{0,0,0}_{L_1,L_2,0}, \quad (9)$$

- Dirichlet inhomogeneous boundary condition on the inner surface of the outer facing:

$$T^{\{1\}}(x,t)=T^{\{2\}}(x_1,x_2,t), x\in P^{0,0,l_1-0}_{L_1,L_2,l_1}; \quad (10)$$

– two conjugation conditions:

$$T^{\{1\}}(x,t)\Big|_{x_3=l_1-0}=T^{\{2\}}(x,t)\Big|_{x_3=l_1+0}, x\in P^{0,0}_{L_1,L_2}, \quad (11)$$

$$\left\{\alpha\left(\vec{\vartheta}\right)\frac{\partial T^{\{1\}}(x,t)}{\partial x_3}\right\}\Big|_{x_3=l_1-0}=\left\{\alpha\left(\vec{\vartheta}\right)\frac{\partial T^{\{2\}}(x,t)}{\partial x_3}\right\}\Big|_{x_3=l_1+0}, x\in P^{0,0}_{L_1,L_2}; \quad (12)$$

– corresponding consistency constraints of the initial functions from (3), (4) and boundary functions from (5)-(10);

– heterogeneous partial differential equation:

$$\frac{\partial T^{\{2\}}(x,t)}{\partial t}=div\left(\alpha\left(\vec{\vartheta}\right)\cdot\overrightarrow{grad}\,T^{\{2\}}(x,t)\right)-\vec{\vartheta}_T(x,t)\cdot\overrightarrow{grad}\,T^{\{2\}}(x,t)+T^{\{1\}}(x,t)+T^{\{3\}}(x,t), x\in \text{int}\,P^{0,0,l_1}_{L_1,L_2,l_2}; \quad (13)$$

– one initial condition:

$$T^{\{2\}}(x,t)\Big|_{t=0}=T_0^{\{2\}}(x), x\in P^{0,0,l_1}_{L_1,L_2,l_2}; \quad (14)$$

– six boundary conditions:

- Dirichlet inhomogeneous boundary condition at the right end of the sapropel-hemp material:

$$T^{\{2\}}(x,t)=T^{\{2\}}_{\text{right}}(x_2,x_3,t),\ x\in P^{0,0,l_1}_{0,L_2,l_2}, \quad (15)$$

- Dirichlet inhomogeneous boundary condition at the left end of the sapropel-hemp material:

$$T^{\{2\}}(x,t)=T^{\{2\}}_{\text{left}}(x_2,x_3,t),\ x\in P^{L_1-0,0,l_1}_{L_1,L_2,l_2}, \quad (16)$$

- Dirichlet inhomogeneous boundary condition at the underside of the sapropel-hemp material:

$$T^{\{2\}}(x,t)=T^{\{2\}}_{\text{inter.}}(x_1,x_3,t),\ x\in P^{0,0,l_1}_{L_1,0,l_2}, \quad (17)$$

- Dirichlet inhomogeneous boundary condition at the upper side of the sapropel-hemp material:

$$T^{\{2\}}(x,t)=T^{\{2\}}_{\text{exter.}}(x_1,x_3,t),\ x\in P^{0,L_2-0,l_1}_{L_1,L_2,l_2}, \quad (18)$$

- Robin boundary condition at the surface of the sapropel-hemp material that is adjacent to the inner surface of the outer facing:

$$h\frac{T^{\{2\}}(x,t)-T^{\{1\}}(x,t)}{\chi\left(\vartheta_{x_3}\right)}=\frac{\partial T^{\{2\}}(x,t)}{\partial x_3},\ x\in P^{0,0,l_1}_{L_1,L_2,l_1}, \quad (19)$$

- Robin boundary condition at the surface of the sapropel-hemp material, which is adjacent to the inner surface of the inner facing:

$$h\frac{T^{\{1\}}(x,t)-T^{\{2\}}(x,t)}{\chi\left(\vartheta_{x_3}\right)} = \frac{\partial T^{\{2\}}(x,t)}{\partial x_3}, x\in P^{0,0,l_2-0}_{L_1,L_2,l_2}; \quad (20)$$

– four conjugation conditions:

$$T^{\{2\}}(x,t)\Big|_{x_3=l_1+0} = T^{\{1\}}(x,t)\Big|_{x_3=l_1-0}, x\in P^{0,0}_{L_1,L_2}, \quad (21)$$

$$\left\{\alpha\left(\vec{\vartheta}\right)\frac{\partial T^{\{2\}}(x,t)}{\partial x_3}\right\}\Big|_{x_3=l_1+0} = \left\{\alpha\left(\vec{\vartheta}\right)\frac{\partial T^{\{2\}}(x,t)}{\partial x_3}\right\}\Big|_{x_3=l_1-0}, x\in P^{0,0,}_{L_1,L_2}, \quad (22)$$

$$T^{\{2\}}(x,t)\Big|_{x_3=l_2-0} = T^{\{3\}}(x,t)\Big|_{x_3=l_2+0}, x\in P^{0,0}_{L_1,L_2}, \quad (23)$$

$$\left\{\alpha\left(\vec{\vartheta}\right)\frac{\partial T^{\{2\}}(x,t)}{\partial x_3}\right\}\Big|_{x_3=l_2-0} = \left\{\alpha\left(\vec{\vartheta}\right)\frac{\partial T^{\{3\}}(x,t)}{\partial x_3}\right\}\Big|_{x_3=l_2+0}, x\in P^{0,0}_{L_1,L_2}; \quad (24)$$

– corresponding consistency constraints of the initial function from (14) and boundary functions from (15), (16);

– heterogeneous partial differential equation:

$$\frac{\partial T^{\{3\}}(x,t)}{\partial t}+R_2\frac{\partial^2 T^{\{3\}}(x,t)}{\partial t^2}-T_{\text{inter.}}(x,t) = div\left(\alpha\left(\vec{\vartheta}\right)\cdot\overrightarrow{grad}\,T^{\{3\}}(x,t)\right), x\in \text{int}\, P^{0,0,l_2}_{L_1,L_2,L_3}; \quad (25)$$

– two initial conditions:

$$T^{\{3\}}(x,t)\Big|_{t=0} = T_0^{\{3\}}(x), x\in P^{0,0,l_2}_{L_1,L_2,L_3}, \quad (26)$$

$$\frac{\partial T^{\{3\}}(x,t)}{\partial t}\Big|_{t=0} = T_1^{\{3\}}(x), x\in P^{a_1,a_2,l_2}_{L_1,L_2,L_3}; \quad (27)$$

– six boundary conditions:

- Neumann homogeneous boundary condition at the right end of the inner facing:

$$\frac{\partial T^{\{3\}}(x,t)}{\partial x_1}=0, x\in P^{0,0,l_2}_{0,L_2,L_3}, \quad (28)$$

- Neumann homogeneous boundary condition at the left end of the inner facing:

$$\frac{\partial T^{\{3\}}(x,t)}{\partial x_1}=0, x\in P^{L_1-0,0,0}_{L_1,L_2,l_1}, \quad (29)$$

- Neumann homogeneous boundary condition at the underside of the inner facing:

$$\frac{\partial T^{\{3\}}(x,t)}{\partial x_2}=0, x\in P^{0,0,l_2}_{L_1,0,L_3}, \quad (30)$$

- Neumann homogeneous boundary condition at the upper side of the inner facing:

$$\frac{\partial T^{\{3\}}(x,t)}{\partial x_2}=0, x\in P^{a_1,L_2-0,l_2}_{L_1,L_2,L_3}, \quad (31)$$

- Dirichlet inhomogeneous boundary condition at the inner surface (that is, the surface that is adjacent to the second layer) of the inner facing:

$$T^{\{3\}}(x,t)=T^{\{2\}}(x_1,x_2,t), x\in P^{0,0,l_2}_{L_1,L_2,l_2}, \quad (32)$$

- Robin boundary condition at the outer surface of the inner facing:

$$-\chi\left(\vec{\vartheta}\right)\frac{\partial T^{\{3\}}(x,t)}{\partial x_3}+\beta_2^{m_2}\left\{T^{\{3\}}(x,t) -\theta_{\text{inter.}}(t)\right\}^{m_2}=0, x\in P^{0,0,L_3-0}_{L_1,L_2,L_3}; \quad (33)$$

– two conjugation conditions:

$$T^{\{3\}}(x,t)\Big|_{x_3=l_2+0} = T^{\{2\}}(x,t)\Big|_{x_3=l_2-0}, x\in P^{0,0}_{L_1,L_2}, \quad (34)$$

$$\left\{\alpha\left(\vec{\vartheta}\right)\frac{\partial T^{\{3\}}(x,t)}{\partial x_3}\right\}\Big|_{x_3=l_2+0} = \left\{\alpha\left(\vec{\vartheta}\right)\frac{\partial T^{\{2\}}(x,t)}{\partial x_3}\right\}\Big|_{x_3=l_2-0} x\in P^{0,0}_{L_1,L_2,b_3}; \quad (35)$$

– from the corresponding consistency constraints of the initial functions from (3), (4) and boundary functions from (5)-(10).

Before proceeding to the description and explanation of the meaning and purpose of the designations that take place in (2)-(35), let us note the following specifics of the mathematical model (2)-(35).

First peculiarity. Obviously, (2)-(12) is a mathematical model for finding a function $T^{\{1\}}(x,t)$, defined only on the first layer (i.e. on the outer facing) of a composite sapropel-hemp slab. Note that this mathematical model includes an unknown function (see (10)-(12)), defined only on the second layer (i.e. on the inner layer – in the sapropel-hemp component) of the composite slab. This means that without knowing the function $T^{\{2\}}(x,t)$, it is impossible to determine the required function $T^{\{1\}}(x,t)$ from (2)-(12).

Second peculiarity. (24)-(34) is a mathematical model for finding a function $T^{\{3\}}(x,t)$, defined only on the third layer (i.e. on the inner facing) of a composite slab. As in model (2)-(12), this mathematical model includes the same unknown function $T^{\{2\}}(x,t)$ (see (32), (34), (35)). This means that, without knowing the function $T^{\{2\}}(x,t)$, it is impossible to determine the desired function $T^{\{3\}}(x,t)$ from (25)-(35).

Third peculiarity. (13)-(24) is a mathematical model for determining the function $T^{\{2\}}(x,t)$, defined only on the second layer (i.e. on the inner layer - in the sapropel-hemp part) of the composite slab. This model includes (see (13), (19)-(24)) both a function $T^{\{1\}}(x,t)$, defined only on the first layer and a function $T^{\{3\}}(x,t)$, defined only on the third layer. This means that without knowing the functions $T^{\{1\}}(x,t)$ and $T^{\{3\}}(x,t)$, it is impossible to determine the desired function $T^{\{3\}}(x,t)$ from (13)-(24).

From the above listed peculiarities of the mathematical model (2)-(35), it becomes clear that this model (2)-(35) consists of three independent mathematical models interconnected by their sought functions $T^{\{1\}}(x,t)$, $T^{\{2\}}(x,t)$, $T^{\{3\}}(x,t)$: of the mathematical model (2)-(12); mathematical model (13)-(24); mathematical model (25)-(35). As a rule, such a situation arises in those studied real problems of mathematical physics, in which the objects under study are multilayer objects or the investigated processes and phenomena occur in layered media [13], [22], [23]. When studying and solving mathematical models of this kind, describing real processes, phenomena or objects in many fields of science and technology, it is imperative to deal with a special class of problems in the theory of ordinary differential equations, called the Sturm-Liouville problem [24], the analysis and solution of which is often a rather cumbersome process and requires from the researcher either special knowledge in mathematics [13], [22]-[24], or the involvement of a professional mathematician in the research, who's scientific interests cover both the theory of differential equations and mathematical physics.

Now let us briefly describe the meaning and purpose of the designations in model (2)-(35).

(A) First of all, we note that in the mathematical model (2)-(35), the sought functions are only two functions: function (1), which characterizes the unsteady temperature field in all three layers of the composite sapropel-hemp slab; function $\vec{\vartheta}(x,t)$, that characterizes the vector velocity of heat propagation in a composite sapropel-hemp slab in directions OX_1, OX_2, OX_3.

(B) Mathematical model (2)-(35) does not contain a separate sub model for determining the required function $\vec{\vartheta}(x,t)$: in the next section, a separate mathematical model will be formulated (see (36)-(47)) to determine this function, or rather, to determine the heat propagation vector velocity averaged by directions OX_1 and OX_2 in a composite sapropel-hemp slab, i.e. to define a scalar function $\vartheta_{x_3}(x,t)$ (see the second peculiarity at the beginning of this section).

(C) $div\vec{A}(x,t) \stackrel{def}{\equiv} \sum_{j=1}^{3} \frac{\partial A_{x_j}(x,t)}{\partial x_j}$, called the divergence operator, is a differential operator that maps a vector field $\vec{A}(x,t)$ to a scalar field. At each fixed moment in time, the operator $div\vec{A}(x,t)$ for each spatial point $x \in \mathbb{R}^3$ determines how much the incoming and outgoing heat fluxes diverge. In the mathematical model (2)-(35), the operator $div(\bullet)$ is present in equations (2), (13) and (25) with vector fields $\vec{A} = \alpha\left(\vec{\vartheta}(x,t)\right)\overrightarrow{grad}\,T^{\{j\}}(x,t)$, $j=\overline{1,3}$, where $\overrightarrow{grad}\,T^{\{j\}}(x,t)$, the called gradient of a scalar function $T^{\{j\}}(x,t)$, $\left(j=\overline{1,3}\right)$ is a vector whose coordinates are the partial derivatives of this scalar function $T^{\{j\}}(x,t)$. In the mathematical model (2)-(35), the gradient $\overrightarrow{grad}(\bullet)$ is present in equations (2), (13), and (25) with scalar functions $T^{\{1\}}(x,t)$, $T^{\{2\}}(x,t)$ and $T^{\{3\}}(x,t)$, respectively.

(D) $R_1 > 0$ from equation (2) and $R_2 > 0$ from equation (24) are referred to as the heat flux relaxation coefficients in the outer facing (i.e. the first layer) and the inner facing (i.e. the third layer), respectively. These numerical coefficients are assumed to be known, for example, being determined experimentally. Further, $\beta_1 > 0$ from the boundary condition (9) and from the boundary condition (33) characterize the averaged heat transfer property of the outer and inner facings, respectively. These numerical parameters are also assumed to be known. Further, $m_1 > 0$ from the boundary condition (9) and $m_2 > 0$ from the boundary condition

(33) characterize the diffusion properties of the outer and inner facings, respectively. These numerical values are also assumed to be known. Further, the meaning of positive numbers L_1, L_2, L_3, l_1 and l_2 is quite obvious from Fig. 1. All these numbers are obviously assumed to be known.

(E) All initial and boundary functions are assumed to be given a priori: initial functions $T_0^{\{1\}}(x), x \in P_{L_1,L_2,L_3}^{0,0,0}$, $T_1^{\{1\}}(x), x \in P_{L_1,L_2,L_3}^{0,0,0}$, $T_0^{\{2\}}(x), x \in P_{L_1,L_2,l_2}^{0,0,l_1}$, $T_0^{\{3\}}(x), P_{L_1,L_2,L_3}^{0,0,l_2}$, $T_1^{\{3\}}(x), x \in P_{L_1,L_2,L_3}^{0,0,l_2}$; boundary functions $T_{\text{right}}^{\{2\}}(x_2,x_3,t), x_2 \in [0,L_2], x_3 \in [l_1,l_2], t \geq 0$, $T_{\text{left}}^{\{2\}}(x_2,x_3,t), x_2 \in [0,L_2], x_3 \in [l_1,l_2], t \geq 0$, $T_{\text{inter.}}^{\{2\}}(x_1,x_3,t), x_1 \in [0,L_1], x_3 \in [l_1,l_2], t \geq 0$, $T_{\text{exter.}}^{\{2\}}(x_1,x_3,t), x_1 \in [0,L_1], x_3 \in [l_1,l_2], t \geq 0$; functions $\theta_{\text{exter.}}(t), t \geq 0$, $\theta_{\text{inter.}}(t), t \geq 0$, meaning the ambient temperature from which the surfaces of the outer and inner facings perform heat exchange according to Newton's law, respectively [13]; functions $T_{\text{exter.}}(x,t), x \in \operatorname{int} P_{L_1,L_2,l_1}^{0,0,0}$, $T_{\text{inter.}}(x,t), x \in \operatorname{int} P_{L_1,L_2,L_3}^{0,0,l_2}$, which characterize the density of heat sources in the environment, with which heat exchange occurs through the surfaces of the outer and inner facings, respectively.

(F) $\alpha\left(\vec{\vartheta}(x,t)\right) = \dfrac{\chi\left(\vec{\vartheta}(x,t)\right)}{c_p \rho\left(\vec{\vartheta}(x,t)\right)}$ is the temperature conductivity coefficient of a composite sapropel-hemp slab, where $\chi\left(\vartheta_{x_3}\right)$ denotes the thermal conductivity coefficient, $\rho\left(\vartheta_{x_3}(x_3,t)\right)$ denotes density, c_p denotes the specific heat capacity. Due to three peculiarities that were presented at the beginning of this section, in the mathematical model (2)-(35) this temperature conductivity coefficient is assumed to be a known step function for $\forall x_i \in [0,L_i]$, $(i=1,2)$:

$$0 < \alpha_{\min} \leq \alpha\left(\vec{\vartheta}(x,t)\right) \approx \alpha\left(\vartheta_{x_3}(x_3,t)\right) = \begin{cases} \alpha_1 \text{ if } 0 \leq x_3 \leq l_1, \\ \alpha_2 \text{ if } l \leq x_3 \leq l_2, \\ \alpha_3 \text{ if } l_2 \leq x_3 \leq L_3, \end{cases}$$

where $\alpha_i, i = \overline{1,3}$ are the constants.

III. Mathematical Model for Desired Vector Velocity of Heat Propagation

As it has been mentioned in the previous section, the function $\vec{\vartheta}(x,t)$ characterizes the vector velocity of heat propagation in a composite sapropel-hemp slab along the directions OX_1, OX_2, OX_3. Assuming that the velocity of heat propagation along the axis OX_3 (i.e. along the thickness/height dimension of the sapropel-hemp slab) is much higher than the velocity of heat propagation in the other two directions (i.e. along the width and length dimensions of the sapropel-hemp slab), then the vector velocity $\vec{\vartheta}(x,t)$ can be averaged along the direction of the OX_1 and OX_2 axes. Then, instead of the vector of the function $\vec{\vartheta}(x,t)$, you can consider only its third component $\vartheta_{x_3}(x,t)$. In this section, a mathematical model is proposed for finding this particular scalar function.

So, let us turn to the formulation of a mathematical model for a function $\vartheta_{x_3}(x_3,t)$, that is present in many places of the mathematical model (1)-(34), but still remains undefined.

It is required to define a function $\vartheta_{x_3}(x_3,t), x_3 \in [0,L_3]$ for $\forall t \geq 0$ from the following one nonlinear equation, one initial condition, four boundary conditions, two conjugation conditions, and four consistency constraints:

– heterogeneous partial differential equation:

$$\frac{\partial \vartheta_{x_3}(x_3,t)}{\partial t} = \frac{\partial}{\partial x_3}\left(\alpha\left(\vartheta_{x_3}(x_3,t)\right)\frac{\partial \vartheta_{x_3}(x_3,t)}{\partial x_3}\right) - \vartheta_{x_3}(x_3,t)\frac{\partial \vartheta_{x_3}(x_3,t)}{\partial x_3} + P(x_3,t), 0 < x_3 < L_3; \quad (36)$$

– initial condition:

$$\vartheta_{x_3}(x_3,t)\big|_{t=0} = \vartheta_0(x_3), \ 0 \leq x_3 \leq L_3; \quad (37)$$

– boundary conditions:

- Dirichlet inhomogeneous boundary condition:

$$\vartheta_{x_3}(x_3,t)\big|_{x_3=0+0} = \theta_{\text{exter.}}(t), \quad (38)$$

- Neumann homogeneous boundary condition:

$$\left.\frac{\partial \vartheta_{x_3}(x_3,t)}{\partial x_3}\right|_{x_3=l_1-0} = 0, \quad (39)$$

- Neumann homogeneous boundary condition:

$$\left.\frac{\partial \vartheta_{x_3}(x_3,t)}{\partial x_3}\right|_{x_3=l_2+0} = 0, \quad (40)$$

- Dirichlet inhomogeneous boundary condition:

$$\vartheta_{x_3}(x_3,t)\big|_{x_3=L_3-0}=\theta_{\text{inter.}}(t); \qquad (41)$$

– conjugation conditions:

$$\vartheta_{x_3}(x_3,t)\big|_{x_3=l_1-0}=\vartheta_{x_3}(x_3,t)\big|_{x_3=l_1-0},\ t\geq 0, \qquad (42)$$

$$\left\{\alpha\left(\vartheta_{x_3}(x_3,t)\right)\frac{\partial\vartheta_{x_3}(x_3,t)}{\partial x_3}\right\}\Big|_{x_3=l_2-0} = \left\{\alpha\left(\vartheta_{x_3}(x_3,t)\right)\frac{\partial\vartheta_{x_3}(x_3,t)}{\partial x_3}\right\}\Big|_{x_3=l_2-0}; \qquad (43)$$

– consistency constraints of the initial function from (37) and boundary functions from (38)-(41):

$$\left.\begin{aligned}&\vartheta_{x_3}(0+0)=\theta_{\text{exter.}}(0+0),\\&\vartheta_{x_3}(L_3-0)=\theta_{\text{inter.}}(0+0),\\&\vartheta'_{x_3}(l_1-0)=\vartheta'_{x_3}(l_2+0)=0.\end{aligned}\right\} \qquad (44)$$

The function $P(x_3,t), x_3\in(0,L_3),\ t\geq 0,$ characterizes the total density of heat sources of the environment external to the composite sapropel-hemp slab. In the mathematical model (36)-(44), all the initial data have already been described in the frames of the mathematical model (2)-(35).

So, the complete mathematical model proposed in this work consists of two mathematical models (listed in the sequence of the solution required): from the mathematical model (36)-(44) with respect to the function $\vartheta_{x_3}(x_3,t)$ of the averaged velocity of heat propagation, and the mathematical model (2)-(35) with respect to the desired unsteady temperature field $T(x,t)=T(x_1,x_2,x_3,t)$ of composite sapropel-hemp slab.

If to find a solution to model (36)-(44), the equation of which can be attributed to the class of equations of the Fisher-Kolmogorov-Petrovsky-Piskunov type [25]-[27], then finding a solution to model (2)-(35) will not cause particular difficulties: this can be implemented by the separating variables method (also known as the Fourier method) [6], [13], [22], [23]. In this paper, we are not dealing with the solution of the one-dimensional initial-boundary value problem (36)-(44), but here we would only like to note that equation (36) using a nondegenerate transformation

$$\left\{\begin{aligned}&\vartheta_{x_3}(x_3,t)=\frac{\partial W(x_3,t)}{\partial x_3},\\&w(x_3,t)=\ln\left[U(x_3,t)\right]^{-\alpha\left(\vartheta_{x_3}(x_3,t)\right)}\end{aligned}\right. \qquad (45)$$

is reduced to a linear equation relating to the new sought for function $U(x_3,t)$. The resulting initial-boundary value problem can also be solved by the separating variables method.

IV. Discussion

The nomenclature of composite materials used in construction is constantly expanding, and innovative methods are developed that make it possible to improve the physical-mechanical, thermophysical, chemical, environmental, economic, etc. characteristics of materials: for example, resulting in substantial improvement of hydrophobicity, fire resistance, intensity of heat exchange processes, statistical and dynamic strength, endurance, energy efficiency, sound insulation, etc. One of the most beneficial from the environmental friendliness and cost-effectiveness standpoint within the nomenclature of the composite construction panels is considered to be a slab made of the hemp shives (acting as filler) and sapropel (acting as binding). Sapropels are a complex organic or organomineral complex of various chemical compounds, both preserved in the original biomass and newly formed in the process of biochemical metamorphism of organic substances [28]. In Latvia, the processes of their formation and accumulation are constantly ongoing, and for many water reservoirs these processes become progressive [28]. In Latvia, the processes of its formation and accumulation are ongoing, and for many freshwater lakes (over 3 thousand with an area larger than 1 ha) and swamps (over 6 thousand) [29]-[31], which are under the control of the "Latvian state forests" governmental institution, these processes are having a progressive nature: according to preliminary estimates, these reservoirs contain over 3 billion m^3 of sapropel. Due to the high degree of destruction of fragments of the original biomass, sapropel are characterized by a homogeneous structure with a high content of fine-grained particles and a high water-holding capacity.

Getting back to the constructed mathematical model (2)-(44), let us note that knowledge of the thermal field inside of a three-layer composite sapropel-hemp slab allows us to calculate (at least in first approximation) the strength of the enclosing and supporting structures built of such slabs under thermal loading conditions: specifically, the temperature changes are the root cause for appearing of additional strain in the structure [32]-[34]. However, in our opinion, in order to carry out an adequate strength calculation for the constructions under thermal loading conditions, it is necessary to consider the mathematical model (2)-(44) in a many component system: this is especially necessary if a construction built of composite sapropel-hemp slabs, refers to: (1) objects of landscape architecture; (2) objects of household facilities in rural areas; (3) self-contained buildings; (4) sites in an urban canyon-like area; (5) objects under the influence of

periodic or almost periodic aero-, hydro-, or lithodynamic flows [34]-[36]. The abovementioned means that the corresponding boundary conditions in (2)-(35) must be "stitched" at the left $P_{L_1,L_2,L_3}^{L_1,0,0}$ and right $P_{0,L_2,L_3}^{0,0,0}$ ends of each of two adjacent sapropel-hemp slabs. Since the construction consists, as a rule, of a multiple sapropel-hemp slabs, it seems that the specified "stitching" of the boundary conditions for each adjacent pair of slabs will significantly complicate the mathematical model (2)-(35) within its computer modeling implementation. In fact, if we consider the mathematical model (2)-(35) in a system of only two bodies/slabs and "stitching" the corresponding boundary conditions to carry out between the right $P_{0,L_2,L_3}^{0,0,0}$ end of the left adjacent slab and the left $P_{L_1,L_2,L_3}^{L_1,0,0}$ end of the right neighboring slab, then this approach will be quite acceptable averaging of the mentioned complex system consisting of many bodies/slabs: there is no need to apply other types of averaging (for instance, see fundamental monograph [34] as well as [37]).

V. Conclusions

In this paper, a 3D mathematical model is proposed to determine the dynamics of the temperature field in a three-layer composite sapropel-hemp parallelepiped slab, in which the outer layers (fireproof facing) are bonded with hemp and sapropel mineralized fill. In the proposed mathematical model, due to the specifics of the material of the inner layer – sapropel-hemp material, it is assumed that, firstly, the temperature conductivity coefficient is a given step function along the vertical axis directed along the thickness dimension of the sapropel-hemp slab, and secondly, the velocity of heat propagation, along with the thermal field, is also considered to be the sought for function. The proposed model consists of a system of three initial-boundary value problems with respect to the temperature function for each layer, respectively, and one initial-boundary value problem with respect to the unknown velocity of heat propagation along the thickness dimension of the composite sapropel-hemp slab.

As it has been already mentioned at the end of Section III, the constructed model (2)-(44) can be solved by the method of separation of variables, by applying it separately to (2)-(35) and to (36)-(44) (to be more precise, to the linear initial-boundary value problem obtained after using the nondegenerate transformation (45)): we managed to find an analytical solution of the model (2)-(44) in a closed form, however, unfortunately, we have not yet managed to implement it in a computer-based model and carry out the corresponding numerical experiments.

Acknowledgements

This work is dedicated to the blessed memory of Professor Janis S. Rimshans, Liepaja University.

The authors of this work would like to express their gratitude to the anonymous reviewers for their equitable critical comments and valuable advices, which we took into account with gratitude.

References

[1] P. Germain, Cours de mécanique des milieux continus: Théorie générale. Paris: Masson et Cie, Éditeurs, 1973.

[2] Yu. I. Burchakov, V. E. Gnedin, and V. M. Denisov, Structural mechanics. Moscow: Higher School, 1983.

[3] A. V. Lykov, Heat conduction theory. Moscow: Higher School, 1967.

[4] R. I. Nigmatulin, Continuum mechanics: Kinematics, dynamics, thermodynamics, statistical dynamics. Moscow: GEOTAR-Media, 2014.

[5] D. A. Frank-Kamenetsky, Diffusion and heat transfer in chemical kinetics. Moscow: Nauka, 1987.

[6] H. S. Carslaw and J. C. Jaeger, Conduction of Heat in Solids. Oxford: Oxford University Press, 1986.

[7] V. S. Zarubin, Modelling. Moscow: "Academy" Publishing Centre, 2013.

[8] V. S. Zarubin, A. V. Kotovich, and G. N. Kuvyrkin, "Temperature state of a plate with temperature-dependent thermal conductivity and energy-release," Mathematics and Mathematical Modeling, vol. 16, no. 3, pp. 18-28, 2016.

[9] V. V. Vasiliev, Mechanics of structures made of composite materials. Moscow: Mechanical Engineering, 1988.

[10] L. N. Tyalina, A. M. Minaev, and V. A. Pruchkin, New composite cmaterials. Tambov: Tambov State Technical University Press, 2011.

[11] M. L. Kerber, Polymer composite materials: Structure, properties, technology. St. Petersburg: Profession, 2008.

[12] V. R. Bensman, "Classification problems for peat bogs and sapropels," Young scientist, vol. 1, no. 1-2, pp. 146-147, 2010.

[13] A. N. Tikhonov and A. A. Samarskii, Equations of Mathematical Physics. Moscow: Nauka, 1977.

[14] Th. L. Bergman, A. S. Lavine, F. P. Incropera, and D. P. Dewitt, Fundamentals of Heat and Mass Transfer. New Jersey: John Wiley & Sons, 2011.

[15] J. H. Lienhard IV and J. H. Lienhard V, A Heat Transfer Textbook. – Massachusetts, Cambridge: Phlogiston Press, 2019.

[16] Y. Ashida, Ke. Saito, and M. Ueda, "Thermalization and heating dynamics in open generic many-body systems," Physical Review Letters, vol. 121, no. 7, pp. 402-408, 2018.

[17] P. P. Volosevich and E. I. Levanov, "Analysis of heat transfer processes taking into account the relaxation of heat flux and bulk energy sources in the medium," Transactions of Russian Higher Educational Institutions: Mathematics, vol. 47, no. 1, pp. 36-42, 2003.

[18] E. I. Levanov, "Heat transfer taking into account the relaxation of the heat flux and energy sources," Mathematical Modelling, vol. 9, no. 2, pp. 53-56, 1997.

[19] D. S. P. Salazar, A. M. S. Macedo, and G. L. Vasconcelos, "Quantum heat distribution in thermal relaxation processes," Physical Review E, vol. 99, no. 2, pp. 2133-2138, 2019.

[20] R. P. Feynman, R. B. Leighton, and M. Sands, The Feynman lectures on physics: Mainly mechanics, radiation, and heat. California: California Institute of Technology Press, 1963.

[21] K. Micadei, J. P. S. Peterson, A. M. Souza, R. S. Sarthour, I. S. Oliveira, G. T. Landi, T. B. Batalhao, R. M. Serra, and E. Lutz, "Reversing the direction of heat flow using quantum correlations," Nature Communications, vol. 10, paper no. 2456, 6 p, 2019.

[22] Sh. E. Guseynov, R. Aleksejevs, J. V. Aleksejeva, "On a 3D initial-boundary value problem for determining the dynamics of impurities concentration in a horizontal layered fine-pore medium," in Proceedings of the 12th International Scientific and Practical Conference "Environment. Technology. Resources", vol. III, Rezekne: Rezekne Academy of Technologies Press, 2019, pp. 60-69.

[23] Sh. E. Guseynov, R. Aleksejevs, J. V. Aleksejeva, and J. S. Rimshans, "On the impurities concentrations dynamics in multicomponent semidisperse semicolloid-high-molecular system: a case study of two-layered anisotropic peat block," Advanced Mathematical Models & Applications, vol.4, no. 2, pp. 99-126, 2019.

[24] A. Zettl, Sturm-Liouville Theory. Providence, Rhode Island: American Mathematical Society Press, 2005.

[25] A. N. Kolmogorov, I. G. Petrovsky, and N. S. Piscounov, "Investigation of the diffusion equation combined with an increase in matter and its application to a biological problem," Bulletin of Moscow State University, Series A: Mathematics and Mechanivs, vol. 1, pp. 1-25, 1937.

[26] R. A. Fisher, "The wave of advance of advantageous genes," Annals of Eugenics, vol. 7, pp. 355-369, 1937.

[27] M.El-Hachem, S.W.McCue, W.Jin, Y.Du, and M.J.Simpson, "Revisiting the Fisher-Kolmogorov-Petrovsky-Piskunov equation to interpret the spreading-extinction dichotomy," Proceedings of the Royal Society A: Mathematical, Physical and Engineering Sciences, vol. 475, no. 2229, Paper ID: 0378, 2019.

[28] S. M. Shtin, Lacustrine sapropels and their complex development. Moscow State Mining University Press, 2005.

[29] N. Brakss, B. Vimba, and A. Kalnins, "On the properties and ways of using sapropels of the Latvian SSR," Transactions of Latvian Academy of Sciences, vol. 133, no. 8, pp. 43-50, 1958.

[30] Central Statistical Bureau of Latvia, "Geographical data," 2009. [Online]. Available: https://data.stat.gov.lv/pxweb/lv/OSP_PUB/START__ENV__DR__DRT/DRT020/. [Accessed: March 19, 2021].

[31] Database, "Lakes," 2009. [Online]. Available: https://www.ezeri.lv/?l=en. [Accessed: March 19, 2021].

[32] R. M. Christensen, Mechanics of composite materials. Mineola: Dover Publications, 2005.

[33] G. L. Gorynin and Yu. V. Nemirovsky, "Mathematical modelling of heat conduction process for 2D-periodic anisotropic composite materials," Mathematical Methods and Physico-Mechanical Field, vol. 57, no. 2, pp. 142-151, 2014.

[34] N. S. Bakhvalov and G. P. Panasenko, Averaging processes in periodic media. Mathematical problems in the mechanics of composite materials. Moscow: Science 1984.

[35] L. C. King, The morphology of the Earth: A study and synthesis of world scenery. Edinburgh: Oliver & Boyd, 1962.

[36] I. P. Baranov, "Using the concept of plastics relief in solving problems modern city planning and architectural planning," in International Conference "InterCarto. InterGIS. Geoinformation Support of Sustainable Development of Territories", vol. 20, 2014, pp. 575-587.

[37] V. I. Gorbachev, "The Bakhvalov-Pobedri averaging method in the mechanics of composites," Bulletin of Lomonosov Moscow State University, Series 1: Mathematics and Mechanics, no. 6, pp. 41-45, 2016.

Environment. Technology. Resources. Rezekne, Latvia
Proceedings of the 13th International Scientific and Practical Conference. Volume 3, 104-109

Exploring the Impact of Burstiness on the Service Process at the Cash Register

Detlef Hartleb
ETSIST, Universidad Polit´ecnica de Madrid
Madrid, Spain
dethar@gmx.de

Andreas Ahrens
Department of Electrical Engineering and Computer Science, Hochschule Wismar, University of Technology, Business and Design
Wismar, Germany

Jelena Zascerinska
Centre for Education and Innovation Research
Riga, Latvia

Abstract **- The service process is the key phase in any queue system applied to business and industry operations. The service process in shops is defined as the payment process at the cash register. The service process consists of two elements or sub-processes: the waiting in the queue to the cash register as well as the payment processing (scanning the goods, giving receipts to customers, etc). Analysis of burstiness as the indicator of the service process has been well-established. Against this background on burstiness as the indicator of the service process, burstiness is also defined as a factor that influences the service process. However, burstiness as a factor in the service process has not attracted a lot of research attention. The aim of this paper is to analyse burstiness as a factor in the service process underpinning the elaboration of scenarios of the service process for the queue management purposes. The present work mostly employs theoretical methods: scientific literature analysis, synthesis, modelling, comparison, and systematization. The theoretical research results in the outline of the conceptual framework for exploring the impact of burstiness on the service process. The key concepts have been identified, namely binary customer behaviour, buyers' burstiness, bottlenecks' emergence at the server, and queue management. The logical chain of the development has been emphasized: binary customer behaviour → buyers' burstiness → bottlenecks' emergence at the check-out station or cash register (server) → queue management. The presented logical chain allows finding out that buyers' burstiness leads to the queue appearance in the service process. In turn, queue appearance requires queue management measures. Hence, buyers' burstiness influences on the decisions in regard to queue management within the service process. Further on, two functions of buyers' burstiness are defined: the indicators of the service process, and the factor that influences the service process. This bi-modal role of buyers' burstiness in the service process highlights the complex nature of the queue management. Five scenarios of the service process will allow using a combination of queue management measures in each scenario or even between scenarios. The findings of the comparative study propose the structure of the service process as the unity of the waiting in the queue to the cash register and the payment processing at the cash register, i.e. scanning of the goods and the payment. The present research has some limitations. Further research tends to validate the model of five scenarios of the service process for the queue management purposes. Comparative studies on buyers' burstiness in the service process will be continued, too.**

Keywords - binary customer behaviour, buyers' burstiness, bottlenecks' emergence at the check-out station (server), queue management.

I. INTRODUCTION

The service process or, in other words, server is a key component in industrial and business operations [1]. Figure 1 as depicted in [1] shows the service process or, in other words, the payment process in the buying process chain [1].

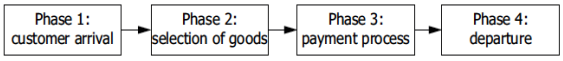

Fig. 1. The key phases in business operations [1].

Figure 2 reveals that the service process includes two sub-processes [1]:

- waiting in the queue to the cash register, and
- the payment processing at the cash register.

Online ISSN 2256-070X
https://doi.org/10.17770/etr2021vol3.6563

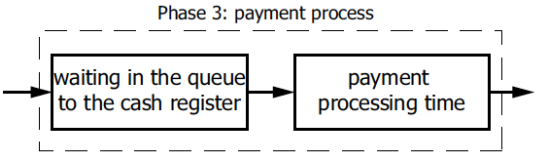

Fig. 2. The elements of the service process [1].

It should be pointed that the service process as the unity of waiting in the queue to the cash register and the payment processing was analysed through generating functions [1] as the generating function offers closed-form solutions when modelling bursty business processes [2]. Closed-form solutions are an advantage when using a single function instead of analysing a sequence of infinite length [2]. In the analysis of the service process, generating functions were used for the analysis of the free time intervals between buyers to the cash register as a part of the payment process [1].

Similar concepts in regard to the presented service process were later presented

- in [3] as illustrated in Figure 3 developed by Kiataramkul and Neamprem [3], and
- in [4] as disclosed in Figure 4 created by Cheong and Chia [4].

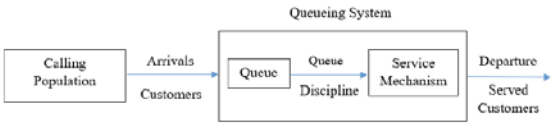

Fig. 3. The basic queueing process [3].

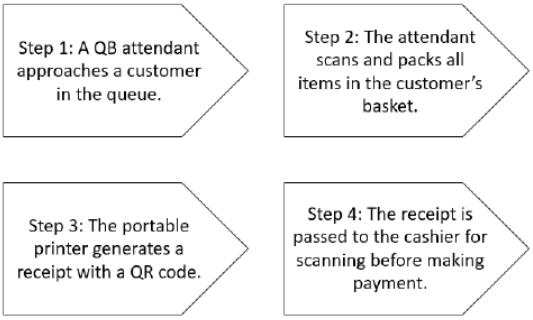

Fig. 4. Process Flow for Queue Buster [4].

Table 1 demonstrates the results of the comparison of the three concepts, namely

- the service process by [1],
- the queueing process by [3], and
- the queue buster [4].

TABLE 1 RESULTS OF THE COMPARISION OF THREE CONCEPTS

Conceptual approach	**Compared elements**		
	Process structure	***Process units of analysis***	***Process indicators***
The service process [1]	• Waiting in the queue to the cash register, • The payment processing	The unity of the two elements: • Waiting in the queue to the cash register, • The payment processing	Burstiness that includes two parameters: • Buyers' probability: buyers' waiting times in the queue and buyers' service (payment processing) times • Buyers' concentration
The queueing process [3]	• Queue • Service mechanism	• Queue • Service channels	• Average queue length, • The average total work in process, • The average waiting time, • The average total time
The queue buster [4]	• Customer approaching in the queue • Scan and pack • QR code generation • Receipt scanning and payment	• Scan and Pack Time/Item • Payment Time • Total Time	• Wait Time, • System Time, • System Length

Table 2 described burstiness as the indicator of the service process.

TABLE 2 BURSTINESS AS THE INDICATOR OF THE SERVICE PROCESS

Indicator	**Indicators elements**			
	Buyers' probability			***Buyers' concentration***
Burstiness	• buyers' waiting times in the queue to the cash register	• buyers' service (payment processing) times at the cash register		• buyers' concentration
		• buyers' service time	• free-time intervals between buyers	

Analysis of burstiness as the indicator of the service process has been well-established [5] - [9].

Against this background on burstiness as the indicator of the service process, burstiness is also defined as a factor [10] that influences the service process [11]. Figure 5 reflects the both functions of burstiness in the service process.

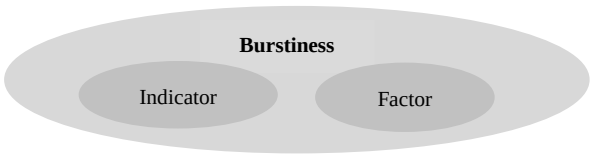

Fig. 5. Burstiness functions.

Hence, burstiness is a bi-modal phenomenon:

- on the one side, burstiness as the indicator is used to determine developmental dynamics of the object [12], and
- on the other hand, burstiness as a factor changes the service process.

It should be noted that by bi-modal phenomenon, a phenomenon that obtains or exhibits two contrasting modes or forms is meant [13].

However, burstiness as a factor in the service process has not attracted a lot of research attention.

The aim of this paper is to analyse burstiness as a factor in the service process underpinning the elaboration of scenarios of the service process for the queue management purposes.

The present work mostly employs theoretical methods: scientific literature analysis, synthesis, modelling, comparison, systematization.

The remaining part of this paper is organized as follows: Section II introduces the conceptual framework of the research. The impact of buyers' burstiness on the service process is theoretically analysed in section III followed by five scenarios of the service process aimed at the queue management. Finally, some concluding remarks are given in Section IV.

II. Conceptual Framework

Burstiness is a factor that influences the service process [1]. It should be noted that by factor, a reason of phenomenon change is meant [14].

Burstiness that influences the service process is related to customers [11]. In the present work, a customer is the overall term. A customer refers to anything and anyone that arrives at a facility and requires service. Examples of customers are shoppers at the check-out station or cars at the traffic light. The term "customer" has received a variety of definitions. In scientific literature, customer and client are synonymously used. Further, the term of "lost customers" is introduced by Sharma [15]. Customer also includes customer abandonment behaviour [16] in regard to a customer who stopped trying to receive a service due to a number of reasons. The term of "blocked customers" describes one who retries to get a service after a random amount of time [15]. Hence, these researchers have established the understanding of the customer behaviour based on the reception of service.

The present research is based on the concept of binary customer behaviour as depicted in Figure 6 [11].

Binary customer behaviour means to buy or not buy [17]. The use of the concept of binary behaviour allows differentiating customers into [17]

- visitors (i.e. who visit a shop but does not buy anything) and
- buyers (who visit a shop and buy a product).

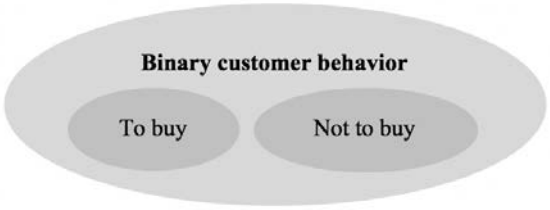

Fig. 6. Elemenst of customer binary option [11].

Buyers are further differentiated into two types [18]:

- highly delay-sensitive but only check-out a few items, and
- highly delay-insensitive but check-out many items.

It should be noted that the authors of the present work have enhanced the buyers' differentiation proposed by Tang, Guo, and Wang [18]. The authors of the present contribution introduce two more types of buyers:

- highly delay-sensitive buyer who only checks-out many items, and
- highly delay-insensitive buyer who checks-out a few items.

Consequently, the overall term "customer" is used in the same meaning by Sharma [15] and the authors of the present work. The terms "lost customer" and "visitor" are used synonymously. Table 3 shows the inter-relationships between customer, client, visitor, lost customer, customer abandonment behaviour, buyer, highly delay-sensitive buyer who only checks-out a few items, highly delay-sensitive buyer who only checks-out many items, highly delay-insensitive buyer who checks-out a few items, and highly delay-insensitive buyer who checks-out many items.

Table 3 Terms Used in the Reserach

Customer / Client				
Visitor, Lost customer, Customer abandonment behaviour	***Buyer***			
	highly delay-sensitive buyer who only checks-out a few items	highly delay-sensitive buyer who checks-out many items	highly delay-insensitive buyer who only checks-out a few items	highly delay-insensitive who checks-out many items

Buyers' burstiness influences the service process [19]. Buyers' burstiness corresponds to an enhanced activity level over a short period of time followed by long periods of inactivity [19]. Buyers' bursty arrival at the server influences the service process at the cash register in a shop.

Buyers' bursty arrival at the server leads to the emergence of a bottleneck [2]. It should be noted that bottlenecks limit the flow of customers, services or products, etc [2]. A bottleneck emerges when single business processes within the business system operate at their capacity limit or beyond [2]. Due to the bottleneck, a queue appears [2]. Hence, the significance of queue management has become apparent.

It should be pointed that Table 4 shows the relationships between queuing systems, customer and server.

TABLE 4 THE RELATIONSHIPS BETWEEN QUEUING SYSTEMS, CUSTOMER AND SERVER

Queuing System	*Customer*	*Server*
Supermarket	Buyer	Cash register
Airport	Passenger	Check in counter
Bank	Client	Cash machine

The elaboration of this conceptual framework allows identifying the key concepts underlying the present research, namely

- binary customer behaviour,
- buyers' burstiness,
- bottlenecks' emergence at the server, and
- queue management.

The study presents a potential model for development indicating how the steps of the process are related following a logical chain: binary customer behaviour → buyers' burstiness → bottlenecks' emergence at the server → queue management. The presented logical chain allows finding out that buyers' burstiness leads to the queue appearance in the service process. In turn, queue appearance requires queue management measures. Figure 7 reveals the inter-relationships between the buyer burstiness, the service process and the queue management.

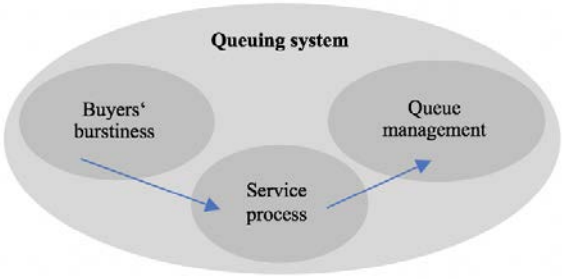

Fig. 7. The inter-relationships between the buyer burstiness, the service process and the queue management.

The presented conceptual framework directs the researchers to explore the impact of burstiness on the service process aimed at queue management.

III. IMPACT OF BUYERS' BURSTINESS ON THE SERVICE PROCESS

Impact is defined as the influence on the decisions (regardless of outcome) that shape people's lives, communities, governance, the environment, and elsewhere [20].

Burstiness is used to support decision making through designation of a tendency in a field of scientific investigation [21] as pointed in Figure 8 [6].

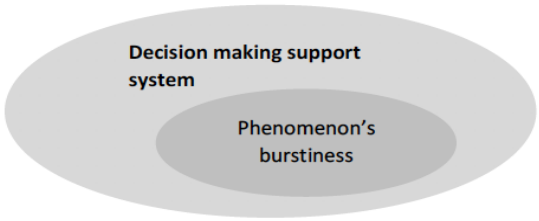

Fig. 8. The inter-connections between decision making support system and phenomenon's burstiness [6].

Consequently, buyers' burstiness influences the decisions on queue management of the service process. By queue management, planning, organizing, leading, and controlling the queuing system aimed at organising an efficient service process in order to reduce customer waiting times in the queue to the cash register or payment processing times at the cash register. The organization of the smooth flow of the service process increases [1]

- the customers' satisfaction with the service, and
- customers' loyalty to the serving company.

For the estimation of the impact of buyers' burstiness on the service process, evaluation of buyers' burstiness can be carried out. One of the reasons of the impact evaluation is the situation where decisions need to be made about whether and/or how to adapt, scale-up, mainstream or replicate projects or processes [22]. Impact evaluations are used in these circumstances because more certainty is required about the changes brought about through these kinds of intervention [22].

It is worth noting that the service process shown in [1] can be described by

- a buyer probability p_e (a visitor becomes with a probability p_e a buyer), and
- a buyer concentration (describing the level of burstiness between buyers α defined in [1]).

For a given level of concentration, probability can be low or high. The probability depends on

- the number of customers in the shop as well as
- on the number of bought goods.

Table 5 presented in [9] indicates buyers' burstiness' constructs and levels for the impact measurement.

TABLE 5 BUYERS' BURSTINESS CONSTRUCTS AND LEVELS [9]

Indicator	**Constructs**	**Levels**				
		1	***2***	***3***	***4***	***5***
		Very low	Low	Average	High	Very high
Burstiness	Probability p_e	Low or high	Low or high	Low or high	Low or high	Low or high
	Concentration $(1-\alpha)$	0.0 – 0.10	0.11 – 0.39	0.41 – 0.59	0.60 – 0.79	0.80 – 1.0

Buyers' burstiness is limiting the service process.

A burstiness level serves as an indicator of bottlenecks [1].

A high level of burstiness, expressed by the buyers concentration, increases the possibilities of bottleneck emergence [1].

The payment processing times at the cash register are quite regular [1]. However, the analysis of the free time intervals at the cash register describing the buyer waiting in the queue to the cash register allows drawing the conclusion on its bursty behaviour [1]. The bursty behaviour of the cashier free time intervals implies long breaks that alternate with many short breaks [1].

TABLE 6 SCENARIOS OF THE SERVICE PROCESS

Process	**The service process**				**Traffic flow**	
Process elements	***Waiting in the queue to the cash register***		***The payment processing***		***Scenario Nr***	***Queue description***
Constructs	Probability	Concentration	Probability	Concentration		
Levels	Low	Low	Low	Low	1	No queuing
	High	Low	Low	Low	2	Pre-Queuing
	High	High	Low	Low	3	Queuing
	High	High	High	Low	4	Pre-traffic jam
	High	High	High	High	5	Traffic jam

Based on these findings of the impact of burstiness on the service process, scenarios of the queue within the service process can be identified. For modelling purposes, Levels 1-3 are used as a low level, and Levels 4-5 – as a high level. Five scenarios of the service process for the queue management purposes are described in Table 6.

IV. CONCLUSIONS

The theoretical research results in the outline of the conceptual framework for exploring the impact of burstiness in the service process. The key concepts have been identified, namely

- binary customer behaviour,
- buyers' burstiness,
- bottlenecks' emergence at the server, and
- queue management.

The logical chain of the development has been emphasized: binary customer behaviour → buyers' burstiness → bottlenecks' emergence at the server → queue management. The presented logical chain allows finding out that buyers' burstiness leads to the queue appearance in the service process. In turn, queue appearance requires queue management measures. Hence, buyers' burstiness influences the decisions in regard to queue management within the service process.

Further on, two functions of buyers' burstiness are defined:

- the indicator of the service process, and
- the factor that influences the service process.

This bi-modal role of buyers' burstiness in the service process highlights the complex nature of the queue management. Five scenarios of the service process will allow using a combination of queue management measures in each scenario or even between scenarios.

The findings of the comparative study presented in Table 1 propose the structure of the service process as the unity of the waiting in the queue to the cash register and the payment processing.

The present research has some limitations. A limitation is the conceptual framework based on the key concepts, namely

- binary customer behaviour,
- buyers' burstiness,
- bottlenecks' emergence at the server, and
- queue management.

Another limitation is the comparative study carried out on the works found via the google search. If the access to other databases would be available, the other findings of the comparative study could be outlined.

The two functions of buyers' burstiness also could limit the investigation of the service process. If other functions of buyers' burstiness within the service process would be determined they could help extend the understanding of the organization of the service process.

Further research tends to validate the model of five scenarios of the service process for the queue management purposes. Comparative studies on buyers' burstiness in the service process will be continued, too.

REFERENCES

[1] D. Hartleb, A. Ahrens, O. Purvinis, J. Zasccerinska, and D. Miceviciene, D. "Internal and External Factor Analysis in Bottleneck Detection in Shop Sales: The Case of Grocery Shops in Lithuania", in Proceedings of the 10th International Conference on Pervasive and Parallel Computing, Communication and Sensors (PECCS 2020), pages 53-60.

[2] D. Hartleb, A. Ahrens, and J. Zascerinska. "Conceptual Framework on Use of Generating Functions for Modeling the Payment Process at Cash Register", in Edited by Piet Kommers and Pedro Isaías. Proceedings of the 19th International Conference e-Society 2021, 3- 5 MARCH, 2021, pp. 269-274. Organised by IADIS, 2021. ISBN: 978-989-8704-26-9.

[3] C. Kiataramkul and K. Neamprem, "Simulation of Queueing System for Commercial Bank in University: Case Study of Bangkok Bank at King Mongkut's University of Technology North Bangkok," in 2019 Research, Invention, and Innovation Congress (RI2C), Bangkok, Thailand, 11-13 December 2019, 2019, pp. 1–4.

[4] M. L. F. Cheong and Y. Q. Chia, "Simulation Model to Evaluate Effectiveness of Queue Management Tool in Supermarket Retail Chain," in 2019 IEEE International Conference on Industrial Engineering and Engineering Management (IEEM), 15-19 December 2019, pp. 606–610.

[5] A. Ahrens, O. Purvinis, D. Hartleb, J. Zaščerinska, and D. Micevičienė. "Analysis of a Business Environment using Burstiness Parameter: The Case of a Grocery Shop", in Edited by Andreas Ahrens, Luis Gomes and César Benavente-Peces, Proceedings of 9th International Joint Conference on Pervasive and Embedded Computing and Communication Systems (PECCS 2019), pp. 49-56. 19-20 September 2019. Vienna, Austria. Printed in Portugal. ISSN: 2184-2817. ISBN: 978-989-758-385-8. Depósito Legal: 460067/19, 2019, pp. 49-56.

[6] A. Ahrens, O. Purvinis, and J. Zaščerinska. "Gap Structure and Characteristic Properties for Analysing Buyers' Burstiness in E-Business process", in Edited by Luis Gomes, Andreas Ahrens, César Benavente-Peces and Mohammad S. Obaidat, Proceedings of 8th International Joint Conference on Pervasive and Embedded Computing and Communication Systems (PECCS 2018), pp. 23-34. 29-30 July 2018. Porto, Portugal. Printed in Portugal. ISSN: 2184-2817. ISBN: 978-989-758-322-3. Depósito Legal: 442620/18. 2018, pp. 23-34.

[7] A. Ahrens and J. Zaščerinska. "E-Shop Visitors' Burstiness as a Predictor of Performance – The Case of eBay", in ICETE 2017 Proceedings of the 14th International Joint Conference on e-Business and Telecommunications Volume 2: ICE-B, Madrid, Spain, July 24-26, 2017, pp. 78-82. ISBN: 978-989-758-257-8. Published by SCITEPRESS – Science and Technology Publications, Lda. Printed in Portugal, 2017.

[8] A. Ahrens and J. Zaščerinska. "Analysing Buyers' Burstiness in E-Business: Parameter Estimation and Practical Applications", in ICETE 2017 Proceedings of the 14th International Joint Conference on e-Business and Telecommunications Volume 2: ICE-B, Madrid, Spain, July 24-26, 2017, pp. 71-77. ISBN: 978-989-758-257-8. Published by SCITEPRESS – Science and Technology Publications, Lda. Printed in Portugal, 2017.

[9] A. Ahrens, O. Purvinis, J. Zaščerinska, and N. Andreeva. "Education for Health Society: Indicators of Burstiness in Research", in Journal Education in a Changing Society, Volume 1 (2016), pp. 28-40. ISSN: 2351-6550, 2016, pp. 28-40. DOI: http://dx.doi.org/10.15181//atee.v1i0.1315.

[10] D. Hartleb, A. Ahrens, O. Purvinis, J. Zascerinska, and D. Miceviciene, "Internal and External Factor Analysis in Bottleneck Detection in Shop Sales: The Case of Grocery Shops in Lithuania," in International Conference on Pervasive and Embedded Computing and Communication Systems (PECCS), Online Streaming, 03.–05. November 2020.

[11] A. Ahrens, O. Purvinis, J. Zaščerinska, and N. Andreeva. "Gap Processes for Modelling Binary Customer Behavior", in Proceedings of the 8th International Conference on Engineering and Business Education 8-9 October 2015, Østfold University College, Fredrikstad, Norway, pp. 8-13. Published by University of Wismar, Germany, 2015, pp. 8-13.

[12] J. Zaščerinska, J. Development of Students' Communicative Competence within English for Academic Purposes Studies. Verlag: Mensch & Buch. 2013, 202 pp. ISBN-13: 978-3-86387-359-2.

[13] A. Ahrens and J. Zaščerinska. "Students' Attitude to Interdisciplinary Research", in Society, Integration, Education. Proceedings of the International Scientifical Conference. Volume I: Higher Education Institutions Pedagogy, School Pedagogy, Pre-School Pedagogy. May, 23th-24th, 2014, – Rēzekne: Rēzeknes Augstskolas Izdevniecība, 2014, pp.13-23.

[14] A. Jacob, A. Ahrens, J. Zascerinska, and C. Benavente-Peces. "AHP-based Evaluation of the Acceptance of Autonomous Driving", in Proceedings of the 10th International Conference on Pervasive and Parallel Computing, Communication and Sensors (PECCS 2020), pages 61-65.

[15] R. Sharma, "Mathematical Analysis of Queue with Phase Service: An Overview," Advances in Operations Research, vol. 2014, Article ID 240926, 19 pages, 2014, Dec 2014. [Online]. Available: https://doi.org/10.1155/2014/240926. [Accessed March 8, 2021].

[16] S. C. Ferrari and R. Morabito, "Application of queueing models with abandonment for Call Center congestion analysis," Gestao & Producao, vol. 27, 2020.

[17] D. Hartleb, A. Ahrens, O. Purvinis, and J. Zascerinska. "Analysis of Free Time Intervals between Buyers at Cash Register using Generating Functions", in Proceedings of the 10th International Conference on Pervasive and Parallel Computing, Communication and Sensors (PECCS 2020) November 3 - 5, 2020 [Online Streaming], 2020, pp. 42-49.

[18] Y. Tang, P. Guo, and Y. Wang, "Equilibrium queueing strategies of two types of customers in a two-server queue," Operations Research Letters, vol. 46, no. 1, pp. 99 – 102, 2018. [Online]. Available: http://www.sciencedirect.com/science/article/pii/S0167637717303243. [Accessed March 8, 2021].

[19] A. Ahrens and J. Zaščerinska. "Gap Processes for Analysing Buyers' Burstiness in E-Business Process", in Edited by Christian Callegari, Marten van Sinderen, Panagiotis Sarigiannidis, Pierangela Samarati, Enrique Cabello, Pascal Lorenz and Mohammad S. Obaidat, Proceedings of the 13th International Joint Conference on e-Business and Telecommunications (ICETE 2016) - Volume 2: ICE-B, pages 78-85. Published by SCITEPRESS – Science and Technology Publications, Lda. Printed in Portugal, 2016, pp. 78-85.

[20] Federation for the Humanities and Social Sciences. "The Impacts of Humanities and Social Science Research. Working Paper", October 2014. Available: http://www.ideasidees.ca/sites/default/files/2014-10-03-impact-project-draft-report-english-versionfinal2.pdf. [Accessed March 8, 2021].

[21] J.B. Pierrehumbert. "Burstiness of Verbs and Derived Nouns", in D. Santos, K. Linden, and W. Ng'ang'a (Eds.) Shall we Play the Festschrift Game?: Essays on the Occasion of Lauri Carlson's 60th Birthday. Springer Verlag, 2012.

[22] Intrac, Impact Evaluation, Intrac for cicil society, 2017. Available: https://www.intrac.org/wpcms/wp-content/uploads/2017/01/Impact-evaluation.pdf. [Accessed March 8, 2021].

Environment. Technology. Resources. Rezekne, Latvia
Proceedings of the 13th International Scientific and Practical Conference. Volume 3, 110-115

Microprocessor System for Temperature Investigation of AC Machines

Totyo Iliev
Department of Electric Power Supply and Equipment
Technical University of Gabrovo
Gabrovo, Bulgaria
totyo_iliev@abv.bg

Tsanko Karadzhov
Department of Mechanical and Precision Engineering
Technical University of Gabrovo
Gabrovo, Bulgaria
karadjov_st@abv.bg

Abstract **- The paper is about four channel microprocessor system for temperature measurement during static and running mode. It incorporates microcontroller type PIC18F452 and employs sensors which convert temperature into voltage. In addition it features optional connection to a PC for storing and processing amassed data. Based on this system a new method is proposed for analysing overheating and cooling of individual parts of asynchronous electric machines. A set of differential equations is derived which later on are processed by MATHCAD software. Obtained results can be presented in tabular or graphic form. The outcome of resolving this task is in the relative ease with which it is possible to establish overheat of various machine parts. Similarly, such approach could be applied with other types of electric machines.**

Keywords - Microprocessor, Microcontroller, Asynchronous Electric Machine, temperature sensor.

I. INTRODUCTION

Both circuits and equipment for temperature measurement find wide range of application in modern industry which in turn necessitates the design of such devices featuring an ever increasing number of function. Using sensor type LM35 a multichannel microprocessor system has been developed, capable of simultaneous measuring of four temperatures.

II. METHOD FOR THERMAL INVESTIGATION OF ASYNCHRONOUS ELECTRIC MACHINES

Two dissimilar approaches are possible to be used in determining the thermal condition of asynchronous machines. [1] [2] [3] [4]

According to the first , an equivalent thermal circuit is set up which usually includes four or five homogeneous bodies such as:

1 – stator pack;
2 – rotor;
3 – stator coil;

All these elements with the exception of the last one do generate thermal losses whose values become evident from experimental measurements or calculations. Each body (element) has its own thermal capacity and all of them are interconnected by thermal conductivity which is conductive and convective.

Convective conductivities are largely dependent on the speed of rotation and, consequently, their values during performance are far more different than the values taken during pause.

With operation mode S4 which is usual for asynchronous machines start-off losses are also to be taken into account. This task entails the set-up of a system of four differential equations and is further to be solved by means of MATHCAD. This results in obtaining thermal dependence for each element from the moment of the transition period start and the quasi-initiation mode.

Such approach is appropriate for practical investigations of thermal processes within the machine. With real functioning machine it is possible to conduct thermal investigations and define thermal parameters with greater accuracy. That, in general, is the essence of this approach.

The above equivalent thermal circuit which contains four homogeneous elements is presented in Fig. 1

Online ISSN 2256-070X
https://doi.org/10.17770/etr2021vol3.6574

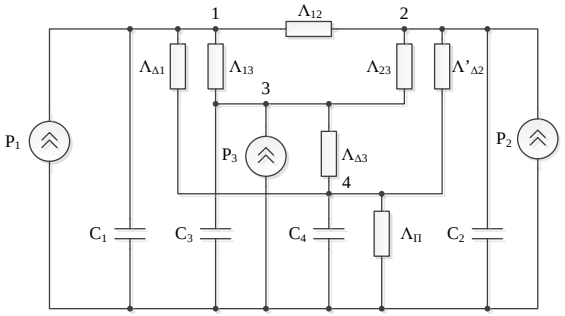

Fig. 1. Equivalent thermal circuit

P1, P2 and P3 are the mean values of losses during operation time t for each operation mode.

$\boldsymbol{\Lambda_{12}}$ – thermal conductivity of the air gap;

$\boldsymbol{\Lambda_{13}}$ – thermal conductivity between copper and steel via channel insulation;

$\boldsymbol{\Lambda_{\Delta 1}}$ – thermal conductivity of contact gap between the pack and the frame;

$\boldsymbol{\Lambda'_{\Delta 2}}$ – thermal conductivity of rotor to the frame via the shaft;

$\boldsymbol{\Lambda_{23}}$ – equivalent thermal conductivity between the second and third body(element);

$\boldsymbol{\Lambda_{\Delta 3}}$ – equivalent thermal conductivity between the third body and the frame;

$\boldsymbol{\Lambda_{\Pi}}$ – thermal conductivity of the frame to the ambience;

$\boldsymbol{C_1, C_2, C_3}$ и $\boldsymbol{C_4}$ – thermal capacities of all four bodies;

$\boldsymbol{\theta_1, \theta_2, \theta_3}$, и $\boldsymbol{\theta_4}$ – overheating of all four bodies.

These parameters are determined by way of experiment and are derived from the measurements made with the developed microprocessor system.

The proposed equivalent circuit allows to compile the following system of differential equations:

$$\frac{d\theta_1}{dt} = -\frac{\Lambda_{11}}{C_1}\theta_1 + \frac{\Lambda_{12}}{C_2}\theta_2 + \frac{\Lambda_{13}}{C_1}\theta_3 + \\ + \frac{\Lambda_{\Delta 1}}{C_1}\theta_4 + \frac{1}{C_1}P_1(1+\alpha_1\theta_1) \quad (1)$$

$$\frac{d\theta_2}{dt} = \frac{\Lambda_{12}}{C_2}\theta_1 - \frac{\Lambda_{22}}{C_2}\theta_2 + \frac{\Lambda_{23}}{C_2}\theta_3 + \\ + \frac{\Lambda_{\Delta 2}}{C_2}\theta_4 + \frac{1}{C_2}P_2(1+\alpha_2\theta_2) \quad (2)$$

$$\frac{d\theta_3}{dt} = \frac{\Lambda_{13}}{C_3}\theta_1 + \frac{\Lambda_{23}}{C_3}\theta_2 - \frac{\Lambda_{33}}{C_3}\theta_3 + \\ + \frac{\Lambda_{\Delta 3}}{C_3}\theta_4 + \frac{1}{C_3}P_3(1+\alpha\theta_3) \quad (3)$$

$$\frac{d\theta_4}{dt} = \frac{\Lambda_{\Delta 1}}{C_4}\theta_1 + \frac{\Lambda'_{\Delta 2}}{C_4}\theta_2 + \frac{\Lambda_{\Delta 3}}{C_4}\theta_3 - \\ - \frac{\Lambda_{44}}{C_4}\theta_4 - \frac{\Lambda_{44}}{C_4}\theta_4 \quad (4)$$

$$\Lambda_{11} = \Lambda_{12} + \Lambda_{13} + \Lambda_{\Delta 1} \quad (5)$$

$$\Lambda_{22} = \Lambda_{12} + \Lambda_{23} + \Lambda'_{\Delta 2} \quad (6)$$

$$\Lambda_{22} + \Lambda_{13} + \Lambda_{23} + \Lambda_{03} \quad (7)$$

$$\Lambda_{44} + \Lambda_{\Delta 1} + \Lambda'_{02} + \Lambda_{\Delta 3} + \Lambda_{\Pi} \quad (8)$$

It should be solved with zero initial conditions. By using Mathcad software we get the solutions for this set of equations: θ_1, θ_2, θ_3 and θ_4. The obtained overheating values θ_1, θ_2, θ_3 and θ_4 for $t=t_1$ are initial conditions for solving the set of equations. Solutions obtained for overheating θ_1, θ_2, θ_3 and θ_4 for $t=t_2$ are in turn the initial conditions for solving the set of equations until quasi-established mode is reached. It is evident that overheating values θ_1, θ_2, θ_3 and θ_4 even in quasi-established mode (S3) pulse in so narrow interval that they could be regarded as constants. This is all the more valid for (S4) mode. In this way the notion of "temperature source" is reached. Power sources can be substituted with overheating sources. Moreover, for this particular case it is convenient to apply the method of average parameters which is stated in [5] [6] [7]

III. PRINCIPLE ELECTRIC DIAGRAM OF MICROPROCESSOR SYSTEM

The diagram is presented on Fig.2

LM35 stand for precision temperature sensors wherein output voltage depends linearly on temperature [8]. They feature a measuring range of:

LM35, LM35A	from -55°C to +150°C
LM35A, LM35CA	from -40°C to +110°C
LM35D	from 0°C to +100°C

Output voltage is changed by 10 mV/°C.

$$U_t = 0{,}01t, [V] \quad (10)$$

Voltage is transferred from sensors' outputs to operation amplifiers LM358 with amplification factor:

$$A = 1 + \frac{R2}{R1} = 5 \quad (11)$$

In this way the entire measuring range of controller's analogue-digital converter is utilized.

Voltage supplied to analogue-digital converter is

$$U_{OU} = 5.0{,}01t, [V] \quad (12)$$

To effectively enable device operation a microcontroller PIC18F452 is used, which features 10-bit analogue-to-digital converter [9]. The controller has enough number of input/output ports and sufficient storage to locate the control program in.

Threshold voltages which determine the converter's measuring range are V_{REF}=0 V and V_{REF+}=5,12 V. Input analogue signal which is supplied to the converter is presented by 2^{10} or 1024 levels.

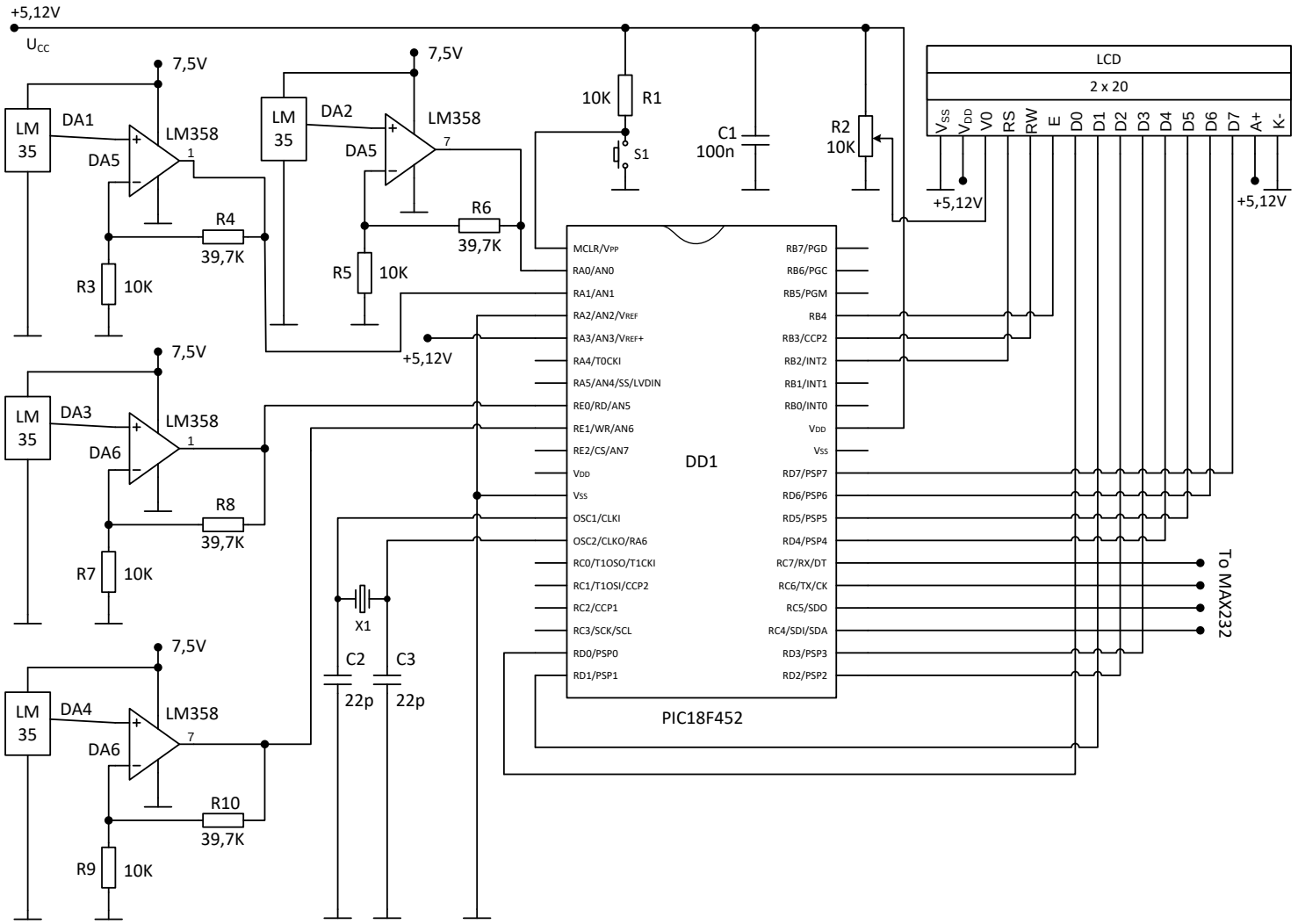

Fig. 2. Principle diagram of Microprocessor System

The step of voltage increment is defined by the formula:

$$\Delta U = \frac{U_{CC}}{2^{10}} = \frac{5{,}12}{1024} = 5\ mV \qquad (13)$$

Supply voltage is selected to be 5.12 V (U_{CC}) for the step to be 5mV.

The function diagram of microprocessor system is composed of four measuring channels each of which incorporates temperature sensor LM35 and measuring amplifier LM358. Voltage is supplied from amplifiers' outputs to the four leads of controller: RA0/AN0, RA1/AN1, RE0/AN5, RE1/AN6 which are configured as analogue inputs. Inputs are switched over. At any point in time voltage is measured at only one input.

Fig. 3 shows a picture of the measuring system.

Fig. 3. Measuring system

Fig. 4 shows how the measuring microprocessor system is linked to a personal computer.

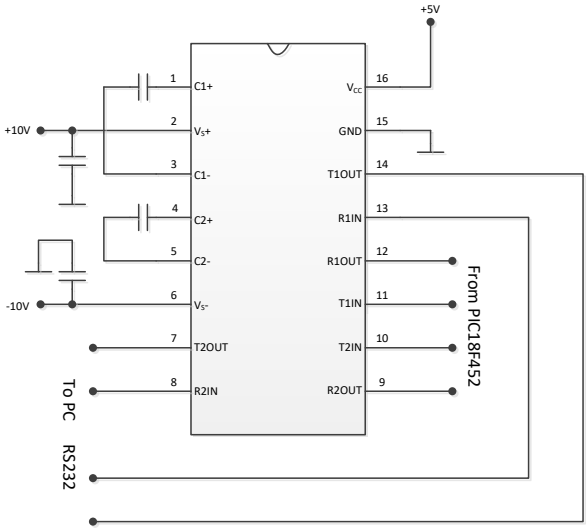

Fig. 4. Microcontroller linked to a PC

Flow chart (block schematic) of program's algorithm

This flow chart is presented in Fig.7 and Fig 8. At the beginning the controller is initialized, constants and variables are defined and storage locations are allocated for them in the data storage. The next step of the program concerns determination of input/output ports. Controller ports are given assignments as digital inputs, analogue inputs and digital outputs. PIC18F452 features four internal module timers. Only Timer 0 is used by means of which program time-lags are assigned and used to synchronize operation of microcontroller and RS232 of computer. The main program is a continuous cycle which is interrupted only when voltage measurement, done by analogue-to-digital converter, is completed.

Processing of each measurement is executed by a subroutine which is started whenever an interruption by analogue-digital converter occurs which signals that measurement has completed.

Input is made followed by processing of measurement result which includes hardware multiplication of measurement value by the assigned constant and conversion of the result from hexadecimal into binary-decimal code. The second stage of the subroutine involves measurement data transfer to the PC. Finally, next measurement is started in the subroutine followed by a return to the main program.

Fig 5 visualizes the dependence of voltages at the output ports of operation amplifiers.

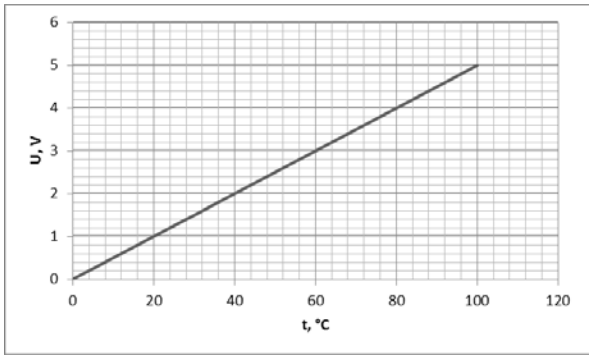

Fig. 5. Transmission characteristic of temperature sensor

IV. Operational Features of the Electronic Device for Temperature Measurement

1. Measurement of four different temperatures on various parts of any machine;
2. Measurement data transfer to a PC;
3. Possible control of four external electric circuits depending on the assigned threshold temperature values;

V. Subroutine for Processing Analogue-Digital Converter Interruption

At the initiation of subroutine a selection of analogue input is made followed by processing of measurement result which includes hardware

multiplication of measurement value by the assigned constant and conversion of the result from hexadecimal into binary-decimal code. The second stage of the subroutine involves measurement data transfer to the PC. Finally, next measurement is started in the subroutine followed by a return to the main program.

The experimental results are given in fig. 7

Fig 6 visualizes the dependence of temperature (θ) at the time of operation (t).

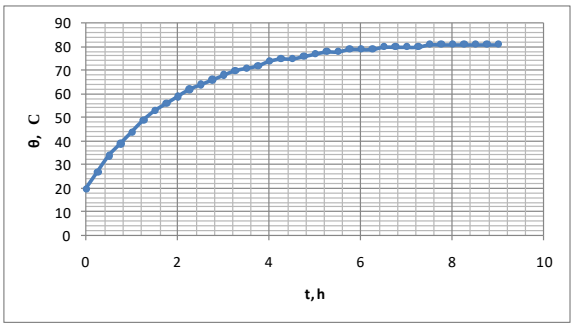

Fig. 6. Experimental results

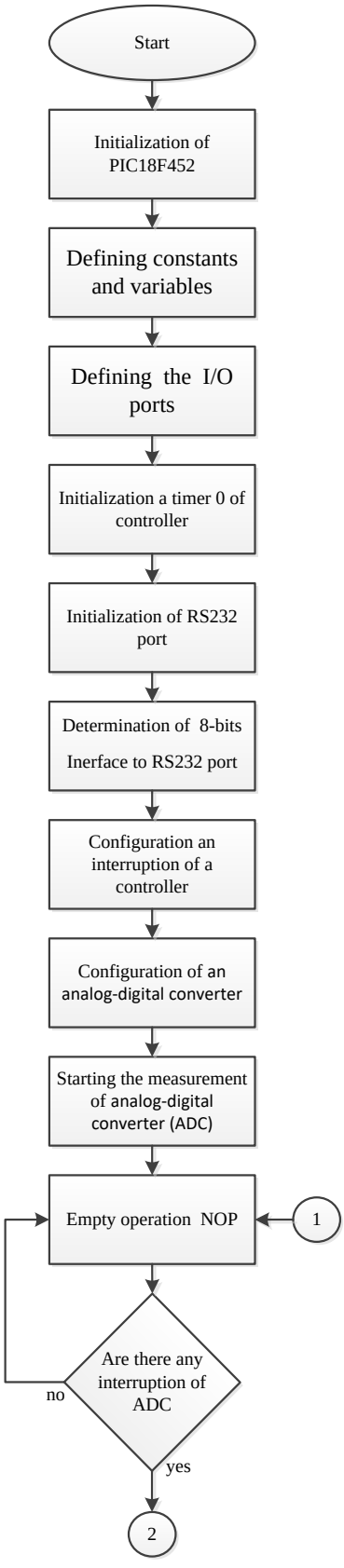

Fig. 7. Algorithm of main program

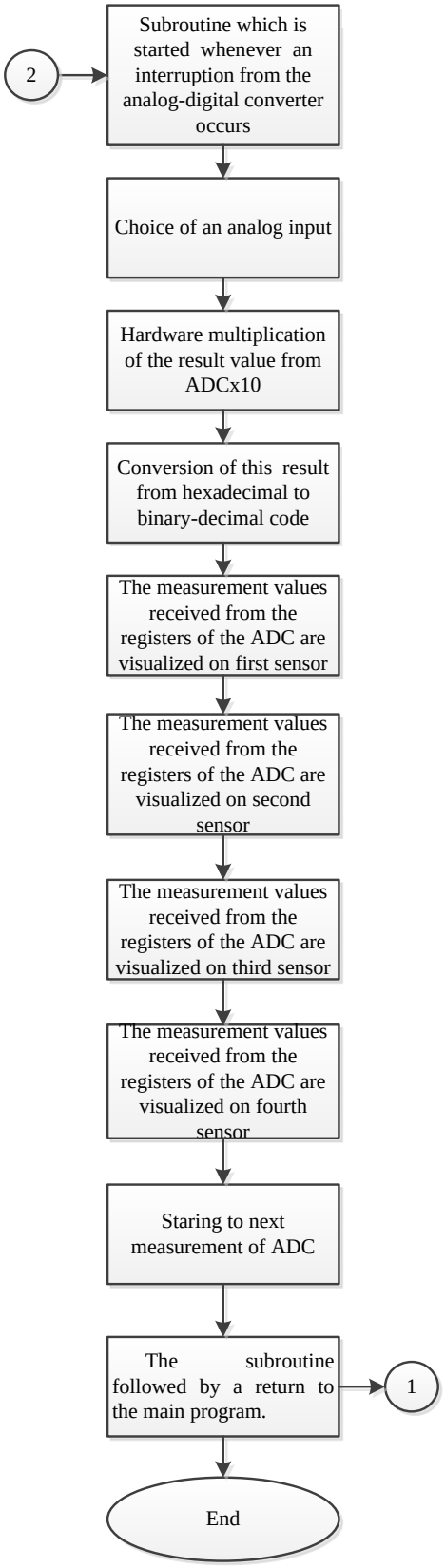

Fig. 8. Algorithm of main program

VI. Conclusion

Generally, the microprocessor system is applicable to electric machines which vary in power capacity and purpose of use allowing to be linked to a PC. In this way it is possible to amass a data array later to be used for thermal analysis. The system is mobile and attachable to every electric machine; its computer link allows for measurement processing with various software, visualization of results and signalling in case of exceeding temperature values.

VII. References

[1] A. Dumcius, V. Augutis and D. Gailius, "The Approximation Aspects of Characteristics of Semiconductor Temperature Sensors," *Electronics and Electrical Engineering*, no. 6(112), pp. 47-50, 2011.

[2] O. Krejcar, I. Spicka and R. Frischer, "Implementation of Full-Featured PID Regulator in Microcontrollers," *Electronics and Electrical Engineering*, no. 7(113), pp. 77-82, 2011.

[3] R. Hajovsky and M. Pies, "Complex Measuring System for Longtime Monitoring and Visualization of Temperature and Toxic Gases Concentration," *Electronics and Electrical Engineering*, no. 6(122), pp. 129-132, 2021.

[4] V. Markevicius and D. Navikas, "Adaptive Thermo-Compensation of Magneto-Resistive Sensor," *Electronics and Electrical Engineering*, no. 8(114), pp. 43-46, 2011.

[5] J. Leskauskaite and A. Dumcius, "The Selection of Thermistors for the Temperature Measurement Gear," *Electronics and Electrical Engineering*, no. 5(111), pp. 59-62, 2011.

[6] B. Gilev, N. Hinov and H. Ibrishimov, "Mathematical Model of Induction Heating with Heat Transfer of Cylindrical Body for Pressing Treatment," in *2019 International Conference on High Technology for Sustainable Development*, Sofia, 2019, DOI: 10.1109/HiTech48507.2019.9128250

[7] N. D. Mazharov, S. M. Hristov, D. A. Dichev and I. S. Zhelezarov, "Some problems of dynamic contactless charging of electric vehicles," *Acta Polytechnica Hungarica*, vol. 14, no. 4, pp. 7-26, 2017, DOI: 10.12700/APH.14.4.2017.4.1

[8] [Online]. Available: http://www.ti.com/lit/ds/symlink/lm35.pdf.

[9] [Online]. Available: http://ww1.microchip.com/downloads/en/devicedoc/39564c.pdf.

Environment. Technology. Resources. Rezekne, Latvia
Proceedings of the 13th International Scientific and Practical Conference. Volume 3, 116-123

Water Discharge Measuring Instruments: an up-to-date Overview

Artem Iukhno
State Hydrological Institute (SHI)
Saint Petersburg, Russia
artem-ardene@mail.ru

Sergei Buzmakov
State Hydrological Institute (SHI)
Saint Petersburg, Russia
s.buzmakov@hydrology.ru

Alisa Zorina
State Hydrological Institute (SHI)
Saint Petersburg, Russia
zorinaalisa@mail.ru

Technological progress could not but affect the sphere of hydrometric measurements. New instruments have been implemented to add to such traditional measuring instruments as mechanical current meters or to replace them. Over the past 20 years, the number of different types measuring instruments has increased dramatically. That is why the analytical review and classification of these devices are needed to help with making appropriate management decisions in the field of streamflow monitoring and surveys. The article presents the multivariable classification of measuring instruments, based on such factors as: morphology scaling (channel width and depth), measuring conditions (open, weed or ice-covered channel), logistical factor (mobile or stationary) and required accuracy. Characteristics of each type of measuring instruments were also considered and the limitations of their applicability were described. The results presented in the paper are expected to expand the horizons of approaches used for estimation of water discharge.

Keywords – current meters, water discharge, ADCP, open channel flow measurement classification

I. PROBLEM INTRODUCTION

The classifications of instruments, used for velocity of the streamflow measuring and further calculation of water discharge, published earlier, are focused on the environmental components and sustainability [1], or on the methods of the physical essence [2], or give general ideas that allow management decision making [3]. One of the last attempts to do such an analytical work in the field of flow measurements was undertaken by Indian scientists under the leadership of Senthil Kumar J [4]. It is worth noting the huge range of the materials covered as well as in-depth development of the ultrasonic flow measurement accuracy tasks, but focused more on pipe- and artificial channel-based equipment. However, this review is not suitable enough for solving problems of instrumental equipment in the field of river (open channel measurements) hydrology and meeting the objectives, outlined in the abstract of this article.

Russian and foreign guiding normative documents in the field of hydrometeorological monitoring and surveys [5, 6] do not provide comprehensive information in a quick and easy-to-use way either. They do not describe all measuring instruments that can be used to measure velocity or any other characteristics, which can be further used for water discharge calculation. Present review is multi-criteria, and each of the above criteria is aimed at the presentation of information about the limits of applicability of a particular method or measurement instrument. In other words, the classification presented in this article can be characterized as applicability-based.

II. CLASSIFICATION IDEA

This multi-criteria classification was developed in order to answer the most challenging and reasonable questions related to the performing the hydrological surveys and monitoring, forming certain level (classifiers) of the classification:

1. Is it necessary to make measurements on-site (continuously) or to make one-time in-situ measurements as part of field work by portable devices? This is how the "Logistic classifier" (A) is formed, or the subdivision into stationary (on-site) and portable measurement instruments, which applicability is limited to use in field surveys.
2. What is the size of the stream on which the measurements are supposed to be made? The answer to this question in a view of expected depths and widths of the channel forms the second level of classification (B) "River-morphological scale".

Online ISSN 2256-070X
https://doi.org/10.17770/etr2021vol3.6613

3. What are the hydrodynamic and associated with it conditions on the river where the measurements are supposed to be made (flow regime, the possibility of immersion of the device)? This is how the third level of grading of the classification (C) "Flow regime and hydrodynamic conditions".
4. What type of devices or methods can be used to determine water discharge, corresponding to a particular previous level of gradation? The (D) "Method or instrument type" level of the classification contains the answer to this question.
5. What is required accuracy of estimating water discharge of a river? The using of color level "expected accuracy" (E) aims to solve this problem.
6. Is it possible to use any other device in unfavorable conditions such as freeze-up channel, high turbulence or when a measuring device or a person, carrying out measurements, is not safe? You can understand this from the graphical classifier (F) "Measurement conditions".
7. Which of the instrument is the most frequently used of those given for a particular classifier? The (G) "Usage frequency" classifier is about it.

The first level (A) realized in the benchmark of this article use two different classifications – for the portable (Figure 1) and on-site instrumental solutions (Figure 2). Levels B and C are implemented directly as branches of one large classification hierarchy. Level D uses a verbal description at one level or another. Classifier E is implemented in the form of shading a block of one or another classification level in the color of the corresponding measurement accuracy. Classifier F is an additional graphic designation in a view of round sign above one or another type of measuring instrument on the right or left above. G level is a sequence of devices in a block of one level - more frequently used devices are locating higher than less used ones within a block of one level.

III. CLASSIFICATION LEVELS

A. The first "Logistic" level of classification divides instruments into stationary (on-site) and portable (in-situ). Stationary devices can operate autonomously, or have such a mode, measuring certain characteristics of the river with the subsequent continuous calculation of water discharge. This is their undoubted advantage, but, even in the time of fast technical progress, the choice of such devices is very limited, and the cost is often very high. It is also worth noting the high research intensity of maintaining the operability of such devices. This requires highly qualified staff that would be responsible for the engineering and manufacturing development, correct installation, operation and maintenance of such equipment. Most of the on-site high-accuracy devices are intrusive, while non-intrusive allow measurements only for general monitoring purposes (accounting for water resources, hydro ecological issues and etc.). Nevertheless, current tendency to transfer national observation network equipment to autonomous regime has been obvious.

Stationary devices include following instruments and methods: hydrometric units of Hydro-electric power stations HEPS (turbines and weirs), hydrometric structures (weirs, flumes); non-contact Doppler and ultrasonic radar flow meters; the slope-area method with using two precise water level gauges; on-site autonomous image velocimetry systems using high-resolution cameras and satellites; bottom submersible and river bank-side ADCP and ultrasonic devices and measuring systems; indirect methods using hydrochemical or physical parameters, stationary tracer dilution and rising bubbles facilities; tilt current meters; noise component analysis method.

Portable instruments and devices are widely spread in hydrological surveys, and actually have achieved a huge number of variations based on vastly different principles. Such devices are used for in-situ measurements, as a rule, by immersing the instrument in the water column or using image velocimetry or radar impingement, or making measurements remotely using drones, aircrafts or satellites. Almost all the devices listed as stationary have portable versions (excluding HEPS facilities). In the field conditions it is also possible to use volumetric and float methods; mechanical, electromagnetic and pressure operated current meters and moving-vessel ADCP devices.

B. "River morphological scale" level aims to classify streams to *creeks*; *minor, medium and large* rivers by morphological principle and *estuaries* by the current distribution factor (with variable backwater phenomena and complex, unique for estuarine areas structure of currents). It is important to realize that this division is not based on the traditional classification of rivers (by the catchment area), but according to the features of using certain measuring instruments and equipment related to them.

The creeks are constituted in a separate category due to the difficulty of immersing the instrument into the water column. That is why the limiting factor for them is a depth of 0.05 m (half of the sensor or propeller diameter of the vast majority of the mechanical or other types of the immersed current meters). Furthermore, it is true (especially for the creeks) that measurements are suitable for volumetric method and portable weirs and flumes.

Minor rivers are characterized by a depth of less than 1.3m - the depth of the river wading.

Medium rivers are determined by the channel width of 100 m - the maximum possible distance between the supports (armors) of hydrometric installations (meter-suspension cables, towing systems and cableways).

Large rivers include rivers where it is impossible to perform measurements from a cableway or towing system. Measurements on large rivers are associated with large labour inputs and large number of additional equipment in the case of using traditional submersible measuring instruments (cranes, balance weights, anchors, reliable floating crafts).

C. "Flow regime and morphological conditions" classifier subdivides rivers into *mountain or sub-mountain and plain.* The slope of the water surface can be considered as a classifying parameter at this level. In such a way, rivers or river sections with slopes of more than 0.2 ‰ are considered to be *semi-mountain*, more than 5 ‰ – *mountain*, less than 0.1-0.2‰ - *plain* or low-land [6]. The slope of the rivers can integrally characterize the hydraulic characteristics of the flows. There are such characteristics for mountain and semi-mountain rivers: a turbulent flow regime, the formation of whirlpools, waves, high flow rates reaching several meters per second. For the plain rivers - a quasi-stationary regime, mild turbulence, low and medium current velocities around 0.1-1 m/s, meandering are specific.

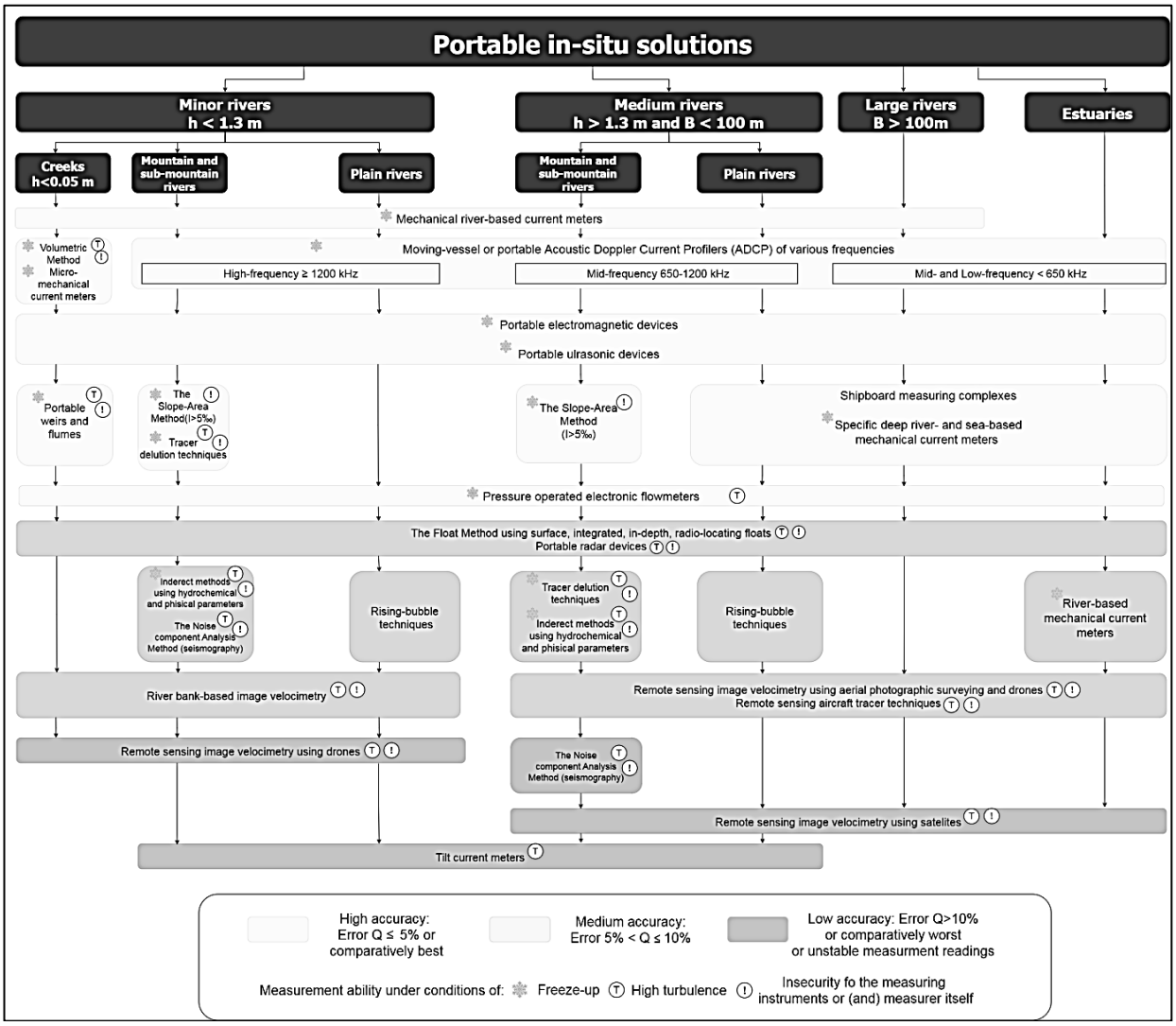

Fig. 1. Portable in-situ instruments and methods for determining water discharge classification (the best quality image can be viewed on the website of the State Hydrological Institute (SHI) [7])

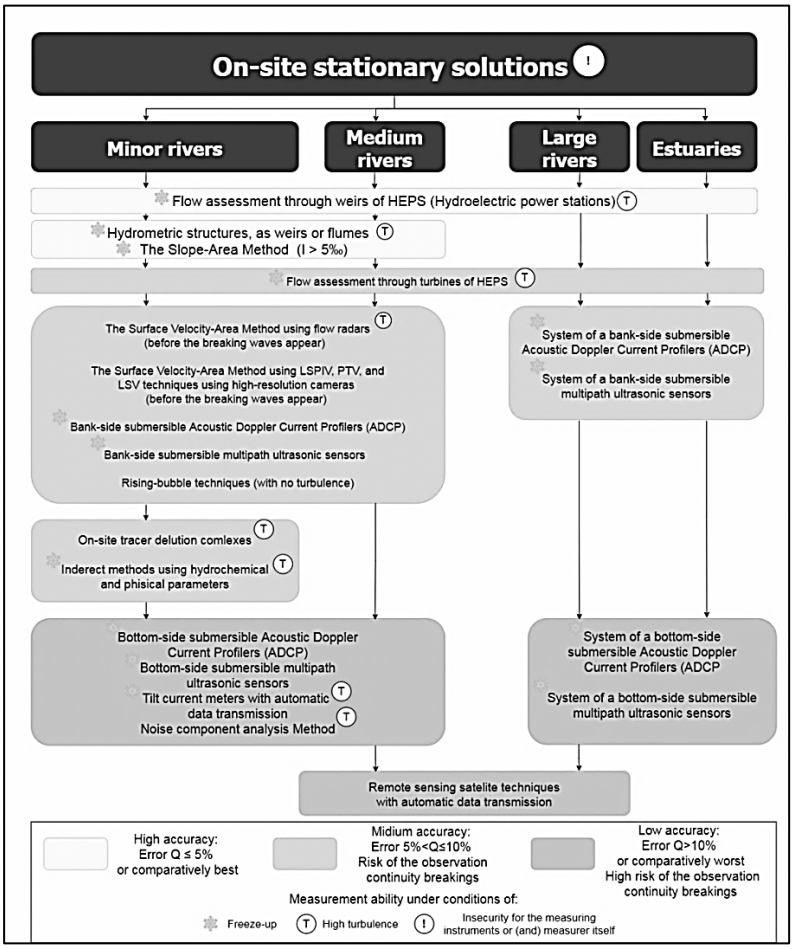

Fig. 2. On-site stationary instruments and methods for determining water discharge classification with (the best quality image can be viewed on the website of the State Hydrological Institute (SHI) [7])

D. At the "Method or instrument type" described different methods or types of the measuring instruments. Below follows the basic principles of operating of the most frequently-used particular method or type of instruments will be briefly considered (with further recommendations on which sources can be found for more detailed information).

Mechanical current meters are the most widely used instruments for measuring current velocity with further calculation of water discharge at the moment. The velocity of flow at a point is proportional to the rate of rotation of the rotor during a fixed period of time.

To date, there has been a huge range of devices manufactured by different countries of the world. In existing models there are such important tasks as: the possibility of fixing simultaneous velocity (due to the use of single-threaded screw with hermetic contact); operation on shallow depths (by reducing the rotor diameter); measurements of low velocities (due to the use of light structural materials of the rotor, increasing its sensitivity); operation under skew-jet conditions (by optimizing the component effect). Besides can be identified: optimized rotor and housing materials and recording and support equipment. According to the level of development of the principles of hydrometric instrumentation (production mechanical flow meters) countries of the world today have approximately the same level. Significant differences lie in the quality of the devices. The devices are manufactured with cup-type and propeller mechanisms [8]. The range of recorded velocities for the river mechanical current meters is from 0.04 m/s to 4-6 m/s and from 0.025 to 2-6 m/s for micro-ones. Specific deep- and sea- based mechanical current meters allow more accurate measurement of velocity when there are reverse currents and high pressure.

Despite the apparent completeness of the development of hydrometric mechanical current meters, there are *unsolved problems* as well. These include [8]:

- lack of an optimal ratio of sensitivity - component, when an increase in the sensitivity of the device would not lead to a significant deterioration component qualities and vice versa (the issue is solved by the layout of the current meter by several replaceable rotors);

- lack of consensus on the influence of the relative diameter of the propeller and its disk-area ration to somewhat different the component properties of the device;
- unsolved issue of ensuring uninterrupted operation of the device in complex conditions (frost, increased mineralization, channel weed);

Methodological aspects of mechanical current meters measurements are outlined in any of the guidelines for stream gauging, for example [9].

Acoustic principle instruments – an Acoustic Doppler Current Profilers (ADCP) and ultrasonic devices. There are two basic types of acoustic current meters: Doppler and Travel Time. Both methods use a ceramic transducer to emit a sound into the water. Doppler instruments are more common. The ADCP works by transmitting "pings" of sound at a constant frequency into the water. As the sound waves traffic, they ricochet off particles suspended in the moving water, and reflect back to the instrument. Due to the Doppler effect, sound waves bounced back from a particle moving away from the profiler have a slightly lowered frequency when they return. Particles moving toward the instrument send back higher frequency waves. The profiler sends out difference in frequency between the waves and the waves it receives is called the Doppler shift. The instrument uses this shift to calculate how fast the particle and the water around it are moving. There are four main types of ADCP devices: portable, moving-vessel and river bank- or bottom immerse-based stationary ones.

Travel time instruments determine water velocity by at least two acoustic signals, one up stream and one downstream. By precisely measuring, the time when water have to travel from the emitter to the receiver, in both directions (the average water velocity) can be determined between the two points. By using multiple paths, the water velocity can be determined in three dimensions.

Travel time meters are generally more accurate than Doppler meters, but they are only record the velocity between the transducers. Doppler meters have the advantage that they can determine the water velocity at a considerable range, and in the case of an ADCP, at multiple ranges.

Acoustic principle-based instruments cover a wide range of measurable velocity from 0.003 m/s to 5-10 m/s in both directions of speed with the accuracy less than 10% for the computed discharge. The profiling depth depends on the frequency of the emitter: for example, high-frequency (1200kHz) ADCPs measure velocity at depths in the range from 0.1 to 7-8 m, medium-frequency (600kHz) - from 0.15-0.2 to 30-40 m, low-frequency (300 kHz or less) - from 1-2 m to 100-300 m for river device versions. In the short term, these devices can replace mechanical current meters due to low labour inputs for measuring and obtaining flow velocities throughout the water column. This process is held back mainly only by high prime cost of ADCPs and Travel Time techniques.

There are many manuals and guidelines for measuring water discharge with ADCP. It might be advised the following ones: [10] for moving vessel measurements and [11] for measurements under ice cover. For using ultrasonic devices there are no regulatory papers yet, but plenty of articles, for example, ones of Japanese researchers [12].

Electromagnetic current meters. The motion of water flowing in a river cuts the vertical component of the Earth‘s magnetic field, and an electromotive force (E_{mf}) is induced in the water, that can be measured by two electrodes. This E_{mf}, which is proportional to the average velocity in the river, is induced along each traverse filament of water, as the water cuts the line of the Earth’s vertical magnetic field. The basic system of an electromagnetic gauging station consists of a coil placed in the bed and the magnetic field, that are induced in the x direction. Since the stream flow is in the z direction, the E_{mf} will be in y direction. Faraday’s law of electromagnetic induction relates the length of a conductor moving in a magnetic field to the E_{mf} generated. The electromagnetic method can be suitable for use in rivers with weed growth, high sediment concentration, or unstable for bed conditions. This method gives a continuous record of the average velocity in the cross-section that can be combined with stage to given an on-site output of discharge [13]. But more often such devices are in portable version.

Their use is governed by the same principles as for mechanical current meters. However, it is worth noting that the measurement methodology should be a little different, but this is not reflected in any of the manuals at the moment. The point is mainly in the approach to averaging the obtained velocity values and their interpretation. Electromagnetic devices are very vulnerable to the direction of flow, therefore they often underestimate the value of the velocity, registering its vector on one or another projection [14]. But this problem is solved by a competent methodological approach (for example, it is possible to recommend taking into account the maximum from the 3-5 measured values with the holding period necessary for the certain flow regime). It is worth noting the low initial threshold of the measured flow velocities - about 1 mm/s, which distinguishes this instrument from a number of others. At the same time, the measurement accuracy is only slightly lower. The upper limit of velocity measurement is 5-10 m/s.

POEM (Pressure Operated Electronic Meter). Depth and velocity measuring instrument that uses a forward-facing pitot tube on the front of a streamlined weight, that houses velocity and depth sensors. This instrument is best

suited to flooded river measurement as the POEM is not precise at water velocities <1 m/s. The average velocity for the vertical is calculated in the POEM software by integrating the depth and velocity readings. Pitot tubes, in one version or another, are also used in laboratory conditions, for measurements on minor streams and creeks [15].

An in-depth comparative study of the tools given above is described in the article [16].

Hydrometric structures. This type includes hydrometric flumes, weirs, hydroelectric power plants of various capacities. As a rule, the water discharge for this type of measuring facilities is determined depending on the water level (or gross head) or recalculated from the characteristics of the hydropower-plant capacity (for HEPS).

It is worth noting the high accuracy of the water discharges obtained in this way, while the main *limiting factors* in the use of structural measures are the large labour inputs during the construction of the structure (and further intrusive impact on the natural self-regulating fluvial-stream system) and the scale of the watercourse. Thus, the maximum flow capacity for hydrometric flumes and weirs does not exceed 50 m^3/s (the minimum is about 60 ml/s).

The construction of HEPS is limited by the commercial importance of its construction, while their throughput capacities can vary from 0.5 to 500 m^3/s for small HEPS, and more than 100 000 m^3/s for large ones. Modern technologies make it possible to automate the process of obtaining a water discharge, which ensures the continuity of observations, and it is an undoubted *advantage*. The practical aspects of using structural flow metering facilities are well covered in [17], methodological aspects – in [18].

Volumetric methods. The simplest way to estimate water discharge of creeks is by direct measurement of the time to fill a container of known volume. The flow is diverted into a channel or pipe which discharges into a suitable container, and the time to fill is measured by stopwatch. The time to fill must be measured accurately, especially when there is only a few seconds. The variation between several measurements taken in succession will give an indication of the accuracy of results.

If the water flow can be diverted into a pipe then it is discharged under pressure, the rate of flow can be estimated from measurements of the jet, or the water column height in the case of vertical upward dislocation. *The main limitation* of the method is a quite low range of possible measuring discharges – from vanishingly small to 50 l/s.

Dilution techniques. The basic principle of dilution gauging is to add a known quantity of a tracer to a stream and to observe its concentration in the stream at a point where it is fully mixed with the flow. The higher the flow is, the more it dilutes the tracer. Dry salt that used as the tracer must be injected at a point that favours rapid dissolution. This creates a salt solution in situ that then disperses into the flow aided by turbulence in the water column. The resulting concentration of salt is measured as electrical conductivity (at a point downstream of the injection point where it is completely mixed). The distance between the injection and measurement points is known as the mixing length (L). The dispersion pattern of conductivity over time is similar in shape to a storm hydrograph. Streamflow Q is calculated dividing the mass of salt (in grams) M by the area under the graph of concentration over time (A). The units of A are milligram-seconds per litre (equivalent to $g \cdot s/m^3$).

Dilution method-based measuring devices are available in both portable and stationary versions. Errors, with meeting all the requirements [19], for turbulent flows with active mixing should not exceed 5-10%, but due to the complexity of dilution processes and hydrodynamic factors for flows unsuitable for measurement by this method, because they can reach 200-300% [19]. In general, this approach can be recommended for mountain rivers with turbulent current and water discharge up to 5-10 m^3/s. Detailed information about the method is presented on the website [19].

Within the scope of this article, it is impossible to cover the entire range of possible water discharge determining equipment, only the main ones have been described above. For less common methods oriented towards more scientific studies, links to research will be provided below. Full information on the applicability of certain means is contained in the classification itself (Figures 1 and 2).

For the slope-area method look at [6], indirect methods using physical and hydrochemical parameters - [20], noise component analysis method [21], tilt current metering - [22], LSPIV (PIV) remote non-intrusive techniques – [23] and the rising bubble techniques – [24].

E. The classifier "Required measurement accuracy" is implemented in a graphical form in a view of shading blocks in one color or another (for more details, see the legends of Figures 1 and 2).

F. Classifier "Possible measuremnent conditions" is an additional graphic designation in round frames above one or another type of measuring instrument on the right or left above. It indicates whether unfavorable conditions as freeze-up channel, high turbulence or conditions of insecurity for the measuring instrument or measurer itself are possible. Special attention should be focused on instruments that are capable for making measurements in insecure conditions, when there is no way to enter the stream (trees carried, large debris, ice floes by the stream and other factors).

INSTEAD OF CONCLUSION

Due to constant technological and scientific progress, the classification presented is doomed to be updated and refined. Therefore, the developers are waiting for your remarks, additions and comments at lgpggi@yandex.ru. By joint efforts, the development of this classification will be faster, and its scientific and practical value will increase.

REFERENCES

[1] P. Dobriyal, R. Badola, Ch. Tuboi & S.A. Hussain, "A review of methods for monitoring streamflow for sustainable water resource management", Applied Water Science, Vol. 7, pp. 2617-2628, Oct. 2016, https://doi.org/10.1007/s13201-016-0488-y

[2] K. D. Jensen, "Flow measurements", J. of the Braz. Soc. of Mech. Sci. & Eng., Vol. 26 №4, pp. 400-419, Dec. 2004, https://doi.org/10.1590/S1678-58782004000400006

[3] R. Gravelle, "Discharge Estimation: Techniques and Equipment". Geomorphological Techniques, Chap. 3, Sec. 3.5, British Society for Geomorphology, pp. 1-8, 2015.

[4] J. Senthil Kumar, A. Kamaraj, C.K. Sundaram, G. Shobana, and G. Kirubakaran, "A comprehensive review on accuracy in ultrasonic flow measurement using reconfigurable systems and deep learning approaches", AIP Advances 10, Vol. 10, Issue 10, (2020), pp. 1063-1078, July 2020, https://doi.org/10.1063/5.0022154

[5] Technical standard of Russian Federation R 52.18.851-2016, "The main measuring instruments of the hydrometeorological purpose, used on the national observation network", Dec.2016.

[6] D.P. Turnipseed, V.B. Sauer, "Discharge measurements at gaging stations: U.S. Geological Survey: Techniques and Methods", book 3, chap. A8, 87 pp., 2010, https://doi.org/10.3133/tm3A8

[6] J.C. Bathurst, "Tests of three discharge gauging techniques in mountain rivers", Hydrology of Mountainous Area, Vol. 190, pp. 93-100, 1990.

[7] Official Laboratory of the Hydrological Instruments page in the web-site of the State Hydrological Institute (SHI) [Web-site. Online]. Available: http://www.hydrology.ru/en/structure/department-hydrological-instruments [Accessed March 3, 2021].

[8] D.E. Klimenko, "Development of hydrometric mechanical current meters in Russia and abroad", Geographical Bulletin of Perm' University, Vol.2, 13 pp., 2010.

[9] WMO Manual on stream gauging, "Volume 1 - Fieldwork", WMO working paper № 1044, 252 pp., 2010.

[10] Environment Canada Manual Book 3-A22, "Measuring discharge with acoustic Doppler current profilers from a moving boat" version adapted for Water Survey of Canada, 62 pp., 2013.

[11] P. Campbell, Materials of the Water Survey of Canada, "Standard operating procedures for under ice discharge measurements using ADCPs. Version 2", 45 pp., 2015.

[12] K. Yokoyama, N. Kashiwaguma, T. Okubo, Y. Takeda, "Flow Measurement in an Open Channel by UVP", 4th International Symposium on Ultrasonic Doppler Method for Fluid Mechanics and Fluid Engineering Materials,, pp. 55-58, 2004, https://www.isud-conference.org/proc/split/ISUD-04_055_Yokoyama.pdf

[13] Standard ISO 9213:2004, "Measurement of total discharge in open channels — Electromagnetic method using a full-channel-width coil"

[14] H. Ryckborst & R. O. Christie, "Feasibility of electromagnetic streamflow measurements using the earth's field", Hydrological Sciences Journal, Vol. 22 (2), pp. 241-255, 2009, https://doi.org/10.1080/02626667709491715

[15] National Environmental Monitoring Standards (NEMS), "Open Channel Flow Measurement: Measurement, Processing and Archiving of Open Channel Flow Data", pp. 77, 2013.

[16] M.L. Soupir, S. Mostaghimi, C.E. Mitchem Jr., "A comparative study of stream-gaging techniques for low-flow measurements in two Virginia tributaries", Journal of the American Water Resources Association, Vol. 45 (1), pp. 110-122, 2009, https://doi.org/10.1111/j.1752-1688.2008.00264.x

[17] Official website of the "Open channel flow manufacture" [Web-site. Online]. Available: https://www.openchannelflow.com/ [Accessed February 20, 2021].

[18] A. J. Clemmens, T.L. Wahl, M.G. Bos, J.A. Replogle, "Water Measurement with Flumes and Weirs", International Institute for Land Reclamation and Improvement, Wageningen, The Netherlands, 384 pp., 2001.

[19] Salt dilution techniques materials on the official website of the Fathom Scientific Ltd. [Web-site. Online]. Available: https://www.fathomscientific.com/category/hydrometrics/salt-dilution/ [Accessed February 20, 2021].

[20] N.V. Ukhov, M.V. Ushakov, "Determination of water discharge in minor rivers by physical and chemical parameters", Scientific notes of the RSHU, Vol. 57, pp. 38-45, 2019.

[21] R.E. Anthony, R.C. Aster, S. Ryan, S. Rathbur, M.G. Baker, "Water current measurements using oceanographic bottom lander LoTUS", Journal of Geophysical Research: Earth Surface, Vol. 123, pp. 210-228, 2017.

[22] M. Kjelldorffa, J. Kuttenkeulera, N. Kirchnerb, J. Krützfeldta, M. Sundberg, "Water current measurements using oceanographic bottom lander LoTUS", Applied ocean research, Vol. 94, 13 pp., 2020, https://doi.org/10.1016/j.apor.2019.101982

[23] W. Lia, Q. Liaob, Q. Ranc, "Stereo-imaging LSPIV (SI-LSPIV) for 3D water surface reconstruction and discharge measurement in mountain river flows", Journal

of Hydrology, Vol. 578, 12 pp., Nov. 2019, https://doi.org/10.1016/j.jhydrol.2019.124099

[24] K. P. Hilgersom and W. M. J. Luxemburg, "Technical Note: How image processing facilitates the rising bubble technique for discharge measurement", Hydrol. Earth Syst. Sci., Vol. 16, pp. 345–356, 2012.

Environment. Technology. Resources. Rezekne, Latvia
Proceedings of the 13th International Scientific and Practical Conference. Volume 3, 124-129

Doppler Non-contact Radar Sensors for Water Discharge Estimation: Advantages and Limitations

Artem Iukhno
State Hydrological Institute (SHI)
Saint Petersburg, Russia
artem-ardene@mail.ru

Sergey Buzmakov
State Hydrological Institute (SHI)
Saint Petersburg, Russia
s.buzmakov@hydrology.ru

Alisa Zorina
State Hydrological Institute (SHI)
Saint Petersburg, Russia
zorinaalisa@mail.ru

The use of non-contact doppler flow radars to determine water discharge is a widespread trend in hydrometeorological surveying and monitoring. However, is it reasonable to consider such an instrument as one of the most suitable and perspective for the hydrological observation network? In-situ testing have been carrying out by authors of this article and the analysis performed in scientific papers cannot provide a single-valued positive conclusion on this issue. Obvious advantage of these radars as independent safe mode of operation seems to overweight their obvious weak points. Many "undercurrents" do not allow this method to be recognized as reliable, such as the problem of transition from surface to medium flow velocities, which consists in the data processing apparatus, reliable positioning of the device, blanking distance task and etc. All in all, this article discusses the main advantages and "vulnerabilities" of the use of such an instrument as non-contact doppler radars to determine water discharge from a scientific and practical points of view.

Keywords – water discharge, non-contact measurements, Doppler radars, non-intrusive river velocimetry

I General information: device kit description and operation principles

Doppler radar flow meters were developed over 40 years ago, but have not yet gained sufficient acceptance in hydrological monitoring. This state of affairs is accompanied by a relatively high cost of instruments, as well as the complexity of the transition from measured surface flow velocities to determining water discharge.

A Doppler radar flow meter consists of a microcontroller, communications and power supply, as well as two sensors: water level (most often a radar sensor is used, but other types of level gauges can be used) and current velocity (local surface current velocity is measured). In most cases, both sensors are placed in the same housing. The current velocity sensor can be used as a separate device, but it is more correct to call such a device a velocimetry.

The radar flow meter measurement is based on the following principle. When water moves, structural relief formations appear on the surface of a turbulent flow - waves that move along with the water mass. If irradiation is performed at an acute angle to such a surface, part of the energy is reflected by inversed manner, while the other is reflected in the direction of the emitter. According to the Doppler effect, the frequency of electromagnetic oscillations of the reflected signal differs from the frequency of the irradiation signal by the value which is calculating using formula 1:

$$f_{extr.} = 2Vcos(\theta)\cos(\frac{\varphi}{\lambda}) \quad (1)$$

Where V – velocity of movement the irradiated object;

λ – the wavelength of the emitted signal;

θ – the angle of the direction of irradiation relative to the flow surface in the vertical plane;

φ – the corresponding angle relative to the direction of flow in the horizontal plane

The mechanism of the flow meter operation. The radar flow meter transmits a signal at a constant frequency of about 24 GHz to the surface of the water at a selected angle. The miniature waves that are present on the surface reflect

Online ISSN 2256-070X
https://doi.org/10.17770/etr2021vol3.6616

the radar waves back to the sensor. To measure the flow velocity, a wave on the water surface of at least 3 mm is required (according to the stated requirements of the vast majority of the equipment manufacturers). The reflected signal is shifted in frequency due to the Doppler effect from the movement of the water surface. Comparing the transmitted frequency with the frequency reflected from the surface, the mathematical apparatus processes the received data and converts it into local velocity.

The flowmeter is installed parallel to the stream flow on a support (for example, on a bridge pier). Installation is possible ashore, but this location does not guarantee good measurement results. The transmitter should be directed at an acute angle to the flow surface of 20-60 ° [1]. The optimum range is 30-45°. The width range of the irradiated spot should not fall to breakers, vegetation, driftwood and other interference.

II. The influence of external environmental and other factors on the reading of the device

The quality of measurements can be influenced by external environmental factors such as wind, rain, vibration, etc.

The wind speed directly over the water surface is about 2% of the wind speed measured at a height of 10 m [2]. For example, with a wind speed at the level of a air vane of 10 m/s, the wind speed above the water surface will be 20 cm/s, and assuming a logarithmic attenuation to the depth of the radar flow velocity measurement, the wind will introduce distortion the measurements by an amount equal to 11 cm/s. Such an error in measuring the flow velocity will occur only if the wind blows exactly in the direction in which the transmitter is directed. For other directions, the error will be less [3].

For *the rain* influence prevention, the most effective solution is to mount the radar so that it points upstream. When it rains, raindrops will drift away from the radar and water will flow towards the radar. Then the radar can distinguish the movement of water from the movement of a rain. Additional rain suppression can be implemented by mounting the radar under some structure (bridge, shield). You should also make sure that no rain or melt water from the bridge leak through the radar's field of view.

In some watercourses, *changes in the direction* of the current are occurring. In such cases, the radar must be configured to register both incoming and outgoing. This radar setting will not filter rain.

The structure supporting the tool (pole, bridge, fence, etc.) must be robust and vibration-free. However, some models have a built-in vibration sensor.

Most measurement inaccuracies caused by environmental factors can be eliminated by properly installing the sensor.

III. Characteristics and specification of manufactured devices

According to the up-to-date marketing research carried out by the employees of the Laboratory of Hydrological Instruments of the State Hydrological Institute [4], the average price of radar flow meters varies around two values: 3800 € and 11000 €. The minimum measurable flow velocity for 95% of radars is 0.1 m/s (some models claim 0.02 m/s). The maximum recorded flow velocity for 90% of the devices is 15 m/s. The velocity measurement error varies from (1% ± 0.025) m/s to (0.5% ± 0.02) m/s. The length of the sensing spot can vary from 0.29 to 49.2 m, the width from 0.12 to 12.8 m.

IV. Case study: Investigation of the applicability of a Doppler non-contact radar flow meter for determining water discharge on the minor river drawing on the example of Polomet' river

The research subject is the Polomet' river in the water discharge section line in the Yazhelbitsy village. The runoff observation period is 1952-2020. The length of the river to the outlet section is 52 km, the catchment area is 631 km^2, the width during the low-flow period is 15m, the mean annual water discharge is 6.7 m^3/s, the maximum is 120 m^3/s.

The scope of the research is the assessment of the accuracy of water discharge measurements on the Polomet' river with the Doppler non-contact discharge radar flowmeter RQ-24 fixed on an overpass across the river. The angle of installation of the device is 55 degrees to the water surface. The minimum recorded velocity of the current is 0.3 m/s. Velocity measurement error (1% ± 0.025) m/s.

The analysed data: water levels and current velocities for the period from March 2016 to June 2020. Discreteness of measurements for the velocity data link - 2 minutes (for the analysis they were reduced to an interval of 1 hour), for the water level data link - 1 hour.

Water level data link analysis. The whole range of measured water levels was divided into 4 categories:

- with an open channel;

- with freeze-up;

- in case of ice phenomena;

- falling into the blind zone of the sensor

Radar readings were compared with reference water levels obtained from averaged data from other automated systems located at the same stream section. Data analysis for each category is shown in Table 1.

With an open channel, the radar demonstrated high measurement accuracy - less than 4% of hourly observation times have an error of more than 3 cm. For the period with ice phenomena (slush ice run, ice drift, etc.),

the radar measurement accuracy was lower, but it can also be used as a reliable water level assessment device.

TABLE 1 ANALYSIS OF THE QUALITY OF THE INITIAL DATA RQ-24 ON THE WATER LEVEL DATA LINK

Periods	Number of readings	Mean deviation, cm	The number of observation times with an error					
			<1cm	%	<2cm	%	<3cm	%
Open channel	26231	-1,298	8440	32,2	19998	76,2	25234	96,2
Freeze-up	5233	0,298	112	2,14	531	10,1	2605	49,8
Ice phenomena	2851	-2,34	113	3,96	839	29,4	2242	78,6
Blind zone of the sensor	108	26,9	3	2,78	9	8,33	38	35,2

During freeze-up, significant deviations from the reference levels can be observed, primarily due to the measurement of snow on ice. The worst results are observed for the highest water levels falling into the blind spot of the instrument.

Estimation of the current velocity data link. The gauge section in which the radar is located is 50 meters upstream from the main one, where the water discharge is measured. Autumn 2020, single full-scale comparative field studies of the local surface flow velocity were performed with a radar flow meter and other instruments of measurement in the radar measurement cross section alignment. The comparison results confirmed the manufacturer's declared accuracy of determining the flow velocity with the RQ-24 flow meter (Table 2).

TABLE 2 SURFACE CURRENT VELOCITY COMPARATIVE MEASUREMENTS DATA AT THE RADAR SECTION

Measurement instrument	Surface velocity, m/s
RQ-24 radar flow meter	0,487
Electromagnetic current meter «Poseidon»	0,485
ISP-1M mechanical current meter with 70mm propeller	0,462
GR-21M1 mechanical current meter with 120mm propeller	0,498
GR-21M1 mechanical current meter with 70mm propeller	0,445

The water discharge calculation data link analysis. The method for calculating water discharge using a radar flow meter is based on the existence of a close relationship between the surface current velocity and the mean flow velocity. Three transition velocity indexes K_1, K_2, K_3 are distinguished depending on the width of the surface velocity measurement zone:

$$K_1 = \frac{V_{mean\ flow}}{V_{mean\ surf.}} \quad (2)$$

$$K_2 = \frac{V_{mean\ flow}}{V_{max.surf}} \quad (3)$$

$$K_3 = \frac{V_{mean\ flow}}{V_{local\ surf.}} \quad (4)$$

Where $V_{mean\ flow}$ – mean flow velocity, m/s;

$V_{mean\ surf.}$ – mean surface velocity, m/s;

$V_{max.surf.}$ – maximum surface velocity, m/s;

$V_{local\ surf.}$ – local surface velocity, m/s.

Since the radar flow meter measures only a certain part of the surface velocity across the width of the river, the K_3 velocity index will be used. The more correct the distribution of velocities in the stream, the closer the connection of the different transition velocity indexes with each other and more accurate mean flow velocity possible to obtain by radar. Most guiding manuals on the use of manufactured radar flow devices recommend indicating a constant value of this factor. The World Meteorological Organization (WMO) and the United States Geological Survey (USGS) recommend using the K_1 velocity index equal to 0.86 for natural channels and 0.90 for artificial channels [5, 6].

A detailed study of this issue was carried out in the 1960s by a group of scientists from the State Hydrological Institute (SHI) under the leadership of D.E. Skorodumov [7]. In his paper it is noted that according to the results of measurements at 38 gauging stations, K_1 can vary from 0.75 to 1.02. It should be noted that these studies set themselves another task - the change in the transition velocity indexes during a high-flow regime, the lower part of the amplitude of water levels fluctuations was almost not studied. However, this article also indicated that adding the lower part of the water level amplitude to the analysis increases the variation in K_1 values.

For the velocity indexes analysis at the main discharge section line, the results of 50 open channel water discharge measurements with a mechanical current meter for 2016-2020 were taken into an account (Figure 1).

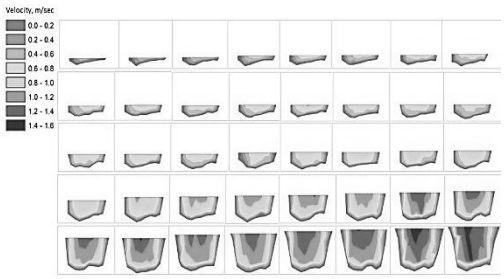

Figure 1 - Distribution of flow velocities at the main discharge section line (according to measured water discharges for 2016-2019 during open channel period)

Since the low-water bed of the river has the correct shape and relatively the same roughness across the width of the river, there is a close relationship between the transition velocity indexes. Figure 2 shows a graph of an increase in the strength of the relationship between the

mean flow velocity and the surface velocity with an increase in the width of the averaging zone (based on the results of 50 measured open channel discharges). Also, with an increase in the width of the averaging zone from 1 m (the width of the averaging zone by the radar flow meter at low water level), which corresponds to the index K_3 up to 15 m (the full width of the low-water bed), which corresponds to the index K_1, the strength of the relationship, expressed in units of a pair nonlinear correlation coefficient, increases from 0.954 to 0.977. Such a slight increase in the strength of the relationship indicates the possibility of using the K_3 index instead of the K_1 index to calculate the water discharge with an acceptable error.

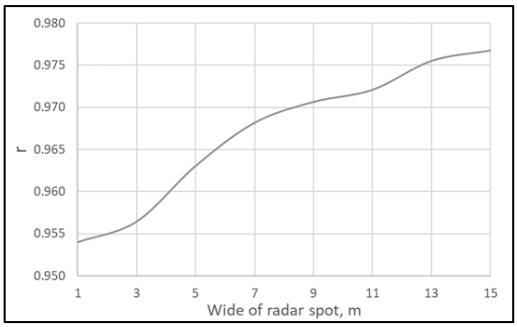

Figure 2 - Graph of an increase in the strength of the relationship between the mean flow velocity and the surface velocity with an increase in the width of the averaging zone

The distribution of the transition velocity indexes for the measured water discharges at the main discharge section line is shown in Figure 3. Thus, the transition indexes from the surface velocity to the average cannot be a constant for the entire amplitude of the water level. In the lower part of the amplitude of water levels, the value of the transition indexes decreases significantly. There is no unambiguous understanding of how these indexes will vary when water flows out to the floodplain.

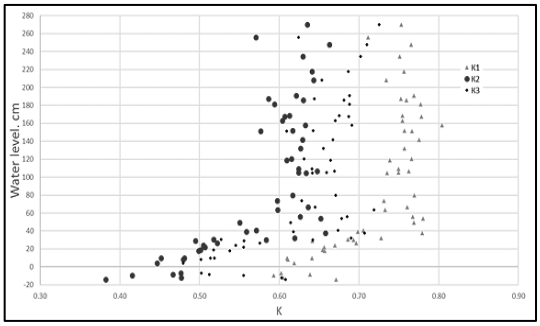

Figure 3 - Dependence of the transition velocity indexes on the water level at the main discharge section line (according to the measured water discharges)

To obtain the transition velocity index K_3 for the radar measurement section line, the following calculation algorithm was carried out:

1 The rating curve Q=f(H) is plotted for the main discharge section line. Since the section between the main discharge section line and the radar measurement section is very short (50 m) and absolutely free of inflows, the slope of the water surface is insignificant in its absolute value, so this dependence was also applied to the radar measurement section.

2 Based on the hourly resolution water level data, the water discharges at the radar measurement section were calculated with an interval of one hour.

3 Using measured cross-sectional profile at the radar measurement section, depending on the water level the water flow areas were calculated for each hour of observation.

4 Based on the data obtained, the average velocity over the entire cross-section of the radar measurement section was calculated with a resolution of 1 hour.

5 By dividing the average velocity by the surface local velocity measured by the radar, the transition velocity index K_3 was obtained (Figure 4). The analysis was performed only for the open channel period and the period with no blind-zone cases.

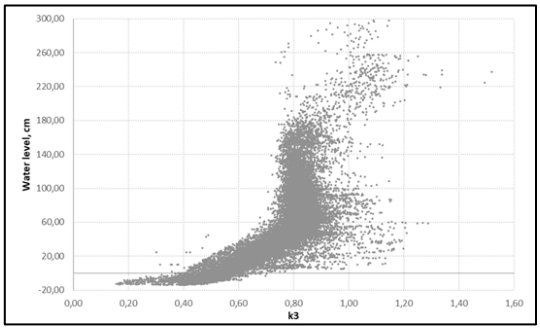

Figure 4 - Dependence of the transition velocity indexes K_3 on the water level for the radar measurement section

The nature of the distribution of points in Figures 3 and 4 is similar, which indicates the correct scheme for calculating K_3 for the radar measurement section. The scatter of points in Figure 4 is primarily due to the different channel capacity of the river at the same water level during the stages of rise and fall. Figure 5 clearly shows that the distribution of the transition velocity indexes on the rise and fall of the rainfall flood, which took place on October 13-17, 2019, is different. Figure 6 shows a complex graph of this flood, on the abscissa axis counting hours from the time of 10/13/2019 13:00. Only three parameters out of five were measured (average velocity and K_3 are calculated parameters with accordance an unambiguous curve Q = f (H). The slope, for the possibility of plotting four characteristics on one axis, is presented in relative units reduced to the variation of the surface velocity. The rise in the level, slope of the water surface and surface velocity began at 24 hours from the start of the countdown, after another 9 hours (33 hours) the values of the slope and surface velocity reached a maximum and began to decrease, while the water level continued to rise and reached its maximum only for 42 hours. From that moment on, the surface velocity began to increase and the level to fall. After approximately 62 hours of observations, the

slope and surface velocity were stabilized at a quasi-constant mode, while the level continued to decline. This course of the main hydraulic elements of the flow, with some changes, is repeated on the example of other rainfall and spring floods. This suggests that at moments of intense change in river flow, the relationship between the current velocity and the water level is inverse, and not direct, which is typical for the entire amplitude of water level fluctuations.

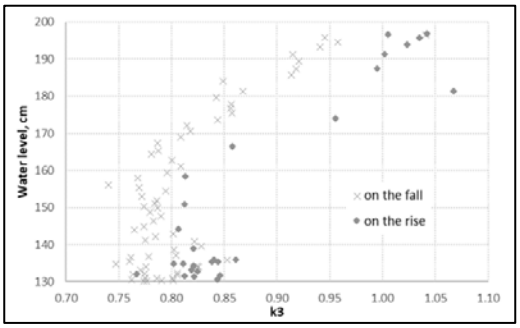

Figure 5 - Dependence of the transition velocity indexes K_3 on the water level for the radar measurement section during the rain flood on October 13-17, 2019

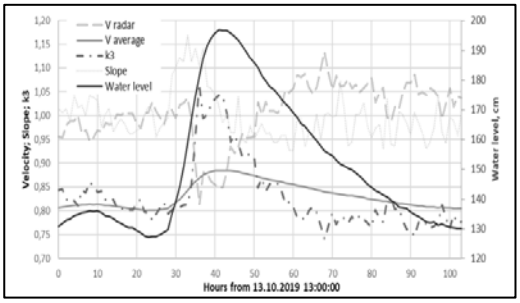

Figure 6 - Comprehensive chart of the hydraulic characteristics of the rain flood on October 13-17, 2019

V. The results obtained

The error in determining the water discharge using a radar flow meter was calculated on the basis of 3 options:

Option 1 - with constant $K_3 = 0.623$ (Figure 7);

Option 2 - with $K_3 = f(H)$, and the water level data of the reference water level gauges;

Option 3 – with $K_3 = f(H)$, and the water level data of the radar-based water level sensor.

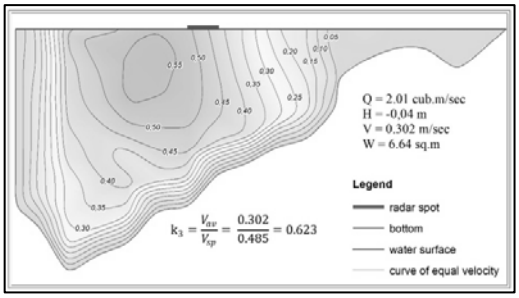

Figure 7- Comprehensive chart of the hydraulic characteristics of the rain flood on October 13-17, 2019

The water discharge calculated by the rating curve Q = f (H) at the main discharge section line was taken as the true value. The results of calculating the error in calculating the water discharge are presented in Table 3.

Table 3 Water discharge calculation error according to use RQ-24 water flow radar

$Q_{calc.}$ error,%	Option 1	Option 2	Option 3
Mean value	7,8	1,1	0,2
Minimum	-280,0	-118,6	-122,7
Maximum	53,5	48,3	47,5
STD	24,3	11,5	11,5
AVG (relative)	20,0	8,5	8,4

The use of a constant value for the transition velocity indexes is not permitted. This leads to an overestimation of the minimum water discharge by 100-280%. The use of the dependence $K_3 = f(H)$ allows you to obtain a water flow rate with an acceptable error, but these observation are complicated and the labour inputs for the determination of this relationship are measure alike with the labour inputs for obtaining a reliable rating curve.

When water flows out to the floodplain, the value of K_3 may vary. Unfortunately, it was not possible to investigate this issue, due to the fact that most of the data at high levels of water outflow to the floodplain fell into the blind zone of the sensor and was rejected. According to the available episodic data, it is possible to assert with a sufficient degree of reliability about an even greater stratification of the $K_3 = f(H)$ dependence in the areas of rise and fall of rainfall and spring floods.

VI. Conclusion and recommendations

As a result of the analysis performed, the following advantages and limitations of using Doppler non-contact flow radar devices to determine the water discharge may be assessed.

Advantages:

+ Safety and contactless measurement. To measure, hydrologist does not need to go into the water and endanger his own life;

+ The possibility of using on mountain rivers with high slopes;

+ The ability to measure the parameter of the mud flood flow passage velocity;

+ The applicability even during the period of slush ice run and ice drift;

+ Using for the rating curve clarification in the periods of the variable wind- and pressure- induced backwater phenomena;

+ A wide range of measured flow velocities from 0.02 to 15 m/s;

+ Permissible error in measuring the flow velocity;

+ Continuity of measurements;

+ The ability to receive data in real time;

+ Low labour inputs for the maintenance.

Limitations (disadvantages):

- Inability to measure in freeze-up channel conditions;

- The water discharge calculation is carried out using a single complexly calculated coefficient of transition from the fictitious discharge to the true one;

- The need for more precise extra measurements of water discharge to plot the dependence of the transition velocity index on the water level, as well as to revise and upgrade the area curve;

- Changes in the averaging area of the surface velocity (radar spot) due to water level fluctuations;

- A mandatory requirement is the presence of microwaves on the surface of the water;

- The presence of a blind zone of the emitter,

- High limit of the minimum fixed velocity (for outdated devices),

- The possible influence of external factors (practically absent in modern devices).

Recommendations:

A. It is impossible to use a radar flow meter to determine the water discharge in an unexplored measuring section of the river without carrying out periodic measurements. It is necessary to obtain the relationship between the transition velocity indexes and the water level, as well as monitor the change in the profile of the river channel at the measurement section line.

B. It is recommended to use radar flow meters at the discharge section lines of mountain rivers with high steep slopes, as well as at section lines of rivers with variable backwater phenomena.

C. In order to study the distribution of current velocities in the flow at different water levels, it is recommended to create gauge sections equipped with several flow meters, in combination with immerse stationary Doppler or ultrasonic profilers (with river bank-based or bottom-based location).

D. Taking into account all the technical requirement and nuances of installation, setup, maintenance and development of transition velocity indexes, you can continuously measure the water flow with an acceptable error.

5 It is necessary to create a methodology for measuring water discharge by the "surface velocity-area" method.

ACKNOWLEDGEMENTS

Employees of the Hydrological Instruments Laboratory of the State Hydrological Institute are open to further cooperation in the field of hydrological surveys and monitoring, share experience and improve their qualifications, keeping a dialogue with experts from all over the world. You can contact us using this email: lgpggi@yandex.ru or emails indicated in the title of the article.

REFERENCES

[1] Methodology instructions. "Determination of water discharge using a radar current velocity meter" (St. Petersburg, Hydrometeoizdat, 1994).

[2] Plant W.J., Wright J.W. "Phase speeds of upwind and downwind traveling short gravity waves", J. Geophys. Res., Vol. 85, p. 3304–3310, 1980.

[3] Costa J. E., Cheng R. T., Haeni F. P., Melcher N., Spicer K. R., Hayes E., Plant W., Hayes K., Teague C., Barrick D. "Use of radars to monitor stream discharge by noncontact methods", Water Resources Research, Vol. 42, Issue 7, p. 14, 2006, https://doi.org/10.1029/2005WR004430

[4] Official Laboratory of the Hydrological Instruments page in the web-site of the State Hydrological Institute (SHI) [Web-site. Online]. Available: http://www.hydrology.ru/en/structure/department-hydrological-instruments [Accessed March 1, 2021].

[5] Manual on stream gauging. Volume I – Fieldwork. WMO-No. 1044, p. 55, 2010.

[6] D. Phil Turnipseed, Vernon B. Sauer, "Discharge measurements at gaging stations", Techniques and Methods 3–A8, Department of the Interior U.S. Geological Survey, p.36, 2010, https://doi.org/10.3133/tm3A8

[7] D.E. Skorodumov, "Determination of water discharge from measured surface velocities in connection with the distribution of velocities in river flows, Proceedings of the State Hydrological Institute, Issue 96, p. 3-57, 1962.

Environment. Technology. Resources. Rezekne, Latvia
Proceedings of the 13th International Scientific and Practical Conference. Volume 3, 130-133

Postprocessor and Macro Program for Calculation of the Displacements of the Working Coordinate Systems when Working by the Method 3 + 2 axes

Tsvetan Kaldashev
Technical university of Sofia
Sofia, Bulgaria
kaldashev.cvetan@abv.bg

***Abstract* - This article discusses the possibility of developing a postprocessor and macro program for automatic calculation and input of the displacements in the working coordinate systems when working by the method 3 + 2 axes. The ability to take the information from the CL Data file and its subsequent use by a macro program for certain calculations is used. For this purpose, a generalized G-POST postprocessor and a specialized FIL language are used.**

Keywords - CNC, 3+2 axis, postprocessor, Euler angles

I. INTRODUCTION

Often, machining of prismatic body parts on five axial machines requires machining in several different positions. In this case the method is 3 + 2 axes, where the two circular axes are used only for adjusting the rotation of the workpiece in the respective machined position. This method has the advantage that the workpiece is processed in one set, which leads to a reduction of the establishment error, and in some cases to compensate for systematic errors [3]. The working coordinate systems used for machining by the 3 + 2 axis method can be set by using a separate working coordinate system G54-G59 for CNC Fanuc and others for each of the machined positions or additional ones - G154 P1-P99 for CNC Haas [1], G54.1 P1-P300 for CNC Mazak [2] or setting using command G68.2 to establish an inclined working plane. In this case a local coordinate system is created, where the values of displacement and rotation of the newly obtained coordinate system are set programmatically with command G68.2, i.e. there is no need to enter an offset in the Offset page of the machine. These various methods of adjustment may be applied as by treatment with machining, and in the methods associated with ball burnishing [5].

II. DEVELOPING A POSTPROCESSOR AND MAKROPROGRAMA

Each CNC machine is characterized by the machine coordinate system O_M (X_M, Y_M, Z_M) (fig. 1) against which the workpieces are established and the coordinate system O_T (X_T, Y_T, Z_T), towards which the cutting tool is oriented.

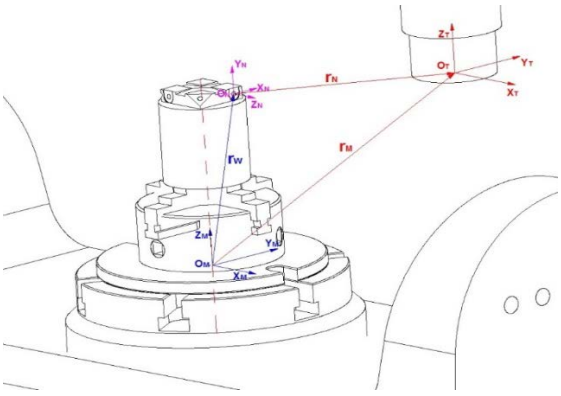

Fig. 1. Relationship between O_M and O_T.

When moving the tool according to a program, in order to be able to achieve the dimensions according to the drawing between these two coordinate systems O_M and O_T, it is necessary to make a dimensional connection. As a result of the attestation of the machine, the components of the vector r_M connecting the coordinate system of the machine O_M and the coordinate system of the tool O_T when the working bodies of the machine are at a reference point are determined. When processing a given surface, it is

Online ISSN 2256-070X
https://doi.org/10.17770/etr2021vol3.6512

necessary to determine the components of the vector r_W connecting the coordinate system of the machine with the working coordinate system O_H (X_N, Y_N, Z_N) (fig. 1). The vector r_N is calculated automatically by the CNC and represents the relative displacement to the O_N coordinate system, where the length of the tool is included.

The treatment of surfaces and holes by the method 3 + 2 axes necessitate adjustment of the working coordinate systems for each of the processed position i.e. to determine the components of vectors r_{W1}, r_{W2}, r_{Wn} (fig. 2)

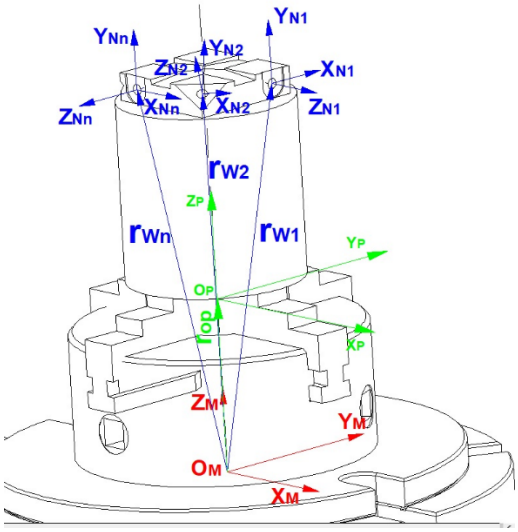

Fig. 2. Determination of the components of vectors r_{W1}, r_{W2}, r_{Wn}

To determine the components of vectors r_{W1}, r_{W2}, r_{Wn}, it is most convenient to use Euler angles. They determine the position of the different coordinate systems O_N relative to the machine coordinate system O_M by rotating sequentially about the three linear axes at an angle ϕ about the X axis, an angle θ around the newly obtained direction on the Y axis and an angle ψ around the newly obtained position on the Z axis.

Macro program (using a subroutine), which performs calculation and automatically input the values of displacement of different coordinate systems working in Offset page by typing:

```
O1000
#16=#26+#503
#104=#24*COS[-#3]-#25*SIN[-#3]
#105=#24*COS[-#1]*SIN[-#3]+#25*COS[-#1]*COS[-
#3]-#16*SIN[-#1]
#106=#24*SIN[-#1]*SIN[-#3]+#25*SIN[-#1]*COS[-
#3]+#16*COS[-#1]
G90G10L2P#2 X#104 Y#105 Z#106
M99
```

The values of variables # 1, # 2, # 3, # 24, # 25, # 26 are set with the command for simple reference to macro program G65 [3, 4] having the form:

G65 P… A… B… C… X… Y… Z…,

where the meaning of the individual arguments is: P - number of the macro program; A - angle of rotation along the A axis; B - register of the coordinate system G54,…, G59; C - angle of rotation along the C axis; X, Y, Z - the displacement along the X, Y and Z axes of the working coordinate system with origin O_N set with respect to O_M

The new position of the working coordinate system is set with the sentence G90G10L2P#2 X#104 Y#105 Z#106, where L defines the category of displacement (L2 for displacement of coordinate systems), P - the register of the coordinate system in which enters the offset (the value is taken from argument B of command G65); X, Y and Z - the calculated offset value defined in variables # 104 (for X axis), # 105 (for Y axis) and # 106 (for Z axis) . Variable # 503 sets the components of the vector r_{OP}, connecting the coordinate system of the machine OM and the reference base of the device device O_P (X_P, Y_P, Z_P) (fig. 2).

The developed postprocessor has the task to extract the values from the CL Data file and set them to arguments A, B, C, X, Y and Z in command G65, which calls the macro program for calculation and introduces the offset of the used coordinate systems.

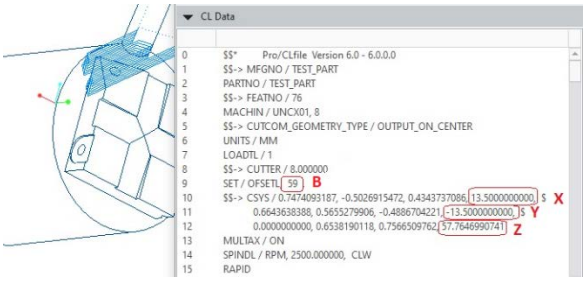

Fig. 3. Argument - value taken from CL Data file

In fig. 3 shows to which argument what value of the CL Data file is assigned. Using a specialized FIL language (Factory Interface Language) and a generalized G-POST postprocessor, I create an array of data about the coordinate systems used and their displacements relative to the reference base of the device. The RESERV command is used to create an array of data for further use. For example, RESERV / A, 4 will allow the following symbol-index combination A (1), A (2), A (3), A (4).

In order to be able to generate the G65 command line when generating the driver, it is necessary to use the Look ahead technique, which allows to read the entire CL Data file and extract the necessary information. In this case, a macro record having the structure is used:

```
G65=MACRO
   CLPOS=POSTF(7,1)+1
   XX=POSTF(13)
   DO/ENDDO,ILOOP=1,100,1
      ILOOP=1
      XX=POSTF(14)
      FCL=POSTF(7,2)
      SCL=POSTF(7,3)
      IF(FCL.EQ.14000) THEN
         ILOOP=101
      ELSE
IF(FCL.EQ.2000.AND.SCL.EQ.ICODEF(SET)) THEN
  IF(POSTF(6,5).EQ.1) THEN
```

```
  CNT=CNT+1
  OFSREG(CNT)=POSTF(7,5)
  IF(OFSREG(CNT).EQ.54) OFSREG(CNT)=1
  IF(OFSREG(CNT).EQ.55) OFSREG(CNT)=2
  IF(OFSREG(CNT).EQ.56) OFSREG(CNT)=3
  IF(OFSREG(CNT).EQ.57) OFSREG(CNT)=4
  IF(OFSREG(CNT).EQ.58) OFSREG(CNT)=5
  IF(OFSREG(CNT).EQ.59) OFSREG(CNT)=6
  ENDIF
ENDIF
IF(FCL.EQ.2000.AND.SCL.EQ.ICODEF(CAMERA))THEN
  XII(CNT)=POSTF(7,4)
  XJJ(CNT)=POSTF(7,8)
  YKK(CNT)=POSTF(7,13)
  ZKK(CNT)=POSTF(7,14)
  XV(CNT)=TEXT/CONVF,POSTF(7,7),10,5,0,0,5
  YV(CNT)=TEXT/CONVF,POSTF(7,11),10,5,0,0,5
  ZV(CNT)=TEXT/CONVF,POSTF(7,15),10,5,0,0,5
  AVAL=ABSF(ATAN2F(YKK(CNT),ZKK(CNT)))
  CVAL=ATAN2F(XJJ(CNT),XII(CNT))
  AV(CNT)=TEXT/CONVF,AVAL,10,5,0,0,5
  CV(CNT)=TEXT/CONVF,CVAL,10,5,0,0,5
 ENDIF
ENDIF
ENDDO) CONTIN
  DMY=POSTF(15,CLPOS)
TERMAC
```

Finding records related to the registers of the coordinate system is performed with the operator IF (FCL.EQ.2000.AND.SCL.EQ.ICODEF (SET)) THEN, which creates an array of data for the used coordinate systems IF (OFSREG (CNT)) .EQ.54) OFSREG (CNT) = 1, IF (OFSREG (CNT) .EQ.55) OFSREG (CNT) = 2, etc. In a similar way, the displacement and angles of rotation of the coordinate systems relative to the machine coordinate system are determined, and together with this the data set is created. This part of the information is processed by the second IF operator (IF (FCL.EQ.2000.AND.SCL.EQ.ICODEF (CAMERA)) THEN).

The output of the created data set is performed at the beginning of the control program, in the records related to the machine. It has the structure:

```
CIMFIL/ON,MACHIN
 XX=POSTF(13)
 CALL/G65
 $$ SEND TO NC PROGRAM
 DO/END02,CNT=1,CURCNT
INSERT/'G65P2013B',OFSREG(CNT),'X',XV(CNT),'Y',Y
V(CNT),'\;'
INSERT/'Z',ZV(CNT)'A',AV(CNT),'C',CV(CNT),';'
    END02)CONTIN
CIMFIL/OFF
```

The output of the data is done using the DO / Loop operator, where the output is performed from the first index of the array (CNT = 1) to the current one (CURCNT). The output of the line with the G65 command is realized with the body of the DO / Loop cycle.

With the postprocessor developed in this way, a control program is generated (only a part of it is shown in fig. 4), for processing the workpiece shown in fig. 5.

```
%
O10
G00G80G90G40
(#503 OPORNA BAZA PO OS Z PRI A=0 I C=0)
#503=161.107
G65 P2013 B1 X0.0 Y0.0 Z60.0 A0.0 C0.0
G65 P2013 B2 X0.0 Y0.0 Z60.0 A5.0 C0.0
G65 P2013 B3 X16.25 Y10.5 Z56.0 A90.0 C90.0
G65 P2013 B4 X-10.5 Y-16.25 Z56.0 A90.0 C0.0
G65 P2013 B5 X0.0 Y0.0 Z60.0 A54.85847 C-90.0
G65 P2013 B6 X13.5 Y-13.5 Z57.7647 A40.83016 C41.63354
T01 M06
S2500 M03
G54 G43 X-30.426 Y-18. Z90. H01
G00 X-30.426 Y-18. Z2.
G01 X-30.426 Y-18. Z0. F250.
```

Fig. 4. Part of NC program

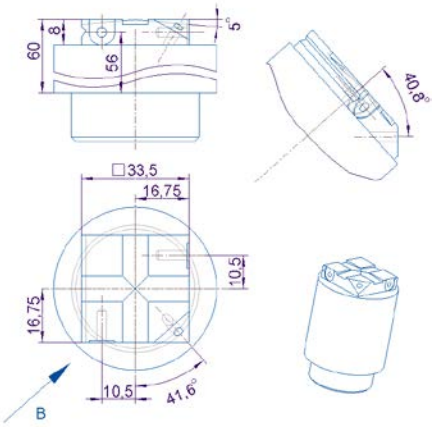

Fig. 5. Test workpiece

The postprocessor was checked - virtual with the use of Vericut and one on a machine with 5 axes and horizontal layout MC032 with CNC Fanuc 6MB and a test workpiece was processed (Fig. 5). In fig. 6 shows the machined workpiece on the machine.

Fig. 6. Machined workpiecenon the machine

III. CONCLUSION

1. The developed postprocessor in combination with the macro program for automatic calculation and loading of the values of displacement of the working coordinate systems when working by the method 3 + 2 axes is correctly working.

2. The proposed postprocessor and macro program are valid for machines with five axes in which the machine

coordinate system coincides with the intersection of the two circular axes A and C.

ACKNOWLEDGEMENTS

The author would like to thank the Research and Development Sector at the Technical University of Sofia for the financial support.

REFERENCES

[1] Haas Mill Operator's manuals, Next Generation Control 96-8210 Revision F December 2017 English

[2] Mazatrol SmoothX Programming manuals, EIA/ISO program, 2019

[3] Hadjiiski P., Programming of CNC machine tools, Tehnical university of Sofia, 2010, ISBN 978-954-438-865-2A

[4] Ben Groves, Macro B programming manual

[5] Slavov, S., Dimitrov, D., Iliev, I., Variability of regular relief cells formed on complex functional surfaces by simultaneous five-axis ball burnishing, (2020) UPB Scientific Bulletin, Series D: Mechanical Engineering, 82 (3), pp. 195-206.

Environment. Technology. Resources. Rezekne, Latvia
Proceedings of the 13th International Scientific and Practical Conference. Volume 3, 134-136

Vericut - Configuring CNC Systems for Turning Center with Sub-spindle

Tsvetan Kaldashev
Technical university of Sofia
Sofia, Bulgaria
kaldashev.cvetan@abv.bg

***Abstract* - This report discusses the configuration of some preparatory and auxiliary commands for the Fanuc 18i TB CNC system for a counter-spindle lathe using special macros called Vericut macros. In most cases, this is necessary because the Vericut library of machines and CNC systems does not have the specific machine and system or do not correspond to the actual ones, i. e. there is no match between them. The need to configure the CNC control system is related to the fact that it is possible to perform simulation, optimization and verification of control programs in a virtual environment before proceeding to the processing of workpieces on the real machine.**

Keywords - Vericut, CNC, verification, turning center, sub-spindle

I. INTRODUCTION

To reduce the risks associated with the defect of the workpiece and reduce the cost of the final product, products are used in which this check can be performed in a virtual environment. When using such a class of products, the stages of technological preparation for processing the workpiece have the structure shown in fig. 1.

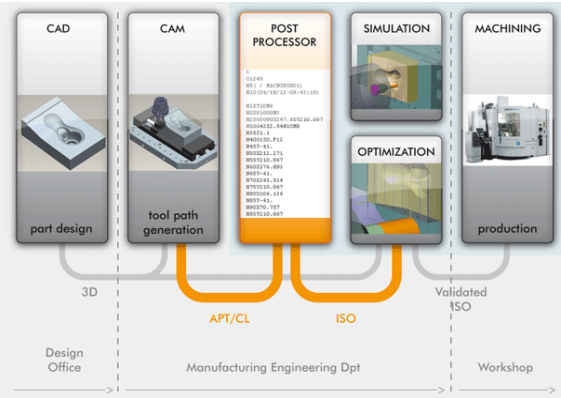

Fig. 1. Stages of technological preparation with the use of products for virtual simulation of the processing [2]

After the simulation stage, an evaluation of the result is performed, after which, based on the obtained result, in some cases optimization is required. Such products are VERICUT, NCSIMUL and others. VERICUT [1] is a product of high grade, that allows for verification and optimization of the tool path, checking for collisions, the simulation of cutting processes. All these possibilities are available for milling, turning, laser, wire erosion discharge machines, turning centers, multi-task machines and robots.

When verifying the tool path, a real machine, tools, holders, workpiece are used, and the simulation is by taking material in a virtual environment. Both the generated driver from the CAM package and the CL data file can be used to simulate the process.

II. CONFIGURING A CNC SYSTEM FOR A TURNING CENTER WITH A SUB-SPINDLE

To solve the problem, Vericut's capabilities for configuring the CNC system are used. In this case, CNC from the Vericut library will be used, where only the necessary M- and G-commands for the Emco Maxxturt 45 machine with Fanuc 18i TB will be configured (added). In fig. 2 shows the kinematic model of the machine [3].

As is well known, the manufacturer of CNC machines determines the purpose of M-commands (other than those standardized by ISO) to control more specific actions. Here is considered the possibility of configuring the M-commands related to the control of the main and counter spindle in the two characteristic modes for the lathe centers, namely the commands with which they are set in the operating mode when they realize the cutting speed, i.e. turning and mode in which they are used as a circular axis. Table 1 gives M-commands [6] with their meaning, which will be configured to control the machine.

Online ISSN 2256-070X
https://doi.org/10.17770/etr2021vol3.6544

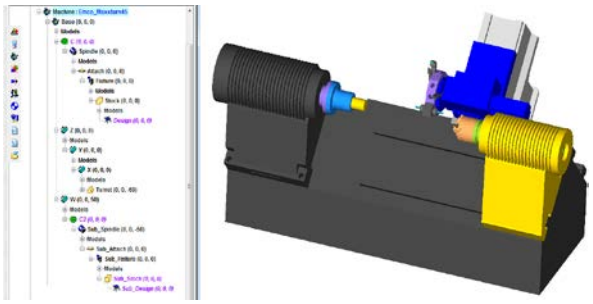

Fig. 2. Kinematic model of the EmcoMaxxturn 45 machine

In turning centers, the typical hole machining cycles have a difference from the machining cycles on drilling and milling machines and machining centers, consisting mainly in the preparation command and on which axis the machining is performed (X-axis or Z-axis). These commands will also be configured.

TABLE 1 M-COMMANDS TO BE CONFIGURED

M-commands	Function
M52	Selection main spindle C-axis
M53	Deselection main spindle C-axis
M69	Open jaws of the main spindle
M168	Open jaws of the counter spindle
M252	Selection counter spindle C-axis
M253	Deselection counter spindle C-axis
M203	Counter spindle ON, clockwise rotation
M204	Counterspindle ON, counter-clockwise rotation
M205	Counter spindle OFF
M303	Driven tool ON, clockwise rotation
M304	Driven tool ON, counter-clockwise rotation
M305	Driven tool OFF

The commands used by the CNC are configured from the G-code Processing window using the so-called Vericut Macro [4]. In essence, these are "macros" developed by Vericut, where their use triggers a certain action. Auxiliary M-commands related to the process of transferring the workpiece between the two spindles are set in the Pick_Off section. This is how the settings for the M69 command are made: in the Add / Modify Word / Address window (fig. 3) the M-command is set. The MacroName uses the ClampCompName macro, which sets the gadget name in the Override Text field in this case Fixture. This field records the name of the device used in the kinematic model of the machine.

The state in which the device is located, set with the macro ClampCompName, ie. the jaws of the chuck (collet device) are open or closed, it is controlled by the macro ClampOnOff. The status is set to 0 off and 1 on. The mode is set in the Override Value field (fig. 3). The other M-commands in the Pick_Off section are configured in a similar way, as for command M168 with macro ClampCompName the name of the equipment of the opposite spindle is set - Sub_Fixture (fig. 3).

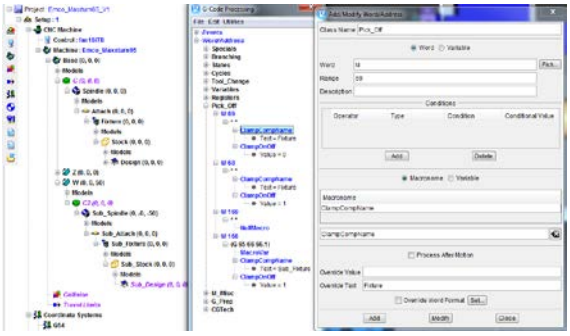

Fig. 3. Windows Add / Modify Word / Address setup commands CNC

In fig. 4 shows the structure and Vericut Macro used to configure the M52 command. After reading command M52, the CNC is able to use the main spindle as a circular axis C1.

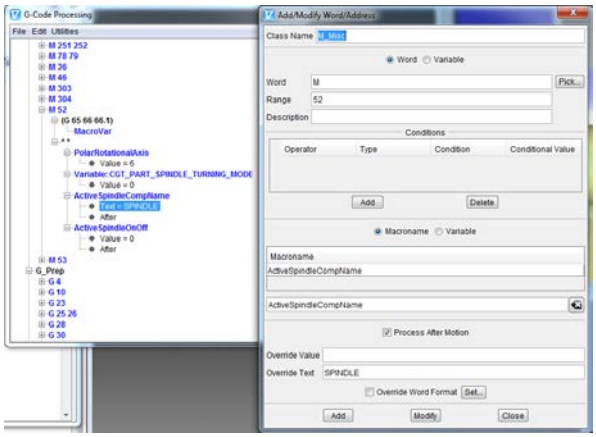

Fig. 4. 4 Structure of the M52 command with the Vericut Macro used to configure it

In practice, this means that the "active" position of the turret is used, i.e. instrumental transitions are made for processing of openings, shifted in relation to the axis of rotation of the workpiece, flat or profile sections are processed, etc. This is also related to the use of polar and cylindrical interpolation mode. Setting this mode is done with the PolarRotationalAxis macro.

In this mode, the axis is set, which is controlled in Cartesian coordinates. The setting is done with a number, where the correspondence number-controllable axis is observed, namely: 4-A, 5-B, 6-C, 10-A2, 11-B2, 12-C2. The variable CGT_PART_SPINDLE_TURNING_MODE is entered by the user who controls the circular axis mode. In this case it is the variable for the main spindle. A value of 0 deactivates the lathe mode and 1-activates the lathe mode. The macro ActiveSpindleCompName specifies which spindle (main or counter) will be set as a circular axis. When using the M52 command, it is necessary to stop the main rotational movement of the spindle. This is controlled with the ActiveSpindleOnOff macro, where the current state of the spindle is set in the Override Value field, with the M52 command running (0-off, 1-on). For commands M252 and M253 proceed in a similar way. To

configure the commands, to control the direction of rotation of the "active" position of the turret of the machine - commands M303, M304, M305, the macro ActiveSpindleActiveTool is used, which activates the tool set in the "active" position of the turret. The direction of rotation of the tool set in the "active" position is done with the already mentioned macros. In fig. 5 shows a screen with the settings made for these commands.

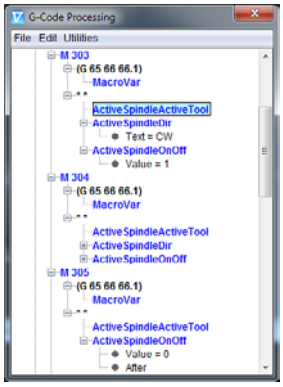

Fig. 5. Configuring commands M303, M304, M305 for drive tools

In cycles G87, G88 and G89 for machining holes perpendicular to the axis of the workpiece, the working movement is along the X axis, ie. in the YZ plane. In FIG. 6 shows a window for setting the G87 command. Vericur macro MotionPlaneYZ is used to set the working plane YZ. The type of the preparatory command is read from the system variable for modal information # 4009 [5].

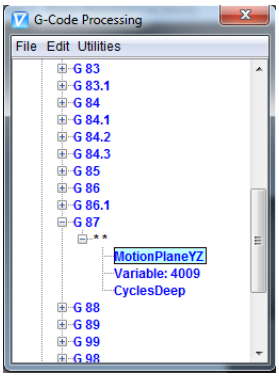

Fig. 6. Configuring G87 command

The type of the cycle is determined by Veicut macro CycleDeep. As already mentioned, in these cycles the working movement is on the X-axis. By default, the working movement is performed on the Z-axis. For this purpose, the settings shown in fig. 7.

In order for the working movement to be on the X-axis, the conditions are introduced:

1. The type cycle is on (Cycle On);

2. The coordinates in the type cycle must be set absolutely or incrementally (ABS_INC);

3. The preparatory command for the cycle is G87, G88 or G89.

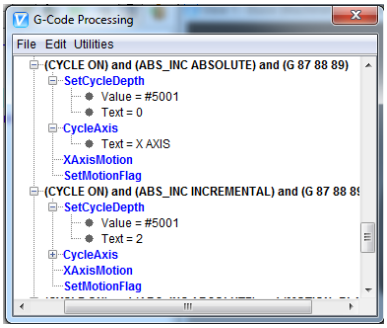

Fig. 7. Settings related to the output of the final coordinate along the X axis when machining holes

If these conditions are met with the SetCycleDepth macro, it is specified that the hole depth will be determined by the system variable for position information # 5001. This is the variable in which the final X-axis coordinate is stored relative to the current operating coordinate system. The Text field of the SetCycleDepth macro is set to 0, which means that the value in the address is set to absolute. The CycleAxis macro determines the axis along which the machining is performed, depending on the selected working plane, in this case the X axis. The XAxisMotion macro indicates movement along the X axis. The G88 cycle settings are made in a similar way, using the CyclesTap macro.

III. CONCLUSION

1. The special M-commands used in the operation of the real machine Emco Maxxturn 45 and control Fanuc 18i TB are configured, using Vericut Macro.

2. Fixed cycles for machining radial holes are configured using Vericut Macro

ACKNOWLEDGEMENTS

The author would like to thank the Research and Development Sector at the Technical University of Sofia for the financial support.

REFERENCES

[1] www.cgtech.com

[2] www.webspring.ncsimul.com

[3] Kaldashev Ts., Developing a kinematic model for turning center with sub-spindle with Vericut, Youth Scientific Conference "Machines, Innovations, Technologies", November 8-9, 2018, "Bulgarian Journal of Engineering Design", pp. 35-40, ISSN 1313-7530, issue №37

[4] Vericut Help

[5] FANUC Operator's Manual Series 18i- MB

[6] Programming/Operation Fanuc 18i – Turning Maxxturn 45, PMC-Emco, V490

Environment. Technology. Resources. Rezekne, Latvia
Proceedings of the 13th International Scientific and Practical Conference. Volume 3, 137-141

Microstructure and Properties of High Chromium White Cast Irons Alloyed with Boron

Julieta Kaleicheva
Faculty of Industrial Technology
Technical University of Sofia
Sofia, Bulgaria
jkaleich@tu-sofia.bg

Krasimir Kirov
Arsenal J.S.Co.
Kazanlak, Bulgaria
kirov_krasimir_1966@abv.bg

Valentin Mishev
Faculty of Industrial Technology
Technical University of Sofia
Sofia, Bulgaria
v_mishev@ tu-sofia.bg

Zdravka Karaguiozova
Space Research and Technology Institute
Bulgarian Academy of Sciences
Sofia, Bulgaria
karazuzi@yahoo.com

***Abstract* - The microstructure and mechanical properties of high chromium white cast iron with composition: 2,6÷3,4% C; 0,9÷1,1% Si; 0,8÷1,1% Mn; 1,0÷1,3% Mo; 12,3÷13,4% Cr, additionally doped with boron in an amount of 0,18% to 1,25% is investigated. The microstructure of six compositions of white cast irons is studied by means of an optical metallographic analysis - one without boron, and the others contain 0,18%; 0,23%; 0,59%; 0,96% and 1,25% boron.**

A test is performed to determine: hardness by the Rockwell method; microhardness; bending strength and impact toughness. It was found that at a boron content of 0,18%; 0,23% and 0,59%, the structure of white cast irons is subeutectic, with impact toughness in the range of 1,80÷1,52 J/cm2; with a boron content of 0,96%, the structure of white cast iron is close to the eutectic, with impact toughness 0,98 J/cm2 ; at a boron content of 1,25% the structure of white cast iron is supereutectic and the impact toughness decreases to 0,68 J/cm2.

With a change in the boron content from 0,8% to 1,25%, the amount of carbide phase in the structure of white cast iron increases, which leads to an increase in hardness from 53 to 59 HRC. The highest bending strength (Rmi=660,85 MPa) was obtained in white cast irons with a boron content of 0,23%.

Keywords* - *high chromium white cast iron, boron, microhardness, hardness, impact toughness, bending strength

INTRODUCTION

High chromium white cast iron is white cast iron with high chromium content between 11% and 30% and carbon between 1,8-3,6%. The presence of high chromium content in the white cast iron volume leads to the replacement of some parts of iron carbide with chromium one. The hardness and the toughness of which is higher than iron carbide in unalloyed white cast iron. The proportional dependence is observed between the carbon and chromium content increase and improvement in the hardness and wear resistance of white cast iron [1, 3, 4, 8]. In the high-chromium irons, as with most abrasion-resistant materials, there is a trade-off between wear resistance and toughness. It is found that the abrasive wear resistance of high chromium cast iron (HCCI) alloys rely on their chemical composition and microstructure [4, 8]. By varying composition and heat treatment, these properties can be adjusted to meet the needs of most abrasive applications [3, 7].

High chromium white cast irons have not only excellent wear but in addition a good corrosion resistance results primarily from the presence of high-volume fraction of very hard eutectic carbides in a strong supporting matrix in their microstructure. Due to inexpensiveness of the high-Cr white cast irons they are used for production impact coal crusher hammers, pulveriser rings, chute liner, and hard facing alloys of rolls or molds [4]. These properties of white cast iron could be improved by adding some elements mostly elements forming strong carbides as molybdenum, vanadium, boron [9-11]. In [1] authors find the formation Mo_2C by molybdenum addition less than 2%. This could not improve its hardness in as-cast condition, but the vanadium and boron addition improve the hardness

Online ISSN 2256-070X
https://doi.org/10.17770/etr2021vol3.6656

of high chromium white cast iron significantly [8]. The influence of both elements is different. Vanadium dissolves into the austenitic matrix and carbide M_7C_3, while boron generates finer structure of eutectic carbide, needle like structure (upper bainite) matrix, and martensite on carbide boundary [1]. In high boron white cast iron with 4 wt% chromium modificated with rare earth magnesium alloy the primary austenite and the eutectic borides are refined. After High temperature heat treatment of this alloy granulation of the borides and the improvement of toughness and tensile strength are observed [2]. Investigation of the destabilization heat treatments undertaken at temperatures of 825, 900 and 975°C for 25 minutes shows for the iron containing boron, a density of carbide particles per square micron at 825°C, is more than this one achieved at 975°C. In the case of the alloy without boron additions, the same relation is defined, but the quantity of the carbides is significantly less. Higher volumes of carbide precipitation imply higher values of bulk hardness and microhardness in the alloys. The results suggest that boron works as nuclei for the precipitation of secondary carbides [5]. A similar effect of hardness and wear improvement is determined due to additions of titanium of 1%, 3% and 5% to a 12%Cr-3%C white iron. Some part of carbon is consumed to form primary TiC during solidification and a decrease in the carbon content in the alloy occurs. The results are decrease in the eutectic M_7C_3 carbide volume fraction and promotion a more martensitic matrix. The best combination of austenite/martensite matrix reinforced with primary TiC carbides was obtained at 3% amount of titanium results in best wear behavior, whereas bulk hardness increases proportionally with the increase in the amount of titanium. Heat treatment leads to the precipitation of secondary carbides occurred within the matrix, which improved the wear resistance of most irons. The best behavior is observed again at 3%Ti iron, which is caused by obtained microstructure; particularly in the well distribution of primary TiC carbides within the matrix [6]. Significant impact of the heat treatment process on the Microstructural Characteristics and Mechanical Properties High-Cr White Cast Iron Alloys is manifested in the work [7]. The work shows an essential role of the temperature increase during heat treatment on the change of the microstructure and therefore on the improvement of the wear resistance through microstructure refinement and in situ formation of fine new carbides. The carbide morphology also influences on the wear and fracture behavior of high chromium white irons. The increase of the carbide volume fraction for the austenitic and martensitic structures is a reason for the hardness increase. The austenite content influence on the abrasion resistance at least to 20-30% level. The quantity above this level of austenite content abrasion resistance is independent. Destabilization heat treatment for high-Cr white cast irons is employed to obtain the martensitic structure for improving the toughness and abrasion resistance of these cast irons [7]. The presence of the carbide forming elements in high carbon cast irons play a significant role in their influence on the wear resistance. Chemical composition of these irons' forms different proportion content between M_7C_3, M_3C and $M_{23}C_6$ which determines their different morphology and hence different exploitation properties. Authors in [8] investigate effect of boron on the structure and properties of 13Cr–2,3C Chromium white irons. Increase in the boron content above 0,39% leads to higher tendency of boron-carbide formation. The prevalence of M_7C_3 carbides and a small quantity of M_3C carbides is observed in the structure of the basic Fe-Cr-C alloy. Increase of the boron content increases the amount of M_3C carbide, while the volume fraction of the M_7C_7 carbides remains unchanged. In the highest boron content about 0,59 wt% secondary M23C6 carbides appear in the structure. The assumption of the formation of complex compounds of the type $M_3(C,B)$ and $M_{23}(C,B)_6$ is suggested [8].

The alloying of ductile cast irons with boron from 0,03 to 0,135% leads to formation of eutectic carbides from 9 to 27% in the iron structure. On the base of this irons new composition of carbide austempered ductile irons (CADI) with structure of lower and upper bainite are produced. These cast irons possess up to 3 times higher wear resistance during abrasive wear compared to this one without boron. In the structure of which there are no eutectic carbides (ADI) [12].

High chromium white cast irons are increasingly used in the practice as a wear-resistant and corrosion-resistant material. The additional alloying of these cast irons affects the chemical composition and dispersion of the carbide phase and the structure of the metal base after casting and heat treatment.

The aim of the present study is to investigate the microstructure, mechanical properties and wear resistance during abrasive wear of high chromium white irons, alloying with boron.

MATERIALS AND METHODS

The samples from high chromium white cast irons alloying with boron from 0,18% to 1,25% are investigated (table 1). These samples are made of test specimens sized Ø30 x 340 mm, cast in sand molds.

The microstructure of six compositions of white cast irons is studied by means of an optical metallographic analysis - one without boron, and the others contain 0,18%; 0,23%; 0,59%; 0,96% and 1,25% boron. The microstructural analysis is performed by means of an optical metallographic microscope NEOPHOT 32. The test samples are processed in the reagent composition: 20g CuSO4, 100ml HCI, 100ml C_2H_5OH.

A test is performed to determine hardness of the studied white cast irons by the Rockwell method (HRC). The microhardness $HV_{0,1}$ of the metal matrix and the carbide phase in the structure of cast irons with loading 100g is defined.

The impact toughness KC is performed by Charpy impact test. The tested samples used are sized 10x10x55 mm without notch.

The bending strength is carried out. The patterns are tested on the universal test machine with a bending device. The bending strength is determined by the formula:

$$R_{mi} = 81.F_{max}/(\pi.d_c^3) \quad (1)$$

where F_{max} is a maximum load, N; d_c is an average diameter of the test body in the load place, mm.

The wear resistance during abrasive wear is investigated as measured loss of mass in terms of dry friction under load of 1,5 kg during 10 min. The tested sample sized ø 30x40 mm circles with speed n=150 min^{-1}, pressed on an abrasive disc 99BA60R7V sized 250x20x20 mm .

TABLE 1 CHEMICAL COMPOSITION OF HIGH CHROMIUM WHITE CAST IRON ALLOYED WITH BORON

Sample №	Chemical element, %					
	C	***Si***	***Mn***	***Mo***	***Cr***	***B***
I	3,23	0,88	1,07	1,08	13,406	-
II	2,58	1,01	1,06	1,28	13,501	0,18
III	3,22	1,11	1,06	1,27	13,351	0,23
IV	2,77	1,00	0,93	1,05	13,175	0,59
V	3,35	0,91	0,85	1,01	12,698	0,96
VI	3,23	1,08	0,89	0,98	12,316	1,25

RESULTS AND DISCUSSION

Fig. 1 show the microstructure of high chromium white cast irons composition presented in table 1. The structure of the cast iron without boron is subeutectic (fig. 1a). Alloyed cast irons with 0,18%; 0,23%; 0,59% boron possess also subeutectic structure, but boron presence in the mentioned content decreases the grain size of the primary austenite and is a reason for the formation of a more dispersed structure (fig. b, c, d). The more quantity of boron in these cast irons persist the increasing part of the carbide eutectic is observed in their structure. At 0,59% boron (fig. 1d) the cast irons structure still is subeutectic, but it contains a large quantity of carbide eutectic. At boron content more than 0,6% to 1% the cast irons structure is approaching the eutectic. The microstructure of high chromium white cast iron with 0,96 % boron is presented in fig. 1e. Besides carbide eutectic a certain amount of primary carbides is observed in this microstructure. At 1,25 % boron content super eutectic structure of the cast irons is noted with rude primary carbides up to 70μm size (fig. 1f).

The increased percentage of the boron content in the tested cast irons structure leads to the quantity of the carbide phase increase (the volume of the carbide eutectic increases and in the cast irons with 0,96 and 1,25% boron primary carbides are formed). This explain hardness increase from 53,5 HRC at 0,18% boron to 57,5 HRC at 1,25% boron (table 2).

The influence of the boron content on the impact toughness of the tested cast irons is shown in fig. 2 and tabl.2. For the cast irons without boron and for those with 0,18 and 0,23 % boron the rates of the impact toughness are close and are in the range from 1,88 to 1,72 J/cm^2. The increased percentage of the boron content is a reason of the quantity increase of the carbide phase in the cast irons structure and results in the impact toughness decrease from 1,52 J/cm^2 at 0,59% boron to 0,68 J/cm^2 at 1,25% boron.

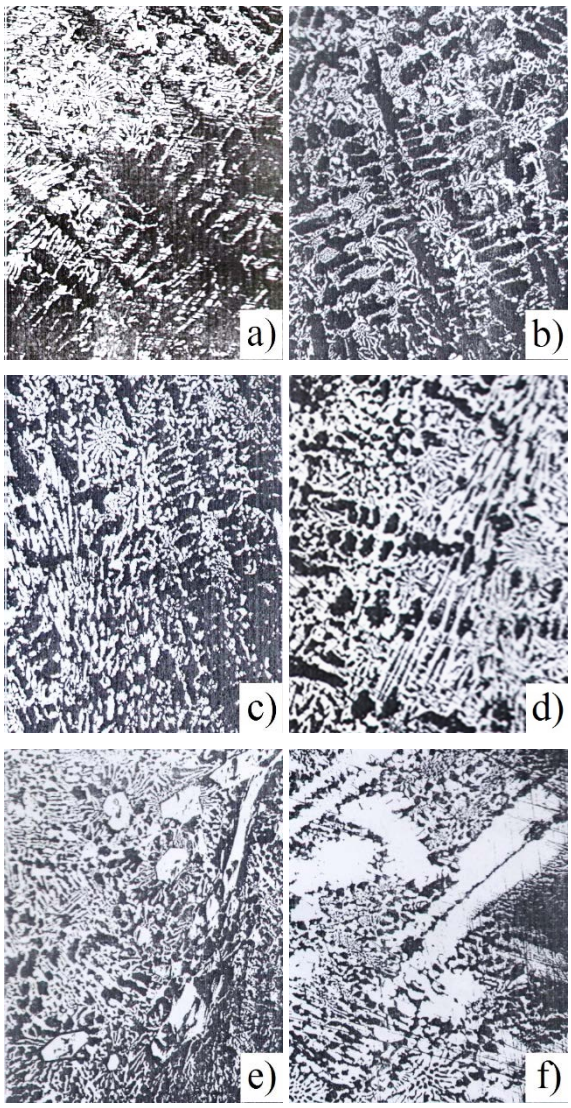

Fig.1. Microstructure of high chromium white cast irons alloyed with boron x100. a) - 0% B; b) - 0,18% B; c) - 0,23% B; d) - 0,59% B; e) - 0,96% B; f) - 1,25% B

TABLE 2 BENDING STRENGTH R_{MI}, IMPACT TOUGHNESS *KC* AND HARDNESS *HRC* OF HIGH CHROMIUM WHITE CAST IRON ALLOYED WITH BORON

Sample №	B, %	HRC	KC, J/cm^2	R_{mi}, MPa
I	-	-	1,88	536,80
II	0,18	53,5	1,80	531,20
III	0,23	54,0	1,72	660,85
IV	0,59	56,5	1,52	391,43
V	0,96	57,0	0,98	374,74
VI	1,25	57,5	0,68	293,27

From the performed bending test the bending strength R_{mi} is defined for the tested high chromium white cast irons with a different boron content (fig.3, table 2). The highest bending strength is achieved for cast irons with 0,23% boron (R_{mi} = 660,85 MPa).

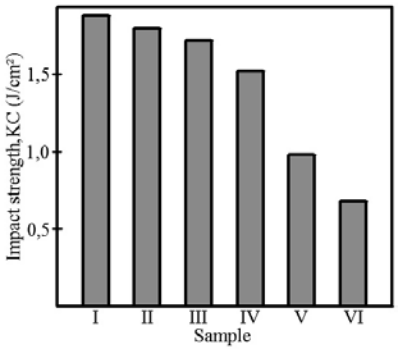

Fig.2. Dependence of the impact toughness *KC* on the boron content in high chromium white cast iron

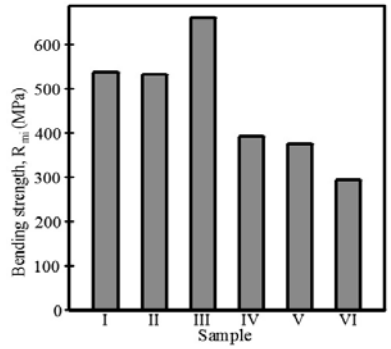

Fig.3. Dependence of the bending strength R_{mi} on the boron content in high chromium white cast iron

The change of the microhardness $HV_{0,1}$ of the metal base and of the carbide phase depending on the boron content in the studied cast irons is presented in fig.4, fig.5 and in table 3. In the alloyed with chromium white cast irons depending on the percentage of the chromium content it is possible to observe the following carbide phase in the eutectic: M_3C, M_7C_3 or $M_{23}C_6$ [3]. In the irons with ~13% chromium the eutectic carbide is M_7C_3. The addition of boron in the cast irons depending of its content this boron can alloy the carbide phases as well as to lead to the appearance of additional carbide phases [3,8]. The highest microhardness of the carbide phase in the boron alloyed cast irons of 1749÷1854 $HV_{0,1}$ (fig. 5) is achieved at 0,96% boron. The dissolving of the boron in the austenite probably increases its resistance to transformation during cooling. The metal base structure at a room temperature could consists as ferrite-carbide mixtures (perlite, sorbite, troostite) as well as nonequilibrium structures (bainite, martensite) and retained austenite. The lowest microhardness is determined for the metal base in the cast irons without boron and the highest - in the cast iron with 0,96% boron (825 $HV_{0,1}$) (fig. 4).

TABLE 3. MICROHARDNESS $HV_{0,1}$ OF THE METAL MATRIX AND CARBIDE PHASE OF HIGH CHROMIUM WHITE CAST IRON ALLOYED WITH BORON

Sample №	B, %	$HV_{0,1}$	
I	-	metal matrix	672
		carbide phase	1427
			1402
II	0,18	metal matrix	766
		carbide phase	1097
			1288
III	0,23	metal matrix	776
		carbide phase	1354
			1226
IV	0,59	metal matrix	786
		carbide phase	1533
			1226
V	0,96	metal matrix	825
		carbide phase	1854
			1749
VI	1,25	metal matrix	766
		carbide phase	1402
			1783

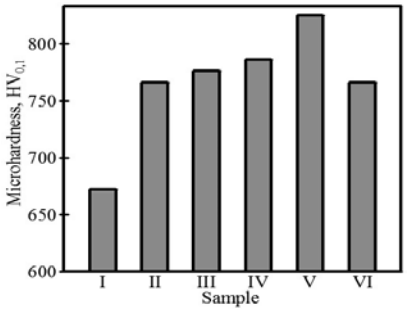

Fig.4. Dependence of the microhardness $HV_{0,1}$ of the metal matrix on the boron content in high chromium white cast iron

The lowest mass loss during abrasive wear test in dry conditions friction is defined for irons alloyed with 0,18 %

boron. The alloyed cast irons with 0,18; 0,23 and 0,59% boron, show higher wear resistance than this one without boron. The highest mass loss is determined during abrasive testing of alloyed cast irons with 0,96 and 1,25% boron (fig. 6, table 4).

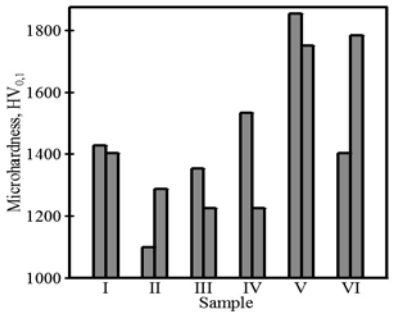

Fig.5. Dependence of the microhardness $HV_{0,1}$ of the carbide phase on the boron content in high chromium white cast iron

TABLE 4. TEST OF WEAR OF HIGH CHROMIUM CAST IRON ALLOYED WITH BORON

Sample №	B, %	m_0, g	m, g	Δ m, g
I	-	142,5032	142,2341	0,2691
II	0,18	147,4415	147,2946	0,1469
III	0,23	145,9076	145,7297	0,1779
IV	0,59	143,6850	143,4546	0,2304
V	0,96	143,8705	143,5771	0,2934
VI	1,25	147,6045	147,2214	0,3831

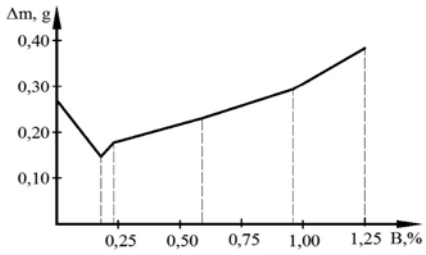

Fig.6. Amendment of the weight loss Δm during abrasive wear test depending on the boron content in high chromium white cast iron

CONCLUSIONS

Additional alloying with boron of the high chromium white cast iron 13,1Cr–3,1C–1,1Mo change the microstructure of the cast iron. The microstructure of the cast irons without boron and with 0,18%; 0,23% and 0,59% boron is subeutectic, with 0,96% boron - is close to the eutectic and with 1,25% boron - supereutectic. Boron alloying decreases grain size of the primary austenite in the subeutectic structure of the cast irons and increases carbide eutectic dispersion. The highest irons impact toughness is achieved in the cast irons without boron and in these of them with 0,18% and 0,23% boron (KC is from 1,88 to 1,72 J/cm^2). The bending strength is highest in the alloyed irons with 0,23% boron (R_{mi}=660,85MPa). The alloyed cast irons with 0,18%, 0,23% and 0,59% boron have higher wear resistance compared to this one of the cast irons without boron.

ACKNOWLEDGMENTS

The authors would like to thank the Research and Development Sector at the Technical University of Sofia for the financial support.

REFERENCES

[1] F. Nurjaman, S. Sumardi, A. Shofi, M. Aryati, and B. Suharno, "Effect of molybdenum, vanadium, boron on mechanical properties of high chromium white cast iron in as-cast condition", *AIP Conference Proceedings*, vol.1711, №020005, February 2016. [Online]. Available: https://aip.scitation.org. [Accessed Sept. 28, 2020].

[2] Xiang Chen, Yanxiang Li and Huiming Zhang, "Microstructure and mechanical properties of high boron white cast iron with about 4 wt% chromium", *Journal of Materials Science*, vol.46, p.957–963, February 2016. [Online]. Available: https://www.researchgate.net. [Accessed Sept. 27, 2020].

[3] A. Nofal, "Metallurgical Aspects of High- Chromium White Irons", www.foundry-planet.com. [Online]. Available: https://www.foundry-planet.com/fileadmin/redakteur/pdf-dateien/13-Adel-Nofal.pdf. [Accessed Sept. 27, 2020].

[4] Kh. Abd El-Aziz, Kh. Zohdy, D. Saber and H. E. M. Sallam, "Wear and Corrosion Behavior of High-Cr White Cast Iron Alloys in Different Corrosive Media", *Journal of Bio- and Tribo-Corrosion* , vol.1, №25, August 2015. [Online]. Available: https://link.springer.com. [Accessed Sept. 25, 2020].

[5] A. Bedolla-Jacuinde, F. V. Guerra, I. Mejía, J. Zuno-Silva and C. Maldonado,"Boron Effect on the Precipitation of Secondary Carbides During Destabilization of a High-Chromium White Iron", *International Journal of Cast Metals Research*, vol.29, issue:1-2, p.55-61, February 2016.[Online]. Available: https://www.tandfonline.com. [Accessed Sept. 25, 2020].

[6] S. Reyna, A. Bedolla-Jacuinde, F.V. Guerra, I. Mejía and M. García, "Effect of amount and distribution of primary TiC on the wear behavior of a 12%Cr-3%C white iron under dry sliding conditions", *Wear*, №203718, February 2021.[Online]. https://www.researchgate.net. [Accessed March. 10, 2021].

[7] Kh. Abdel-Aziz, M. El-Shennawy* and Adel A. Omar, "Microstructural Characteristics and Mechanical Properties of Heat Treated High-Cr White Cast Iron Alloys", *International Journal of Applied Engineering Research*, vol.12, №14, p.4675-4686, January 2017. [Online]. https://www.researchgate.net. [Accessed March. 2, 2021].

[8] S. M. Tomovic-Petrovic, S. V. Markovic and S. Zec, "The effect of boron on the amount and type of carbides in chromium white irons", *Journal of the Serbian Chemical Society*, vol.67(10), p.697–707, January 2002. [Online]. https://www.researchgate.net. [Accessed Sept.. 28, 2020].

[9] K. Ibrahim, " Investigation of improving wear performance of hypereutectic 15% Cr-2% Mo white irons", *China Foundry*, vol.7(4), p.438-446, November 2010. [Online]. https://www.researchgate.net. [Accessed Sept.. 29, 2020].

[10] C. Scandian, C. Boher, J.D.B de Mello and F. Rezai-Aria, "Effect of molybdenum and chromium contents in sliding wear of high-chromium white cast iron: The relationship between microstructure and wear", *Wear*, vol.267, issues:1-4, p.401-408, May 2009.[Online]. https://www.sciencedirect.com. [Accessed Sept.. 29, 2020].

[11] J.D.B. de Mello, A. A. Polycarpou,"Abrasive wear mechanisms of multi-components ferrous alloys abraded by soft, fine abrasive particles", *Wear* , vol.269, issues:11–12, p.911-920, October 2010. [Online]. https://www.sciencedirect.com. [Accessed Sept.. 29, 2020].

V.P.Todorov, "Influence of the carbide phase on the mechanical and operational characteristics of bainitic cast irons", Ph.D. dissertation, Technical University - Gabrovo, Gabrovo, Bulgaria, 2016.

Environment. Technology. Resources. Rezekne, Latvia
Proceedings of the 13th International Scientific and Practical Conference. Volume 3, 142-147

Power Unit for Power Supply of an Autonomous Facility Having Ability to Connect to General Industrial Power Supply in Recuperative Microgeneration Mode

Alexander Khitrov
Pskov State University
Electric Power Engineering, Electric Drive and Automation Systems Department
the Russian Federation
khitrov-pscov@mail.ru

Andrei Khitrov
Pskov State University
Electric Power Engineering, Electric Drive and Automation Systems Department
the Russian Federation
khitrov.aa@gmail.com

Sergei Loginov
Pskov State University
Electric Power Engineering, Electric Drive and Automation Systems Department
the Russian Federation
lsy1@mail.ru

Yulia Domracheva
Pskov State University
Electric Power Engineering, Electric Drive and Automation Systems Department
the Russian Federation
juli-politeh@yandex.ru

Evgeny Veselkov
Pskov State University
Electric Power Engineering, Electric Drive and Automation Systems Department
the Russian Federation
wes_el@bk.ru

***Abstract* - Fundamental and exploratory research in the field of energetics and rational nature management is currently focused on getting results in the field of the effective development and functioning of energy systems. Such systems are based on modern electrical equipment, including electrical machines and controlled power converters (active rectifiers and regenerative units (AC/DC), direct voltage converters (DC/DC), inverters (DC/AC)), conventional and non-traditional electric power based on renewable energy sources (RES).**

The Program of basic research in the Russian Federation on a long-term period (2021-2030 years) comprises the actual problems of development of energy supply, energy efficiency, renewable and alternative sources in industry and agriculture, including the issues of production technology, of conversion and storage of electric power.

Electric power from the renewable energy sources requires its continuous correction, equalization and buffering i.e. a control system for the system operating modes.

The paper presents a project of the power unit that provides both autonomous and traditional operation of a power plant having the possibility of recuperating electrical energy into the network. The structure and the composition of such a power unit is proposed, basic control strategies for an autonomous power generating plant having a capacity of up to 15 kW, operating from the variable low speed engine, also having the other sources of alternative energy with the possibility of power accumulation are considered.

Keywords - autonomous power facility, microgeneration, module power systems control, recuperation.

I. INTRODUCTION

Federal Law of the Russian Federation of December 27, 2019 No. 471 "On the amendments of the Federal Law "On Electric Power" in part of the microgeneration development" has defined the concept – "microgeneration facility"[1]. It is the facility for the production of electrical energy belonging on the right of ownership or on other legal grounds to a consumer of electrical energy, and its power receivers are technologically connected to power

Online ISSN 2256-070X
https://doi.org/10.17770/etr2021vol3.6517

supply network facilities with a voltage level of up to 1000 V, as well operating on the basis of using renewable energy sources (including but not limited to). The facility is used by the consumer for the production of electrical energy for both covering his own household or industrial needs and selling it in the manner prescribed by the main provisions of retail markets functioning if the amount of electric power produced by this facility does not exceed the maximum value of the connected power receivers of the consumer and is not more than 15 kW [1-2].

In other words, it is made possible to sell excess electricity to the network and subsequently to have an income, in agreement with the utilities company, from the autonomous power source on the basis of using renewable energy sources (wind power plant, solar panels, hydrogenerator set on water body, etc.) having a power of up to 15 kW of the three-phase load (3x400 V, 50 Hz).

Electric power from renewable energy sources requires continuous correction, equalization and buffering of the power values, that is, a control system for operating modes.

The project seems to be relevant, given the New Professions Atlas up to 2030. In the field of energy generation and accumulation new professions include [3]:

- local power supply systems specialist;
- recuperation systems designer;
- microgeneration systems developer;
- power generation systems modernization manager.

Local power systems specialist is engaged in development, implementation and maintenance of low power generation systems (wind, solar, bio, etc.). This type of competence can be used for the owners of country houses as well as in designing vertical farms.

Recuperation system designer is a specialist who develops technological solutions for capturing excess power of moving vehicles, primarily during braking of road transport, subway trains and urban electric transport. There is nothing revolutionary in electric energy recuperation, as it applied now mostly in railway transport, trams and trolleybuses. But recuperation in autonomous power supply systems has just been started practicing.

Microgeneration systems developer is a specialist in developing and designing new technological solutions related to energy microgeneration according to customer requirements. Microgeneration is rapidly growing all over the world including Russia but it is often the case that the standard solutions cannot be used for one reason or another, for example, due to climate, and the development of specialized systems to meet the particular factors is required.

In addition, expenditure on the elements of an autonomous-network electric power plant is getting reduced in the structure of production costs for the reason of expanding production of solar panels, inverters, accumulator storage batteries and supercapacitors. There has been a downward tendency of the cost of the permanent magnet synchronous motors (PMSM) that are increasingly used as starter-generators for autonomous-network electric power plants.

II. BASIC POWER FACILITY MODULES

According to forecasts, private alternative energy will be actively being developed in the next 10-20 years. Technologies for production, transferring and storing energy will be automated with the optimization of the operating modes.

The starting data for the power facility design are determined by the desire to create an autonomous power plant for the own needs having the three-phase power of up to 15kW and the possibility of accumulating electrical energy and recuperating it to the network.

Let's determine the main modules for the power facility – microgeneration module system.

The algorithm for switching the operating modes of the facility is designed for solid-state relays (SSR) applying. SSR is module semiconductor block made using hybrid technology and consisting of power switches using MOSFETs, IGBTs, thyristors, triacs and the optocoupler control circuit that performs the function of a conventional electromagnetic relay coil (Fig. 1).

Modern SSRs using MOSFETs are capable of withstanding overvoltages of up to 400V whereas SSRs using IGBTs – up to 1700V at currents of 320-400A, and SSR using thyristors – up to 1600V at currents of 320A in single-phase networks and at currents of 120A in three-phase networks.

Fig 2. shows the network part **M1** of the autonomous-network electric power plant. The input of the system is global electrical network (3x400V four-wire circuit) with a bidirectional electric energy meter (e.g. A1820RAL-P4G-DW-4) [4]) connected to the object by circuit breaker QS.

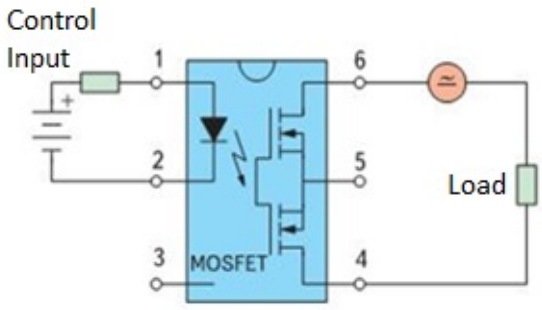

Fig. 1. Solid-state relay.

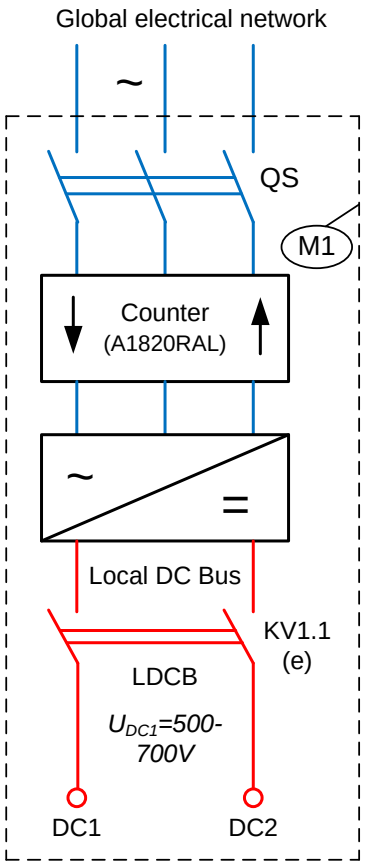

Fig. 2. The network module of the power facility.

Power module of active front end (AFE) rectifier (recuperative converter) (e.g. *EPV-R-TPPT-32-380-600*, Manufacturer: «*CHEAZ-ELPRI*», Cheboksary, RF) is designed to interact with network. It provides the creation of the local direct current bus (LDCB) for connection to one or more sources of power generation and storage as well as to local controlled frequency converters with induction motors (pumps, fans, air conditioners, etc.).

Direct current SSR **KV1.1** provides the connection of adjustable voltage U_{DC1} (500-700V, 40A, e.g. *5P20.10G1-40-6*, Manufacturer: CJSC «*Proton-Impuls*», RF) both when consumers are powered by network and in the mode of transferring (selling) the excess power produced by alternative source (recuperation mode).

Fig. 3 schematically shows the power facility renewable energy sources, at least one three-phase electric generator converting potential or kinetic energy, the solar battery modules conventionally connected, forming a single-phase alternating voltage when SSR **KV1.0** is switched on, and providing the battery charger, if necessary, when SSR **KV2.0** is switched on (L, N to Fig. 4).

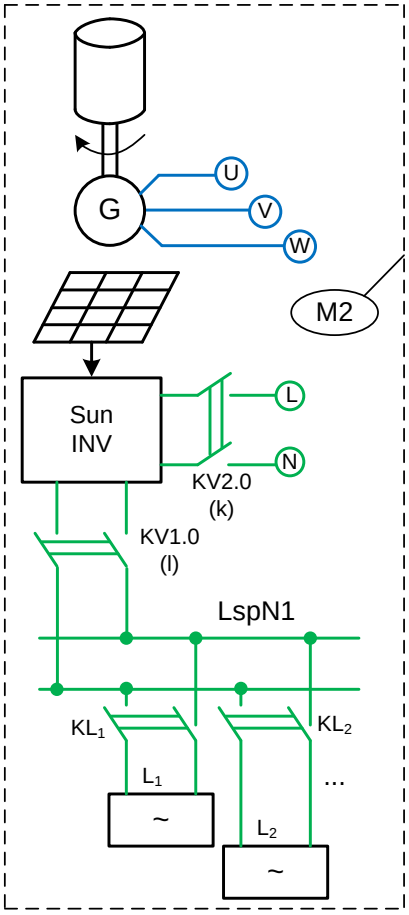

Fig. 3. The renewable energy sources module of the power facility

Renewable energy sources module **M2** may include: solar panels (sources of DC voltage of the required level with an inverter (Sun INV in Fig. 3)), wind generator or wind park, some other prime mover using thermal energy (rotary-vane external combustion engine, Stirling engine, gas electric generator using the energy of the natural gas stored in the gasholder) or hydroelectric generator using potential and kinetic energy of water.

The number of these sources is determined by the power requirements of the whole power facility and by technical and economic parameters including the costs of implementation.

Solar panels and an inverter (e.g. solar inverter SOFAR 5KTLM-G2 [5]) create the local single-phase AC network (LspN1 connected with SSR **KV1.0**, e.g. MD-xx44.ZD3 from *KIPPRIBOR*, RF) having a power of up to 5kW. Switching on SSR **KV2.0** provides, if necessary, recharging the battery pack (or 48V supercapacitor) – module **M4** (Fig. 4). Fig. 4 shows the basic structure of the power unit forming a three-phase local AC network (3x400V, 50Hz) and providing the communication with M1 and M2 modules. The dashed parts M1 and M2 of Fig. 4 are the corresponding parts of the modules presented in Fig. 2 and Fig. 3 (DC1 and DC2 in Fig. 2 and Fig. 4; L, N, U, V, W in Fig. 3 and Fig. 4).

Energy storage device M4 is connected with direct current SSR **KV1.2** which can be switched on to start initially a vertical-shaft-type wind turbine (together with three-phase SSR K3.Start) using an inverter (INV, e.g. Unidrive SP). The second local single-phase AC network (LspN2) can be created, if necessary, using the network single-phase inverter NetINV (48DC/220AC, e.g. TS-1500-248B (48-220V), MeanWell (MW)). In the structure designed, there is an option of providing the local single-phase AC network by switching SSR **KV1.3** and connecting the inverter to the buck DC/DC converter having an output voltage of 42-60V (U_{DC4}).

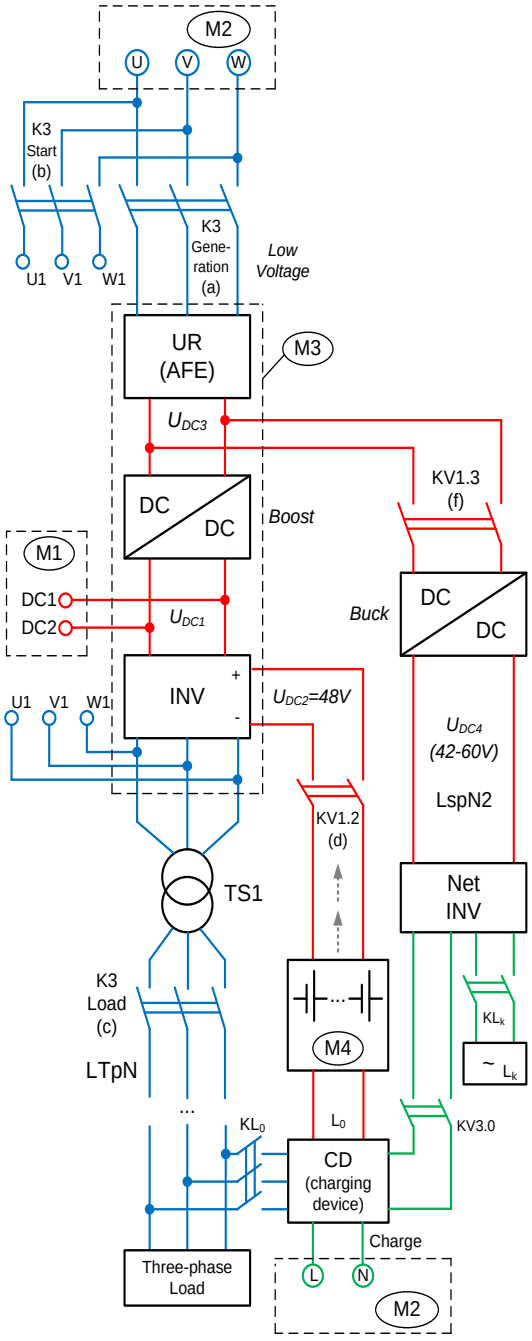

Fig. 4. The power unit of the power facility.

The rectifier-inverter unit **M3** is the core of the whole power unit. It provides the generating local three-phase AC network (LTpN) and connecting sources, power receivers and energy storage via DC bus using is the boost DC/DC converter [6].

Three-phase AC voltage LTpN of the microgeneration module system is formed at the output of M3 inverter INV and the electric load is connected via transformer TS1. The load may include charging device CD for recharging the accumulator batteries of M4.

A large number of types of the autonomous power plants can have a variable speed of the prime mover (e.g. wind turbines having the Savonius rotor system, rotary-vane external combustion engine, hydrogenerator). The variables speed of the system in the range from 300 to 750 rpm does not allow to ensure the normal functioning of the three-phase inverter or requires applying the generators of a special construction with a large number of poles.

One of the tasks of the microgeneration module system is to provide the consumer with the constant frequency of the three-phase supply voltage (50Hz, 3x400V). For variable shaft speed systems the PMSM having the speed of 1500 or 3000 rpm can be used. (e.g. PMSM of *VDM*-100 type from JSC “Uralelectro”, RF [7]).

The technical implementation of module M3 is a complex task, such modules are not produced by industry but become a viable proposition. The connection to generation source is made with three-phase SSR K3.Generation.

The module comprises an active front end rectifier (AFE) or uncontrolled rectifier (UR), a DC/DC converter and an inverter having the option of connecting to LDCB via DC1 and DC2 of M1 (DC+ and DC- inputs), for example, frequency converters of the series Unidrive (Control Techniques) or ACS (ABB).

One of the implementation variants is presented in [8]. For transferring electric power from PMSM to LDCB a DC/DC converter is provided. The DC/DC converter includes the uncontrolled rectifier, H-bridge having 2 or 4 high-speed power IGBTs, high-frequency transformer working at a frequency of 20-100kHz, and the bridge performed with a half-wave rectification and Schottky diodes and connected to the secondary winding of the transformer.

III. BASIC STRATEGY FOR CONTROLLING POWER FACILITY OPERATING MODES

Let’s consider the main operating modes of the microgeneration module system in accordance with the structure given in Fig. 4from the standpoint of the traditional logic of technological processes control.

Let’s introduce the Boolean variables a, b, c, d, e, f (in brackets in Fig.2 and Fig.4).

a – switching on/off the mode of power generation from the prime mover (from PMSM).

b – switching on/off the starting mode from 48V DC source.

c – switching on/off the load for the local three-phase network (LTpN) of the power facility.

d – connecting/disconnecting the energy storage M4 to the DC bus of M3.

e – connecting the global electrical network to the DC bus of M3.

f – providing the local single-phase network (LspN2) using a buck DC/DC converter.

For control of the power facility operating modes the AC and DC SSR controlled with the direct voltage of up to 24V by a programmable logic controller (PLC) may be used.

Following the analysis of the four input variables (a-d), let's introduce new variables:

- $G = a \cdot c \cdot \overline{b + d}$ – establishes the generation mode from the renewable energy source.

This mode should be switched on when the load of the local network is connected (c = 1), the generation mode from the PMSM has already switched on (a = 1), and start of the PMSM had been completed after the DC source M4 had been disconnected (b + d = 0).

- $S = b \cdot d \cdot \overline{a + c}$ – establishes the start mode for PMSM when connecting the DC source 48V.

Table 1 shows the states of the four variables for determining the basic operating modes of the power facility. The rows with forbidden modes have been excluded from the table.

The basic operating modes of the microgeneration module system are highlighted in bold.

For the basic operating modes 7-9 the Boolean functions Y1, Y2, Y3 has been synthesized.

$Y1 = G \cdot \overline{e} \cdot \overline{f}$ – control function for operation of the local three-phase network (LTpN).

$Y2 = G \cdot \overline{e} \cdot f$ – control function for operation of the local three-phase network (LTpN) and the option of the local single-phase network (LspN2).

$Y3 = a \cdot \overline{b} \cdot \overline{c} \cdot \overline{d} \cdot e$ – control function for providing the recuperation of excess electric power generated to the global electrical network (QS = 1).

Fig. 5 shows the test bench having a power of 1,5kW set up at the Electric Power Engineering, Electric Drive and Automation Systems Department of Pskov State University (PskovSU).

TABLE 1 OPERATING MODES

№	G	S	e	f	Operating Mode
0	0	0	0	0	Switched Off
1	0	0	0	1	**Power supply from the solar panels of M2 module if available and connected to SSR KV1. Providing the local low-power single-phase AC network for supplying the single-phase AC load using using the DC/DC converter and the network single-phase inverter.**
2	0	0	1	0	**Operating from the global three-phase AC network via the recuperative module M1 providing the local network 3x400V having a power of up to 15kW. Reactive energy accumulation. QS = 1.**
3	0	0	1	1	DC bus U_{DC4} is additionally created. A buck DC/DC converter is used.
4	0	1	0	0	Starting a wind power plant from an external 48V DC source.
5	0	1	0	1	DC bus U_{DC4} is additionally created. A buck DC/DC converter is not reqired.
6	0	1	1	0	Starting a wind power plant from the global electrical network while the 48V DC source is disconnected from inverter INV. Carried out briefly by the operator for the initial start.
7	1	0	0	0	**Generation from a wind power plant. Providing the local autonomous network 3x400V having a power of up to 15kW (output variable Y1).**
8	1	0	0	1	**Generation from a wind power plant. Providing the local autonomous network 3x400V having a power of up to 15kW and additionally DC bus U_{DC4}. A buck DC/DC converter is used (output variable Y2).**
9	1	0	1	0	**Energy recuperation to the global electrical network after switching off the local 3x400 network (variable *c* changes from 1 to 0, and variable *e* from 0 to 1) (output variable Y3).**

The test bench allowed to carry out the studies, that confirmed the efficiency of the innovative microgeneration module system presented in the authors publications [6, 9, 10].

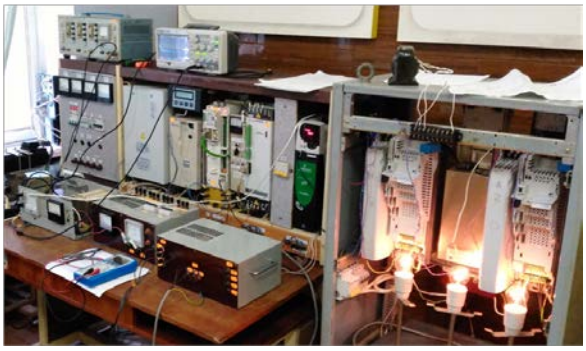

Fig. 5. Test bench.

The studies carried out correlate with the data published in [11], which indicated that "one of the problems of electromechanics, which has not received a high effective

solution, is the conversion of the mechanical energy of the driving shaft having the variable speed into the electrical energy with the specified quality indicators: stabilized AC voltage and frequency or stabilized DC voltage".

IV. CONCLUSIONS

1. The module structure for the microgeneration facility has been developed.

2. It is recommended to apply a permanent magnet synchronous machine (PMSM) as the electric generator for the wind power plant [12].

3. The limited possibilities of output voltage control in the structures with PMSM without applying mechanical or electrical multiplicators require the creation of the special power unit of the module type, consisting of a rectifier module (controlled or uncontrolled), a boost DC/DC converter and a conventional three-phase inverter.

4. The experimental studies have shown the efficiency of the individual modules of the power facility with the admissible values of the indicators of electrical power quality [9, 13].

REFERENCES

[1] Federal Law of the Russian Federation of December 27, 2019 No. 471 "On the amendments of the Federal Law "On Electric Power" in part of the microgeneration development". (In Russian).

[2] Order of the Government of the Russian Federation No. 3684-r of December 31, 2020 "Program of fundamental scientific research in the Russian Federation for the long-term period 2021-2030. (In Russian).

[3] T.A. Tonunts. Atlas of New Professions. Power generation and energy storage. Professions that will appear before 2030. *Izdatel'skie reshenija* [Publishing solutions]. 2020, 40 p.(In Russian).

[4] Alpha A1800. Multifunctional microprocessor-based electricity meters of the ALFA series. Moscow: Elster Metronica, 2010. 25 p.

[5] Omega. Solar Inverter for Water Pump. User manual. [Online]. Available: http://www.masterbattery.es/manuales/ Omega_Water_Pump.pdf [Accessed: Mar. 20, 2021].

[6] Khitrov A.A., Khitrov A.I., Ilyin A.V., Domracheva Y.V, Fedorov D.S. Electric energy generation in autonomous energy supply module having rotary expansion engine. Environment. Technology. Resourses. Proceeding of the 12th International Scientific and Practical Conference. June 20, 2019. Volume III. p. 109-113.

[7] Electrotechnical plant "Uralelectro" of Mednogorsk. [Online]. Available: http://ural-motor.ru/[Accessed: Mar. 20, 2021].

[8] Wind farm with several wind turbines. Patent RU 2 725 167 C1. Brombach, Johannes (DE), Penalty, Christian (DE). Application 2019133661,23.03.2018. Published 30.06.2020 Bul.№19.

[9] Khitrov A.A., Khitrov A.I., Veselkov E.L., Tikhonov V.I. Investigations of Electric Power Quality in Autonomous Low Power Plant. Environment. Technology. Resourses. Proceeding of the 11th International Scientific and Practical Conference. June 15-17, 2017. Volume III. p.136-139. Rezekne.

[10] Plokhov I.V., Khitrov A.A., Khitrov A.I. *Starter-generatornaya ustanovka dlya avtonomnoy sistemy elektrosnabzheniya na baze rotorno-lopastnogo dvigatelya s vneshnim podvodom teploty*. [Starter-generator set for autonomous power supply system for external combustion rotary-vane engine]. Patent RF №144521. 27.08.2014. (In Russian).

[11] Mytsyk G.S. About modern solutions of machine-electronic generating systems for small-scale power generation and mobile objects. *Elektrichestvo* [Electricity]. 2020, №7, pp.22-32. (In Russian).

[12] Permanent magnet synchronous motor 3 to 350 kW - 1500 to 5500 rpm. [Online]. Available: http://acim.nidec.com/ motors/leroy-somer/products/permanent-magnet-synchronous-motors/ lsrpm-dyneo [Accessed: Mar. 20, 2021].

[13] State Standard 32144-2013. Electric Energy. Electromagnetic compatibility. Standards of quality of electric energy in general-purpose power supply systems. (In Russian).

Environment. Technology. Resources. Rezekne, Latvia
Proceedings of the 13th International Scientific and Practical Conference. Volume 3, 148-153

Aluminum Based Composites Obtained by FSP (Review)

Christo Kondoff
IMSETCH "Acad. A Balevski" - Bulgarian Academy of Sciences
Sofia, Bulgaria
hriko61@gmail.com

Radostina Zaekova
IMSETCH "Acad. A Balevski" - Bulgarian Academy of Sciences
Sofia, Bulgaria
rzaekova@mail.bg

Marina Manilova
IMSETCH "Acad. A Balevski" - Bulgarian Academy of Sciences
Sofia, Bulgaria
mamanil@abv.bg

***Abstract* - The composites based on aluminum alloys obtained by friction stir processing (FSP) combine the advantages of lightweight aluminum composites with the well-refined structure obtained by deformation in plastic state. When reinforcing elements in the form of powders or nanoplates are introduced in the process, of mixing they are evenly distributed in the processes zone, which acquires a fine-grained structure. The study examines specific results in the use of various tools and materials, as well as some basic parameters of the process in terms of surface smoothness, defects and some performance characteristics of the tested samples, such as strength, ductility, hardness and corrosion resistance.**

Keywords* - *aluminum alloys composites, friction stir processing (FSP), fine-grained structure, nanoplates

I. INTRODUCTION

The composite materials, called "composites" for brevity, have a complex of useful qualities and are widely used nowadays. In most cases the application of metal matrix composites (MMC), and in particular aluminum matrix composites (AMC), is limited due to their high cost despite their high performance combined with low weight [1]. Extremely good opportunities for creating composites are provided by the technology for friction stir processing (FSP) [2], [3] and the technology friction stir welding (FSW) for in non-detachable joining.

Both processes FSW and FSP, as the former is developed by TWI Cambridge, UK [4] in 1991 and the latter is developed by Mishra, India [2] in year 2000, are based on the same principles. The main parameters of the process, which determine the properties of the processed layer, are the applied load, tool rotation velocity, traverse velocity of processing, and tool type and geometry. The process FSP has acquired worldwide spread due to the following advantages [5] - [7]:

- Can be realized on universal metalworking machines and machining centers;
- No expensive consumables, additive materials or gasses, etc. are required;
- No specialized power source is required;
- The temperatures are lower than those for conventional overlay welding and the alloying elements are preserved;
- The material is not melted but only plasticized, so there is no distortion and stability of the geometric dimensions is ensured;
- Allows surface processing of dissimilar materials;
- The costs for pre-cleaning and sanding after processing are reduced;
- Allows to process a specific area of the surface;
- The process is clean and protects the environment and human health;
- Refinement of the microstructure due to the intensive mixing. The results achieved after FSP are grain refinement, breaking the non-metallic inclusions and the coarse dendritic structure, and occurrence of dynamic recrystallization, characterized by a large number of high-angle grain boundaries [6].

Online ISSN 2256-070X
https://doi.org/10.17770/etr2021vol3.6640

FSP is used as an excellent technique for making MMK with reinforcing or modifying powders introduced and uniformly dispersed in the processed area.

II. GEOMETRY OF THE TOOLS FOR FSP

The geometry of the tool is one of the most important factors in FSP, which plays a key role for stirring the material. The speed with which FSP is carried out depends on the tool geometry. The tool for FSP consists of shoulder and pin, as is shown in Fig. 1.

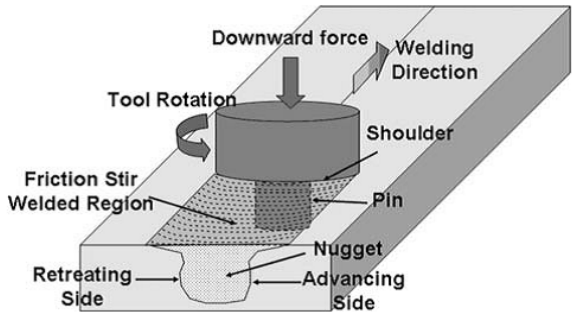

Fig. 1. Scheme of FSP [8].

The tool has two main functions: (a) local heating, and (b) stirring the material. On the initial stage of entering the tool, the heating is obtained mainly by the friction between the pin and the part. Additional heat is released as a result of the deformation of the material. The tool penetrates the material until the shoulder comes in contact with the top surface. The friction between the shoulder and the part leads to the release of a large amount of heat. From the point of view of the heat released, the relative size of the pin and the shoulder is important.

The second function of the tool is to "mix" and "move" the material. The uniformity of the microstructure and the properties, as well as the efforts in the process depend on the design of the tool. The most commonly used tool combines a concave shoulder with threaded cylindrical pins, see Fig. 2 [9].

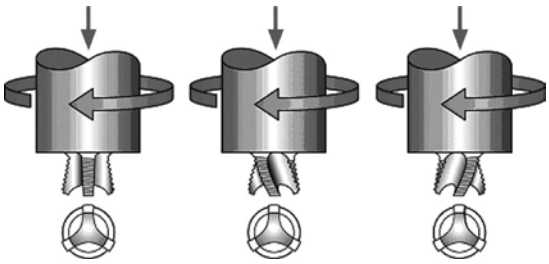

Fig. 2. Flared-Triflute TM tools developed by TWI, UK: (a) neutral flutes, (b) left flutes, and (c) right hand flutes (after Thomas et al.) [9].

The main factor determining the advantage of tools with threaded pins and flutes over the conventional cylindrical pins is the ratio of the entrained volume of the material during rotation to the volume of the pin itself, i.e. ratio between the "dynamic volume" and the "static volume", which is important to ensure adequate flow during mixing. Typically, this ratio for pins with similar root diameters and lengths is 1.1: 1 for conventional cylindrical pin, 1.8:1 for pin model WhorlTM, and 2.6:1 for pin model MX TrifluteTM (in welding plate with thickness 25 mm) [9].

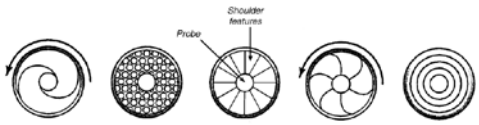

Fig. 3. Tool shoulder designs [10].

Different tool shoulder profiles are designed to suit different materials and conditions of processing, see Fig. 3. These shoulder profiles improve the quality of processing and ensure reintroduction of the plasticized material into the stirring zone.

The profile of the pin in Fig. 4 has a significant impact on hardness, strength and wear resistance [11].

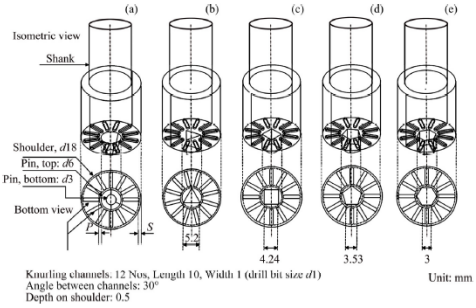

Fig. 4. Tools used in FSW process showing knurling shoulder feature [11].

As a result of the research performed regarding the type of instrument, the following conclusions can be made:

- Defects, such as delamination, tunnel defects and imperfections, are observed in the microstructures of the areas processed with the individual tools, which are probably due to the unstable flow of the plasticized material due to improper combination of geometry of the pin and the shoulder.
- The best results are observed with a tool having square pin and shoulder with knurling re-entrant channels, which ensures uniform distribution of the plasticized material, both on the advance side and the retreat side of the weld.
- The instrument with a square pin and a shoulder with knurling re-entrant channels also shows the best values for ultimate tensile strength of 182 MPa and hardness of HV78.

TABLE 1 FORCE, TORQUE AND MECHANICAL PROERTIES OF WELDS WITH DIFFERENT TOOLS [11]

Sample No.	Tool	Number of sides (n)	Static to dynamic volume ratio	Axial force#/kN	Tool torque#/ (kN·m)	UTS*/ MPa	Avg. micro-hardness in stir zone* (HV)
1	Taper cylindrical pin shaped tool (T_C)		1	6.5	58.9	172±0.5	70.2
2	Triangular pin shaped tool (T_C)$_T$	3	2.4	5.4	48.5	178±1.0	62.1
3	Square pin shaped tool (T_C)$_S$	4	1.57	6.0	54.0	182±0.8	78.2
4	Pentagonal pin shaped tool (T_C)$_P$	5	1.32	5.9	53.1	171±0.6	80.6
5	Hexagonal pin shaped tool (T_C)$_H$	6	1.2	6.4	56.7	172±1.2	78.1

*Average of three reading values; # Maximum recorded force/torque in entire welding

Similar results are obtained in FSP of composites based on Al-Mg alloy (4 wt% Mg) reinforced with 1wt% SiC and 1wt% graphite particles [12]. In addition to providing reliable joining, the FSP carried out significantly affects the mechanical properties of hardness, tensile strength and wear resistance. The reduction of the grain size, according to the mathematical dependence derived by Hall–Petch, gives information about the quantitative change of the mechanical characteristics. The heat released due to friction of a tool with a square-head pin is significantly less than that in case of hexagonal- or octagonal-head pins. The smaller grain growth in the stirring zone occurs in the process of cooling to room temperature. This means that the use of a tool with a square head pin provides enhanced mechanical properties.

Aluminum alloys of all series can be subjected to FSP. There are data for FSP of alloys of dissimilar composition. There are a number of techniques used to obtain AMCs using FSP, which are described below.

III. OBTAINING AMC BY INCORPORATING REINFORCING PARTICLES INTO THE MATRIX THROUGH CHANNELS AND FURTHER FSP WITH A TOOL WITHOUT PIN OR A TOOL WITH TAPERED PIN [7].

Fig. 5 [7] shows the scheme of FSP for obtaining AMC based on alloy AA 6061-T6 with different concentrations of reinforcing Al2O3 particles.

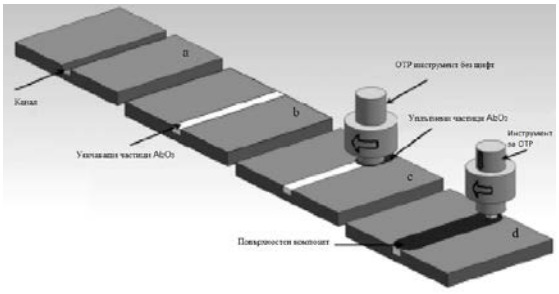

Fig. 5. Obtaining AMC through FSP [7].

The microstructures of nano composites obtained through different modes of FSP are shown in Fig. 6.

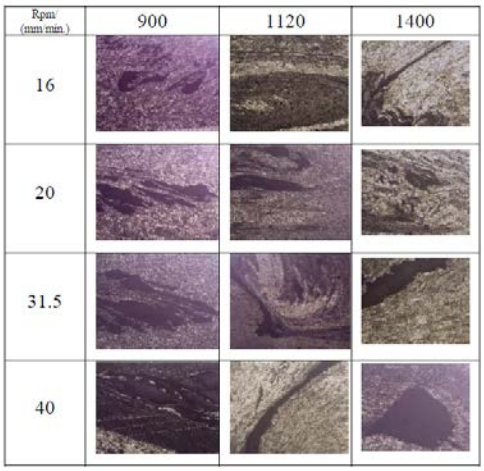

a)

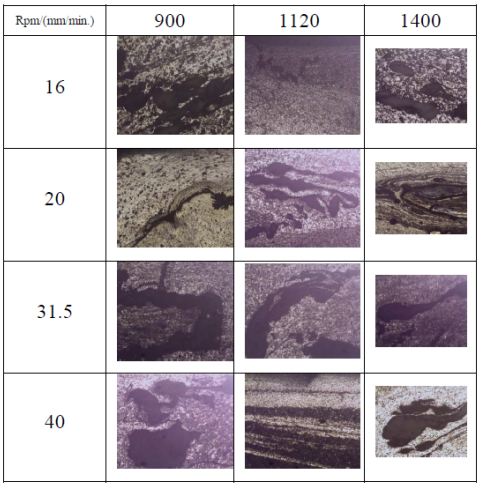

b)

Fig. 6. Microstructures of composites with concentration of nano particles (a) 2%, and (b) 6% [7].

It was found that a defect-free structure was obtained at concentration 2 vol. % of the reinforcing nano particles, tool rotation speed 1120 rpm, traverse speed 16 mm/min and a threaded taper pin tool with concave shoulder. Fig. 7 displays the comparison between the hardness of composites with 2 vol. % and 6 vol.% nanoparticles with respect to the raw material.

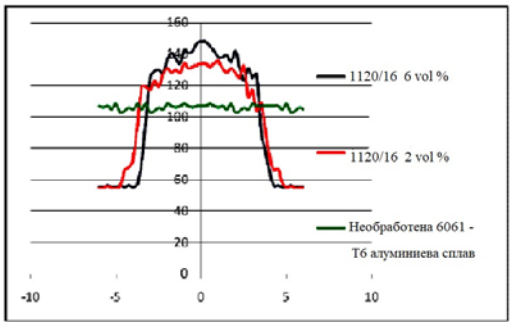

Fig. 7. Hardness of the composites [7].

It is obvious that at rotational speed 1120 rpm, traverse speed 16 mm/min, and 6 vol. % concentration of Al2O3 nano particles the hardness of the obtained composite reaches 132 HV.

IV. OBTAINING AMK BY INCORPORATING REINFORCING PARTICLES INTO THE MATRIX BY DRILLING CYLINDRICAL HOLES AND FURTHER FSP [13].

AMK based on alloy 7075-T651 with reinforcing nanoparticles of SiC and ash in ratio 60:40, 75:25 and 90:10 and concentrations 4%, 8% and 12% volume percentages are obtained by FSP [13]. The processing is performed under the following parameters:

- Tool rotation speed 500, 1000 and 1500 rpm;
- Traverse speed 20, 30 and 40 mm/min.

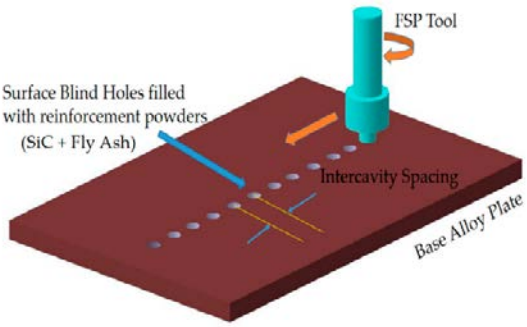

Fig. 8. FSP by introduction of the reinforcing powder in blind holes [13].

The influence of these parameters on the microstructure of composites, wear rate and microhardness is studied.

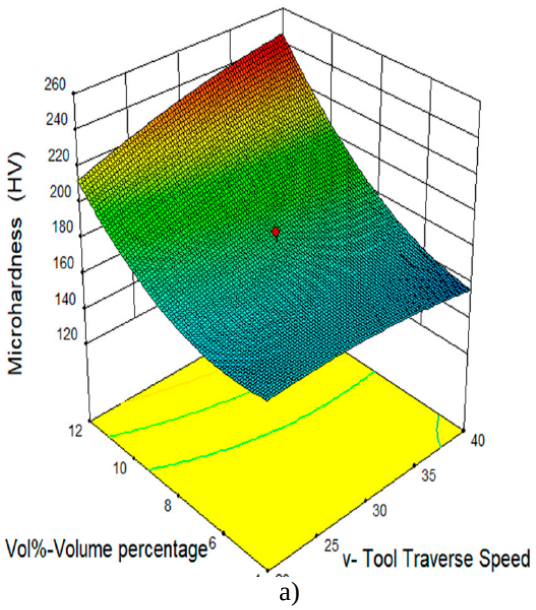

a)

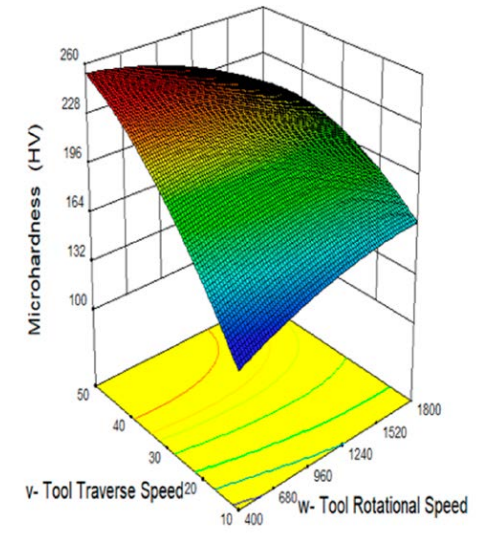

b)

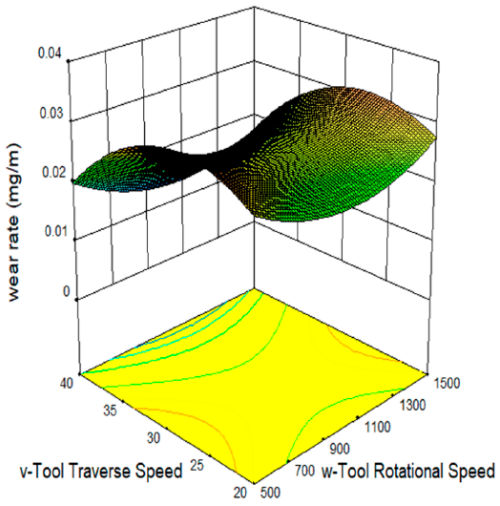

c)

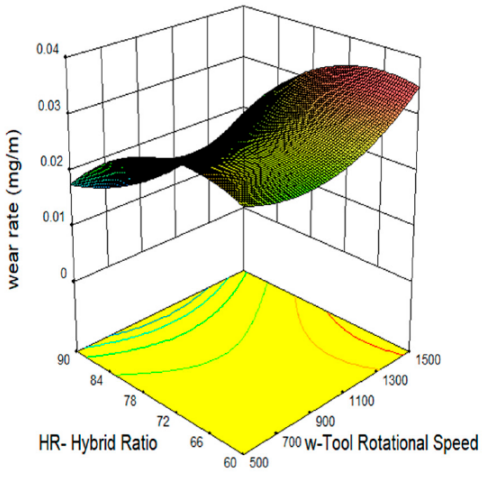

d)

Fig. 9. Effects of tool rotational speed, traverse speed and hybrid ratio on the wear rate and microhardness of AA7075-SiC/fly ash composites: a), b), c), d [13]

The degree of uniformity of distribution of SiC reinforcing particles mixed with industrial powder in the base alloy AA7075 is most important for improving the microhardness and wear resistance of composites.

The minimum wear rate is achieved in the sample processed with combination of parameters w=1000 rpm, v=40 mm/min, HR=75:25, concentration 8 vol. %; and the maximum hardness of 241,2 HV is achieved in the sample processed with combination of parameters w=500 rpm, v=40 mm/min, HR=90:10, concentration 12 vol.%.

V. OVERLAPPING FSW OF ALUMINUM ALLOY AA6061 WITH INTERMEDIATE GRAPHENE LAYER

The main disadvantage of aluminum based MMCs is the poor weldability when applying conventional fusion welding technologies [14], [15]. The defects observed are inclusions, porosity, chemical interaction between the materials of reinforcement and matrix, high residual stresses and cracking due to the substantial difference between the coefficients of thermal expansion of matrix material and reinforcement [16], [17]. Their presence reduces the weld efficiency up to 50% than that of the base material [18]. Another substantial reason for the reduced efficiency in fusion welding of MMCs are the metallurgical aspects, such as the increase of grain size up to 10 times compared to the base material, along with the large heat affected zone (HAZ) [19]. These problems can be effectively overcome by the method of friction stir welding (FSW).

Over the last decade, graphene has been developed as a promising reinforcement for various aluminum-based composites. Its low density and exceptional mechanical and thermal properties make it ideal reinforcement in various low density alloys [20]. The large surface of the graphene sheets favours its strong interfacial connection with the metal phase of the composite. In solid state preparation of Al-graphene composite by FSW, a huge decrease in the degree of wear is also observed [21]. In another study conducted by Jeon et al. [22] the thermal conductivity of a graphene-reinforced composite is increased by near 15% when obtained by FSW. Khodabakhshi et al. [23] also observe a near 50% increase in hardness and a threefold increase in strength of graphene-containing aluminum as reinforcement.

Despite graphene is efficient enough to substantially increase the strength of the alloy or composite, its implementation is limited by its lower corrosion resistance in aluminum alloys, since graphene layers activate the corrosion of aluminum due to occurrence of galvanic corrosion [24].

The study reported in [25] shows the increase of strength of aluminum alloys welded by FSW with overlapping (Fig. 10), using an intermediate layer of graphene nanoplatelets (GNP) in the interface of the weld joint.

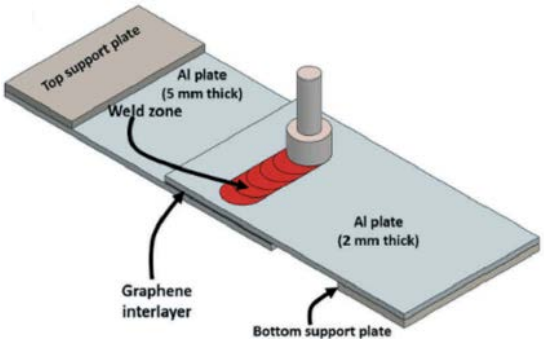

Fig. 10. Schematic representation of FSW [25].

The study shows that when using GNP as an intermediate layer, the strength of the welded joint increases by 121% and the percentage elongation increases by 53% compared to the weld without an intermediate layer. In the case of an intermediate layer weld, the bottom of the top plate on the retreating side acts as a potential fracture site due to the presence of an interfacial defect and an undeformed GNP layer. The strengthening of the weld is due to various primary reinforcement mechanisms such as thermal discrepancy, grain refinement, Orowan mechanism, and load transfer.

The following advantages are also observed when using an intermediate layer of GNP:

- the type of destruction changes from brittle to plastic; - the grain size in the welding zone decreases by ~ 38%;
- the height of the Hook Defect HD (CD) and the cold lap defect CLD decreased by 26% and 41% respectively;
- preventing the formation of a layer of Al2O3 on the surface of the overlap and thus contributing to a significant strengthening of the welded joint.

The technique of FSW of aluminum alloys with overlapping and GNP can also be used to obtain hybrid metal matrix composites.

Acknowledgements

The authors thank the Bulgarian Scientific Research Fund for funding according to the contract KP-06-India/10, as well as Prof. Adepu Kumar and Dr. Krishna Kishore for sharing some of their work ideas and articles.

REFERENCES

[1] M. J. Jweed, A. M. Takhakh, N. K. Kareem, "Comparison between Friction stir welding (FSW) and Friction stir processing (FSP) of AA5086 aluminum alloy", International Journal of Technical Research and Applications, Volume 3, Issue 6 (November-December,2015), pp 205-210.

[2] R.S. Mishra, M.W. Mahoney, S.X. McFadden, N.A. Mara, A.K. Mukherjee, Scripta Mater. 42 (2000) 163

[3] R.S. Mishra, M.W. Mahoney, Mater. Sci. Forum 357–359 (2001) 507

[4] W.M. Thomas, E.D. Nicholas, J.C. Needham, M.G. Murch, P. Templesmith, C.J. Dawes, G.B. Patent Application No. 9125978.8 (December 1991).

[5] Z.Y. Ma, R.S. Mishra, M.W. Mahoney, Acta Mater. 50 (2002) 4419

[6] R. Kapoor, N. Kumar, R.S. Mishra, C.S. Huskamp, K.K. Sankaran, "Influence of fraction of high angle boundaries on the mechanical behavior of an ultrafinegrained Al-Mg alloy". Mater. Sci. Eng., 2010 A 527, 5246–5254, http://dx.doi.org/10.1016/j.msea.2010.04.086

[7] P. Naresh, A. Kumar "Effect of Nano Reinforcement On Fabrication Of Al/Al2O3 Surface Composite By Friction Stir Processing", Materials Science forum, Vols. 830-831, pp 467-471

[8] R.S. Mishra, Z.Y. Ma / Materials Science and Engineering R 50 (2005) 1–78

[9] W.M. Thomas, K.I. Johnson, C.S. Wiesner, Adv. Eng. Mater. 5 (2003) 485.

[10] W.M. Thomas, E.D. Nicholas, S.D. Smith, in: S.K. Das, J.G. Kaufman, T.J. Lienert (Eds.), „Aluminum 2001—Proceedings of the TMS 2001 Aluminum Automotive and Joining Sessions," TMS, 2001, p. 213.

[11] A. Kumar, K.K. Mugada "Effect of knurling shoulder design with polygonal pins on material flow and mechanical properties during friction stir welding of Al−Mg−Si alloy" Trans. Nonferrous Met. Soc. China 29(2019) 2281−2289

[12] A. M. Hassan, T. Qasim, and A. Ghaithan, "Effect of Pin Profile on Friction Stir Welded Aluminum Matrix Composites", Materials and Manufacturing Processes, 2012, 27: 1397–1401,

[13] P. A. Namdev, R. P. Srinivasa, O. B. Mamat and A. M. Lubis, Effect of SiC/Fly Ash Reinforcement on Surface Properties of Aluminum 7075 Hybrid Composites, Coatings, June 2020, 10, 541, doi:10.3390.

[14] B. Sahoo, S. D. Girhe, J. Paul, "Influence of process parameters and temperature on the solid state fabrication of multilayered graphene-aluminium surface nanocomposites". J. Manuf. Process. 2018, 34, 486–494

[15] B. Sahoo, D. Narsimhachary, J. Paul, "Tribological behavior of solid-state processed Al-1100/GNP surface nanocomposites". J. Mater. Eng. Perform. 2018, 27, 6529–6544. DOI: 10.1007/s11665-018-3727-6.

[16] V. K. Parikh, A. D. Badgujar, N. D. Ghetiya, "Joining of metal matrix composites using friction stir welding: a review", Mater. Manuf. Process. 2019, 34, 123–146. DOI: 10.1080/10426914.2018.1532094.

[17] T. Prater, "Solid-state joining of metal matrix composites: a survey of challenges and potential solutions.", Mater. Manuf. Process. 2011, 26, 636–648. DOI: 10.1080/10426914. 2010.492055.

[18] T. K. Pal, "Joining of aluminium metal matrix composites". Mater. Manuf. Process. 2005, 20, 717–726. DOI: 10.1081/AMP-200055116.

[19] A. Sharma, V. M.Sharma, B. Sahoo, S. K. Pal, J. Paul, "Effect of multiple micro channel reinforcement filling strategy on Al6061-graphene nanocomposite fabricated through friction stir processing", J. Manuf. Process. 2019, 37, 53–70. DOI: 10.1016/j. jmapro.2018.11.009.

[20] R. Maurya, B. Kumar, S. Ariharan, J. Ramkumar, K. Balani, "Effect of carbonaceous reinforcements on the mechanical and tribological properties of friction stir processed Al6061 alloy", Mater. Des. 2016, 98, 155–166. DOI: 10.1016/j.matdes.2016.03.021.

[21] J. B. Fernandez, E. J. Macias, J. S. Muro, L. Caputi, D. Miriello, R. De Luca, A. S. Roca, H. C. Fals, "Tribological behavior of AA1050H24-graphene nanocomposite obtained by friction stir processing", Metals (Basel). 2018, 8, 113. DOI: 10.3390/met8020113.

[22] C. H. Jeon, Y. H. Jeong, J. J. Seo, H. N. Tien, S.T. Hong, Y. J. Yum, S. H. Hur, K. J. Lee, "Material properties of graphene/aluminum metal matrix composites fabricated by friction stir processing", Int. J. Precis. Eng. Manuf. 2014, 15, 1235–1239. DOI: 10.1007/s12541-014-0462-2.

[23] F. Khodabakhshi, M. Nosko, A. P. Gerlich, "Effects of graphene nano-platelets (Gnps) on the microstructural characteristics and textural development of an Al-Mg alloy during friction-stir processing", Surf. Coatings Technol. 2018, 335, 288–305. DOI: 10.1016/j.surfcoat.2017.12.045.

[24] F. H. Latief, E. S. Sherif, A. A. Almajid, H. Junaedi, "Fabrication of exfoliated graphite nanoplatelets-reinforced aluminum composites and evaluating their mechanical properties and corrosion behavior", J. Anal. Appl. Pyrolysis. 2011, 92, 485–492. DOI: 10.1016/j.jaap.2011.09.003.

[25] A. Sharma, V. Sharma, A. Gugaliy, P. Rai, S. K. Pal, and J, Paul, Friction stir lap welding of AA6061 aluminium alloy with a graphene interlayer", Materials and Manufacturing Processes, January 2020,

DOI: 10.1080/10426914.2020.1718694.

Environment. Technology. Resources. Rezekne, Latvia
Proceedings of the 13th International Scientific and Practical Conference. Volume 3, 154-158

Experimental Compare of the Mechanical Properties of Pultruded Glass Fibre Reinforced Plastic Based on Polyester and Vinylester Resin

Andrejs Kovalovs
Institute of Materials and Structures
Riga Technical University
Riga, Latvia
andrejs.kovalovs@rtu.lv

Andrejs Morozovs
COMPOR Ltd
Riga, Latvia
andrejs.morozovs@compor.lv

***Abstract* - The main purpose of this study is an experimental investigation and comparison of the mechanical properties of pultruded glass fibre reinforced polymer composite based on polyester and vinylester resin. For this purpose, the specimens were cut from the walls of square tube pultruded profile along to the fibres direction. The mechanical properties of the pultruded composite such as ultimate tensile strength and ultimate bending strength, tensile modulus and flexural modulus were obtained. It was observed that using of vinyl ester resin in pultruded composite instead of polyester resin enhanced the ultimate tensile and flexural strength from ~13% to ~24% in dependence of composite specimen's thickness.**

Keywords - Pultruded unidirectional GFRP lamina, tensile testing, flexural testing

I. INTRODUCTION

Modern composites are widely used now in different engineering constructions due to their high stiffness-to-weight and strength-to-weight ratios [1], [2] and high dissipative properties [3], [4]. The mechanical properties of composite materials are estimated in most cases by using conventional fracture methods [5]-[6], ultrasonics [7] and inverse technique based on low-frequency vibrations [8]–[10].

Pultrusion is one of the fastest growing manufacturing processes within the composites market. It is a continuous and cost-effective technology and is widely used for a production of high strength fibre-reinforced polymer composite profiles with different cross-sections [11].

During the manufacturing process, the reinforcement materials (fibres in the form of roving and mats) are pulled through an impregnation bath, containing a resin, and then fed into a heated forming where shaped into the geometry of pultruded profile. Finally, the profile is pulled out of the heated mould and cut according to desired length [12].

In literature, many different numerical and experimental techniques are carried out to design pultrusion processes. Mostly, thermo-chemical modelling in transient and steady state analyses are developed for a better understanding of pultrusion processes to analyse the distributions of temperature and degree of cure inside the die, using the finite element methodology [13]-[15] finite difference methodology, based on the nodal control volume method [16], [17].

Modern pultruded fibre reinforcing polymer (FRP) are becoming significantly important for the production of a large variety of products due to their light weight, higher tensile strength, good environmental resistance, high durability and electromagnetic neutrality [18], [19]. These characteristics ensure extensive application in civil engineering. Pultruded profiles are widely used as main structural component in bridge and building construction instead of the traditional materials [20]-[22].

The most common pultruded FRP composites used continuous fibres in the form of rovings, mats, woven fabrics and various type resin materials, including polyester, epoxy and vinyl ester. Combinations of these materials allows obtain the necessary mechanical properties of composite used for construction purpose [23]. The knowledge about mechanical properties of various pultruded GFRP composites significantly grow in last few years. Many researchers reported advantageous of pultruded composites by means of mechanical properties. A systematic study on material properties of pultruded GFRP composites is very important for extend application these materials in civil engineering [24]-[26] and simulation on mechanical behaviour of structures under

Online ISSN 2256-070X
https://doi.org/10.17770/etr2021vol3.6644

loading. Characterization of mechanical behaviour is not only an important study for entire structures under loading, but also for the separate parts in time of their production, since stresses and deformations caused by the process may occur [27]- [29].

One of the main component in pultrusion is a type of resins. Polyester resins is the most widely used type of resin used in manufacture of pultruded composite. This resin can be used in the manufacture of anything composite and has an excellent resistance to corrosion in aggressive environments. Disadvantage of this polyester resin in compare to the vinylester resin is low long-term durability. In addition, the vinylester resin faster in cure and offers exceptional moisture resistance. The strength of vinylester is higher than polyester resin but polyester resin is the cheapest [30], [31].

The main aim of this investigation is an experimental determination the mechanical properties of pultruded GFRP composite based on polyester and vinylester resin and their comparison. Mechanical characteristics include tensile and flexural modulus of elasticity and ultimate tensile and bending strength. Specimens with two thickness and different structures used in this study.

II. Materials and Methods

The pultruded GFRP specimens involved in this study were manufactured by COMPOR Company. They cut off from E-glass/polyester and E-glass/vinylester sheets with 6.3 mm and 3 mm thickness, respectively. The sheets cut off from walls of square tubes. GFRP square tube were fabricated with unidirectional glass fibre yarn (4800g/1000m) and continuous filament mat (CFM) layers embedded in polyester or vinylester resin matrix through pultrusion process. Wall with thickness of 6 mm consist of outer and internal middle layer of CFM with density 600 g/m^2 and inside layer with density 450 g/m^2. The wall with thickness of 3 mm consist of two CFM as outer and inside layer with density 450 g/m^2. It can be note that difference in construction of specimens can lead to distinction in mechanical properties.

The tension tests were carried out according to ASTM D3039 [32] in order to determine the ultimate tensile strength and longitudinal elastic modulus. Specimens were tested using a universal testing machine ZWICK100 with a capacity of 100 kN and crosshead movement speed of 2 mm/min. The dimension of specimens are 250 mm long in the direction of roving fibres and 25 mm wide. Gauge length of extensometer in tensile testing was 50 mm. The resulting average values of tensile test results were taken by repeating nine tests.

The ultimate tensile strength (σ_T) and longitudinal tensile modulus (E_T) were calculated using Equations (1) and (2).

$$\sigma_T = P_{max}/A \quad (1)$$

$$E_T = \Delta\sigma/\Delta\varepsilon \quad (2)$$

where, P_{max} is the force that caused failure (N); A is the cross-sectional area (mm^2); $\Delta\sigma$ is the difference in applied tensile stress between the two strain points (MPa); $\Delta\varepsilon$ is the difference between the two strain points

The flexural properties of pultruded GFRP composite specimens were determined according to ASTM D790 [33] using an Instron E3000 testing machine. The three-point bending flexural test were carried out to determine values of elastic modulus and ultimate flexural stress. Flexural tests were carried out at crosshead speed of 5 mm/min and using a 3 kN load cell. The dimension of flexural specimens for thickness 6.3 mm are 120 mm long in direction of roving fibres and 23 mm wide. The span was chosen according to recommendation of ASTM D790 standard. Span-to-thickness ratio, L/t, must be 16:1. Thus span between two supports is 100 mm. Specimens with 3 mm thickness has 60 mm long and 11 mm wide. Span between two supports is 48 mm. The resulting average values of bending test results were taken by repeating seven tests.

The ultimate flexural stress (σ_f) and flexural modulus (E_f) were calculated using Equations (3) and (4).

$$\sigma_f = 3P_{max}L/2bt^2 \quad (3)$$

$$E_f = L^3\Delta F/4bh^3\Delta s \quad (4)$$

where: P_{max} is the failure force (N); L is the support span (mm); b is the width of specimen (mm); t is the thickness of specimen (mm); Δs is the difference in specimen mid-point deflections (mm); ΔF is the difference in loads at Δs respectively (N).

III. Results and Discussions

A. Tensile and Flexural Strength

Table 1 and Table 2 represent the comparison between tensile and flexural average strength for two pultruded composite with two type of resins and two thickness, respectively. The largest value in the tensile and flexural strength of the pultruded composites were obtained for composites with vinylester resin.

Replacement of a polyester resin (PE) by vinylester resin (VE) increases ultimate tensile strength of pultruded composites (Table 1). The maximum tensile stress reached 448.6 MPa and 353.7 MPa for pultruded composites with thickness 6.3 mm and 3 mm. The replacement of a polyester resin (PE) by vinylester resin (VE) gives an increase of ~18% and ~16%, respectively.

Table 1 Tensile strength

Specimen	Number of tests	Aver	Standard Deviation	Coefficient of Variation
		GPa	GPa	%
VE t=6.3 mm	9	448.6	21.58	5.07
PE t=6.3 mm	9	367.5	23.10	6.62
VE t=3 mm	9	353.7	24.99	7.45
PE t=3 mm	9	295.9	22.97	7.76

A similar increase is observed for the flexural strength in the pultruded composites (Table 2). Differences of the maximal stress between two resins achieve ~13% for specimens with thickness 6.3 mm and ~24% for specimens with thickness 3 mm.

TABLE 2 FLEXURAL STRENGTH

Specimen	Number of tests	Mean	Standard Deviation	Coefficient of Variation
		GPa	GPa	%
VE t=6.3 mm	7	506.0	20.24	4.00
PE t=6.3 mm	7	439.0	18.24	4.16
VE t=3 mm	7	268.6	21.80	8.12
PE t=3 mm	7	203.0	15.10	7.44

Averaged tensile stress-elongation curves of pultruded composites with two type of resins is plotted in Fig. 1. The stress-elongation curves for both type of resins were linear up to break. It can be observed that elongation at break for pultruded composite with polyester resin less than for composite with vinylester resin.

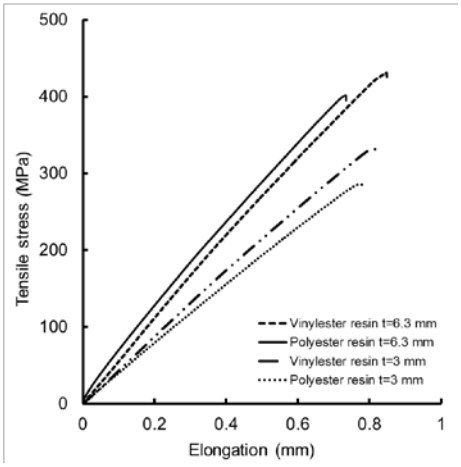

Fig. 1. Tensile stress-elongation curves of pultruded GFRP specimens with different thickness and resin.

Fig. 2. shows average flexural stress-displacement curves of pultruded composites with two type of resins. The displacement at failure had similar values for the pultruded composite with polyester and vinylester resin with the same thickness. The stress increased linearly until failure. The local destruction of the specimens begins on the lower surface in the middle of the span.

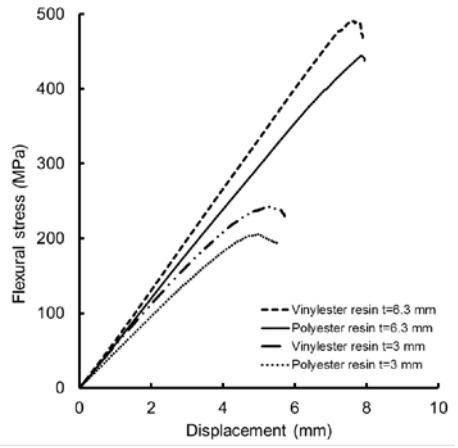

Fig. 2. Flexure stress-displacement curves of pultruded GFRP specimens with different thickness and resins.

B. Tensile and Flexural Elastic Modulus

The average results obtained for the tensile and flexural modulus with two type resin of the pultruded composites are presented in Table 3 and Table 4, respectively.

TABLE 3 TENSILE ELASTIC MODULUS

Specimen	Number of tests	Mean	Standard Deviation	Coefficient of Variation
		GPa	GPa	%
VE t=6.3 mm	9	28.36	3.41	12.04
PE t=6.3 mm	9	29.25	1.46	4.97
VE t=3 mm	9	22.60	2.34	10.36
PE t=3 mm	9	22.84	2.25	9.84

The pultruded composite with polyester and vinylester resin have approximately the same results in tensile modulus (Table 3). Percentage difference between polyester and vinylester resin does not exceed ~3% and ~1% for composites with thickness 6.3 mm and 3 mm, respectively.

Comparing the flexural modulis of the pultruded composite with two type of resin when thickness of specimens is 6.3 mm no significant differences were observed between them ~3%.

TABLE 4 FLEXURAL ELASTIC MODULUS

Specimen	Number of tests	Mean	Standard Deviation	Coefficient of Variation
		GPa	GPa	%
VE t=6.3 mm	7	19.78	1.37	6.90
PE t=6.3 mm	7	19.14	1.75	9.15
VE t=3 mm	7	9.90	0.96	9.68
PE t=3 mm	7	7.23	0.66	9.08

The replacement of a polyester resin by vinylester resin had the negligible influence on the flexural modulus of elasticity for composites with thickness 6.3 mm (table 3). The greatest increase of flexural modulus was obtained only for composites with thickness 3 mm and achieves ~27%. The flexural modulus of elasticity increased from 7.23 to 9.90 GPa.

The pultruded composite with thickness of 3 mm has a lower tensile and flexural modulus in compared to the corresponding values of composites with thickness of 6 mm. Different number of continuous filament mat in construction of pultruded composite may explain this difference.

IV. CONCLUSIONS

In the present research, the mechanical properties of pultruded GFRP composite with combination of two resin were studied. The knowledge about mechanical properties of pultruded glass fibre reinforced polymer composite based on polyester and vinylester resin are important because this product is relatively light and can be used in specific places. The experimental testing and analysis of pultruded GFRP composite were performed with the aim to investigate the influence of vinylester resin and polyester resin on the ultimate tensile and flexural strength, elastic and flexural modulus. For this reason, the composite specimens with two thickness and two type of resin were investigated experimentally. The results obtained allow us to conclude:

- The ultimate tensile strength was obtained for the pultruded composite with vinylester resin. The ultimate tension strength increase by ~18% and ~16% for pultruded composites with thickness of 6.3 mm and 3 mm, respectively.
- The ultimate flexural strength of pultruded composites with thickness 6 mm was increased by ~13% from 439.0 to 506.0 MPa. Composite with thickness 3 mm had the greatest percent increase in strength ~24%.
- The pultruded composite with polyester and vinylester resin have approximately the same results of tensile modulus.
- The replacement of a polyester resin by vinylester resin had the neglible influence on the flexural modulus of elasticity for composites with thickness 6.3 mm. The greatest increase of flexural modulus was obtained only for composites with thickness 3 mm and achieves ~27%. The flexural modulus of elasticity increased from 7.23 to 9.90 GPa.

ACKNOWLEDGEMENTS

This work was supported by the European Regional Development Fund, project No. 1.1.1.1/18/A/053 “An effectiveness improvement of conventional pultrusion processes”.

REFERENCES

[1] E. Barkanov, E. Eglitis, F. Almeida, M. C. Bowering, G. Watson, "Optimal Design of Composite Lateral Wing Upper Covers. Part I: Linear Buckling Analysis," Aerosp Sci Technol, vol. 38, pp.1-8, 2014. https://doi.org/10.1016/j.ast.2014.07.010

[2] E. Barkanov, E. Eglitis, F. Almeida, M. C. Bowering, G. Watson, "Optimal design of composite lateral wing upper covers. Part II: Nonlinear buckling analysis," Aerosp. Sci. Technol. vol. 51, pp. 87-95, 2016. https://doi./org/10.1016/j.ast.2016.01.020

[3] W. Hufenbach, L. Kroll, C. Holste, O. Täger and E. Barkanov, "Design of Dynamically Loaded Fiber-Reinforced Structures with Account of Their Vibro-Acoustic Behavior," Mech. Compos. Mater., vol. 37(2), pp. 145-152, 2001.

[4] Y. Koutsawa, W.L. Azoti, S. Belouettar, R. Martin and E. Barkanov, "Loss Behavior of Viscoelastic Sandwich Structures: a Statistical-Continuum Multi-Scale Approach," Compos. Struct., vol. 94, pp. 1391-1397, 2012. https://doi.org/10.1016/j.compstruct.2011.11.003

[5] R.F.S Hearmon, Introduction to Applied Anisotropic Elasticity, Oxford: Oxford University Press, 1961.

[6] V. Lusis, A. Krasnikovs, O. Kononova, V. Lapsa, R. Stonys, A. Macanovskis, A., Lukasenoks, "Effect of short fibers orientation on mechanical properties of composite material - fiber reinforced concrete," J. Civ. Eng. Manag., vol. 23(8), pp.1091-1099, 2017. https://doi.org/10.3846/13923730.2017.1381643.

[7] L. Filipczynski, Z. Pawlowski, J. Wehr, Ultrasonic Method of Testing Materials, London: Butterwoths, 1966.

[8] E. N. Barkanov, M. Wesolowski, P. Akishin and M. Mihovski, "Techniques for Non-Destructive Material Properties Characterisation," in Non-Destructive Testing and Repair of Pipelines, E. N. Barkanov, A. Dumitrescu, I. A. Parinov, Eds. Springer International Publishing, 2018, pp. 191-207.

[9] E. Barkanov, M. Wesolowski, W. Hufenbach and M. Dannemann, "An Effectiveness Improvement of the Inverse Technique Based on Vibration Tests," Comput. and Struct., vol. 146, pp. 152-162, 2015. https://doi.org/10.1016/j.compstruc.2014.10.006

[10] M. Wesolowski and E. Barkanov, "Improving Material Damping Characterization of a Laminated Plate," J. Sound Vib., vol. 462, 114928, 2019. https://doi.org/10.1016/j.jsv.2019.114928

[11] E. Barkanov, P. Akishin, R. Emmerich, M. Graf, "Numerical simulation of advanced pultrusion processes with microwave heating," in: Proceeding of the VII European Congress on Computational Methods in Applied Sciences and Engineering, 2016, pp. 7720-7738. https://doi.org/10.7712/100016.2368.5953

[12] N. Uddin, Developments in Fiber-reinforced polymer (FRP) Composites for Civil Engineering, Woodhead Publishing, 2013.

[13] E. Barkanov, P. Akishin, N.L. Miazza, S. Galvez, "ANSYS-based algorithms for a simulations of pultrusion processes, "Mech. Adv. Mater. Struc., vol. 5, pp. 377-384, 2017, https://doi.org./10.1080/15376494.2016.1191096

[14] E. Barkanov, P. Akishin, N.L. Miazza, S. Galvez, N. Pantelelis, "Experimental validation of thermo-chemical algorithm for a simulation of pultrusion processes, " IOP Conf. series: Journal of Physics:Conf. series, vol. 991, 2018, https://doi.org/0.1088/1742-6596/991/1/012009

[15] E. Barkanov, P. Akishin, E. Namsone, A. Bondarchuk, N. Pantelelis, "Real time characterization of pultrusion processes with a temperature control," Mech. Compos. Mater., vol. 56(2), pp. 135-148, 2020. https://doi.org/10.1007/s11029-020-09868-4

[16] Y. R. Chachad, J, A, Roux, J. G. Vaughan, E. S. Arafat, "Thermal model for three-dimensional irregular shaped pultruded fiberglass composites," J. Compos. Mater, vol. 6, pp. 692-721, 1996. https://doi.org/10.1177/002199839603000604

[17] I. Baran, C.C. Tutum, J. H. Hattel, "The effect of thermal contact resistance on the thermosetting pultrusion processes," Composites: Part B, vol. 45, pp. 995-1000, 2013, https://doi.org/10.1016/j.compositesb.2012.09.049

[18] A.S. Mosallam, A. Bayraktar, M. Elmikawi, S. Pul, S. Adanur, "Polymer composites in construction: an overview," vol. 2, p. 25, 2015. http://dx.doi.org/10.15226/sojmse.2014.00107

[19] A. Vedernikov, A. Safonov, F. Tucci, P. Carlone, I. Akhatov, "Pultruded materials and structures: A review," J. Compos. Mater., vol. 54(26), pp. 4081–4117, 2020. https://doi.org/10.1177/0021998320922894

[20] L.C. Bank, "Composites for Construction: Structural Design with FRP Materials, " John Wiley & Sons, 2006.

[21] A. K. Gand, T.-M. Chan, J. T. Mottram, "Civil and structural engineering applications, recent trends, research and developments on pultruded fiber reinforced polymer closed sections: a review," Front. Struct. Civ. Eng., vol. 7(3), pp. 227–244, 2013. https://doi.org/10.1007/s11709-013-0216-8

[22] H. Xin, Y. Liu, A.S. Mosallam, J. He, and A. Du, "Evaluation on material behaviors of pultruded glass fiber reinforced polymer (GFRP) laminates," Compos. Struct., vol. 182, pp. 283–300, 2017. https://doi.org/10.1016/j.compstruct.2017.09.006

[23] R.W. Meyer, Handbook of Pultrusion Technology. Springer-Verlag, NJ, 1985

[24] J. R. Correia, M.M. Gomes, J.M. Pires, F.A. Branco, "Mechanical behaviour of pultruded glass fibre reinforced polymer composites at elevated temperature: Experiments and model assessment," Compos. Struct., vol. 98, pp. 303–313, 2013. https://doi.org/10.1016/j.compstruct.2012.10.051

[25] E. Madenci, YO.. Özkılıç, L. Gemi, "Experimental Experimental and theoretical investigation on flexure performance of pultruded GFRP composite beams with damage analyses," Compos. Struct., vol. 242, pp. 112-162, 2020. https://doi.org/10.1016/j.compstruct.2020.112162

[26] A. Landesmann, C.A. Seruti, E.M. Batista, "Mechanical Properties of Glass Fiber Reinforced Polymers Members for Structural Applications," Mat. Res., vol. 18(6), pp. 1372–1383, 2015. https://doi.org/10.1590/1516-1439.044615

[27] E. Barkanov, P. Akishin, E. Namsone, J. Auzins, A. Morozovs, "Optimization of Pultruzion Processes for an Industrial Application," Mech. Compos. Mater., vol. 56(6), pp. 697-712, 2021, https://doi.org/10.1007/s11029-020-09868-4

[28] V. Antonucci, A. Cusano, M. Giordano, J. Nasser, L. Nicolais, "Cure-induced residual strain build-up in a thermoset resin," Composites: Part A, vol.37, pp. 592-601, 2006, https://doi.org/10.1016/j.compositesa.2005.05.016

[29] O. Kononova, A. Krasnikovs, G. Harjkova, V. Lusis, "Numerical simulation of mechanical properties for composite reinforced by knitted fabric," in: Proceeding of the 11th World Congress on Computational Mechanics (WCCM) / 5th European Conference on Computational Mechanics (ECCM) / 6th European Conference on Computational Fluid Dynamics (ECFD), 2014, pp. 2925-2932.

[30] A.M. Fairuz, S.M. Sapuan, E.S. Zainudin, C.N.A. Jaafar, "Polymer composite manufacturing using a pultrusion process: a review," Am J. Appl. Sci., vol. 11, pp. 1798–1810, 2014. https://doi.org/10.3844/ajassp.2014.1798.1810

[31] J.M. Sousa, M. Garrido, J.R. Correia, S. Cabral-Fonseca, "Hygrothermal ageing of pultruded GFRP profiles: Comparative study of unsaturated polyester and vinyl ester resin matrices," Composites Part A: Applied Science and Manufacturing, vol. 140, 106193, 2021. doi:10.1016/j.compositesa.2020.106193

[32] ASTM D3039. Standard Test Method for Tensile Properties of Polymer Matrix Composite Materials, ASTM International, West Conshohocken, PA (2017).

[33] ASTM D790. Standard Test Methods for Flexural properties of Unreinforced and Reinforced Plastics and Electrical Insulating Materials, ASTM International, West Conshohocken, PA (2017).

Environment. Technology. Resources. Rezekne, Latvia
Proceedings of the 13th International Scientific and Practical Conference. Volume 3, 159-162

Application of Artificial Neural Networks in the Context of Active Magnetic Bearing Control Systems

Alexander Kravtsov
Department of Electric Power Engineering, Electric Drive and Automation Systems
Pskov State University
Pskov, Russia
avkravtsov@inbox.ru>

Konstantin Vukolov
Department of Electric Power Engineering, Electric Drive and Automation Systems
Pskov State University
Pskov, Russia
kasyanvukolov@yandex.ru

Igor Plokhov
Department of Electric Power Engineering, Electric Drive and Automation Systems
Pskov State University
Pskov, Russia
igor_plohov@list.ru

Igor Savraev
Department of Electric Power Engineering, Electric Drive and Automation Systems
Pskov State University
Pskov, Russia
igor_savraev@mail.ru

Sergey Loginov
Department of Electric Power Engineering, Electric Drive and Automation Systems
Pskov State University
Pskov, Russia
lsy1@mail.ru

Abstract **- The article is devoted to the application of neural network methods and genetic algorithms in solving problems of controlling an electric drive of an active magnetic suspension. The method of rolling moment for eliminating an imbalance is considered. The scheme of the neural network controller and the curves of the transients in the open single-mass electromechanical system and in the system c of the neurocontrollers are presented.**

Keywords - Active magnetic bearing, neural network the neural network controller, transient simulation.

I. INTRODUCTION

Active magnetic bearing (AMB) is a complex mechatronic device, which makes it possible to achieve the noncontact suspension of electric machine rotor towards a stator. The process of fitting the stable rotor position is accomplished by the magnet gravity power, that influences the rotor from the side of electromagnets [1]. The AMB control loop configures the current in magnet coils, according to measures from the rotor displacement sensors or by the signal from magnetic flux sensor. The primary advantages of an AMB system are meant to be relatively high carrying capacity, high-level mechanical resistance, ability to gain a persistent non contact body bearing, a broad range to vary stiffness and buffering and opportunity to apply the AMB system in cases of high-speed rotation, in low and high temperatures. Negative points of applicable AMB devices are the large cost of a final target device and the high complexity of both system engineering and controller implementation [2].

There is a number of issues, which could finally get a resolution and thus make it possible to reduce both engineering self-cost and operation cost. One of such issues is the minimisation of human labour from the perspective of system design and operational process. The other relevant problem is the complete AMB diagnostic system synthesis. These above-described topics can be considered in terms of artificial intelligence, including neural network application, that now becomes common use in control system realisations and in diagnostics of electromechanic facilities.

Online ISSN 2256-070X
https://doi.org/10.17770/etr2021vol3.6531

II. Review of Current Investigations in the Problem Spaces

A. Modern view on electromechanic system diagnostics and operation using neural network technologies

One of the viable approaches in order to improve the inspection system functional efficiency and to achieve better AMB diagnostics could be the application of complex intelligent computer technologies. The idea of NN usage in terms of gaining required diagnostic and propagation results leads to a sufficient attenuation of the electromechanical system diagnostics process. The ways of neural network usage in the electromechanical diagnostics systems are listed below:

- NN application for parameter-oriented valuation of AMB elements. Here NN provides the ability to compare the current AMB state and the non-defect element model.
- NN application for electromagnetic system parameters propagation. Developing appropriate techniques allows to formulate variable relations as polynomials.
- NN application in pattern recognition systems. NN provides a common classification of an equipment state, namely the distribution of the current state to one of state classes (accurate or inaccurate with a concrete defect type), that is rated by the given trial type or measure type.

NN application in diagnostics and in electromechanic facility propagation tasks carries out these several positive points:

- For neural network algorithm implementation the minimum of object info is required.
- In case if NN synthesis it is possible to evaluate a parallel information processing, that, firstly, improves the system operational speed, and, secondly, leads to a higher system reliability [3].

B. Direct electric motor torque control using a neural network

One of the vital issues in electrical motors area is the problem of current control systems modification via new non-conventional approaches and control algorithms, which could be artificial neural networks (NN) and fuzzy-logic. Among these are the NN stator flux-linkage observer and the special direct torque control device, published in IJAREEIE [4, 5].

The main difference of the fuzzy-logic direct control system in respect of the traditional one, based on an optimized switch table, is that there occurs a neural block that identifies the electrical motor parameters and the parameters of a rotation speed fuzzy controller, see Figure 1. The duty of the neural network block is to calculate electromotor characteristics [6]. The neuro-fuzzy controller appears to be an artificial neural network, that is trained by the regular laws of rotor rotation speed proportional-integral controller.

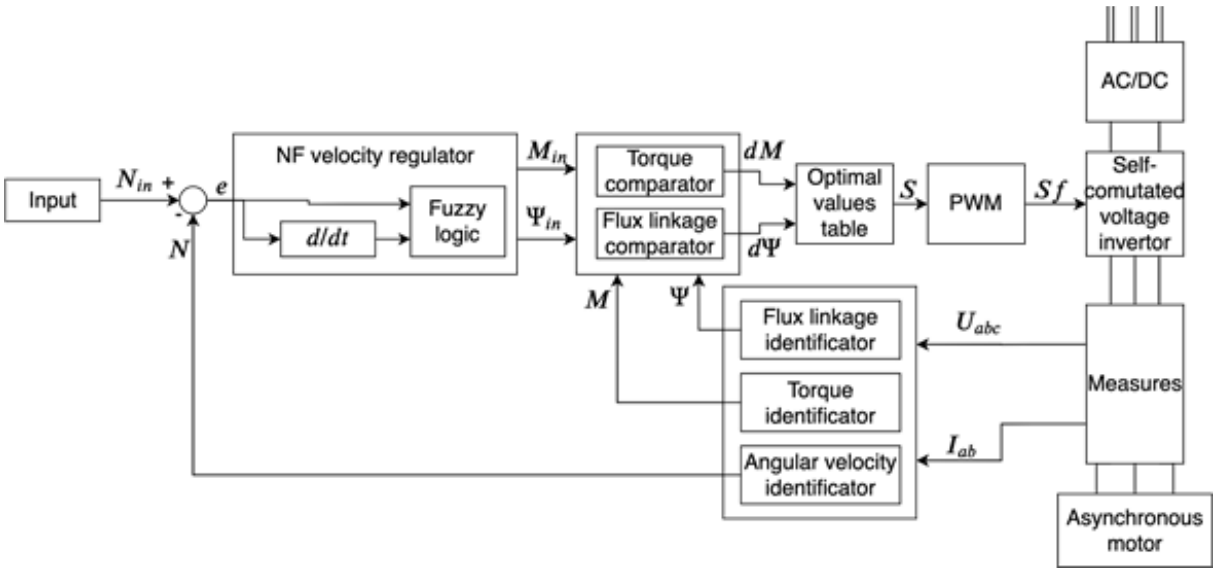

Fig. 1. An asynchronous motor control system with neural network block, N_{in} - velocity threshold, N - rotor velocity, ψ - magnetic flux, M - torque on the motor shaft, S - control signal, Sf - modulated signal, U - motor coil voltage, I - motor coil current.

The main difference of the fuzzy-logic direct control system in respect of the traditional one, based on an optimized switch table, is that there occurs a neural block that identifies the electrical motor parameters and the parameters of a rotation speed fuzzy controller, see Figure 1. The duty of the neural network block is to calculate electromotor characteristics [6]. The neuro-fuzzy controller appears to be an artificial neural network, that is trained by the regular laws of rotor rotation speed proportional-integral controller.

The rotor rotation speed controller provides better quality and higher speed of the transient process. Therefore, the combination of fuzzy controller and

parameters identifier block in the electrical motor system would lead to the speed improvement of the controller itself, as well as to higher adaptiveness due to data integrating.

C. AMB control torque method using multilayer perceptrons

The current discovery is about the neural network application in terms of AMB control with torque method. This new method can be applied to the active magnetic bearing in order to eliminate the unbalance [7].

Torque method is used for training the NN with the aim to minimize the error between an estimated model and the real model of the AMB. The dynamic equation of the AMB is given by (1) [8].

$$D(q)\ddot{q} + h(q,\dot{q}) + T = u \qquad (1)$$

where *D*- tensor of inertia, q - rotor position matrix, h - rotor Coriolis matrix, *T* - rotor mechanical energy, *U* - external torque matrix.

Since there are always uncertainties, the ideal error response cannot be achieved in general. The neural network controller is introduced to compensate these uncertainties.

The new control law can be written as (2).

$$u(t) = \widehat{D}(q)v(t) + \widehat{h}(q,\dot{q}) + \tau_n \qquad (2)$$

where υ - rotor acceleration matrix, τ_n - neural network output value, *u(t)* - control signal.

The NN output τ_n cancels out the uncertainties caused by the inaccurate model in the computed torque controller.

The NN controller scheme is depicted on the Figure 2 [9].

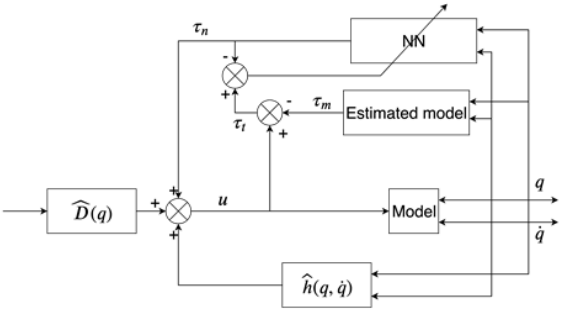

Fig. 2. Representation of the neural network controller, τ_n - neural network output, *u* - rotor external moment matrix, τ_m - math model output, $\tau_t = u - \tau_m$, $\hat{D}$ - estimated tensor of inertia, $\hat{h}$ - estimated rotor Coriolis matrix, *q* - rotor position matrix

Current study discovers the performance of the proposed NN controller. System temporal responses are investigated via modelling both standard PID-controller and the NN controller in Matlab. The process is modelled on five AMB axes, three choices of estimated model are highlighted. Figure 3 shows, for instance, the results for the variable estimated model.

Simulations done in the study show very clearly the improvement of responses by NN controller for a magnetic bearing under a computed torque control, compare with classical controllers.

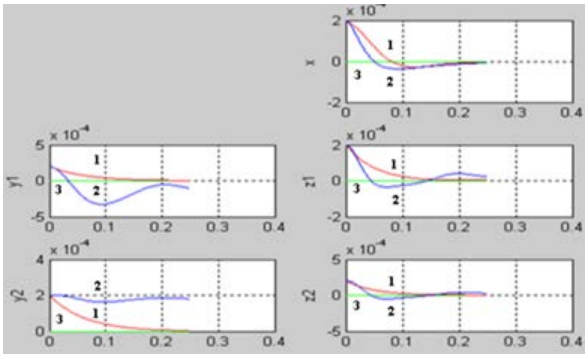

Fig. 3. Diagram representing the answers on the five axes for the variable estimated model, in red-1: System with MLP, in blue-2: PID alone, and in green-3: the desired answer

D. The application of NN approaches and genetic algorithms in objectives of electric motor control

Although the existing approaches of electromotor automatic control system synthesis, as, for instance, modal control approach, make it possible to develop well-controlled systems, the practical realization of such systems leads to a variety of technical problems. These are namely the necessity to get hard-to-measure control variables (such as the moment of elasticity) and in some cases the inability to built synthetic parameters in practice because of restrictions, that exist on real electrical motors. The replacement of linear controllers that are in service with non-linear ones can provide the proper output control response using less signal-from-coordinate dependencies. The opportunity for such a replacement is achieved owing to a non-linear controller, designed as the neural controller, which is actually a neural network (NN) [10].

In current topic the usage of NN and genetic algorithms with electrical motor devices lies over the concrete object assignment, which is about suppressing the self-excited frictional oscillations in electromechanic set-ups with a non-linear friction pair load.

With the NN usage, the solution is based on a single feedback of an easy measured axis, and such NN approach provides, apart from the steadiness, both the motor axis limitations required and the transient process quality.

As result there is a stable configuration build, transient processes of the system are depicted in Figure 4. Auto oscillation is gone and dynamical quality indexes are quite good enough.

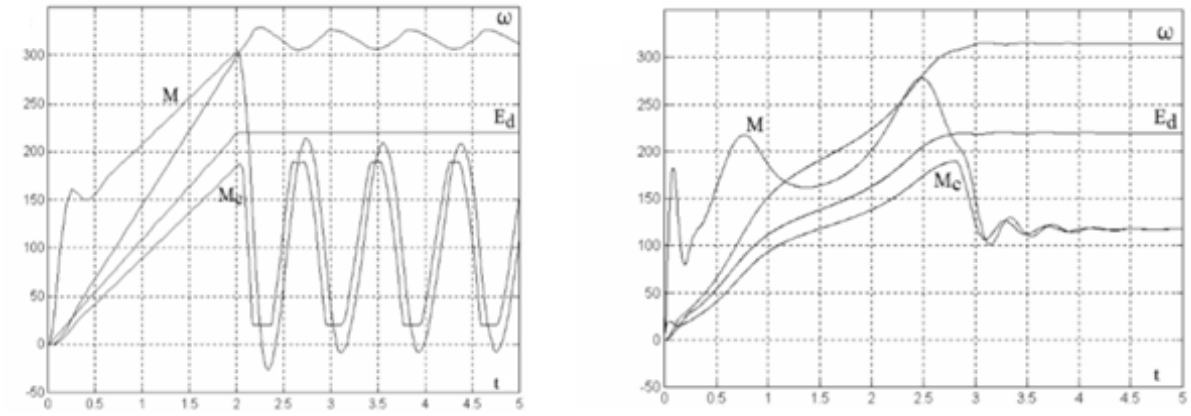

Fig. 4. Transient responses in the open-loop electromechanical configuration (on the left) and in the NN controller system (on the right), M - control torque, M_c - friction pair load, E_d - control signal, ω - rotor velocity, t – time.

CONCLUSIONS AND PERSPECTIVES

From the point of current discovery, it can be concluded, that a variety of investigations is being done in the area of NN application in electromechanic control and electromechanic diagnostics. Nevertheless, AMB control and AMB parameters optimization using NN, as well as NN usage in AMB diagnostics are quite unexplored and have a large potential for future investigations, so the researches and development in this area are certainly relevant.

REFERENCES

1. Zhuravlev U.N. Activnye magnitnye podshipniki: teoriya, raschet, primenenie [Active magnetic bearings: theory, calculations, application]. Saint-Petersburg.: Politekhnica Publ., 2003. pp. 22–30. (in Russian).

2. Bleuler H. Magnetic levitation: a challenge for control design in mechatronics. Toshiba Chair for Intelligent Mechatronics, 2011. pp. 578–583.

3. Bobokin G.I., Shprekher D.M. Primenenie neyronnykh setei dlya diagnostiki elektromekhanicheskikh sistem [Neural networks application in the field of electromechanical system diagnostics], 2003. Available at: https://cyberleninka.ru/article/n/primenenie-neyronnyh-setey-dlya-diagnostiki-elektromehanicheskih-sistem (in Russian).

4. Wang Ping, Li Bin, Huang Ruixiang, Li Guidan. Diangong jishu xuebaoTrans. China Electrotech, 2003. pp.5-8.

5. Gottapu K., Prashanth Y., Mahesh P., Sumith Y. Simulation of DTC IM Based on PI& Artificial Neural Network Technique. International Journal of Advanced Research in Electrical, Electronics and Instrumentation Engineering vol. 2, no. 7, issue 7, 2013.

6. Mamdani E.H., Assilian S. An experiment in linguistic synthesis with a fuzzy logic controller. Int. J. Man-Mach. Stud., vol. 7, pp.1-13, 1975.

7. F. Matsumura and T. Yoshimoto. System modeling and control design of horizontal shaft magnetic bearing system. IEEE Trans. Magn., vol. Mag-22, no. 5, 1986.

8. K. Noami and H. Yamaguchi. Robust control of magnetic bearing systems by means of sliding mode control. Proc. Int. Symp. Applicat. Electromagnetism, vol. ISEM 91, no. 1, 1991.

9. J. De Miras, A. Charara, B. Caron. Nonlinear control of a magnetic levitation system without premagnetization. IEEE Transactions on Control Systems Technology, vol.4, no.5, 1996, pp.513-523.

10. Narendra K.S., Parthasarathy K. Identification and control of dynamical systems using neural networks. IEEE Trans. on Neur. Net, vol. 1, no. 1, 1990, pp. 4-27.

Environment. Technology. Resources. Rezekne, Latvia
Proceedings of the 13th International Scientific and Practical Conference. Volume 3, 163-167

Investigation of the Influence of the Number of Repetitions on the Process of Laser Marking of HS6-5-2-5 Steel

Lyubomir Lazov
Rezekne Academy of Technology
Rezekne, Latvia
lyubomir.lazov@rta.lv

Nikolay Angelov
Technical University of Gabrovo
Gabrovo, Bulgaria
angelov_np@abv.bg

Edmunds Teirumnieks
Rezekne Academy of Technology,
Rezekne, Latvia
edmunds.teirumnieks@rta.lv

Abstract **- Today, methods for marking parts and components in industrial production are constantly improving, and they must meet several basic criteria for active traceability by consumers. The parameter that is of paramount importance for the quality of the marking is related to the contrast of the marked sign or QR code. To achieve optimal contrast, a number of technological factors and the functional relationships between them must be taken into account.**

The report examines the role of the number of repetitions on contrast in raster marking of HS6-5-2-5 tool steel products. The dependences of the number of repetitions on the speed and frequency are also taken into account - the main factors in the process of laser ablation. Graphs of the depth of the marking are drawn depending on the number of repetitions and the linear density of the pulses. The experiments were made with a fiber laser. By the performed analyses the working intervals of processing between the studied factors are deduced, allowing to achieve the desired optimal result.

Keywords **-** ***laser marking, fiber laser, HS6-5-2-5 steel, number of repetitions, linear density of the pulses, speed, power density, contrast.***

I. INTRODUCTION

Laser marking of metals and alloys is a technological process that is widely used in production. It is used in mechanical engineering, automotive, aircraft, military industry, electronics, in the production of medical equipment, household goods and more.

The technological process of laser marking has been studied in the work of some authors [1 – 8]:

The paper [1] presents a study of laser micro processing of metals by using a high repetition rate femtosecond laser. On stainless steel (AISI 304), copper and aluminium the impact of the significant laser processing parameters onto the machining process was investigated, such as laser fluency, repetition rate, lateral pulse distance and polarisation. The machining results were evaluated by the ablation rate, surface roughness, process efficiency, material removal rate and the wall-angle. For complementary discussions the experimental data are compared with results achieved in theoretical analysis. Outgoing from the results appropriate laser processing parameters are derived in order to optimise the machining process.

The basic factors affecting the laser marking of products – volumetric density of the absorbed energy and the number of repetitions, were studied in the publication [2]. Experiments were conducted of marking the samples of stainless steel with fiber laser. The dependence of the contrast of marking from the power density for different number of repetitions, and also the volumetric density of the absorbed energy from speed was obtained and the experimental results analysed.

The report [3] presents the results of the measurements and analysis of the influence of laser process parameters on the color contrasting obtained. In this case, the relevant parameter, the field of high frequencies and low pulse energy were examined. It describes studies a properties of the laser radiation, such as, pulse width, average power, the intensity and beam diameter.

Laser marking tests are carried out on AISI 304 steel, using a Q-switched diode pumped Nd:YAG laser in [4].

Online ISSN 2256-070X
https://doi.org/10.17770/etr2021vol3.6567

The aim is to determine the correlation occurring between working parameters (i.e. pulse frequency, beam scanning speed, and current intensity) and resulting mark visibility. The latter is evaluated as the contrast index measured from digital images of the marks. To characterize mark features, its width and roughness are estimated, and analyses employing optical and scanning electron microscopy coupled with energy dispersive X-ray technique were carried out. An empirical model was built, and from it the best processing conditions for optimum mark visibility, taking into account the operating constraints of the laser system used, were drawn.

The paper [6] presents the results of the measurements and analysis of the influence of laser process parameters on the colour obtained. The study was conducted for titanium (Grade 2) using a commercially available industrial pulsed fiber laser. It was determined how a variety of different laser process parameters, such as laser power, the scanning speed of the material, the temperature of the material, the size of the marked area, and the position of the sample, relative to both the focal plane and the centre of the working field of the system, affect the repeatability of the colours created. Additionally, a comparison of the results for titanium with those obtained for stainless steel in a previous study is presented.

The influence of a number of basic quantities on the process of laser marking of metals and alloys as well as their mutual connection during the realization of the process is still not clarified. Also, lasers and laser marking systems are constantly being improved, which undoubtedly expands their application capabilities [9 – 12].

The aim of the development is to study the influence of the overlap coefficient when marking HS6-5-2-5 tool steel products with a fiber laser for different values of speed and linear density of the pulses.

II. THEORETICAL ASPECTS

The laser marking process is influenced by a number of physical quantities such as power density, speed, frequency and duration of pulses, pulse power, pulse energy, linear pulse density, linear energy density, effective energy, overlap coefficient, fill factor, coefficient of reflection, absorption capacity, wavelength of laser radiation, coefficient of thermal conductivity, coefficient of diffusivity, specific heat capacity, etc. In each specific case of marking (depending on the material, laser, marking method) studies must be performed. Numerical and / or real experiments can be performed to determine the optimal parameters of the technological process. The speed and linear density of the pulses are quantities that have a significant impact on the studied process.

Marking speed is one of the most important parameters of the technological process. The time of impact on the sample and the energy that is absorbed in the material in the impact zone depend on it. It is decisive in choosing the method of marking.

The requirements for the speed in the technological process of laser marking are contradictory: on the one hand, the speed must be high in order to reduce the time for performing the operation, and therefore to obtain greater efficiency in the production of the product; on the other hand, it must be relatively small in order to be able to absorb the required amount of energy under the influence in order to reach the required temperature and contrast of the marking. By taking into account the other factors influencing the process, a balance must be found between these contradictory requirements and optimal technological parameters must be obtained to achieve laser marking with the required contrast.

Linear density of the pulses is a physical quantity equal in number to the number of pulses dropped per unit length

$$L_p = \frac{\nu}{v} \ , \tag{1}$$

where ν is the frequency, v – the marking speed.

It is a quantity of complex character. It is determined both by a quantity related to the laser source (marking speed) and by a quantity related to the technological process (marking speed). Linear density of the pulses affects the contrast and homogeneity of the resulting marking.

For each drawn square, the contrast was determined by measuring the Grey colour saturation of the resulting marking J_x and the background of the sample J_f. The contrast of the marking was determined by the formula.

$$k* = \frac{J_x - J_f}{J_b - J_f} \times 100\% \tag{2}$$

where J_b is the saturation of the black colour

III. MATERIAL AND LASER SYSTEM

The experiments were performed with samples of HS6-5-2-5 rapid tool steel. It is widely used in industry. Steel HS6-5-2-5 is used for making cutters, turning knives, cutting strips for wood and steel, for roughing and semi-finishing tools when machining advanced alloy and stainless steels in conditions of increased heating of the cutting edge. It is high carbon steel and has a high content of chromium, molybdenum, tungsten, vanadium and cobalt. Some physical characteristics of the steel are given in Table 1.

TABLE 1. BASIC PHYSICAL CHARACTERISTICS OF THE HS6-5-2-5 RAPID TOOL STEEL

Characteristic	Value
Coefficient of thermal conductivity k, W/(m.K)	27
Specific heat capacity c, J/(kg.K)	460
Density ρ, kg/m^3	8200
Coefficient of diffusivity a, m^2/s	7.16×10^{-6}

The experiments were performed with a laser technological system with a fiber laser. Some of its basic parameters are presented in table. 2. The fiber laser is an innovative laser operating in pulsed mode. The wavelength of its radiation is in the near infrared region. It has

extremely high beam quality and high efficiency. The laser system has high positioning accuracy.

TABLE 2. BASIC PARAMETERS OF A LASER TECHNOLOGICAL SYSTEM WITH A FIBER LASER

Parameter	Value
Wavelength λ, nm	1064
Power P, W	20
Diameter of working spot d, μm	35
Frequency ν, kHz	80
Pulses duration τ, ns	100
Pulse energy E_p, mJ	0.25
Pulse power P_p, kW	2.50
Beam quality M^2	< 1.1
Positioning accuracy, μm	2.5
Efficiency, %	40

IV. EXPERIMENTS

The study of the influence of the number of repetitions on the process of laser marking of samples of alloy tool steel HS6-5-2-5 was performed in two directions:

1. Investigation of the dependence of the contrast of the marking on the speed

Samples of the study steel were prepared. A raster method of marking was applied. Squares with a side of 5 mm were marked once, twice, three times and five times. The marking speed varied in the interval $v \in [40, 220]$ mm/s throug 20 mm/s. The parameters that are kept constant are presented in Table 3. The marked sample from HS6-5-2-5 steel is given in Fig. 1. The contrast for each mark was determined. Five contrast measurements were made at different locations in each square and the mean contrast value was determined.

TABLE 3. PARAMETERS THAT DO NOT CHANGE DURING THE EXPERIMENTS.

Parameter	Value
Power density q_s, W/m^2	$7.66.10^9$
Diameter of work spot d, μm	35
Frequency ν, kHz	20
Pulse duration τ, ns	100
Raster step Δx, μm	50
Defocus Δf, mm	0

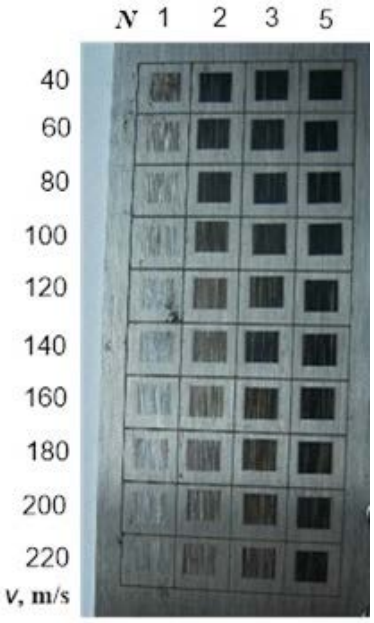

Fig. 1. Sample of tool steel HS6-5-2-5 marked with fiber laser

Results analysis

The graphs of the experimental dependence $k^* = k^*(v)$ are presented in Fig. 2 for different number of repetitions of the marked squares: N = 1; 2; 3 and 5. The following conclusions can be done from their analysis:

- As the number of repetitions increases, the contrast of the laser marking increases nonlinearly;
- When the speed changes in the interval интервала $v \in [40, 100]$ mm/s in the double raster marking of the lines the contrast k^* increases by about 62% compared to their single marking (the graphics in orange and red, respectively). When the speed changes in the interval $v \in [100, 220]$ mm/s this increase is about 2 times. The explanation for this experimental result is that the first treatment increases the absorption capacity in the impact zone. Thus, when re-acting on the treated surface, more energy is absorbed by the incident laser radiation;
- The number of repetitions N = 3 and N = 5 results in a higher contrast k^* of the marked area compared to that of N = 2, but the increase in contrast is about 25% and 40% respectively. These results show that for laser marking of the studied tool steels it is not necessary to do a large number of repetitions (greater than N = 2). This leads to a loss of time and energy to perform the marking, which increases the production cost of

the product. In this case, the quality of the marking does not change noticeably;

- Double marking should also be used when the power of the laser source is not sufficient to obtain a quality marking on a single marking. For example, a contrast k^* = 37% is obtained (see Fig. 2) at a speed v = 40 mm/s for the used power density and the marking is well perceived when using special readers. A contrast k^* = 60% is obtained (see Fig. 2) for double marking at the same parameters and the marking is well perceived both visually and when using special readers.

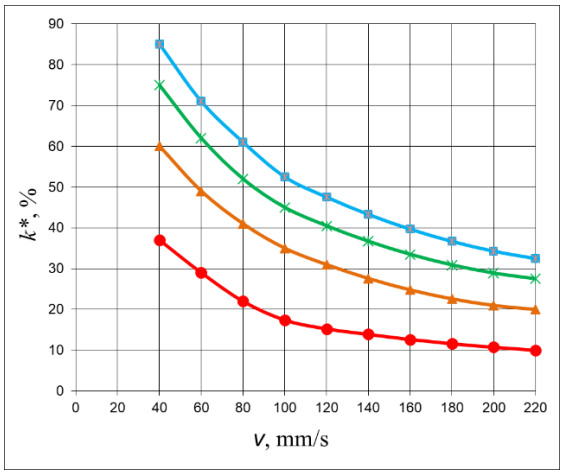

Fig. 2. Graphs of the experimental dependence $k^* = k^*(v)$ for marking with fiber laser at number of repetitions: red color - N = 1; orange color - N = 2; green color - N = 3; blue color - N = 5.

2. Investigation of the dependence of the contrast of the marking on the linear density of the pulses

The raster marking method was used again. Squares with a side of 5 mm were marked once, twice and three times. The linear pulse density varied in the interval $L_p \in$ [125, 1000] mm^{-1} throug 125 mm^{-1}. The parameters that are kept constant are presented in Table 4. The contrast was determined for each marked square. Figure 3 shows a sample with a single (top row) and double marking (bottom row) with power density q_s = 7.66.10^9 W/m^2.

TABLE 4. PARAMETERS THAT DO NOT CHANGE DURING THE EXPERIMENTS.

Parameter	Value
Power density q_s, W/m^2	7.66.10^9
Diameter of work spot d, μm	35
Speed v, mm/s	80
Pulse duration τ, ns	100
Raster step Δx, μm	50
Defocus Δf, mm	0

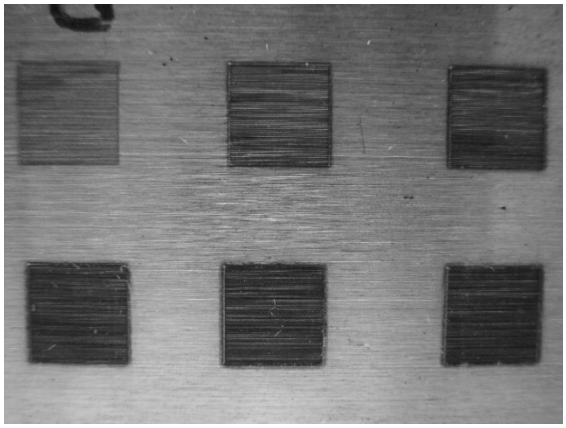

Fug. 3. Single (top row) and double (bottom row) raster marked fields with fiber laser

Results analysis

The graphs of the experimental dependence $k^* = k^*(L_p)$ are presented in Fig. 4 for different number of repetitions of the marked squares: N = 1; 2 and 3. Several conclusions follow from the analysis of the graphs:

- As the linear density of the pulses increases, the contrast of the marking increases nonlinearly for all three graphs;;
- In the interval $L_p \in$ [125, 375] mm^{-1} the curves are significantly steeper than in the interval $L_p \in$ [375, 1000] mm^{-1};
- At number of repetitions N = 2 the contrast is from 25% to 55% higher than at number of repetitions N = 1 for the whole studied interval of the linear pulse density;
- At number of repetitions N = 3 the increase of the contrast is from 40% to 100% greater than at number of repetitions N = 1 for the whole studied interval of the linear density of the pulses;
- Again, it is seen that the required number of repetitions should not be greater than N = 2.

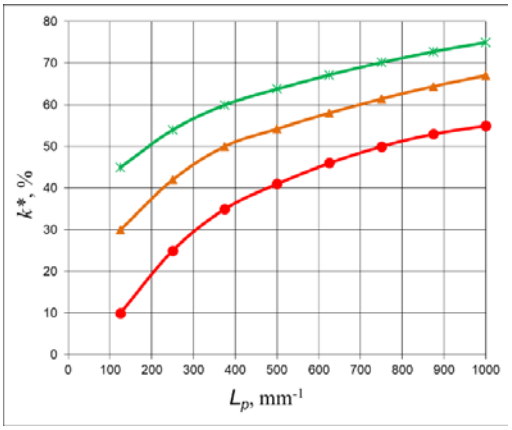

Fig. 4. Graphs of the experimental dependence $k^* = k^*(L_p)$ for marking with fiber laser at number of repetitions: red color - N = 1; orange color - N = 2; green color - N = 3.

V. CONCLUSIONS

The study we present in this report shows the direct relationship between the contrast in the marking area and the number of repetitions. The relationship between the contrast and the processing speed in the range from 40 mm/s to 220 mm/s with single and multiple repetitions of the laser impact zone was also analysed.

The influence of the linear energy density (pulse tracking frequency in combination with the processing speed) on the contrast in single and multiple repetitions of the marked area was also analysed.

The correct assessment of the impact of these technological parameters on the contrast of the marking made on samples of HS6-5-2-5 rapid tool steel contributes to the optimization of the production process and increases the wear resistance of the marking and the efficiency of automated QR codes reading to track the quality of the products.

REFERENCES

[1] Schille, J., et al., Micro processing of metals using a high repetition rate femto second laser: from laser process parameter study to machining examples. in Proc. of 30th Int. Congress on Appl. of Lasers and Electro-Optics (ICALEO 2011), Orlando FL, USA, 2011, DOI: 10.2351/1.5062326

[2] Angelov, N., Investigating the Influence of the Number of Repetitions and Volumetric Energy Density on Laser Marking of Products, Contemporary Materials V-2, Vol. 5 No. 2, 250-253, 2014, DOI: https://doi.org/10.7251/cm.v2i5.1738

[3] Lazov, L., H. Deneva, P. Narica, Factors Influencing the Color Laser Marking, Environment. Technology. Resources, Rezekne, Latvia, Proceedings of the 10th International Scientific and Practical Conference. Volume I, 102-107, 2015, DOI: 10.17770/etr2015vol1.223

[4] Leone, C., S. Genna, G. Caprino, I. De Iorio, AISI304 stainless steel marking by a Q-switched diode pumped Nd:YAG laser", Journal of Materials Processing Technology 210, 1297-1303, 2010, DOI: https://doi.org/10.1016/j.jmatprotec.2010.03.018

[5] Dolchinkov, N., Practical Research Of Marking And Cutting Of Textiles With Increased Resistance, Using CO_2 Laser, Journal of Physics: Conference Series , Volume 1681, 2020 012014 IOP Publishing DOI: 10.1088/1742-6596/1681/1/012014

[6] Antonczak, A., B. Stepak, P. aweł E. Koziol, K. Abramski, Krzysztof, The Influence of process parameters on the laser induced coloring of titanium, Applied Physics A 115(3):1003-1013, 2013, DOI: 10.1007/s00339-013-7932-8

[7] Wellershoff, S.-S., Untersuchungen zur Energiere-laxationsdynamik in Metallen nach Anregung mit ultrakurzen Laserpulsen, in Fach-bereich Physik, Freie Universität Berlin: Berlin, 2000, 159 p., ISBN 3898251322, 9783898251327

[8] Dichev, D., I. Zhelezarov, T. Karadzhov, N. Madzharov and D. Diakov, "Method for measuring motion parameters of moving objects," 12th International Scientific and Practical Conference on Environment, vol. 3, 27-31, 2019, DOI: 10.17770/etr2019vol3.4131

[9] Yasa, E,J.-P. Kruth, Investigation of laser and process parameters for Selective Laser Erosion, Precision Engineering, Volume 34, Issue 1, 101-112, 2010, DOI: https://doi.org/10.1016/j.precisioneng.2009.04.001

[10] Nolte, S., et al. High Repetition Rate Ultrashort Pulse Micromachining with Fiber Lasers. in Fiber Laser Applications: Optical Society of America, 2011, DOI: https://doi.org/10.1364/FILAS.2011.FThC1

[11] Dolchinkov, N., N. Nichev, Structure and Management of the National Automated System for Permanent Control of the Radiation Gamma Background in Bulgaria, Land Forces Academy Review, Vol. XXII, No 2(86), 115-121, 2017, DOI: https://doi.org/10.1515/raft-2017-0016

[12] Pencheva T., D. Pulov, B. Gyoch, M. Nenkov, Design of CCD Optical System for Thermal IR Spectral Region. In pr. 29-th International Spring Seminar fn Electronics Technology, St. Marienthal, Germany, Verlag Dr. Markus A. Detert, 413-418, 2006, ISBN 3-934142-23-0, DOI: 10.1109/ISSE.2006.365380

Environment. Technology. Resources. Rezekne, Latvia
Proceedings of the 13th International Scientific and Practical Conference. Volume 3, 168-172

On the Possibility of Marking Eggs with a CO_2 Laser

Lyubomir Lazov
Rezekne Academy of Technologies
Rezekne, Latvia
llazov@abv.bg

Pēteris Čeirs
Rezekne Academy of Technologies
Rezekne, Latvia
ceirs@inbox.lv

Imants Adijans
Rezekne Academy of Technologies
Rezekne, Latvia
imants.adijans@rta.lv

***Abstract* - A number of policies and standards regarding food safety issues and quality management have been established for the food industry. One of these requirements is related to the marking of food products describing the expiration date, content and quality. The report examines the possibility of using laser technology to mark chicken eggs. The contrast of the laser marking is the main criterion for determining its quality. The study examines the functional dependences of the contrast on the main technological parameters of the marking process: laser output power (7 – 20.3 W) and processing speed (50 - 300 mm/s). As a result of the research, optimal parameters for marking with a technological laser system CO_2 have been determined.**

.

Keywords - laser marking, marking of eggs, CO2 laser, laser engraving

I. INTRODUCTION

Today, in most countries of the world, food safety is very important. A number of norms and standards for food safety and quality have been developed for the food industry [1]. One of these requirements is related to the marking of food products describing the expiration date, content, quality, etc. Tracking is one of the key tools for achieving quality and safety standards. Tracking allows you to determine the current location of the product, its origin and expiration date, and also provides information about processing, retailing and the final purpose of goods [2]. To ensure high quality in the trading network, automated systems are often used. Technologies for automated identification of goods and data collection are based on barcodes, QR codes, optical recognition of encoded information, etc.

One of the most popular foods is chicken eggs. According to the International Independent Institute for Agrarian Policy (МНИАП), since 2000, the total production of chicken eggs has increased by 1.4 times, and by 2035 the consumption of eggs in the world will increase by 50% [3]. Chicken eggs are usually marked with an alphanumeric code. Fresh eggs of class "A" - intended for human nutrition, are marked with a code consisting of numbers and letters [4] (see figure 1).

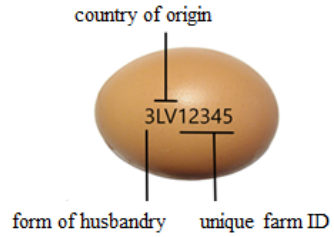

Figure 1. Marking a chicken egg with an alphanumeric code.

Traditionally, eggs are marked with an ink seal. This method of marking has such disadvantages as the need for chemical dyes, environmental pollution, the need for time for the ink to dry.Laser technology has developed at a very fast pace in recent decades. One of the main applications of laser technology is laser marking. Laser marking is also used in the food industry. The laser creates markings on the eggshell without the need for additional materials such as ink, while ensuring outstanding marking quality and consistency. Unlike ink markings, laser markings are not erased or smudged. The advantages of laser marking also include high speed, repeatability, efficiency and low operating costs. The method is non-contact, does not require a special working environment and can be easily automated and integrated into production lines. [5,6,7,14,15]

The aim of the present study is to analyse the capabilities of one industrial CO_2 laser system for marking eggs, to determine the optimal operating intervals for power and processing speed to achieve optimal marking contrast [8].

Online ISSN 2256-070X
https://doi.org/10.17770/etr2021vol3.6625

II. PROCESS RESEARCH EQUIPMENT

In the experimental studies we performed for marking the eggs we used a CO_2 laser technological system with a wavelength λ = 10.6 μm. Synchronous control of the on / off laser generation and the movement of the laser beam focusing system along a given contour along the X, Y axes, as well as the change in the laser radiation parameters, is carried out using a special computer program. A schematic diagram of an experimental setup for marking chicken eggs is shown in figure 2a. In the experiments we used the raster laser marking method (figure 2b).

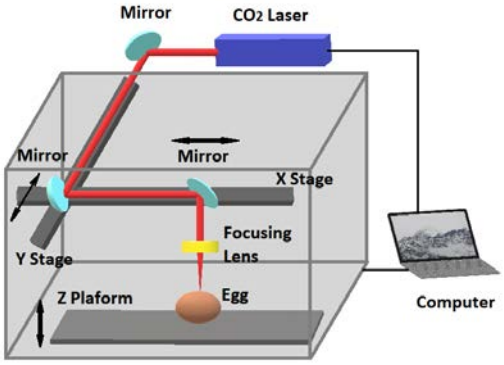

Figure 2a. Schematic diagram of an experimental setup for marking chicken eggs using a CO_2 laser.

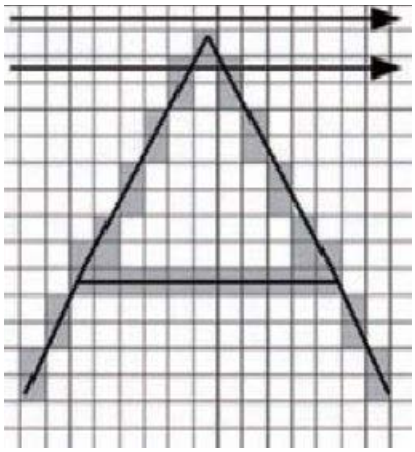

Figure 2b. Raster method of laser marking.

The main technical parameters of the CO_2 laser system SUNTOP ST-CC9060, with which the experiments were performed, are listed in table 1.

TABLE 1. TECHNICAL PARAMETERS OF CO2 LASER SYSTEM SUNTOP ST-CC9060

Laser type	CO_2 laser
Operation mode	CW
Laser wavelength	10.6 μm
Max. laser power	100 W
Process size	900 x 600 mm
Scanning speed	0 – 1000 mm/s
Positioning accuracy	<0.02 mm
Focal length	63.5 mm

The Ocean Optics STS VIS microspectrometer was used to determine the contrast in the measurements, measuring the reflectivity *R* [%] of the treatment area and comparing it with that of the surrounding surface. A schematic diagram of measuring the reflectance *R* [%] of the egg shell surface using a microspectrometer is shown in figure 3a. The reflected light spectrum from the unmarked egg shell surface (brown) and from the CO_2 laser marked egg shell surface is shown in Figure 3b.

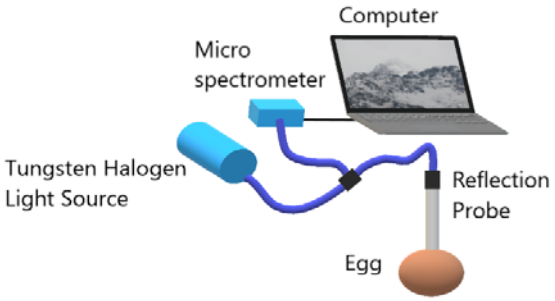

Figure 3a. Schematic diagram of measuring the reflectance *R* [%] of the surface of the shell of chicken eggs.

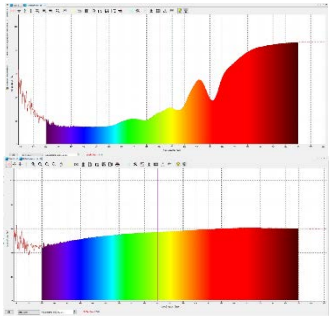

Figure 3b. The reflected light spectrum from the unmarked egg shell surface (above) and from the CO_2 laser marked egg shell surface (below).

III. SPECIFICS, PROPERTIES AND STRUCTURE OF THE MATERIAL SUBJECTED TO LASER TREATMENT

The shell of a chicken egg is a hard, porous shell. From above, the shell is covered with a thin over-scaled shell - cuticle, and from below it is firmly connected with a two-layer under-scaled shell. The cuticle is not strong and is easily destroyed by mechanical action (washing with brushes, etc.), but it protects a fresh egg from the influence of the external environment. The basis of the shell is a network of collagen-like protein fibers and an intermediate inorganic substance, which contains mainly carbonate and phosphate salts of calcium and magnesium, which provides a certain strength and resistance to mechanical stress. [9]

For a chicken egg, the shell has a thickness of 0.34 – 0.40 mm. The thickness of the eggshell depends on the mineral content of the feed. In the structure of the shell, two layers are distinguished. The outer layer is spongy and occupies 2/3 of the entire thickness. The inner layer is prismatic. The shell of a chicken egg has about 7000 through pores with a diameter of 4 to 40 microns. As a result, the shell is

permeable to gases, water and water vapor. The permeability of the shell to air is the same in both directions (from the inside and from the outside). Water enters from the outside into the middle as slowly as from the inside into the external environment. The permeability of the shell for carbon dioxide is better than for air, and vice versa for oxygen. The density of the shell is 2.14 – 2.17g/cm^3. [9,10]

Figure 4 shows the microstructure of an eggshell. The shell of a medium-weight chicken egg consists of 1.6% (0.1 g) of water, 98.4% (6 g) of dry substances, including organic - protein 3.3% (0.2g), lipids 0.03 (traces) and 95.1% (5.8 g) of inorganic substances. The shell mineral is 99% calcium carbonate. In eggs of birds with a hard shell, it exists in the most thermodynamically stable form - calcite. Inorganic phosphate, magnesium, zinc, copper, manganese, selenium and other elements that are present in small quantities can have a certain effect on the quality of the shell. [9]

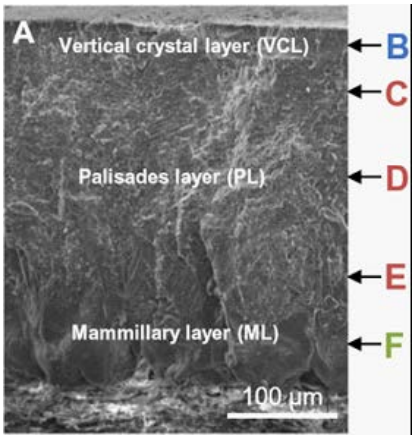

Figure 4. Microstructure of poultry eggshell, SEM (Scanning Electron Microscope) image. [11]

For chicken eggshell typical is structure with nano granules of various sizes (from 50 to 100 nanometres). Five layers can be distinguished with different average sizes of nanostructures, and this size increases from the outer layers of the shell to the inner ones. Figure 4: B - outer vertical crystalline layer VCL; C, D, E - middle columnar (palisade) layer PL, F - inner layer of hemispherical aggregates (mammillary) ML. [9,12]

IV. FACTORS AFFECTING THE PROCESS OF MARKING, AND METHODOLOGY FOR THE EXPERIMENT

In general, factors that affect the laser marking process can be divided into 3 main groups (figure 5a). Depending on the choice of the technological system and the mode of operation (pulse or CW mode), as well as the method of marking, the process affecting factors also change. In our study, due to the fact that the CO2 laser technological system operates in CW mode and only two methods are used (ablation and engraving), there are six factors that affect the contrast of the marking (figure 5b). These are: laser power density qs [W/cm2] (respectively the energy density Es [J/cm2]); marking speed v [mm/s]; distance between raster strokes Δx [mm] (raster step); focus offset Δf; number of repetitions; color of the treated surface. Laser power density represents laser source parameters. Marking speed, raster step, focus offset, and number of repetitions represent the parameters of the technological system and the method used. In terms of material properties, this is the color of the treated surface. In our specific case, the color of the examined chicken eggs is brown.

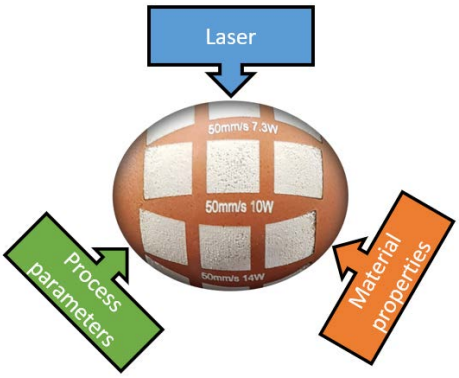

Figure 5a. Three main groups of factors that affect the laser marking process.

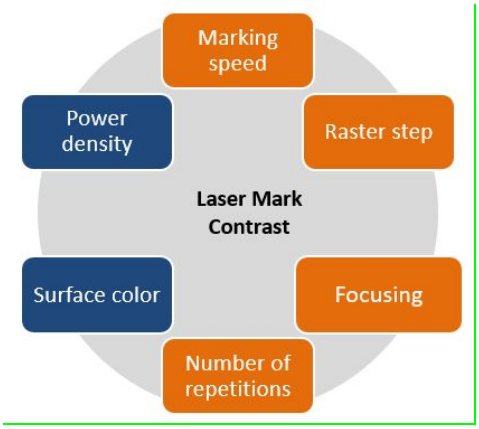

Figure 5b. Six factors that affect the contrast of the marking

The methodology of the experiment in the present study is related to the analysis of the contrast *k* as a function of the processing speed *v* and the power *P* of the laser radiation. Two series of experiments were carried out in which one of the two main parameters, processing power *P* and the speed *v* of the beam on the treated surface, was kept constant. The rastering method of marking is used to fill in a 10x10 mm square with a constant pitch between the raster lines Δx = 0.1 mm. This size made it possible to subsequently measure the reflectance *R* of the treated area

using a microspectrometer (figure 5a) and calculate the contrast *k*.

In the first series of experiments *k = k (P)*, the contrast *k* is studied in the range of power *P* change from 7.3 W to 20.3 W at six constant marking speeds *v*, respectively (50; 100; 150; 200; 250; 300 mm/s).

In the second series of experiments *k = k (v)*, the contrast *k* is investigated in the range of variation of the velocity *v* from 50 mm/s to 300 mm/s sequentially for six constant laser radiation powers *P*, respectively (7.3; 10; 12; 14; 17; 20.3 W). A total of 72 experiments were carried out and related measurements of the reflectivity *R*. The choice of research ranges for power *P* and speed *v* was made on the basis of our previous studies [13] related to the study of the functions *b = b (P)* and *h = h (v)*, where *b* and *h* are the width and depth of the marking lines on the treated surface. The aim was to achieve the depth *h* of the treated area less than 1/5 of the thickness of the chicken egg shell (0.34 ÷ 0.40 mm) and at the same time to achieve the maximum contrast *k* of the marking area. It should be borne in mind that the depth of the stained area per eggshell is only 150μm.

V. Results of Experimental Studies

The results of experimental studies of the effect of laser radiation power on the contrast of the marking zones are shown in figure 6a. We can see contrast versus power graphs for three different processing speeds: 50 mm/s; 150 mm/s and 300 mm/s. It is clearly seen from them that in the range from 7.3 W to 14 W, the contrast *k* increases nonlinearly for all three marking speeds, and in the range from 14 to 20.3 W, the dependence is almost linear. For the entire studied interval of power *P*, the contrast *k* in absolute value increases by about 14-16%. In order to better find out which of the two working intervals is more advantageous for operation from a technological point of view, ratio *Δk/ΔP* was calculated in the power range from 7.3 W to 14 W and from 14 W to 20.3 W. The results of these calculations are shown in Table 2.

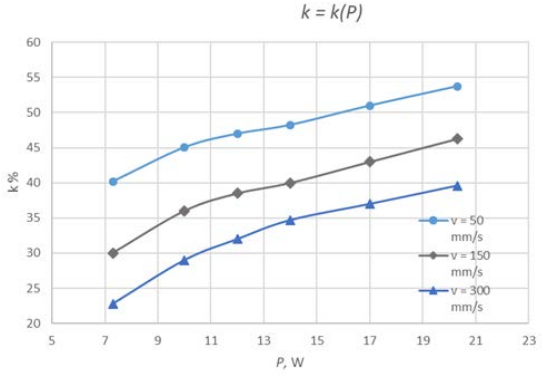

Figure 6a. Contrast *k* as a function of power *P*.

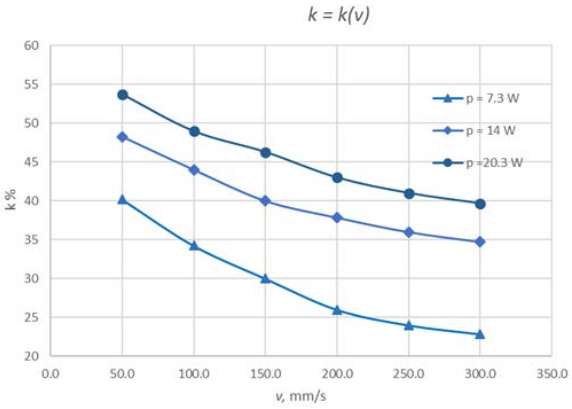

Figure 6b. Contrast *k* as a function of speed *v*.

The analysis of the results of experimental studies of the effect of the processing speed *v* on the contrast *k* is summarized and presented in the graphs (figure 6b). The graphs shows three dependences of the contrast *k* on the velocity *v* for three different laser radiation powers 7.3 W; 14 W and 20.3 W. For the investigated range of velocity *v* from 50 mm/s to 300 mm/s, a nonlinear decrease in contrast *k* is observed for all three laser powers. Comparing the three power graphs shows that the graph with *P* = 7.3 W has a greater slope than with 14 W and 20.3 W.

In order to better find out where the most successful working intervals are from the technological point of view, the rate of contrast change *Δk/Δv* was calculated in the speed range *v* from 50 mm/s to 300 mm/s. For better visualization of the analysis, the interval of velocity *v* is divided into two sections: 50 ÷ 200 mm/s and 200 ÷ 300 mm/s. The results of these calculations *Δk/Δv* are shown in Table 2.

Table 2. The rate of contrast change ΔK / ΔP, [%/W] in the power range and the rate of contrast change Δk/Δ *v* [%/mm·s-1] in the speed range.

Speed *v*, (mm/s)	Power *P*, 7.3 ÷14 W	Power *P*, 14 ÷20.3 W	Power *P*, (W)	Speed *v*, 50÷200 mm/s	Speed *v*, 200÷300 mm/s
50	1.8	0.70	7.3	0.093	0.03
150	1.5	0.95	14.0	0.07	0.035
200	1.2	0.75	20.3	0.073	0.04

Analysis of the graphs and tables shows that the lowest values of the contrast change rate are in the range for powers *P* - 14 ÷ 20.3 W and for processing speeds *v* - 200 ÷ 300 mm/s.

Finally, the following recommendations can be made from this analysis: In this research, as the recommended operating interval for optimal contrast (more than 35%) for the studied power ranges *P* = 7.3 ÷ 20.3 W and speed *v* = 50 ÷ 300 mm/s.

There may be recommendations as follows:

P = 14 ÷ 20.3 W. in the range for processing speed *v* = 200 ÷ 300 mm / s.

In this analysis, we were guided by two factors that are related to the optimization process:

- on the one hand - reading the markings, both visually and with the help of automatic recognition systems.
- on the other hand - to achieve a high processing speed *v* (200 ÷ 300 mm/s) with an optimal operating power *P* (14 ÷ 20.3 W) for a specific technological CO_2 laser system.

Another feature that we registered during the research is that in the area of marking there is no melting of the main material from which the eggshell is made. The interaction of the marking process is related to the sublimation method of processing, i.e. we have direct destruction and dusting of the base material.

VI. Conclusion

The ability to spot the right area, label and evaluate a product right on production lines is critical for laser marking of food and especially for chicken eggs. This study was divided into three phases.

First, the study was aimed at clarifying the geometry of the marking zone and its functional dependencies on technological processing parameters. The results of this study were published at the scientific conference "Radiation Safety in the Modern World" of the National Military University "Vasil Levski" in year 2019 in Bulgaria.

At the second phase - there was a research of the influence of the power of technological parameters P and the processing speed v on the achievement of the optimal contrast k in the range from 35% to 55%, which was the subject of this study.

The third phase - future of our research is related to the development of algorithms for determining the optimal position of the marking on the surface of chicken eggs. This is due to the fact that the eggs have a specific oval shape, which, in turn, affects the focusing and defocusing of the workpiece during laser processing.

The generalization of these three studies will ultimately lead to optimization of laser marking parameters and providing contrast, and stable marking that is correctly positioned on the working surface of the eggs.

VII. References

[1] Myo Min Aung, Yoon Seok Chang. Traceability in a food supply chain: Safety and quality perspectives. https://doi.org/10.1016/j.foodcont.2013.11.007

[2] Bruno Peres, Nicolas Barlet, Gérard Loiseau, Didier Montet. Review of the current methods of analytical traceability allowing determination of the origin of foodstuffs. https://doi.org/10.1016/j.foodcont.2005.09.018

[3] https://www.agroinvestor.ru/analytics/news/28981-potreblenie-yaytsa-v-mire-vyrastet-v-1-5-raza/

[4] https://www.agri.ee/ru/markirovka-kurinyh-yaic

[5] https://www.videojet.com/content/dam/pdf/NA%20-%20English/Application-Notes/an-inkjet-vs-laser-for-egg-coding-us.pdf

[6] Ming-Fei Chen, Wen-Tse Hsiao, Wei-Lun Huang, Chun-Wei Hu, Yu-Pin Chen. Laser coding on the eggshell using pulsed-laser marking system. https://doi.org/10.1016/j.jmatprotec.2008.02.075

[7] Ming-Fei Chen, Yan-Hsin Wang, Wen-Tse Hsiao. Finite element analysis and verification of laser marking on eggshell. https://doi.org/10.1016/j.jmatprotec.2008.02.065

[8] B. J. Bartholomeusz, M. C. Gupta. Laser Marking of Thin Organic Films. DOI: 10.1364/AO.31.004829

[9] http://www.cnshb.ru/AKDiL/0062/base/RS/000488.shtm

[10] https://www.researchgate.net/figure/Cross-section-of-the-eggshell-and-distribution-of-known-matrix-proteins_fig2_41110738

[11] https://advances.sciencemag.org/content/4/3/eaar3219/tab-figures-data

[12] https://nplus1.ru/news/2018/04/02/cracking-eggshells

[13] P Čeirs, I Adijāns, Analysis of the possibility of laser marking of eggs using CO_2 laser, Сборник доклади от научна конференция Радиационната безопасност в съвременния свят. „Васил Левски" 22 ноември 2019 г. ISSN 2603 4689 стр. 174-182.

[14] L. Lazov, N. Angelov, E. Teirumnieks and E. Teirumnieka, "Preliminary numerical analysis for the role of speed onto laser technological processes". Environment. Technology. Resources. Proceedings of the 12th International Scientific and Practical Conference. Volume III. – Rezekne, 2019. – pp. 137. – 142. http://dx.doi.org/10.17770/etr2019vol3.4154

[15] P. Narica, L. Lazov, A. Teilans, P.Grabusts, E. Teirumnieks and P. Cacivkins, "Method for Color Laser Marking Process Optimization with the use of Genetic Algorithms". Environment. Technology. Resources. Proceedings of the 11th International Scientific and Practical Conference. Volume II. – Rezekne, 2017. – pp. 101. – 106. http://dx.doi.org/10.17770/etr2017vol2.2607

Environment. Technology. Resources. Rezekne, Latvia
Proceedings of the 13th International Scientific and Practical Conference. Volume 3, 173-180

Methods for Measuring Laser Power

Lyubomir Lazov
Rezekne Academy of Technologies
Rezekne, Latvia
llazov@abv.bg

Tsanko Karadzhov
Technical University of Gabrovo
Gabrovo, Bulgaria
karadjov_st@abv.bg

***Abstract* - Today we are witnessing the rapid development of the laser industry. Laser sources with new wavelengths, higher powers and energies, different modes of operation (generation of laser pulses), as well as various applications in industry, medicine, environmental protection etc. are emerging. This requires the development of new physical methods and principles for accurate measurement of power, energy, and other parameters of laser sources. In different types of laser technological processes, accurate measurement of laser power is extremely important in terms of quality, repeatability, and validation of the process. In most cases, accurate laser power measurement is a difficult task, especially when working with high-power lasers or having to perform real-time measurements.**

The report analyses and systematizes the physical principles and methods on which existing laser measuring instruments are based. This research also aims to help researchers and technologists find and develop new approaches to solving this challenging measurement problem.

Keywords - laser power, measurement methods, types of measuring devices, physical principles

I. INTRODUCTION

In recent years, the laser industry has developed extremely fast, with more new laser sources with new wavelengths, higher power and energy, frequencies, and modes of operation. All this is a prerequisite for the emergence of new applications in various fields of industrial production.

The result and the quality for each specific laser technology such as laser welding, cutting, marking, engraving, drilling, etc. They depend on many factors, including material properties, processing speed, type of shielded gas, laser parameters, including - laser power [1] [2].

Laser power or more precisely the power density together with the processing speed (respectively the exposure time) are two of the main factors determining the degree of energy absorbed in the material. Therefore, to characterize in a qualitative aspect a technological operation for qualification, it is necessary to specify/quantify the power delivered by the laser in the processing area.

As laser technology is significantly ahead of the methods for measuring the parameters of laser radiation, it is necessary in recent years to look for new opportunities for improvement and refinement of technologies for measuring the power / energy of laser sources. [3] [4] [5]

1. The system requirements for accurate power output or energy become higher. Years ago a tolerance of ± 10% of power was considered good, today the requirements are higher to ± 5%, and in some cases even higher ± 1%. Today, some pulsed laser applications require pulsed power stability of up to 0.2%.
2. Lasers have become not only more powerful, but with versatile applications. For example, lasers are available on the market emitting 300 J/s or 10 kW of pulsed power in the processing area, the energy density and power reaches values of the order of several hundred J/m² or over 10 kW/cm². For such power densities, new constructions and methods for measuring the energy parameters of the laser are needed.

Today, power and energy meters have to deal with increasingly difficult and difficult tasks due to the fact that they have to measure large intervals of change in power, energy (from power pW up to 10 kW; pJ energy to hundreds of J), the length of the wave (from far UV to far IR), the diameter of the beam, for example the pulse duration and the repetition rate. An example of this great variety of measuring devices offered on the market of different types, operating ranges and based on different methods, can be seen from just one portfolio of one of the world's leading companies Coherent [6].

Online ISSN 2256-070X
https://doi.org/10.17770/etr2021vol3.6565

TABLE 1

Laser Type	Measurement Needed	Power Range	Wavelength Range	Sensor Type
CW	Avg Power	10 nW to 50 mW 200 µW to >5 kW	250 nm to 1800 nm 0.15 µm to 12 µm	Optical – Power Mode Thermopile
Pulsed	Avg Power	200 µW to >5 kW	0.15 µm to 12 µm	Thermopile
Pulsed	Energy Per Pulse	100 nJ to >10J	0.15 µm to 12 µm	Pyroelectric
Pulsed	Energy Per Pulse	10 pJ to 800 nJ	325 to 1700 nm	Optical – Energy Mode

Table 1 Different types of measuring devices offered by Coherent with their operating ranges of: power and wavelengths.Measurement and monitoring of laser power is a continuous process from the beginning - the moment when the laser is first manufactured, to its integration and operation by the end-user, who will use the laser system in various types of applications that we know are so wide from industrial applications to those in medicine and research. The choice of the appropriate measuring equipment for the work in the specific technological applications is no less important than the choice of the appropriate laser for the realization of a specific technological process.

Currently, available laser measuring devices use different measuring methods and sensors. The choice of a specific meter for a given application depends on the spectral range, sensitivity or minimum required response and trigger threshold.

The most commonly used methods for measuring laser power are given in the following table2.

TABLE 2

Method	Features and specifics of the method
with pyroelectric sensors	• Measures the energy of pulsed lasers and can only work with pulsed lasers • The average power is calculated by multiplying the pulse repetition frequency by the pulse energy.
with thermopile sensor	• Measures the power of CW lasers and integrates the energy of pulsed lasers to determine the average measured power. • It can also be used to measure the energy of a pulse - most often to measure the energy of medical and industrial lasers with wide pulses.
with optical sensors - Photodiode	• Used to measure low CW laser power. • It is also used in some sensors to measure low-pulsed laser power.

The variety of sensitivity ranges of different types of sensors operating in different circuit solutions and serving concrete methods of power measurement are also in a wide range. Figure 1 presents the possible ranges of operation of two types of sensors used in thermal and optical methods. The graph shows that thermopile sensors cover a wider range than optical / diode laser radiation sensors.

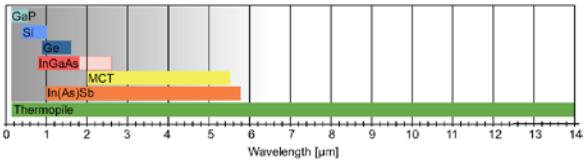

Fig. 1. The sensitivity of two types of sensors (photodiode detectors and thermopiles) for measuring power relative to the wavelengths of laser radiation [7]

When choosing a meter for the power of laser radiation, it is necessary to take into account two factors, the method of measurement and the range of operation of the sensor. The importance of this parameter for two spacing measurement methods is sowed by the diagram in Figure 2.

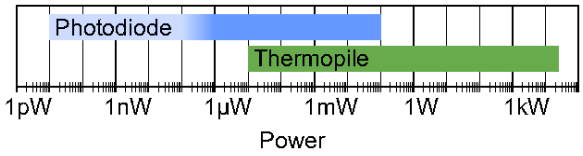

Fig. 2. Operating ranges of laser power measuring devices based on two different methods using photodiode and thermopile detectors [7].

Both types of detectors cover a large dynamic range of powers. It is clear from the figure that devices based on the thermal method are preferred when measuring high laser power powers of the order of kW, and photoelectric methods based on diode sensors are preferred at low powers in the range pW to mW.

Some several key steps and considerations need to be taken in the specific selection of the measuring device. This is because, as there are many different types of lasers with very different specifications, also there are different measurement technologies that are suitable for specific types of lasers and tailored to specific laser specifications. In this article, we will try to discuss the basic approaches and methods of measuring the power and energy of the laser and we will try to give you a small contribution to the selection process faced by each user of laser technology equipment.

II. THERMAL MEASUREMENT METHODS

The thermal method using thermopile sensors is a great universal technology suitable for measuring the power of many lasers. They can be successfully used to measure the power of CW lasers as well as the average power of pulsed lasers. In some special cases, they can also be used to measure the energy of individual long pulses. The basic physical principle on which this type of power meter has based the conversion of the absorbed electromagnetic energy of the laser into heat. With the help of a heat radiator, this heat is transferred to the environment by convective cooling or water cooling. The temperature difference between the temperature of the sensor/absorber and the radiator/cooler is converted into an electrical signal by a thermocouple.

Photodiodes are sensitive for powers down to 10 pW. Incoming radiation above 100 mW leads to a saturation of the electrical signal, setting the limit for the maximum

power. The power saturation is critical when monitoring e.g., ultrafast pulse lasers. Although the average power might be rather low (and within the power range of the detector), the power of the short pulses greatly exceeds the upper power limit of the detector leading to saturation of the signal and hence distorted measurement results. Additionally, industrial applications use photodiodes typically from 500nW upwards (when detecting stray light or fractions of the beam), giving a very small dynamic range and complicating its integration into the system. For such applications, a thermopile detector is preferable, since it has a broad dynamic range and integrates the signal of the individual pulses, therefore monitoring the average power.

Thermopile sensors are used to monitor laser beams of up to 25 kW. The upper limit for those detectors is mainly attributed to the ability to cool the sensor efficiently. In recent years, the minimum detectable power has been shifted more and more into the range of photodiodes and has reached 10 µW. The company greenTEG offers a resolution below 1 µW. [7]

Measurement of laser radiation power with thermocouple

Thermopile sensors are the best choice for measuring average powers from 10 µW upwards. Especially outside the visible range, where photodiode technologies are expensive, thermopiles should be considered. Photodiodes, on the other hand, are the best choice when single pulses need to be analysed or when power levels in the nW range should be resolved.

Most power meters are based on the principle of a thermal detector: They convert optical power to heating power via an absorber structure with a black coating. They use a thermopile to measure the resulting temperature rise (or the temperature difference between the absorber and the mount). Thermal power meters are useful for average powers between about 10 mW and several kilowatts. Thermal power meters are moderately precise, have a sensitivity that is independent of wavelength, and are relatively slow.

In many cases, these meters use thermocouples. The measured laser beam falls on one side of the thermocouple, it is heated by the laser, and on the other side, there is a radiator or cooler, which aims to maintain a constant temperature. The laser energy absorbed by the thermocouple material is converted into heat. The temperature difference on both sides of the thermocouple creates an electromotive voltage. This voltage is proportional to the temperature difference, which is proportional to the measured power. on the laser. This voltage is measured to provide laser power readings in watts fig. 3.

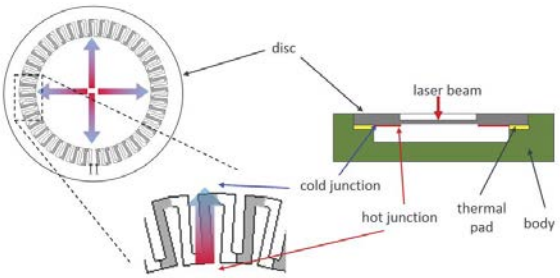

Fig. 3. Disk with thermocouple [8]

The material used to absorb the energy of the laser beam is essential because the parameters and characteristics of the detector depend on its properties. This material absorbs most of the laser's optical energy and converts it into heat. A portion of the laser beam is reflected, which can vary from a few percent to 50 percent of the total optical power, depending on the material.

The laser beam falls in the center of the disk and the heat energy passes radially from the center to the periphery. The total amount of heat passing through the disk does not depend on the size of the disk and the position of the beam.

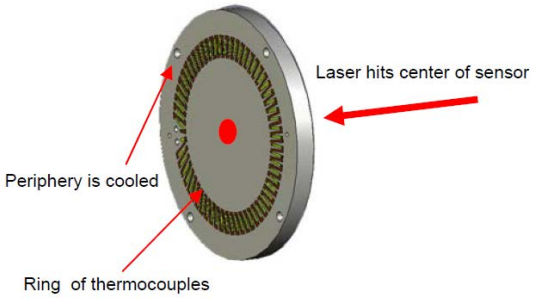

Fig. 4. Thermocouples

The thermal power meter is not measuring the absolute temperature of the sensor but rather the temperature drops across the thermopile fig. 4. Therefore, the reading is quite independent of ambient temperature. If the temperature of the cooled periphery goes up, the temperature of the inside of the thermopile goes up correspondingly and the temperature drop – hence the reading – remains the same.

Thermopile laser measurement is almost wavelength-independent, durable, and reliable. It is therefore the mainstay of laser power/energy measurement. It cannot, however, measure repetitive pulses or very low powers and energies.

Pyroelectric power meters

The pyroelectric sensor used in laser power measuring devices consists of a crystal that polarizes when heated. These detectors work as follows:

When a laser pulse hits the surface of the detector, it heats up and polarizes the crystal, thus creating an even and opposite charge on both surfaces of the detector. The surface of the detector is metallized so that the charge

collects on the parallel capacitor, regardless of where the laser beam hits the surface. In this way, the charge of the capacitor is proportional to the energy of the pulse. Once the pulse is complete, the capacitor voltage is read, and the capacitor is discharged electronically to be ready for the next pulse.

Pyroelectric detectors are especially useful for repetitive pulses and can measure up to thousands of pulses per second. They are also quite sensitive. However, they are not very durable, so for higher energies and powers, an attenuator/diffuser is placed in front of the sensor crystal to reduce the energy on the pyroelectric crystal.

Pyroelectric power meters are relatively fast meters. They cannot be used to measure the continuous power of the laser. The output signal of this type of laser power meter is proportional to the changes in the incident input energy.

Pyroelectric sensors for measuring radiant energy are sensitive in a very wide range of wavelengths and can measure energy from laser sources with different powers up to 10 J. Most of these sensors have a ceramic coating to withstand high energy density of laser radiation. The sensors can be connected directly to a high input impedance amplifier or oscilloscope via a BNC connector.

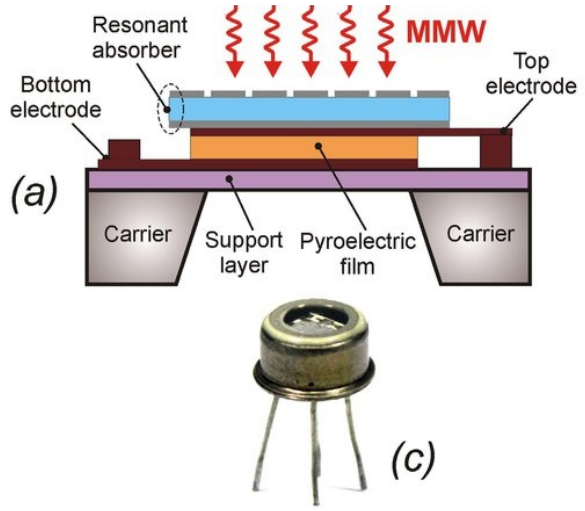

Fig. 5. Pyroelectric sensor [9]

III. PHOTOELECTRIC MEASUREMENT METHODS

The most commonly used sensors for measuring low laser power are photodiodes due to their speed. In them, as in other sensors, light is absorbed by materials and converted into an electric current called photocurrent, which is proportional to the power of the radiation. Depending on the material from which they are made, photodiodes are sensitive to laser beams with different wavelengths. Photodiodes made of Si, Ge and InGaAs are sensitive in the near infrared region up to 1800 nm. Using materials such as HgCdTe (MCT) and In (As) Sb, the measurement range is extended to about 6000 nm. Photodiodes made of GaP are used to measure the power of ultraviolet lasers.

The principle of measuring with photodiodes is one of the most common methods for measuring the power of laser radiation. It has both advantages and some significant disadvantages. The action of the photodiode is based on increasing the reverse current of the p-n junction during its illumination, which is practically used to measure the intensity or power of laser radiation.

The photodiode has the highest speed of all optoelectronic photodetectors, which is its biggest advantage. It can be used to measure fast-changing laser radiation. The photodiode can operate in two modes - photodiode and photo galvanic mode, and both modes can be used to measure the intensity of light or laser fluxes. So-called PIN photodiodes are used to measure the power of pulsed lasers, which have an even higher speed than traditional photodiodes with a PN junction.

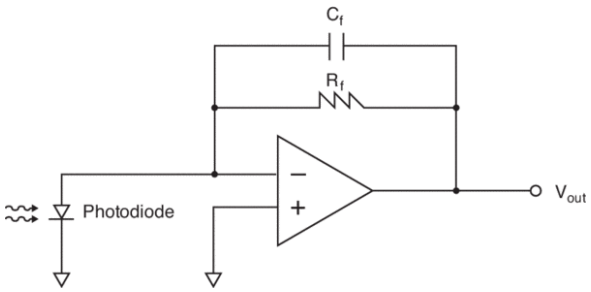

Fig. 6. Light-to-voltage converter

Most laser power measurement circuits use light to voltage converter at which the output voltage is proportional to the luminance over the active area of the photodiode created by the laser beam fig. 6.

There are also power meters that use light to frequency converter with a photodiode at the input. This is a programmable light to frequency IC that outputs a pulse train or a square wave (50% duty) with the frequency that is directly proportional to the incident light intensity. Uses a simple TTL output for easy interfacing to a microcontroller.

For example, the S9705 is a photo IC that combines a photodiode and a current-to-frequency converter on a CMOS chip. Output is a square wave (50 % duty ratio) with frequency directly proportional to light intensity incident on the photodiode. The CMOS level digital output allows direct connection to a microcontroller or other logic circuitry. The S9705 has a wide dynamic range and light intensity can be easily measured when used with a digital counter [10].

Features
Converts light intensity to frequency
Wide dynamic range: 5 orders of magnitude
Excellent linearity
Output timing reset function
Digital output for direct interface to microcontroller
4-pin plastic package.

In rare cases, semiconductor phototransistors and photoresistors can be used as photosensitive elements.

IV. PONDEROMOTIVE ACTION MEASUREMENT METHODS

Another method is based on the physical phenomenon of optical radiation pressure. In this method, the measurement of the laser beam power is realized without the need to absorb it, as is necessary, for example, in the calorimetric method. There is no need for thermal control of the absorbed laser energy and the reaction and recovery time after each measurement in the receiver.

The idea of the radiation pressure or the momentum of photons was first proved by the Russian scientist Peter Nikolaevich Lebedev in 1899 [11]. Figure 1 shows a schematic diagram of the idea of the experiment proposed by Lebedev.

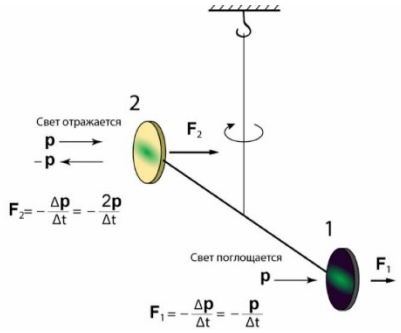

Fig. 7. Lebedev's experiment

It consists of two circular plates, one of which is blackened and absorbs light, and the other, shiny, reflects light fig. 7. The plates are fixed at opposite ends of a light rod suspended by a thin quartz thread. The whole structure was placed in a glass vessel from which air was evacuated. When reflected from a mirror, light transmits to it twice as much pulse per unit time as light falling on an absorbing plate of the same area, which leads to twisting of the filament, which was measured by P.N. Lebedev. It is worth noting that the actual installation was somewhat more complicated since it was necessary to avoid the effects associated with an insufficiently high vacuum level and uneven heating of the installation parts.

The light flux propagating in space carries with it a certain momentum, when interacting with a substance it transmits its momentum, changing its direction of propagation. For example, if the momentum carried by a light beam is p, then the force F transmitted by it to the substance (mirror) depends on the rate of change of this pulse.

$$F = \frac{dp}{dt} \quad (1)$$

Since the magnitude of the pulse is defined by the amount of energy E divided by the speed of light c.

$$|p| = \frac{E}{c} \quad (2)$$

Then for a beam with optical power $P = dE / dt$, reflected from without diffusion and absorption by an ideal mirror will reflect the radiation of incident light, generating a force $F = 2P / c$ on the mirror. Thus, the light falling on a mirror with perfect reflection will press the mirror with force fig.8:

$$F = \frac{2P}{c} r\cos\theta \quad (3)$$

where r is a function of the reflectivity R and the absorption A = (1 - R), as well as the α part of the un-reflected light absorbed by the mirror

$$r = R + (1 - R)\alpha/2 \quad (4)$$

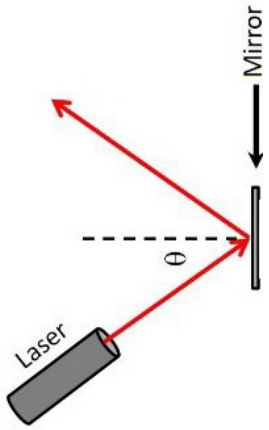

Fig. 8. The laser radiation, incident at θ angle to the mirror, exerts a force F on it.

Here the fact is considered that the absorbed photon gives its whole momentum, and the reflected photon gives twice its momentum to the mirror.

Equation (3) describes a maximum power conversion factor in force of $2/c = 6.67 \times 10^{-9}$ N/W for a normal frequency of a perfectly reflecting mirror.

The first successful experiments demonstrating the light radiation pressure date back to the early 20th century [12] [13]. The presence of small forces at powers of the order of 100 mW of incident light on the plates of the scale is demonstrated using torsion scales.

These as well as later developments by many authors [14] [15] [16] [17] [18] [19] fully confirm the validity of the radiation pressure. This method with the use of a torsion balance has a high sensitivity but is not suitable for working in a non-laboratory environment. That is why it has been neglected for many years and can be said to have been forgotten.

Today, highly sensitive scales and dielectric mirrors with very high reflectivity are available (usually> 99.99% for optical and> 90% for RF). This is precisely the prerequisite for a new stage in the development of this method of measurement - mainly for measuring high laser power. Such devices are already available from several research laboratories. They are based on the physics of the interaction of incident photons on a strongly reflecting mirror [20]. The advantage of the device offered by these authors is the ability to directly deflect the laser beam from the measuring mirror, in which case the measurement is performed without interrupting the laser technology

process itself. However, this proposed design solution has one significant drawback, namely sensitivity to inertial forces (acoustic vibrations and tilt-dependent gravity projection).

Ivan Ryger et al. [21] in their publication demonstrate a miniaturized version of a radiation pressure sensor that can potentially overcome the above-mentioned drawback, namely by avoiding the impact of the environment (acoustic vibrations and tilt-dependent gravity projection) on the sensor readings, thus closer to the needs of users of technological systems. A schematic diagram of the sensor proposed by the authors is shown in figure. 9. The sensor consists of a silicon micromachined parallel plate capacitor, both of whose disk electrodes (diameter 20 mm) are attached to a rigid frame through weak springs (width 465 μm, thickness 380 μm, length 45 mm) in the shape of an Archimedean spiral (see fig,9). For the optical sensor, a highly reflective dielectric mirror (optimized for reflectance with a value of 0.9992 ± 0.0002 at 1.07 μm wavelength and 45° angle of incidence) is deposited onto the front side of one disk electrode.

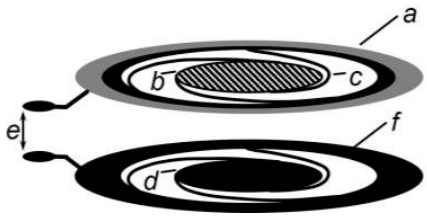

Fig. 9. Schematic diagram of a sensor for measuring laser radiation pressure using an Archimedean spiral for a damper. [22]

To obtain a calibration between the measured electrical signal and the applied optical radiation on the sensor, it is necessary to know exactly the electromechanical parameters (spring constant, the distance between the capacitor plates and the capacity gradient concerning the distance between the plates). For this purpose, Ivan Ryger et al. in [22] offers an optoelectronic characterization technique, where a time-varying voltage of electrostatic deviation is applied to the electrodes of the capacitor and measuring the axial displacement of the mirror.

V. OTHER MEASUREMENT METHODS

Piezo-resistance method for measuring laser radiation pressure

Piezoelectric sensors are based on the physical piezo effect. When charged with pressure on the piezoelectric materials on their opposite surfaces, electric charges appear. When the magnitude and direction of the pressure changes, the magnitude and type of electric charge also change fig. 10.

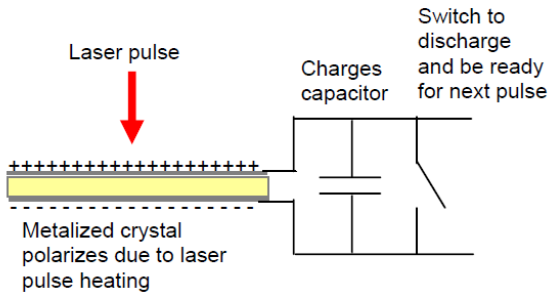

Fig. 10. Schematic diagram of a pressure sensor based on the piezoelectric effect

Piezo-resistance pressure sensors based on micro-electro-mechanical systems (MEMS) on a silicon substrate can also be successfully used to measure the laser pressure. The sensor is made of a thin silicon membrane, hermetically covering the space below it, and four piezo resistors applied on its surface, the resistance of which depends on the pressure and temperature.

Any change in the external pressure under the action of laser radiation causes deformation of the membrane and a change in the resistance of the piezo resistors connected in a bridge circuit fig. 11.

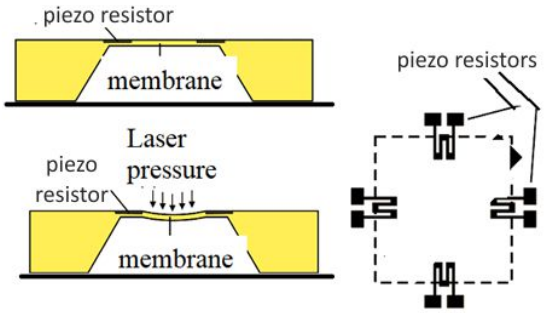

Fig. 11. Schematic diagram of membrane type pressure sensor in combination with piezo resistors

Nonlinear optical method effects for measuring the energy (power) of a laser radiation.

A method for measuring the energy or power of laser radiation, based on nonlinear optical effects arising from the passage of laser radiation through a substance, the main of which are the effect of optical rectification, the effect of optical polarization, generation of harmonics and Raman scattering.

Photochemical method for measuring the energy (power) of a laser radiation.

A method for measuring the energy or power of laser radiation based on the use of photochemical reactions with a known quantum yield arising from absorption laser radiation by substance.

Photographic method for measuring the energy (power) of a laser radiation.

A method for measuring the energy or power of laser radiation, based on the photochemical effect of laser radiation on photographic materials and functional dependence the optical density of blackening *D* of the

photosensitive layer from the irradiation of this layer *E* and the exposure time t, determined by the formula:

$$D = [\lg(E.t^p)]$$

where *D* is the optical density of blackening; E is the irradiance of the photosensitive layer; *t* is the exposure time; p is the Schwarzschild parameter depending on *E* and *t*.

VI. CONCLUSION

The present study aims to help users of laser equipment in the correct selection of a laser measuring system. From all that has been said so far, the first step must begin with an analysis of a detailed examination of the laser (or lasers), the parameters of which must be measured:

Key laser parameters in this analysis should be minimum and maximum average power of the laser source, the wavelength of the laser radiation, and the output diameter of the laser radiation.

When working with a pulsed laser, it is important to consider: the minimum and maximum pulse energy as well as the width of the laser pulse and the frequency of repetition of the pulses. (If the repetition rate is adjustable, it will be useful to know the maximum repetition rate at maximum energy, thus obtaining the maximum average number of powers.) Taking these parameters and factors into account in the mode of operation of the laser will help to determine how much heat will be absorbed/absorbed if a sensor system is selected.

The following considerations/guidelines should be considered when determining the appropriate measurement method for a laser technology system:

- Water cooling is used in all modern thermal sensors to measure powers greater than 300 W. And at high powers of the order of kilowatts, a specialized high-speed water line is provided in most cases for cooling the sensor.
- Thermopile sensors are preferable to use when it is necessary to measure the power of pulsed lasers with a pulse repetition frequency higher than 10 kHz. If the frequency of the pulsed laser is less than 10 kHz, it is preferable to use a pyroelectric sensor.
- To measure the power of lasers operating at low power and emitting in the far infrared region of the electromagnetic spectrum, it is preferable to use devices based on the photoelectric method. Semiconductor photodiode sensors are often used, which have a good response to low light levels. This type of method and measurement sensors can be successfully applied to lasers operating in CW and pulsed mode, but with low average output power.
- The next step after selecting the appropriate sensor for a given measurement is to select a compatible meter with the required measuring range and the required sensitivity. This step is very important to perform quality registration and visualization of the measurement. Usually the signal from the sensor is converted from analog to digital signal on the measuring display. The measuring device can also perform digital signal processing and other correction algorithms, such as wavelength or temperature compensation.

VII. REFERENCES

[1] N. Angelov, "Investigation the Influence of the Number of Repetition and Volumetric Energy Density on Laser Marking of Products," *Journal of the Academy of Sciences and arts of the Republic of Srpska „Contemporary Materials*, vol. V, no. 2, pp. 250-253, 2014, DOI: 10.7251/cm.v2i5.1738

[2] N. Angelov, "Determination of Working Intervals of Power Density and Frequency for Laser Marking on Samples from Steel HS18-0-1," *Proceedings of the Union of Scientists - Ruse*, vol. 12, pp. 125-130, 2015.

[3] A. L. Cullen, " Absolute power measurement at microwave frequencies," *Proc. IEEE* , vol. 92, pp. 100-111, 1952.

[4] D. Ma, J. L. Garrett and J. N. Munday, "Quantitative measurement of radiation pressure on microcantilever in ambient environmnent," *Appl. Phys. Lett*, vol. 106, 2015, DOI: 10.1063/1.4914003

[5] K. Agatsuma, D. Friedrich, S. Ballmer, G. DeSalvo, S. Sakata, E. Nishida and S. Kawamura, "Precise measurement of laser power using an optomechanical system," *Opt. Express*, vol. 22, pp. 2013-2030, 2014, DOI: 10.1364/OE.22.002013

[6] [Online]. Available: https://www.coherent.com/measurement-control/main/laser-power-and-energy-meters.

[7] S. Dröscher, "White Paper: Technologies for Laser Powe monitoring," [Online]. Available: https://www.greenteg.com/template/userfiles/files/White%20Paper_Detector%20Technologies%20Laser%20Power.pdf.

[8] [Online]. Available: https://www.newport.com/t/optical-power-measurement.

[9] S. A. Kuznetsov, A. G. Paulish, M. Navarro-Cía and A. V. Arzhannikov, "Selective Pyroelectric Detection of Millimetre Waves Using Ultra-Thin Metasurface Absorbers," *Scientific Reports*, vol. 6, 16 Feb 2016, DOI: 10.1038/srep21079

[10] [Online]. Available: https://www.hamamatsu.com/us/en/product/type/S9705/index.html.

[11] P. N. Lebedev, "Experimental examination of light pressure," *Ann. Phys*, pp. 1-26, 1901.

[12] E. F. Nichols and G. F. Hull, "A preliminary communication on the pressure of heat and light radiation," *Phys. Rev*, vol. 13, p. 307–320, 1901, DOI: 10.1103/PhysRevSeriesI.13.307

[13] E. F. Nichols and G. F. Hull, "The pressure due to radiation," *Astrophysical. Journal*, vol. 17, pp. 315-351, 1903.

[14] J. J. Cook, W. L. Flowers and C. B. Arnold, "Measurement of laser output by light pressure," *Proc. IRE* , vol. 50, 1962.

[15] M. Stimler, Z. I. Slawsky and R. E. Grantham, "Torsion pendulum photometer," *Rev. Sci. Instrum*, vol. 35, pp. 311-313, 1964, DOI: 10.1063/1.1718813

[16] G. Roosen and C. Imbert, "Measurement of laser output by light pressure," *Opt. Eng*, vol. 20, pp. 437-439, 1981.

[17] G. T. Gillies, "Photomechanical laser power measurements with magnetically suspended rotors," *Fizika*, vol. 19, pp. 407-420, 1987.

[18] Y. Yuan, "A new pulse laser energy meter," *Rev. Sci. Instrum*, vol. 61, p. 1743–1746, 1990, DOI: 10.1063/1.1141144

[19] G. T. Gillies and R. C. Ritter, "Torsion balances, torsion pendulums, and related devices," *Rev. Sci. Instrum*, vol. 64, no. 2, p. 283, 1993, DOI: 10.1063/1.1144248

[20] P. Williams, J. A. Hadler, F. C. Maring, R. Lee, K. A. Rogers, B. J. Simonds, M. T. Spidell, A. D. Feldman and J. H. Lehman, "Portable, high-accuracy, non-absorbing laser power measurement at kilowatt levels by means," *Opt. Express* , vol. 25, p. 4382–4392, 2017.

[21] I. Ryger and et al, "MEMS Non-Absorbing Electromagnetic Power Sensor Employing the Effect of Radiation Pressure," in *Proceeding at the Eurosensors* , Graz, Austria, 2018, DOI: 10.3390/proceedings2130767

[22] I. Ryger, A. B. Artusio-Glimpse, P. Williams, N. Tomlin, M. Stephens, K. Rogers, M. Spidell and J. Lehman, "Micromachined force scale for optical power measurement by radiation pressure sensing," *IEEE Sens. J.* , vol. 18, p. 7941–7948, 2018, DOI: 10.1364/OE.385502

Environment. Technology. Resources. Rezekne, Latvia
Proceedings of the 13th International Scientific and Practical Conference. Volume 3, 181-186

On the Possibility of Laser Stripping of Communication Cables with Low-Power CO_2 Laser

Lyubomir Lazov
Rezekne Academy of Technology
Rezekne, Latvia
Lyubomir.Lazov@rta.lv

Andris Sniķeris
Rezekne Academy of Technology Rēzekne, Latvia
snikeris_a@protonmail.com

***Abstract* - Laser engraving is one of the most commonly used laser procedures for interacting with laser material. The speed, ease of use and high precision make it an attractive process for use by manufacturers and for removing insulation from various cables. Cable stripping is a particularly common operation in aeronautics. The aircraft is equipped with several hundred kilometers of cables to control and operate the various systems of the aircraft and most of these cables must be stripped at both opposite ends to allow the cable to be connected to different terminals.**

This report examines the possibility of removing polyvinyl chloride (PVC) insulation from telecommunication cables of different colours and thicknesses up to 600 [µm]. The experimental measurements of the study were performed with a low-power continuous CO_2 laser system. The main functional dependence of the width and depth of the ablation zone on the main technological parameters, such as the average power and the processing speed, have been experimentally studied. The zones of laser impact are observed with a laser microscope. The graphic dependencies are analyzed in order to determine the optimal working intervals.

The analysis aims to help solve problems related to the application of small diameter communication cables in the production of various communication devices and components for the needs of industry.

Keywords* - *ablation, cable, CO_2 laser, polyvinyl chloride

I. INTRODUCTION

Polyvinyl chloride is one of the major types of plastics, which is widely used in various industries like electrical, automotive equipment, packaging, construction, aeronautics, and applications such as windows, flooring, bottles, pipes, fittings, cables, etc. [1]. At the global level, demand for PVC exceeds 35 million tonnes per year, and it is rated second only after polyethylene as volume leader in the plastics industry [2]. Due to its low cost and good dielectric and processing properties, PVC is one of the most widely used insulating materials [3]. It also has stable chemical properties, has excellent fire resistance due to the presence of chlorine, is easily process able, has good insulation and dielectric performance, and is environmentally friendly [4,5].

Nowadays in manufacturing, the ability to strip insulation of various materials and materials from cables or wires is very important. For “state-of-the-art” applications it is necessary to be able to strip insulation layers with high precision and efficiency, without damaging the conductor. For copper (CU) cables laser wire stripping mechanisms achieve this by their ability to selectively remove insulating material while leaving copper intact. It is very important to find a balance between the intensity of laser radiation and the preservation of cable characteristics to achieve an optimal cable stripping process.

One of the most commonly used laser types for wire-stripping systems is the CO_2 laser. CO_2 lasers play a large role in the laser-material processing industries. CO_2 laser offers good beam quality and low cost per watt. Numerous discrete output wavelengths from 9 to 11 microns in the far-IR spectrum. Specific wavelengths can be selected with the use of isotopes in a laser gas mixture. Radiation in this wavelength is strongly absorbed by a large amount of commonly used materials including PVC [6].

Online ISSN 2256-070X
https://doi.org/10.17770/etr2021vol3.6615

The CO_2 laser beam does not damage the conductor part of the CU cable, because copper is very reflective to the CO_2 laser beam and has high thermal conductivity, but the insulating materials tend to be highly absorbing. As the laser beam passes through the cable, it cuts precisely through the insulation, which which allows easy removal of the insulating layer of the cable [7].

Martnyuk has researched the usage of frequency quadrupled Nd: YAG laser for wire stripping [8]. Iceland has researched the usage of CO_2 and Nd:YAG lasers in wire-stripping equipment [9]. Miller has researched the ability of a 10.6 [μm] CO_2 laser to selectively remove the insulation of various materials [10].

The main purpose of this study is to determine the necessary parameters of a CO_2 laser system to completely remove the outer isolation layer of communication cables, deriving the functional dependencies of the depth of laser ablation on power, speed, the raster step distance and influence of material's colour on twisted pair CU cables outer insulation layer made of PVC with a thickness of up to 600 [μm].

II. INSULATION REMOVAL TECHNIQUES

The cable stripping process is the removal of the insulation, which covers the electrically conducting wire or wires of a cable, to make the cable-ready insertion in the cable connector. Conventional cable stripping technologies include abrasive, chemical, thermal, and mechanical methods. Each of those methods has its drawbacks in one or several areas such as damage to a copper conductor, low precision, quality, or poor processing speed.

In precise manufacturing applications where perfect insulation removal is needed it is unacceptable to have such deficiencies. Mechanical cable-stripping methods are not well suited to strip cables that do not have regular cross-sections like twisted pair cables, which are very frequently used in telecommunications. The quality of this process highly depends upon the skill and experience of the crafts-person to cut through the protective cover without damaging or stressing the elements [11]. Twisted pair cable (TPC) is composed of two conductors which are twisted together. The twisting is used to cancel electromagnetic interference from external sources and to reduce the cross-talk with surrounding wires (typically within large bundles) and it is also used to protect the environment from its radiation [12]. Chemical cable-stripping methods have a long processing time and environmental issues. Successful thermal cable-stripping requires very precise calibration and temperature control and it needs a secondary operation to completely remove all insulation from a selected area of the cable.

Laser cable stripping has a faster processing time, better process control, and very good precision compared to other methods. Laser cable stripping is a contact-less process and using appropriate laser type and laser power is important to significantly reduce the risk of damage to the copper conducting part. The laser beam can create a variety of patterns such as cross-cut end strips, angled cuts, mini-windows, or any programmable patterns and selected points of cable or wire. A list of insulation types strippable by CO_2 laser includes rubber, fabric, Teflon, polyvinyl chloride, Kapton, and fiberglass.

III. EQUIPMENT AND MATERIALS

ST-CC9060 laser systems were used in the experimental process for sample processing. Parameters of ST-CC9060 laser are shown in table I. This laser is specially designed for interaction with non-metallic materials. This system has and a high-speed XY coordinate table, with unique fully sealed cavity construction shown in Fig. 1.

Principle of operation: the resonator tube of the CO_2 laser is filled with a gas mixture as a laser-active medium. A laser discharge generates when high voltage is applied to the electrodes of the laser resonator, this process causes the molecules in the CO_2 gas mixture to release laser radiation in form of emissions. After amplification, in laser resonator photons leaves it through the output resonator. These photons, who are directional, monochromatic, and coherent from the laser beam with help of optical systems are directed to the work surface.

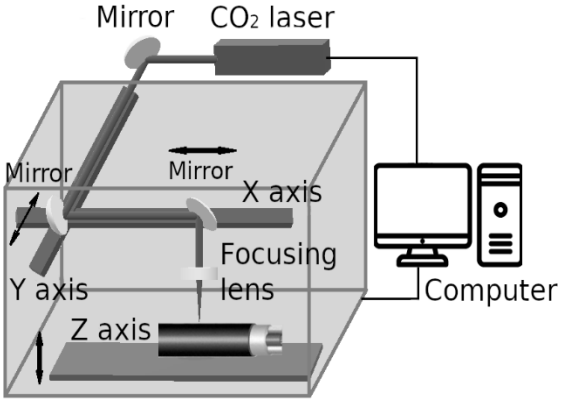

Fig. 1. Scheme of the operational stand

TABLE I. PARAMETERS OF ST-CC9060 LASER

Laser Power *P*	100W
Laser Wavelength λ	10640nm
Marking Area *S*	900 mm x 600 mm
Marking Speed *v*	0-1000mm/s
Repetition Accuracy	±0.02mm
Power Consumption	1.5 kW
Power Supply	220v/50Hz/10A
Cooling system	water cooling & protection system
Focal Length *f*	65 mm

For the parameter measurement of the heat-affected zone, an OLS-5000 SAF laser microscope (Fig. 2) was used. Magnification of 20x with repeatability – 0.03 [μm] was used for determining the width and depth of the heat-affected zone.

Fig. 2. OLS-5000 SAF confocal laser microscope

IV. MATERIALS / EXPERIMENTAL SAMPLES

PVC is a thermoplastic material, meaning that it can be softening when heated and hardening when cooled and it can undergo these processes many times without any noticeable change. Properties of PVC can vary depending on its molecular weight and additives (plasticizers, fillers, pigments, etc.) PVC is extremely cost-effective in comparison to other plastics with a high degree of versatility in end-use and processing possibilities. It is durable, easily maintained, and can be produced in a variety of colours. It has good stiffness, impact strength, good chemical resistance, and non-flammability [13, 14].

There are different types of PVC available on the market which can be used as an insulation material. The most common types are rigid PVC (PVC-U) and plasticized PVC (PVC-P) PVC-P is usually used for stranded cables where the flexibility of the cable is necessary. PVC-U is used for solid cables which are more useful for heavy-duty applications [13]. The most important parameters of PVC-P and PVC-U are shown in Table II. Another important factor that influences the absorbability of laser light for PVC is the colour of the material. colour or PVC depends on the amount and type of pigment additives present in the material.

TABLE II. PARAMETERS OF RIGID AND PLASTICISED PVC [13]

Property	**Rigid**	**Plasticized**
Density (g/m^3)	1.34-1.39	1.29-1.34
Tensile modulus (GPA)	2.41-2.45	-
Tensile strenght (MPa)	37.2-42.4	14-26
Density (g/m^3)	1.34-1.39	1.29-1.34
Elongation at break (%)	-	250-400
Notched izod (kJ/m)	0.74-1.12	-
Hardness	R107-R122 (Rockwell)	A71-A96 (Shore)

V. METHODOLOGY

Depth *h* of a single slit cut and 10 x 10 mm window cut area was measured as a function of laser power *P*, raster step distance *Δx*, and processing speed *v*. PVC-P strips of different colours (white, yellow, red, green, blue and black) with a size of 20 x 200 [mm], thickness - 0.6 [mm] were prepared for the experimental series. The focal length *f* and the spot size of laser beam *d* are constant throughout the entire experimental study – *d* = 92.7 [μm], *f* = 65 [mm]. Laser interaction time - *t* and laser power density – *W* were measured for all measurements. Error calculation was made for all measurements. Every experiment was repeated 4 times to achieve more reliable results. A 10 x10 [mm] window cut area of each sample was performed using a raster scanning method. (Figure 3.) Raster step distance *Δ x* is the distance between the lines of the trajectory of the laser beam.

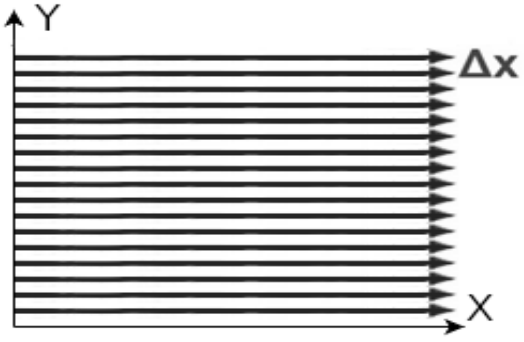

Fig. 3. Raster scanning method

Experimental part of the study is divided in four parts.

In the first section of the experimental process, ablation depth *h* was examined as a function of processing speed *v* - *h* = *h* (*v*) for 10x10 [mm] area

ablation for samples of six different colours. Values of P and Δx are constant through experimental series. P = const = 4.5, 7.3, 10.5, 14 W, Δx = *const* = 20 [μm]. v = 100 ÷ 345 [mm/s].

In the second section of the experimental process, ablation depth h was examined as a function of laser power P : $h = h\ (P)$ for 10 x 10 [mm] area ablation for samples of six different colours. Values of laser power P used in these series: 1, 2.2, 3.5, 4.5, 6.1, 7.3, 9, 10 [W]. Values of v and Δx are constant through experimental series. v = const = 150, 225 and 300 [mm/s], Δx = *const* = 20 [μm].

In the third section of the experimental process, ablation depth h was examined as a function of laser power P - $h = h\ (P)$ for a single-slit cut samples of six different colours. Values of laser power P used in these series: 1, 2.2, 3.5, 4.5, 6.1, 7.3, 9, 10, 12, 14, 17.6, 20, 23.6, 27.6, 30, 34.5, 38.5, 43 [W]. Values of v and Δx are constant through experimental series. v = const = 200 [mm/s].

In the fourth section of the experimental process, ablation depth h was examined as a function of raster distance Δx: $h = h\ (\Delta x)$. Values of P and v are constant through experimental series. P = *const* = 4.5 [W], v = *const* = 100 [mm/s], Δx = 10 ÷ 80 [μm].

VI. Results of Experimental Studies

Results of the first set of experiments are shown in Fig. 4 and Fig. 5. Fig. 4 shows the depth of 10x10 [mm] laser-ablated zone as a function of the laser processing speed of four different colours – white, yellow, green, and black samples to make the graph clearer. Experiments where cable isolation was fully ablated (h > 600 [μm]) and the values of those measurements are not shown in Fig. 4.

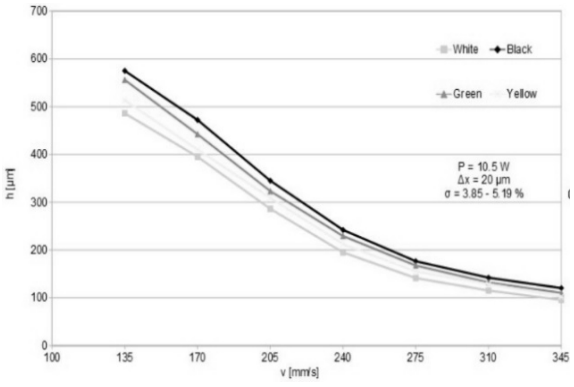

Fig. 4. Depth of the laser-ablated area as a function of laser processing speed

Data shown in Fig. 4 shows an increase of depth h of the laser-ablated zone by decreasing the laser processing speed. The trajectory of change of h is similar for samples of all colors, however, white-colored samples consistently are showing the lowest depth of laser-ablated area as black-colored samples have the deepest zone of ablation among experimental samples. Difference of h between black and white sample groups are between 15.4% at v = 135 mm/s and 20.5% at v = 345 mm/s. Fig. 5 shows how the depth of heat-affected zone h changes as a function of laser processing speed for four different values of laser power P.

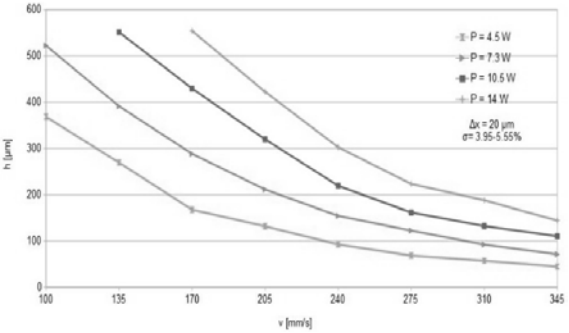

Fig. 5. Depth of the laser-ablated area as a function of laser processing speed of blue-coloured samples

A non-linear function can be observed. Changing laser power from 4.5 [W] to 14 [W] (311% increase) depth of laser-ablated zone at measured processing speed values where does not exceed (170 – 345 [mm/s]) increases by 320.9 – 330.6 %. Depth of the laser-ablated zone increases proportionally to increase the laser power.

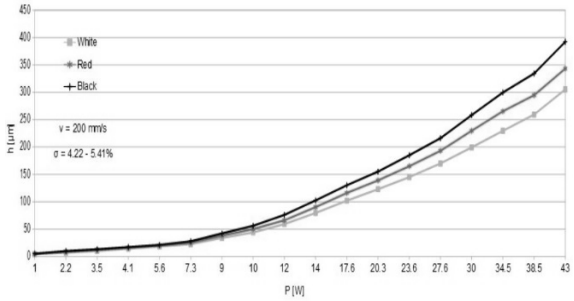

Fig. 6. Depth of the laser-ablated area as a function of laser power

Increasing laser power increases the depth of the laser-ablated zone exponentially as seen in Fig. 6. To analyze the way how increasing laser power P changes the depth of the laser-ablated zone, measured results were divided into four distinct intervals. Interval 1 – 1 to 10 [W]. Interval 2 – 10 to 20 [W]. Interval 3 – 20 to 30 [W] and interval 4 – 30 to 43 [W]. Increasing P of black-coloured sample in interval 1 - from 1 [W] (5.32 [μm]) to 10 [W] (56.13 [μm]) increases h by 1055%. This corresponds to a 5.65 [μm] increase in depth of the laser-ablated zone h per 1 [W]. Increasing P of the black-coloured sample in interval 2 - from 10 [W] (56.13 [μm]) to 20 [W] (155.09 [μm]) increases h by 176.3%. This corresponds to a 9.90 [μm] increase of h per 1 [W]. Increasing P of the black-coloured sample in interval 3 - 20 [W] (155.09 [μm]) to 30 [W] (258.36 [μm]) increases h by 66.6%. This corresponds to a 10.33 [μm] increase of h per 1 [W]. Increasing P of black-coloured samples in interval 4 - 30 [W] (258.36 [μm]) to 43 [W] (392.27 [μm]) increases h by 51.2%. This corresponds to a 10.30 [μm] increase of h per 1 [W].

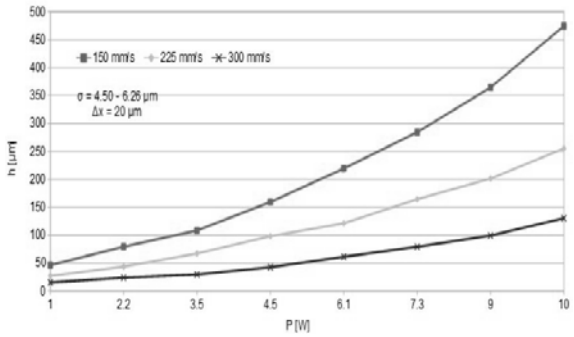

Fig. 7. Depth of the laser-ablated area as a function of laser power for three different processing speed values

Fig. 7 shows the dependence of 10 x10 [mm] laser-ablated zone on laser power *P* for three different laser processing speed values – 150, 225, and 300 [mm/s]. Results of red-coloured samples are shown in Figure 7 however a similar trajectory of change of *h* is noticeable for other tested colours, but the value of *h* slightly differs due to the absorbency of PVC plastic insulation for each colour. At *P* = 10 [W], *v* = 150 [mm/s], depth of laser-ablated area is 3.64 times larger than at *P* = 10 [W], *v* = 300 [mm/s].

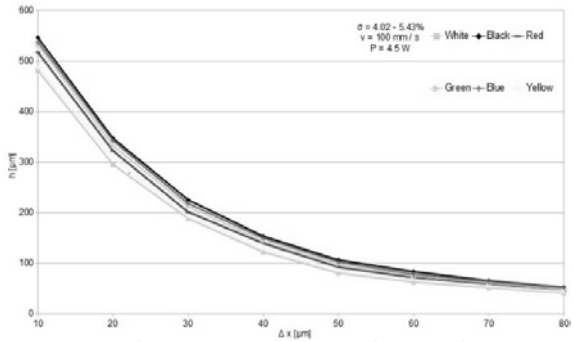

Fig. 8. Depth of the laser-ablated area as a function of raster step distance

Fig. 8 shows the dependence of the depth of laser-ablated area *h* on raster step distance *Δ x* at *v* = 100 [mm/s] and *P* = 4.5 [W] for all 6 tested colours. Due to the beam diameter *d* = 92.7 [µm] and TEM_{00} laser beam, change of *h* between *Δx* = 70 [µm] and *Δx* = 80 [µm] is relatively small. As the value of *Δx* is decreased further, *h* increases exponentially.

VII. Summary

The following statements can be made from the analysis of the experiments:

- Using the selected methodology laser type and mode, it is possible to perform quick and effective ablation of commercially available telecommunication cable isolation. Laser power *P*, procession speed *v*, and raster step distance *Δx* (for area ablation) are the most important parameters in the ablation process of PVC for single slit cuts and 10 x 10 area ablation. [15, 16] The chemical composition of specific insulation material and its colour also considerably influence the ablation process.
- Experimental dependencies of these parameters and depth of laser-ablated area *h* can be used to properly adjust laser stripping of the cable insulation, depending on the thickness of the insulation layer and diameter of the cable core according to necessary safety standards, its functionality, and specific needs of a customer. These parameters can be changed at will to adjust to different insulation material, its colour, or thickness to make the process more efficient, for example, increasing processing speed *v* and laser power *P*, adjusting raster step distance *Δx*.

VIII. Conclusion:

Finding the optimal operating parameters for specific insulation material type and thickness and understanding how a change of parameters influences the geometry of the laser-ablated area are very important steps to achieve optimal laser-material interaction. Results of this study can be of interest to different industries, which manufacturing process include cables, wires, or other applications where it is necessary to remove an area of insulating material.

The present study examines the depth of the laser-ablated area as a function of parameters such as laser power *P*, laser processing speed *v*, raster step distance *Δx* as well as the influence of colour on the process of laser ablation on a PVC-P CU twisted pair cable outer layer isolation layer with a thickness of 600 [µm].

References

[1] J. Brandrup and W. Michaeli, Eds, *Recycling and recovery of plastics*. Hanser Verlag, 1996.

[2] M. Sadat-Shojai, and G. R. Bakhshandeh, "Recycling of PVC wastes." *Polymer degradation and stability*, *96*(4), 404-415, 2011. [Online]. Available: ScienceDirect, https://www.sciencedirect.com [Accessed February 25, 2021], https://doi.org/10.1016/j.polymdegradstab.2010.12.001

[3] N. M . Abdel-Gawad, A. Z. El Dein, D. E. A. Mansour, H. M. Ahmed M. M. F. Darwish, and M. Lehtonen, "Multiple enhancement of PVC cable insulation using functionalized SiO2 nanoparticles based nanocomposites., " *Electric Power Systems Research*, *163*, 612-625, 2018. [Online]. Available: ScienceDirect, https://www.sciencedirect.com [Accessed February 25, 2021], https://doi.org/10.1016/j.epsr.2017.11.011

[4] K. Barber and G. Alexander, "Insulation of electrical cables over the past 50 years," *IEEE Electrical Insulation Magazine*, *29*(3), 27-32, 2013. [Online]. Available: IEEE Xplore, https://ieeexplore.ieee.org/Xplore/home.jsp [Accessed March 1, 2021], https://doi.org/10.1109/MEI.2013.6507411

[5] W. V. Titow, "Commercial PVC Polymers." *PVC Technology* (pp. 37-58). Springer, Dordrecht, 1984.

[6] A. J. DeMaria, and T.V. Hennessey, "The CO_2 laser: the workhorse of the laser material processing industry,"*SPIE Professional Magazine*, 1-27, 2010. [Online]. Available : https://spie.org/Documents/Membership/laser_co2_demaria_hennessey.pdf

[7] P. A. Lykov, E. V. Safonov, and A.M. Akhmedianov," Selective laser melting of copper," *Materials Science Forum* (Vol. 843, pp. 284-288). Trans Tech Publications Ltd, 2016. [Online]. Avaivable: Scientific.net, https://www.scientific.net

[Accessed March 5, 2021], https://doi.org/10.4028/www.scientific.net/MSF.843.284

[8] J. Martyniuk, "UV laser-assisted wire stripping and micro-machining," *Lasers as Tools for Manufacturing* (Vol. 2062, pp. 30-38). International Society for Optics and Photonics., 1994. [Online]. Available: SPIE Digital Library, https://www.spiedigitallibrary.org [Accessed March 3, 2021] https://doi.org/10.1117/12.167593

[9] W. F. Iceland, "Design and development of equipment for laser wire stripping," *Industrial Applications of High Power Laser Technology* (Vol. 86, pp. 68-72). International Society for Optics and Photonics, 1976. [Online]. Available: SPIE Digital Library, https://www.spiedigitallibrary.org [Accessed March 2, 2021], https://doi.org/10.1117/12.954963

[10] T.R. Miller, "Laser Wire Stripping", *Proc. SPIE 0744, Lasers in Motion for Industrial Applications*, 1987.

[11] A.S. Cale, J.D. Danley, D.L. Dean Jr, T.L. Cooke, C.B. Mabry III, & D.M. Miller, *U.S. Patent No. 8,052,836*. Washington, DC: U.S. Patent and Trademark Office, 2011.

[12] C. Jullien, P. Besnier, M. Dunand, and I. Junqua, "Advanced modeling of crosstalk between an unshielded twisted pair cable and an unshielded wire above a ground plane," *IEEE transactions on electromagnetic compatibility*, *55*(1), 183-194, 2012. [Online]. Available: IEEE Xplore, https://ieeexplore.ieee.org/Xplore/home.jsp [Accessed March 1, 2021], https://doi.org/10.1109/TEMC.2012.2206599

[13] S.G. Patrick, Practical Guide to Polyvinyl Chloride, 53-83, 2005.

[14] L. Lazov, A. Snikeris, I. Balchev, I. and E. Teirumnieks, "Laser marking and engraving of household and industrial plastic products". Journal of Physics: Conference Series, 1859 (1), 012016. https://doi.org/10.1088/1742-6596/1859/1/012016

[15] L. Lazov, N. Angelov, E. Teirumnieks and E. Teirumnieka, "Preliminary numerical analysis for the role of speed onto laser technological processes". Environment. Technology. Resources. Proceedings of the 12th International Scientific and Practical Conference. Volume III. – Rezekne, 2019. – pp. 137. – 142. http://dx.doi.org/10.17770/etr2019vol3.4154

[16] P. Narica, L. Lazov, A. Teilans, P.Grabusts, E. Teirumnieks and P. Cacivkins, "Method for Color Laser Marking Process Optimization with the use of Genetic Algorithms". Environment. Technology. Resources. Proceedings of the 11th International Scientific and Practical Conference. Volume II. – Rezekne, 2017. – pp. 101. – 106. http://dx.doi.org/10.17770/etr2017vol2.2607

Environment. Technology. Resources. Rezekne, Latvia
Proceedings of the 13th International Scientific and Practical Conference. Volume 3, 187-194

Laser Ablation of Paint Coatings in Industry

Lyubomir Lazov
Rezekne Academy of Technology
Rezekne, Latvia
lyubomir.lazov@rta.lv

Nikolay Angelov
Technical University of Gabrovo
Gabrovo, Bulgaria
angelov_np@abv.bg

Edmunds Teirumnieks
Rezekne Academy of Technology,
Rezekne, Latvia
edmunds.teirumnieks@rta.lv

Imants Adijāns
Rezekne Academy of Technology,
Rezekne, Latvia
imants.adijans@rta.lv

Antons Pacejs
Rezekne Academy of Technology,
Rezekne, Latvia
antons.pacejs@rta.lv

Ērika Teirumnieka
Rezekne Academy of Technology,
Rezekne, Latvia
erika.teirumnieka@rta.lv

***Abstract* - A comparison is made between the laser and sandblasting methods for removing paint from industrial facilities. The advantages of laser ablation are discussed. The possibilities of laser paint removal systems - stationary and moving - are shown. The main factors influencing the laser ablation process and the indicators that determine the quality of the obtained surface are systematized. Researchers' publications on this technological process are analyzed.**

Keywords* - *laser ablation, paint, advantages, factors, laser paint cleaning system

I. INTRODUCTION

Paint removal is a process that finds application in some specific areas such as maintenance of vessels, aircraft, cars and more. In industrial conditions, two main methods are used - sandblasting method and laser method. Both methods are widely used at the present stage of development of science and technology. It should be noted that the laser method is gradually expanding its position due to a number of its advantages over the sandblasting method:

- Nature is less polluted

The fine grits used in the sandblasting method are difficult to clean, which is too unfavorable for the environment. In the laser method, the coating is thermally removed and blown;

- The health of the workers is spared

The application of the sandblasting method requires strictly specialized clothing due to the strong dusting of the working environment, while the laser method uses only goggles and normal workwear.

- Mobility

The laser beam is easily delivered to the impact area, as it can be transported there by means of glass fiber.

- Flexibility

The paint can be removed without any surface damage or a surface with the necessary roughness can be obtained for easier repainting

- Low cost price

There is a lasting tendency to reduce the cost of the process. The improvement of laser sources and laser technology systems and the competition of manufacturing companies have led to a significant reduction in their market prices while expanding their capabilities. At the same time, the prices of consumables for the sandblasting method are slightly increasing.

- Processing of hard-to-reach places;
- Higher productivity;
- Easy maintenance of the laser technology system;
- High quality;
- Precision;
- Lack of direct mechanical or chemical contact with the substrate.

Laser ablation of paints is a complex process that is influenced by some basic factors. They are in complex

Online ISSN 2256-070X
https://doi.org/10.17770/etr2021vol3.6662

relationships with each other and both the specific influence of each factor and the complex influence of the main factors must be studied [4], [20], [25 – 27].

The aim of the publication is to systematize the various techniques for the implementation of the technological process of laser ablation of paint from industrial facilities, to discuss their capabilities and to analyze the main factors influencing the process.

II. PRESENTATION

Laser cleaning can be defined as the removal of unwanted layers or the extended contamination of the unwanted layers from a solid substrate. In particular, laser ablation of paint from the surface of solids is an essential part of this technological process [17], [22].

Laser ablation can be viewed as a process, in which the rapidly applied heat can cause thermal expansion and propagation of a pressure shockwave, which when applied effectively can be implemented in the removal of coatings. The laser ablation process can be schematically represented as the rapid heating of the surface layers of the material undergoing ablation there by forming a plasma, which in turn creates a shockwave that ejects the ablated material outwards as fine particles (see Fig. 1). The substrate below the coating that is targeted for removal is protected from damage by keeping the laser energy density below the damage threshold. The laser ablation process is shown schematically in Figure 1 [23], [20].

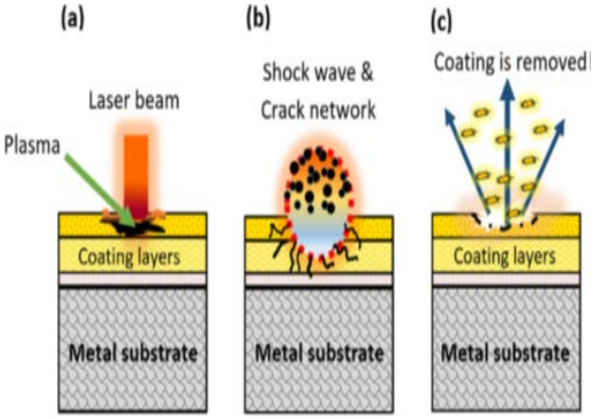

Fig. 1. Graphical illustration of the laser ablation mechanism: (a). Laser vaporizes the coating layer and creates a plasma formation. (b). Plasma creates a shock wave and crack network. (c). The top clear coat has been removed in the ablation mechanism.

In the publications of a number of authors the process of laser ablation of paint from metal surfaces is considered and researched. Various technical solutions are offered.

II.1. Laser paint cleaning systems

II.1.1. Stationary laser paint cleaning systems

An experimental system with Nd:YAG laser (λ = 1064 nm) was proposed in [18] (Fig. 2). The sample is horizontally placed on the X-Y axis platform with the laser beam perpendicularly irradiates on it. A suction pump is used to absorb the ablated paint debris. The thickness of the paint covered on steel is ~360 μm and a square of 40 mm × 40 mm is ablated by laser for performance evaluation of laser cleaning.

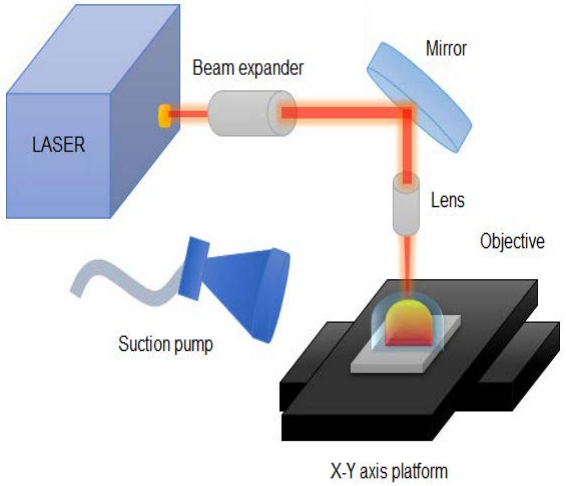

Fig. 2. Paint removal experimental setup

In the publication [10], the results are analyzed in view of the use of the system for industrial paint removal in a variety of circumstances (Fig. 3), but specifically for the use in a nuclear environment for decommissioning. The experimental work is performed using a Rofin Sinar DL025 stacked HPDL, emitting at approximately 900 nm. The working distance used between laser optics and coating surface was around 5 cm, with a spot size of around 12 mm × 7 mm. The system optics were protected by a nozzle assembly, allowing for protective air flow over the lens to prevent combustion products from depositing on the front surface.

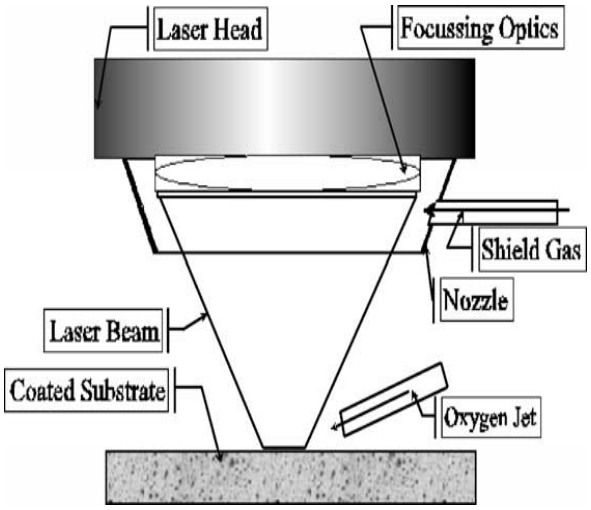

Fig. 3. Schematic of the laser–nozzle–substrate arrangement used in the experiments.

II.1.2. Moving laser paint cleaning system

The sample surfaces in [3] are irradiated while utilizing a CW fiber laser (YLS-2000, IPG Photonics, Oxford, MA, USA) with a maximum average power of 2 kW, wavelength of 1070 nm. The laser beam spot is perpendicular to the substrate surface and the laser spot size is 5.0 mm. The beam quality factor (M^2) is 1.2 measured by a laser beam quality analyzer (SP620U). The laser head is installed on a six-axis robot arm (ABB, Zürich, Switzerland). The auxiliary device includes a water-cooled chassis for the laser and an argon canister, which serves to protect the laser head lens. Argon process gas is blown over the surface in this case, in order to minimize the combustive effects. The nozzle assembly protects the system optics that allows for protective airflow through the lens to prevent combustion products from depositing on the front surface. Figure 4 presents a schematic diagram of the experimental setup.

The laser technological system can be configured for both manual and robotic tool positioning. Figure 5 shows a standard laser system with power 400 W installed in a maintenance hangar at U.S. Naval Air Station, Patuxent River, MD. The gray laser cabinet connects to the hand-held laser tool via a 50-meter, orange-colored fiber optic umbilical cable [24].

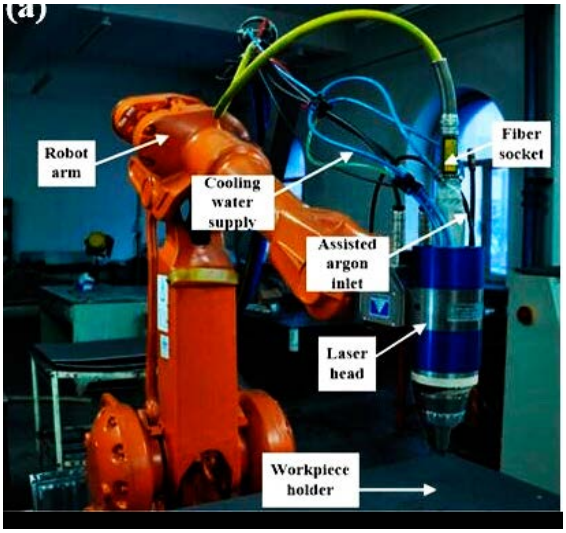

Fig. 4. Schematic diagram of experimental setup

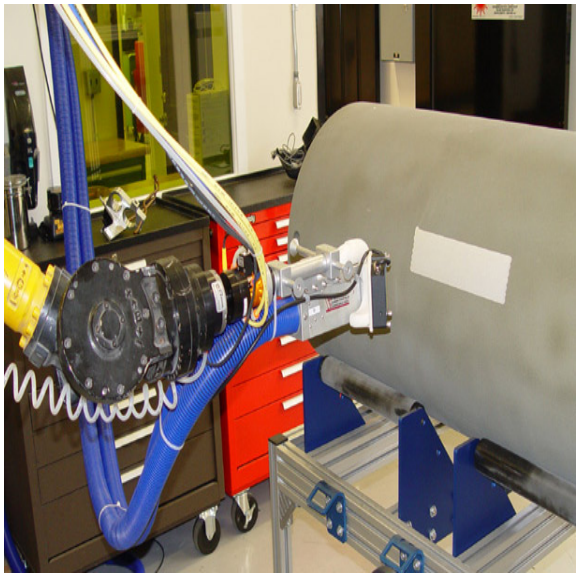

Fig. 5. A laser system in use by the US Naval Undersea Warfare Center, Keyport, WA, for cleaning test torpedoes

The manual laser tool in Figure 6 with extended fiber optic umbilical can easily reach surfaces difficult or impossible for human access. An optional video camera in the tool and heads-up operator's display enables stripping of surfaces in confined spaces, e.g., voids and tanks, or in difficult to reach spaces such as beneath or behind equipment [24].

Fig. 6. Heads-up display for confined space access

The characteristics of lasers and laser paint ablation systems are presented in Table 1. It can be seen that lasers operating in both continuous and pulsed mode are used. CO_2 lasers have less power than fiber lasers, Nd: YAG lasers and diode lasers, because the absorbency of dyes for radiation with a wavelength of 10.6 μm (far infrared area) is greater than this for wavelength of about 1 μm (near infrared area). In addition, it should be noted that the

radiation of fiber lasers, Nd: YAG lasers and diode lasers is easily transmitted along the glass fiber to the area of impact. It is impossible to transfer CO_2 laser radiation via glass fiber.

TABLE 1. SOME CHARACTERISTICS OF LASERS AND LASER SYSTEMS USED FOR LASER PAINT ABLATION

Laser / Characteristic	Fiber laser	Nd:YAG laser	Diode laser	CO_2 laser
Wavelength, nm	1064	1064	800 ÷ 950	10600
Operating mode	Pulse mode CW	Pulse mode Q-switch mode CW	Pulse mode CW	CW
Power, W	500 ÷ 2500	500 ÷ 2500	500 ÷ 2500	100 ÷ 1000
Diameter of work spot, mm	1 ÷ 5	1 ÷ 5	1 ÷ 5	1 ÷ 10
Frequency, kHz	20	20	20	–
Pulse duration, nm	100	100	250	–
Beam quality M^2	1.2	1.5	10	6
Efficiency	40	30	50	20
Possibility to transmit radiation along glass fiber	Yes	Yes	Yes	No

II.2. Main factors influencing the process and experimental results of their research

The main factors influencing the laser ablation process are related to the laser source (wavelength, power density, working spot diameter, pulse duration, frequency), the technological process (speed, defocusing) and the physical and chemical properties of the coating. Their reporting and research as well as taking into account the physical mechanisms in the implementation of the process will lead to high quality processing (Table 2).

A number of scientists have studied the main factors influencing the process of laser ablation of paint from metals and alloys in their publications.

The influence of power, absorbed energy, frequency and speed of scanning on the process of laser ablation of paint is studied in [18]. Technological parameter are also pulse duration 100 ns and diameter of work spot 100 μm. They are determined experimentally. The performance of the laser cleaning was evaluated. An experiment was performed with repainted coating after laser ablation. Excellent adhesion strength of 20 MPa is achieved between the repainted coating and the substrate, which is higher than what is required by shipyard applications.

The removal of paint from the surface of metal samples using fiber lasers operating in continuous and pulsed mode was studied in [8]. They choose the specific energy as a quantity that determines the realization of the process. In cw mode the specific energy reduced with the increase of laser scan speed and corresponding increase of laser power. In case of repetitive pulsed mode the specific energy was found to depend on the pulse on-time as well as on the time interval between two successive pulses. At 1 kHz repetition rate, the specific energy reduced with the increase of duty cycle and corresponding increase in scanning speed, but at relatively low frequencies of 50–150 Hz and 50% overlap between two pulses specific energy was found to increase with increasing duty cycle. Irrespective of the mode of operation specific energy increased with the increase of average line energy. During the laser paint irradiation a plume of burning fume was formed over the surface and the variation in specific energy with laser processing parameters has been attributed to the absorption of laser radiation in the plume.

In the publication [10], the authors present work on investigating the suitability and characteristics of a 2.5 kW CW high power diode laser (HPDL) for the removal of chlorinated rubber (CR) and epoxy resin type paints from concrete and steel surfaces. The experimental dependence of the removal rate on the output laser power for coverage from chlorinated rubber (CR) paint, is obtained. Process characteristics, safety issues, as well as costing issues and various practical matters are discussed.

TABLE 2. REALIZATION OF THE PROCESS OF LASER ABLATION OF PAINT

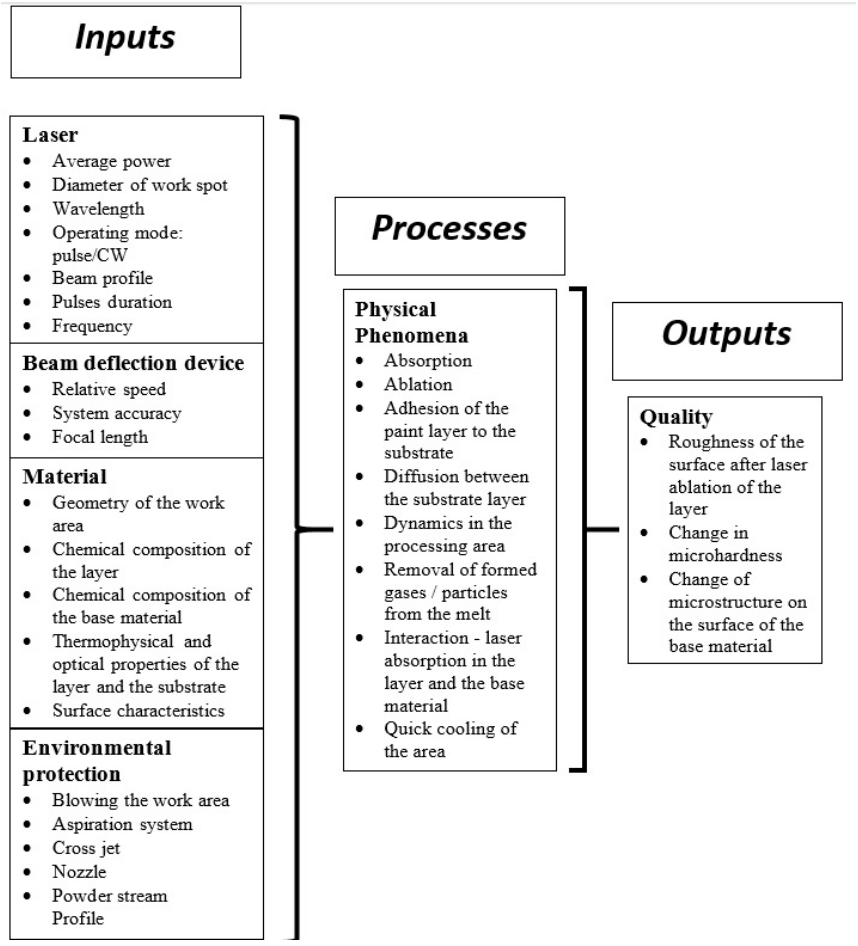

In the publication [2], authors research removal of a thin oxide layer from a tungsten ribbon. They use the fundamental (λ = 1064 nm), second (λ = 532 nm) and third harmonic (λ = 355 nm) radiation from a Q- switched Nd-YAG laser. It was found that beyond the threshold, oxide removal was achieved at all wavelengths for a wide range of influence values. The removal mechanism of the oxide layer was found to be dependent on both wavelength and influence of the incident radiation and has been identified as ejection or sublimation. The un-cleaned and cleaned surfaces were analyzed by scanning electron microscopy (SEM), energy dispersive X-ray analysis (EDS) and atomic force microscopy (AFM). Laser cleaned tungsten ribbons were used in a thermal ionization mass spectrometer (TIMS) to determine isotopic composition of Neodymium atoms.

In the paper [3], the research about continuous wave (CW) laser cleaning technique is employed to clean the paint on the substrate of aluminum alloy, using in the shipbuilding. The track width and depth of laser ablated craters are measured to study the removal rates. The analysis of cw laser cleaning is performed to explain the removal process that is theoretically based on the model, created from the authors. The model uses the heat equation with the corresponding initial and boundary conditions. It makes it possible to determine the temperature profile in the area of impact, the thermal stress profiles, the adhesion and the cleaning force. Experimental studies have also been conducted. The sample surfaces are irradiated while utilizing a cw fiber laser. The laser beam spot is perpendicular to the substrate surface and the laser spot size is 5.0 mm. The following results were obtained:

- A relationship between the removal depth rate and the power density for epoxy polyester (EP) coatings;
- The removal rate of the EP paint depending on the output power of the laser;
- The relationship between laser power density and roughness on the cleaned surface;
- The relationship between scanning velocity and the roughness on the cleaned surface;

- The dependence of HV hardness on the center of the scan line and the upper surface.

The parametric and morphological studies indicate that the cleaned surface of aluminum alloy could be achieved at proper parameters.

In [6], laser cleaningis researched as a proces with significant advantages over the conventional cleaning techniques. It is a well-controlled process with unique properties, such as precise treatment, high selectivity, and high flexi-bility. A cleaning technique using a high-power fibre laser is developed for the surface preparation of steel. Fibre laser has advantages of compact system, automation capability, and low maintenance cost. They report the laser cleaning results using a 500-W pulsed high-power fibre laser. The laser cleaning is able to meet the requirements of the International Organization for Standardization (ISO) standard 8501.

Laser assisted cleaning of oxide films on stainless steel plates is studied both experimentally and theoretically in [1]. The highly oxidized surfaces with oxide scales of about 25 mm thickness are irradiated with Q-switched pulsed Nd:YAG lasers with and without frequency doubling, i.e., at 1064 nm and 532 nm wavelengths. Both multiple irradiation on single spots and scanning with pulsed lasers are employed. The variables studied are laser wavelength, pulse duration, number of pulses, and scanning velocity. Laser cleaning experiments were performed in which the cleaned samples were at rest and in motion. The results indicate that heavily oxidized stainless steel surfaces can be cleaned with short, high power density pulses. Shorter laser wavelength, higher power density, and irradiation with multiple pulses improve the surface cleaning. No loss of the underlying metal layer is observed during treatment.

In the publication [12], the authors show that thermal stress is the main mechanism in the process of paint removal by Q-switched Nd:YAG laser (λ = 1064 nm, t = 10 ns). A theoretical model of paint removal by short-pulse laser is established from the perspective of thermal stress. Thermal stress is generated by thermal expansion, and the temperatures of different samples are calculated according to the one-dimensional heat conduction equation. The theoretical cleaning threshold can be obtained by comparing thermal stress with the adhesion of paint, and the theoretical damage threshold is obtained by calculating the temperature. Moreover, the theoretical calculations are verified by experimental results.

In the paper [16], authors show results of the investigation into the feasibility of using a CO_2 laser technology to perform critical cleaning of gas-turbine aero-engine components for manufacture. They report the results of recent trials and relate these to a thermal model of the cleaning mechanisms, and describe resultant component integrity. The paper defines the experimental conditions for the laser cleaning of various aerospace-grade contaminated titanium alloys, using a continuous wave CO_2 laser. Laser cleaning of Ti64 proved successful for electron beam welding, but not for the more sensitive Ti6246. For diffusion bonding the trials produced a defective standard of joint. Effects of oxide formation is modelled and examined experimentally.

The paper [7] investigated the feasibility and the efficiency of removal of rust from the ship steel using CO_2 pulsed laser. The results show that CO_2 pulsed laser can effectively clean the rust by using suitable parameters without damage the substrate. A cleaning threshold for stripping rust of power density exists. Also, the effect of the process parameters on the efficiency and performance as well as the removal mechanism were studied in this paper.

An investigation in the paint stripping of a single-layer epoxy polyester hybrid coating from an aluminium substrate highly suitable for recycling process is made in [11]. The feasibility of a diode laser source without any assistance of oxygen flow was checked and the best operative conditions were sought. Attention was first paid on the deposition of the polymeric film on aluminium substrates so as to perform the paint stripping process on coatings with the closest geometrical tolerances and dimensional accuracy. Then, a full factorial experimental design was led in order to study the influence of main process variables, that is, the interaction time, the power density, the focusing length, the absorption coefficient and the number of passes on the effectiveness of paint stripping expressed in terms of paint removal depth. Finally, several process maps were developed as a support in identifying the best way to lead the paint stripping process. Process characteristics, leading mechanisms and a simple regression linear model, easily applicable to a wide range of paint stripping contexts, were also discussed in detail.

Experiments to investigate the potential for practical laser graffiti-removal systems are reported in [19]. A universal engineering curve for the time needed for removal of paint from nonconductive substrates that was valid over a range of 10^7 W/cm^2 in intensity was measured with a variety of lasers. Comparable times were measured for conductive substrates, when pulses shorter than the thermal conduction times were used. The influence of the power, pulse energy, frequency, pulses duration and exposure time has been researched. Analysis suggests that Q-switched Nd:YAG lasers may be the most efficient means for removing graffiti and other unwanted paint. An 1-m2 area of paint 14 μm thick can be removed in approximately 10 min with a 50-Hz laser system of 15-W average power.

In the paper [21], the application of laser cleaning in the conservation of cultural assets is reviewed - stone and metal artifacts along with wall and easel paintings. The innovative part is entirely dedicated to the extension of the application perspective of the Nd:YAG lasers by exploiting the significant versatility provided by their different pulse durations. Besides extensively discussing the specific conservation and physical problems involved

in stone and metal cleaning, a significant effort was also made to explore the application potential for wall and easel paintings. The study of the latter was confined to preliminary irradiation tests carried out on prepared samples. The authors characterized the ablation phenomenology, optical properties, and photomechanical generation associated with the irradiation of optically absorbing varnishes using pulse durations of 10 and 120 ns. Further results concern the nature of the well-known problem of the yellowish appearance in stone cleaning, removal of biological growths and graffiti from stones, cleaning of bronze and iron artifacts and related aspects of laser conversion of unstable minerals, removal of calcareous stratification from wall paintings, and other features.

III. Conclusions

In summary, the proposed methods of laser ablation deepen the knowledge of technologists and operators in this field. They can make a choice of suitable technical devices for laser ablation of paint. In addition, they can evaluate the influence of various factors on the laser ablation process. Systematizing these factors makes it easier for them to plan their experiments when working with different paints or laser sources.

IV. References

[1] Guo, H, R. Martukanitz, T. DebRoy, Laser assisted cleaning of oxide films on SUS409 stainless steel, *Journal of Laser Applications*, 2004, 16(4): 236–244. DOI: https://doi.org/10.2351/1.1809639

[2] Kumar, An., V. Sonar, D. Das, R. Bhatt, P. Behere, M. Afzal, Ar. Kumar, J. Nilaya, D. Biswas, Laser cleaning of tungsten ribbon, *Applied Surface Science*, 2014, 308: 216–220., DOI: https://doi.org/10.1016/j.apsusc.2014.04.138

[3] Brygo, F., C. Dutouquet, F. Le Guern, R. Oltra, A.Semerok, J. Weulerssea, Laser fluence, repetition rate and pulse duration effects on paint ablation, *Applied Surface Science*, 2006, 252(6): 2131–2138. DOI: 10.1016/j.apsusc.2005.02.143

[4] Chen, G., T. Kwee, K. Tan, Y. Choo, M. Hong, Laser cleaning of steel for paint removal, *Applied Physics A*, 2010, 101(2): 249–253, DOI: https://doi.org/10.1007/s00339-010-5811-0

[5] U.S. Department of the Navy Carderock Division; Naval Surface Warfare Center; Peterson Builders Inc.,The National Shipbuilding Research Program: Surface Preparation and Coating Handbook; IIT Research Institute: Chicago, IL, USA, 1994. https://apps.dtic.mil/sti/pdfs/ADA447625.pdf

[6] Chen, G., T. Kwee; K. Tan, Y. Choo, M. Hong, High-power fibre laser cleaning for green shipbuilding. Journal of Laser Micro / Nanoengineering, 2012, 7(3):249-253. DOI: 10.2961/j1mn.2012.03.0003

[7] Ke, L.; H. Zhu, W. Lei, Z. Cheng, Laser cleaning of rust on ship steel using TEA CO2 pulsed laser. In Photonics and Optoelectronics Meetings (POEM) 2009: Industry Lasers and Applications; International Society for Optics and Photonics: Bellingham,WA, USA, 2009; Volume 7515, 75150G1-75150G8, DOI: 10.1117/12.846775

[8] Madhukar, Y., S. Mullick, D. Shukla, S. Kumar, A. Nath, Effect of laser operating mode in paint removal with a fiber laser, Applied Surface Science, 2013, 264, 892–901, DOI: https://doi.org/10.1016/j.apsusc.2012.10.193

[9] Tsunemi, A., K. Hagiwara, N. Saito, K. Nagasaka, Y. Miyamoto, O. Suto, H. Tashiro, Complete removal of paint from metal surface by ablation with a TEA CO_2 laser, Applied Physics A, 1996, 63, 435–439, https://link.springer.com/article/10.1007/BF01571670

[10] Schmidt, M.J.J.; Li, L.; Spencer, J.T. An investigation into the feasibility and characteristics of using a 2.5 kW high power diode laser for paint stripping, Journal of Materials Processing Technology, 2003, 138, Issues 1-3, 109–115, DOI: https://doi.org/10.1016/S0924-0136(03)00057-8

[11] Barletta, M.; Gisario, A.; Tagliaferri, V. Advance in paint stripping from aluminium substrate, Journal of Materials Processing Technology, 2006, 173, Issue 2, 232–239, DOI: https://doi.org/10.1016/j.jmatprotec.2005.11.029

[12] Zou, W., Y. Xie, X. Xiao, X. Zeng, Y. Luo, Application of thermal stress model to paint removal by Q-switched Nd: YAG laser, Chinese Physics B, Volume 23, Number 7, 074205, 2014, DOI: 10.1088/1674-1056/23/7/074205

[13] Lu, Y.F.; Song,W.D.; Ang, B.W.; Hong, M.H.; Chan, D.S.H.; Low, T.S. A theoretical model for laser removal of particles from solid surfaces, Applied Physics A, 1997, 65, 9–13, DOI: https://doi.org/10.1007/s003390050533

[14] Tam, A., W. Leung, W. Zapka, W. Ziemlich, Laser-cleaning techniques for removal of surface particulates, Journal of Applied Physics, 1992, 71, 3515–3523, DOI: https://doi.org/10.1063/1.350906

[15] Kelley, J.D.; Hovis, F.E. A thermal detachment mechanism for particle removal from surfaces by pulsed laser irradiation, Microelectronic Engineering, 1993, 20 (1-2), 159–170, DOI: https://doi.org/10.1016/0167-9317(93)90213-O

[16] Turner, M., P. Crouse, L. Li, A. Smith, Investigation into CO_2 laser cleaning of titanium alloys for gas-turbine component manufacture, Applied Surface Science., 2006, 252 (13), 4798–4802, DOI: https://doi.org/10.1016/j.apsusc.2005.06.061

[17] Gathers, G., Thermophysical properties of liquid copper and aluminum International Journal of Thermophysics, 1983, 4, 209–226, DOI: https://doi.org/10.1007/BF00502353

[18] Li, X., T. Huang, W. Chong, R. Zhou, Y. S. Choo, M. Hong, Laser cleaning of steel structure surface for paint removal and repaint adhesion, Opto-Electronic Engineering, 2017, 44(3): 340-344, DOI: 10.3969/j.issn.1003-501X.2017.03.009

[19] Liu, K., E. Garmire, Paint removal using lasers, Applied Optics 34(21):4409-4415, 1995, DOI: 10.1364/AO.34.004409

[20] Razab, M., A. Noor, M. Jaafar, N. Abdullah, F. Suhaimi, M. Mohamed, N. Adam, N. Jusuf, A review of incorporating Nd: YAG laser cleaning principal in automotive industry, Journal of Radiation Research and Applied Sciences, Vol. 11, Issue 4, 2018, DOI: https://doi.org/10.1016/j.jrras.2018.08.002

[21] Siano, S., J. Agresti, I. Cacciari, D. Ciofini, M. Mascalchi, I. Osticioli, A. Mencaglia, Laser cleaning in conservation of stone, metal, and painted artifacts: state of the art and new insights on the use of the Nd: YAG lasers, Applied Physics A, Volume 106, Issue 2, 419-446, 2012, DOI: https://doi.org/10.1007/s00339-011-6690-8

[22] Bergström, D., J. Powell, A. Kaplan, The absorptance of steels to Nd: YLF and Nd: YAG laser light at room temperature, Applied Surface Science Vol. 253 Issue 11 (2007): 5017-5028, DOI: https://doi.org/10.1016/j.apsusc.2006.11.018

[23] Mongelli, G., Portable handheld laser small area supplemental coatings removal system retrieved from Dayton, Ohio, United States, 2005, https://apps.dtic.mil/sti/pdfs/ADA451223.pdf

[24] Laser Paint Stripping, Laser Cleaning and Coating Removal Solutions, Lasertronics.com, General Lasertronics Corporation, www.lasertronics.com/wp/applications/ship-maintenance/

[25] Dichev, D., I. Zhelezarov, T. Karadzhov, N. Madzharov and D. Diakov, "Method for measuring motion parameters of moving objects," 12th International Scientific and Practical Conference on Environment, vol. 3, 27-31, 2019, DOI: 10.17770/etr2019vol3.4131\

[26] G. Cvetanov, T. Karadzhov and R. Miteva, "Determination of the elastic displacements in plain strained condition of involute cylindrical gears with asymmetric profile," in 46th International Conference on Applications of Mathematics in Engineering and Economics, Sofia Bulgaria, 2021. DOI: 10.1063/5.0042511

[27] Zlateva-Petkova, T., Human Resources Quality as a Factor for Competitive Power of Organizations, State University SUMI, vol. 3, pp. 207-212, Ukraine, 2011, ISSN 2218-4511, https://www.researchgate.net/publication/279473856_Human_resources_quality_as_a_factor_for_competitive_power_of_organizations

Environment. Technology. Resources. Rezekne, Latvia
Proceedings of the 13th International Scientific and Practical Conference. Volume 3, 195-197

Technological Optimization of Positioning Prismatic-Body Details in Holding Devices

Angel Lengerov
Technical University - Sofia, Plovdiv Branch
Plovdiv, Bulgaria
anlen@tu-plovdiv.bg

Abstract - **The aim of the present work is to propose and substantiate a scheme of a device for positioning prismatic-body details on two holes with parallel axes and a plane, perpendicular to them. This will help to achieve high accuracy of linear and angular orientation of the workpiece. Thus the requirements for the accuracy of the center-to-center distance of the base holes will be reduced and the process of assembling the workpiece to the grip pawls will be simplified.**

Keywords - accuracy, optimization, prismatic –body details,

I. INTRODUCTION

The process of prismatic-body details positioning, based on two holes with parallel axes and a plane perpendicular to them, is performed on support plates with different combinations of mounting pawls: a cylindrical and a sheared pawl; two cylindrical pawls, one of which may be of reduced diameter relative to the base hole; two conical, sinking pawls; two elastic grip pawls [1, 2] and others. The most common and most precise in terms of accuracy of orientation of the workpiece is the first of these solutions. The main disadvantage of positioning by means of a cylindrical and a sheared pawl is the need for achieving high accuracy of the center-to-center distance between the base holes of the workpiece during their prefabrication. This makes the technological process more expensive and is not justified in cases when the base openings are not used in mounting and assembling, but have a purely technological purpose. In addition, the operation of these devices reveals [3, 4] some difficulties in assembling the workpiece on the pawls.

The aim of the present work is to propose and substantiate a scheme of a device for positioning of prismatic-body details on two holes with parallel axes and a plane perpendicular to them, which would allow to achieve the highest possible accuracy of linear and angular orientation of the workpiece with reduced requirements to the accuracy of the center-to-center distance of the base holes and greater ease when assembling the workpiece to the pawls in a positioning process.

II. METHODOLOGY

The construction and the principle of operation of the proposed device are clarified in Fig.1. The workpiece 1 is mounted on the support plates 2 on the base surface. The pawls 3 are cylindrical. This is determined by the presence of a tolerance T_L at a distance L between the axes of the base holes, as a result of which, when positioning a batch of workpieces, the position of one of the pawls (Fig. 1 b) is shared between two boundary positions. The diagram shows that the area enclosed by the intersection of the two boundary circumferences belongs to all workpieces in the batch. The diameter of the right-hand pawl must fall into this area and its tolerance must be equal to T_L.

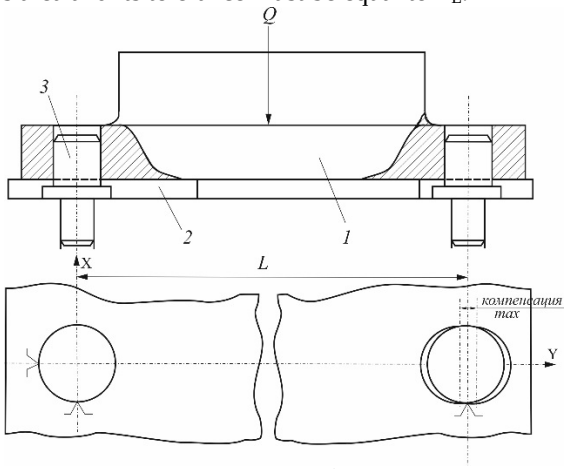

Fig.1. Model design of the device

The linear movement of the detail in the direction of Ox and Oy axes is limited within the clearance between the fixed pawl and the base hole, assembled with it. In this respect, the proposed scheme is completely equivalent to the scheme of positioning on a cylindrical and a sheared pawl.

Online ISSN 2256-070X
https://doi.org/10.17770/etr2021vol3.6523

The limiting values for the displacement of the workpiece from the middle position are:

$$J_{3\min 1} = \frac{J_{\min 1}}{2}$$
$$J_{3\max 1} = \frac{J_{\min 1} + T_1 + T_1^{'} + T_{w1}}{2} \quad (1)$$

where $J_{3\min 1}$ and $J_{3\max 1}$ are the limiting operating radial clearances;

$J_{\min 1}$ - the minimum guaranteed clearance;

T_1 - the tolerance of the base opening;

$T_1^{'}$ - the tolerance of the diameter of the pawl;

T_{w1} - the tolerance for the wear of the pawl.

The role of the movable pawl, similar to the role of the sheared one, is to limit the rotation of the detail around the axis of the fixed pawl. The largest angle of rotation α (Fig. 2) from the middle position can be determined by the formula

$$\sin\alpha \approx \frac{J_{3\max 1} + J_{3\max 2} + \frac{J_{3\max 3}}{\cos\beta} + \frac{T_L}{2}\sin\beta + f_y}{L} \quad , (2)$$

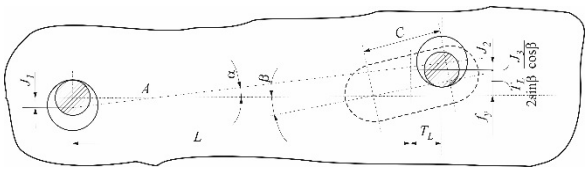

Fig. 2. Scheme for determining the error of the workpiece rotation

where $J_{3\max 2}$ is the maximum operating radial clearance between the movable pawl and the base hole;

$J_{3\max 3}$ - the maximum operating radial clearance between the movable pawl and the guide channel;

β - the angle between the direction of the center-to-center distance and the axis of the channel, obtained as a result of inaccuracy in its fabrication;

f_y - the linear inaccuracy in the channel fabrication, representing the distance between its middle part and the direction of the center-to-center distance.

The clearance $J_{3\max 2}$ is analogous to $J_{3\max 1}$ and depends on the same elements as the ones, specified in (1), but taken for the connection pair movable pawl - base hole. The maximum displacement of the movable pawl in the guide channel is determined by the expression:

$$J_{3\max 1} = \frac{J_{\min 3} + T_3 + T_3^{'} + T_{w3} + T_{w3}^{'}}{2} \quad (3)$$

where $J_{\min 3}$ is the minimum guaranteed clearance;

T_3, T_{w3} are the tolerances for fabrication and wear of the pawl;

$T_3^{'}$, $T_{w3}^{'}$ - the tolerances for fabrication and wear of the channel.

In case of positioning on a cylindrical and a sheared pawl, the maximum error of rotation of the detail, determined by the rotational angle α, is:

$$\sin\alpha = \frac{J_{3\max 1} + J_{3\max 2} + f_y}{L} \quad , \qquad (4)$$

In the above dependence, the clearances $J_{3\max 1}$ and $J_{3\max 2}$ completely cover by meaning the notation in (2), while f_y is an analogous inaccuracy in the position of the sheared pawl.

The analysis of the errors in the angular position of the workpiece for the two positioning schemes, expressed by (2) and (4), shows that in the proposed scheme the error is greater, because in (3) the expressions $\frac{J_{3\max 3}}{\cos\beta}$ and $\frac{T_L}{2}\sin\beta$ are added. This conclusion is still not sufficient grounds to reject the scheme, however. The performed calculations show that in practice the difference between the errors in the two schemes is small and acceptable for the production conditions.

The quantity $\frac{T_L}{2}\sin\beta$ can be neglected as infinitesimal, since the tolerance T_L is a small number and the angle β is also small (β <1 °). As it can be seen from (3), $J_{3\max 3}$ depends on the accuracy of manufacturing both the pawl and the channel, as well as on their wear. The capabilities of the modern tool shops allow for making both elements with high accuracy and a small minimum guaranteed clearance. Moreover, this accuracy should be considered in relation to the required accuracy of positioning the detail. The wear of both the pawl and the channel is very small due to the fact that the relative displacement path is small and the two details are in constant contact (unlike the case with the connection pair pawl-base hole).

The influence of the tolerance T_L of the center-to-center distance on the accuracy of the angular orientation remains implicit, as it manifests itself in different directions. When positioning on a cylindrical and a sheared pawl, the increase of T_L leads to inadmissible sharpening of the sheared pawl, and after a certain value of T_L - to elimination of the cylindrical band. In these cases the scheme is not applicable, and the only way out is to increase the dimensional accuracy L of the

workpieces. The inaccuracy of the device additionally interferes with this scheme.

The proposed positioning scheme with two cylindrical pawls, one of which movable, allows for full compensation of the tolerance of the size *L* both for the workpiece and for the device, without limiting their nominal practical values. This is achieved at the expense of the free run of the movable pawl. The length of the channel (Fig. 2) when ignoring its angular error is determined by the condition:

$$C \geq T_L + T_L^{'} - J_{\min 1}$$

.

(5)

Two operational advantages of the proposed scheme follow from the above, compared to the case of positioning on a cylindrical and a sheared pawl - greater ease of assembly of the workpiece to the pawls and applicability in large-sized details processing.

III. CONCLUSIONS

1. The proposed scheme for body details positioning on two cylindrical pawls, one of which movable, provides high accuracy of angular positioning of details, comparable to the accuracy of positioning on a cylindrical and a sheared pawl. This is achieved by practically unlimited deviations in the center-to-center distance of the base openings.

2. The technological process of pretreatment of the base openings is simplified and the prime cost of the product is reduced, while the technological possibilities of the scheme expand toward large-sized details positioning.

3. In terms of details linear orientation accuracy both schemes are equal.

4. The introduction of a movable pawl determines greater ease when assembling the workpiece to the pawls in a positioning process.

REFERENCES

[1] G. Jordanov, Technological equipment, Sofia, 2014, (In Bulgarian).

[2] I. Zamfirov, Technological equipment, Ruse, 1994, (In Bulgarian).

[3] H. Metev, M. Vlahova, Modeling of the process selection of clamping devices in the design of fixtures for the locating of workpieces during machining. International scientific conference UNITECH'20, Gabrovo, vol.2, p. 33-38, 2020, (In Bulgarian).

[4] Z. Zlatanov, R. Raychev, Ch. Pashinski, Matrix examination of static undefined planar frame under static load", International Scientific Conference "TechSys 2018" – ENGINEERING, TECHNOLOGIES AND SYSTEMS, Technical University of Sofia, Plovdiv Branch, 17-19 May 2018, Plovdiv, Bulgaria.

Environment. Technology. Resources. Rezekne, Latvia
Proceedings of the 13th International Scientific and Practical Conference. Volume 3, 198-201

Investigation of the accuracy of details positioning in devices with elastic grip pawls

Angel Lengerov
Technical University -Sofia, Plovdiv Branch
Plovdiv, Bulgaria
anlen@tu-plovdiv.bg

***Abstract* - This paper presents the results of a study of the accuracy of fixing body details on a flat surface and two elastic grip pawls. The obtained experimental results, concerning the displacement of a detail in longitudinal and transverse direction, have been compared with the analytically obtained errors, resulting from positioning a detail on both a cylindrical and a sheared grip pawl. It has been found that the results for the accuracy of details positioning in devices with elastic grip pawls are better than those, related to using a sheared grip pawl and a cylindrical one.**

Keywords - accuracy, elastic grip pawls, device

I. INTRODUCTION

The fixtures are a work-holding or support devices used in the manufacturing industry. They are used to accurately locate and position the workpiece in a specific location and orientation and support it during machining, with respect to the tool in order to maintain the specified tolerances under the cutting and clamping forces [5].

The devices used by CNC machines should not limit the technological capabilities and flexibility of the machines, which defines some basic requirements for them as [2]: the need for a complete orientation of the part in the fixture, because the dimensions are obtained automatically by CNC machining systems; Need for complete orientation of the device and parallelism of its coordinate axes with those of the machine.

Fixtures used in CNC machines are classified as general purpose, modular, flexible or reconfigurable workholders. There has been significant research on automated flexible, reconfigurable and modular fixtures design [1]. Engineering analysis methods such as kinematic analysis, finite element analysis and expert systems are often used in the CAFD. Expert systems have been developed for assisting the fixture design and selection. They are built on rule based systems, which consist, synthesizing rules, constraining rules and strategic rules [4].

The location of small and medium-sized prismatic parts is often done on a flat surface and two pins, one of which is made cylindrical and the other is cut [2]. This scheme has become necessary due to its significant advantages: simple construction of the fixture, the ability to comply with the principle of unity of the bases, the accessible a approach direction of the cutting tool from different sides of the workpiece and more. But it also has a significant disadvantage, which is emphasized in the following particular case: with a small diameter of the holes, the distance between the center of holes and pins must be made with particularly high accuracy.

To eliminate these defects, a method has been proposed for positioning prismatic parts on a flat surface in two elastic pins. The two base pins are cylindrical and assemble the holes in a transition joint. The error of distance between the center of the holes is compensated by the elastic deformation of the console part of the pins, which has a reduced cross section.

The aim of the present work is to investigate the accuracy of locating prismatic details in a fixture with elastic pins. The obtained results can be used in the design of fixtures, as well as in the development of expert systems for CAFD.

II. METHODOLOGY

The experimental setup (system) of the study is shown in Fig.1. The error of the position of the part when basing it in the fixture is determined in the fixed to the workpiece, coordinate system XYZ. Control points on the surface of the part, through which the error of the establishment in space can be registered, are selected according to the principle the 3-2-1 locating principle (6 points location) [2, 5, 6]. Their position is chosen depending on the

Online ISSN 2256-070X
https://doi.org/10.17770/etr2021vol3.6524

configuration of the part and at the maximum possible distance between them.

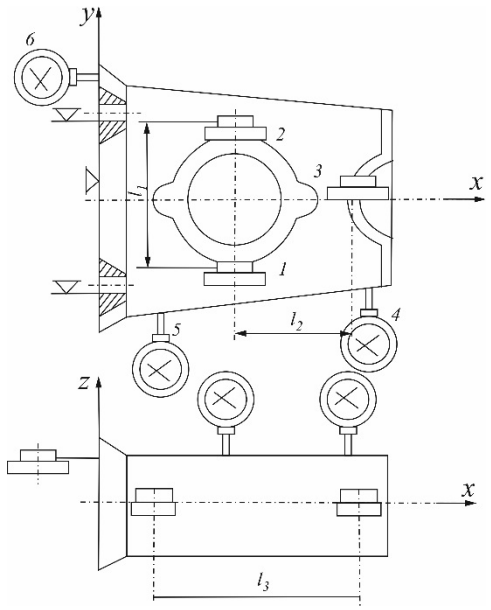

Fig. 1. The experimental setup

Points 1, 2 and 3 determine the position of the part in the plane xOy and rotation relative to the x and y axes, and points 4 and 5 - the movement along the y-axis and rotation relative to the z-axis. The sixth point determines the movement of the part along the x-axis. The error of the position of the part at each of these points is reported by means of measuring clocks with a division value of 0,001 mm, fixed to the mass of the machine by means of magnetic holder.

III. RESULTS AND DISCUSSION

100 attempts were performed for three details with an error of the distance between the centres of holes of 0 mm, -0,25 mm and +0,25 mm.

The rotations relative to the three coordinate axes were calculated for each experiment using the equations:

$$\alpha_x = \frac{\Delta_1 - \Delta_2}{l_1} \quad , \qquad (1)$$

$$\alpha_y = \frac{\frac{\Delta_1 + \Delta_2}{2} - \Delta_3}{l_2} \quad , \qquad (2)$$

$$\alpha_z = \frac{\Delta_4 - \Delta_5}{l_3} \quad , \qquad (3)$$

where α_x , α_y , α_z are the angular deviations from the three coordinate axes;

Δ_i - the measured deviation of the respective clock;

l_1 , l_2 , l_3 - the distances between the clocks, according to fig.1.

The obtained results are statistically processed and are shown in Table. 1 and graphically in Fig. 2 and Fig. 3.

TABLE 1

Error in the center-to-center distance	Error character-ristics	Positioning errors				
		α_x, s	α_y, s	α_z, s	by the y axis	by the x axis
0 *mm*	Mean value	4	5	3	0,7	2,3
	Dispersion	5	8	8	5,8	2,7
	Deviation zone	19	34	34	25,9	11,9
- 0,25 mm	Mean value	2	6	16	-1,73	-0,07
	Dispersion	8	7	8	7,34	1,94
	Deviation zone	36	29	35	32,8	8,7
+0,25 mm	Mean value	19	15	13	2,4	2,8
	Dispersion	9	5	6	10,6	V7
	Deviation zone	33	22	3	47,4	6,4

In Fig. 2 shows the experimental and theoretical curves of the distribution of the obtained error along the y-axis, and Fig. 3 - along the x-axis, in case of deviation the distance between the centers of the holes.

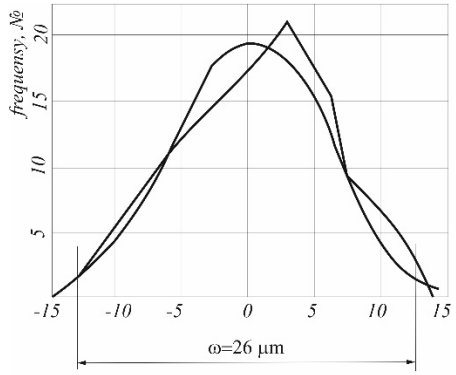

a)

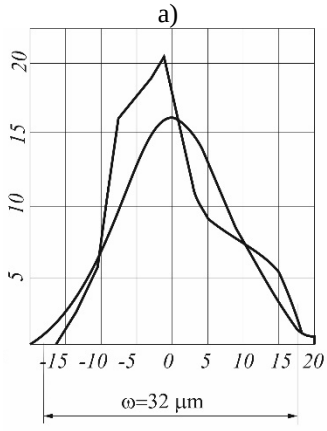

b)

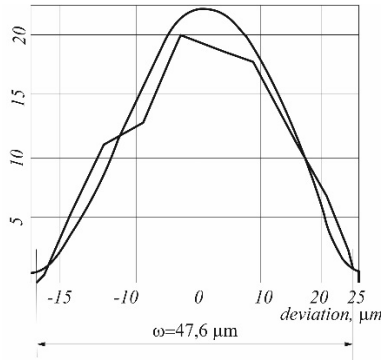

c)

Fig. 2. Error of displacement of the part in the transverse cros direction in case of error of the center distance: a) 0 mm; b) -0,25 mm; c) + 0mm

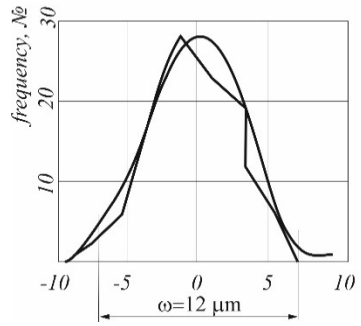

a)

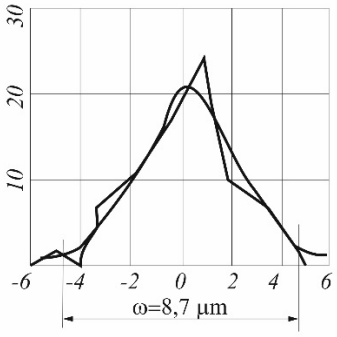

b)

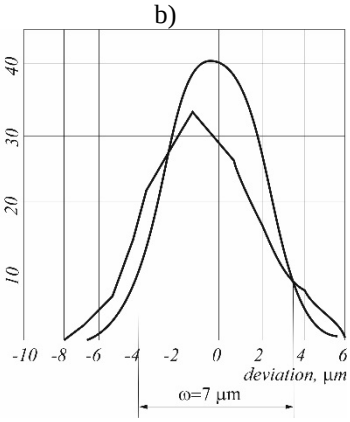

c)

Fig. 3. Error of displacement of the part in the transverse direction in case of error of the center distance: a) 0 mm; b) -0,25 mm; c) + 0mm

It can be seen from the figures that there is a good agreement of the experimental curve with the normal distribution law, which is confirmed by Pearson's criterion χ^2.

Larger deviations of the center-to-center distance result in larger scattering dispersion fields. This does not contradict the physical meaning of the elastic deformation of the pins.

An estimate of the error obtained by establishing on a flat surface and two elastic pins can be made by comparing it with the error when establishing a cylindrical and cut pin for the same conditions. As no such device is available, this comparison is made analytically.

The width b of the cut pin is determined by the condition [3]:

$$J_{\min} + \frac{d}{b} J_{\min} \geq T_{L\,\det} + T_{L\,dev} \quad , \qquad (4)$$

where $J_{\min}$ - the minimum guaranteed clearance fit between the pins and the holes;

d - diameter of the cut pin;

b - width of the cut pin;

$T_{L\,\det}$ - tolerance of between the center distance of the holes for the part;

$T_{L\,dev}$ - tolerance of between the center of the pins from the device.

For specific conditions, when clearance fit $\phi 8 \frac{H7}{f7}$ with a minimum guaranteed clearance $J_{\min} = 0,013\,mm$, when the tolerance of the center-to-center distance $T_{L\,dev} = \pm 0,02$ according to [3] for the width of the cut pin obtained in b = 0,198 *mm*. A pin of this width cannot guarantee the normal operation of the device.

To obtain a width b = 2,5 *mm*, the tolerances of the center-to-center distances must be adjusted accordingly $T_{L\,\det} = \pm 0,02\,mm$, $T_{L\,dev} = \pm 0,005\,mm$, which means that the base holes of the part must be machined on a coordinate borring with an optical device for coordinate reading. Such a solution is unacceptable in the conditions of large-scale and mass production.

With the same tolerances at center distances, a sufficient width of the cut pin can be ensured by increasing the diameter of the holes. For the above conditions, it is obtained b = 3 *mm* when clearance fit $\phi 51 \frac{H7}{f7}$ the pins with the holes. Such a solution is also impermissible, since the diameter of the holes is determined by the construction of the part.

When establishing a cylindrical and cut pin, the displacement of the workpiece in a direction perpendicular

to the axis of the pins is determined by the maximum clearance J_{max} between the pin and the hole according to [3]:

$$J_{max} = J_{min} + \frac{T_1}{2} + \frac{T_1^{'}}{2} + \frac{T_{1w}}{2} \quad , \qquad (5)$$

where T_1 is the tolerance of the hole diameter;

$T_1^{'}$ - the tolerance of the diameter of the pin;

T_{1w} - the wear tolerance of the pin.

At clearance fit $\phi 51\frac{H7}{f7}$, $J_{max} = 0,075\ mm$ is obtained. The study gives $W_{max} = 48\ \mu m$.

The largest angle of rotation when establishing a cylindrical and cut pin can be determined by the relation

$$\sin\alpha = \frac{J_{max} + J_{max}^{'}}{L}$$

where $J_{max}^{'}$ is the clearance between the hole and the cut pin;

L - center distance.

For the specific case we get $\alpha^{'} = 3^{'}$. The study obtained a maximum rotation $\alpha_x = 36"$.

IV. CONCLUSIONS

A comparative study of the error of establishing on a flat surface and two elastic pins and the popular scheme with a cylindrical and cut pins performed in this paper.

The conducted researches show that when establishing on flat surfaces and elastic pins, admissible linear and angular errors of the position of the workpiece are obtained for conditions under which the establishment on the cylindrical cut pin is impossible or inexpedient.

REFERENCES

[1] V. Ivanov, Process-Oriented Approach to Fixture Design. In Book: Advances in Design, Simulation and Manufacturing (pp. 42-50), 2019.

[2] G. Jordanov, Technological equipment, Sofia, 2014, (In Bulgarian).

[3] I. Zamfirov, Technological equipment, Ruse, 1994, (In Bulgarian).

[4] D. Stephanson, J. Agapiou, Metal cutting theory and praktice, Taylor & Francis, Inc. 2016.

[5] O. Mihaylov, G. Nikolcheva, An integrated RBR fixture design system, Vol. 5, CBU International Conference Proceedings, 2017.

[6] H. Metev, T. Kuzmanov, K. Krumov, Determining the accuracy taking into account the phenomenon of technological heredity, TU-Gabrovo, vol.49, pp.22-28, ISSN 1310-6686, 2015, (In Bulgarian).

Environment. Technology. Resources. Rezekne, Latvia
Proceedings of the 13th International Scientific and Practical Conference. Volume 3, 202-207

Selection of Locators in Automated Design of Fixtures for Locating Workpieces During Machining

Hristo Metev
Department of Mechanical Engineering Equipment and Technologies
Technical University of Gabrovo
Gabrovo, Bulgaria
hmetev@abv.bg

Kalin Krumov
Department of Mechanical Engineering Equipment and Technologies
Technical University of Gabrovo
Gabrovo, Bulgaria
kalin_krasimirov_krumov@abv.bg

Ali Gitan
Department of Mechanical Engineering Equipment and Technologies
Technical University of Gabrovo
Gabrovo, Bulgaria
homam@abv.bg

***Abstract* - Using the systematic approach, the possible basing schemes of the workpieces in the machining attachments have been discovered and systematized with a view to their use in automated design. The analysis shows that the use of the proposed systematization in computer-aided design is significantly more rational, since the structure reflects the sequence of choice of the optimal basing scheme - analysis of the theoretical basing scheme, analysis of the geometry of the workpiece, formation of the possible list of the basing schemes. An analysis was performed with the help of which the criteria for geometric compatibility were revealed, allowing to make a choice of a basing scheme, satisfying the geometric shape of the workpiece. An algorithm for selection of locators has been developed. The development is part of a system for automated design of fixtures for locating of workpieces during machining.**

Keywords* - *locating of workpieces; fixtures; basing schemes; locators; computer aided design.

I. INTRODUCTION

The development of systems for automation of engineering work has necessitated the development of systems for automated design and in particular fixtures for locating workpieces, which include newer tools, libraries, functional applications and levels of integration.

Compared to manual design, the use of CAD /CAE systems makes it possible to reduce manual labor and increase the quality of design, but does not allow complex automation, as the key stages (choosing the optimal scheme of basing (SB), calculating clamping forces, selection of construction of the locators) is done manually [1] - [5].

One of the most complex tasks in the automated design of fixtures is the selection of an optimal scheme of basing the workpieces, so *the purpose of this work is to systematize the possible schemes of basing and selection of locators in order to use them in automated design*.

II. GENERAL REGULATIONS

- *Systematization of the schemes of basing the workpieces*

The analysis of the existing systematizations of the possible schemes of basing shows that the most rational is the one proposed in [6], in which several possible realizations correspond to one theoretical SB, the number of which depends on the geometric shapes of the surfaces used for location technological bases (LTB).

Since the workpieces are based on planar (P), external (Cl^e) and internal (Cl^i) cylindrical, external (Cn^e) and internal (Cn^i) conical surfaces, different combinations of geometric shapes of the base surfaces are obtained (PPP, $PPCl^e$, etc.), occurring in practice, and a different number of realizations of SB from these combinations. Moreover, several possible combinations of geometric shapes of workpiece surfaces, used for LTB, correspond to a theoretical SB [6],[7].

The workpieces are based on one or several LTB, one of which is the main, providing the best orientation of the workpiece, depriving it of three (main plane LTB), four (double guide LTB) or five (support guide LTB) degrees of freedom.

Online ISSN 2256-070X
https://doi.org/10.17770/etr2021vol3.6603

A surface ensuring a stable position of the workpiece in the fixture is chosen as the main base. The relatively largest surface area of the workpiece is chosen.

The main LTB, depending on the degrees of freedom taken away and their symbols are given in Table 1, and the most frequently used locators - in Table 2. According to the number of deprived degrees of freedom and the geometric shape of LTB, locators are grouped as shown in Table 3.

TABLE 1 TYPES OF LOCATIONS ON TECHNOLOGICAL BASES

Geometric shape of the surface	**Deprived degrees of freedom**	**Name**	**Definition**
Plain (P)	3	main (primary)	MP
	2	guide	G
	1	support	S
Cylindrical (Cl)	4	double guide	DG
	3	main	MCl*
	2	double support (centering)	DS
	1	support	S**
Conical (Cn)	5	support guide	SG
	3	support centering	SC
	2	double support (centering)	DS***
Spherical (Sp)	3	triple support	TS
* When using a floating (self-locating) long V-blok [8] ** When using a floating (self-locating) short V-blok *** Floating center or movable rear center			

Combining the possible LTB with the possible used locators, the possible schemes of full basing were obtained (Table 4) [8].

The choice of LTB for a particular operation depends on various factors. Thus, the use of this systematization in computer-aided design is significantly more rational, as its structure reflects the sequence of selection of optimal LTB - analysis of the theoretical LTB, analysis of the geometry of the workpiece, formation of a possible list of LTB.

If the described system is applied to a specific workpiece, it is noticed that not all SB are applicable, which is determined by the geometric incompatibility of the workpiece and locators, which implement it. An important role is played by the geometric characteristics of the workpiece: the presence of stamping or casting slopes; location of the bases of the workpiece, not allowing the implementation of the selected combination of locators, etc.

TABLE 2 LOCATORS

Locators	**Definition**
Support (cylindrical or flat)	S
V-block long	V_l
V-block long floating	V_{lf}
V-block short	V_s
V-block short floating	V_{sf}
Pin cylindrical	P
Diamond pin cylindrical	P_d
Cylindrical mandrel	M_c
Diamond mandrel cylindrical	M_{cd}
Taper mandrel	M_t
Bushing cylindrical long	B_{cl}
Bushing cylindrical short	B_{cs}
Taper bush long	B_{tl}
Taper bush short	B_{ts}
Centre hard	C_h
Centre rotating	C_r
Centre floating	C_f

TABLE 3 APPLICATION OF LOCATORS

Geometric shape of LTB	**Deprived degrees of freedom**				
	5	4	3	2	1
P	-	–	S	S	S
Cl^e	-	V_l, B_{cl}	V_{lf}	S, V_{lf} , V_s, B_{cs}	S, V_{sf}
Cl^i	-	M_c	C_h	P, M_{cd}, C_f	P_d
Cn^e	B_{tl}	-	B_{ts}	-	-
Cn^i	M_t	-	C_h	C_f, C_h	-
Sp	-	-	S	-	-

When choosing the construction of locators should take into account the criteria:

- theoretical scheme of basing;
- type of locators;
- shape of the surface used for LTB;
- quality of the surface used for LTB (rough, finish, presence of casting or stamping slopes);
- maintainability;
- possibility to combine with another locator.

- *Algorithm for automated selection of locators*

The choice of the construction of the locators is made according to the scheme shown in Fig. 1, systematizing the construction of the locators according to the above criteria.

TABLE 4 POSSIBLE SCHEMES FOR BASING OF THE WORKPIECE

Theoretical SB	Surfaces	Realizations	Theoretical SB	Surfaces	Realizations
MP + G (DS) + S	PPP	SSS	DG + S + S (DG + G)	Cl^ePP	V_lSS
	$PPCl^e$	SSS			$B_{cl}SS$
		SSV_{sf}		Cl^ePCl^e	V_lSS
	$PPCl^i$	SSP_d			$B_{cl}SS$
	PCl^eP	SSS			V_lSV_{sf}
		SV_{lf} S			$B_{cl}SV_{sf}$
		SV_sS		Cl^ePCl^i	V_lSP_d
		$SB_{cs}S$			$B_{cl}SP_d$
	PCl^eCl^e	SSS		Cl^eCl^e	V_lV_s
		SV_sS			$B_{cl}V_s$
		$SB_{cs}S$			V_lS
		SSV_{sf}		$Cl^eCl^eCl^i$	V_lSP_d
		SV_sV_{sf}			$B_{cl}V_{sf}P_d$
		$SB_{cs}V_{sf}$			V_lV_{sf} P_d
	PCl^eCl^i	SS P_d			$B_{cl}SP_d$
		$SV_{lf}P_d$		Cl^eCl^i	V_lP
		SV_sP_d			$B_{cl}P$
		$SB_{cs}P_d$		$Cl^eCl^iCl^i$	V_l P_dP_d
	PCl^iP	SP_dS			$B_{cl}P_d$ P_d
		S $M_{cd}S$		Cl^iPP	M_cSS
	PCl^iCl^e	SPS		Cl^iPCl^e	M_cSS
		$SM_{cd}S$			M_cS V_{sf}
		$SM_{cd}V_{sf}$		Cl^iPCl^i	M_cSP_d
		SP V_{sf}		$Cl^iCl^eCl^i$	M_cSP_d
		SPP_d			M_cV_{sf} P_d
	PCl^iCl^i	$SM_{cd}P_d$		Cl^iCl^i	M_c P
		S C_fP_d			M_c M_{cd}
SG + S	Cn^eP	$B_{tl}S$	SC+DS+S	Cn^iCn^iP	C_hC_hS
	Cn^eCl^e	$B_{tl}V_{sf}$			C_f C_f S
	Cn^eCl^i	$B_{tl}P_d$			
	Cn^iP	M_tS			
	Cn^i Cl^e	M_tV_{sf}			
	Cn^iCl^i	M_tP_d			

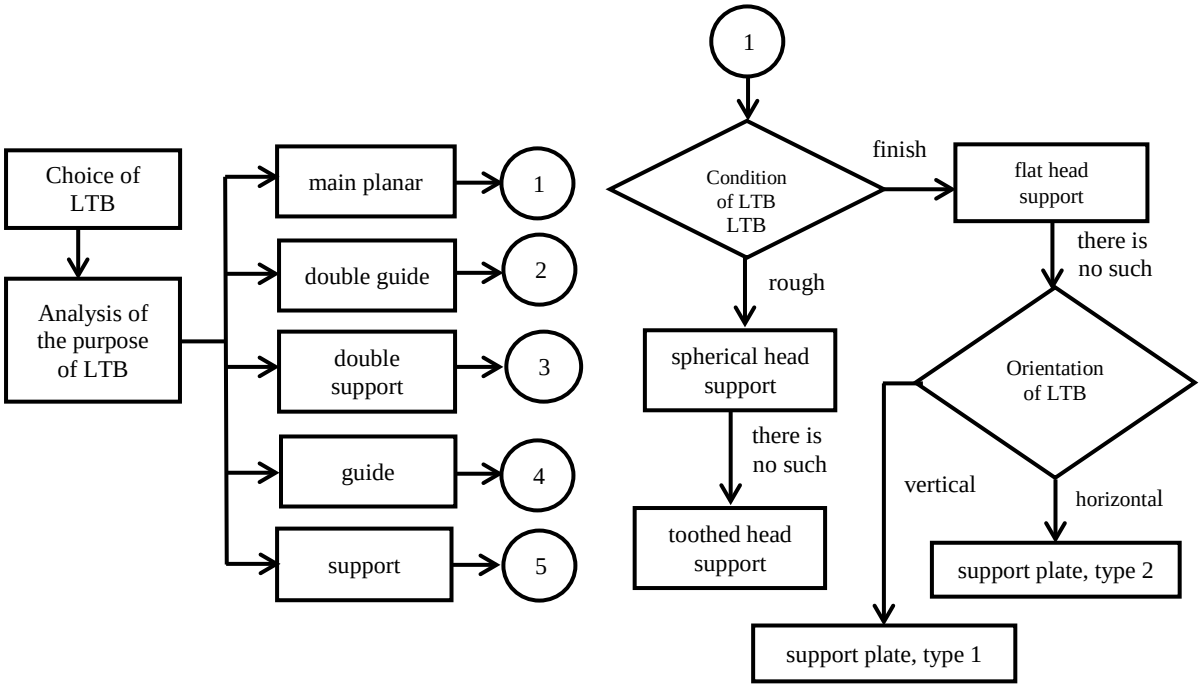

Fig. 1. Selection of locators

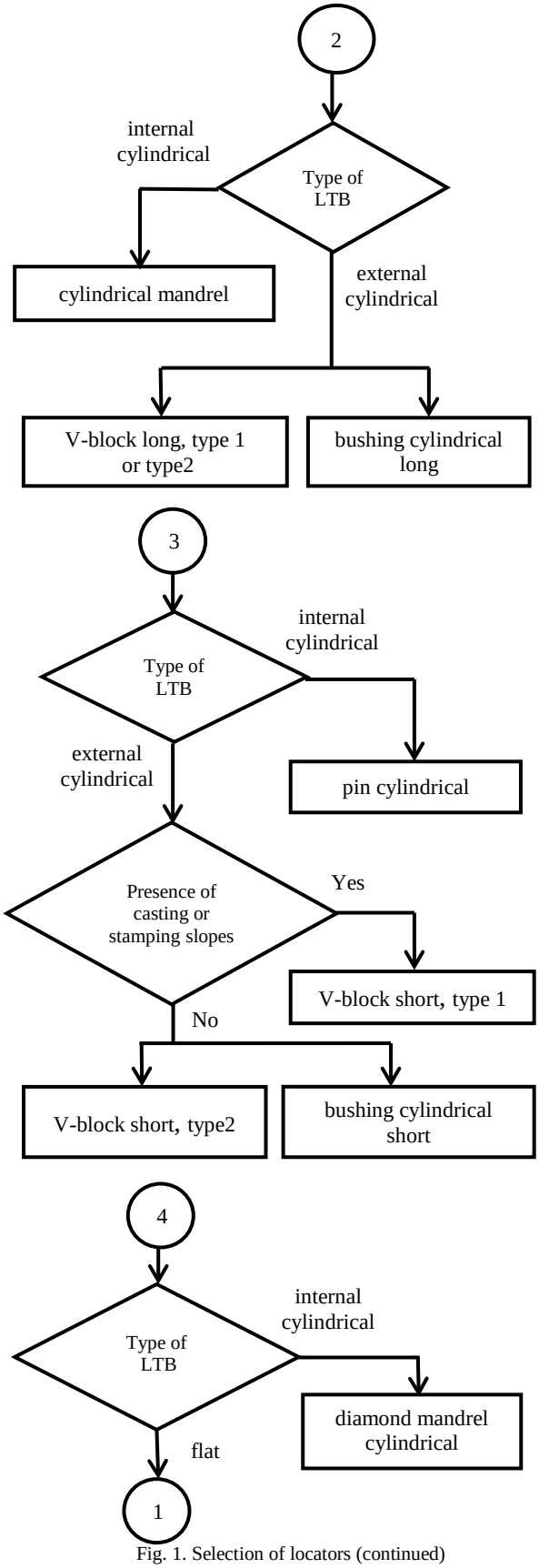

Fig. 1. Selection of locators (continued)

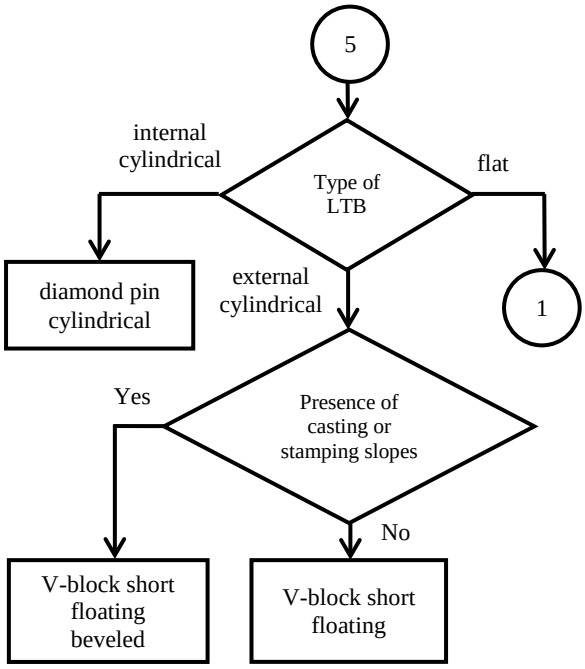

Fig. 1. Selection of locators (continued)

A database with models of locators of the fixtures in the Solid Works software environment and tables for their automated selection in the MS Excel software environment has been built, some of which are shown in Fig. 2.

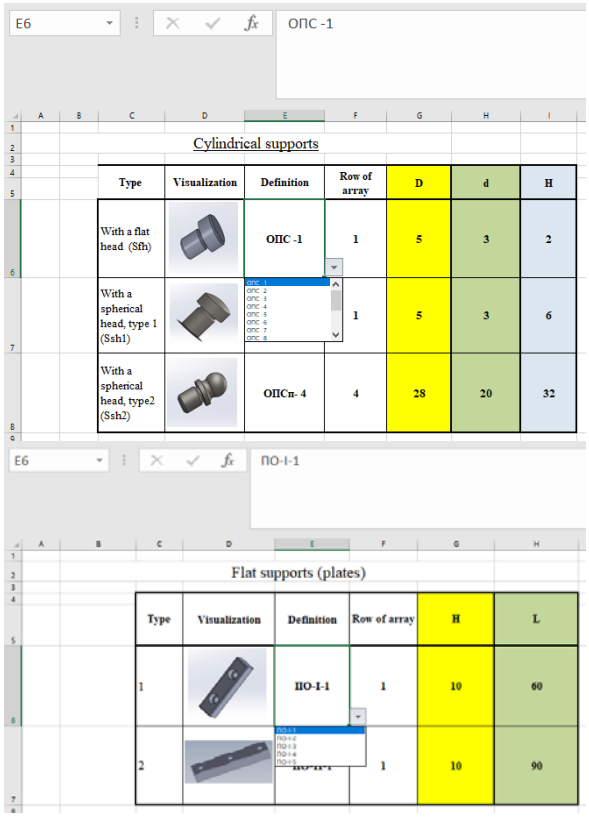

Cylindrical supports

Type	Visualization	Definition	Row of array	D	d	H
With a flat head (Sfh)		ОПС -1	1	5	3	2
With a spherical head, type 1 (Ssh1)			1	5	3	6
With a spherical head, type2 (Ssh2)		ОПСп- 4	4	28	20	32

Flat supports (plates)

Type	Visualization	Definition	Row of array	H	L
1		ПО-I-1	1	10	60
2			1	10	90

Fig. 2. Tables for automated selection of locators

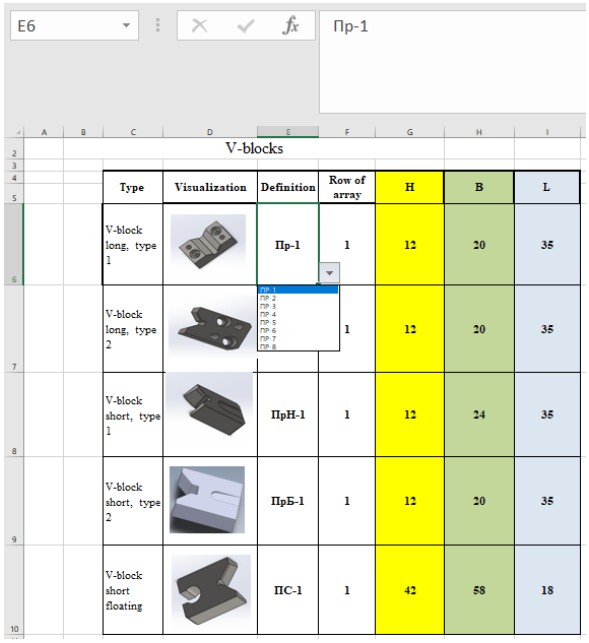

V-blocks

Type	Visualization	Definition	Row of array	H	B	L
V-block long, type 1		Пр-1	1	12	20	35
V-block long, type 2			1	12	20	35
V-block short, type 1		ПрН-1	1	12	24	35
V-block short, type 2		ПрБ-1	1	12	20	35
V-block short floating		ПС-1	1	42	58	18

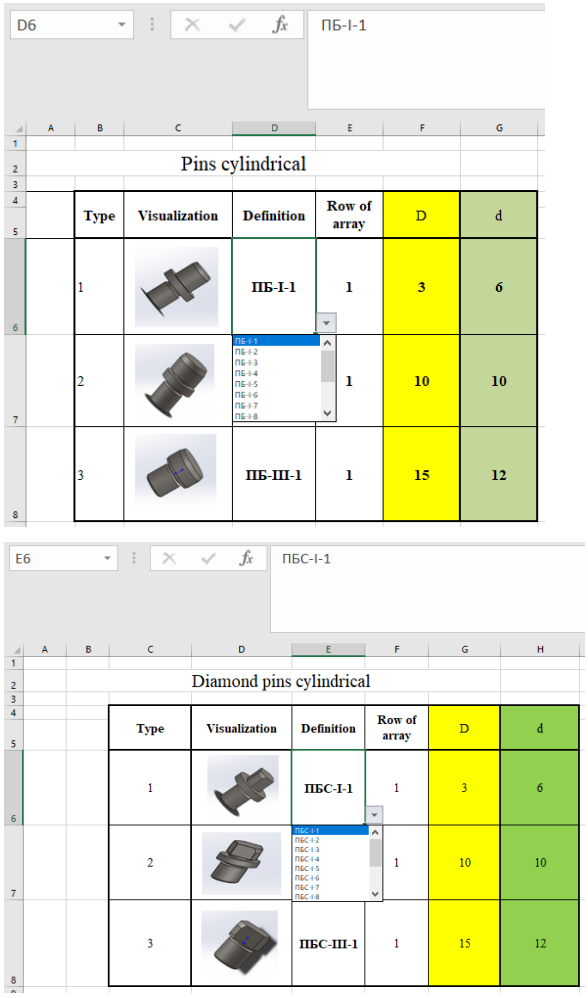

Pins cylindrical

Type	Visualization	Definition	Row of array	D	d
1		ПБ-I-1	1	3	6
2			1	10	10
3		ПБ-III-1	1	15	12

Diamond pins cylindrical

Type	Visualization	Definition	Row of array	D	d
1		ПБС-I-1	1	3	6
2			1	10	10
3		ПБС-III-1	1	15	12

Fig. 2. Tables for automated selection of locators (continued)

CONCLUSION

1. Systematization of the possible schemes of basing the workpieces in the fixtures for locating during machining with a view to use and in automated design has been performed.
2. An algorithm for selection of locators has been developed.
3. A database with locators has been created and tables for their automated selection have been developed. The database allows the inclusion of new construction elements.
4. The obtained results are a stage of the development of a system for automated design of fixtures for locating of workpieces during machining.

REFERENCES

[1] Z.M. Bi, W.J. Zhang, Flexible fixture design and automa-tion: review, issues and future direction. International Journal of Production Research, vol.39 (13), p. 2867–2894, 2001.

[2] Raev M., Metev H., Mitev J. Analysis methods of design of arrangements for the estabilishment of the preparations for machining. International scientific conference UNITECH'15, Gabrovo, Bulgaria 2015г., vol.3, p. 101-106, 2015.

[3] Metev H., Raev M., Mitev J. Methodology and algorithm for computer-aided design of fixtures for the locating of workpieces in the mechanical treatment. Journal of the Technical University of Gabrovo, vol.48, p. 35-39, 2014.

[4] Vukelic D., Hodolic J. Computer aided fixtures design. University of Novi Sad. Faculty of Technical Sciences. 47-th anniversary of the faculty. 2007: 21-26.

[5] G. Nikolcheva, O. Mihaylov, Automation of the selection of the points in location by the 3-2-1 principle using a SolidWorks intigradet locating module, Scientific Proceedings Of the Scientific-Technical Union Of Mechanical Engineering, vol.3, XIII International Congress "Machines, Technologies, Materials 2016", Varna, Bulgaria, p. 72-75, 2016.

[6] Ilickij V., B. Zotina. Design of technological equipment. Bryansk. c.123. BGTU, 2006.

[7] Metev H., Gitan A., Selection of optimal basic schemes in automatic design of fixtures for the locating of workpieces during machining. International scientific conference UNITECH'19, Gabrovo, Bulgaria, vol.2, p. 206-211, 2019.

[8] Kuzmanov T., Metev H., Tsvyatkova I. Basing workpieces analysis in mechanical working. International scientific conference UNITECH'03, Gabrovo, Bulgaria, vol.1, p. 541-543, 2003.

Environment. Technology. Resources. Rezekne, Latvia
Proceedings of the 13th International Scientific and Practical Conference. Volume 3, 208-215

Influence of Forest Stand Density on Pinus Sylvestris Roundwood Quality in Even-Aged Mixed Scots Pine Stands in Myrtillosa Mel. Mesotrophic Site Type

Ziedonis Miklašēvičs
Rezekne Academy of Technologies
State Stock Company "Latvijas Valsts Meži" (Latvia's State Forests)
Rēzekne, Latvia
Email: (Ziedonis Miklašēvičs): z.miklasevics@lvm.lv

***Abstract* - Among different development directions for better forest utilization, the purposefully detailed assessment of wood quality as raw material, faciliating improved wood utilization in manufacturing of traditional roundwood products as well as brand new products, proves to be very perspective. Roundwood quality features substantially differ depending on forest stand geographic location, growing site conditions, tending of forest stands and other circumstances [2], [3], [11]. Therefore, the economical estimation of more important tree species in Latvia should not be based only on scientific conclusions made in other countries, so particular research is needed for this purpose. Pine (Pinus sylvestris) is the most widespread tree species in Latvia, therefore a research work provided the characteristic of round wood obtained from pine tree stem is an actual point from several aspects, as it is necessary;**

- **to create early prediction models of roundwood quality;**
- **to plan harvesting purposes;**
- **to create the data basis of economically more relevant domestic tree species;**
- **to provide the further development of roundwood quality assessment methods;**
- **to estimate the competitiveness of Latvia pine timber in the world market**

The main goal of study is to work out the quality characteristic of pine roundwood manufactured in final felling sites depending on timber formation damages- bark abrasion caused side drought.

Keywords* - *bark abrasion, side drought, mature stands, medium aged stands, stands at harvesting age. stands above harvesting age.

I. INTRODUCTION

In order to ensure sustainable forest management it is very important to know the forest health and viability. The representing quality features like heartwood, sapwood, wood cells e.t.c. characterize the whole tree and its parts. Parametric characteristic of quality features depends on many circumstances. The quality of forest - plantation on the whole and growing trees are mostly affected by growing conditions [5], [6], methods of reforestation [3], [4], tending methods [11], tree bark diseases [1] forest stand density and tree competition [2], [8], [12].

At the same time due to various factors as high forest stand density and natural damage caused by wind-falls and snow breaks a part of forest stands lose their viability and die [11]. Stand damage can be classified according to location as damage to the stem or root system. Stem damage occurs above the root collar while root damage occurs below in the stem or roots "Fig. 1".

The majority of damage to the residual stand occurs during the felling stage when falling trees collide with residual tree stems. The injury can be designed further as a superficial or deep wound depending on its depth. In *Picea abies* stands, damage suffered almost inevitably leads to decay. In *Pinus sylvestris* stands, damage suffered leads to side drought with or without decay "Fig. 2".

Online ISSN 2256-070X
https://doi.org/10.17770/etr2021vol3.6611

Fig. 1. Stem damage above root collar and root damage caused side drought

Pinus sylvestris stands are more resistant to heartwood rot but in case of *Picea abies* the situation Latvia is really serious-almost a quater of trees have decay in stem and can be used mostly as energy wood or pulp wood.

Fig.2. Side drought in *Pinus sylvestris* stands with and without decay

Harvesting in Latvia has been regulated by legislation [12], which determine the final felling age and diameter according to tree species and soil quality in forest lands. Current Latvian legislation permits the final felling in *Pinus sylvestris* stands where the trees of the dominant stand have reached the mean age of 101 years or the mean diameter of 35cm.

Nevertheless by observing the instructions provided in the regulatory dokuments and when final felling in hight stands density has been performing, round timber with high volume features have been harvested, e.g. *side drought*, sweep e.t.c. which reduce the timber value “Fig. 3”.

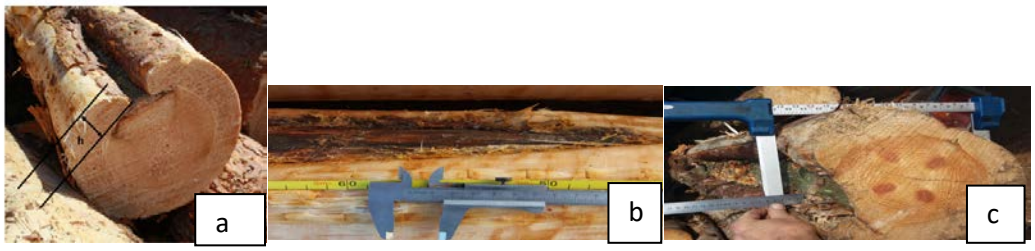

Fig.3. The depth (h) limit of side draught (a) according to the roundwood assortiment’s quality requirements: 1cm for wood poles (b); 2cm for sawlogs (c)

Pinus sylvestris is the most widespread conifer tree specie in Latvia. According to Latvian National Forest Inventory data (2013-2017), pine stands comprise 856.4 thousand ha or 26.5% of the total forest area (www.silava.lv; according to forest defination - at least 1000 trees/ha, able to reach the height of 5 m).

4.7% from the total forest area is Myrtillosa and 22% is Hylocomiosa. The total wood standing volume in Myrtillosa stands (age 101>) reaches 310m^3/ha and 365 m^3/ha in Hylocomiosa stands, where *Pinus Sylvestris* standing volume respecxtively 206m^3/ha in Myrtillosa and 178m^3/ha in Hylocomiosa [11].

Because forest that grow today will ensure Latvia with forest resources after several decades, therefore, it is especially important that its value is not decreasing.

II. STUDY GOAL

The main task of forestry is the growing forest with its most important indicator - wood resources stored in living trees. In contrast, timber companies have an additional interest not only in the volume of timber harvested, but mainly in the quality indicators of round timber. Therefore, it is important to predict possible wood defects of growing trees, which may limit the applicability of the produced round timber to high value-added sawn timber, building construction elements, etc. production.

The main goal of study is to work out how the forest stand density at the harvesting age as a most important factor determine Correlation coef r=0.66 at $r_{0.05}$=0.12 between *Pinus Sylvestris* stock volume and stand density [11] impacts the quality of roundwood assortiments and to evaluate the damages of side draughts as timber formation damages caused by wind-falls and snow in high forest stand density felling areas of mesotrophic site type (*Myrtillosa mel.)*

The following objective was set to achieve the study goal:

To clear up the characteristic of timber formation damage – *Side drought* in the commercial part of pine stems (10-15m section, devided in 4 zones) harvested as wood poles “type A. Fig.1” in overstockled young stands with overdue thinning where Scots pine current rotation age are older than 101 years and forest stand density higher than 0.7.

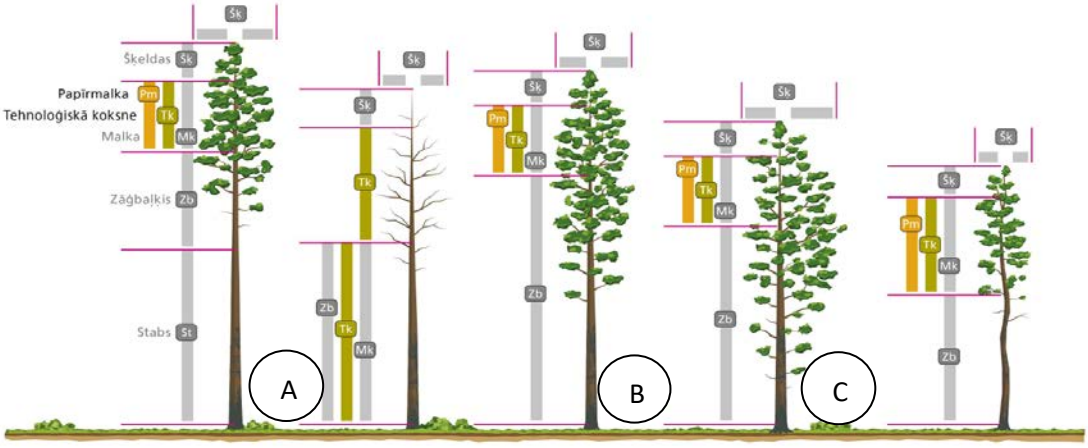

Fig.4. Harvested products from different pine stems types, where: A; B; C -pine stem types, St - wood poles; Zb- saw logs; Pm- pulp wood; Tk- technological wood; Mk- fire wood; Šķ-wood chips

III. MATERIALS AND METHODS

A field study was carried out at the period April - June of 2020 in Zemgale region of Latvia and in energy company JSC “Sadales tīkli”. Wood poles which were harvested in Myrtillosa mel. forest type where the age of pine stands according to the forest inventory description were more than 105 years old were selected in the investigation. “Table 1. ”

TABLE 1

DATA CHARACTERIZED HARVESTING SITE

Woodland type	**Myrtillosa mel.**	
Regeneration year	1905	1900
Species	6P3E1B11510E85	9P1E120+B12010E80
Area (ha)	0.70	1.3
Previous managment operation isn’t registred		

The average age of trees before harvesting in the felling area was determined by drilling 20-25 trees at the butt swelling using Presler drill and counting the annual rings of increment core.

TABLE 2

DATA CHARACTERIZED HARVESTING SITE AND HARVESTING RESULTS

Harvesting site identification	Area (ha)	Amount (m^3)	Species	Harvested amount (m^3)	Stems
493380285996	1.99	969.03	Birtch	31	66
			Spruce	360	946
			Black alder	12	47
			pine	581	584
			Total	985	1643

Traceability of wood poles was ensured. In order to gather information about impact of *side draught* on wood pole's quality parameters, the following approach, methods and data was collected:

- data characterized the wood felling area: coordinates of wood felling area; forest type; growing stock; growth conditions; site quality classes; species composition index and the age of species;
- data characterized the wood pole's visual quality parameters: lengh of wood pole; wood pole top, butt diameter and diameters measured with the interval 1m, wood pole diameter at a side draught positions; a side draught possition measured from the wood pole butt and a width/number of annual rings characterized the age of injury.

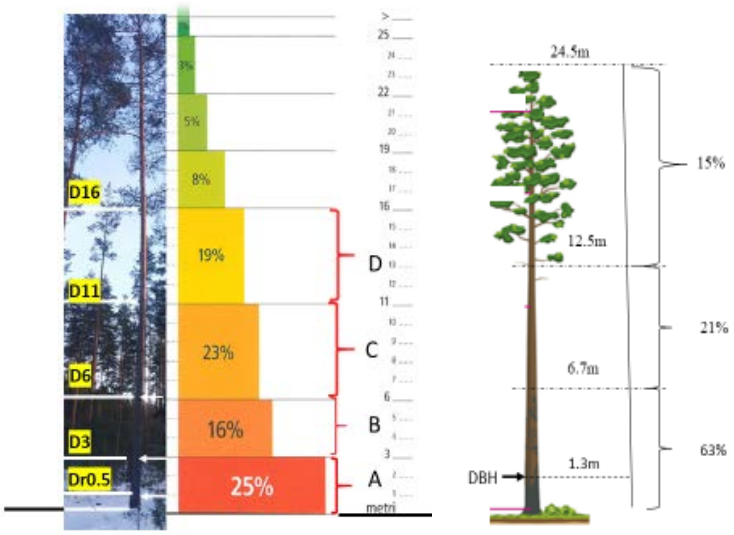

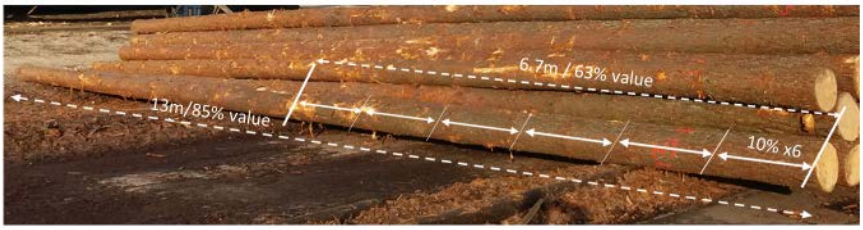

Fig. 5. The methodical distribution of pine stem by volume, zone and by timber value when stem lenght H- 24,5m, DBH -36cm; H/D=0.68

The methodical scheme of the investigation is given in "Fig. 5", where the commercial parts of pine stems manufactured as wood poles are devided in 4 zone which represents more than 84% of roundwood value.

The quality control of each of harvested 221 pcs. wood poles "Table 3, 4" was done in harvesting sites and JSC "Sadales tīkli" in each stage of technological process.

TABLE 3

HARVESTED AMOUNT OF WOOD POLES

Wood poles lenght (m)	**Pcs/ m^3**	**Average 1pcs volume (m^3)**
10	48/22.14	0.5
12	118/72.1	0.689
13	26/20.06	0.768
14	29/24.80	0.852
Total	221/139.1	

The data characterized quality of harvested wood poles are given in "Table 4".

TABLE 4

THE QUALITY OF HARVESTED WOOD POLES

Quality appreciations	**Volume pcs /(m^3)**	**% from harvested volume**	**% from harvested stem**
Defect (Curvature)	75/35.02	25.19	32.94
Defect (Side draughts)	38/25.71	18.49	18.19
Corresponds to the quality	108/78.27	56.32	48.87
Total	221/139.1		

The measurement example of side draught characterized parameters is given in "Fig. 6".

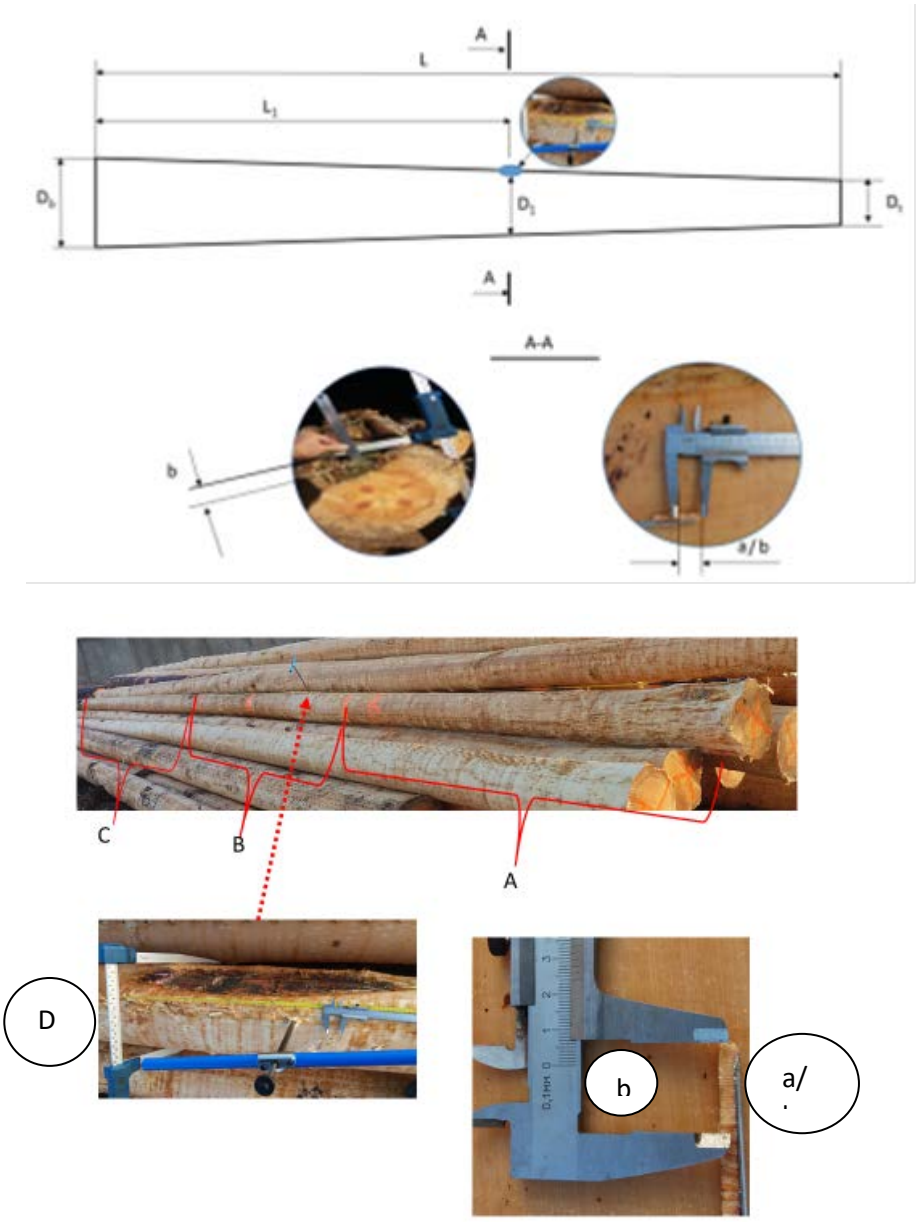

Fig. 6. The measurement example of side draught characterized parameters, where: A, B, C- zone of side draught position place; D_1-wood pole diameter at side draught position, mm; b- side draught depth, mm; a/b- number/thickness of annual rings characterized the age of injury; L_1- distance of side draught position measured from butt, cm; L- the lenght of wood pole, cm; D_t - the wood pole top diameter, mm; $D_b / D_{b\,0.5}$ - the wood pole (from B zone) butt diameter / the wood pole (from A zone) butt diameter measured 0.5m from the butt, mm

IV. RESULTS AND DISCUSSION

Harvesting development in Latvia is regulated by Cabinet Regulation No. 935 "Regulations on Tree Felling", which determines the age and diameter of the main felling according to the dominant tree species and quality. However, following the instructions provided in the regulatory documents and performing felling in forest stands with high density, round timber with an increased amount of wood faults, such as dry sides, curvature is obtained. etc., which reduces the industrial value of timber. With no or delayed felling of such stands in such harvesting sites, the amount of dead wood increases, which exceeds the natural growth. Respectively, the biological value of the forest stand increases, but the industrial value decreases. Various literature sources [11] indicate that the current growth of wood in mature stands is approx. 6.5m^3/ha, in felling age stands approx. 5.2m^3/ha. At the same time, the natural growth of the stock in uncultivated stands is close to zero or even negative. The preservation of such stands is in

stark contrast to the tasks of modern forestry - the product produced in logging is defective [9], [14].

According to the methodical requirements the measurement results characterized damages of pine stems caused by side draughts are given in "Fig. 6","Table 5".

TABLE 5
THE MEASUREMENT RESULTS CHARACTERIZED DAMAGES OF PINE STEMS CAUSED BY SIDE DRAUGHTS

Zone	**A**	**B**	**C**	**D**
Diameters	Dr0.5 / D1 / D2	D3 / D4 /D5	D6 / D7 / D8 / D9 /D10	D11 / D12 / D13/ D14/D15
Taper (mm/m) (221wood poles)				
Average	7.0			
Stdev	0,57			
Median	6.89			
Wood pole diameters (mm) measured according to the methodical requirements (221wood poles) "Fig. 2"				
Average	301/294/288	287/280/273	267/260/253/246/240	237/231/227/ 229/223
Stdev	30/30/29	26/26/25	25/25/25/25/25	22/22/21/16/16
Median	295/288/281	287/280/274	267/261/254/248/241	241/234/231/ 233/227
Wood pole diameters (mm) at side draught positions according to damaged zone (38 wood poles) "Fig. 2"				
Average	300	265	245	211
Stdev	30	42	40	25
Median	290	247	252	207
The depth of side draught (mm) "Fig. 2"				
Average	20.4	22.1	18	17
Stdev	8.6	8.9	4.8	4.1
Median	21	22	18	15.5
The width of annual rings (mm) characterized stem wound age "Fig. 2"				
Average	0.98	1.09	0.91	1.06
Stdev	0.22	0.19	0.15	0.19
Median	1.10	1.15	1.08	1.11
Years before side draught damages (mm)				
Average	20.8	20.2	19.7	16.0

V. CONCLUSIONS AND RECOMENDATIONS

The results of the study indicated the following:

- About 18.19% of inspected wood poles (pine stands) harvested in felling areas in Myrtillosa mel. forest type where the mean age of pine trees were 115-120 years old were damaged by timber formation damages -side draughts.
- About 18.49% from harvested pine stems volume (wood poles) were rejected due to timber formation damages -side draughts which average depth (mm) exceeds 20mm.
- The data characterized stem wound age shows that the biological value of the pine stand starts to increase, but the industrial value decreases in mesotrophic site type (*Myrtillosa mel.)* harvesting sites where the age of stems is more than 100 year.
- There are advisible to raise the issue of reducing the felling criteria (age of the main felling (in years) depending on the quality and average diameter of the stand) in non-cultivated felling stands in felling stands where there is no purposefully created tree stands structure, by evaluating socio-economic and ecological aspects.
- In forests with this kind of management history the application of the current rotation age (101 years) will likely be a grave mistake. The existing management model should be altered.

VI REFERENCES

[1] N. Arhipova, T. Gaitnieks, J. Donis, J. Stenlid and R. Vasaitis, "Butt rot incidence, causal fungi and related yield loss in Picea abies stands of Latvia". Canadian Journal of Forest Research, 41 (12 VI.): 2011, pp. 2337-2345.

[2] I. Baumanis, "A complex research project: factors in Latvia affecting the health of pine (planting stock and young plantations), and recommended protective measures". Proceedings of the Latvian Academy of Sciences, Section B, 7(552), 1993, pp. 79-80.

[3] I. Baumanis , Ā. Jansons and U. Neimane, Selection, genetics and seeding in Latvia. Daugavpils, 2014, p. 324.

[4] R. A. Blanchette. "Decay and canker formation by Phellinus pini in white and balsam fir". Can. J. For. Res. 12. 1982, pp. 538-544.

[5] C. J. Earle "*Pinus sylvestris* (Scots pine) description. In: The Gymnosperm Databaswe".2011, http://www.conifers.org/pi/Pinus_sylvestris.php [archived in July, 2014]

[6] D. E. Etheridge "True heartrots of British Columbia. Canadian Forest" Service, Pacific Forest Research Center, Victoria, BC.Forest Pest Leaflet No. 55. 1972, p. 14.

[7] R. S. Hunt and D. E. Etheridge "True heart-rots of the Pacific Region". Forest Pest Leaflet No.55, Pacific Forestry Centre. 1995, p. 8.

[8] M. J. Larsen and F. F. Lombard, "A new variety of Phellinus pini associated with cankers and decay in white firs in southwestern Oregon and northern California". Can. J. For. Res. 9: 1979, pp. 31-38.

[9] Z. Lībiete, J. Jansons and T. Zālītis, "Age structure and productivity of conifer stands in Latvia". Mežzinātne / Forest Science 19(52): 2009, pp. 28-48.

[10] Z. Miklašēvičs, "Evaluation of heartrot caused by Phellinus Pini and related yield loss in pinus sylvestris stands".// The 12th international conference reports, Rezekne 2019, pp. 166-171.

[11] P. Zālītis and J. Jansons, Structure of purposefully established stands. LVMI "Silava", 2009, pp. 70-75.

[12] Cabinet Regulations N^{O}935. Regulations on tree felling.

[13] Evaluation of the effects of heart rot fungi on live treestructuralstability. https://www.for.gov.bc.ca/.../WTReport-Effects-of-HeartRotFungi-June.

https://www.zm.gov.lv/public/ck/files/ZM/mezhi/.../1_pielikums.pdf. [Accessed 2007].

[14] Opinion on the draft guidelines on forest and related development guidelines for 2015-2020, VSS-489 ldf.lv/sites/default/files/faili/Par_mums/LDF_vestules/80_ldf_msnp_vss489.doc [Accessed 2014].

Environment. Technology. Resources. Rezekne, Latvia
Proceedings of the 13th International Scientific and Practical Conference. Volume 3, 216-225

Evaluation of Damage of Roundwood Assortiments Caused by Varied Construction, Technical Solutions and Conditions of Harvester Head Feed Rollers

Ziedonis Miklašēvičs
Rezekne Academy of Technologies
State Stock Company "Latvijas Valsts Meži" (Latvia's State Forests)
Rēzekne, Latvia
Email: (Ziedonis Miklašēvičs): z.miklasevics@lvm.lv

***Abstract* - The purpose of this study was to evaluate the depth of damages caused by harvester head feed roller spikes to birtch veneer logs, harvested according to top diameter group (18x25cm, 25<cm), spruce sawlogs (6x10cm), spruce and pine sawlogs according to top diameter group (10x14cm, 14x18cm).**
Thirteen technical solutions and conditions of the harvester head soft feed rollers (Moipu Standard, Rib), standard feed rollers (Multi-Tree Handling (MTH), Steel Thumbnail) and agreesive feed rollers (TP) were tested in this study.
Regulation parameters of hydraulic system and angles of delimbing knife blades during the harvesting of stems in different woodland types and seasonality using single grip harvesters: John Deere 1270E, John Deere 1070E and John Deere 1070D equipped with harvester heads: H754; H480C and H460 were examined in clearcutting and thinning operations in twenty four wood felling sites in Kurzeme and Vidzeme region of Latvia.

Key words - soft feed rollers, standard feed rollers, agressive feed rollers, timber damages, roundwood assortiments

I. INTRODUCTION

The useful outcome of sawmaterials when sawlogs are manufactured, quality of rotary cut veneer when veneer logs are rotary peeling, wood surface quality when wood poles for power lines, building timber and posts are manufactured, depends on mechanical damages caused by harvester head feed rollers. The severity of the damage influence technical solutions and conditions of the harvester head feed rollers, regulation parameters of hydraulic system, angle of tooth of delimbing knifes, bark thickness, wood density, seasonality, professional skills of harvester operator and e.t.c. [4], [11], [1], [10], [6], [9].
According to the investigation results made by [7] the depth of damage in the tested species exhibited broad dispersion: birch 1.8-6.0, pine 4.2-8.7 and spruce 4.3-8.7 mm, with mean values of 3.7, 5.5 and 5.8 mm, respectively. Investigation results made by [4] revealed that the mean damage to the pine and spruce was 5.9 and 3.9 mm, respectively. According to the investigation results made by [4] damage caused by harvester head feed rollers in the tested species wasn't deeper 10 mm.
How the depth of damage in 10mm caused by harvester head feed rollers impacts the roundwood quality?
In rotary cut veneer manufacturing when the thickness of veneer is 1.26mm and the birch veneer log rotary cilinder is 25cm, the lenght of gained veneer in peeling process is 28.9m. If the cilinder surface damage caused by feed rollers reaches 10mm, veneer in lenght 3.1m (10.7%) will be rejected because of inadequate quality.

Online ISSN 2256-070X
https://doi.org/10.17770/etr2021vol3.6609

Fig.1. Cut veneer manufacturing process (a;b) and rejected veneer (c) caused by feed roller penetration in timber

In posts manufacturing process, if the roundwood (top diam.10cm) surface damage caused by feed rollers reaches 10mm, a greater depth of wood requires to be removed. The technological timber loss in manufacturing process will reaches 19%.


Fig.2. Roundwood surface damage caused by feed roller penetration in timber

The optimal force with which the feed rollers and delimbing knives clamp the roundwood is achieved by setting the pressing force of the hydraulic cylinders. Too low feed roller pressure comparing to delimbing knives pressure or poor technical conditons of the feed rollers and incorrect geometry of the cutting edge and sides of the knife causes bark loosening and damage on the wood surface as rollers slip. Too high pressure also causes deep roundwood damages.

Investigations in this area have been conducted in Finland, Sweden, Canada, Russia, Poland and other countries [1], [4], [6], [7], [11]. According to the investigation results made by [3], [7]. the problem related to feed roller damage has increased in Sweden and other countries, including Latvia.

II. STUDY GOAL

The goal of this study was to evaluate the depth of damages caused by harvester head feed roller spikes to birtch veneer logs, harvested according to top diameter group (18x25cm, 25<cm), spruce sawlogs (6x10cm), spruce and pine sawlogs according to top diameter group (10x14cm, 14x18cm). The following objectives were set to achieve the study goal:

(i) to evaluate the technical solutions and conditions of the harvester head soft feed rollers (Moipu Standard, Rib), standard feed rollers (Multi-Tree Handling (MTH), Steel Thumbnail) and agreesive feed rollers (TP), tested in this study;

(ii) to evaluate the geometry of cutting edge and sides of the harvester upper delimbing knives;

(iii) to evaluate the harvester head feed rollers and delimbing knives pressure settings according to species and diameters of harvested assortiments;

(iv) to measure the depth of damages caused by harvester head feed roller spikes;

Online ISSN 2256-070X
https://doi.org/10.17770/etr2021vol3.6609

(v) to collect and analyse all measurement results

III. MATERIALS AND METHODS

A field study was carried out at the period Juni of 2016 – March of 2017, in Kurzeme and Vidzeme region of Latvia. Investigations were made in Myrtillosa, Vacciniosa, Hylocomniosa, Myrtillosa turf. mel., Oxalidosa, Myrtilloso-polytrichosa; Caricoso-phragmitosa and Aegopodiosa forwest types. In study thirteen technical solutions and conditions of the harvester head soft feed rollers (Moipu Standard, Rib), standard feed rollers (Multi-Tree Handling (MTH), Steel Thumbnail) and agreesive feed rollers (TP) were tested in clearcutting and thinning operations in twenty four wood felling sites. The technical information of the studied harvester head feed rollers is given in Table1. The investigation of feed rollers was conducted with John Deere 1270E, John Deere 1070E and John Deere 1070D equipped with harvester heads: H754; H480C and H460. In order to gather information about the depth of damages caused by harvester head feed roller spikes to birtch veneer logs, harvested according to top diameter group (18x25cm, 25<cm), spruce sawlogs (6x10cm), spruce and pine sawlogs according to top diameter group (10x14cm, 14x18cm), the following approach, methods and data were collected:

- data characterized the technical solutions and conditions of the studied feed rollers by measuring the average lenght of spikes, mm;
- data characterized the technical conditions of upper delimbung knives by measuring sharpening angles and back bevel shape using blade gauge F681744;
- data characterized regulation adjustments of feed rollers and delimbung knives according to wood species and diametrs of harvested roundwood;
- data characterized the deepest penetration point (u.b.) in most damaged zone of objected assortiment caused by inner or outer feed rollers.

Data characterized wood damage caused by harvester head feed roller slip weren't reflected in this study to avoid incorrect conslusions. The main reasons caused feed roller slip are low level of harvester operator professional skills, incorrect adjustments of hidraulic system, proportion of high-average branches, e.t.c.

IV. RESULTS AND DISCUSSION

Data characterized the technical solutions and conditions of the studied feed rollers is given in "Table1". According to the investigation objective, the average lenght of the spikes were measured for each of the feed roller of observed 14 equipment (Fig. 3).

Fig.3. The lenght measurement of the feed roller spikes and evaluation the visual quality

JOHN DEERE HARVESTER HEADS, SIDE AND INNER FEED ROLLER TECHNICAL SOLUTIONS AND TECHNICAL CONDITIONS

Equipment	**A**	**B**	**C**	**CI**	**D**	**E**	**F**
Harvester head	H754	H460	H754	H754	H754	H754	H754
Outer feed rollers (average spike height)	 Soft roller *Moipu Standard* (15mm)	 Soft roller *Moipu Standard* (15mm)	 Standard roller *MTH Rib Classic* (12mm)	 Standard roller *MTH Rib Classic* (atfer renovation) (8.5mm)	 TP-roller (12mm)	 Soft roller *Moipu Standard* (13 mm)	 Soft roller *Moipu Standard* (15mm)
Inner feed roller (average spike height)	 Soft roller *Rib* (12mm)	 Standard roller *Steel Thumbnail* (12mm)	 Standard roller *Steel Thumbnail* (13mm)	 Standard roller *Steel Thumbnail* (12mm)	 Standard roller *Steel Thumbnail* (15mm)	 Standard roller *Steel Thumbnail* (atfer renovation) (11mm)	 Standard roller *Steel Thumbnail* (13mm)

Environment. Technology. Resources. Rezekne, Latvia
Proceedings of the 13th International Scientific and Practical Conference. Volume 3, 216-225

HARVESTER HEADS, SIDE AND INNER FEED ROLLER TECHNICAL SOLUTIONS AND TECHNICAL CONDITIONS

Equipment	**G**	**H**	**L**	**M**	**N**	**O**
Harvester head	H754	H754	H754	H754	H754	H480C
Outer feed rollers (average spike height)	 Standard roller *MTH Rib Classic* (12mm)	 Standard roller *MTH Rib Classic* (12mm)	 Standard roller *Steel Thumbnail* (12mm)	 Standard roller *Steel Thumbnail* (15mm)	 Soft roller_Moipu Standard. (15mm)	 Standard roller *Steel Thumbnail* (12mm)
Inner feed roller (average spike height)	 Standard roller *Steel Thumbnail* (12mm)	 Standard roller *Steel Thumbnail* (12mm)	 Standard roller *Steel Thumbnail* (12mm)	 Standard roller *Steel Thumbnail* (12mm)	 Standard roller *Steel Thumbnail* (12mm)	 Standardt roller_*Steel Thumbnail* (15mm)

Environment. Technology. Resources. Rezekne, Latvia
Proceedings of the 13th International Scientific and Practical Conference. Volume 3, 216-225

Data characterized the deepest penetration point in most damaged place of objected assortiment caused by inner or outer feed rollers is given in Table 2.

TABLE 2

FEED ROLLER DAMAGES OF SPRUCE, PINE AND BIRCH ROUNDWOOD ASSORTIMENTS

				Feed roller penetration depth (median/ average) **in timber** (u.b., mm) p.s. *inner roller*						
				Spruce roundwood (top diameter, cm)			**Pine** roundwood (top diameter, cm)		**Birch** roundwood (top diameter, cm)	
Equipment	Type of cutting	Cutting period	Woodland type	**6x10**	**12x14**	**14x18**	**12x14**	**14x18**	**20x30**	**30>**
A	Clear cutting	09	Myrtillosa		*2.2/3.0* 5.7/5.4			*1.9/1.9* 4.7/4.8		
B	Thin-ning	07	Vacciniosa	*2.5/3.2* 2.8/3.2	3.6/3.8	2.9/3.1	*3.0/2.5*	*2.8/2.2* 3.6/3.4	*1.8/1.5* 2.7/3.2	*1.3/1.2* 3.4/3.4
C	Thin-ning	09	Vacciniosa		*5.8/5.9* 3.8/3.4			*5.4/5.4* 3.7/3.8		
C1	Thin-ning	09	Vacciniosa			*3.5/3.8*	*5.5/5.4*	*5.9/6.0*		
D	Clear cutting	06	Hylocom-niosa	1.8/2.2	2.4/2.4		2.4/2.2	*3.6/3.8* 4.4/4.3	*2.4/2.6*	
E	Clear cutting	07	Hylocom-niosa		3.5/3.3	5.5/5.4	3.4/3.6	3.5/3.4	*2.0/2.1* 1.3/1.1	
		08	Myrtillosa turf. mel.	3.3/3.2	3.8/3.7	6.3/6.4	3.4/3.6	3.5/3.4	*3.0/3.2* 3.4/3.5	
F	Thin-ning	07	Oxalidosa	*2.5/2.5* 2.5/2.3		3.9/3.0	*3.0/3.2*	*3.6/3.8* 1.8/1.7	*1.7/1.8* 3.5/3.6	
	Clear cutting	12 02 03	Oxalidosa Oxalidosa Hylocomniosa			3.6/.3.3	5.1/ 4.9	7.2/ 7.6 3.1/3.4	3.8/3.8 4.8/5.2	3.5/3.4
G	Thin-ning	07	Oxalidosa; Myrtilloso-polytrichosa;	*5.2/5.2* 4.5/4.2		*6.5/6.6* 3.5/3.8		3.7/3.6		
		11	Caricoso-phragmitosa		3.8/3.6	3.9/3.9				
H	Thin-ning	08	Hylocomniosa; Myrtillosa mel.; Oxalidosa			*4.5/4.6* 2.4/2.4		3.7/3.6	*4.2/4.1* 3.4/3.7	
L	Clear cutting	11	Hylocomniosa		2.0/2.3	2.2/2.3		3.7/3.6	3.3/3.3	3.1/3.2
M	Clear cutting	08	Hylocomniosa	0.5/0.6	1.2/1.3	2.7/3.6			2.5/2.7	2.5/2.6
N	Clear cutting	10	Oxalidosa	3.4/3.7	3.6/3.8	3.5/3.8		3.1/3.1	2.9/3.2	3.3/3.8
O	Clear cutting	08	Aegopodiosa		3.5/4.2					

The deepest penetration point in most damaged zone of objected assortiment caused by inner or outer feed rollers was measured under bark (u.b.) by using penetration calliper (Fig. 2). The measurement zone was chosen in 50cm lenght. The measurements were taken in sampling plots which average area was about 60m^2. According to the investigation task the penetration depth caused by feed rollers were observed and measured in each of objective assortiments (Fig. 4).

Fig. 4. The measurement of feed roller damage depth in timber

The technical conditions and back bevel shape of upper delimbung knives were evaluated by measuring angles of cutting edge and surface flatness using blade gauge F681744 (Fig. 5).

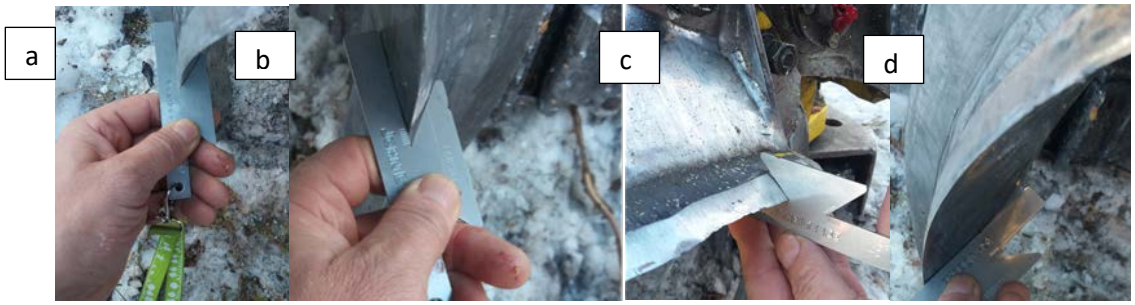

Fig. 5. The measurement of angle of cutting edge and surface flatness of top and upper delimbing knives (d) using blade gauge F681744, where (a; c) – correctly sharpened knife (36deg.); (b)- uncorrectly sharpened knife(>36 deg.)

Observation results of delimbing knives and fixed top knife is given in Fig. 6.

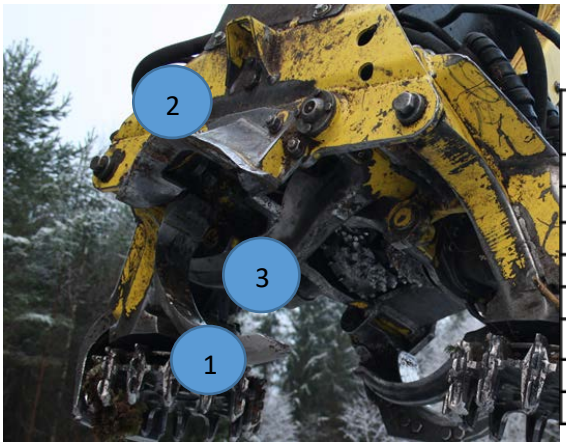

Equipment	Angles of cutting		
	1	2	3
A	>36^0	36^0	>36^0
C	36^0	36^0	36^0
C1	>36^0	36^0	36^0
E	36^0	36^0	>36^0
F	36^0	36^0	36^0
H	36^0	36^0	36^0
L	<36^0	36^0	36^0
N	36^0	36^0	36^0

Fig. 6. The points of measurement and observation results, where 1 - right upper delimbing knife; 2- top knife; 3 - left upper delimbing knife

Data characterized regulation adjustments of feed rollers and delimbung knives according to wood species and diametrs of harvested roundwood is given in Table 3 .

TABLE 3

REGULATION ADJUSTMENTS OF FEED ROLLERS AND DELIMBING KNIVES OF EQUIPMENTS A;C;C1;E;F;H;L;N ACCORDING TO WOOD SPECIES AND DIAMETERS OF HARVESTED ROUNDWOOD

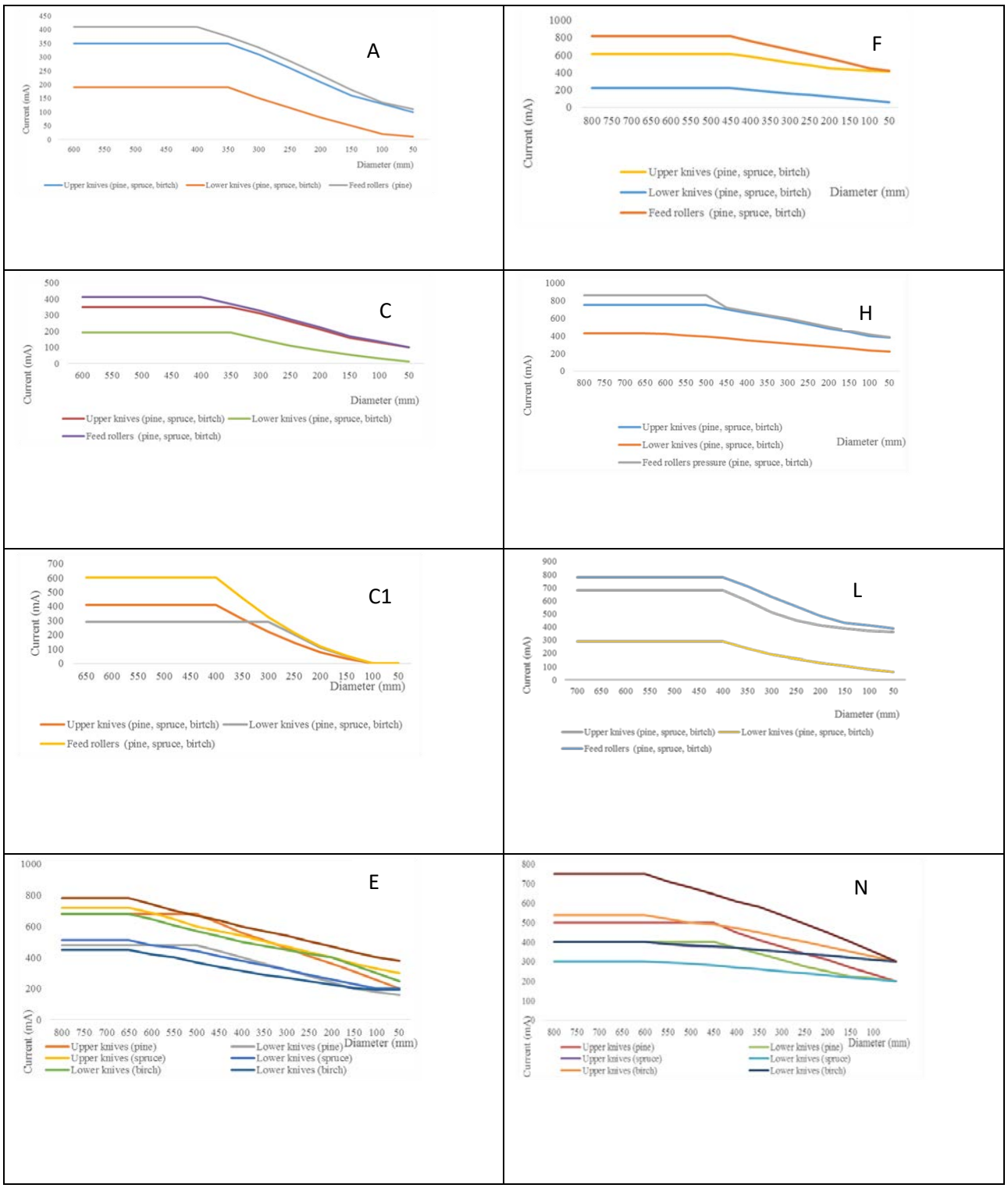

V. CONCLUSIONS AND RECOMENDATIONS

The results of the study indicated the following:

1. The incorrect maintenance of the fixed knife and upper delimbing knives when the actual angle of cutting exceed the recommended 36^0 causes cutting them into the stem. Therefore, the penetration depth in timber caused of spikes of harvester head feed rollers increases.The main reasons when the actual angle of cutting differs from the recommended are:
   - 1.1.the surface deterioration of upper delimbing knifes exceeds the recommended (>2mm);
   - 1.2.the width of delimbing knife reaches the critical, when the correct maintenance is impossible due to designed parameters of the knife;
   - 1.3.ignorance of recommended angle of cutting in the process of sharpening
2. If the lenght of the feed roller spikes of inner feer roller are longer comparing to the outer feed rollers, the deepest penetration in timber made the inner feed roller.
3. In cases when inner feed roller is aggressive or standard but outer feed rollers respectively standard or soft, the deepest penetration in timber made inner feed roller.
4. The deepest feed roller damages (median) caused by:
   - 4.1. inner feed roller were observed in spruce roundwood (14x18cm) when the penetration depth in timber reached 6.5mm;
   - 4.2.outer feed rollers were obseved in pine roundwood (14x18cm) when the penetration depth in timber reached 7.2mm
5. The deepest feed roller damages (median) of spruce roundwood (6x10cm) made inner roller 5.2mm.
6. The deepest feed roller damages (median) of spruce roundwood (12x14cm) made inner roller 5.8mm.
7 The deepest feed roller damages (median) of pine roundwood (12x14cm) made inner roller 5.5mm.
8. The deepest feed roller damages (median) of birch roundwood (20x30cm) made outer rollers 4.8mm.
9. The deepest feed roller damages (median) of birch roundwood (30<cm) made outer rollers 3.5mm.
10. To reduce the depth of penetration in timber caused by feed rollers, the following recomendations are given:
    - 5.1.to inspect regulary feed roller spikes technical conditions, angles of cutting and tehnical conditions of delimbing knifes;
    - 5.2.to maintain optimal pressure settings of feed rollers and delimbing knifes according to wood species and harvested roundwood diameters;
    - 5.3.the pressure of feed rollers should be at least 20 bar. higher comparing to upper delimbing knifes;
    - 5.4.to set up the harvester head with the same tape and conditions inner and outer feed rollers when (Multi-Tree Handling (MTH), Steel Thumbnail) and agreesive feed rollers (TP) are used;
    - 5.5.in cases when soft feed rollers (Moipu Standard,Rib) are used as outer feed rollers, the inner should be standard feed rollers with the same lenght parametrs of spikes.
    - 5.6. to avoid using soft feed rollers as inner rollers due to clotting them with bark what caused slippage and deep timber damades.

VI . REFERENCES

[1] Y. Gerasimov, A. Seliverstov, and V. Syunev, Industrial round-wood damage and operational efficiency losses associated with the maintenance of a single-grip harvester head model: A case study in Russia. Forests 3: 2012, pp. 864-880.

[2] John Deere. Operation and Maintenance Manual for Harvester Head John Deere 758HD; John Deere: Moline, IL, USA, 2008.

[3] P .Jönsson and B. Hannrup, 2007. Virkesvärdestest 2006 – virkesskador [Timber-value tests 2006 – timber damage and defects]. Skogsforsk Resultat 2007 (7). 4 p.

[4] Z. Karasewski and A. Lacka, "Damage caused by harvester head feed rollers to alder, pine and spruce". Drewno 2016, Vol. 59.

[5] A. Kariniemi, Kuljettajakeskeinen hakkuukonetyönmalli – työn suorituksen kognitiivinen tarkastelu [Operator-specific model for mechanical harvesting – cognitive approach to work performance].Helsingin yliopiston metsävarojen käytön laitoksen julkaisuja 38, 2006, 126 p.

[6] P. S. Mederski, Możliwości zastosowania harwestera do pozyskiwania drewna w mieszanych drzewostanach brzozowo-sosnowych (The potential of harvester use for thinning operations in mixed birch-pine stands). Wydawnictwo Uniwersytetu Przyrodniczego w Poznaniu, Poznań 2013.

[7] Y.Nuutinen and K.Väätäinen, "Operational efficiency and damage to sawlogs by feed rollers of the harvester head". Silva Fenn., 44, 2010, pp. 121–139.

[8] H. Ovaskainen,"Timber harvester operators'working technique in first thinning and the importance of cognitive abilities on work productivity". Dissertationes Forestales 79, 2009, 62p.

[9] R. Spinelli and N. Magagnoti , "Work quality and veneer value recovery of mechanized and manual log-making in Italian poplar plantations". European Journal of Forest Research 130, 2011, pp.737-744.

[10] K.Väätäinen and H. Ovaskainen, Hakkuukoneenkuljettajan hiljaisen tiedon merkitys hakkuutulokseen työpistetasolla (The significance of harvester operator's tacit knowledge on cutting with single grip harvester). Metsäntutkimuslaitoksen tiedonantoja 937, 2005, 100 p.

[11] A. Węgrzyn and N. Leszczyński N, "Rolki posuwu głowic harwesterowych (Feed rollers in harvester heads)." Technika Ogrodnicza Rolnicza i Leśna 3. 2014, pp. 6-8.

Environment. Technology. Resources. Rezekne, Latvia
Proceedings of the 13th International Scientific and Practical Conference. Volume 3, 226-231

Features of Alloyed a Matry of Water-Dispersed Iron Powders

Ivanka Miteva
Faculty of Mechanical and Precision Engineering
Technical University of Gabrovo
Gabrovo, Bulgaria
idmiteva_prestij@abv.bg

Ivan Vinev
Faculty of Mechanical and Precision Engineering
Technical University of Gabrovo
Gabrovo, Bulgaria
ivinev@abv.bg

Ivan Mitev
Faculty of Economics
Technical University of Gabrovo
Gabrovo, Bulgaria
imitev@tugab.bg

***Abstract* - The publication examines the peculiarities of alloying a matrix of water-dispersed iron powders of the type ASC 100.29, AHC 100.29 and ABC 100.30. The possible ways of alloying in powder metallurgy are presented. The influence of the main alloying elements - copper, nickel, phosphorus, molybdenum, etc. was traced. on the technological process in the production of powder metallurgical details. A special place is given to the alloying elements intensifying the process of coagulation of the pores in the matrix during sintering - copper and phosphorus. Graphical dependences for the influence of copper on the dimensional changes of the iron matrix at different sintering temperatures are presented.**

Keywords - copper, nickel, phosphorus, powder metallurgy, water-dispersed iron powders.

I. INTRODUCTION

General purpose sintered structural materials from iron powders and alloyed iron matrices represent a major part of powder metallurgical production. In developed industrial countries, the relative share of these parts for the needs of automotive, machine and instrument making, electronics, as well as in a number of other areas of the metalworking industry is significant [8,14,15,16,17,19]. With the correct selection of the initial composition of the charge in many cases the parts obtained by the method of powder metallurgy have similar operational properties with those of the parts obtained by conventional technologies (by casting) [7]. The main advantage of the products obtained by the method of powder metallurgy is the absence or insignificant mechanical processing without loss of the material in the form of shavings, high degree of preservation of the dimensions and quality of the surfaces, accuracy of the mass, etc.[9,11].

Structural products in powder metallurgy, similar to those in conventional ones, are usually made of alloys. Pure metals are used only if the products require special physical properties. Obtaining certain physical and mechanical properties requires the use of alloyed iron powders. Many of the alloying elements used in ferrous metallurgy to improve the properties of iron are used by analogy in powder metallurgy. However, there are some significant features [7,9,17]:

- the application of some alloying elements widely used in ferrous metallurgy - chromium, manganese, silicon, titanium and vanadium - is difficult due to their strong affinity for oxygen;
- the surface layer of the corresponding oxide, which is formed during oxidation, is very difficult to reduce under normal sintering conditions, moreover, as a result of reactions with the sintering medium and the oxygen present in the iron powder, additional oxidation often takes place during the sintering process, due to which diffusion is difficult and a material with low physico-mechanical properties is obtained, therefore the oxides of the alloying additives, which are mixed with the iron powder, must be reduced more easily during sintering than the oxides of the iron itself;
- in powder metallurgy some elements that are used to a limited extent in ferrous metallurgy - copper and phosphorus - are widely used for alloying;
- in powder metallurgy some elements that are used to a limited extent in ferrous metallurgy - copper and phosphorus - are widely used for alloying;

Online ISSN 2256-070X
https://doi.org/10.17770/etr2021vol3.6580

- comparison with classical metallurgy larger quantities of alloying additives are needed here in order to obtain the desired properties;
- important factor in selecting the type and quantity of the alloying element is its influence on the accuracy of the dimensions of the sintered products.

For these reasons, the chemical composition of a large proportion of sintered steels differs significantly from the composition of ordinary steels with the same field of application.

In the present publication the aim is to study the peculiarities of alloying an iron matrix based on water-dispersed iron powders with copper, nickel and other alloying elements.

II. Materials and Metods

Samples based on water-dispersed iron powders type ASC 100.29, AHC 100.29 and ABC 100.30 were used in the research process. The iron matrix is alloyed with copper, nickel, phosphorus and carbon.

The samples are pressed with a force of 200÷800 MPa. The measured density after sintering varies in the range of 6.00 ÷ 7.00g /cm^3.

The determination of the mechanical characteristics of the tested samples is done according to the standardized methods for determining the tensile strength, the relative elongation and the change in the linear dimensions [12].

An increase in the size of the parameter of the crystal lattice of iron during its alloying with copper was determined by the method of X-ray diffraction analysis [13].

III. Results and Discussion

The final complex of physical and mechanical properties of the sintered materials largely depends on the way of introducing the alloying elements in them. In powder metallurgy, several methods of alloying are used: mechanical mixtures; alloy powders, partially alloyed powders - Fig.1 [19].

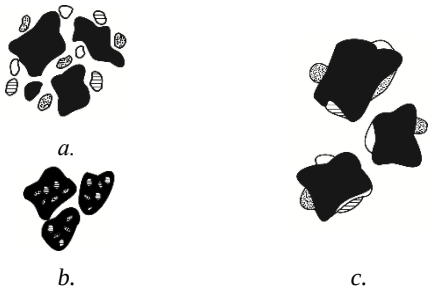

Fig. 1. Alloying schemes in powder metallurgy:
a - mechanical mixture; b - alloyed powder;
c - partially alloyed powder.

From Fig. 1, it can be seen that the most suitable for use in production seems to be the finished alloyed powder, because the individual powders particles have the same composition as the final product. Such powders are obtained by sputtering, mechanical grinding and co-reduction. The method of pulverization of metal melts has found the widest industrial application [1,6,17]. In this way, alloys of many non-ferrous metals are obtained - bronze, brass, aluminium alloys, as well as low- and high-alloy steels.

The use of alloyed powders makes it possible to maximize the use of alloying elements, to obtain alloys with high homogeneity of structure, and hence with the greatest uniformity of properties and accuracy of the geometric parameters of the products. Due to their higher hardness, however, alloy powders have a relatively poor compaction, which is of great importance when pressing parts with a more complex configuration. In such cases, high-energy molding methods are suitable - hot dynamic pressing, high-speed pressing, etc. [6,11].

Until now, the compression of mechanical mixtures of the necessary components has been more widely used in powder metallurgy, as the desired alloys are formed by diffusion during sintering [6,17].

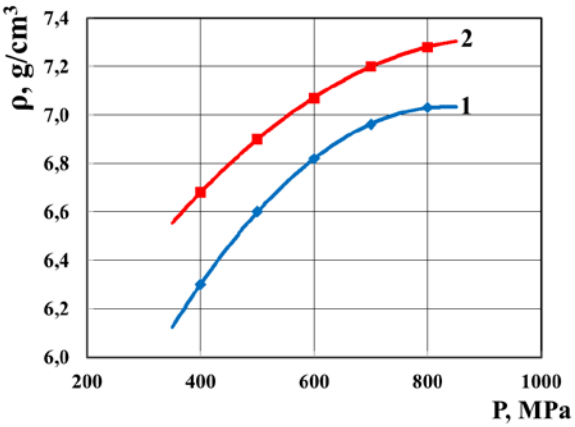

Fig.2.Compactness of alloyed powders- 1 and mechanical mixtures -2
with composition Fe + 2% Ni + 0.5% Mo + 0.5% C

Figure 2 shows experimental results proving a much better compaction of a mechanical mixture compared to an alloyed powder with the same composition.

The use of mechanical mixtures requires much better mixing of the components before pressing, higher temperature and longer duration of the sintering process in order to homogenize the alloy. In some cases, in order to obtain materials with special properties - for example, with high wear resistance, the creation of nonequilibrium structures is resorted to.

A compromise between alloy powders and mechanical mixtures is pre-alloyed powders. During sintering, the alloying elements diffuse relatively quickly into the base metal, which allows the process to be carried out under more favourable technological conditions. The heat treatment is carefully controlled so that the interaction

between the alloying elements and the iron powder is in the initial stage.

The alloying of iron with copper or with copper in combination with other elements makes it possible to obtain alloys with very good physical and mechanical properties [3,10,17]. Iron-copper alloys are usually obtained from mechanical mixtures. A specific method of alloying in this case is the impregnation of a porous iron skeleton with molten copper or its alloys. Copper is also used in the preparation of pre-diffusion-doped powders and much less frequently in ready-made alloy powders.

The formation of the structure of the alloy during sintering of a mechanical mixture of iron and copper powder is of both theoretical and practical interest. The iron-copper system has a limited solubility of the components in the solid state - at a temperature of 1094ºC iron dissolves about 8% Cu, and copper in turn can dissolve about 4% Fe [10]. As the temperature decreases, the mutual solubility decreases. Eutectoid decay occurs at 850°C and a mixture of α- and ε-mixed crystals is observed at room temperature. In a solid solution with iron remains less than 0.15% copper, and above this amount of copper in the structure is in free form. The size and shape of the copper inclusions depend on: the cooling rate; the total amount of copper; temperature and duration of sintering.

The most commonly used powder materials based on water-dispersed iron powders of the type ASC 100.29, AHC 100.29 and ABC 100.30 are alloyed with 1÷10% copper. Unlike conventional metallurgy in powder metallurgy, copper is the main alloying element, and its advantages are as follows [2,7]:

- good mixing with iron powder;
- easy reducibility of copper oxides;
- formation of a liquid phase during sintering at relatively low temperatures.

This is the most pronounced difference in the goals set for alloying in conventional technologies and in powder metallurgy.

Together with the increase of the strength characteristics during sintering, the copper helps to increase the parameters of the crystal lattice of the iron depending on the copper diffused in it – fig.3. This helps to compensate for the shrinkage of the iron matrix during sintering.

Our experiments show that when alloying an iron matrix of water-dispersed iron powders ABC 100.29 with 2.0% copper after a single double-sided pressing and sintering at 1000÷1200ºC for 1h, practically no changes in the linear dimensions of the parts are registered. – fig. 4.

The figure shows that an increase in the copper concentration in the iron matrix leads to an increase in the volume of sintered parts, as this increase is most significant at a concentration of copper in the iron briquette - 8 ÷ 10%.

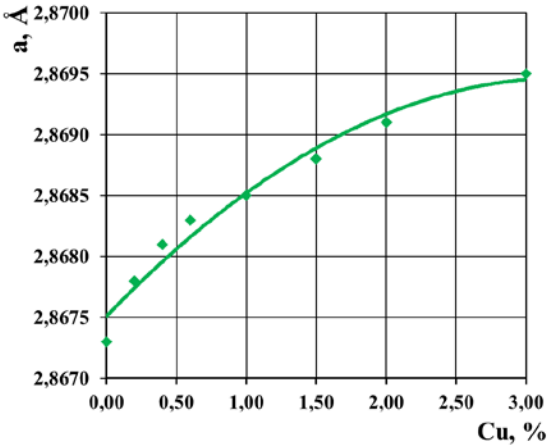

Fig. 3. Changing the parameter of the crystal lattice of iron during alloying with copper

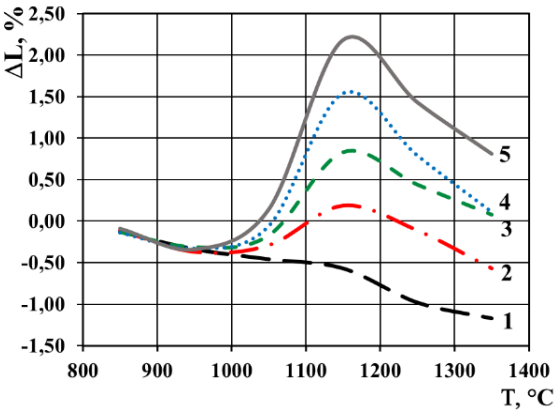

Fig. 4. Dimensional changes depending of an iron matrix of ABC 100.29 alloyed with copper: 1 - 0% Cu; 2 - 2% Cu; 3 - 4% Cu; 4 - 6% Cu; 5 - 8% Cu.

The addition of other alloying elements can affect the process in one direction or another. It was found that the addition of carbon to the iron-copper system leads to a reduction in the size of the workpiece. The same is found when adding nickel and tungsten. These limit the solubility of copper in iron and thus reduce the increase in the volume of the parts. Therefore, in combination with the alloying elements, powder metallurgical alloys with increased strength can be realized while satisfactorily preserving the size of the workpieces.

Highly alloyed with copper - up to 20%, powder steels can be obtained by infiltration of pre-sintered carcasses or water-dispersed iron powder pre-alloyed with copper. As the iron frames can be pressed to the required dimensions, high-precision powder products are obtained by infiltration. From the experimental results of Fig.5. it is seen that the sintered steels double their strength after infiltration with copper.

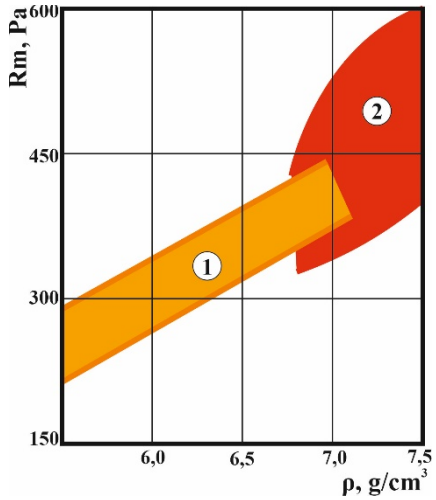

Fig.5. Tensile strength of iron matrix based on powders ASC 100.29, ABC100.29 and AHC 100.30 after alloyed with 2%Cu -1 and infiltration with 20% Cu - 2.

The measured tensile strength after diffusion annealing and disperse hardening of powder materials based on iron powders ABC 100.29, containing 1.0% carbon and 15% copper depending on their density reaches 1150 ÷ 1250 MPa, at relatively high values of relative elongation - 4 ÷ 6%.

In powder metallurgy after copper, the next most common alloying element is nickel. Like copper, it has a weak affinity for oxygen. Its introduction makes it possible to obtain appropriate values for strength and ductility. The Fe-Ni system refers to the case of unlimited solubility of solid components [1,7]. Iron and nickel form a continuous series of solid solutions without brittle compounds. Unlike the Fe-Cu system, here the partial diffusion coefficients differ insignificantly and the effect of volume increase is almost imperceptible. Nickel has a high activating ability during sintering, which manifests itself at relatively high temperatures - above 1150ºC, and a longer process duration. Alloying iron with nickel slows down the growth of crystals during sintering, which helps to increase shrinkage during the final stages of the process.

In the conducted experiments it was found that the way of doping has a great influence on the structure of Fe-Ni products. When working with finished alloy powders after firing, the structure remains homogeneous, single-phase and is externally similar to the structure of non-alloy iron powder products. When using mechanical mixtures of iron and nickel powder, the final structure depends exclusively on the firing mode. At temperatures up to 850ºC, regardless of the duration of sintering, there is practically no interaction between the nickel and iron particles in the matrix.

As the temperature rises, nickel dissolves in iron. The alloys obtained under such conditions are characterized by a spotted, inhomogeneous structure. Only when the temperature rises to 1250ºC and the sintering duration exceeds 120 min does the alloy acquire a single-phase structure.

From the experimental results obtained in the study of iron-nickel samples, it was found that the properties of copper-alloyed steel steels can be significantly improved by adding nickel powders to the charge. The measured values for the tensile strength of samples doped with 3% copper and 2.5% nickel vary in the range of 450 ÷ 550 MPa, and when the concentration of nickel increases to 5%, the values for the tensile strength increase by approximately 100 MPa. When optimizing the concentration of copper and nickel in the briquette of iron powder ABC 100.29 (4.5% copper and 5% nickel) the measured values for tensile strength reach 750 MPa. But at the expense of significantly reducing the values for elongation. If for iron-nickel steels with 5% Ni the measured elongation is of the order of 14 ÷ 16%, then for the considered triple system it is only 4%.

We managed to increase the tensile strength values found in the experiments by adding 0.5% C to the ternary system, but at the expense of the results for the relative elongation. The measured mechanical characteristics of powder samples based on ABC 100.29 iron powders alloyed with 7% Ni, 2.0% Cu and 0.5% C at a briquette density of 7.01 g / cm3 are - tensile strength 635 MPa, elongation 2.5÷3% and hardness HRB 87. After heat treatment (hardening of 950ºC in oil), the tensile strength increases to 1055MPa, the hardness HRC47, but the relative elongation is only 1÷2%.

The main representative of the alloying elements from the group of non-metals in powder metallurgy is phosphorus [4,5]. In ferrous metallurgy it is considered an undesirable impurity, as in steels it increases the tendency to liquation and favours the formation of brittle phosphides. For strength reasons, the concentration of phosphorus in powder steels is limited to 0.3 ÷ 0.6%.

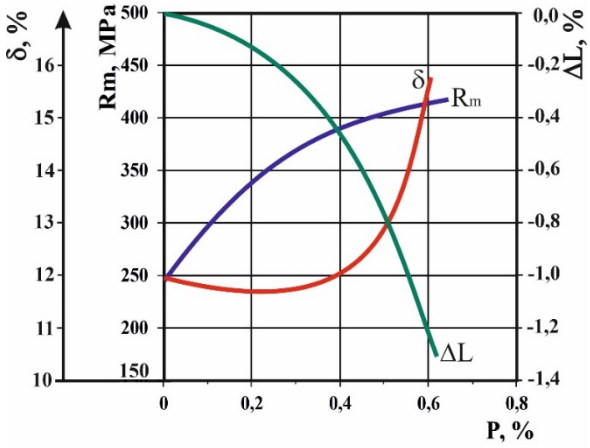

Fig.6. Dependence of tensile strength - Rm, elongation - δ and change of linear dimensions – ΔL, on the concentration of phosphorus in the iron matrix

As a result of the formation of a solid solution of iron with phosphorus, the ferrite component in the tested samples is stabilized. The tensile strength of samples of iron powder ASC100.29 and ABC 100.30 alloyed with 0.5% phosphorus is in the range of 400 ÷ 450MPa - Fig.6, but thanks to the stabilized ferrite phase the plasticity of the

parts is very high and the relative elongation of the parts reaches - 14 ÷ 16% - Fig.6.

As a result of the formation of solid solutions with iron, phosphorus stabilizes Fe α . The iron-phosphorus state diagram shows that in the case of alloys with a phosphorus concentration ⩾0.55%, the sintering process practically proceeds without phase transformations. The increased rate of self-diffusion in the α - phase favours the migration of atoms during sintering, which allows the process to be realized at temperatures of the order of 1000ºC. In the case of an iron matrix doped with 0.3% phosphorus, the achieved hardening of the solid solution of phosphorus in the iron reaches values similar to those in the case of alloying the iron matrix with 2% copper. However, it should be borne in mind that the measured relative shrinkage of the parts at a phosphorus concentration ⩾ 0.4% may exceed 1% - fig. 6. Therefore, alloying the iron matrix with phosphorus is not recommended for the manufacture of products with increased dimensional accuracy requirements.

In order to increase the strength characteristics of the studied iron matrices in the presence of phosphorus in them and to preserve the linear dimensions of the products, tests were also performed on samples with the addition of copper or nickel.

In the triple systems Fe-Cu-P and Fe-Ni-P at sintering temperatures above 950ºC the process takes place in the presence of a liquid phase which accelerates the process of sintering and coagulation of the pores. Under certain conditions, in particular in the case of the Fe-Ni-P ternary system, as a result of solid solutions formed in the initial stage of sintering, instead of shrinking the blanks, their size increases, which can be used as a compensating mechanism of shrinkage.

IV. CONCLUSIONS

The following more important conclusions can be formulated from the conducted research and the results obtained:

- Powder metallurgy is a technological process that allows the production of unique materials that are impossible to obtain by applying conventional metallurgical technologies. The mechanical mixing in solid state of the components allows the use of copper and phosphorus as alloying elements, which in practice do not find application in conventional metallurgical technologies.

- The alloying of the ferrous matrix in powder metallurgy can be realized in three ways - by mechanical mixtures, partially and completely alloyed powders. It has been proven that with the same pressing forces the compaction of the mechanical mixtures is 0.30 g/cm^3 higher than the pre-alloyed powders.

- The alloying of iron matrices from water-dispersed powders with copper and phosphorus allows the sintering process to be realized in the presence of a liquid phase. This favours the coagulation of the pores, leads to compaction of the blanks and increase their mechanical properties.

- Alloying iron with nickel slows down the growth of crystals during sintering, which helps to increase shrinkage during the final stages of the process.

REFERENCES

[1] N. Manukyan, Technology Powder Metallurgy. Yerevan, Aystan, 1986, p.232

[2] I.May, L. Schetky, Cooper in iron and steel, John Wiley and sons. Toronto, 1988, p.307, ISBN 0-471-05913-7

[3] I. Mitev, Tensile strength after sintering and aging iron-copper cermet. Yearbook of TU-Varna, 2001, p.104 ÷ 110.

[4] I. Mitev, I. Vinev, Properties of Iron Powder Materials Alloyed with 0.45% Phosphorus, Machine Building and Machine Science, Vol. 9, 2009, p.61÷64, ISSN 1312-8612.

[5] I. Mitev, I.Vinev, Sintering Powder Metallurgy Materials from Iron-phosphorus System, International Conference "Unitech, 10", Gabrovo, 2010, Volume II, s.178 ÷ 184, ISSN 1313-230X

[6] Mitev, I., Powder Metallurgy – part I (Receive powder metallurgy materials and products, University Press „V. Aprilov", Gabrovo, 2004, ISBN 954-4683-233-2

[7] I. Mitev, Powder Metallurgy – part II (Powder Metallurgical Products with Sructural and Instrumental Purpose, University Press „V. Aprilov", Gabrovo, 2004, ISBN 954-4683-234-0.

[8] I. Mitev, Contemporary industrial technologies - part III / Progressive methods for mechanical forming /, EX-PRESS, Gabrovo, 2016, ISBN 978-954-490-511-8

[9] I. Mitev, Modern Industrial Technology - part III, (Progressive methods of mechanical shaping), EX-PRESS, Gabrovo, 20016, ISBN 978-954-490-511-8

[10] I. Mitev, Copper in two-component powder metallurgical systems, EX-PRESS, Gabrovo, 2019, ISBN 978-954-490-632-0

[11] I. Mitev, Technologies for chipless forming, EX-PRESS, Gabrovo, 2021, ISBN 978-954-490-492-6

[12] I. Mitev, Structural Analysis,, EX-PRESS, Gabrovo, 2013, ISBN 978-954-490-363-3

[13] I. Mitev, Crystallography, EX-PRESS, Gabrovo, 2012, ISBN 978-954-490-3610-7

[14] N. Nikolova, Intellectual Capital Management used for Optimizing the Activities of Modern Small and Medium Enterprises / Companies, 4th International Conference ″Economics and Management-Based on New Technologies″, EMoNT 2014, 12-15 June 2014, Vrnjačka Banja, Serbia., pp.258-262, ISBN 978-86-6075-045-9

[15] N. Nikolova, Entrepreneurial "BLUE" Practices for Sustainable Development and Resources Efficiency, 12th International Scientific and Practical Conference "ENVIRONMENT. TECHNOLOGY. RESOURCES.", June 20-22, 2019, Rezekne Academy of Technologies, Rezekne, Latvia, Volume I, 198-203, ISSN 1691-5402, ISSN 2256-070X

[16] D. Petrova, Intelligent, Innovative and Sustainable Industryin Bulgaria – Prospekts and Challenges, Environment. Technology. Recourses – Proceeding of the 12-th International Scientific and Practical Conference, Rezekne Academy of Technologies, Rezekne, Latvia, 2019, ISSN 1691-5402, p.210-215.

[17] R. Todorov and other, Materials and Equipment for Powder Metallurgical Construction Products, Publishing BAS, Sofia, 1988

[18] P. Tomchev, N. Nenov, R. Ivanova, Instantaneous water heater with induction heater operating with grid frequency, „Research and Development in Mechanical Industry“ RaDMI 2012, 13-17 September 2012, Vrnjačka Banja, Serbia, SaTCIP Ltd., Technical-Mechanical School in Trstenik, ISBN 978-86-6075-036-7, Volume II, pp.1214-1218.

[19] I.Vinev, Peculiarities of iron matrix alloying in powder metallurgy, MNK UNITECH-18, Gabrovo, volume II, p.239 ÷ 244, 2018, ISSN 1313-230X

Environment. Technology. Resources. Rezekne, Latvia
Proceedings of the 13th International Scientific and Practical Conference. Volume 3, 232-235

Investigation of Residual Stresses and Deformations of a Pultruded Thin Beam Profile

Endija Namsone
Institute of Materials and Structures
Riga Technical University
Riga, Latvia
endija.namsone@inbox.lv

***Abstract* - In the present study, a coupled 3D transient thermo-chemical analysis together with 2D plane strain mechanical analysis is carried out for the pultrusion process. For the mechanical analysis, a cure hardening instantaneous linear elastic (CHILE) approach is used of a thin beam profile made of glass fibre and epoxy resin. The applied approach is efficient and fast to investigate the residual stresses and deformations together with the distributions of temperature and degree of cure obtained from the thermo-chemical analysis.**

Keywords* - *finite element method, pultrusion, residual stresses, thermo-mechanical.

I. Introduction

Characterization of mechanical behaviour is not only an important study for entire structures under loading [1]-[3], but also for the separate parts in time of their production [4] since stresses and deformations caused by the process may occur.

Pultrusion is a continuous and cost-effective process and is widely used for a production of high strength fibre-reinforced polymer composite profiles with different cross-sections [5], [6]. During pultrusion, the fibres are saturated with the resin in a tank and after that are continuously pulled through a heated die. In literature, many different numerical and experimental techniques are carried out to design pultrusion processes. Mostly, thermo-chemical modelling in transient and steady state analyses are developed for a better understanding of pultrusion processes to analyse the distributions of temperature and degree of cure inside the die, using the finite element methodology [7]-[9] finite difference methodology [10], [11], based on the nodal control volume method.

It is well known, that in time of manufacturing process of thermoset matrix composites, material characteristics of resin vary during the glass transitions from rubbery to solid state. It follows that, this change of resin material directly influences its mechanical properties, which are temperature- and degree of cure-dependent and can occur as unwanted residual deformations. Therefore, the investigation of process-induced variations like residual stresses and deformations should be performed for a better control of mechanical behaviour of pultrusion process.

In addition of thermo-chemical studies in literature, a thermo-chemical-mechanical analysis of pultrusion for glass-fibre reinforced profiles are developed in [12]-[14]. For this reason, in the present study a thermo-mechanical analysis is applied by coupling a 3D thermo-chemical model with a 2D plane strain mechanical model, like described in [15], [16]. The thermo-mechanical finite element model is created in the finite element code ANSYS Mechanical, based on the cure hardening instantaneously linear elastic method (CHILE) as in [17] to investigate the residual stresses and deformations of pultruded beam profile made of glass fibre and epoxy resin.

II. Materials and Methods

A. Formulation of multi-physical problem

The simulation of 3D thermo-chemical pultrusion process can be solved by three governing energy equations:

$$\rho c_p \frac{\partial T}{\partial t} - \frac{\partial}{\partial x}\left(k_x \frac{\partial T}{\partial x}\right) - \frac{\partial}{\partial y}\left(k_y \frac{\partial T}{\partial y}\right) - \frac{\partial}{\partial z}\left(k_z \frac{\partial T}{\partial z}\right) = 0 \quad (1)$$

$$\bar{\rho}\bar{c_p}\left(\frac{\partial T}{\partial t} + u\frac{\partial T}{\partial x}\right) - \frac{\partial}{\partial x}\left(\overline{k_x}\frac{\partial T}{\partial x}\right) - \frac{\partial}{\partial y}\left(\overline{k_y}\frac{\partial T}{\partial y}\right) - \frac{\partial}{\partial z}\left(\overline{k_z}\frac{\partial T}{\partial z}\right) - q = 0 \quad (2)$$

$$\left(\frac{\partial T}{\partial t} + u\frac{\partial T}{\partial x}\right) = R_r \quad (3)$$

Online ISSN 2256-070X
https://doi.org/10.17770/etr2021vol3.6635

where T is the temperature, u is the pull speed, c_p is the specific heat, ρ is the density, k_x, k_y and k_z are the thermal conductivities in x, y and z directions, q_b is the rate of energy, α is the degree of cure. Accordingly, $\bar{\rho}$ is the lumped density, $\overline{c_p}$is the lumped specific heat, $\overline{k_x}, \overline{k_y}$ and $\overline{k_z}$ are the lumped thermal conductivities of the composite material in x, y and z directions. The generative term q in a relation of internal heat generation and due to the exothermic reaction of resin can be expressed by the following equation:

$$q = V_r + \rho_r + H_{tr} + R_r \tag{4}$$

where V_r is the resin volume fracture, H_{tr} is the total heat of reaction, ρ_r is the density of resin and R_r is the resin reaction rate, which can be described as in [18]:

$$R_r(\alpha, T) = \frac{\partial \alpha}{\partial t} = \frac{1}{H_{tr}} \frac{dH(T)}{dt} = K(T) \cdot f(\alpha) \tag{5}$$

$f(\alpha)$ is the reaction function and $K(T)$ can be defined by the Arrhenius relationship:

$$K(T) = K_0 \exp(-\frac{E}{RT}) \tag{6}$$

where R is the universal gas constant and E is the activation energy. E and K_0 could be determined by a fitting procedure of the experimental heat flow curves obtained from differential scanning calorimetry tests.

For the thermo-chemical simulation of pultrusion process in this study, the equations above are solved using the finite element code ANSYS Mechanical and the nodal control volume method is applied to obtain the evolution of temperature and degree of cure.

Since the resin state changes during the process from rubbery to glassy state, the CHILE approach method is applied to capture the transition mechanically for the thermo-mechanical analysis. In this case, the resin modulus is described:

$$E_r(\alpha, T) =$$

$$\begin{cases} E_r^0 & T^* < T_{C1} \\ E_r^0 + \frac{T^* - T_{C1}}{T_{C2} - T_{C1}}(E_r^\infty - E_r^0) \quad for & T_{C1} \le T^* \le T_{C2} \\ E_r^\infty & T^* > T_{C2} \end{cases} \tag{7}$$

where E_r^0 and E_r^∞ are the uncured and cured resin moduli, T_{C1} and T_{C2} are the critical temperatures at the begin and completion of the glass transition and T^* is the difference between the instantaneous glass transition and resin temperature: $T^* = T_g - T$. The evolution of the glass transition is described as:

$$T_g = T_g^0 + (T_g^\infty - T_g^0) \frac{\lambda \alpha}{1 - (1 - \lambda)\alpha} \tag{8}$$

T_g^0 and T_g^∞ are the temperatures of glass transition of uncured and cured resin, λ is a constant fitting parameter.

The chemical shrinkage of resin is calculated:

$$\Delta \varepsilon_r = \sqrt[3]{1 + \Delta V_r} - 1 \tag{9}$$

where $\Delta V_r = \Delta \alpha \cdot V_{sh}$ - the incremental volume resin shrinkage as a function of change in the degree of cure and total volume shrinkage V_{sh}=6.9% .

The thermo-mechanical problem is solved by using the obtained distributions of temperature and degree of cure from the thermo-chemical analysis. For the finite element simulations in ANSYS, the incremental linear elastic approach is applied to calculate the residual stresses and deformations. The incremental thermal strains:

$$\Delta \varepsilon_i^{th} = \alpha_i \cdot \Delta T \tag{10}$$

Mechanical properties of fibre and resin, fibre volume fracture and as well as the chemical resin shrinkage strains are affecting the incremental chemical shrinkage strains. Assuming the fibre phase mechanical properties are cure independent$\Delta \varepsilon_{1f} = \Delta \varepsilon_{2f} = \Delta \varepsilon_{3f} = 0$, then incremental chemical strain:

$$\Delta \varepsilon_1^{ch} = \frac{\Delta \varepsilon_r E_r (1 - V_f)}{E_{11f} V_f + E_r \cdot (1 - V_f)} \tag{11}$$

$$\Delta \varepsilon_2^{ch} = \Delta \varepsilon_3^{ch} = (\Delta \varepsilon_r + v_r \Delta \varepsilon_r)\big(1 - V_f\big) - (v_{12f} V_f + v_r\big(1 - V_f\big))\Delta \varepsilon_1^{ch} \tag{12}$$

where E_{11f} and v_{12f} is the longitudinal elastic modulus and Poisson's ratio of the fiber, E_r and v_r – of the resin, V_f is the fibre volume ratio. $\Delta \varepsilon_1^{ch}$ - incremental chemical strain in the longitudinal direction, $\Delta \varepsilon_2^{ch}, \Delta \varepsilon_3^{ch}$ - in the transverse directions.

B. Thermo-chemical model

A 3D transient thermo-chemical analysis is carried out for a thin beam profile [12]. The pultrusion die for this profile is with following dimensions 915 x 38.1 x 38.1 mm and 1.59 x 12.7 mm for the cross-section of it. The materials used for a production of beam are fiberglass and epoxy resin. The finite element model is created in ANSYS mechanical using 3D thermal solid finite elements Solid 70 and only a quarter is modelled due to the symmetry (see Fig.1). The total number of elements is 11102 and 3660 mm from the die exit of profile is continued to extend the thermo-chemical analysis. The initial conditions:

- at time t=0 all nodal points have the room temperature and degree of cure is 0;
- pull speed 20 cm/min;
- solution time step is 4.5 s.

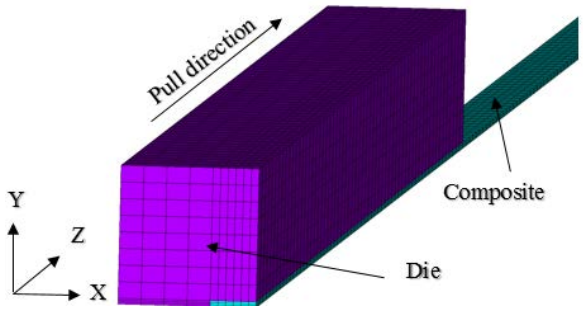

Fig. 1. Fragment of the finite element model for the thermo-chemical analysis.

C. *Thermo-mechanical model*

During the 2D thermo-mechanical analysis, the cross-section of beam profile is moved through the pull direction. The finite element model of profile cross section in ANSYS Mechanical is created by 2D plane strain solid finite elements Plane 182. The model has following boundary conditions – symmetry boundary conditions on the symmetry line and sliding conditions on the contact surfaces.

The mechanical properties of fibre and resin are given in Table 1. The value of CTE of resin in a glassy state is 2.5 times smaller than in a rubbery state. The critical temperature at the onset and competition of glass transitions is assumed $T_{C1} = -45.7°C$ and $T_{C2} = -12°C$. For the T_g calculation in equation (8), T_g^0 is assumed 0 °C and $T_g^\infty = 195$ °C. The fitting parameter $\lambda = 0.4$.

III. RESULTS AND DISCUSSIONS

It should be noted that all results for the thermo-mechanical analysis should be viewed together with the distributions of temperature and degree of cure obtained from the thermo-chemical analysis, which were measured in two different control points. As the temperature and degree of cure distributions are almost uniform all over the cross-section of profile, the results are practically the same for both control points. For this reason, the results of thermo-chemical analysis are presented only for one control point B (see Fig. 2).

TABLE 1 MECHANICAL PROPERTIES OF FIBRE AND RESIN

Property	**Value**		
	Symbol (unit)	***Fibre***	***Resin***
Young's modulus	E_r^0 (MPa)	-	3.447
	E_r^∞ (MPa)	-	$3.447 \cdot 10^3$
	E_{11} (MPa)	$7.308 \cdot 10^4$	Eq. 11 [1]
	E_{22} (MPa)	$7.308 \cdot 10^4$	Eq. 11 [1]
Shear modulus	G_{12} (MPa)	$2.992 \cdot 10^4$	Eq. 13 [1]
	G_{13} (MPa)	$2.992 \cdot 10^4$	Eq. 13 [1]
Poisson's ratio	ν_{12}	0.22	0.35
	ν_{13}	0.22	0.35
Coefficient of thermal expansion (CTE)	α_1 (1/°C)	$5.04 \cdot 10^{-6}$	$5.76 \cdot 10^{-5}$
	α_2 (1/°C)	$5.04 \cdot 10^{-6}$	$5.76 \cdot 10^{-5}$

The values of effective Young's moduli at the end of the pultrusion process are describing the final stiffness of beam profile. These values are found to be 48 238.5 MPa in the longitudinal direction and 12 439.9 MPa in the transverse direction. Comparing them with the recommended values found in literature [19], which is in the range of 35 000 to 50 000 MPa for glass fibre reinforced composite, it can be concluded that the stiffness of this beam is adequate.

The evolution of corresponding strains are given in Fig.3. In this case, thermal strain is the incremental thermal strain and chemical strain is the linear chemical strain. The total strain is the process induced strain obtained by counting together thermal strain with chemical strain. The maximum value of thermal strain is ε_{max}^{th}=0.01116.

IV. CONCLUSIONS

In the present study, a thermo-chemical-mechanical analysis was performed with the aim to investigate the residual stresses and deformations for the pultrusion process of a rectangular thin beam profile. For this reason, a 3D thermo-chemical model was coupled with a 2D plane strain mechanical model performed in finite element code ANSYS Mechanical. In order to obtain the resin modulus, which is dependent of temperature and degree of cure, the CHILE based approach was utilized.

During the thermo-chemical analysis, uniform distributions of temperature and degree of cure were obtained all over the profile in both control points, where the process of curing were occurred very similarly at the same time.

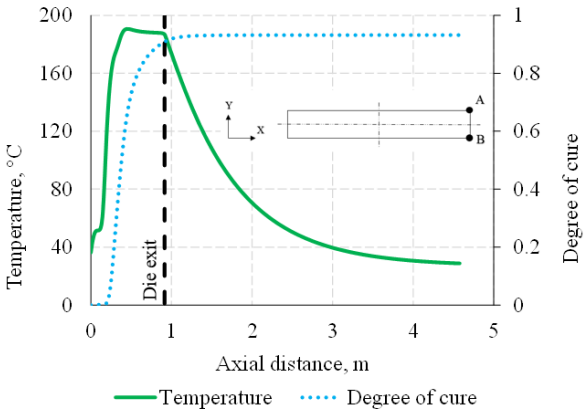

Fig. 2. The distribution of temperature and dregee of cure in the control point B.

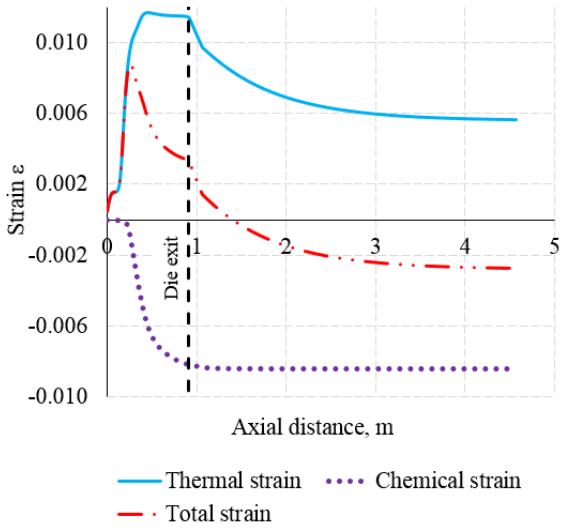

Fig. 3. The strain evolution in the control point B.

The obtained values of the effective elastic modulus of the composite material were analysed and compared with the recommendations in the literature, it can be concluded that the stiffness of beam profile is appropriate.

The applied method was found to be quite fast and efficient for the investigation of the residual stresses and deformations together with the distributions of temperature and degree of cure. It could be performed for further studies also for more complex pultruded profiles for different structures, where the geometrical precision is more important.

ACKNOWLEDGEMENTS

This work was supported by the European Regional Development Fund, project No. 1.1.1.1/18/A/053 "An effectiveness improvement of conventional pultrusion processes".

REFERENCES

[1] P. Masarati, M. Morandini, J. Riemenschneider, P. Wierach, S. Gluhih, E. Barkanov, "Optimal Design of an active twist 1:2.5 scale rotor blade,"in: Proceedings of the 31st European Rotorcraft Forum, Firenze, Italy, pp. 37.1-37.14, 2005.

[2] E. Barkanov, E. Eglītis, F. Almeida, M. C. Bowering, G. Watson, "Optimal design of composite lateral wing upper covers. Part II: Nonlinear buckling analysis," Aerosp. Sci. Technol. Vol. 51, pp. 87-95, 2016, https://doi./org/10.1016/j.ast.2016.01.020

[3] E. Barkanov, A. Kovalov, P. Wierach, J. Riemenschneider, "Optimised comparative analysis of an active twist for helicopter rotor blades with C and D-spar designs," Mech. Compos. Mater. Vol. 5., pp. 553-566, 2018, https://doi.org/10.1007/s11029-018-9764-2

[4] V. Antonucci, A. Cusano, M. Giordano, J. Nasser, L. Nicolais, "Cure-induced residual strain build-up in a thermoset resin," Composites: Part A, vol.37, pp. 592-601, 2006, https://doi.org/10.1016/j.compositesa.2005.05.016

[5] P. Akishin, E. Barkanov, A .Bondarchuk, "Finite element modelling and analysis of conventional pultrusion processes," IOP Conf. Series: Materials Science and Engineering, vol. 96, p. 10, 2015, http://iopscience.iop.org/article/10.1088/1757-899X/96/1/012012

[6] E. Barkanov, P. Akishin, R. Emmerich, M. Graf, "Numerical simulation of advanced pultrusion processes with microwave heating," in: Proceeding of the VII European Congress on Computational Methods in Applied Sciences and Engineering, 2016, pp. 7720-7738, https://doi.org/*10.7712/100016.2368.5953*

[7] E. Barkanov, P. Akishin, N.L. Miazza, S. Galvez, "ANSYS-based algorithms for a simulations of pultrusion processes," Mech. Adv. Mater. Struc., vol. 5, pp. 377-384, 2017, *https://doi.org./10.1080/15376494.2016.1191096*

[8] E. Barkanov, P. Akishin, N.L. Miazza, S. Galvez, N. Pantelelis, "Experimental validation of thermo-chemical algorithm for a simulation of pultrusion processes," IOP Conf. series: Journal of Physics:Conf. series, vol. 991, 2018, 0.1088/1742-6596/991/1/012009

[9] E. Barkanov, P. Akishin, E. Namsone, A. Bondarchuk, N. Pantelelis, "Real time characterization of pultrusion processes with a temperature control," Mech. Compos. Mater., vol. 56, pp. 135-148, 2020, https://doi.org/10.1007/s11029-020-09868-4

[10] Y. R. Chachad, J, A, Roux, J. G. Vaughan, E. S. Arafat, "Thermal model for three-dimensional irregular shaped pultruded fiberglass composites," J. Compos. Mater, vol. 6, pp. 692-721, 1996, https://doi.org/10.1177/002199839603000604

[11] I. Baran, C.C. Tutum, J. H. Hattel, "The effect of thermal contact resistance on the thermosetting pultrusion processes," Composites: Part B, vol. 45, pp. 995-1000, 2013, https://doi.org/10.1016/j.compositesb.2012.09.049

[12] I. Baran, C. C. Tutum, M. W. Nielsen, J. H. Hattel, "Process induced residual stresses and distortions in pultrusion," Composites:Part B, vol. 51, pp. 148-161, 2013, http://dx.doi.org/10.1016/j.compositesb.2013.03.031

[13] I. Baran, J. H. Hattel, R. Akkerman, "Investigation of process induced warpage for pultrusion of rectangular hollow profile," Composites:Part B, vol. 68, pp. 365-374, 2015, http://dx.doi.org/10.1016/j.compositesb.2014.07.032

[14] T. A. Bogetti and J. W. Gillesprie, "Process-induced stress and deformation in thick-section thermoset composite laminates," J. Compos. Mater., vol. 26, pp. 626-660, 1992, https://doi.org/10.1177/002199839202600502

[15] A. Johnston, R. Vaziri, A. Poursartip, "A plane straine model for process-induced deformation of laminated composite structures," J. Compos. Mater., vol. 35, pp. 1435-1469, 2001, https://www.researchgate.net/publication/254112346

[16] I. Baran, J. H. Hattel, R. Akkerman, C. C. Tutum, "Mechanical modelling of pultrusion process: 2D and 3D numerical approaches," Appl. Compos. Mater., vol. 22, pp. 99-118, 2015, https://doi.org/10.1007/s10443-014-9394-3

[17] I. Baran, J.H. Hattel and C. C. Tutum, "The impact of process parameters on the residual stresses and distortions in pultrusion ," in 19th International Conference on Composite Materials, 2013, pp. 6328-6337.

[18] P. Akishin, E. Barkanov, N. Miazza, S. Galvez, "Curing kinetic models of resins for microwave assisted pultrusion," Key Eng. Mater., vol. 721, pp. 92-96, 2017, https://doi.org/10.4028/www.scientific.net/KEM.721.92

[19] D. Zenkert and M. Battley, Laminate and Sandwich Structures: Foundations of fibre composites. 2nd edition. Denmark: Polyteknisk Forlarg, 2009.

Environment. Technology. Resources. Rezekne, Latvia
Proceedings of the 13th International Scientific and Practical Conference. Volume 3, 236-241

Production of Magnesium Binder Composites Using Local Raw Materials and Technogenic Products

Elvija Namsone
Riga Technical University
Faculty of Civil Engineering Institute of Materials and Structures
Riga, Latvia
elvija.namsone@inbox.lv

Genadijs Sahmenko
Riga Technical University
Faculty of Civil Engineering Institute of Materials and Structures
Riga, Latvia
genadijs.sahmenko@rtu.lv

Aleksandrs Korjakins
Riga Technical University
Faculty of Civil Engineering Institute of Materials and Structures
Riga, Latvia
aleks@latnet.lv

***Abstract* - Building sector is known as one of the biggest polluters, causing environmental pollution and carbon dioxide emissions, most of which are generated during the production process of building materials. Therefore, researchers and manufacturers have become increasingly interested in environmentally friendly materials with low energy consumption. Magnesium based cements are being studied as an alternative to a widespread material as Portland cement, thus reducing the temperature required for calcination. During this research, magnesium binder-based composites using two types of magnesium (local dolomite waste material and caustic magnesia) were produced. Within the framework of this study, several regimes of thermal treatment were used to produce low carbon dioxide and environmentally friendly magnesium binder composites. Physical, mechanical and thermal properties of obtained specimens were tested.**

Keywords* - *magnesium binder composites, magnesium-based cements, dolomite waste material, magnesium oxychloride cements

I. Introduction

Portland cement is currently one of the most produced and consumed materials in the world, with an average annual amount of production of 4.6 billion metric tons [1] – [3]. Building industry has significant impact on environment. About 8 % of the world's anthropogenic carbon dioxide (CO_2) emissions are related to the cement and concrete industries; cement is responsible for 95 % of the emissions during the production of concrete [1], [4].

Growing concerns excessive CO_2 emissions led to proposals for low-CO_2 alternative binders [1], [5], [6]. Such binders include magnesium oxide cements which, in combination with other materials, may be used as magnesium oxychloride cements, magnesium phosphate cements, magnesium silicate hydrate cements, etc. [1], [7]

Magnesite ($MgCO_3$) calcination is mainly used for the production of magnesium oxide to be used as raw materials of magnesium oxide-based cements [8], [9]. As another source of magnesite serves dolomite ($CaMg(CO_3)_2$) with larger deposits than magnesite [8], [10]. Magnesium oxide (MgO) forms during the calcination process of dolomite ores and dolomite has been already used as raw material to produce MgO-based cement [8], [11], [12]. Currently the most studied magnesium cements are magnesium oxychloride cement (MOC) and magnesium phosphate cement (MPC) [13].

Magnesium phosphate cement is obtained by a chemical reaction between MgO and soluble acid phosphate. These cements possess vital properties as follows: fast setting, high early strength, excellent fluidity, low shrinkage, high bonding strength, good biocompatibility [8], [14] – [17]. Therefore, MPC have been applied in the following areas: rapid repair, hazardous waste stabilization, biological materials, for the preparation process of foamed concrete and others [8], [13].

Magnesium oxychloride cement, also known as Sorel cement, first was invented in 1867 shortly after the invention of Portland cement [18], [19]. MOC is

Online ISSN 2256-070X
https://doi.org/10.17770/etr2021vol3.6641

TABLE 1 CONTENT OF DOLOMITE SAMPLES

Content	Samples	
	LP	***LS***
$CaMg(CO_3)_2$ [%]	92 - 94	93 - 95
$CaCO_3$ [%]	2.1 – 3.6	1.5 – 2.5
SiO_2 [%]	other	other

obtained by a chemical reaction between MgO and magnesium chloride ($MgCl_2$) solution at ambient temperature, creating ternary system of MgO, $MgCl_2$ and water [23].

Compared to traditional Portland cement, MOC possesses: light weight, high early strength, good abrasion and corrosion resistance properties, low thermal conductivity [13], [18], [20] – [22]. MOC is widely used at: industrial floor production, grinding wheels. MOC is useful for decorative, fire protection, sound and thermal insulation panels production [18], [19].

Compared to the calcination temperature required for the production of Portland cement, it is many times lower for the production of MOC. Consequently, there is some interest in the construction industry for MOC, because these materials are energy efficiency and has been considered as environmentally friendly [23].

II. MATERIALS AND METHODS

A. Used materials

Magnesium binder compositions were prepared in laboratory conditions. Magnesium oxide (MgO) served as the main component and two types of magnesium were added during the experiment.

Caustic MgO CCM RKMH-F, produced by Austrian company "RHI AG Ltd" with 76 % MgO purity, calcined at 750°C and size distribution 90 % < 30μm was used in the first experimental part.

Magnesium, produced from locally available dolomite waste material, obtained from Pļaviņu and Sīļukalns quarries in Latvia, was added in the second part of the research (compositions LP and LS).

TABLE 2 CAUSTIC MAGNESIUM BINDER COMPOSITIONS

Components [weight proportions]	Magnesium binder compositions					
	T1	***T2***	***T3***	***T4***	***T5***	***T6***
Sand	2.25	2.25	2.25	2.25	2.25	2.25
MgO	1	1	1	1	1	1
$MgCl_2$	0.75	0.63	0.50	0.75	0.63	0.50
H_2O	0	0.25	0.38	0	0.25	0.38
SF	0	0	0	0.13	0.13	0.13

TABLE 3 LIGHTWEIGHT MAGNEISUM BINDER COMPOSITIONS

Components [weight proportions]	Magnesium binder compositions	
	λ1	***λ2***
MgO	1	1
$MgCl_2$	0	0.87
H_2O	0.82	0.64
KP	0.92	0.60
PB-LUX	0.92	0.92

To determine $CaMg(CO_3)_2$ and $CaCO_3$ content in the samples with dolomite waste material, mineralogical analysis (XRD or X-ray diffraction analysis) was performed; the results are presented in Table 1. Performing literature review and differential thermal (DTA) and thermogravimetric (TGA) analyses, three regimes of calcination temperature (730°C, 760°C and 790°C) were used.

Magnesium chloride hexahydrate $MgCl_2 \cdot 6H_2O$ (known as bischofite) containing 47 % $MgCl_2$ served as brine solution and was used at a ratio of 1:1 of mass to water.

Natural, washed sand with fraction size 0-1 mm, supplied by local company "Sakret", Latvia was added as a filler.

Microsilica or silica fume (SF) has fine particle size in a range from 1 μm to 15 nm. SF is pozzolanic additive with complementary cementing properties that helps to improve water resistance and durability of material [1], [24].

B. Magnesium binder compositions

In the first part of experimental study, magnesium binder compositions using technogenic product - caustic MgO were obtained. Six compositions (T1, T2, T3, T4, T5 and T6) with MgO/sand ratio 0.44 and containing variable amount of $MgCl_2$, SF and water were produced, see data in Table 2.

Two compositions (λ1 and λ2) of lightweight magnesium concrete were made. Monopotassium phosphate KH_2PO_4 fertiliser (KP) 0-52-35, supplied by "Prayon S.A." and with P_2O_5 content of at least 51.6 % was used for hardening of magnesia. Synthetic foaming agent "PB-Lux" was added with a ratio of PB-Lux/MgO 0.92 (data summarized in Table 3).

In the second part of the experimental research, compositions using local dolomite waste material were obtained (LP and LS, adding dolomite waste material from

Pļaviņu and Sīļukalna quarries, accordingly, see Table 4.) Magnesium oxychloride cement or Sorel cement mixes with three different calcination regimes and water/binder rations 0.4 and 0.35 were prepared.

TABLE 4 COMPOSITIONS USING DOLOMITE WASTE MATERIAL

Properties	**Magnesium binder compositions**	
	LP	***LS***
Temperature of calcination [ºC]	730	730
	760	760
	790	790
Ratio of water/binder	0.4	0.35

The use of recycled porous glass ceramic aggregates with three particle sizes (0.63-1.25 mm, 1.25-2.5 mm and 2.5-5.0 mm) resulted in lightweight concrete compositions (λP and λS) with water/binder ratio of 0.45, see Table 5.

C. Testing methods

To provide the maximum of MgO phase and the minimum of CaO phase, calcination of dolomite powder using three temperature regimes of 730ºC, 760ºC and 790ºC was performed.

In order to obtain a binder powder with a uniform consistency, the calcined dolomite material was subjected to grinding. The process of grinding was done by using planetary ball mill "Retsch PM 400" 220-230 V; 50/60 Hz and rotation speed 300 rpm. Fig.1 presents the obtained material before and after grinding. Dolomite material from Pļaviņu quarry (LP) was grinded 3.5 min and grinding time of dolomite from Sīļukalns quarry (LS) was 5.5 min. The results of grinding fineness are 75.6 % and 76 % (for LP and LS dolomites, respectively).

Universal testing machine "Zwick Z100" with the maximal test force of 100 kN was used to conduct the compressive strength test. The pressure was applied with 0.0005-600 mm/min speed. The samples were exposed under relative humidity conditions (~90-95 %) and temperature 15-20ºC; the dimensions of the test samples 50x50x50mm.

TABLE 5 LIGHTWEIGHT MAGNEISUM BINDER COMPOSITIONS

Properties	**Magnesium binder compositions**					
	λP			***λS***		
Particle fraction size [mm]	0.63-1.25	1.25-2.5	2.5-5.0	0.63-1.25	1.25-2.5	2.5-5.0
The amount of particles [wt%]	-	-	100	-	-	100
	20	40	40	20	40	40
Bulk density [kg/m^3]	225	186	170	225	186	170
Ratio of water/binder	0.45			0.45		

Fig. 1. Dolomite material before and after grinding.

Testing of thermal conductivity was carried out according to guidelines of the LVS EN 12667 standard. It was recorded by equipment for measuring the thermal flow "Laser Comp's FOX 600" with thermal conductivity range 0.01-0.2 W/mK. Testing parameters were determined at 0ºC for the upper and at 20ºC for the lower panel.

Specimens-plates were tested in a hardened and dried condition with the following geometry: 300x300x48 mm, 300x300x40 mm, 300x300x50 mm and 300x300x47 mm (for λ1, λ2 – compositions being prepared using caustic MgO and for λP and λS – compositions being made adding local dolomite waste material).

III. RESULTS AND DISCUSSION

A. Density and compressive strength

Samples obtained by adding both caustic MgO (compositions T1-T6) and dolomite powder from local quarries (compositions LP and LS) were subjected to a 7-day compressive test.

Analysing the results of caustic magnesia compositions, it can be seen that as the amount of $MgCl_2$ decreases, so do the strength values (data presented in Fig.2). For example, reducing the amount of $MgCl_2$ in the compositions T1-T3 by 66%, the compressive strength decreases in the range from 29.5 MPa to 9.2 MPa.

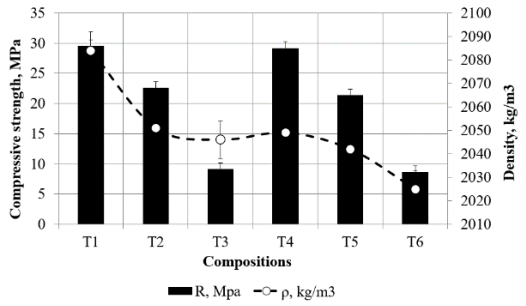

Fig. 2. Results of compressive strength test (using caustic magnesia).

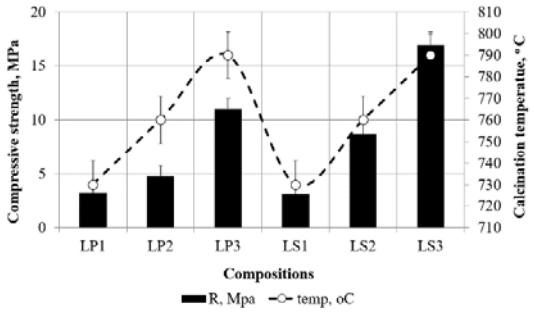

Fig. 3. Results of compressive strength test (using local dolomite waste material)

Summarizing the obtained data from the compositions in the production of which local dolomite powder was added, it can be concluded that the strength values depend on the calcination temperature (data presented in Fig.3). As the calcination temperature increases, the compressive strength also increases.

Maximal compressive strength values of the tested samples were obtained when more magnesium oxide was released during the calcination process. For both series (LP and LS), when dolomite powder from Pļaviņu (LP) and Sīļukalns (LS) quarries was added during production, the maximal strength was observed at a temperature of 790ºC and was 7.73 MPa and 13.82 MPa higher than at 730ºC calcination.

B. Water/binder ratio – compressive strength

A following relationship was observed between the water/binder ratio and the compressive strength (the corelation of water/binder ratio and compressive strength is presented in Fig.4): a higher water/binder ratio resulted in lower strength values.

The water/binder ratio increased from 0.25 to 0.45 and the values of compressive strength decreased from 29.5 MPa to 8.7 MPa when testing the specimens produced using technogenic product (caustic magnesia).

Compositions from local raw material (dolomite powder) included two water/binder ratios 0.4 (LP mixes) and 0.35 (LS mixes); the maximal strength value between LP series samples was 11.0 MPa while it was 17.0 MPa when LS series samples were tested.

C. Thermal conductivity

Thermal properties were tested on samples with caustic magnesia and synthetic foaming agent (λ1, λ2 compositions) and on samples with dolomite waste material and granulated aggregate (porous ceramics) (λP, λS compositions), see the results of thermal conductivity test in Fig.5.

Density values of 348 kg/m^3 and 305 kg/m^3 were obtained using synthetic foaming agent (λ1, λ2), but for compositions with porous glass ceramics (λP, λS) it was about two times higher. With the increase of density values, the coefficient of thermal conductivity also increased. The coefficient was 0.088 W/mK and 0.07 W/mK for the compositions with technogenic product used (caustic magnesia), and it was 0.115 W/mK and

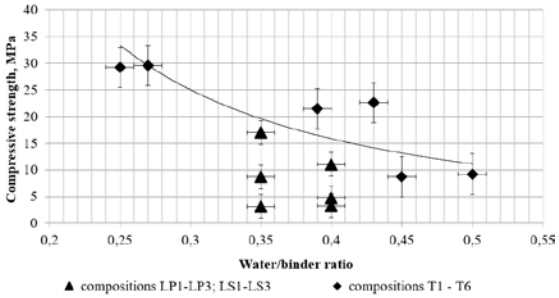

Fig. 4. Corelation of water/binder ratio and compressive strength

0.097 W/mK for the compositions with local raw material (dolomite powder).

Comparing to the results from similar mixes, it can be concluded that the values of coefficient of thermal conductivity decrease with the increase of the amount of $MgCl_2$ (caustic magnesia compositions). When comparing to the data obtained using the porous ceramics of three fractions, it can be seen the results are quite similar: density of λP – 613 kg/m^3 and of λS – 600 kg/m^3.

IV. CONCLUSIONS

In the experimental part of the research, two series of magnesium binder compositions were prepared by using technogenic product (caustic magnesia, produced by "RHI AG", Austria) with an average density value 2050 kg/m^3 and 7-day compressive strength value 20.1 MPa (values were in the range of 8.7-29.5 MPa); and by using local raw material (dolomite powder from Pļaviņu and Sīļukalna quarries in Latvia) with the values of 7-day compressive strength 3.27-17.0 MPa.

The results of the research allow to conclude that calcination temperature affects the strength values. Analysing local dolomite powder compositions, it was observed that with the increase of the calcination temperature, when more magnesium oxide is released, the maximal strength values of these samples were obtained. Specimens produced using dolomite from Pļaviņu quarry at calcination temperature 790ºC showed average strength value 11.0 MPa, but samples using Sīļukalns dolomite material at the same temperature had 7-day compressive

strength of 17.0 MPa. While testing the prepared specimens with a calcination temperature of 730°C, about 70 % and 81 % lower compressive strength values were obtained.

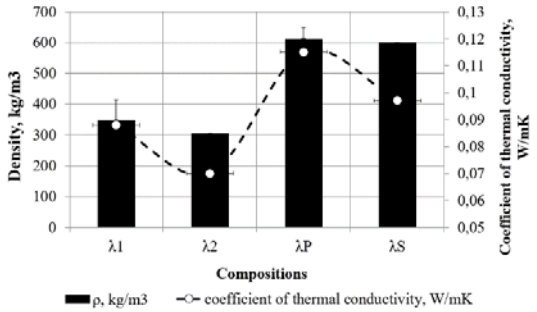

Fig. 5. Results of thermal conductivity test

It was also observed that the amount of magnesium chloride also affects the strength values – as the magnesium chloride content of the mixtures decreased, the compressive strength values also decreased. Addition of 66 % less magnesium chloride to the compositions resulted in a 70 % reduction in strength values (for the T4-T6 compositions from 29.2 MPa to 8.7 MPa).

The results of the study show that a higher water/binder ratio resulted in lower 7-day compressive strength values. Using caustic magnesia, the tested specimens showed about 70.1 % lower values when increasing water/binder ratio from 0.25 to 0.45. Using dolomite waste material and increasing the ratio by 13%, an average compressive strength values decreased in a range from 9.6 MPa to 6.3 MPa.

The use of synthetic foaming agent in the production of lightweight magnesium binder compositions resulted in 43.2 % and 49.2 % lower density values, and in 23.5 % and 28 % lower values of coefficient of thermal conductivity, comparing to the results of the specimens being prepared by adding porous glass ceramics aggregate.

REFERENCES

[1] A.Pivák, M.Pavlíková, M.Záleská, M.Lojka, O.Jankovský, Z.Pavlík, "Magnesium oxychloride cement composites with silica filler and coal fly ash admixture," Materials. June 2020; vol. 13(11), p. 2537, doi: 10.3390/ma13112537

[2] K.L.Scrivener, V.M.John, E.M.Gartner, "Eco-efficient cements: potentioal economically viable solutions for a low-CO_2 cement-based materials industry," Cem. Concr. Res., vol.114, pp. 2-26, Dec.2018, https://doi.org/10.1016/j.cemconres.2018.03.015

[3] G.V.P.Bhagatg Singh, K.V.L.Subramaniam, "Production and characterization of low-energy Portland composite cement from post-industrial waste," J. Clean. Prod., vol. 239, p. 118024, Dec.2019, https://doi.org/10.1016/j.jclepro.2019.118024

[4] N.Lippiatt, T.Ch.Ling, S.Y.Pan, "Towards carbon-neutral construction materials: Carbonation of cement-based materials and the future perspective," J. Build. Eng., vol. 28, p. 101062, March 2020, https://doi.org/10.1016/j.jobe.2019.101062

[5] J.Gieskam, J.R.Barrett, P.Taylor, "Construction sector views on low carbon building materials," Build. Res. Inf., vol. 44, pp. 423-444, Oct.2015, https://doi.org/10.1080/09613218.2016.1086872

[6] E.Gartner, T.Sui, "Alternative cement clinkers," Cem. Concr. Res., vol.114, pp. 27-39, Dec.2018, https://doi.org/10.1016/j.cemconres.2017.02.002

[7] L.Wang, L.Chen, J.L.Provis, D.C.W.Tsang, Ch.S.Poon, "Accelerated carbonation of reactive MgO and Portland cement blends under flowing CO_2 gas," Cem. Concr. Compos., vol. 106, p. 103489, Feb.2020, https://doi.org/10.1016/j.cemconcomp.2019.103489

[8] J.Yu, J.Qian, F.Wang, J.Qin, X.Dai, Ch.You, X.Jia, "Study of using dolomite ores as raw materials to produce magnesium phosphate cement," Constr. Build. Mater., vol. 253, p. 119147, Aug.2020, https://doi.org/10.1016/j.conbuildmat.2020.119147

[9] A.Sam, J.L.Provics, "Magnesia-based cements: a journey of 150 years, and cements for the future?," Chem. Rev., vol. 116 (7), pp. 4170-4204, March 2016, https://pubs.acs.org/doi/10.1021/acs.chemrev.5b00463

[10] K.Sasaki, X.H.Qiu, Y.Hosomomi, S.Moriyama, T.Hirajima, "Effect of natural dolomite calcination temperature on sorption of borate onto calcined products," Micropor. Mesopor. Mater., vol. 171, pp. 1-8, May 2013, https://doi.org/10.1016/j.micromeso.2012.12.029

[11] Z.Z.Liu, S.Wang, J.Huang, Z.H.Wei, B.W.Guan, J.H.Fang, "Experimental investigation on the properties and microstructure of magnesium oxychloride cement prepared with caustic magnesite and dolomite," Constr. Build. Mater., vol. 85, pp. 247-255, June 2015, https://doi.org/10.1016/j.conbuildmat.2015.01.056

[12] M.Altiner, M.Yildirim, "Study of using dolomite as starting material resource to produce magnesium oxychloride cement," J. Adv. Concr. Technol., vol 15, pp. 269-277, 2017, https://doi.org/10.3151/jact.15.269

[13] Y.Hao, Y.Li, "Study on preparation and properties of modified magnesium oxychloride cement foam concrete," Constr. Build. Mater., vol. 282 (3), p. 122708, May 2021, https://doi.org/10.1016/j.conbuildmat.2021.122708

[14] B.W.Xu, H.Y.Ma, H.Y.Shao, Z.J.Li, B.Lotchenbach, "Influence of fly ash an compressive strength and micro-characteristics of magnesium potassium phosphate cement mortars," Cem. Concr. Res., vol. 99, pp. 86-94, Sep.2017, https://doi.org/10.1016/j.cemconres.2017.05.008

[15] Y.Li, B.Chen, "Factors that affect the properties of magnesium phosphate cement," Constr. Build. Mater., vol. 47, pp. 977-983, Oct.2013, https://doi.org/10.1016/j.conbuildmat.2013.05.103

[16] J.H.Qin, J.S.Qian, C.You, Y.R.Fan, Z.Li, H.T.Wang, "Bond behaviour and interfacial micro-characteristics of magnesium phosphate cement onto old concrete substrate," Constr. Build. Mater., vol. 167, pp. 166-176, Apr.2018, https://doi.org/10.1016/j.conbuildmat.2018.02.018

[17] B.Kanter, A.Vikman, T.Bruckner, M.Schamel, U.Gbureck, A.Ignatius, "Bone regeneration capacity of magnesium phosphate cements in a large animal model," Acta Biomater., vol. 69, pp. 352-361, March 2018, https://doi.org/10.1016/j.actbio.2018.01.035

[18] Ch.Hu, B.Xu, H.Ma, B.Chen, Z.Li, "Micromechanical investigation of magnesium oxychloride cement paste," Constr. Build. Mater., vol. 105, pp. 496-502, Feb.2016, https://doi.org/10.1016/j.conbuildmat.2015.12.182

[19] Z.Li, C.K.Chau, "Influence of molar ratios on properties of magnesium oxychloride cement," Cem. Concr. Res., vol. 37 (6), pp. 866-870, June 2007, https://doi.org/10.1016/j.cemconres.2007.03.015

[20] R.Siddique, T.R.Naik, "Properties of concrete containing scrap-tire rubber – an overview," Waste Manage., vol. 24(6), pp. 563-569, 2004, https://doi.org/10.1016/j.wasman.2004.01.006

[21] G.Z.Li, Y.Z.Yu, "Experimental study on urban refuse/magnesium oxuchloride cement compound floor tile," Cem. Concr. Res., vol. 33(10), pp. 1663-1668, Oct.2003, https://doi.org/10.1016/S0008-8846(03)00136-4

[22] N.Li, Q.Wang, M.Zhang, "Research on water resistance of magnesium oxychloride cement," Sichuan Cement, vol. 12, pp. 8-11, 2014

[23] L.Wei, Y.Wang, J.Yu, J.Xiao, S.Xu, "Feasibility study of strain hardening magnesium oxychloride cement-based composites,"

Constr. Build. Mater., vol. 165, pp. 750-760, March 2018, https://doi.org/10.1016/j.conbuildmat.2018.01.041

[24] H.Qing, W.Jing, L.Ying, Z.Weixin, C.Chenggong, D.Jinmei, M.Yangyang, Z.A.Yuan, X.Xueying, "The effect of silica fume on the durability of magnesium oxychloride cement," Ceramics-Silikaty, 2019, vol. 63(3), pp. 338-346, https://dx.doi.org/10.13168/cs.2019.0029

Environment. Technology. Resources. Rezekne, Latvia
Proceedings of the 13th International Scientific and Practical Conference. Volume 3, 242-244

Optical Properties of Laser-Colouring Marked Stainless Steel

Pavels Narica
Faculty of Engineering
Rezekne Academy of Technologies
Rezekne, Latvia

Svetlana Pan'kova
Department of Physics
Pskov State University
Pskov, Russian Federation
psvvit@mail.ru

Vladimir Solovyev
Department of Physics
S. M. Budienny Military
Telecommunications Academy
St. Petersburg, Russian Federation
Department of Physics
Pskov State University
Pskov, Russian Federation
solovyev_v55@mail.ru

Alexander Vanin
Department of Applied Informatics
and Modelling
Pskov State University
Pskov, Russian Federation
a.ivanin@mail.ru

Mikhail Yanikov
Department of Physics
Pskov State University
Pskov, Russian Federation
losthighway@mail.ru

***Abstract* - Laser colour-marking method often displace conventional marking techniques. Complicated technology of laser-induced periodic surface structure creation on stainless steel samples allows changing their surface morphology and optical properties, which were studied in this work by atomic force microscopy (AFM), laser scanning microscopy, reflectance spectroscopy and ellipsometry. Reflectance spectra of the samples demonstrate reflectance maxima correlate with the visible colours of the samples and with the extrema in the non-monotonic spectral dependences of the derivative of real part of complex dielectric permittivity extracted from the ellipsometric data. Thus, the most intensive light scattering takes place when the real part of complex dielectric permittivity falls down quickly with changing wavelength. We did not observe any "azimuth anisotropy" in our optical measurements at constant incidence angle: the spectra were the same independently of the light incidence plane orientation (parallel or perpendicular to the previous laser light spot scanning direction). We suppose that this selective resonance-like light scattering is due to the sample surface inhomogeneity, which is the result of previous laser treatment. This assumption agrees with estimations based on laser microscope and AFM images as well as with predictions of Mie theory. Thus, the colours of the samples under study are due to the light scattering by randomly distributed surface species with different sizes.**

Keywords* - *laser colour-marking, stainless steel, optical properties.

I. INTRODUCTION

Two main methods of laser colouring of metals are mentioned in the literature [1]. The first one utilizes a laser as a heat source, which fabricates a transparent or semitransparent oxide film on the metal surface. White light illuminating the sample is reflected from the surface of both the oxide and metal. As a result of interference of the reflected light beams, a colour effect can be obtained. The thickness of the oxide layer, its refractive index, and the order of interference determine the colour spectrum. If one uses the second method, colour can be obtained on the metal surface by the formation of laser-induced periodic surface structures (LIPSS), acting as diffraction gratings.

Our experimental results demonstrate one more additional reason for colour appearance on the metal surface after laser treatment: the colours of the sample may be due to the light scattering by randomly distributed surface species with different sizes.

II. MATERIALS AND METHODS

We used the samples of stainless steel with dimensions of 100 × 100 mm and thickness of 1 mm. Before the experiment, the plates were washed with isopropyl alcohol in an ultrasonic cleaner. The samples were marked in atmospheric air with the help of industrial laser marking system „DFL Ventus Marker II" (Firma ACI). Fiber laser with wavelength 1062 nm, average output power 20 W,

Online ISSN 2256-070X
https://doi.org/10.17770/etr2021vol3.6516

pulse peak power 12 kW, variable pulse duration and pulse frequency 1-1000 kHz was used. Details of the sample preparation have been described in [2], [3].

AFM images were obtained by scanning probe microscope «NanoEducator». Surface morphology was also studied by KEYENCE 3D Laser Scanning Microscope VK-X100/X200.

Angular resolved reflectance spectra $R(\lambda)$ of the samples under study were measured under illumination by unpolarized white light from a tungsten lamp using a collimated beam. Reflected light was analyzed by USB650 Red Tide spectrometer (Ocean Optics, Inc.).

Ellipsometry determines the change in polarization of reflected light from a sample by measuring two parameters Ψ and Δ that characterize the relative change in the amplitudes of the *p*- and *s*- polarized waves and the phase shift between them:

$$\exp(i\Delta)\tan\Psi = \frac{R_p}{R_s},$$

where R_p and R_s are the reflection coefficients.

After these measurements of ellipsometric parameters, one can carry out calculations of important physical characteristics (refractive index *n*, extinction coefficient *k*, real (ε') and imaginary (ε'') parts of complex dielectric permittivity etc.) of the sample using Fresnel formulae [4] and some theoretical models (semi-infinite effective medium is the simplest one).

In this work, we used spectroscopic ellipsometer "Ellips-1891", working at static photometric mode without any rotating elements or modulators [5].

III. Results and Discussion

Reflectance spectra of the samples No. 2, 3, 4, 5 (having blue, green, orange and red colour, respectively) measured at the angle of light incidence $\theta = 50^0$ are shown in fig. 1. One can see rather wide reflectance bands with maxima at approximately 475, 570, 635 and 705 nm, respectively. The similar results correlating with the visible colours of the samples were obtained at the angle of light incidence $\theta = 30^0$ (fig. 2).

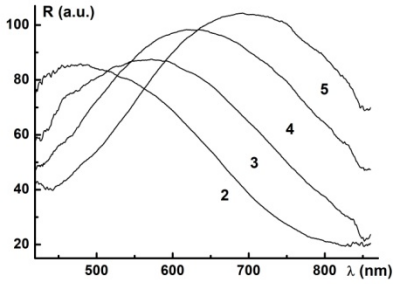

Fig. 1. Reflectance spectra of the samples No. 2, 3, 4 and 5 at the angle of light incidence $\theta = 50^0$.

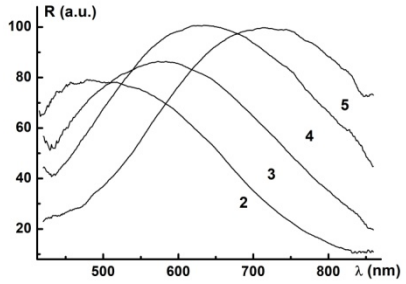

Fig. 2. Reflectance spectra of the samples No. 2, 3, 4 and 5 at the angle of light incidence $\theta = 30^0$.

Fig. 3 demonstrates spectral dependences of ellipsometric parameters Ψ and Δmeasured at the angle of light incidence $\theta = 50^0$ for one of the samples. It should be emphasized, that we did not observe any "azimuth anisotropy" in our optical measurements at constant angle of light incidence value: the spectra was almost the same independently of the plane of light incidence orientation (parallel or perpendicular to the previous laser light spot scanning direction) – see solid and dotted lines in fig. 3. Thus, the colours of the samples under study are not caused by the "diffraction grating effect".

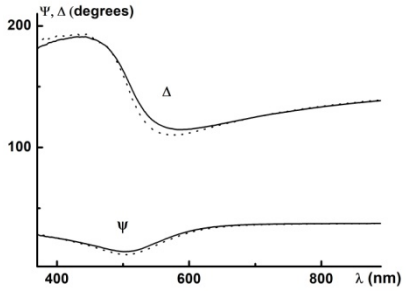

Fig. 3. Spectral dependences of ellipsometric parameters of the sample measured at the angle of light incidence $\theta = 50^0$. Solid and dotted lines correspond to the plane of light incidence orientation (parallel or perpendicular to the previous laser light spot scanning direction, respectively).

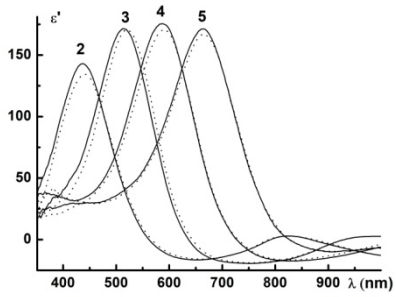

Fig. 4. Spectral dependences of the real part of complex dielectric permittivity ε' for the samples No. 2, 3, 4 and 5 measured at the angle of light incidence $\theta = 50^0$. Solid and dotted lines correspond to the plane of light incidence orientation (parallel or perpendicular to the previous laser light spot scanning direction, respectively).

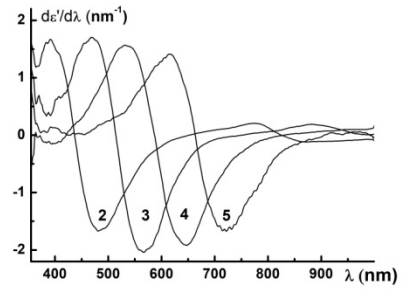

Fig. 5. Spectral dependences of the derivative of the real part of complex dielectric permittivity $d\varepsilon'(\lambda)/d\lambda$ for the samples No. 2, 3, 4 and 5 measured at the angle of light incidence $\theta = 50^0$.

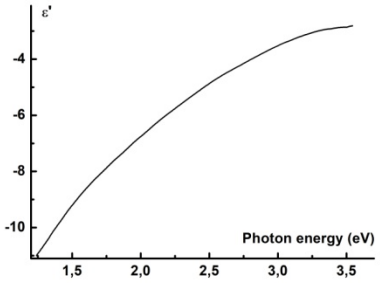

Fig. 6. Spectral dependence of the real part of complex dielectric permittivity ε' for the initial stainless steel ("substrate") measured at the angle of light incidence $\theta = 70^0$.

Figs 4 and 5 show non-monotonic spectral dependences of the real part of complex dielectric permittivity ε' and those of its derivative $d\varepsilon'(\lambda)/d\lambda$ extracted from the ellipsometric data for the samples No. 2, 3, 4 and 5. Note that no extrema could be observed in the monotonic spectral dependence of the negative ε'value for the initial stainless steel ("substrate") in the investigated intervals of photon energy and the angles of light incidence (see, e.g., graph in fig. 6 which is typical for metals [6]).

One can see that all the maxima positions in fig. 1 correspond with minima in fig. 5. Thus, the most intensive light scattering takes place when the real part of complex dielectric permittivity ε' value falls down very fast with changing wavelength λ. This behaviour is specific for dissipating systems, where significant dispersion of ε'value (usually near the resonance frequency) leads to energy dissipation, high dielectric losses etc.

We suppose that this selective resonance-like light scattering [4], [7] is caused by the sample surface inhomogeneity which, in its turn, may be the result of previous laser treatment [8]. Qualitative estimation based on laser microscope and AFM images [3] leads to the conclusion that the characteristic size of randomly distributed surface species increases with the sample number (from 2 to 5), correlating with the shift of the peculiarities in figures 1 and 5 to the longer wavelengths. This statement agrees with the predictions of Mie theory, concluding that scattering characteristics of spherical particles depend upon the non-dimensional parameter $q = 2\pi a/\lambda$ [4], [7], where $2a$ is the sphere diameter. From this point of view, particle size growth has to increase corresponding resonance scattering wavelength; this prediction is in consistency with our experimental results.

IV. CONCLUSIONS

Laser colouring of metal surface may be caused not only by interference in thin oxide films and/or by diffraction of light on laser-induced periodic surface structures. We suggest one more possible mechanism of colour laser marking: selective resonance-like light scattering due to the sample surface inhomogeneity, which is the result of previous laser treatment. This assumption agrees with optical data and estimations based on laser microscope and AFM images as well as with predictions of Mie theory. Thus, the colours of the stainless steel samples may be due to the light scattering by randomly distributed surface species with different sizes appeared after laser irradiation.

V. ACKNOWLEDGMENTS

The authors are grateful to Professor L. Lazov for choosing a research direction and helpful discussions.

REFERENCES

[1] A. J. Antonczak, B. Stepak, P. E. Kozioł, K. M. Abramski, "The influence of process parameters on the laser-induced coloring of titanium", Applied Physics A, vol. 115, pp. 1003–1013, 2014.

[2] L. Lazov, H. Deneva, P. Narica, "Factors influencing the color laser marking", Environment. Technology. Resources: Proceedings of the 10th International Scientific and Practical Conference, Rezekne, Latvia, vol. 1., pp. 102-107, 2015.

[3] P. Narica, "Chromium-nickel steel surface colour laser marking process optimization," Doctoral thesis, Daugavpils University, Daugavpils, Latvia, 2017.

[4] M. Born and E. Wolf, Principles of Optics. Oxford: Pergamon Press, 1964.

[5] V. A. Shvets, E. V. Spesivtsev, S. V. Rykhlitskii, N. N. Mikhailov, "Ellipsometry as a high-precision technique for subnanometer-resolved monitoring of thin-film structures", Nanotechnologies in Russia, vol. 4, pp. 201–214, 2009.

[6] S. A. Maier, Plasmonics: Fundamentals and Applications. NY: Springer, 2007.

[7] C. Bohren and D. Huffman, Absorption and scattering of light by small particles. Wiley, 1983.

[8] C. Y. Yap, C. K. Chua, Z. L. Dong, Z. H. Liu, D. Q. Zhang, L. E. Loh, and S. L. Sing, "Review of selective laser melting: Materials and applications," Applied Physics Reviews, vol. 2, pp. 041101 (1-21), 2015.

Environment. Technology. Resources. Rezekne, Latvia
Proceedings of the 13th International Scientific and Practical Conference. Volume 3, 245-251

Industry 4.0 - Development and Consequences for Sustainable Development of Bulgaria

Neli Nikolova
Department Management
Technical University of Gabrovo
Gabrovo, Bulgaria
e-mail: nik_nel@abv.bg

***Abstract* - The report presents analytical information about the state of play of the processes of the Fourth Industrial Revolution in different areas of the Bulgarian economy and industry. Based on a survey conducted in Bulgarian SMEs, the respondents' idea of the challenges and obstacles faced by company guides in its implementation in production, digital education, qualification and training in the course of the work is summarized. Data from a survey on key skills and competences needed to work in digitalization conditions have been released. Recommendations and sample applications have been formulated to ensure a successful symbiosis of Industry 4.0 with Industry 5.0.**

Keywords* - *digital education, challenges, competences, Industry 4.0

I. INTRODUCTION

The digitalization coming into the world poses new challenges for Bulgarian organizations from different economic sectors. The COVID-19 pandemic has led to numerous changes, and the economic crisis has affected the whole world. Many business and non-profit organisations have been placed in a new business environment where consumer's behaviour has changed and conditions have become even more precarious. The most affected by the crisis is the small business. This sector of the economy is most vulnerable because it represents over 90% of the entire business in Bulgaria. In turn, the average occupies only about a percentage, and the large one – below 0.5% (as of 2019) Given the situation, digitalization has proved to be the key to the flexibility and adaptability of each company.

II. EXPOSITION

In the exceptional difficult conditions in which modern business is to function, Industry 4.0 has become ubiquitous in the following economic areas, characterized by enhanced digital connectivity and mobility of people of active working age, whose existence has become part of the large digital community:

- information and communication technologies;
- cyber-physical systems;
- storage and processing of large-scale data sets (so-called cloud systems);
- systems for modeling, simulating and virtual presentation of information;
- tools for interaction between humans and computing machines.

A significant proportion of companies surveyed by university lecturers [5],[6] put new materials into their production using computer systems for production management, the essential elements of which are the minimization of waste and the use of technology for their recovery. In 40% of them, new information technologies have entered into administrative activity, accounting, pricing, stock and order management. About 1/2 of the companies surveyed do not yet have developed a comprehensive system for training and upskilling of the staff needed for working in the conditions of Industry 4.0. About 1/3 of the companies are in the process of developing such a system, and the remaining 20% already have a developed and operational system. In recent decades, it has become obvious to everyone that the problems faced by organizations are becoming more complex, dynamic and multidimensional. These include transformation in all areas of the business related to automation and digitization of workflows, constant economic uncertainty, employee engagement, etc. The internal dynamics of these problems are constantly changing and complicated by the advancing Industry 5.0, in which people and machines will have to interact as harmoniously as possible in order to maintain their competitiveness and adapt to the new way of working.

Many SMEs have managed to reap the benefits in the country for creating added value and successfully

Online ISSN 2256-070X
https://doi.org/10.17770/etr2021vol3.6543

participating in industry 4.0 processes. Positives for the digital transformation of the Bulgarian industry are: well-developed ICT infrastructure with high-speed broadband; excellent tradition in the IT sector; access to European programmes; widespread use of the Internet.

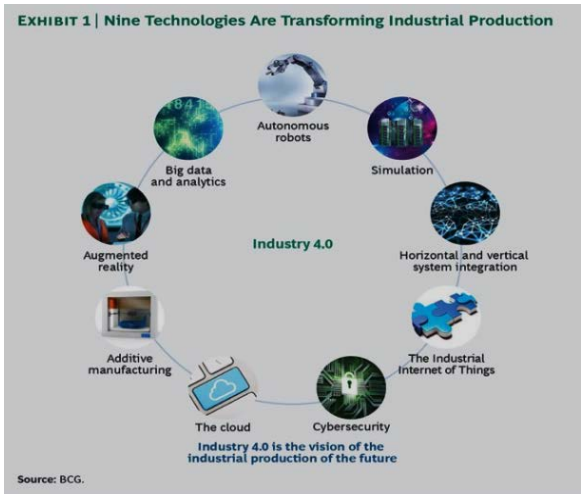

Fig. 1. Vision of Industry 4.0
Source: Industry 4.0: The Future of Productivity and Growth in Manufacturing Industries

The unfolding global pandemic has accelerated the digital transformation process in almost all sectors and united industries in their efforts to be more cooperative for a functional digital future. The ability to use digital tools and channels has become a major tool for entrepreneurs trying not only to survive the current crisis, but also to make the most of it. In a world of forced contactlessness, a huge part of the interaction of companies with their customers and employees must take place virtually. In many of these cases, the digital presence becomes the only way for the Bulgarian small, medium and large business to survive in the conditions of forced closure and social isolation.

When looking at the issues of "Industry 4.0" in the context of the sustainability of the national economy, we need to address not only the industrial sector, but also the other areas relevant to the management of sustainable development.

1. Socio-economic development
2. Sustainable consumption and production
3. Social inclusion
4. Demographic changes
5. Public Health
6. Climate change and clean energy
7. Sustainable transport
8. Natural resources
9. Global Partnership
10. Effective management

The digital transformation of the business is studied and analyzed in the publications of a number of Bulgarian researchers through different approaches [1], [2], [3], [4]. Flexible adaptation of modern enterprises to dynamic changes requires the development and use of new business models.

Through them, management teams can respond quickly and adequately to ever-evolving technologies, enabling them to collaborate in a new ecosystem, effectively manage data as a valuable asset and tackle cybersecurity.

Fig. 2. Technological aspects of Industry 4.0 [11]

The following figure traces innovations during individual industries in the course of their evolution:

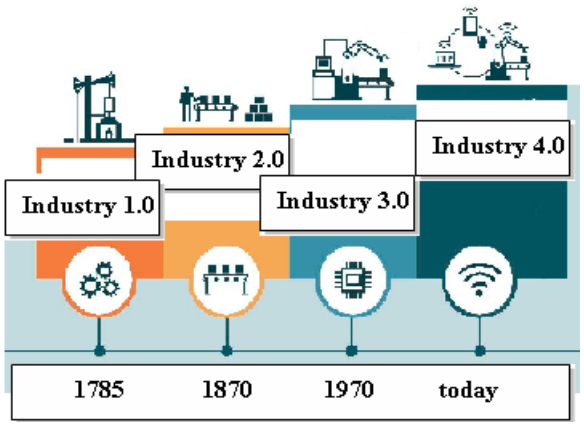

Fig. 3. Industry development

Legend:
- **Industry 1.0** - mechanization, steam power; weaving loom
- **Industry 2.0** - mass production, assembly line; electric energy;
- **Industry 3.0** - automation, computers, electronics]
- **Industry 4.0** - cybernetic systems, the Internet of Things, networks.
- **Industry 5.0** – the future industry – collaboration between robots and humans, the so-called "koboti"

The Internet of Things, cloud technologies, large databases and analytical tools, mobile communications and social networks are the strategic solutions needed for digital transformation of organizations. They all set up a quality new business model that achieves maximum operational efficiency through data mining, forecast modelling and forecast analysis; development of a digitised ecosystem of products and services. The digital

skills of the workforce combine digital and technical skills with problem-solving skills; create new job descriptions, incentives and career paths for the recruitment and retention of skilled employees; flexibility in the workplace; build global teams.

IMD's Global Digital Business Transformation Centre has developed a so-called „grand piano model“ in which it describes seven areas of organisational change presented in Figure 4: [7]

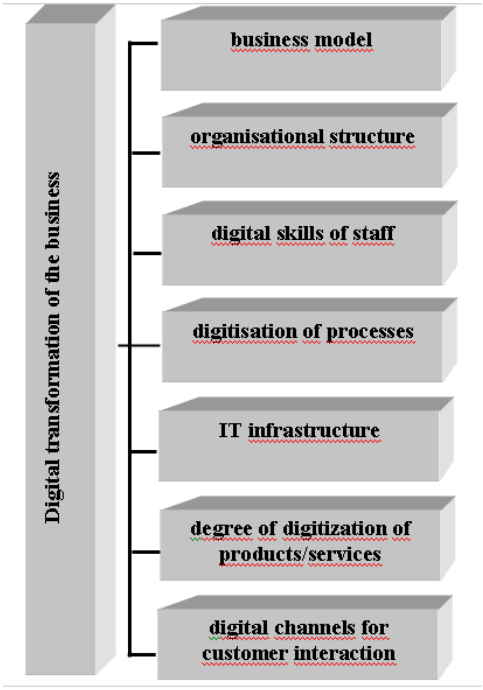

Fig.4. Digital Royal

The new draft digital transformation strategy in the country for the period 2020-2030, prepared by the Ministry of Transport, Information Technology and Communications, sets out the implementation of the following main objectives:

- deployment of secure digital infrastructure;
- ensuring access to adequate technological knowledge and digital skills;
- unlocking the potential of the data;
- digitisation in favour of a circular, low-carbon economy;
- improving the efficiency of government and the quality of public services.

Gigabit connectivity will be ensured by 2030 for all major socio-economic drivers such as schools, transport hubs and major public service providers, as well as digitally intensive enterprises. Support for high-speed connectivity will be accompanied by trainings for acquiring new or improving key competences and professional qualifications; new skills for specific new jobs. Strategic measures include enhancing citizens' digital skills and stimulating demand for internet-based services from the population and businesses.

Bulgarian small and medium-sized enterprises (SMEs), which make up more than 99.8% of enterprises in Bulgaria, face many challenges posed by digitization and Industry 4.0.

Purpose of the study and methodology

This publication aims to explore the potential of Industry 4.0 for Bulgarian SMEs and their level of readiness (digital, infrastructure, etc.). The arguments formulated above are set out in the questions of a questionnaire, with the help of which, in the framework of project 2009C "Management of technological change as a structured process for finding effective and flexible solutions through Industry 4.0, funded by the Research Fund for 2020, a study has been carried out on the problems related to digitization in Bulgarian SMEs. Some of the answers to the questions received in the survey are presented graphically.

For respondents were selected company managers, as well as managers from the average management levels – mainly operating managers, who are directly related to the implementation of Industry 4.0 in their enterprises. The results obtained, although the relatively small number of SMEs surveyed cannot be claimed to be of great representativeness, are interesting and indicative of the problems and what is to be done for the preparation of Bulgarian SMEs for the implementation of Industry 4.0. The survey covers 86 companies from different districts in the country By subject of activity they are allocated as follows:

- processing industry – 42%;
- services – 50%;
- mechanical engineering – 8%.

By their size, the sampleD SMEs are relatively "evenly distributed": medium – 35%, small – 32.5% and micro – 32.5% (Fig. 5).

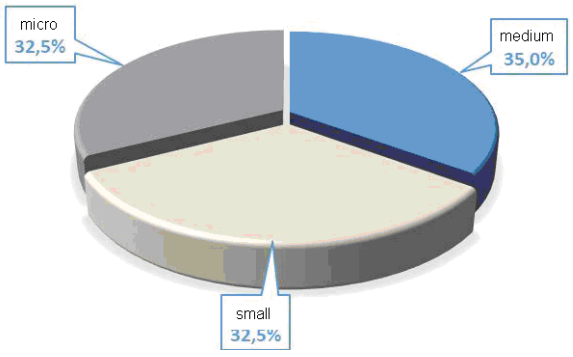

Fig. 5. Structure by size of SMEs

According to a poll conducted, more than 80% of respondents rated the role of digital in their company as "decisive" or "very significant." With regard to the current level of digitisation, more than half of respondents replied that it was above average. Nearly 90% of the companies where the survey was done indicated that within three years they would have already taken steps towards

digitizing the processes. The survey participants were asked the questions:

1. What topics were discussed in the companies surveyed last year?

We received the following responses, calculated in percentage terms of the figure:

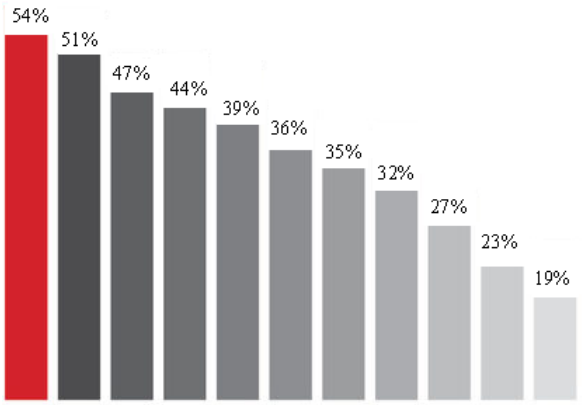

Fig. 6. Topics discussed in companies

Legend:

- development and implementation of innovations – 54%;
- productivity gains – 51%;
- achieving growth – 47 %;
- expansion of markets – 44 %;
- introduction of new business models – 39%;
- implementation of modern technologies – 36%;
- attitude of the staff for change – 35%;
- minimizing operating costs –32%;
- protection against cyber attacks – 27%;
- achieving competitive advantages -23%;
- management of creative human resources (talents) – 19%.

2. In which of these areas will Industry 4.0 have the greatest impact on the public?

Each respondent gave up to three answers:

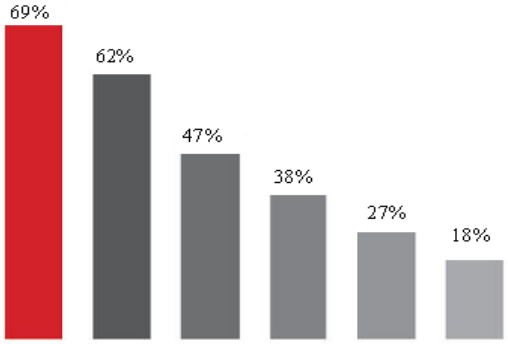

Fig. 7. Influence of Industry 4.0

Legend:

- public sector – 69%;
- private sector – 62%;
- state regulators – 47%;
- intergovernmental cooperation - 38%;
- electoral attitudes- 27%;
- non-governmental organizations – 18%.

3. What are the most common difficulties (obstacles) in digital transformation of company processes?

The surveyed top managers formulate several main obstacles in developing new business models to ensure strategic competitiveness of the companies they manage.

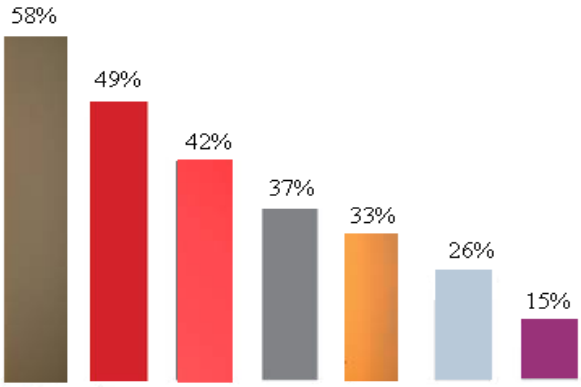

Fig. 8. Barriers to introduction of Industry 4.0

Legend:

- lack of internal ranking of strategic objectives - 58%;
- lack of cooperation with external partners - 49%;
- lack of a specific business case to justify investments in the necessary IT structure – 42%;
- lack of adequate complex skills to absorb the approach to Industry 4.0 – 37%;
- difficulties in coordinating the actions of the different units – 33%;
- insufficient attitude and motivation to participate in radical transformation – 26%;
- undesirables for changes by elderly employees in enterprises – 15%;

4. How will the process optimization help you grow your business?

Only strategic managers in the companies where the survey was carried out answered this question. Of these, 25% working in SMEs and 34% of large enterprises pointed to automatic connectivity with suppliers and customers.

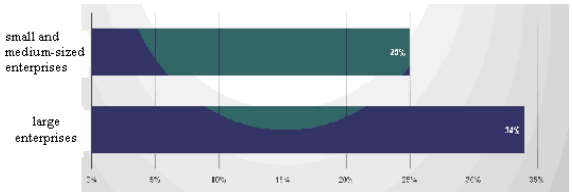

Fig.9. Automatically connected business processes with suppliers and customers

Fig.10 presents survey data among regional managers on the necessary competencies of their employees:

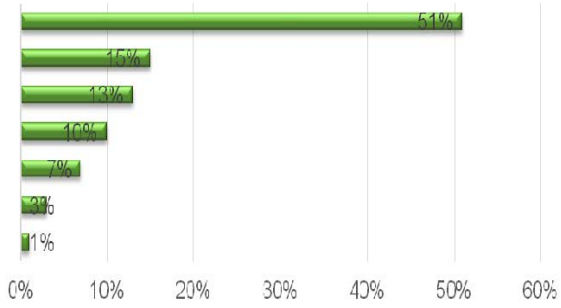

Fig.10. Key competences of HR

Legend:
- digital skills – 51%;
- technical competences – 15%;
- entrepreneurial attitudes – 13%;
- creativity – 10%;
- organizational skills – 7%;
- communication – 3%;
- others – 1%.

5. What challenges do company executives face from the entry of Industry 4.0 into their organizations?

When interviewing linear and functional managers, we ranked the following challenges for SMEs related to Industry 4.0:

- security and cybersecurity issues;
-reliability and stability in critical communication;
- the need to preserve the integrity of production processes;
- avoiding costly large interruptions;
- protection of industrial know-how in control files for industrial automation;
- risk of redundancies in IT departments;
- challenges in integrating data from different sources.

The analysis of challenges identifies a number of new specific opportunities and management solutions in the context of digital transformation.

Findings

Industry 4.0 has different aspects that can affect Bulgarian SMEs. It can transform business models and value chains by connecting built-in systems and intelligent manufacturing processes.

Nearly 50% of the study participants believe that Industry 4.0 can significantly change their production systems. Some 23% of respondents said that the 4th Industrial Revolution could affect their business in all aspects, while 15.6% of them believe that only IT systems can benefit from the concept of Industry 4.0.

Based on the survey results, 36.8% of respondents stated that the lack of internal digital culture and training, insufficient opportunities for the introduction of new business models, as well as dynamically changing market requirements are the most critical barriers to the implementation of Industry 4.0 in their organizations.

After conducting extensive interviews with some of the managers in the machine building industry, they point out that not only technological and product company renewal is necessary, but also the implementation of modern technologies contributing to environmental protection, in accordance with national and European requirements.

Challenge analysis identifies a number of new specific opportunities and management solutions in the context of digital transformation.

On the other hand, the world's data on consumption and nutrition of the population is extremely worrying - over a billion and a half people on the planet suffer from malnutrition. Between 30 and 50 per cent of all food produced in the world is thrown away, according to a sensational report by the British Association of Engineers. This equates to between 1.2 and 2 billion tonnes per year. In the UK itself, 30% of vegetables produced are not even picked because they do not meet the appearance requirements of distributors. Half of the food bought in the US and UK goes to rubbish bins dumped by shoppers. Globally, about 550 billion cubic meters of water are wased each year to grow crops that never reach consumers. The energy costs of supply exceed at times the energy costs of producing a particular unit of each type of fruit and vegetables. In this aspect, Industry 4.0 can provide crucial support for optimal use of fertile areas and the development of modern agriculture.

The solutions consist in the design and commissioning of integrated complexes for organic production, harvesting and delivery of fruit and vegetables on indoor and outdoor areas, based on existing technologies, technological solutions and finished elements. In order to be efficient, integrated production complexes need to be introduced on large vacant areas. They are suitable for the territory of the Republic of Bulgaria and due to the lack of labour. Variant of the application of Industry 4.0. are mobile autonomous robots (drones, drones and ground robots) used in the country for precise grain production.

In recent decades, large enterprises in the Bulgarian mining industry have been among the leading ones in Europe in the pace of introduction of new technologies in all aspects of their activities. Modern solutions are integrated both to achieve high safety at work in mining sites and to minimise environmental footprints and greenhouse gas emissions. Modern digital technologies are successfully implemented and implemented programs for complete digital transformation of production processes. They cover automation, mining equipment management and monitoring systems. The results are higher productivity, better cost and quality of the finished product, as well as the possibility of optimal and longer utilization of natural resources. Mining companies can observe different aspects of the modern concept of the circular economy, which are actually implemented.

With the development of automated vehicles, the use of clean technologies and, in particular, the emergence of low-emission trucks and electric vehicles is increasing. New digital technologies in the transport and logistics industry reduce costs and improve efficiency by offering automated analyses for business in real time.

In Bulgaria there are good examples of digital transformation in both the leading sector of information

and communication technologies, as well as in traditional sectors and banking services. Over the past five years there has been a rapid growth rate of employees in information technology (by 56.2%) Bulgaria is at the forefront of ICT start-ups in the EU.

Outside of the information and communication technology sector and digital marketing agencies, good examples of a holistic approach to these processes have some of the banks in the country. Factors for the success of the digital transformation in the Bulgarian banking sector are the provided financial resource and the targeted work to change the attitude of employees towards replacing traditional processes with digital ones. With regard to customers, the digital transformation is aimed at narrowing the market segments based on more precise processing of information, increasing the access opportunities and speed of the service, as well as the individualization of promotional offers in branch banking structures.

Digital innovation for the Bulgarian banking market is the introduction of the Factoring.bg. The platform shortens the time and effort in the exchange of information, improves the speed and transparency of factoring transactions, speeds up advancepayments, minimizes manual document filling and ensures transparency throughout the process.

The force majeure circumstances has accelerated the processes for the digitization of the Bulgarian economy, from which it will continue to benefit in the long term. The digital revolution achieved in a short time significant objective advantages, some of which are:

- Increased efficiency. The digital economy has the undoubted potential to optimize operations and automate processes in a number of industries. As a result, each company can optimize its time and human resources, minimize its waste and environmental footprint, and focus on revenue-generating activities.

- Improve the customer experience. The Internet of Things (Internet of Things or IoT) is the basis for creating a "smart world" - a reality built of objects, devices and infrastructure connected to the Internet and, accordingly, to each other. IoT has the capacity to accelerate and refine a number of processes across industries. The digitization of trade can be based on technologies such as IoT and artificial intelligence to offer its customers the personalization of next-generation services and respond to needs already in the bud of their emergence.

- Excellent security. Contrary to some outdated perceptions, technologies such as blockchain and decentralised data storage could make digital processes far more secure and reliable than easily manipulative physical reality.

- Adaptability. The digital economy gives tremendous leeway in a physically limited world. It opens the door to the practices of the future - remote teams, virtual operations, omnichannel marketing, automated payments and flexible co-op terms with partners and customers.

- Repeated return on investment. Digitization is a complex process that requires a certain amount of time and capital investment. Virtual operations save extremely much time, resources and losses in the long term, providing a much wider scope and adaptability of the business to competition.

The digital trend for working from home achieves much more connectivity and many more people learn to use the digital environment, which means that there are many more consumers for the digital products that entrepreneurs create.

Short-term consequences

One of the most obvious consequences we are likely to see in the coming years is the decline in demand for labour. This will be the result of the slowdown of the global, European and Bulgarian economies. The most endangered groups will be older workers, as well as people with lower education and skills. The decline can be offset somewhat by demand in other sectors that will remain less affected by the crisis. Employment will hold certain levels as the virus flows less lightly in people of working age.

Long-term consequences

Social isolation required many companies to introduce compulsory work from home - something that before the pandemic was typical of only a few of them, especially the liberal professions. On the one hand, if working from home proves just as productive as working from an office, it can become much more prevalent after the end of the virus crisis. If it delivers well, many companies will have more confidence in people in their teams to work outside the office. At the same time, the offices of many companies may prove to be an unnecessary cost of rent, consumables and overhead.

This would also depend on the dynamics of working at home and what results companies will show. Technological developments will be one of the few positive long-term consequences of the crisis. The need for remote work will speed up the process of developing new and improving existing technologies. The projected expectations are for an increase in the rise of high technology and the number of software and hardware specialists without which remote operation is impossible.

The industry, in particular manufacturing, will continue on the path of robotisation, but at a higher rate due to market needs. Automation is one of the solutions to curb the pandemic in the manufacturing sector, where many people usually work in the same room. This will provide more personal space for employees in factories and other manufacturing plants.

The social distance will inevitably also require changes in the work of the state administration. New electronic administrative services and optimisation of existing ones will need to be introduced. The inability to physically go to the institutions will also require the administration to change the way it works.

Many sectors will suffer huge economic losses. One of the first sectors concerned is transport, as the production and supply of raw materials and goods will decline. Trade, restaurant business, culture and sport are also among the most affected industries. Last but not least comes tourism, which suffers severe consequences.

CONCLUSION

In conclusion, we can say that the 2020 pandemic has opened the doors of the digital economy, which is currently creating its "creative destruction" - a process in which an outdated system collapses and goes into the past to pave the way for something new, more accurate, smarter and better. COVID-19 has become the catalyst for digital transformation.

The results of the survey show a high level of awareness of the Bulgarian managers for Industry 4.0. Respondents demonstrated widespread use of IT infrastructure in their accounting and financial systems (78%), and also had significant benefits in supply management and set-aside/stocks (around 67%). participants in the survey indicate the existence of a developed company strategy for the implementation of Industry 4.0, yet most top managers are working on creating one and intend to invest up to 10% of their realized profit in the digitization of their processes in the next 1-2 years.

The new industrial revolution has the potential to improve productivity as well as life and quality of jobs, if properly accompanied by a stable mix of policies for inclusive and sustainable, innovation-driven growth.

REFERENCES

[1] Miteva, I. Mitev, T. Kovachev, Influence of the pressing force on the strength properties of sintered materials based on water-dispersed iron powders alloyed with cooper, IJSTII “Machines Technologies Materials”, years XV, Issue 1/2021, ISSN PRINT 1313-0226, ISSN WEB 1314-507X, pp 34÷37

[2] Kovachev, T., I.Miteva, I.Mitev, Influence of Pressure Force on Density Before sintering of Iron Powder materials Obtained by Reduction, AJ Industrial Technologies, Issue7/2020, ISSN 1314-9911, pp. 23÷27.

[3] Nenov., N., P., Tomchev, R., Ivanova, Study of the Ion Radiation Influence on the Parameters of Unijunction Transistors, *Proceedings of the 9th International Scientific and Practical Conference “Environment. Technology. Resources”. Vol.1*, Latvia, Rēzekne, 20-22 June, 2013. Rēzekne: Rēzeknes Augstskola, RA izdevniecība, 2013, ISSN 1691-5402, ID in database – 16424, pp.137-139.

[4] Petrova, D., Analysis of SMEs in Bulgaria – Assessment of Their Innovation Activities, Rezekne 2013, Latvia, Rezekne Higher Education Institution, Faculty of Engineering, Scientific Institute for Regional Studies, Environment. Technology. Resources, Proceedings of the 9th International Scientific and Practical Conference June 20-22, 2013, Volume 3, ISSN 1691-5402,pp 46-49. scopus

[5] Petrova, D., Intelligent, Innovative and Sustainable Industry in Bulgaria – Prospekts and Challenges, Environment. Technology. Recourses – Proceeding of the 12-th International Scientific and Practical Conference, Rezekne Academy of Technologies, Rezekne, Latvia, 2019, ISSN 1691-5402, p. 210-215.

[6] Tomchev, P., N., Nenov, R., Ivanova, Instantaneous water heater with induction heater operating with grid frequency, „Research and Development in Mechanical Industry“ RaDMI 2012, 13-17 September 2012, Vrnjačka Banja, Serbia, SaTCIP Ltd., Technical-Mechanical School in Trstenik, ISBN 978-86-6075-036-7, Volume II, pp. 1214-1218.

[7] Wade, M,. Digital Business Transformation. A Conceptual Framework 2015 Available online at

[8] http://www.imd.org/uupload/IMD.WebSite/DBT/Digital%20Business%20Transformation%20Framework.pdf

[9] https://cio.bg/management/2017/09/20/

[10] http://ebox.nbu.bg/sec16/pdf/59.pdf

[11] https://eniware.org/What is Industry 4.0

[12] https://www.investor.bg/analizi/85/

Environment. Technology. Resources. Rezekne, Latvia
Proceedings of the 13th International Scientific and Practical Conference. Volume 3, 252-255

Analysis Of Optical Methods For Monitoring The Working Surface State Of The Grinding Wheel

Alexander Orlov
Institute of Engineering Sciences
Pskov State University
Pskov, Russia
sashaorlov.m@gmail.com

Igor Nikiforov
Institute of Engineering Sciences
Pskov State University
Pskov, Russia
nikiforov.i.p@mail.ru

Pavel Maltsev
Institute of Engineering Sciences
Pskov State University
Pskov, Russia
inertan@gmail.com

Anton Usik
Institute of Engineering Sciences
Pskov State University
Pskov, Russia
usik.tosha@yandex.ru

***Abstract* - The article describes an analysis of non-contact optical methods for monitoring linear wear and the working surface condition of the grinding wheel during dry grinding. The presented methods are based on computer processing of photo and video materials, 3D models surface construction of the grinding wheel, the machine vision and using of the optical equipment. The advantages and disadvantages of this methods were analyzed. As a result of the conducted research, it was concluded that the usable area of the considered methods depends on the circle material, cutting parameters, control objectives, including the requirement for on-line control, and also the available material and technical equipment.**

Keywords* - *Grinding, tool wear, laser, triangulation, machine vision, light polarization

I. INTRODUCTION

Condition monitoring of a working surface of a grinding wheel has an important role in quality assurance of the machined surface. During grinding process the wheel wears out, becomes salted, and its geometric shape changes. Workable state providing of the grinding wheel surface is an actual task because of shaping treated surface is the result of the interaction of the abrasive tool with the surface of the work piece.

The control can be provided by contact and non-contact methods. All contact methods have a significant drawback. It is the wear of the probe during its interaction with the abrasive grains of the grinding wheel. Therefore, non-contact methods (optical, pneumatic, hydraulic) are becoming more applying. Optical monitoring methods are analyzed in this work, which are based on these basic principles: laser scanning, polarized light using, 3D surface modeling based on static micrographs. At the same time, special software are widely used, such as with statistic analysis using.

II. MATERIALS AND METHODS

Non-contact method of texture analysis for wear determination of a grinding wheel by using machine vision is known [1]. This method consists in obtaining images of the grinding wheel working surface by using a CCD camera (CCD is a charge-coupled device) at different times during the grinding process and their subsequent analysis by existing statistical and fractal methods.

Other non-contact optical method for detection of grinding wheel wear is based on a digital profile grinding machine by using a CCD is also known [2]. A machine vision system with a scheme for visual measurement of the grinding wheel profile has been developed, which consist of a profile grinding machine, a CCD camera GC2441M with a telescoping lens, a controller and a computer processing the received data. To measure the wheel profile photographs of its working surface in different parts are made. It is provided by repeatedly turning the grinding wheel at 45° from the previous position within one full turn. Then received images are transferred to the computer memory, where they are processed by software.

System for active control of surface roughness by measuring the degree of polarization of the reflected radiation is also known [3]. The control method which is

Online ISSN 2256-070X
https://doi.org/10.17770/etr2021vol3.6548

used in this system is an analysis of radiation polarization characteristics, roughness value in the reflected radiation and their relationship. As a result, a model is built (experimental curve), which allows to monitor state of the grinding wheel, focusing on it in real time. The surface roughness control system consists of a radiation source, a workpiece (rough surface), a linear polarizer, an optical image capturing instrument and a data processing device. The optimal angles of incidence and reflection is 45° that was established empirically. Angles of 0° and 90° were also used in the formula to determine the degree of polarization.

Next considered non-contact method for analyzing grinding wheel working surface state by using three-dimensional scanning has been proposed in work [4]. The 3D scanning system includes a Nanovea CHR150 chromatic white light sensor with a specially designed circle positioning scheme. It consists of three tables - horizontal, vertical and rotating, and a motor that drives the grinding wheel. Due to this method, white light passes through a lens with a high degree of chromatic aberration, thus refracting and separating into its constituent colours. The light ray length that hits the interest area of surface is reflected and returned to the lens, while the other rays are scattering. In this case, the reflected ray length is equal to the distance from the lens to the grinding wheel working surface. The 3D scanning system is controlled by using a special LabView software package and the analysis and editing of a grinding wheel surface 3D model is performed by using the Nanovea Mountains 3D Analysis software. This system has a homing subsystem that allows scanning the same area multiple times during multiple grinding tests.

Also known optical method for monitoring of the grinding wheel surface state, in which the wheel is repeatedly photographed by an electron microscope [5]. 3D model of the grinding wheel working surface is created from array of photographs. During the experiment, images of the interest area of the grinding wheel surface are recorded by using a Supereyes B008 digital microscope. Photographs are collected and processed by using the special software Helicon Focus Professional; as a result, the 3D model is formed. Then the grinding wheel has been processing a carbide workpiece for 15 minutes, after that it is photographed again and new 3D model with changes is created. Then the two models are compared by using the same computer program.

Similar to the previous method is a method for analysis the 3D parameters of the diamond grinding wheels working surface by using laser scanning [6]. A significant difference of this method is the using of a laser scanning device instead of a digital microscope. Laser scanning allows obtaining a 3D model of the analyzed surface without using an array of photographs and its subsequent processing. The laser processes the grinding wheel scanned profile, transfers it in digital form to a computer and allows simultaneously showing to nine parameters of the working surface. The result of the analysis is a digital volumetric surface relief, indices of the standard deviation of the profile, the height from the top of the grains to the centreline, the average step of irregularities, deviation from the standard, the height of irregularities by ten points, and the value of the relative reference surface area, showing the contact area of the grinding wheel with the surface of the processed workpiece.

Also, a method of colorimetric computer analysis of the working surface parameters and defects of a superhard material is proposed in work [6]. In the course of analysis by a metallographic microscope, images of the grinding wheel surface are obtained in polarized light rays. The authors have developed the corresponding software in the Borland Delphi 5.0, based on the Pascal programming language. It allows determining grain wear by using the obtained photographs as a percentage of the total number of pixels in the image. Varying the tint components of the photographs in the RGB color system allows selecting the required colors in the image, calculating their exact number in pixels to determine the surface quality of the grinding wheel.

A predictive model for grinding surfaces based on the topography of a wheel for modeling grinding is presented in work [7]. The measurement is carried out by a laser triangulation sensor mounted on the machine. The obtained result is imported into the software for modeling of the processing. Measuring of the grinding tool surface by using laser triangulation allows describing the wear behaviour with high accuracy.

The use of focus variation microscopy to assess active surfaces is considered in article [8]. The principle of the method is that the light reflected from the surface returns to the optical system of the microscope and through the ray splitter to the active area of the photometric detector. In which an image containing information about color, brightness, contrast, length and width are forming. The signal processing unit searches only those parts of the image on which the light ray has been focused, then these parts are reconstructed and finalized. To create a 3D model, surface microtopography is required, for which scans are carried out along the Z axis. This method is used for measuring and analyzing the active surfaces of abrasive tools of various types. Focus variation microscopy is a promising measuring method with greater potential for development, especially with its hardware implementation.

Also known method on-machine measurement of the grinding wheels 3D surface topography using a laser displacement sensor [9]. The coarse diamond grinding wheel is attached to the vertical spindle; the laser sensor is attached to the work table. To ensure an accurate measurement, the laser ray should be aligned with the centre axis of the spindle. After the laser ray is reflected through the controller, the point height is determined. The laser sensor moves downward along the spindle axis with low speed, thus scanning the entire circumference of the grinding wheel surface along a spiral path. The results obtained are processed in the Matlab. This method allows to approximately revealing the shape of each grain. The model determines the following three parameters: active grain volume, active grain-containing amount, and active grain. Knowing these parameters, it is possible to estimate the real characteristics of the grinding wheel.

Creation of a triangulation model of the grinding wheels working surface relief consists in creating a set of photographs of a working surface fragment with different height orientation of the depth field [10]. Then happens layer-by-layer photography with a step-by-step shift of the digital microscope optical system. After that the set of photographs is processed in the Helicon Focus Professional application, as a result of which an OBJ-model of a fragment of the grinding wheel working surface is obtained. Using the MechLab application, the OBJ-models are converted into an STL-model, and then into a DBF-image (triangulation model). Topological analysis consists in the determination of the Euler-Poincare characteristic, the kind of surface, the analysis of the adjacency of faces and edges. With the help of the triangulation model integral characteristics (linear, angular, surface and volumetric) can be determined.

III. Results and Discussion

The advantages and disadvantages of the considered methods are summarized in Table 1.

TABLE 1. OPTICAL METHODS FOR MONITORING THE WORKING SURFACE STATE OF THE GRINDING WHEEL

Name of the method	Authors	Advantages	Disadvantages
Texture analysis by using machine vision [1]	N. Arunachalam, B. Ramamoorthy	Obtaining reliable values with minimal errors.	Impossibility of obtaining data in real time, and when rotating manually.
Grinding wheel wear detection based on profile grinding using a CCD camera [2]	F.Fana, L.M.Xub, Z.Zhangc, .J.Chaod, C.Fane, L.Shif	High measurement accuracy comparable to the data obtained during the verification of the experimental results with a profilometer.	Impossibility to analyze in real time; the process is not automated - manual rotation of the wheel to the desired angle is required to provide CCD camera access from the required angle.
System for active control based on measuring the degree of polarization of the reflected radiation [3]	Ziyatdinov R.R., Shabaev A.A., Valiakhmetov R.R	The ability of using method in real time; automation of changing cutting conditions; high reliability.	Indirectly monitoring - reaching a certain degree of polarization indicates a degradation of surface quality and wear.
Analysis of the grinding wheel working surface state by using three-dimensional scanning [4]	A. Darafon	Automated, has a high speed of data collection; suitable for testing wheels made of various materials; varying data sampling intervals, image resolution, spot size.	Impossibility to receive data in real time; removing the grinding wheel from the machine is required.
Evaluation of the working surface relief development of diamond wheels on a metal bond [5]	V. L. Dobroskok, Ya. N. Garashchenko, A. N. Shpilka	The ability to obtain a large amount of statistical data; visual representation of the state of the wheel working surface as 3D models, graphs and histograms.	Impossibility to receive data in real time; large number of images is required to create 3D models.
Analysis of 3D parameters of the diamond wheels surface by using laser scanning [6]	A. I. Grabchenko, V. A. Fedorovich	Reducing the time for obtaining a 3D surface model; increased accuracy; the possibility of analysis various grinding materials; universal using.	Impossibility to receive data in real time and with a rotating grinding wheel.
Colorimetric computer analysis of parameters and defects of the superhard working surface [6]	A. I. Grabchenko V. A. Fedorovich	High accuracy of results; applicability to the analysis of the surface condition of grinding wheels made of various materials.	Impossibility to receive data in real time, because each photo is saved manually and processed separately.
Wheel topography method [7]	R. Hockauf, V. Böß, T. Grove B. Denkena	Measuring of the grinding tool surface using laser triangulation allows high accuracy describing of the wear.	Impossibility to receive data in real time.
Focus variation microscopy to assess active surfaces of the grinding wheel [8]	W. Kapłonek, K. Nadolny, G. M. Królczyk	High measurement efficiency, resolution, reproducibility, speed; simple control; software with a number of useful features.	Restrictions at large angles of inclination; measurement errors or their absence (appearance of unmeasured points).
Topography of the wheel by using a laser displacement sensor [9]	Y. Pan, Q. Zhao, B.Guo	The possibility of using the method to analysis a rotating wheel while machine processing; applicability to universal surface grinding machines.	Possibility of inaccuracy during measuring the grain shape of the grinding wheel.
Triangulation model of the wheel working surface relief [10]	V. L. Dobroskok, A. N. Shpilka, V. B. Kotlyarov	The ability to obtain adequate 3D models by analyzing the geometric characteristics of the shadows.	The measurement results depend on the resolution of the matrix and the optical system, and the software features.

IV. Conclusions

Each of the considered methods has its own field of application, depending on the resolution, measurement accuracy, degree of automation, and the possibility of obtaining data in real time.

Based on the analysis of existing methods, it can be concluded that the most promising direction of optical control of the grinding wheels surface state is the use of laser sensors for creating 3D models of the working surfaces by using the triangulation method.

The authors are conducting research on the use of high-resolution webcams in three main direction:

1) analysis of the colour scale of microphotographs of the grinding wheel surfaces and the workpiece and their statistical processing (the goal is to determine the moments of occurrence of burns and the dynamics of salting);

2) determination of the amount and size of sludge particles on the grinding wheel surface based on pattern recognition (the goal is to determine the optimal dressing time);

3) analysis of the correlation between the degree of salting (according to microphotographs) and the amount of radial wear during grinding of various materials (according to the indications of pneumatic-electric-contact transducers [11]).

REFERENCES

[1] Texture analysis for grinding wheel wear assessment using machine vision, N Arunachalam and B Ramamoorthy Department of Mechanical Engineering, Indian Institute of Technology Madras, Tamilnadu, India; November 2006.

[2] In-situ fast measurement of grinding wheel wear and compensation of wheel profile error F.Fana *, L.M.Xub, Z.Zhangc, X.J.Chaod, W.C.Fane and L.Shif School of Mechanical Engineering, Shanghai Jiao Tong University, Shanghai 200240, China country.

[3] In-process monitoring system to control surface roughness based on measurement of polarization degree of reflected radiation. Ziyatdinov R.R., Shabaev A.A., Valiakhmetov R.R. Basic research. – No. 12–2. – 2017, pp. 287–291.

[4] Measuring and Modeling of Grinding Wheel Topography by Abdalslam Darafon, Dalhousie University Halifax, Nova Scotia April 2013. chapter 6. characterization of grinding wheel surface topology using a white chromatic sensor, pp.110–141.

[5] Evaluation of the development of the relief of the working surface of diamond circles on a metal bundle, V. L. Dobroskok, Ya. N. Garashchenko, A. N. Shpilka. Scientific and technical creativity: problems and prospects: collection of articles of the 10th All-Russian Conference-seminar, ed. – Samara : SamSTU, 2015, pp. 22–29.

[6] 3D processes of diamond-abrasive processing. Monograph. Grabchenko A. I., Fedorovich V. A. - Kharkiv: NTU "KHPI", 2008, pp. 59–64, pp. 85–87.

[7] Prediction of Ground Surfaces by Using the Actual Tool Topography, Rolf Hockauf, Volker Böß, Thilo Grove and Berend Denkena, Institute of production engineering and machine tools, Leibniz Universität Hannover, 30823 Garbsen, Germany; May 2019.

[8] The Use of Focus-Variation Microscopy for the Assessment of Active Surfaces of a New Generation of Coated Abrasive Tools Wojciech Kapłonek, Krzysztof Nadolny, Grzegorz M. Królczyk; Measurement science review, 16, (2016), no. 2, pp.42-53

[9] On-machine Measurement of the Grinding Wheels' 3D Surface Topography Using a Laser Displacement Sensor. Yongcheng Pan, Qingliang Zhao, Bing Guo School of Mechatronics Engineering, Harbin Institute of Technology, Harbin, 150001, China; August 2014.

[10] Obtaining a triangulation model of the relief of the working surface of grinding wheels / V. L. Dobroskok, A. N. Shpilka, V. B. Kotlyarov // Cutting and tool in technological systems = Cutting & tool in technological system: international scientific and technical collection-Kharkiv : NTU "KHPI", 2014. – Issue 84. pp. 85–92.

[11] Grinding wheel monitoring system // Nikiforov, I., Maltsev, P., Kulakova, M. Vide. Tehnologija. Resursi - Environment, Technology, Resources, 2019, 3, pp. 193–196.

Environment. Technology. Resources. Rezekne, Latvia
Proceedings of the 13th International Scientific and Practical Conference. Volume 3, 256-260

Investigation of the Influence of the Modifiers P, Sr, Ti and Combinations of them on the Structure and Mechanical Properties of AlSi25 Alloy

Ivan Panov
Technical University - Sofia, Plovdiv Branch
Plovdiv, Bulgaria
specialista57@abv.bg

Boyan Dochev
Technical University - Sofia, Plovdiv Branch
Plovdiv, Bulgaria
boyan.dochev@gmail.com

Desislava Dimova
Technical University - Sofia, Plovdiv Branch
Plovdiv, Bulgaria
desislava608738@gmail.com

***Abstract* - The most commonly used elements to modify primary silicon crystals in the structure of hypereutectic aluminum-silicon alloys are phosphorus and sulfur. Phosphorus has been shown to have the highest coefficient of modification with respect to the primary silicon and is therefore a preferred modifier. There are also data on the positive effect of the modifiers Sb, Sr, Ti, and B on the silicon crystals in the structure of this type of alloys. The influence of the modifiers phosphorus, strontium, titanium and combinations of them on the size and shape of both the primary silicon crystals and the silicon crystals in the composition of the eutectic of the AlSi25 alloy has been studied in this work. Mechanical tests have been performed to determine both the strength and the plastic parameters of the investigated alloy (in unmodified and modified state). The classic for this type of alloys modifier - phosphorus - has been introduced into the melt by the ligature CuP10. Strontium has been introduced by the ligature AlSr10, and titanium - by the ligature AlTi5B1, the two ligatures in the form of rods. The investigated alloy has also been modified by combinations of the used modifiers: phosphorus and strontium, phosphorus and titanium. The influence of the used modifiers on the structure and mechanical properties of AlSi25 alloy has been discussed.**

Keywords* - *hypereutectic aluminum-silicon alloy, modification, structure, mechanical properties

I. Introduction

Modification is a process of metallurgical processing of the melt, in which by introducing small amounts of special additives - modifiers [1], the structure of the aluminum-silicon alloys changes unnaturally.

According to the generally accepted classification of P.A. Rehbinder [2], the modifiers are divided into two groups. Type I modifiers are surfactants, adsorbed on the crystalline germs and reducing the growth rate of the solid phase. Type II modifiers are usually refractory substances with a crystal lattice, identical in appearance and with parameters close to those of the crystallizing alloy. For higher efficiency it is desirable that the particles have a maximum size of less than 5 μm. [3]. Distributed in the melt in a finely dispersed to colloidal-dispersed state, they become independent centers of crystallization or form such centers as a result of the interaction with the melt.

The modification of aluminum-silicon alloys is a two-stage process in which two main types of treatment are required – refinement of the grains of the α-solid solution using Al-Ti-B agents and modifying the eutectic (αAl + Si) by Na (classic example of a type I modifier) or sodium salts (NaF, NaCl, Na3AlF6), Sr or Sb. The modification of the eutectic silicon in the structure of the hypoeutectic aluminum-silicon alloys is performed with Na (0.005-0.01 wt%), Sr (0.01-0.04 wt%) or Sb (up to 0.2 wt%). In unmodified alloys, the eutectic silicon is separated in the form of coarse needles or plates, which, under certain conditions, serve as stress concentrators. In modified alloys, the silicon crystallizes in the form of small particles with a spherical or thread-like (filamentous) shape. The disadvantages of the modification with Na [4], [5] are that the tendency of gas saturation of the alloys increases, the thinness decreases, the modifier burns quickly, which leads to the need to introduce it every 30-40 minutes in the form of chlorine- or fluorine-containing salts, which is not environmentally friendly. Strontium (Sr) and antimony (Sb) have a long-lasting modifying effect (up to 4 hours). However, contamination of the melt with traces of chlorine and sodium can eliminate their action. The methods used in modern casting practice for refining the α-grains and

Online ISSN 2256-070X
https://doi.org/10.17770/etr2021vol3.6554

modifying the eutectic of Al-Si alloys are considered the literature [6], [7], [8], [9], [10], [11], [12], [13]. Most often, the melt is treated with ligatures in the form of rods with a diameter of 10-15 mm, obtained by pressing or rolling cast workpieces of aluminum ligatures. During the deformation treatment, the non-metallic elements, present in the ligatures, get crushed, their quantity increases and the modifying effect intensifies [6]. To modify the eutectic, Al-Sr ligatures are added at a dosage of 0.04 wt. % Sr max, while for refining the α-grains - double Al-Ti ligatures with a dosage of 0.2% Ti max and triple Al-Ti-B with a dosage of 0.006% B max are introduced. Triple Al-Ti-C ligatures are also used, as their advantage over the Al-Ti-B ligatures consist in the relative simplicity of preparation and the comparable effect. Compositions with different ratios of Ti, B and C [8], [12], [13] are experimented to optimize the treatment with Al-Ti-B and Al-Ti-C ligatures.

The modification of the primary Si coarse crystals in the hypereutectic silumins is performed with phosphorus or sulfur, and the formed AlP or AlS, respectively, serve as crystallization germs [45], [51]. It is known that the mechanical properties of the piston aluminum-silicon alloys depend both on the size, quantity and distribution of the eutectic silicon, and on the quantity, size and shape of the primary silicon crystals [14].

II. Materials and methods

The object of this study was a two-component hypereutectic aluminum-silicon alloy AlSi25 with a chemical composition shown in Table 1.

TABLE 1 CHEMICAL COMPOSITION OF ALSI25 ALLOY

Si	Cu	Mn	Mg	Cr	Fe	Al
25,7	0,084	0,01	0,006	0,0012	0,17	rest

Phosphorus (P) in the amount of 0.04 wt%, strontium (Sr) - 0.05 wt% and titanium (Ti) - 0.2 wt% were used to modify the studied alloy. A combined modification treatment was performed both with the combination of phosphorus and strontium, and with phosphorus and titanium. Phosphorus is a classic modifier for refining the primary silicon crystals in the structure of hypereutectic aluminum-silicon alloys. Ti is most often used to modify the α-grains in the structure of hypoeutectic aluminum-silicon alloys. Sr is used to modify the eutectic silicon in the structure of hypoeutectic and eutectic aluminum-silicon alloys. There are data on the positive effect of both titanium (Ti) and strontium (Sr) at certain concentrations on the primary silicon crystals in the structure of hypereutectic aluminum-silicon alloys [4].

All experiments were performed under the same conditions. Test samples were cast from all studied compositions, from which sections were prepared for microstructural analysis and standard test specimens were made for conducting mechanical tests.

III. Results and discussion

The main amount of primary silicon crystals in the structure of the unmodified AlSi25 alloy are irregular in shape and large in size - 190μm. The eutectic silicon crystals in the alloy structure are in the form of plates with a length of 10 to 40μm (Fig. 1).

After modification of the alloy with phosphorus in the amount of 0.04 wt%, refinement of the primary silicon crystals in the structure of the alloy is observed, they are regular in shape, evenly distributed in the structure of the studied alloy and measure in the range of 25-55μm. Phosphorus also modifies the eutectic silicon crystals and they are in the form of plates with a maximum length of 7μm (Fig. 2). The microstructural analysis proves the claim that phosphorus has a complex modifying effect on the structure of hypereutectic aluminum-silicon alloys, i.e. it works as a modifier of both types - I and II - at the same time.

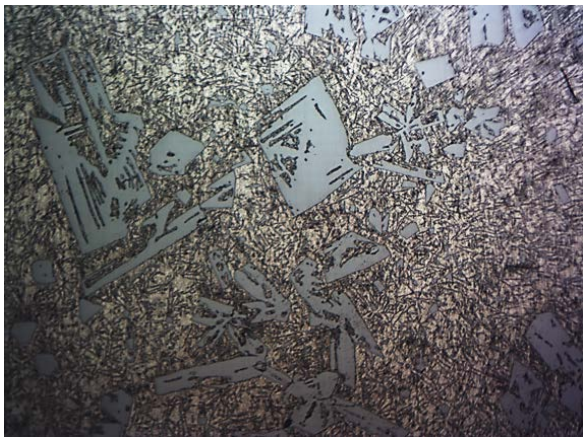

Fig. 1. Structure of unmodified alloy AlSi25 x200

Fig. 2. Structure of modified by 0.04% P alloy AlSi25 x200

The results of the microstructural analysis show that the primary silicon crystals in the structure of the AlSi25 alloy, modified by titanium in an amount of 0.2 wt%, have an irregular shape and size of 150µm. The silicon crystals in the eutectic composition have a rounded shape and dimensions of the order of 4-5 µm (Fig. 3). The size of the primary silicon crystals in the structure of the alloy, modified with the help of Ti - 0.2 wt% is refined by 21%, compared to the unmodified alloy. This confirms the opinion that this modifier affects the size of the primary silicon crystals, but does not change their shape and does not favor their uniform distribution in the structure of the alloy. Due to the used amount of the modifier titanium (Ti), the eutectic silicon crystals become highly refined and have a rounded shape.

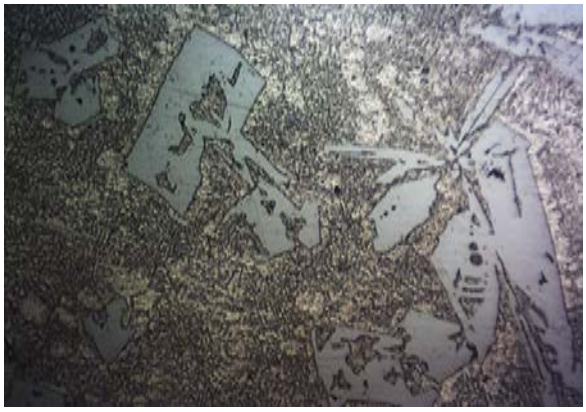

Fig. 3. Structure of AlSi25 alloy, modified by 0.2% Ti x200

The primary silicon crystals in the structure of the studied AlSi25 alloy, when modified by strontium (Sr) in the amount of 0.05 wt%, have an irregular (star-like) shape and measure 110µm. The silicon crystals in the composition of the eutectic are also highly refined and have dimension of the order of 4-5µm (Fig. 4). The primary silicon crystals in the structure of the alloy, modified by Sr - 0.05 wt%, are refined by about 42%, in comparison with the unmodified alloy. This confirms the opinion that this modifier affects the size of the primary silicon crystals, but does not change their shape, nor does it affect their distribution in the structure of the alloy. Due to the used amount of the modifier strontium (Sr), the eutectic silicon crystals become highly refined and get a rounded shape.

After carrying out a combined modifying treatment of the studied AlSi25 alloy with phosphorus 0.04 wt% and titanium 0.2 wt%, the primary silicon crystals take the form of straight-walled polygons with dimensions of the order of 10-30µm, evenly distributed in the structure of the alloy. The silicon crystals in the eutectic composition of the alloy, modified this way, are refined, with a filamentous shape and dimensions of the order of 4-5 µm (Fig. 5).

The results of the microstructural analysis of the studied alloy AlSi25, when modified by the combination, consisting of phosphorus 0.04 wt% and strontium 0.05 wt%, show that the primary silicon crystals are in the form of straight-walled polygons with dimensions of the order of 20-35µm and are evenly distributed in the structure of the alloy. The silicon crystals in the eutectic composition of the modified alloy are refined and have the form of plates with dimensions in the range of 4-5 µm (Fig. 6).

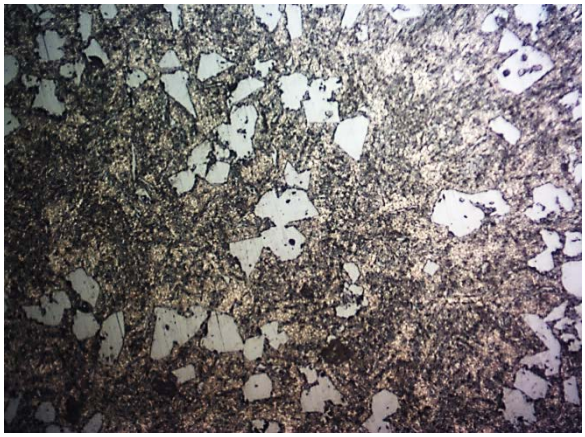

Fig. 4. Structure of AlSi25 alloy,modified by 0.05% Sr x200

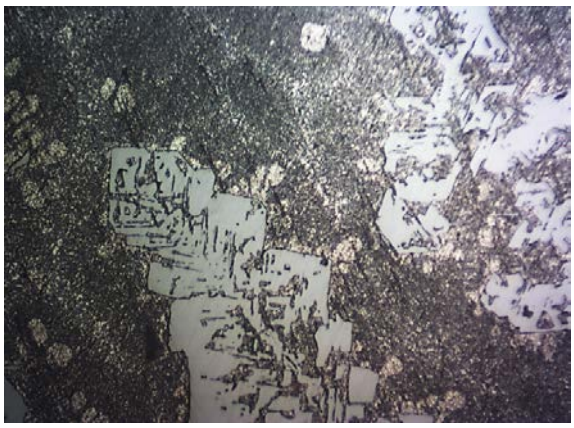

Fig. 5. Structure of the AlSi25 alloy, modified by 0.04% P and 0.2% Ti x200

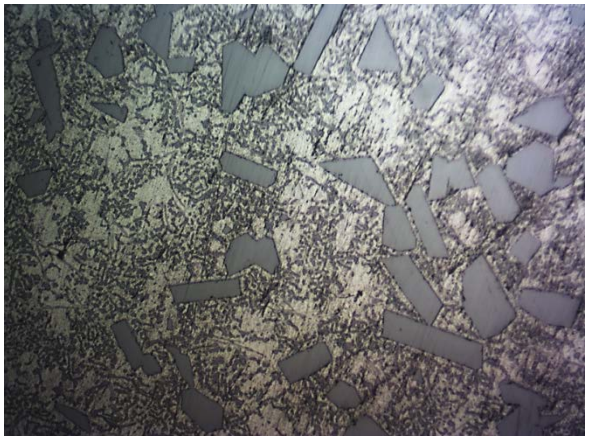

Fig. 6. Structure of the AlSi25 alloy, modified by 0.04% P and 0.05% Sr x200

The results of the performed microstructural analyses of the hypereutectic aluminum-silicon alloy AlSi25 - unmodified, modified by phosphorus, titanium, or strontium and by the combinations phosphorus plus titanium and phosphorus plus strontium are shown in Table 2.

Table 3 shows the results of the mechanical tests of all studied compositions.

TABLE 2 RESULTS OF MICROSTRUCTURAL ANALYSIS

Alloy	Modifier	Si, μm	$Si_{e,}$ μm
AlSi25	Unmodified	190	10-40
AlSi25	0,04% P	25-55	7
AlSi25	0,2% Ti	150	4-5
AlSi25	0,05% Sr	110	4-5
AlSi25	0,04% P+0,2% Ti	10-30	4-5
AlSi25	0,04% P+0,05% Sr	20-35	4-5

TABLE 3 RESULTS OF MECHANICAL TESTS

Alloy	Modifier	R_m, MPa	A_5, %	HB 2,5/62,5/30
ALSI25	Unmodified	58,8	1,8	61,1
ALSI25	0,04% P	78	-	64,3
ALSI25	0,2% Ti	55,3	0,8	65,4
ALSI25	0,05% Sr	41,1	-	62,8
ALSI25	0,04%P 0,2% Ti	84	-	73
ALSI25	0,04%P 0,05% Sr	73,8	-	70,4

IV. CONCLUSIONS

The classical modifier phosphorus (P) in the used concentration of 0.04 wt% has a complex modifying effect on the structure of the studied AlSi25 alloy. The primary silicon crystals get refined (25-55μm), have a more compact shape and are evenly distributed in the structure of the alloy. The eutectic silicon is in the form of plates and threads up to 7 μm long. Both the tensile strength and the hardness of the investigated alloy increase, compared to the unmodified one.

When modifying the alloy by titanium (Ti), the size of the primary silicon crystals reduces by about 21%, but their shape is not affected by this modifier in the used concentration of 0.2 wt%. In contrast, the silicon crystals in the eutectic are highly refined and rounded. This leads to a decrease in the level of hardness and an increase in ductility (A5-0.8%) compared to the phosphorus-modified alloy, while the strength decreases by about 30%.

The strontium (Sr)-modified alloy has the lowest values of hardness and mechanical strength of all studied modified compositions. The eutectic silicon in it is highly refined - 4-5μm, while the shape and the distribution of the primary silicon crystals are not affected by this modifier in the used concentration of Sr - 0.05%.

The alloy, modified by the combination of phosphorus and titanium has the best strength parameters. Not only the primary silicon crystals become refined here (10-30μm), but also the silicon crystals in the composition of the eutectic - 4-5μm.

The alloy, modified by the combination of phosphorus and strontium, has lower but comparable strength parameters with the alloy, modified by phosphorus and titanium combined. It is noteworthy that the complex modification (P + Ti; P + Sr) leads to greater refinement of the primary silicon crystals compared to the modification by phosphorus alone. In addition, the eutectic silicon crystals in the case of complex modification are significantly smaller and compact in shape.

The structures, obtained after complex modification, suggest an increase in abrasion resistance. This assumption, however, needs to be proven by additional tribological tests.

Acknowledgments: The authors would like to thank the Research and Development Sector at the Technical University of Sofia for the financial support

REFERENCES

[1] R.Slavov R., M. Manolov, V. Atanasova. Handbook for casting non-ferrous metals and alloys. Sofia, Tehnika, 1976 (In Bulgarian).

[2] P.A Rehbinder, Surface phenomena in dispersed systems, In the book Physico-chemical mechanics. M., Science, 1979, 143-154 .

[3] Modification of aluminum alloys using ligatures with dispersed intermetallics. - Non-ferrous metals, 1989, № 5, 93-96 (In Russian).

[4] G.B.Stroganov, V.A Rotenberg, G.B Gershman, Aluminum alloys with silicon. M., Metallurgy, 1977 (In Russian).

[5] R.Simon, R. Smetek MTS 1500 – an automated melt treatment system for aluminium alloys utilizing granular fluxes. WFO Technical Forum, June 2007 –GIFA, Düsseldorf, 106-108.

[6] V.I.Napalkov., B.I. Bondarev, V.I .Tararishkin, M.V. Chukhrov. Ligatures for the production of aluminum and magnesium alloys, M., Metallurgy, 1983, 160 pp. V.G Kokulin, M.P Borgoyakov, E. M. Hilderbrant (In Russian).

[7] Victor Vladimirovich Novokreshchenov, Thesis on the topic "Technology of manufacture of castings of especially difficult configuration from silumin for engine building", Ministry of Education and Science of the Russian Federation, the South Ural state university, Chelyabinsk, 2014 (In Russian).

[8] F.J.Feikus, Leichtmetall-Sand-und-Kokillenguss (Teil 3: Schmelzen, Gie□en und Erstarren). –Giesserei, 94, 6/2007, 230-235.

[9] G.P. Jones and J. Pearson., Factors affecting the grain-refinement of aluminum using titanium and boron additives, Metallurgical Transactions B, Vol. 7, Nr.2, (1976), p. 223-234.

[10] S. A. Kori, B. S. Murty and M. Chakraborty, Development of an efficient grainrefiner for Al–7Si alloy and its modification with strontium, Materials Science and Engineering A, Vol. 283, Issues 1-2, 15 May 2000, Pages 94-104.

[11] Rao Arjuna, B.S. Murty and M. Chakraborty, Role of zirconium and impurities in grain refinement of aluminium with AI-Ti-B, Mater. Sci. Technol., Vol.13, №9, (1997), p. 769-777.

[12] W.Schneider (Bonn), P.Hoefs und W.Reif (Berlin) und M.Kearns (London). Entwicklung einer AlTiC-Vortlegierung für die Kornfeinung von Aluminum. ALUMINIUM, 74, 1996, 7/, 536-538.

[13] W. Schneider, D. Granger. Aluminium Grain refinement in DC casting of aluminium, Part II. – Aluminium, vol. 83, 6/2007,74-75.

[14] Choi Hongseok, Hiromi Konishi, Xiaochun Li. Al2O3 nanoparticles induced simultaneous refinement and modification of primary and eutectic Si particles in hypereutectic Al–20Si alloy. Materials Science and Engineering A 541 (2012) 159– 165 (Department of Mechanical Engineering, University of Wisconsin-Madison, Madison, WI 53706, USA)

Environment. Technology. Resources. Rezekne, Latvia
Proceedings of the 13th International Scientific and Practical Conference. Volume 3, 261-265

Investigation of the Influence of Different Modifiers on the Eutectic Si in the Composition of AlSi18 Alloy

Ivan Panov
Technical University - Sofia, Plovdiv Branch
Plovdiv, Bulgaria
specialista57@abv.bg

Boyan Dochev
Technical University - Sofia, Plovdiv Branch
Plovdiv, Bulgaria
boyan.dochev@gmail.com

Valentin Manolov
Institute of Metal Science, Equipment, and Technologies "Acad. A. Balevski" with Center for Hydro- and Aerodynamics at the Bulgarian Academy of Sciences
Sofia, Bulgaria
v.manolov@ims.bas.bg

Angel Velikov
Institute of Metal Science, Equipment, and Technologies "Acad. A. Balevski" with Center for Hydro- and Aerodynamics at the Bulgarian Academy of Sciences
Sofia, Bulgaria
anmabg@abv.bg

Vanya Dyakova
Institute of Metal Science, Equipment, and Technologies "Acad. A. Balevski" with Center for Hydro- and Aerodynamics at the Bulgarian Academy of Sciences
Sofia, Bulgaria
v_diakova@mail.bg

***Abstract* - The structure of hypereutectic aluminum-silicon alloys consists of primary silicon crystals arranged in a eutectic matrix. In the present work the influence of different types of modifiers on the size and shape of the silicon crystals in the composition of the eutectic of the AlSi18 alloy has been studied. The classic for this type of alloys modifier (phosphorus), as well as the nanomodifiers SiC and nanodiamonds (ND) have been used. The results of the microstructural analysis show that the three modifiers used affect differently the shape and size of the eutectic silicon of the investigated alloy.**

Keywords* - *hypereutectic aluminum-silicon alloy, modification, nanomodifiers, eutectic silicon

I. INTRODUCTION

Hypereutectic aluminum-silicon alloys are characterized by good mechanical properties, wear resistance, corrosion resistance and low coefficient of linear expansion. These are the main reasons why such alloys are the preferred material for making pistons for internal combustion engines. The primary silicon crystals in unmodified hypereutectic aluminum-silicon alloys are in the range of 80-100 μm and have a rough irregular shape. Therefore, they have a strong notching effect on the structure of the alloys and significantly impair their mechanical and operational properties. In order to increase the mechanical properties of the alloys, it is necessary to grind the primary silicon crystals, to ensure their uniform distribution in the structure of the alloy and to give them a compact shape, thereby reducing their notching action. This is achieved by a modifying mode of treating the alloys. Apart from the modification of the primary silicon crystals, in order to increase the properties of this type of alloys, it is necessary to strengthen the eutectic matrix in which they are located, i.e. the silicon crystals in the eutectic composition must also be modified. The published studies, based on a two-stage type of modifying treatment of hypereutectic aluminum-silicon alloys, using phosphorus and sodium (sulfur and sodium), show unsatisfactory results due to the formation of NaP or NaS and loss of the modifying effect of the used modifiers, which necessitates other solutions to be searched. [1].

To modify the α-phase in the composition of the eutectic in the structure of hypoeutectic and eutectic

Online ISSN 2256-070X
https://doi.org/10.17770/etr2021vol3.6555

aluminum-silicon alloys, new types of modifiers - nanomodifiers - have recently been used. These modifiers work in the alloys as surfactants (modifiers of the first order); they block the growth of the α-phase and, accordingly, of the silicon crystals in the eutectic, so the silicon crystals get refined for this reason as well [2], [3], [4]. , [5], [6], [7], [8], [9], [10]. This is a prerequisite for the use of such modifiers to treat the eutectic, on the one hand, and to treat hypereutectic aluminum-silicon alloys in order to modify the eutectic silicon crystals in them,

II. Materials and methods

The object of study in this work was a two-component hypereutectic aluminum-silicon alloy AlSi18. The content of alloying elements in the composition of the alloy was minimized, and the impurity elements were insignificant. This was done in order to obtain results that can only be explained by the action of the used different types of modifiers on the structure of the studied alloy. The chemical composition of the alloy is shown in Table 1.

The following modifiers were used to modify the investigated alloy: phosphorus (0.04wt%), nanomodifier SiC (β-modification) in the amount of 0.1wt%, and nanodiamonds (ND) nanomodifier in the amount of 0.1wt%. Phosphorus was introduced into the melt of the investigated alloy by the ligature CuP10, SiC - in the form of an aluminum composite rod, and the ND nanomodifier was packed in the form of an aluminum cartridge. For better wetting and absorption by the melt, the nanoscale modifiers are coated with various metal protectors. The SiC nanomodifier, used in this case, was Cu-coated and the ND nanomodifier - plated with Ni.

Table 1 Chemical composition of AlSi18 alloy

Si	Cu	Mn	Mg	Cr	Fe	Al
17,6	0,03	0,05	0,001	0,001	0,12	rest

Experiments were conducted with unmodified AlSi18 alloy, as well as with the same alloy, modified by P, SiC and ND. To ensure comparability of the obtained results, all experiments were performed under the same conditions. The alloys were refined with a coating refining flux in the amount of 0.5 wt% of the amount of the alloy, the melts were degassed by blowing with argon for 3 min at a temperature of 760° C, and the modifying treatment was carried out at a temperature of 810° C. The casting temperature of the investigated compositions was 760° C, and the temperature of the used metal equipment - 210° C. Sections for microstructural analysis were prepared from the cast test samples.

III. Results and discussion

The results of the microstructural analysis show that the silicon crystals in the eutectic composition of the unmodified AlSi18 alloy are up to 250-260 μm long and are in the form of well-shaped elongated plates, looking like needles in the plane of the microscopic observation (Fig. 1). There are also small silicon crystals with a size of several microns, which form groups or are located next to each other and at small microscopic magnifications resemble a broken needle (Fig. 2). In another area of the microscopic field, fine silicon crystals can be seen, resembling a "fishbone" (Fig. 3). Particles with a shape, characteristic of non-metals, are observed in the eutectic (Fig 4).

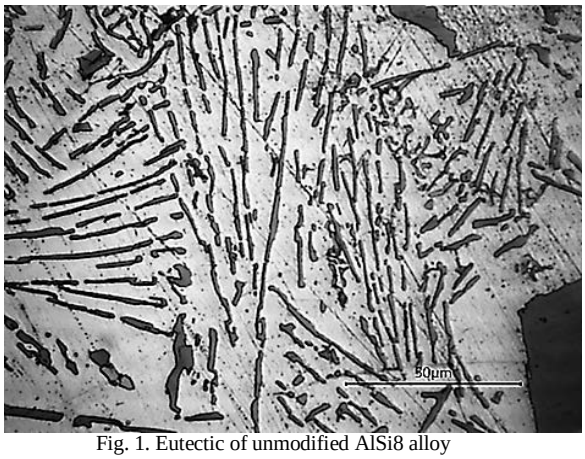

Fig. 1. Eutectic of unmodified AlSi8 alloy

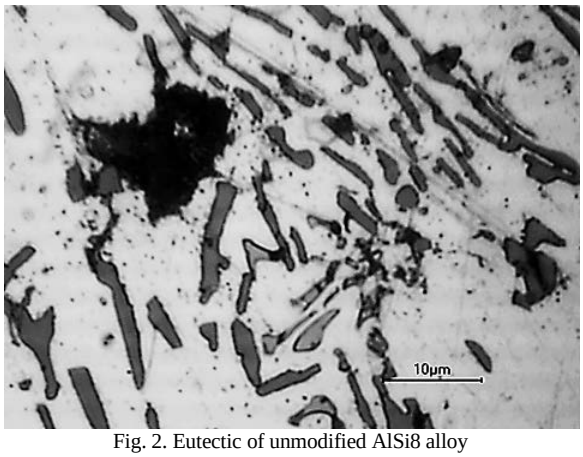

Fig. 2. Eutectic of unmodified AlSi8 alloy

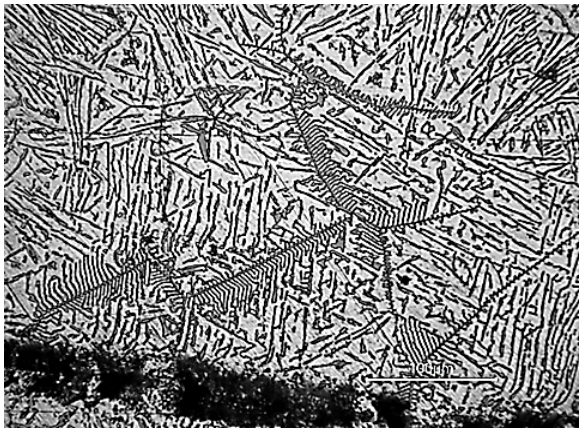

Fig. 3. Eutectic of unmodified AlSi8 alloy

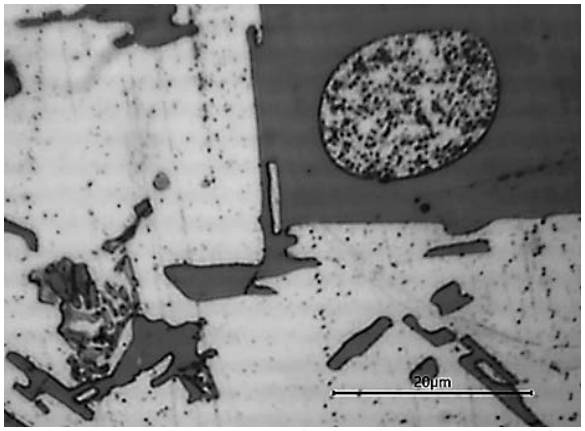

Fig. 4. Eutectic of unmodified AlSi8 alloy

Fig. 5. Eutectic of phosphorus-modified AlSi18 alloy

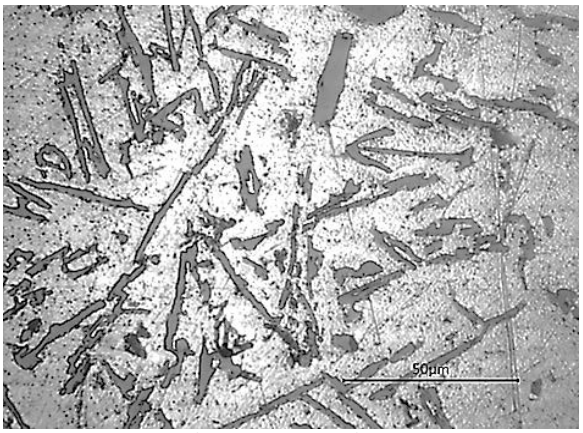

Fig. 6. Eutectic of phosphorus-modified AlSi18 alloy

The silicon crystals in the eutectic composition of the phosphorus-modified hypereutectic aluminum-silicon alloy AlSi18 are refined. They are in the form of plates (needles) and reach a length of 115-135 µm (Fig. 5). There are also small rounded silicon crystals, which are like clusters and resemble broken needles (Fig. 6). Given that modifiers most often have a double action, we assume that (P) could also be adsorbed at the grain boundaries of the alpha phase (solid solution of silicon in aluminum), not allowing the grains of the alpha phase to increase this way, which means that phosphorus has an impact on the structure as a modifier of the first order as well. Due to the prevention of the alpha-phase grains from growth, the distances between the branches of the dendrites remain small, and this is exactly where the discrete silicon crystals are distributed during the formation of the eutectic. In our opinion, this is the reason why phosphorus (P) influences the size of the silicon crystals in the composition of the eutectic of the studied alloy as well.

After the microstructural analysis of the hypereutectic aluminum-silicon alloy AlSi18, modified by the nanomodifier SiC, the results show that the silicon crystals in the composition of the eutectic are very small, and whole "needles" rarely occur. Most often there are a series of small silicon crystals arranged next to each other, not longer than 4-5 µm (Fig. 7 and Fig. 8). It can be assumed that the nanomodifier (SiC) is adsorbed at the grain boundaries of the alpha phase, thus inhibiting the growth of the alpha crystals, and, in result of concentration fluctuations, many silicon crystals are formed on the branches of the dendrites, also not having the chance to significantly increase their size. This is most likely the reason why the silicon crystals in the eutectic are so highly refined.

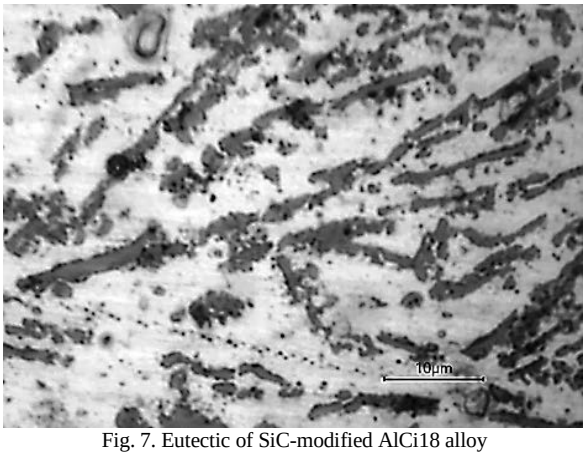

Fig. 7. Eutectic of SiC-modified AlCi18 alloy

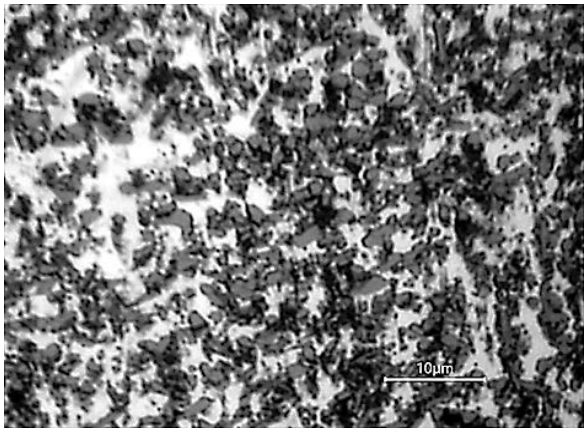

Fig. 8. Eutectic of SiC-modified AlCi18 alloy

In the hypereutectic aluminum-silicon alloy AlSi18, modified by a ND nanomodifier, the silicon crystals in the eutectic composition are significantly refined. The amount of silicon in the form of plates (needles) is insignificant, their average maximum length is about 15-16 µm. However, the share of small equiaxed silicon particles increases (Fig. 9 and Fig. 10). Given the claim that some of the modifiers, used to modify aluminum-silicon alloys, have a double action, we can assume that the nanodiamond (ND) nanomodifier is a complex modifier, i.e., it has a modifying effect both on the crystals of primary silicon and on the alpha phase in the composition of the eutectic, respectively on the silicon crystals in the composition of the eutectic as well. This is a prerequisite for the structure-formation process of the studied hypereutectic aluminum-silicon alloy AlSi18, modified by a nanodiamonds (ND) nanomodifier, to proceed in accordance with both the adsorption theory and the theory of overcooling at the same time.

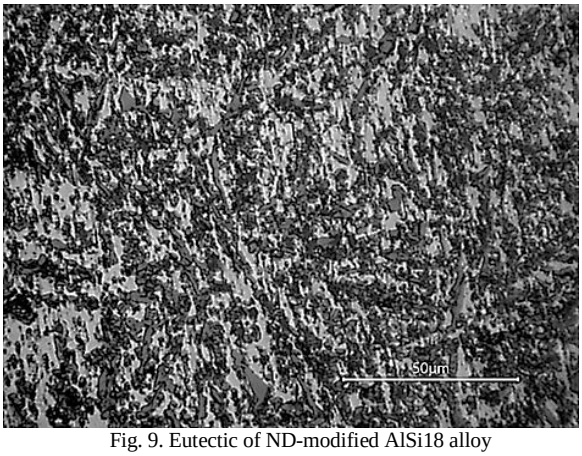

Fig. 9. Eutectic of ND-modified AlSi18 alloy

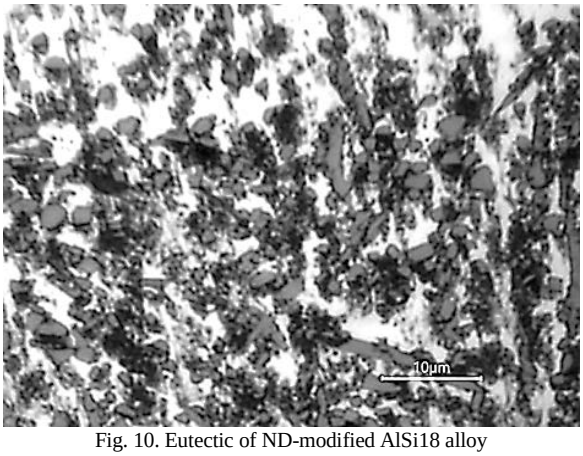

Fig. 10. Eutectic of ND-modified AlSi18 alloy

Table 2 shows the results from the performed microstructural analysis of the studied AlSi18 alloy in unmodified and modified state.

TABLE 2 RESULTS OF MICROSTRUCTURAL ANALYSIS

Modifier	-	P	SiC	ND
Size of Si in the composition of the eutectic	250-260 µm	115-135 µm	4-5 µm	15-16 µm

IV. CONCLUSIONS

It has been proven that the classic modifier (P) affects the shape and size of the primary silicon crystals in the structure of the investigated hypereutectic alloy. Moreover, the conducted studies show that it also has a modifying effect on the size of the silicon crystals in the composition of the eutectic of the AlSi18 alloy.

The modifier SiC has the strongest modifying effect on the silicon crystals in the composition of the eutectic. It affects both their size and their shape, having a pronounced compacting effect on the eutectic silicon in the structure of the studied alloy.

The nanodiamond ND modifier also considerably affects the size of the eutectic silicon crystals. In addition

to the significant reduction in their size, we find again a tendency toward globulisation and compaction of the eutectic silicon crystals, similar to the case when the AlSi18 alloy is modified by SiC. We can assume that the reason behind this similar action of the SiC modifier and the nanodiamonds is hidden in their size (20-50 nm).

Acknowledgments: The authors would like to thank the Research and Development Sector at the Technical University of Sofia for the financial support

REFERENCES

[1] G.B Stroganov, B.A.Rotenberg, G.B.Gershman, Alloys of aluminum with silicon, M., Metallurgy, 1977 (In Russian);

[2] V. Manolov, A.Cherepanov, R. Lazarova and S. Konstantinova, March, 22-25, 2011, Properties of the aluminium alloy AlSi7Mg, modified by refractory nanopowders, Interaction of highly concentrated energy flows with materials in promising technologies and medicine, IVth all-Russan conference, Novosibirsk, 186-190, ISBN 9785-93089-034-1

[3] R. Lazarova, N. Bojanova, R. Dimitrova, I. Panov and V. Manolov, Influence of Nanoparticles Introducing in the Melt of Aluminum Alloys on Castings Microstructure and Properties, https://link.springer.com/article/10.1007/s40962-016-0033-7

[4] V. Manolov, A. Cherepanov, R. Lazarova, and S. Konstantinova, Influence of nanopowder inoculars on the structure and the properties of the AlSi7Mg alloy, Foundry, M., № 11, 11-14, ISSN: 0024-449X, IF 0,088

[5] R. Lazarova, V. Gaidarova, V. Manolov, M. Manchev, S. Konstantinova, A. Cherepanov, Investigation of the influence of modifying nanopowders on the characteristics of metal alloys. - Proceedings of the VII International Scientific-Technical Congress "Machines, Technologies, Materials" - MTM'2010, Sofia, Bulgaria, May 2010, 48-53.

[6] V N Gaidarova, R L Lazarova, S V Vaseva, V K Manolov, and S G Konstantinova, June 2010, Microstructure and Mechanical Properties of AlSi7Mg Alloy: Effect of Added Nanodiamond, In: Explosive Production of New Materials: Science, Technology, Business, and Innovations. Edited by A.A. Deribas and Yu.B. Scheck, Moscow, TORUS PRESS, ISBN 978-5-94588-073-3, p. 25 (Proceedings of the X International Symposium EPNM-2010 Bechichi, Montenegro)

[7] S. Iman El-Mahallawi, Ahmed Yehia Shash and Amer Eid Amer, Metals 2015, 5(2), 802-821; Nanoreinforced Cast Al-Si Alloys with Al2O3, TiO2 and ZrO2 Nanoparticles, doi:10.3390/met5020802

[8] Hongseok Choi, Hiromi Konishi, Xiaochun Li. Al2O3 nanoparticles induced simultaneous refinement and modification of primary and eutectic Si particles in hypereutectic Al–20Si alloy. Materials Science and Engineering A 541 (2012) 159– 165 (Department of Mechanical Engineering, University of Wisconsin-Madison, Madison, WI 53706, USA)

[9] El-Mahallawi, H.Abdelkader, L.Yousef, A.Amer, J.Mayer, A.Schwedt Influence of Al2O3 nano-dispersions on microstructure features and mechanical properties of cast and T6 heat-treated AlSi hypoeutectic Alloys. Materials Science&Engineering A 556 (2012) 76–87.

[10] K.. Borodianskiy, A. Kossenko, M. Zinigrad, Improvement of the mechanical properties of Al-Si alloys by TiC nanoparticles, Metallurgical and Materials Transactions A, Nov. 2013, Vol.44, Iss.11, pp 4948-4953.

Environment. Technology. Resources. Rezekne, Latvia
Proceedings of the 13th International Scientific and Practical Conference. Volume 3, 266-269

Gas Dynamics of Working Fluid Inlet into Chamber of Rotary Expansion Machine

Andrey Perminov
Department of Electric Coupling and Automation Systems
Pskov State University
Pskov, Russia
alp-mail@mail.ru

Alexander Ilyin
Department of Electric Coupling and Automation Systems
Pskov State University
Pskov, Russia
al.ilyin@yandex.ru

Sergey Tikhonov
Department of Automobile Transport
Pskov State University
Pskov, Russia
sit42@rambler.ru

Dmitriy Fedorov
Department of Electric Coupling and Automation Systems
Pskov State University
Pskov, Russia
dmitriy-fedorov-2012@mail.ru

Sergey Drozdov
Department of Electric Coupling and Automation Systems
Pskov State University
Pskov, Russia
sergei_drozdov@inbox.ru

***Abstract* - In this article, a mathematical model of working fluid inlet into chamber of rotary expansion machine from source of superheated steam. The main practical problem that can be solved on the basis of this model is to determine dependence of torque on the angular velocity, i.e. in the construction of mechanical characteristics of rotary expansion machine.**

Keywords* - *rotary expansion machine; gas dynamics; mathematical model.

I. INTRODUCTION

Rotary vane and rotary machines have a number of advantages over engines of other designs, for example, connecting rod and piston: lower specific gravity, high specific liter power, can work stably at low speeds, less mechanical losses due to the absence of reciprocating movements, significantly less vibration due to design balance score. When implementing a thermodynamic cycle in a rotary machine with an external heat supply, it is possible to achieve high efficiency values, use various types of fuel, and ensure high environmental friendliness. Work on the development of engines and installations based on machines of rotary blade and rotary type has been carried out by the research team of Pskov State University for more than ten years, and the main research results are published in [2], [3], [8] – [15].

The subject of this article is a rotary expansion machine (patent RU 2619391 [1]). The device and the principle of operation of the rotary expansion machine are described in detail in [4], [5].

II. INITIAL RELATIONS

A diagram of the process of filling the chamber with a fresh gas charge is shown in Fig. 1. It is assumed that in the source from which the charge enters the chamber, it is maintained constant values of pressure p_0 temperature T_0 and isobaric heat capacity c_{p0} [6], [7].

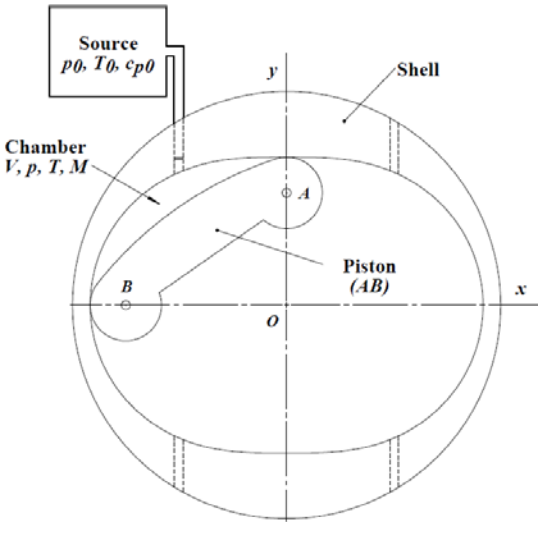

Fig. 1. Chamber inlet scheme.

Online ISSN 2256-070X
https://doi.org/10.17770/etr2021vol3.6514

The gas enters the chamber through inlet port, flow area of which $f(\alpha)$ is a known function of shaft rotation angle α. The dependence of chamber's volume $V(\alpha)$ on the angle, and angle of beginning of opening α_{BO} and angle of end of closing α_{EC} of inlet window are also set.

In this process, three variables are unknown: the pressure p of gas in chamber, its mass M and temperature T.

We will assume that gas flow, which has enthalpy $i_0 = c_{p0}\,T$ and velocity v at entrance to chamber, slows down inside chamber. The enthalpy of stalled flow increases by $v^2/2$ and becomes equal to

$$i_0{}^* = c_{p0}\,T_0 + v^2/2 \tag{1}$$

Assuming that intake process is quasi-stationary, we will use the first law of variable mass thermodynamics to describe it. According to him, enthalpy flow entering chamber along with mass flow goes to change internal energy of gas and perform expansion work:

$$i_0{}^* dM - dQ_W = d(Mu) + p\,dV, \tag{2}$$

where $u = c_V\,T$ is the specific internal energy of gas (c_V is isochoric heat capacity); dQ_W is heat removed as a result of heat exchange of gas with chamber walls.

Equation (3) taking into account (1) is reduced to the form:

$$\left(c_{p0}\,T_0 + v^2/2\right)dM = Mc_V\,dT + c_V T\,dM + p\,dV + dQ_W. \tag{3}$$

Next, we perform following transformations of this equation.

We divide both sides of Eq. (3) by the internal energy Mc_VT of the gas in the chamber and write it in the form

$$\frac{dT}{T} = \left(\frac{c_{p0}\,T_0 + v^2/2}{c_V T}\right)\frac{dM}{M} - \frac{p\,dV}{Mc_VT} - \frac{dQ_W}{Mc_VT}. \tag{4}$$

Considering Mayer's formula for the gas constant

$$R = c_p - c_V, \tag{5}$$

the equation of state is reduced to the form $pV = \left(c_p - c_V\right)MT$, or

$$pV = (k-1)Mc_VT, \tag{6}$$

where k is the adiabatic exponent:

$$k = \frac{c_p}{c_V}. \tag{7}$$

Taking into account (6), the second term on right-hand side of equation (4) takes the form

$$\frac{p\,dV}{Mc_VT} = (k-1)\frac{dV}{V}, \tag{8}$$

and equation (4) is written as

$$\frac{dT}{T} = \left(\frac{c_{p0}\,T_0 + v^2/2}{c_V T} - 1\right)\frac{dM}{M} - (k-1)\frac{dV}{V} - \frac{dQ_W}{Mc_VT}. \tag{9}$$

Next, we will apply following mathematical trick. Let us take natural logarithm of both sides of equation of state $pV = RMT$: $\ln p + \ln V = \ln R + \ln M + \ln T$. Differentiating by angle of rotation of shaft α, we obtain $\frac{1}{p}\frac{dp}{d\alpha} + \frac{1}{V}\frac{dV}{d\alpha} = \frac{1}{M}\frac{dM}{d\alpha} + \frac{1}{T}\frac{dT}{d\alpha}$, whence we find

$$\frac{dT}{T} = \frac{dp}{p} + \frac{dV}{V} - \frac{dM}{M}. \tag{10}$$

Equating the right-hand sides of equations (9) and (10), we obtain

$$\frac{dp}{p} = \frac{c_{p0}\,T_0 + v^2/2}{Mc_VT}dM - \frac{k}{V}dV - \frac{dQ_W}{Mc_VT}. \tag{11}$$

Dividing (11) by differential $d\alpha$, we obtain the differential equation

$$\frac{dp}{d\alpha} = p\left[\frac{c_{p0}\,T_0 + v^2/2}{Mc_VT}\frac{dM}{d\alpha} - \frac{k}{V}\frac{dV}{d\alpha} - \frac{1}{Mc_VT}\frac{dQ_W}{d\alpha}\right]. \tag{12}$$

III. Flow Rate and Mass Change

It is known that the flow at the chamber entrance has a velocity

$$v = \varphi\sqrt{RT_0}, \tag{13}$$

where $R = c_p - c_V$ is gas constant; φ is a factor that, depending on flow regime (subcritical or critical), takes on values

$$\varphi = \sqrt{2\frac{k}{k-1}\left[1 - \left(\frac{p}{p_0}\right)^{\frac{k-1}{k}}\right]}\ for\ p \geq p_{cr};\ \ \varphi = \sqrt{2\frac{k}{k+1}}\ for\ p < p_{cr}. \tag{14}$$

Here $k = c_p/c_V$ is the adiabatic exponent; p_{cr} is critical value of pressure in the chamber

$$p_{cr} = \beta_{cr}p_0,\ \beta_{cr} = \left(\frac{2}{k+1}\right)^{\frac{k}{k-1}}. \tag{15}$$

So, for diatomic gases $k = 1.4$ and $\beta_{cr} = 0.527$; for polyatomic gases and superheated steam $k = 1.3$ and $\beta_{cr} = 0.546$. At $p < p_{cr}$, the coefficient φ for these gases takes on the values $\varphi = 1.08$ and $\varphi = 1.06$, respectively, while outflow velocity has a constant maximum value equal to speed of sound in this medium.

Let the intake port have an area f_0. In the processes of opening and closing the window, the area of its passage for gas section, which we denote by $f(\alpha)$, varies in range $0 \leq f(\alpha) \leq f_0$. Then the second mass flow rate of gas through window is determined by formula

$$\frac{dM}{M} = \mu\rho\upsilon f(\alpha), \tag{16}$$

where $\rho = M/V$ is gas density; μ is the flow coefficient taking into account compression of jet and aerodynamic drag, approximate value of which is

$$\mu \cong 0.37. \tag{17}$$

Taking into account that $dt = d\alpha/\omega$, the differential dependence follows

$$\frac{dM}{d\alpha} = \frac{\mu}{\omega}\frac{M}{V(\alpha)}\upsilon f(\alpha), \tag{18}$$

IV. EXHAUST HEAT

During the time interval dt of the working fluid through the chamber wall heat is removed

$$dQ_W = \beta_T F\,(T - T_W)dt, \tag{19}$$

where β_T is instantaneous value of heat transfer coefficient by forced convection, averaged over current surface of walls with area F; T and T_W are current temperatures of working fluid and walls, respectively.

The shaft rotates with an angular velocity $\omega = d\alpha/dt$. Since $dt = d\alpha/\omega$, the last term on the right-hand side of equation (12) takes the form

$$\frac{1}{Mc_V T}\frac{dQ_W}{d\alpha} = \frac{\beta_T F}{\omega M c_V T}\,(T - T_W). \tag{20}$$

V. INTAKE EQUATIONS

Adding the equation of state $pV = MRT$ to equations (12) and (18), we have a closed system of three equations for determining three unknowns p, M, T as functions of angle α in range $0° \leq \alpha \leq 90°$.

$$\begin{cases} pV = MRT\,, \\ \dfrac{dp}{d\alpha} = p\left[\dfrac{c_{p0}\,T_0 + \upsilon^2/2}{Mc_V T}\dfrac{dM}{d\alpha} - \dfrac{k}{V}\dfrac{dV}{d\alpha} - \dfrac{1}{Mc_V T}\dfrac{dQ_W}{d\alpha}\right] \\ \dfrac{dM}{d\alpha} = \dfrac{\mu}{\omega}\,\dfrac{M}{V(\alpha)}\,\upsilon\, f(\alpha) \end{cases} \tag{21}$$

The initial conditions for solving these equations are values p_2, M_2, T_2 and V_2 of state of gas remaining after its previous release from this chamber.

VI. SIMULATION RESULTS

The resulting system of equations was used to build a simulation model in the MatLab Simulation system. A series of computational experiments were carried out on the simulation model to confirm the adequacy of the obtained mathematical model. The results of the experiments are shown in Fig. 2–5. The results are presented in relative units for a shaft rotation speed of 31.42 rad/s, working fluid is air, and calculated machine power is 10 kW.

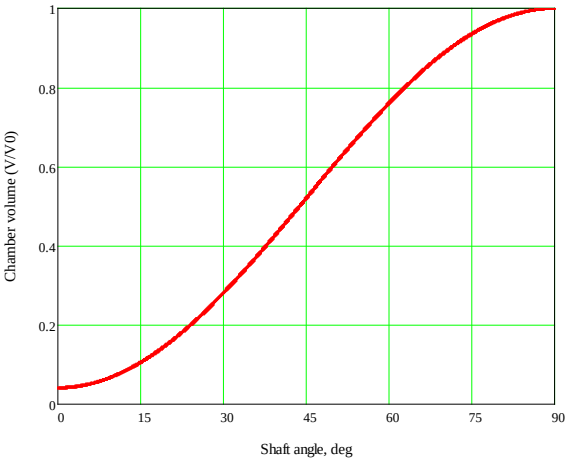

Fig. 2. Dependence of chamber volume on shaft angle.

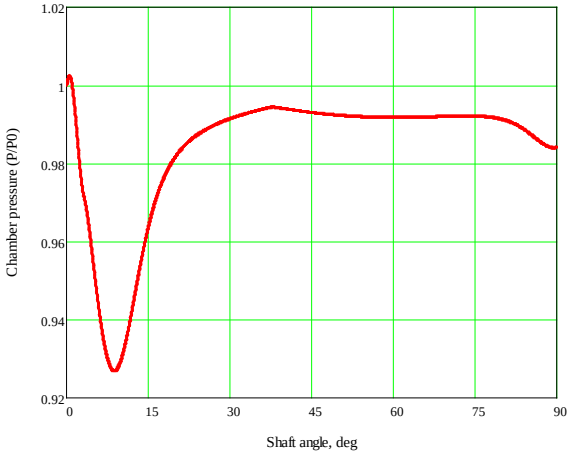

Fig. 3. Dependence of chamber pressure on shaft angle.

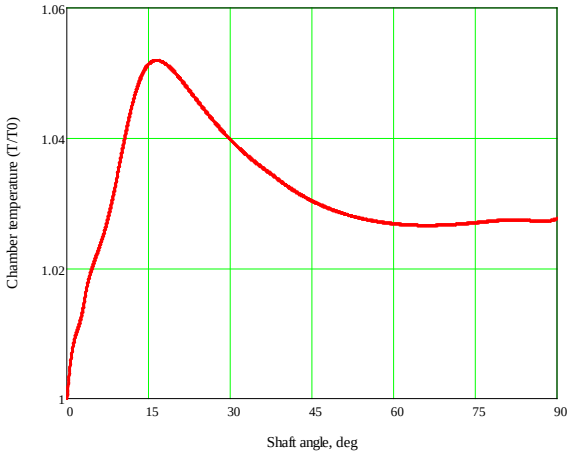

Fig. 4. Dependence of chamber temperature on shaft angle.

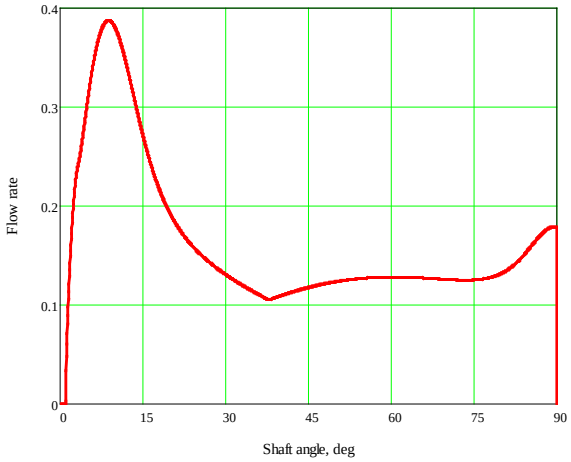

Fig. 5. Dependence of flow rate on shaft angle.

The resulting simulation model makes it possible to study the effect of various working fluids on the efficiency of a rotary expansion machine.

VII. Conclusion

In this article, a mathematical model of process of admitting superheated steam from a heat source to chamber is constructed. In formulation of problem, an assumption was made, according to which superheated steam, being a real gas, is considered an ideal gas. This assumption allowed us to simplify the model, which can be useful as a first approximation.

The main practically necessary problem, which can be solved on basis of this model, is to determine dependence of torque on angular velocity, i.e. in construction of mechanical characteristics of a rotary expansion machine.

References

[1] RF Patent 2619391 for an invention. Int. Cl. F01C1/44. Rotary Expantion Machine / Y.N. Lukyanov, Y.N. Zhuravlev et al. Publ. 15.05.2017.

[2] RF Patent 2374526 for an invention. Int. Cl. F16H25/04. Mechanism for converting motion / Y.N. Lukyanov, Y.N. Zhuravlev et al. Publ. 27.11.2009. Bull. Number 33.

[3] RF Patent 2387844 for an invention. Int. Cl. F01G1/077, F02G1/044. Rotary-vane engine with an external supply of heat / Y.N. Lukyanov, Y.N. Zhuravlev et al. Publ. 27.04.2010. Bull. Number 12.

[4] Y.N. Zhuravlev, I.V. Plokhov, Y.N. Lukyanov, and others, Calculation and Design of Rotaty-blade Machine with External Heat Supply. Monogrphy. Pskov, 2012.

[5] Y. N. Zhuravlev, I. V. Plokhov, Y. N. Lukyanov, and others, Mathematical Models of Physical Processes in Rotary-blade Engine with External Heat Supply. Monogrphy. Pskov, 2012.

[6] Perminov A., Lukyanov Y., Ilyin A., Zhuravlev Y., Tikhonov S., Determination of chamber and piston geometry for a rotary type expansion machine. “Environment. Technology. Resources. Proceedings of the 12th International Scientific and Practical Conference”, 2019, 3, стр. 197–200, https://doi.org/10.17770/etr2019vol3.4060

[7] Zhuravlev Y., Perminov A., Lukyanov Y., Tikhonov S., Ilyin A., Construction of piston outer profile for rotary type expansion machine. “Environment. Technology. Resources. Proceedings of the 12th International Scientific and Practical Conference”, 2019, 3, p. 257–260, https://doi.org/10.17770/etr2019vol3.4059

[8] S.Semyonov, S.Tikhonov, Y.Lukyanov, A.Perminov, Analysis method of calculation parameters of heat and mass transfer processes in the stirling engine. “Environment. Technology. Resources. Proceedings of the 11th International Scientific and Practical Conference”, 2017, 3, p. 298–303, https://doi.org/10.17770/etr2017vol3.2513

[9] S.Semyonov, S.Tikhonov, Y.Lukyanov, A.Perminov, Optimization of mechanical strength of rotary-vane engine. “Environment. Technology. Resources. Proceedings of the 11th International Scientific and Practical Conference”, 2017, 3, p. 357–360, https://doi.org/10.17770/etr2017vol3.2511

[10] Perminov A., Lukyanov Y., Tikhonov S., Ilyin A. Thermodynamic cycle with two-component working fluid. “Environment. Technology. Resources. Proceedings of the 11th International Scientific and Practical Conference”, 2015, https://doi.org/10.17770/etr2015vol2.261

[11] Y. N. Zhuravlev, A. L. Perminov, Y. N. Lukyanov, S. I. Tikhonov, S. N. Semenov, Minimization of Mechanical Strength of Rotary-blade Heat Engine with Cam-and-lever Motion Transformer. Bulletin of Pskov State University. Series: Engineering scinces, 2016.

[12] A. L. Perminov, A. A. Khitrov, A. I. Khitrov, Mechatronic System “Magneto-electric Synchro Motor – Active Rectifier” for Autonomous Energy Station Using Rotary-blade Machine with External Heat Supply. “Proceedings of VII International (VIII Russian) Conference on Automotization Electrical Drives AEP-2012”, Ivanovo State Energy University, Ivanovo, 2012. P. 330–335

[13] Andreev M., Zhuravlev Y., Lukyanov Y., Perminov A. Autonomous Power Station Based on Rotary-Vane Engine with an External Supply of Heat. Environment. Technology. Resources. Proceedings of the 9th International Scientific and Practical Conference. Volume 2. 2013, https://doi.org/10.17770/etr2013vol2.842

[14] A.L. Perminov, Y.N. Lukyanov, S.I. Tikhonov, Electrogenerators fot Energy Sets. “Electrical Engineering. Electrical Energy. Information Techlogies. Proceedins of I International Research and Prctice Seminar”, Pskov. 2018. P. 52–55.

[15] Perminov A.L., Luk'yanov YU.N., Tikhonov S.I., Il'in A.V. Elektrogeneratory dlya energoustanovok. Elektromekhanika. Elektroenergetika. Informatsionnyye tekhnologii Sbornik materialov 1-go Mezhdunarodnogo nauchno-prakticheskogo seminara. 2018. pp. 52-55.

Environment. Technology. Resources. Rezekne, Latvia
Proceedings of the 13th International Scientific and Practical Conference. Volume 3, 270-273

Synthesis of a Lever-Cam Motion Transducer for a Rotary Vane Pump

Andrey Perminov
Department of Electric Coupling and Automation Systems
Pskov State University
Pskov, Russia
alp-mail@mail.ru

Alexander Ilyin
Department of Electric Coupling and Automation Systems
Pskov State University
Pskov, Russia
al.ilyin@yandex.ru

Sergey Tikhonov
Department of Automobile Transport
Pskov State University
Pskov, Russia
sit42@rambler.ru

Alexander Khitrov
Department of Electric Coupling and Automation Systems
Pskov State University
Pskov, Russia
khitrov-pscov@mail.ru

Yury Zhuravlev
Pskov, Russia
drakon426@mail.ru

***Abstract* - The article solves problem of synthesizing a lever-cam motion transducer that converts rotary motion of input shaft of a rotary pump into motion of its vanes required for volumetric pumping of gases and liquids. Analytical expressions for theoretical profile of cam of lever-cam transducer of the movement of rotary vane pump are obtained. The cam profile was built according to analytical expressions.**

Keywords* - *rotary vane pump, lever-cam motion transducer, volumetric pumping gas.

I. INTRODUCTION

The creation of a pump that provides volumetric pumping of a working fluid regardless of the working fluid type (gas, liquid and gas-liquid mixture) that enters the pump inlet is very important for a number of industries (gas, oil, pharmaceutical, etc.)

An alternative to existing types of pumps with volumetric pumping is a rotary vane pump with a lever-cam motion converter [1] – [3].

Structurally pump consists of a rotary vane group and a lever-cam motion transducer (Fig. 1).

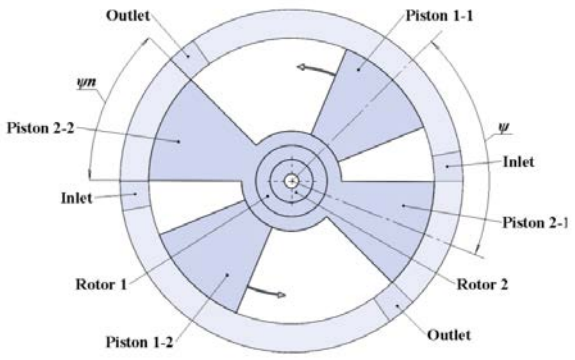

Fig. 1. Rotary vane pump design.

The rotor-vane group consists of a body and two coaxial rotors, each of which carries a vane of two diametrically located pistons. Pistons have an angular dimension ψ_n. Body has two inlet and two outlet ports. Inter-piston space contains four chambers of variable volume. Opening and closing of windows is done by respective piston surfaces [4], [5].

Pump works as follows. Volume of chamber opposite open inlet window increases to a maximum value and is filled with a working fluid. Then, this volume of working fluid with closed inlet port is transferred to outlet zone, and with open outlet port, release occurs with a decrease in chamber volume to a minimum value.

Online ISSN 2256-070X
https://doi.org/10.17770/etr2021vol3.6513

On one revolution of output shaft, each chamber makes two releases of working fluid and, therefore, with four chambers, pump makes eight releases. Moreover, pumping process is really voluminous, i.e. it is volume that is pumped, regardless of whether gas or liquid fills its volume when entering chamber.

The type of working fluid affects only power of drive motor.

II. ORGANIZATION OF MOVEMENT

To organize motion of vanes described above, it is proposed to use a lever-cam motion transducer. A similar mechanism was first proposed in patent RU 2374526 [1] for a rotary vane engine with external heat supply [2]. The kinematic diagram of the mechanism is shown in Fig. 2.

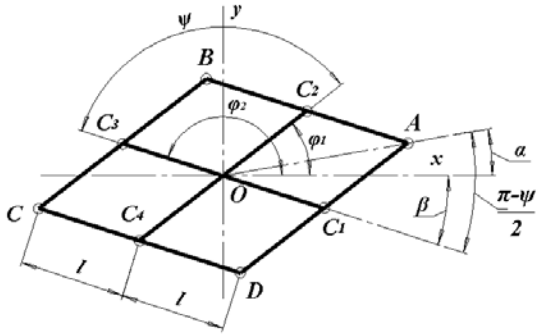

Fig. 2. Kinematic diagram of mechanism.

Four links *AB*, *BC*, *CD* and *DA* of length $2l$ each are pivotally connected to each other and form a rhomboid. Fork C_1C_3 of vane 1 and fork C_2C_4 of vane 2 are pivotally attached to centers of links of rhomboid. Axes of vanes have angular coordinates φ_1 and φ_2, respectively.

Rhomboid vertices *A*, *B*, *C*, and *D* are equipped with rollers that roll on cam. A cam profile is such that it makes the axes of rollers A, B, C and D move along so-called theoretical cam profile, which sets law of motion of vanes. Profile of the cam itself is equidistant (internal or external) to theoretical profile. The cam used in rotary vane pump has a theoretical profile in polar coordinates ρ and α of form

$$\rho(\alpha) = 2l\sin(a + b\cos(2\alpha)), \tag{1}$$

here $a = \pi/4$, $b = \pi/4 - \psi_{min}/2$. Profile (1) provides a change in the angle between axes of vanes according to the harmonic law $\psi(\alpha) = 2a + 2b\cos(2\alpha)$, which cannot be used for pump under consideration [6], [7].

Taking this circumstance into account, we formulate the problem as follows. It is required to synthesize a cam profile that would ensure that one vane stops, while other blade would move at which the angle ψ between axes of vanes either decreases from value ψ_{max} to ψ_{min} (outlet), or increases from ψ_{min} to ψ_{max} (inlet), and also the movement of the inlet isolated volume to the outlet/inlet area.

III. GEOMETRIC RELATIONSHIPS

The configuration of rhomboid is completely determined by links length $2l$ and the angles φ_1 and φ_2 of vanes axes C_1C_3 and C_2C_4 with the *x*-axis. These angles are input variables of four-link structure. For output parameters we take length of half–diagonal $OA = \rho$ (polar radius) and angle α between OA and *x*-axis (polar angle). Obviously, function $\rho(\alpha)$ defines theoretical cam profile.

An important geometric parameter is angle $\psi = \varphi_1 - \varphi_2$ between vanes axes, which can vary within limits $\psi_{min} \le \psi \le \psi_{max}$, $\psi_{max} = \pi - \psi_{min}$, where value ψ_{min} is set for design reasons.

From Fig. 2 we have

$$\beta = \pi - \psi - \varphi_2,$$
$$\alpha = \frac{\pi-\psi}{2} - \beta = \frac{\varphi_1+\varphi_2}{2} - \frac{\pi}{2},$$
$$\rho = 2l\cos\left(\frac{\pi-\psi}{2}\right) = 2l\sin\left(\frac{\psi}{2}\right), \tag{2}$$

whence next geometric relations follow:

$$\psi = \varphi_1 - \varphi_2, \tag{3}$$
$$\varphi_1 + \varphi_2 = 2\alpha + \pi, \tag{4}$$
$$\varphi_1 = \alpha + \frac{\psi}{2} + \frac{\pi}{2},\ \varphi_2 = \alpha - \frac{\psi}{2} + \frac{\pi}{2}, \tag{5}$$
$$\rho(\alpha) = 2l\sin\left(\frac{\psi}{2}\right),\ \bar{\rho}(\alpha) = \frac{\rho(\alpha)}{2l} = \sin\left(\frac{\psi}{2}\right), \tag{6}$$

where $\bar{\rho}$ is dimensionless polar radius.

IV. FIRST STAGE

First stage begins from position $\alpha = 0$, in which angle between axes of vanes $\psi = \psi_{max}$, and the angles φ_1 and φ_2, according to (5), have the following values:

$$\varphi_1 = \varphi_{10} = \frac{\psi_{max}}{2} + \frac{\pi}{2},$$
$$\varphi_2 = \varphi_{20} = -\frac{\psi_{max}}{2} + \frac{\pi}{2}. \tag{7}$$

At this stage, the vane 1 must remain stationary, so angle φ_1 must have a constant value φ_{10}. Vane should move to approach vane 1 and according to (4), the angle $\varphi_2(\alpha) = 2\alpha + \pi - \varphi_{10} = 2\alpha - \psi_{max}/2 + \pi/2$. In this case, angle ψ changes according to law

$$\psi(\alpha) = \varphi_{10} - \varphi_2(\alpha) = \psi_{\max} - 2\alpha. \tag{8}$$

Starting stage ends when angle ψ reaches value ψ_{min}. Value of angle α, at which this stage ends, will be denoted by α^* and found from relation (8):

$$\alpha^* = \frac{\pi}{2} - \psi_{min}. \tag{9}$$

Vertex of rhomboid A in this segment moves along trajectory

$$\bar{\rho}_A(\alpha) = \sin\left(\frac{\psi_{max}}{2} - \alpha\right),\ 0 \le \alpha \le \alpha^*. \tag{10}$$

and at the same time $\alpha = \alpha^*$ will take the position A^*. Thus, the polar radius $\bar{\rho}_A$, which at $\alpha = 0$ has largest value

$\bar{\rho}_A(0) = \sin\left(\frac{\psi_{max}}{2}\right) = \bar{\rho}_{max}$ decreases with increasing α, and at $\alpha = \alpha^*$ takes smallest value $\bar{\rho}_A(\alpha^*) = \sin\left(\frac{\psi_{min}}{2}\right) = \bar{\rho}_{min}$.

The vertex of rhomboid B corresponds to the polar radius $\bar{\rho}_B$, which is related to the radius $\bar{\rho}_A$; the obvious relation is $\bar{\rho}_A^2 + \bar{\rho}_B^2 = 1$, which implies $\bar{\rho}_B(0) = \cos\left(\frac{\psi_{max}}{2} - \alpha_A\right)$. Considering that $\alpha_A = \alpha_B - \pi/2$, we obtain the equation of the cam profile in the BB^* section:

$$\bar{\rho}_B(\alpha) = \sin\left(\alpha - \frac{\psi_{max}}{2}\right), \frac{\pi}{2} \le \alpha \le \left(\alpha^* + \frac{\pi}{2}\right). \quad (11)$$

Polar radius $\bar{\rho}_B$, which at $\alpha = \pi/2$ has smallest value $\bar{\rho}_{min} = \sin\left(\frac{\psi_{min}}{2}\right)$, at $\alpha = \pi/2 + \alpha^*$ takes largest value $\bar{\rho}_{max} = \sin\left(\frac{\psi_{max}}{2}\right)$, (Fig. 3).

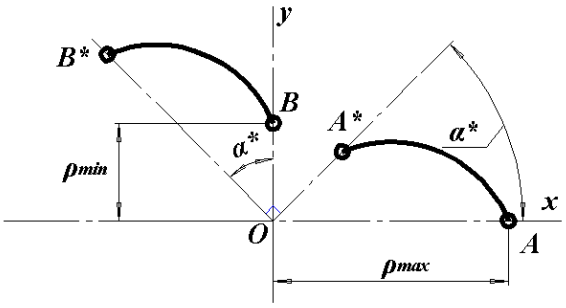

Fig. 3. First stage.

At the end of the starting stage, the working fluid is displaced in one pair of diametrically located chambers, and filling occurs in the other pair of chambers.

V. SECOND STAGE

At this stage, all four chambers are moved without changing volume: one pair of chambers to filling zone, other to discharge zone. Therefore, points A^* and B must be connected by an arc of a circle of radius $\bar{\rho}_{min}$, and points B^* and C – by an arc of a circle of radius $\bar{\rho}_{max}$, with center of both circles at point O (Fig. 4). We have:

$$\bar{\rho}(\alpha) = \bar{\rho}_{min} = \sin\left(\frac{\psi_{min}}{2}\right) = \text{const}, \alpha^* \le \alpha \le \frac{\pi}{2};$$

$$\bar{\rho}(\alpha) = \bar{\rho}_{max} = \sin\left(\frac{\psi_{max}}{2}\right) = \text{const},$$

$$\left(\alpha^* + \frac{\pi}{2}\right) \le \alpha \le \pi. \quad (12)$$

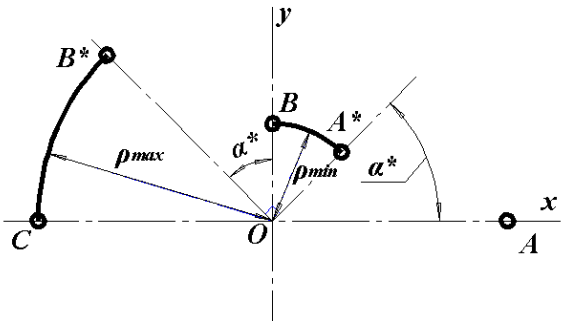

Fig. 4. Second stage.

VI. CAM PROFILE EQUATIONS IN POLAR COORDINATES

In the range $0 \le \alpha \le \pi$, the cam profile is described by equations (10) – (12). The function $\bar{\rho}(\alpha)$ has period π, therefore, in the interval $\pi \le \alpha \le 2\pi$, we have

$$\bar{\rho}(\alpha) = \sin\left(\alpha - \frac{\psi_{max}}{2}\right), \pi \le \alpha < (\alpha^* + \pi);$$

$$\bar{\rho}(\alpha) = \bar{\rho}_{min} = \sin\left(\frac{\psi_{min}}{2}\right), (\alpha^* + \pi) \le \alpha < \frac{3\pi}{2};$$

$$\bar{\rho}(\alpha) = \sin\left(\frac{\psi_{max}}{2} - \alpha\right), \frac{3\pi}{2} \le \alpha < \left(\alpha^* + \frac{3\pi}{2}\right);$$

$$\bar{\rho}(\alpha) = \bar{\rho}_{max} = \sin\left(\frac{\psi_{max}}{2}\right), \left(\alpha^* + \frac{3\pi}{2}\right) \le \alpha \le 2\pi. \quad (13)$$

Equations (10) – (13) can be used to construct a theoretical cam profile. The theoretical profile for $\psi_{min} = 45°$ is shown in Fig. 5. Profile is built in relative units.

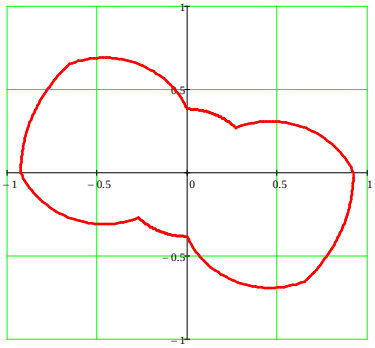

Fig. 5. Theoretical profile.

Using an equidistant offset from theoretical profile, actual cam profile is obtained. The appearance of cam is shown in Fig. 6.

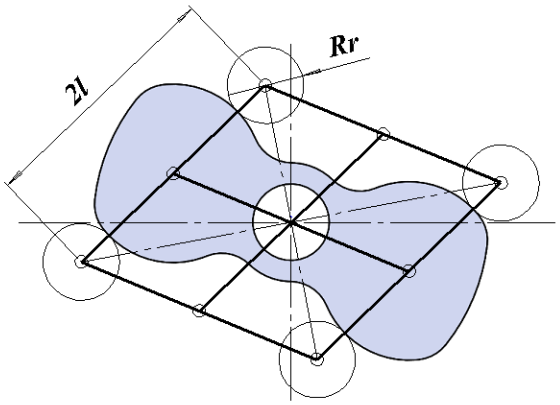

Fig. 6. Cam profile.

Angle between axes of vanes ψ changes according to law shown in Fig. 7. As can be seen from the graph, synthesized profile ensures that one vane stops, while other vane moves at which angle ψ between axes of vanes increases from ψ_{min} to ψ_{max} (inlet), and decreases from ψ_{max} to ψ_{min} (outlet). Also, the inlet isolated volume moves to the outlet/inlet zone.

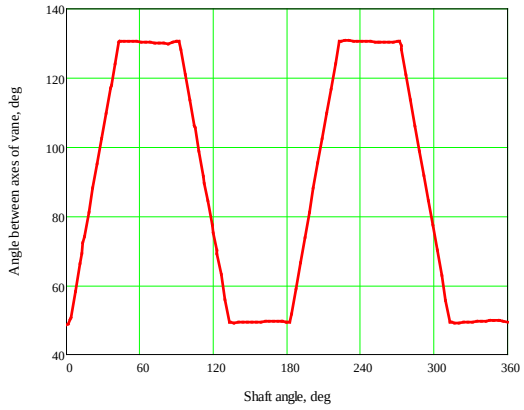

Fig. 7. Angle between axes of vanes ψ.

VII. Conclusion

In this article, analytical expressions are obtained for theoretical profile of cam of lever-cam transducer of movement of a rotary vane pump. Cam profile was built according to analytical expressions.

Results of article can be used in design and manufacture of rotary vane pumps that provide volumetric pumping of both gas and liquid working bodies , as well as other machines of a similar type [8] – [11].

References

[1] RF Patent 2374526 for an invention. Int. Cl. F16H25/04. Mechanism for converting motion / Y. N. Lukyanov, Y. N. Zhuravlev et al. Publ. 27.11.2009. Bull. Number 33.

[2] RF Patent 2387844 for an invention. Int. Cl. F01G1/077, F02G1/044. Rotary-vane engine with an external supply of heat / Y. N. Lukyanov, Y. N. Zhuravlev et al. Publ. 27.04.2010. Bull. Number 12.

[3] RF Patent 2619391 for an invention. Int. Cl. F01C1/44. Rotary Expantion Machine / Y. N. Lukyanov, Y. N. Zhuravlev et al. Publ. 15.05.2017.

[4] Perminov A., Lukyanov Y., Ilyin A., Zhuravlev Y., Tikhonov S., Determination of chamber and piston geometry for a rotary type expansion machine. “Environment. Technology. Resources. Proceedings of the 12th International Scientific and Practical Conference”, 2019, 3, p. 197–200, https://doi.org/10.17770/etr2019vol3.4060

[5] Zhuravlev Y., Perminov A., Lukyanov Y., Tikhonov S., Ilyin A., Construction of piston outer profile for rotary type expansion machine. “Environment. Technology. Resources. Proceedings of the 12th International Scientific and Practical Conference”, 2019, 3, p. 257–260, https://doi.org/10.17770/etr2019vol3.4059

[6] Y. N. Zhuravlev, I. V. Plokhov, Y. N. Lukyanov, and others, Calculation and Design of Rotaty-blade Machine with External Heat Supply. Monogrphy. Pskov, 2012.

[7] Y. N. Zhuravlev, I. V. Plokhov, Y. N. Lukyanov, and others, Mathematical Models of Physical Processes in Rotary-blade Engine with External Heat Supply. Monogrphy. Pskov, 2012.

[8] S. Semyonov, S. Tikhonov, Y. Lukyanov, A. Perminov, Analysis method of calculation parameters of heat and mass transfer processes in the stirling engine. “Environment. Technology. Resources. Proceedings of the 11th International Scientific and Practical Conference”, 2017, 3, p. 298–303, https://doi.org/10.17770/etr2017vol3.2513

[9] S. Semyonov, S. Tikhonov, Y. Lukyanov, A. Perminov, Optimization of mechanical strength of rotary-vane engine. “Environment. Technology. Resources. Proceedings of the 11th International Scientific and Practical Conference”, 2017, 3, p. 357–360, https://doi.org/10.17770/etr2017vol3.2511

[10] Perminov A., Lukyanov Y., Tikhonov S., Ilyin A. Thermodynamic cycle with two-component working fluid. “Environment. Technology. Resources. Proceedings of the 11th International Scientific and Practical Conference”, 2015, https://doi.org/10.17770/etr2015vol2.261

[11] Y. N. Zhuravlev, A. L. Perminov, Y. N. Lukyanov, S. I. Tikhonov, S. N. Semenov, Minimization of Mechanical Strength of Rotary-blade Heat Engine with Cam-and-lever Motion Transformer. Bulletin of Pskov State University. Series: Engineering scinces, 2016.

Environment. Technology. Resources. Rezekne, Latvia
Proceedings of the 13th International Scientific and Practical Conference. Volume 3, 274-280

An Alternative Approach to Reducing Aging of Innovative Industrial Products in Terms of Industry 4.0

Desislava Petrova
Department Management
Technical University of Gabrovo
Gabrovo, Bulgaria
e-mail: des_petrova@abv.bg

***Abstract* - The rapid progress in the field of industrial and information-communication techno-logies and their impact on production systems are putting increasing pressure on the engineering structure. That is why modern technological deve-lopment has created conditions in which innova-tive obsolescence already takes precedence over physical. A particularly important point in this direction is the correct determination of the degree of influence of innovative aging on products and processes in order to establish its impact on the technical, economic and social results of industrial activity. In addition, the impact of this process is globalizing, resulting in innovative obsolescence of technology and lagging behind the level of advan-ced technologies from modern ones world-wide. The further use of innovatively obsolete equipment and technological processes leads to certain losses, the amount of which will depend on the degree of this lag. This report proposes an alternative approach to reducing the innovative obsolescence of industrial products by modernizing and creating sustainability in the engineering space. At the same time, innovative progress in the future will put increasing pressure on the technological structure and on the distinctive features of this process. A theoretical attempt has been made to calculate mathematically innovative aging, and the impact of destructive innovations is difficult to capture with this model.**

Keywords* - *innovative aging, engineering space, modernization.

I. INTRODUCTION

Industry 4.0 is a concept that encompasses several aspects of the fourth industrial revolution. It should be noted that the main innovation of Industry 4.0 is the redesign of technological and organizational processes as a result of the integration of different sources of information with management and production pro-cesses. It is the result of non-traditional use and a combination of existing technologies to create new business solutions that satisfy customers. The develop-ment of the production capacities is related to the service life of the machines and their physical and innovative obsolescence. This obsolescence can be partially predicted and controlled if the following alternative actions are performed: monitoring their reliability and renewal, reducing downtime, improving machinery and equipment, improving the production cycle, monitoring and, if necessary, adjusting the monitored indicators [1].

The condition and development of the equipment in the process of its operation depends on the change of its parameters. This change can be managed if the influencing factors are studied and the relative share of the dominant parameters in determining the capacity of the equipment itself in the particular company is determined. Innovative aging is linked to the life cycle of innovation. At the current stage of technical deve-lopment, two factors have a significant impact on innovative aging:

- innovative development in the field of machinery and technology in the industries producing means of production;

- designed and implemented in the production of new, more modern, more productive and with better technical and economic indicators machines in comparison with the previously produced ones.

Taking into account these factors that characterize the quality side of innovative development allows to reveal not only the mechanism of its impact on the indicators of production efficiency, but also its impact on different aspects of the production process [2]. Process reengineering is not always the optimal solution, but it is a tool for their improvement and leads to economic, technical

Online ISSN 2256-070X
https://doi.org/10.17770/etr2021vol3.6507

and environmental effects. Digitalization is entering all spheres of life and will inevitably affect the technological processes in the industry and in particular the innovative aging. The time for registration of a Patent or Utility Model is not a constant value, and the innovations do not stop, which is a prerequisite for the delay of their registration. A new approach is needed for their registration, thus there will be no factor delaying the introduction of innovations in industrial practice. This can be solved with the help of a Global Database in which to innovate and move forward without bureaucratizing the process and wasting time and resources. The innovative obsolescence of industrial products is the subject of research by a team of the following authors Dimitar Damyanov, Siika Demirova, Beata Vlahova in their works, to which I belong [1, 2, 12].

The impact of innovative development is globali-zing, as a result of which there is an innovative obsolescence of technology and lagging behind the level of commissioned technologies from modern ones. The further use of innovatively obsolete equipment and technological processes leads to certain losses, the amount of which will depend on the degree of this lag. Thus, there is a certain relationship between productivity as a world-class level and technical development. It is expressed in the achieved technical stages of development, taking into account the differences in the respective levels and the increase of productivity. The indicators determining the technical levels and productivity are closely related and interdependent, as they are defined by technological development at a given time, which in turn is a result of the achieved productivity of technology as a degree of development of scientific and technological progress. The physical essence of these dependencies is expressed in shortening the periods of creation of new technical solutions, inventions, technologies, modern constructions, know-how, etc. and increasing their productivity in absolute and relative terms for each new period. Therefore, the periods of innovative obsolescence of technology become shorter over time, and technical levels - higher for each subsequent period. These are objective technical laws, which with the technological development mark accelerated steps for each subsequent period. The future development of industrial activities will be characterized by ever higher technical levels and higher productivity, rapid innovative aging and global intensification of processes and activities. At the same time, these dependencies form new spheres, generating a new environment of development, flexibly balanced by the influence of internal and external factors. Now we can not talk only about individual innovations and innovation processes, but about innovative production, considered in a complex way. The impact of the external environment determines the basic requirements for the technological behaviour of companies and creates the prerequisites and conditions for a new attitude to innovation as an integral and necessary part of the global development of industry and society. The impact of innovative development is globalizing, as a result of which there is an innovative obsolescence of technology and lagging behind the level of commissioned technologies from modern ones. The use of innovatively obsolete equipment and technological processes leads to certain losses, the amount of which will depend on the degree of this lag. The future development of industrial activities will be characterized by ever higher technical levels and higher productivity, rapid innovative aging and global intensification of processes and activities [7]. Technological development and more precisely its consequences, manifested in the form of innovative obsolescence of products and processes, lead to a kind of attitude of manufacturers to seek ways and means to improve and change their parameters.

II. EXPOSITION

The essence of the problem - innovative aging and modernization

Modernization is one of the most effective forms of rapid implementation of new technical and technolo-gical advances in the practice and process of renewal of production in the conditions of Industry 4.0. Therefore, modernization will mean the improvement of those components that determine the level of the product or process, which will give it advantages inherent in simi-lar products and processes, but with more modern parameters and higher productivity. By innovative obsolescence we will understand the lag of the level of the put into operation equipment and technologies from the newly produced innovative machines and techno-logies [2]. As a consequence of this lag, they become more uncompetitive, which leads to certain losses.

Innovative obsolescence imposes conditions that companies must comply with. This stems from both the technological attitude and the strong impact of consumer interest in new products [4]. That is why more and more companies are starting to apply flexible technological and organizational forms of behavior to the surrounding industrial and market world. In essence, this means that a global innovation policy is beginning to take shape, the manifestation of which is beginning to take flexible technological and organizational forms in specific companies [5]. This policy is increasingly adapting to the global industrial behavior of innovations as a resource for their future development. The main directions, providing an effective way out of the limitations imposed by the rapid innovative obsolescence in the creation of competitive innovative products, are actively applied by many companies in the automotive and electronics industries [3]. This new approach, quickly adopted by industrial companies, is already showing its advantages in the competitive qualities of both industrial products and in increasing the efficiency of its application.

The rapid innovative obsolescence of products and services poses to humanity the solution to the problem of eliminating the harmful effects of its impact. This is especially necessary when issuing protection docu-ments, such as patents, where the term for their issuance is longer than the emergence of a new innovative solution [6]. Or we can say that the innovative product is innovatively obsolete before it is even put into operation. With the current development of information and communication

technologies, this problem can be solved with the creation of a European or World Information Center, with open access to a database. Thus, to grant patents only for such products and technologies that have a proven long innovative life. For all other inventions, open access to them should be made and used for a fee [10].

We can summarize that innovative development, innovative aging and modernization are interrelated manifestations of the same process, they are constella-tion-bound. In addition, innovative obsolescence can be studied, controlled and controlled through moderni-zation methods and forms of application. To this end, an approach and a way to determine the magnitude and extent of innovative aging can and should be proposed. Also to determine in a timely manner the coefficient of modernization of technical means that are not equipped in the enterprise. The aim of this thesis is to analyze the impact of technologies in the environment of Industry 4.0 on the sustainability of the integrated engineering space throughout the production chain, with the industrial benefit to focus on the synergistic effect of its overall application [7].

Modernization as conditions for integration of engineering components in the production chain

The development of engineering is inconceivable without the computerization of the management of engineering processes. The role and goals of the engineering processes in the modern conditions, through the sphere of production, turn to the requirements of the end user, flooding him with powerful flows of individualized products. The requirements for the quality of the processes are also increasing, and they must be faster, more accurate, more economical. Characteristically, the information support of the engineering and reengineering (modernized) process has been radically changed. Currently, the integration of reengineering activities is carried out primarily with the introduction of information systems [8].

One of the main requirements in this direction is the correct formulation of the concept of information flow and information system. The information flow is a set of information modules that are distributed in the engineering system and between it and the external environment, necessary for the management and control of engineering operations. Modern engineering information flow can only exist in the form of electronic media. Therefore, the automation of engineering components, or the modernization of these activities as an element of company development are also considered as a complex solution with automation of company activities [11]. The characteristic here is that the engineering chain includes both the internal company connections and those that define the external influences for the need to modernize the automation equipment. In this way, the information engineering activity forms a fully integrated information space.

The functional dependence between the engineering information systems (EIS) and the internal and external connections can be expressed by the following formula:

$$EIS = f(S_v, S_w) \quad (1)$$

Where:

S_v - internal interconnections;
S_w - external interconnections.

The internal-structural interrelations are studied and arranged by significance and belonging according to certain features to the engineering information system. These are the interrelationships between the engineering of technology and the material flow realized through the Internet of Things. Therefore, this is the possibility to use a digital engineering and reengineering information system, which is related to machines and automation equipment within the company. This includes the construction of a reengineering virtual model in virtual reality with a mirror image - software implementation.

External links are related to the types of engineering subsystems, including those with external suppliers, customers, etc. throughout the engineering chain.

The second no less important issue is the construction of engineering information systems in terms of their functionality (functional structure).

Before talking about the functionality of the engineering information system, they must determine the types of information flows that penetrate the system itself. The specificity of the engineering information system is determined by the fact that the flow management is performed both within the industrial company and between the various participants in the engineering and reengineering chain of the intelligent innovative and flexible Industry 4.0.

In this regard, information flows are divided into two main types:

- Strategic (coordinating) and
- Functioning.

Individual functions (functional subsystems) can be included in both types of data flows (in inventory management).

The strategic (coordinated) flow also includes key functions of the logistics information system, which is part of the digital engineering system [12].

Digital intelligence in the engineering and modernized information system

The methodology of digital intelligence forms a set of requirements that are necessary for the future functioning of the engineering and reengineering information system in the environment of digitalization and Industry 4.0. This requirement is imposed from the point of view of preliminary construction of the technical levels of the system. In this aspect, the engineering information system adapts the following levels:

- Technical level of the system (electronic levels of engineering and reengineering information system of a specific industrial company);

- Technical level of the site (virtual or real engineering or reengineering information object);
- Artificial intelligence (control intelligence), which includes: a range of functions that artificial intelligence can perform (1… .n) and functions that have a complete replacement of man (F of the total number of n-functions) by introducing engineering and reengineering information systems.

Formation of engineering and modernized information depots for storage in virtual reality of information modules

This includes the possibilities for self-differentiation of functions in the re-engineering information systems and their adaptation as modules for incorporation in other processes, which are characterized by the following engineering activities:

- Approach for construction of information depots for storage of information systems built into the reengineering process.
- Delivery of information services via the Internet (embedded information systems - software). They are coded independently and separated by functions and purpose systems (software product), offered on the market as a commercial product for the needs of engineering and reengineering.
- Approach for building engineering and reengineering information systems in the cloud.
- Offering virtual engineering and reengineering reality in the cloud [13].
- Cyber security of processes.

In order to more accurately and correctly account for the benefits and effects of innovative development and innovative aging, the development of the problem should be considered comprehensively. This means that the qualitative nature of components such as the degree of innovation, innovation activity, innovation obsolescence and alternative solutions to rapid innovation aging should be considered as a comprehensively integrated solution approach. The integration nature of this approach is based on the fact that it involves more influential factors that affect the efficiency of innovation activity of industrial companies [12].

The structure of the solution includes several models defined as:

- Model for determining the degree of innovation;
- Model for innovation activity [15];
- Model for innovative aging;
- Model for alternative solutions.

Model for determining the degree of innovation

Mathematical models can be applied to determine the degree of innovation of products and processes, and specific indicators are used to solve them, defining the concept of innovation as novelty, applicability and commercialization.

- Technical indicators (novelty);
- Indicator determining the consumer nature (applicability);
- Commercial realization (market).

The model for determining the degree of innovation is used to calculate the novelty in cases where it is sufficient for a particular purpose of research to focus on the innovative nature of the problem.

In the development of innovative products, technical, consumer and market indicators or

$$C_{imo} = C_{teh} + C_{pot} + C_{mt} \quad (2)$$

are used, and the degree of innovation is defined as the sum of the results of the separated indicators, taken as relative weights subject to the condition:

$C_{teh} \leq 1$; $C_{pot} \leq 1$; $C_{mt} \leq 1$;

$C_{ino} \leq 3$ - Degree of innovation.

Technical indicator (C_{teh}) (novelty) - calculates the savings of materials, labor, energy, quality improvements, etc. of the new product compared to the old or similar.

User indicator (C_{pot}) - the number of users (C_{pot}) who will accept the new product is predicted and we use empirical dependencies for diffusion of innovations.

Market indicators (C_{mt}) - for sales and include three components: C_{inv} - investment (production) costs; C_{kk} - quality and C_{eko} - ecology.

Model for innovation activity [1

The definition of innovation activity for a given period of time, with pre-set parameters, can also be modeled [16]. The model of innovation activity reveals how products are perceived as attractive between real and potential consumers. The innovation activity model can be widely used in product and technology forecasting. The mathematical basis of the innovation activity model is the diffusion model. The wording of the model is based on:

$$S(t) = m.f(t) \quad (3)$$

Where:

f(t) - the degree of change of the received or introduced activity;

m - potential;

S(t) - the sale or degree (value) of the change in the accepted introduced activity, i.e. perception.

Then the innovation activity can be expressed by S(t) or:

$$S(t) = \frac{m(p+q)^2}{p} \cdot \frac{e^{-(p+q)t}}{1+\frac{q}{p}e^{-(p+q)t}} \quad (4)$$

p - the coefficient of innovation, taking into account external influences or advertising effect;

q - the coefficient taking into account the internal influences or the effect of the functionality;

Values of p and q are experimental.

The model is suitable for use in a wider range of innovative products, although the solutions vary widely, mainly in pricing and advertising [1, 2].

Model for innovative aging

Innovative obsolescence is measured by the degree of depreciation of some of the functions of old machine constructions compared to those of newly manufactured innovative ones. Their determination is performed in the following sequence according to the formula:

$$M = W.C \quad (5)$$

Where:

M - innovative aging (depreciation of the functions of old machines) (BGN);

W - initial value of the old machine (BGN);

C - Coefficient taking into account the level (%) of innovative obsolescence (0 ^ 1).

C moves in the range 0 < C < 1, where:

C = 1 has no innovative obsolescence (the machine is 100% innovative).

C = 0.5 the machine is half innovatively obsolete or 50%.

C = 0 the machine is completely innovatively obsolete or 0% innovative.

C - defines innovation only in the range from 0 to 1.

C = (1 - E) where:

E - degree of innovation of the machine at a given time (at the time of measurement).

Research and determination of the coefficient for innovative aging and modernization

The study was conducted in the following areas:

- Dynamic change in the value of the new industrial product to the value of the old product at certain intervals.
- Dynamic change of the productivity of the new industrial product (of certain indicators) to the productivity of the old industrial product.

Degree of innovative aging

The degree of innovation (E) determines how much more innovative a machine is (%) with the comparable machine. It is defined as follows:

$$E = \frac{D_1}{D_2} \quad (6)$$

$$D_1 = \frac{V_1}{V_2} \quad (7)$$

$$D_2 = \frac{Q_2}{Q_1} \quad (8)$$

Where:

D_1 - ratio of the value of the new machine to the value of the old one.
D_2 - ratio of the productivity of the new machine to the productivity of the old one.
V_2- Value of the new machine.
V_1- Value of the old machine.
Q_2- Productivity of the new (innovative) machine.
Q_1- Productivity of the old machine.

We replace and receive:

$$K = 1 - \frac{D_1}{D_2} \quad (9)$$

Additional explanations to the main indicators given above:

1. The ratio $\frac{D_1}{D_2}$ must be positive (+), which indicates that we have innovation, or the degree of innovation of the machine is growing. With a negative ratio (-) the conclusion is that the innovation of the machine decreases or the machine is not innovative. In essence, this means that D_2 must take precedence over D_1 or the price of the new machine must be in optimal proportion to the price of the old machine. And the productivity of the new machine must always be higher than the productivity of the old machine.

2. For $V_2 = 0$ and $Q_2 = 0$ then
both $D_1 = 0$ and $D_2 = 0$;

3. Determining the duration of the production periods of the types of machine constructions such as:

- Conventional or class A, these are traditional machines and class A_1, these are machines for which the reliability /warranty/ service life indicators are the same over time.
- Mechatronic (on a modular basis) with an optimal ratio between the indicators reliability/warranty period/service life.
- Machines for cyber systems.

4. The ratio (1- E) can be at the nth degree, when we follow the development of the innovation process of innovations with world novelty.

n_1 - the next innovation against which it is measured (serves as a base).

h - scale factor (from 0.5 to 1.00) or range of manifestation.

h = 1, at n = 1, only applies to world-class innovations.

h = 0.5 at n = 0.5, only applies to innovations with a regional scale of innovation impact.

Then:

$$C = (1 - E) = \frac{D_1}{D_2} \quad (10)$$

TABLE 1 BASIC DATA

Indicator	Contents	Value
V_2	New price	500 to 450
Q_2	Productivity of the new machine	150 to 100
V_1	Old price	300 const
Q_1	Productivity of the old machine	100 const
$\frac{V_1}{V_2}$	Price ratio	$D_1 = \frac{V_1}{V_2}$
$\frac{Q_2}{Q_1}$	Productivity factor	$D_2 = \frac{Q_2}{Q_1}$
K_n	Modernization coefficient	K_n

The following results were obtained, shown in Figures 1, 2 and 3.

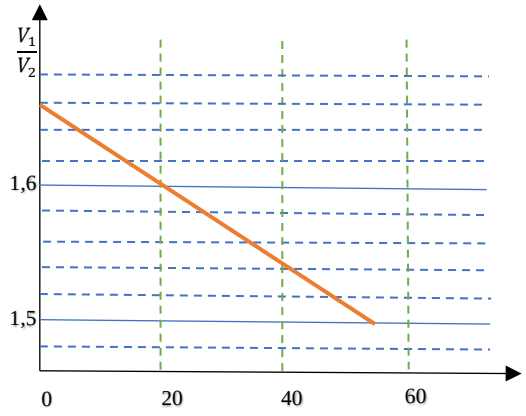

Fig. 1. Price ratio (D_1)

The results from the above graphs show the following:

Initial $\frac{V_1}{V_2} = 1.66$ and final data $\frac{V_1}{V_2} = 1.5$ are shown in Fig.1.

Fig. 2. Productivity factor (D_2)

Initial $\frac{Q_2}{Q_1} = 1.5$ and final data $\frac{Q_2}{Q_1} = 1$ are shown in Fig.2.

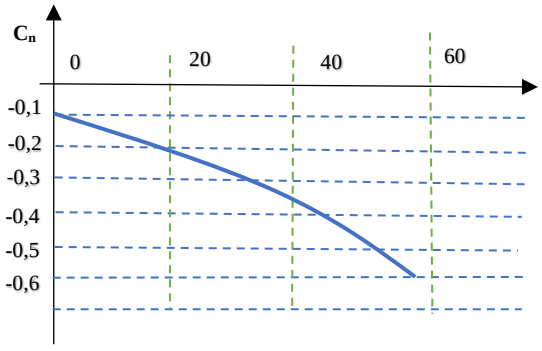

Fig. 3. Modernization coefficient (K_n)

Initial C_n = -0.11 and final data C_n = -0.5 are shown in Fig.3.

The strategic policy of industrial companies is inconceivable without a well-developed, assessed and meaningful policy for technical development, which takes into account the innovative aging, as a major factor in this development [9]. It is theoretically substantiated and practically proved that moderniza-tion approaches and methods can largely eliminate the harmful effects of innovative aging. Therefore, industrial policy actually forms the concept of technical and economic indicators of the company and is a major factor for its prosperity [14]. It should not be overlooked that the rapid technical progress in the field of industrial and information technology and its impact on production systems will put increasing pressure on both their structure and the distinctive features of this process. Borders will increasingly blur and the structure of production will change significantly. The striving for complex improvement of the technolo-gical, auxiliary and information activities will be more and more necessary as a main factor for the development of the modern production. This means that based on new communication and computer advances, nanotechnologies and other technical solu-tions, the structure of production will change globally. In the future, production will be considered as a whole, including technology, technological and information processes, as well as functionally integrated production components, throughout the engineering cycle. The study presented in this topic analyzes the impact of technology on the sustainability of the integrated engineering space throughout the production chain and the role of modernization in this process.

III. CONCLUSION

Based on the above, it can be concluded that the defining characteristics of engineering information

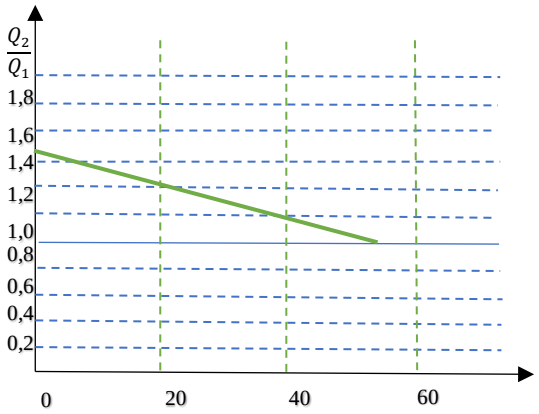

systems are derived, which define a higher level in the functional spectrum of engineering systems. They create an opportunity to expand the scope of the integrated

engineering information space. In this direction, the guidelines for the formation of re-engineering information depots for storage of information modules in virtual reality are determined.

In conclusion, it can be said that innovative development, innovative aging and modernization are interrelated manifestations of the same process. In addition, innovative aging can be studied, controlled and controlled through modernization methods and forms of application. For this purpose, an approach and a way of determining the size and calculating the amount of innovative obsolescence of products and processes and determining the coefficient of modernization are proposed. A toolkit for practical use and application of the coefficients is also proposed.

The constellation connectivity of innovative development, innovative aging and modernization are decisive for this process. It is important to note that innovative obsolescence can be studied, mastered and controlled through modernization methods and forms of application. This is achieved by determining the magnitude and calculation of the amount of innovative obsolescence of products and processes and by determining the coefficient of modernization in technology and systems.

REFERENCES

[1] Demirova, S., Innovative obsolescence and its impact on pro-duction development of industrial products, International scientific journal "Innovation", Year VI, ISSUE 1/2018, pp.7-9

[2] Damianov, D., Modern alternatives to rapid innovative aging, Scientific Bulletins of NTS in Mechanical Engineering, Year XXVI, Vol. 3/224, ISSN 1310–3946, 27 ISTC “ADP 2018”, June 2018, pp. 278-283.

[3] Kartunov S., D. Petrova, Database management system for automated design of micromechanical components for products in microsystem engineering, Proceedings of the 3rd International Conference „Research and Development in Mechanical Industry“, Volume 3, Herceg Novi, Serbia and Montenegro, Trstenik: High Technical Mechanical School, Kruševac: Institute IMK “14 Ovtomber” and Podgorica: Institute of Mechanical Engineering, 2004, p. 1154-1586, ISBN 86-83803-08-2, p.1546-1552.

[4] Kartunov, S., N., Nenov, Training in and development of Mechatronics and micro- and nano-systems technology in the Technical university of Gabrovo, Bulgaria, 6th International Conference “Competence of Contemporary Specialist: The unity of Theory and Practice”, Kaunas, 2012/6(I), ISSN 2029-4557, p. 79-84.

[5] Mitev,I., Influence of the Type of Iron Powder of the Tensile Strength of Iron Carbon Powder Materials Alloyed with Cooper, International Journal of Engineering and Advanced Technology (IJEAT), Volume 4, Issue 4, 2015, pp.156÷159, ISSN (online) 2249-8958.

[6] Mitev,I, Dimensional Change During Sintering of Samples of the Fe-Cu System, International Journal of Emerging Technologies in Computational and Applied Sciences (IJETCAS), ISSUE 8, vol.5, 2014, p.433÷436, ISSN (online) 2279-0055, ISSN (print) 2279-0047.

[7] Mitev,I., Optimizing of induction heating depending of the electromagnetic field – part|II, 13th International conference RaDMI 2013, Kopaonik, Serbia, 12÷15 September, 2013, vol.2, p.888÷893.

[8] Nenov., N., P., Tomchev, R., Ivanova, Study of the Ion Radiation Influence on the Parameters of Unijunction Tran-sistors, 9th International Scientific and Practical Confe-rence “Environment. Technology. Resources”. *Vol.1*, Latvia, Rēze-kne, 2013. Rēzekne: Rēzeknes Augstskola, RA izdevniecība, 2013, ISSN 1691-5402, ID in database – 16424, pp.137-139.

[9] Nikolova, N., Information man under the knowledge change conditions – SATERRA 2001, Journal of the University of Applied Sciences Mittweida, SATERRA 2001, Band II, p.33-38, Internationale Wissens chaftliche Konferenz, ISSN 1437-7624

[10] Nikolova, Neli, Intellectual Capital Management used for Optimizing the Activities of Modern Small and Medium Enterprises/Companies. 4th International Conference Econo-mics and Management-Based on New Technologies, EMoNT 2014, 12-15 June 2014, Vrnjačka Banja, Serbia., pp.258-262, ISBN 978-86-6075-045-9.

[11] Nikolova, Neli, Entrepreneurial “Blue” Practices for Sus-tainable Development and Resources Efficiency, 12th Inter-national Scientific and Practical Conference “Environment. Technology. Resources”, June 20-22, 2019, Rezekne Academy of Technologies, Rezekne, Latvia, Volume I, 198-203, ISSN 1691-5402, ISSN 2256-070X.

[12] Petrova, D., Analysis of SMEs in Bulgaria – Assessment of Their Innovation Activities, Rezekne 2013, Latvia, Rezekne Higher Education Institution, Faculty of Engineering, Scientific Institute for Regional Studies, Environment. Technology. Resources, Proceedings of the 9th International Scientific and Practical Conference June 20-22, 2013, Volume 3, ISSN 1691-5402,pp 46-49. scopus

[13] Petrova, D., Intelligent, Innovative and Sustainable Industry in Bulgaria – Prospekts and Challenges, Environment. Technology. Recourses – Proceeding of the 12-th International Scientific and Practical Conference, Rezekne Academy of Technologies, Rezekne, Latvia, 2019, ISSN 1691-5402, p. 210-215.

[14] Tomchev, P., N., Nenov, R., Ivanova, Instantaneous water heater with induction heater operating with grid frequency, „Research and Development in Mechanical Industry“ RaDMI 2012, 13-17 September 2012, Vrnjačka Banja, Serbia, SaTCIP Ltd., Technical-Mechanical School in Trstenik, ISBN 978-86-6075-036-7, Volume II, pp. 1214-1218.

[15] http.www.mee.government.bg

[16] http.www.eib.org

[17] http.www.mag.innov.ru

Environment. Technology. Resources. Rezekne, Latvia
Proceedings of the 13th International Scientific and Practical Conference. Volume 3, 281-285

Resonant Electromagnetic Processes at Unstable Operation of Sliding Current Collector Units of Turbogenerator

Igor Plokhov
Department of Electric Power Engineering, Electric Drive and Automation Systems
Pskov State University
Pskov, Russia
igor_plohov@list.ru

Igor Savraev
Department of Electric Power Engineering, Electric Drive and Automation Systems
Pskov State University
Pskov, Russia
igor_savraev@mail.ru

Alexander Ilyin
Department of Electric Power Engineering, Electric Drive and Automation Systems
Pskov State University
Pskov, Russia
al.ilyin@yandex.ru

Oksana Kozyreva
Department of Electric Power Engineering, Electric Drive and Automation Systems
Pskov State University
Pskov, Russia
ks_33n@mail.ru

Alexander Dementiev
Institute of Engineering
Pskov State University
Pskov, Russia
techno@pskgu.ru

***Abstract* - The article is devoted to study of the resonance electromagnetic oscillations arising during unstable operation of the sliding current collection unit of turbo-generators. Mathematical modeling of these processes is carried out. It has been established that it is these processes that are the main cause of increased sparking and "ring fire" or "breakdown of commutation" on contact rings.**

Keywords* - *sliding current collector units, resonance, mathematical model, computer simulation.

I. INTRODUCTION

The operation of sliding electrical contacts (SC) is accompanied by mechanical vibrations causing modulation of current flowing through the contact. If the disturbing influences exceed pressing force on the brush, the current transmission becomes unstable, currentless pauses appear [1]. During the operation of parallel sliding electrical contacts, specified disturbances can occur simultaneously at some part of brushes.

In DC electric machines, the main cause of brush sparking is the commutation process. For current collector assemblies with slip-ring contacts, the causes of sparking have so far not been adequately explained. Attempts to explain the sparking on the contact rings [2] boil down mainly to the fact that due to the high current density in the transition layer of SC causes melting and evaporation of the surface layers of the contact parts, leading to the release of red-hot particles in the direction of rotation of the contact rings (CR). However, the release of particles occurs only at very high levels of sparking. It is impossible to explain in the indicated way the most common point sparking and increased sparking under the entire running edge of the SC without the release of sparks. In addition, thermal calculations show [3] that the temperatures of contact clusters in the transition layer of SC very rarely reach the melting and evaporation temperatures of SC materials (steel and graphite: 1500–3200 °C, 3900–4200 °C). A spark discharge cannot occur when the voltage drop on the contact is 2.5–3 V. To ensure the breakdown of the air gap and dielectric surface membranes, kilovolts of voltage are required, which occur in the modes of parametric resonances. There is a very indicative practical case of fighting the circular fire, which leads to the conclusion about insufficiency of theoretical substantiation of causes of increased sparking and circular fire [2, 4, 5]. At the request of the management of the power plant, the

Online ISSN 2256-070X
https://doi.org/10.17770/etr2021vol3.6530

authors of this brochure [2] did not indicate the reasons for the occurrence of an all-round fire in the brush-contact apparatus of a new turbogenerator with a capacity of 500 MW, despite promptly accepting (flow-through, "repolarization", sealing of the brush-contact apparatus (BCA), purging, cleaning of a ring, replacement of brushes and etc.). Sparking on the negative ring appeared in January 2010 and was observed constantly, despite the measures taken. After 1.5 months, an emergency shutdown occurred due to strong sparking on the negative (inner) ring. The slip rings were sanded, the polarity was changed (the outer ring – negative, the inner one – positive), and the EG-2AF1 type brushes were replaced with 611OM type brushes. Since oil from the bearing had previously penetrated into the BCA measures were taken to prevent oiling of the rings. Then the second emergency shutdown of the generator occurred 10 days after the first due to strong sparking also on the negative (in this case, already on the outer) ring. Again the rings were polished and the polarity of the rings reversed (the outer ring – plus and the inner ring – minus.).To prevent possible oil ingress into the BCA, a new sealing of BCA was installed on the bearing side, an oil trap was upgraded, and cloth filters were installed at the air inlet to the BCA. However, the measures taken did not give any result and the third emergency shutdown occurred due to the all-round fire again on the negative slip ring 9 days after the second shutdown. Its vibration before the shutdown was 298–320 microns. The wear of the brushes on the ring was increased: they fell into disrepair 2 hours after installation. After the turbogenerator was stopped, the inner ring was sanded again. As a result, due to repeated grinding, its diameter has decreased unacceptably. The serviceability of thyristors was repeatedly checked. There were no comments relating to any faults. A transition was made from the working excitation to the reserve (electric machine exciter), but the sparking was not eliminated. After 7 months after the repairs carried out, strong sparking reappeared due to which the generator had to be stopped.

This practical example clearly shows that there are hidden reasons for increased sparking and all-round fire that are not described in instructions and other literature. The authors of this paper found that these reasons are high-amplitude parametric resonances in the electromagnetic circuits of the BCA. When the sparking brushes were shunted with a damping capacitance, the sparking almost completely disappeared, which indicates the importance of electromagnetic resonance causes of sparking [6, 7].

Practice shows that sparking on contact rings usually occurs with unbalanced distribution of current over parallel brushes [8], low quality of contact surface of the rings and increased vibration of the electric machine. These factors are external visible causes of sparking, but it is more important to identify internal energy release mechanisms in the contact layer. This will allow the development of new methods for reducing sparking in the BCA of the turbogenerator.

As the measurements show, the sliding contact has an electric capacity which varies within thousands and hundreds of μF depending on the type of brush and its mode of operation. The "direct" contact intervals are characterized by the largest value of contact capacity, which is shunned by the small transition resistance of one hundred and one thousand fractions of Ohm for various SC. In case of contact failure, the flow of power current in the transition layer is practically stopped, the transition resistance reaches units and tens of kOhm, and the contact capacity is reduced due to the increase in the distance between the contacting micro-reliefs. In addition, the current conductors, together with the accompanying current conducting elements, have a resistance of micro-Ohm and an inductance ranging from one to hundreds of micro-Henry.

II. SIMULATION OF THE DYNAMICS OF CURRENT DISTRIBUTION

Based on the above considerations, we will construct an design model of the group SC. The brushes are divided into two groups: 1) contacting continuously; 2) contacting with the probability of current transmission failure.

Let's consider the replacement scheme of the sliding current collector unit (SCCU) of the turbo generator and its mathematical description.

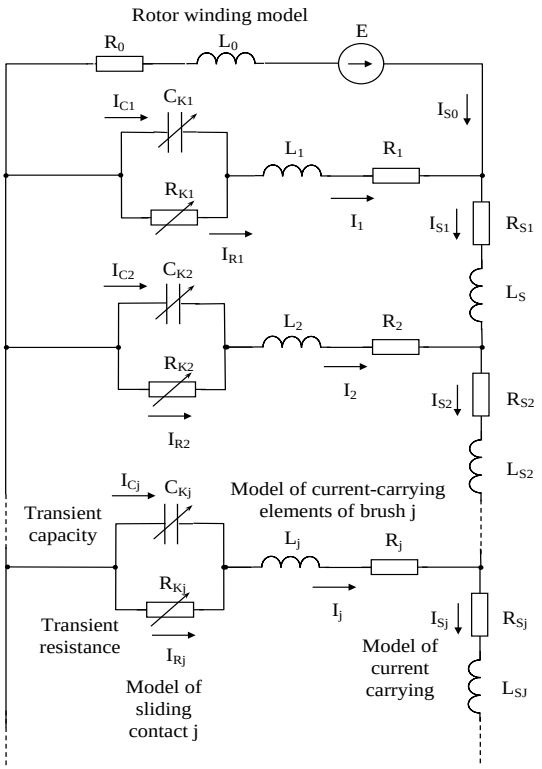

Fig. 1. General replacement scheme of sliding current collection unit.

The dynamics of current distribution will be described by the system of differential equations

$$\begin{cases} I_0R_0 + L\frac{dI_0}{dt} + I_1R_1 + L\frac{dI_1}{dt} + I_{R1}R_{K1} = E \\ I_{j+1}R_{j-1} + L_{j-1}\frac{dI_{j-1}}{dt} + I_{Rj-1}R_{Kj-1} - \\ -I_jR_j - L_j\frac{dI_j}{dt} - I_{Rj}R_{Kj} - I_{Sj-1}R_{Sj-1} - \\ -L_{Sj-1}\frac{dI_{Sj-1}}{dt} = 0 \\ I_jR_j + L_j\frac{dI_j}{dt} + I_{Rj}R_{Kj} - I_{j+1}R_{j+1} - \\ -L_{j+1}\frac{dI_{j+1}}{dt} - I_{Rj+1}R_{Kj+1} - I_{Sj}R_{Sj} - \\ -L_{Sj}\frac{dI_{Sj}}{dt} = 0 \\ I_{Sj-1} - I_j - I_{Sj} = 0,\ \sum_j I_j - I_0 = 0 \\ I_{Rj}R_{Kj} - \frac{1}{C_{Kj}}\int U_{cj}dt = 0 \end{cases} . \quad (1)$$

Parameters R_{Kj} and C_{Kj} are transient resistance and SC capacity depend on contact pressure, which is modulated by kinematic perturbation effects:

For simplicity, let's consider the characteristics of the system with two SC in a parallel branch, each of which can be represented as a synchronously operating group of contacts. Moreover, in the process of simulation we will conditionally set the transient resistance and capacity of the stable group of brushes constant, and for the unstable group we introduce modulation of these parameters: sinusoidal, polyharmonic, relay or pulse.

The scheme of replacement of the CCU comprising two brushes in a parallel branch is shown in Fig. 2.

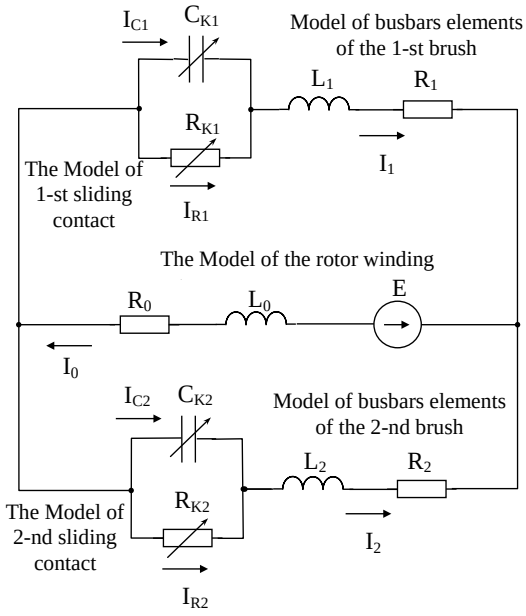

Fig. 2. The scheme of replacement of sliding current collection unit comprising two sliding contacts or two groups of SC.

Let's describe the dynamics of current distribution by the system of integro-differential equations

$$\begin{cases} I_1R_1 + L_1\frac{dI_1}{dt} + I_{R1}R_{K1} + I_0R_0 + L_0\frac{dI_0}{dt} = E \\ I_2R_2 + L_2\frac{dI_2}{dt} + I_{R2}R_{K2} + I_0R_0 + L_0\frac{dI_0}{dt} = E \\ I_{R1}R_{K1} - \frac{1}{C_{K1}}\int_0^T I_{C1}dt = 0 \\ I_{R2}R_{K2} - \frac{1}{C_{K2}}\int_0^T I_{C2}dt = 0 \\ I_1 + I_2 - I_0 = 0 \\ I_1 - I_{C1} - I_{R1} = 0 \\ I_2 - I_{C2} - I_{R2} = 0 \end{cases} . \quad (2)$$

We will bring this system to the operator form

$$\begin{cases} I_1(p) = \frac{1}{p}\frac{1}{L_1}[E - I_1(p)R_1 - \\ -I_{R1}(p)R_{K1} - I_0(p)R_0] - I_0(p)\frac{L_0}{L_1} \\ I_2(p) = \frac{1}{p}\frac{1}{L_2}[E - I_2(p)R_2 - \\ -I_{R2}(p)R_{K2} - I_0(p)R_0] - I_0(p)\frac{L_0}{L_2} \\ I_{R1}(p) = \frac{1}{p}I_{C1}(p)\frac{1}{R_{K1}C_{K1}} \\ I_{R2}(p) = \frac{1}{p}I_{C2}(p)\frac{1}{R_{K2}C_{K2}} \\ I_0(p) = I_1(p) + I_2(p) \\ I_{C1}(p) = I_1(p) - I_{R1}(p) \\ I_{C2}(p) = I_2(p) - I_{R2}(p) \end{cases} . \quad (3)$$

Using equations (3) we will construct a dynamic simulation model in the environment SIMULINK MATLAB (Fig. 3).

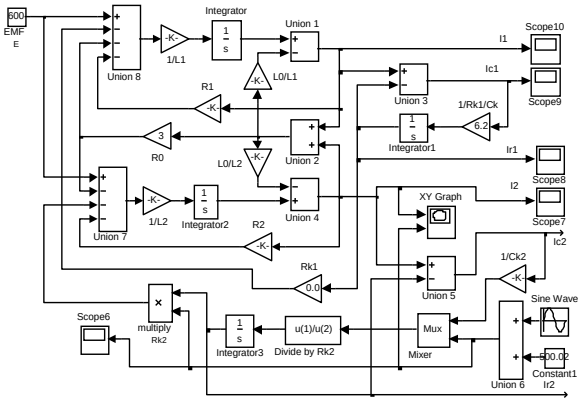

Fig. 3. Simulink-model of a current collection node with two SC or two groups of SC.

The model allows us to study dynamic processes occurring in parametric perturbations of various types. In this figure, in particular, a sine wave generator with a constant offset is used, the signal of which modulates the transient resistance of the brush. Under certain conditions, the system loses stability. As shown by the computational experiments the loss of stability and the sharp increase in the amplitudes of oscillating processes of current transmission are bound to the increase of instability of brush contact.

As an example, Fig. 4 shows the phase current trajectory $I_2(t)$ on the XY Graph plotter (Fig. 3) with a

sinusoidally pulsating law of transient resistance variation of the second brush $R_{K2}(t)$ within 0.02–1000 Ohm.

The oscillations of the output value (Y axis) in a very short time acquire an amplitude exceeding 1000 A at a frequency of at least 1 MHz.

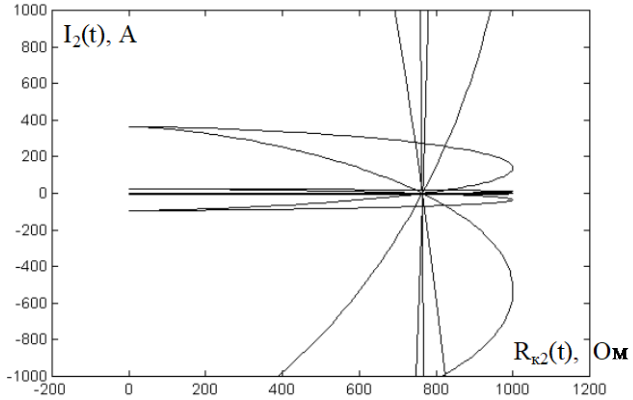

Fig. 4. Phase current trajectory $I_2(t)$ calculated using the Simulink-model. It illustrates the characteristic picture of the development of divergent self-oscillating current distribution process in CCU.

Frequency dependency analysis shows that the system has resonance peaks the location and configuration of which depends on the R_{K2} and C_{K2} parameters. Since in the course of operation there is practically a relay periodic change of the specified parameters, which causes a change of all basic characteristics, the CCU can be classified as a class of dynamic systems with a variable structure (VSS) [8].

In our case, all the subsystems of the VSS being analyzed are stable, while the aggregate system is unstable in certain modes. This is due to the fact that the system has nonlinear characteristics of structural units and it is open. In open stochastic systems, synergistic phenomena associated with the formation of self-developing structures or processes arise under certain conditions [9] – [10]. The increase in quantitative changes can occur in an avalanche-like manner and with weak limiting factors lead to the destruction of the structure of the object.

Various computer simulation systems were used in the simulation process. The mode of divergent self-oscillating current distribution (DSCD) was revealed for all models.

III. DSCD Mode as a Cause of Circular Fire on Contact Rings

A series of computational experiments using the Electronics Workbench simulation system from Interactive Image Technologies (Canada) was conducted to confirm the results and study the properties of the model.

It can be seen from the plots obtained during the simulation that the currents of brush groups in the mode of unstable contact take high instantaneous values exceeding nominal values by tens and hundreds of times. In addition, as shown by calculations higher harmonics of vibration acceleration have a major influence on the magnitude of current emissions. In this connection, the effect of frequency and duty cycle of regular SC disorders on the dynamic current distribution process was investigated (Fig. 5 and Fig. 6).

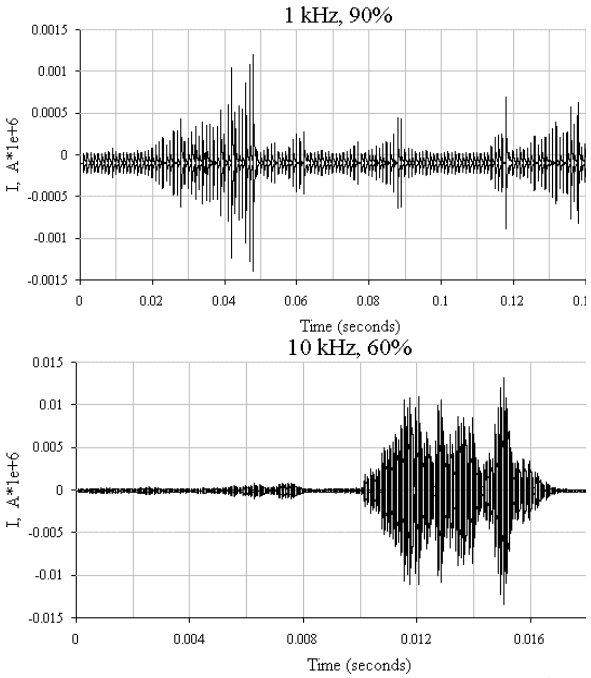

Fig. 5. Dynamic current distribution with regular disturbances of the sliding contact.

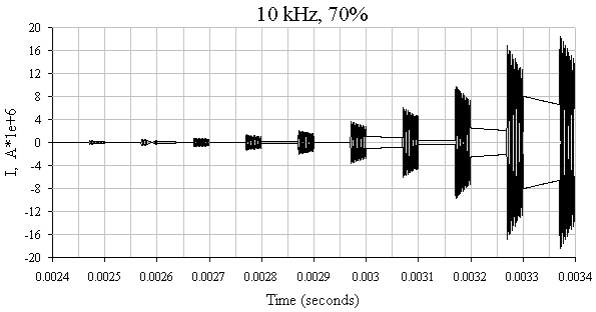

Fig. 6. Divergent process of dynamic current distribution.

Each of these graphs shows two curves, one shows the change in the current of the stable group of brushes, and the other demonstrates unstable current transmission with regular contact violations.

Based on the results of their analysis it can be said that there are combinations of duty cycle and frequency of contact violations in which current amplitudes reach very large values. Such processes should be accompanied by strong sparking of sliding contacts. In addition, a number of results were obtained in which the oscillatory process of dynamic current distribution became divergent, i.e. the system lost the stability.

To clarify the nature and dynamics of current distribution over several brush sets in conditions of unstable contact, the model was complicated. Five brush sets exposed to polyharmonic vibration accelerations, shifted in phase relative to each other in accordance with the placement of the sets along the perimeter of the contact

ring, were introduced into consideration. The results obtained in this case confirmed the possibility of developing DSCD processes at certain harmonic perturbation compositions.

IV. CONCLUSIONS

From the foregoing, it follows that diverging resonant electromagnetic processes of this type are one of the main electromagnetic causes of the occurrence of circular fire or "breakdown of commutation" at the contact rings of turbogenerators. Moreover, the probability of developing a divergent self-oscillating current distribution (DSCD) is the higher, the greater the instability of the contact of the BCA.

The result of the theoretical and experimental studies was the development of a method and a device for reducing sparking on the contact rings of the turbo-generator and excluding the emergency mode of the DSCD by introducing damping capacities into the electromagnetic circuits of the current collection unit, which reduce the amplitude of electromagnetic oscillations [13, 14].

It is possible to recommend the introduction of the above technique for analyzing the regions of electromagnetic resonances and a device for suppressing the sparking of the BCA for large power turbine generators.

REFERENCES

[1]. Mechanics of sliding contact / V.I.Nellin, N.Y.Bogatyrev, L.V.Lozhkin et al. – M.: Transport. 1966. 255 p. (in Russian).

[2]. Samorodov Y. N. Paradoxical properties of sliding contact in BCA. – M.: NTF "Energoprogress", 2013.56 p. (in Russian).

[13]. Device for reducing spark formation in the node of a sliding current collector / Plokhov I. V., Ilyin A.V., Isakov A. N., Kozyreva O. I. Patent for utility model No. 132630, publ.: 2013.09.20. (in Russian).

[14]. Device for reducing sparking in the sliding current collector assembly / Kotkov N. A., Plokhov I. V., Kozyreva O. I., Ilyin A.V., Savraev I. E. Patent for invention No. 2685695, publ.: 23.04.2019. (in Russian).

[3]. Ilyin, L., Plokhov I., Kozyreva, O., and etc. Synergetic model of electro-friction interaction. Environment. Technology. Resources. Rezekne, Latvia. Proceedings of the 12th International Scientific and Practical Conference, June 20–22, 2019. Volume III. P. 208–213, http://dx.doi.org/10.17770/etr2019vol3.4072

[4]. Typical instructions for the operation and repair of the slip ring assembly and brush apparatus of turbine generators with a capacity of 63 MW and above. RD 153-34.0-45.510-98. M.: SPO ORGRES, 2000. (in Russian).

[5]. Braude L. I., Borozinets B. V., Maslov V. V. Operational control of serviceability of brush-contact devices of turbogenerators. – Electric power stations, 1998, No. 1. (in Russian).

[6]. Oksana Kozyreva, Igor Plokhov, Nikita Kotkov, and etc. Experimental investigations of effect of LC-circuits on sparking and thermal state of sliding electric contact unit. Environment. Technology. Resources, Rezekne, Latvia, Proceedings of the 11th International Scientific and Practical Conference. Volume III, 2017. P.150–153, http://dx.doi.org/10.17770/etr2017vol3.2575

[7]. Oksana Kozyreva, Igor Plokhov, Igor Savraev, and etc. Reducing sparking in the transient layer of the sliding electrical contact unit. 19th International Scientific Conference on Electric Power Engineering, Brno, Czech Republic, 16–18 May 2018. P.223–227, https://dx.doi.org/10.1109/EPE.2018.8395969

[8]. Popov I. N., Zrazhevsky S. M., Kalmykov A.V. On condition monitoring and tuning of brush-contact devices of turbogenerators. Electronic publication on the website "Electric networks": https://leg.co.ua/arhiv/generaciya/o-kontrole-sostoyaniya-i-nastroyke-schetochno-kontaktnyh-apparatov-turbogeneratorov.html. (in Russian).

[9]. Theory of systems with variable structure // Emelyanov S. V., Utkin V. I., Taran V. A., et al. Ed. Emelyanova S. V. – M.: Nauka. 1970. 592 p. (in Russian).

[10]. Haken G. Synergetrics. M.: World. 1980. 400 p. (in Russian).

[11]. Haken G. Synergetrics Hierarchy of instabilities in self-regulating systems. M.: World. 1985. 419 p. (in Russian).

[12]. Fuller B.R. Sinergetics. N.Y.: MacMillan. 1982. 350 p.

Environment. Technology. Resources. Rezekne, Latvia
Proceedingsofthe 13th InternationalScientificandPractical Conference. Volume 3, 286-290

Optoelectronic Device for Measuring the Power of Laser Radiation

Dimcho Pulov
Department of Mechanical and Precision Engineering
Technical University of Gabrovo
Gabrovo, Bulgaria
pulov@mail.bg

Tsanko Karadzhov
Department of Mechanical and Precision Engineering
Technical University of Gabrovo
Gabrovo, Bulgaria
karadjov_s@abv.bg

***Abstract* - A device for measuring the power of the laser radiation.has been designed. The device consists of transmitter and receiving part. The transmitter includes optical radiation source and optical system for collimation of radiation. The receiver part consists of silicon photodiodes, electronic signal processing unit and unit for measurements.**

Keywords - Gaussian laser beam; Galilean beam expander; receiver the laser source ; photodiodes

I. INTRODUCTION

Lasers are monochromatic coherent sources of optical radiation characterized by a low degree of divergence and high intensity. These properties determine their wide application in different fields. The power of the laser radiation is of great importance when used for practical purposes. This requires development of new methods and devices for measuring and reducing the power of laser radiation.

II. EXPOSITION

The purpose of this article is to develop a device for measuring the power of high-energy and highly concentrated optical fluxes. Such fluxes are formed during the generation of laser radiation.

The set goal can be achieved by accomplishing the following tasks:

- Development of a block functional diagram of the device;
- Development of the optical diagram of laser beam expander;
- Development schematic electrical diagram of the device.
- Development of the algorithm of the control program

A. Spatial profile of the laser beam

The design of the optical laser systems to a certain extent repeats that of the classic optical devices but taking into account the features of laser radiation [5], [8], [18]. Such a feature is the spatial structure of the laser beam. In its consideration the concept of Gaussian beam is of fundamental importance. This is a beam in the cross section of which the energy is distributed according to Gauss's law (Fig. 1). The Gaussian beam corresponds to the fundamental mode TEM_{00} which is formed by a stable resonator with an arbitrary configuration. Its intensity in the cross section is determined by the expression

$$I(r) = I(0)\cdot e^{-2\left(\frac{r}{\omega}\right)^2} = \frac{2P}{\pi[\omega(z)]^2}\cdot e^{-2\left(\frac{r}{\omega}\right)^2}$$

where: r is a radial distance from the axis of the beam; $I(r)$ and $I(0)$ are the intensity of the beam at distance r and the axis ; ω is beam radius at which the intensity decreases e^2 times; P is the full power of the beam

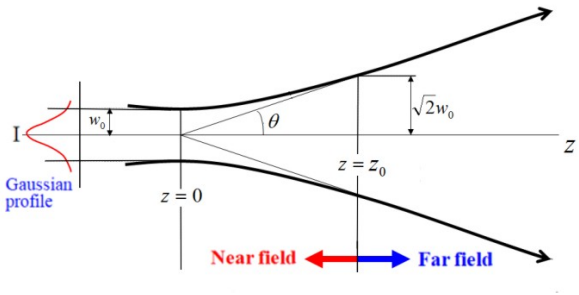

Fig. 1. Spatial profile of the Gaussian laser beam

Online ISSN 2256-070X
https://doi.org/10.17770/etr2021vol3.6590

Laser beams are coherent and their propagation in space is described by the laws of diffraction. Depending on the longitudinal distance z there is Fresnel diffraction (near zone) and Fraunhofer diffraction (far zone). The Rayleigh range ($z = z_0$) is taken as the notional line between the two zones. The Rayleigh range represents the distance from the waist of the beam at which its radius increases $\sqrt{2}$ times, and the area of its cross section – 2 times.

In the near zone Gaussian beam will at first get closer to the axis and reach a minimum cross section in the waist of the beam, where its radius is

$$\omega_0 = \omega(z=0) = \sqrt{\frac{\lambda z_0}{\pi}}$$

After the waist the Gaussian beam undergoes a diffraction divergence and moves away from the axis. Its cross section increases and in the far zone at distance z from the waist the beam radius assumes the value

$$\omega_z = \omega_0 \sqrt{1+\left(\frac{z}{z_0}\right)^2}$$

The wave front of the oscillations occurring in the resonator in the paraxial region is spherical. The radius of the wave front depends on the longitudinal coordinate z and is determined by the expression

$$R_z = z\left[1+\left(\frac{z_0}{z}\right)^2\right] \qquad (1)$$

It follows from (1) that at a distance $z = z_0$ the radius of the wave front is minimal and has a value $R_z = 2z_0$. This corresponds to a spherical wave front. As z decreases and increases the radius R_z increases. R_z increases faster when z decreases. The wave front is flat in the waist of the beam ($z = 0$).

The spatial structure of the Gaussian beam during its propagation in space for level $1/e^2$ is given by hyperbolic isophotes. The asymptotes of the enveloping hyperbolas make an angle θ with the axis of the beam. This angle is equal to the angle of diffraction of the fundamental mode TEM_{00} in the far zone. The angle θ describes the divergence of the beam in the far zone ($z >> z_0$) and can be expressed as

$$\theta = \frac{\lambda}{\pi\omega_0} \qquad (2)$$

The full divergence of the beam is $\Theta = 2\theta$.

It follows from expression (2) that the smaller the waist of the beam the greater the divergence of the beam. Therefore, to form a well collimated beam, it is necessary to reduce its divergence at the expense of increasing its cross section.

B. Block functional diagram of the device

The optoelectronic device for measuring the power of laser radiation consists of a transmitting and receiving part [9], [11], [16], [17]. The transmitting part includes laser source and collimating optical system. A laser is used as radiation source. The collimating system is an afocal optical system which acts as a beam expander while reducing its angular divergence. The receiving unit consists of silicon photo receivers, an electronic processing unit and a unit for visualization of measurement result. Fig. 2 shows a block chart of the device.

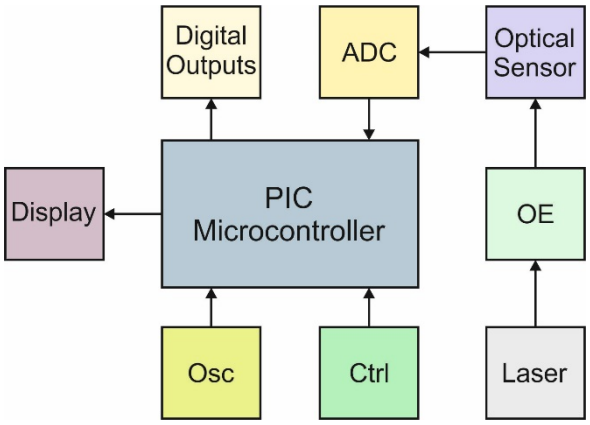

Fig. 2. Block chart of an optoelectronic device for measuring the power of laser radiation

C. Beam expander

When designing the optical system (OS) of the laser, it is assumed that the source of radiation is at infinity and its angular dimensions are determined by the divergence of the beam [3], [4], [12], [13], [14]. In order to achieve optimal coordination between the laser and the optical system it is necessary to place the entrance pupil of the optical system in the area of the beam waist [1], [7], [10], [15].

The main task of the OS is to expand the input beam by some coefficient M defined by the ratio of the diameters of the beam waist after the expander and before the expander. This can be achieved by reducing the divergence of the output beam. Such conversion of the laser beam can be achieved by using telescopic afocal reversing system. There are two types of such systems: Galilean and Keplerian. Galilean system was chosen on the basis of the following advantages:

a) Lack of internal focus. This avoids the production of high energy densities, which is important when using high power sources.

b) The first element in Galilean system is negative and it has a positive spherical aberration. The second element is positive and its spherical aberration is negative. Thus, with correct selection of optical forces and shape of

the elements, it is possible to easily obtain a system with corrected spherical aberration.

c) Galilean system is more compact.

Propagation of a Gaussian beam through an Galilean expander is shown in Fig. 3. The first element (Lens 1) focuses the beam in its focal plane. Its purpose is to reduce the cross section of the beam waist. In Galilean system, the first element is negative and therefore the waist after it is virtual and located on the left.

The divergence of the beam before lens 1 is determined by expression (2). The radius of the waist after the first element is

$$\omega'_0 = \frac{\lambda}{\pi\omega_0} \cdot f'_1$$

The divergence of the beam after the first lens is

$$\theta' = \frac{\lambda}{\pi\omega'_0}$$

After lens 1 the beam increases its divergence. The purpose of the second element (lens 2) is to reduce the divergence and to collimate the beam radiation. For this reason, the beam waist after lens 1 is located in the rear focal plane of lens 2. The focal distance f'_2 of lens 2 is selected from the required expansion M and the degree of beam collimation to be achieved. The greater the f'_2 the greater the beam expansion and the smaller the divergence. The beam waist after lens 2 is determined by the expression

$$\omega''_0 = \frac{\lambda}{\pi\omega'_0} \cdot f'_2$$

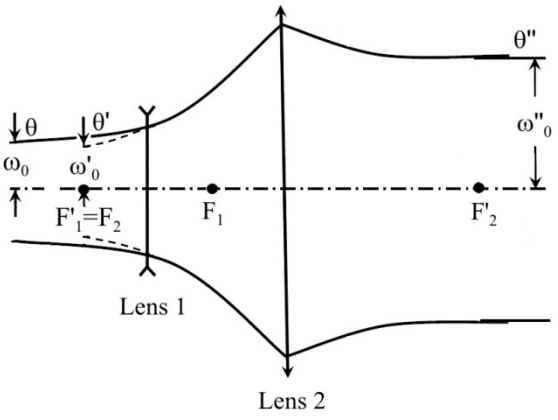

Fig. 3. Propagation of a Gaussian beam through an Galilean expander

The beam divergence after the second lens is

$$\theta'' = \frac{\lambda}{\pi\omega''_0}$$

Therefore the coefficient of expansion can be written as follows:

$$M = \frac{\omega''_0}{\omega_0} = \frac{f'_2}{f'_1} = \frac{\theta}{\theta''}$$

Fig. 4 shows the optical diagram of the designed beam expander, and Table 1 shows its design parameters. The expander has an magnification $M = 5^x$, his diameter of the entrance pupil is 3 mm and diameter of the exit pupil is 15 mm.

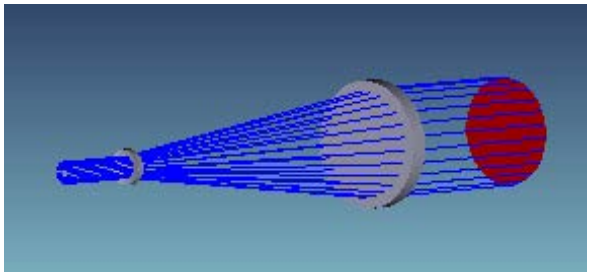

Fig. 4. Optical scheme of the Galilean expander

TABLE 1 GALILEAN EXPANDER DESIGN PARAMETERS

Surface		Radius	Thickness	Glass
Lens 1	***1***	-4,4	0,76	N-SF8
	2	-8,45	48,64	
Lens 2	***3***	∞	3,35	N-SF8
	4	-44,72		

The optical system of the designed expander does not form images of complex objects, but only transmits the laser radiation energy. Therefore, the main requirements for its quality are not related to transmitting fine structure of the image, but to the implementation of the necessary expansion and minimization of the divergence of the output laser beam.

The Marechal criterion $W_{RMS} > \frac{\lambda}{14}$ is used to evaluate the quality of the expander. The RMS value of the wave aberration at the output of the expander is $W_{RMS} = 0{,}007\lambda$. Therefore, it can be assumed that it is of diffraction-limited quality. In Fig. 5 the OPD graph is shown at the output of the expander.

D. Schematic electrical diagram of the device

Fig. 6 shows the schematic electrical diagram of the device. Precision high speed TSL254 light-to-voltage converters are used as photo receivers.

These converters consist of silicon photodiode with photosensitive area 1mm and high impedance operational amplifier with $1M\Omega$ feedback resistor. The output voltage is proportional to the illuminance. Fig. 7 shows the diagram of the photo converter. The sensitivity of the sensor is $60\,{}^{mV}\!/_{\mu W/cm^2}$ at $\lambda = 880nm$.

Fig. 5. OPD graph of the expander

An 8 bit PIC18F452 microcontroller is used to control the operation of the device, which has a 10 bit analog-to digital converter. The threshold voltages that determine the measuring range of the analog-to-digital converter are $V_{REF} = 0V$ and $V_{REF+} = 5{,}12V$ respectively and are applied to terminals RA2 and RA3. The input analog signal that enters the ADC is represented by 210 or 1024 levels. The step of voltage increase is determined by the formula:

$$\Delta U = \frac{U_{REF+}}{2^{10}} = \frac{5{,}12}{1024} = 5mV$$

Four photo converters are included in the functional diagram of the device. The measured power is proportional to the average voltage of the photo converters. The voltages at the output of the photo converters are determined when calibrating the device – which values of the laser radiation power they correspond to and accordingly to be entered as correction coefficients in the control program [2,6].

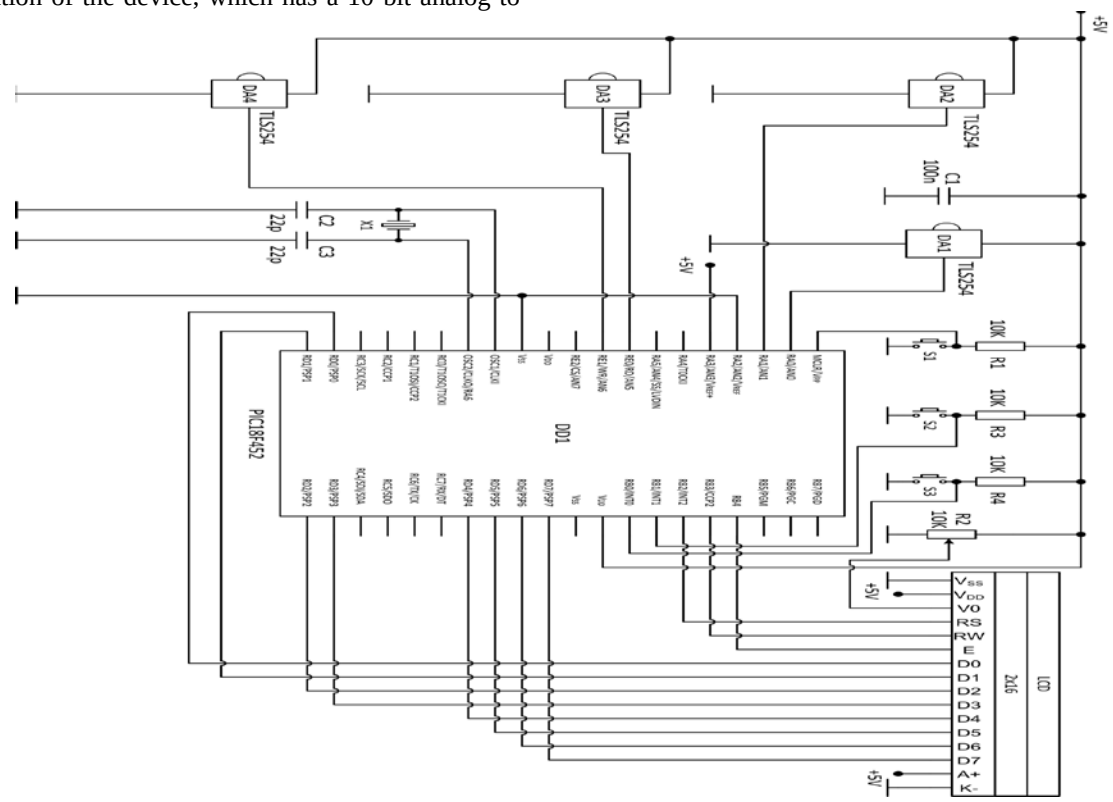

Fig. 6. Schematic electrical diagram of the device

E. Block chart of the algorithm of the program

The block chart of the algorithm of the control program is shown in fig. 8. At the beginning, the controller is initialized, constants and variables are defined and the corresponding cells from data memory are reserved for them. The next stage of the program is related to determining the input/output ports used. The pins of the microcontroller that will be digital inputs, analog inputs and digital outputs respectively are defined. PIC18F452 has 4 internal timer modules.

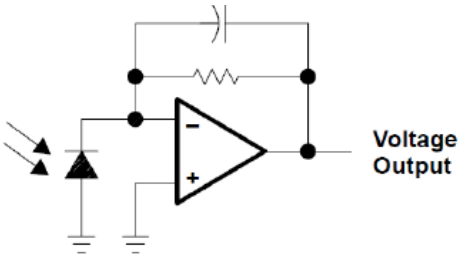

Fig. 7. Diagram of the photo converter

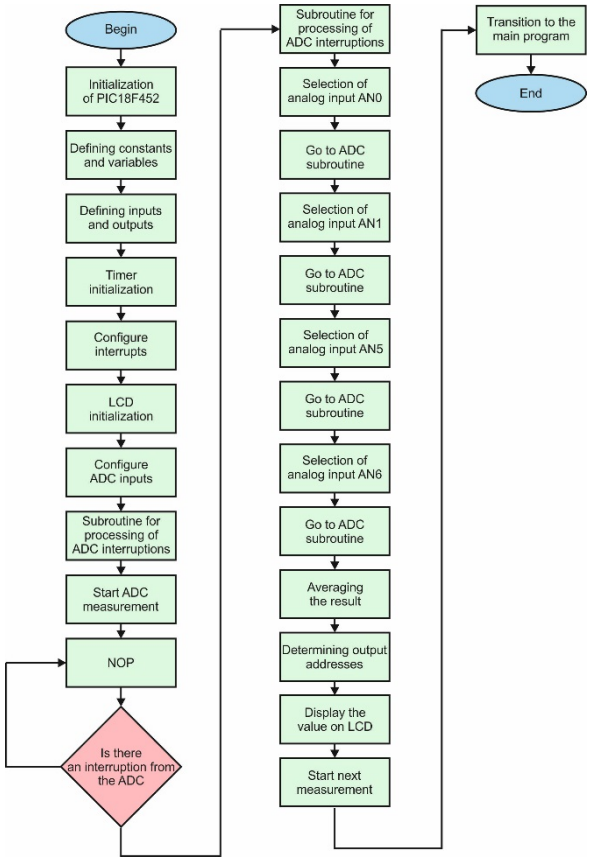

Fig. 8. Block chart of the algorithm of the program

Only Timer 1 is used. It sets time delays in the program which are used to synchronize the operation of the microcontroller and the alphanumeric liquid crystal display. Next, an initialization of the display is performed. The main program is a continuous cycle which stops only when the voltage measurement from the ADC has been completed. The processing of the result of each measurement takes place in a subroutine which starts when an ADC interrupt occurs.

III. Conclusion

Optoelectronic device for measuring laser radiation power has been developed. 5^x Galilean beam expander which has a low divergence has been designed. A scheme with four photo receivers has been used, which increases the measurement accuracy compared to a single photo receiver.

References

[1] G. I. Cukanova,A. V. Baholdin, Specialnie razdeli prikladnoj optiki,SPb,GUITMO, 2007.

[2] D. Dichev, H. Koev, T. Bakalova and P. Louda, "A Measuring Method for Gyro-Free Determination of the Parameters of Moving Objects", Metrology and Measurement Systems, Vol. 23, Issue 1,2016, pp. 107-118, DOI: 10.1515/mms-2016-0001.

[3] H.J. Eichler, J. Eichler and O. Lux, Lasers: Basics, Advances and Applications, Springer Series in Optical Sciences, Springer Nature Switzerland AG, 2018.

[4] I.A. Konyakhin, A. Merson, A.N. Timofeev and A.I. Konyakhin , „Optoelectronic system on the base of the anamorphic element for the measuring of the elevation angles", in Proc. of SPIE, Sixth International Symposium on Precision Engineering Measurements and Instrumentation 2010, Vol. 7544, p. 75443N, DOI: 10.1117/12.885594.

[5] L. Lazov, N. Angelov, E. Teirumnieks, Method for Preliminary Estimation of the Critical Power Density in Laser Technological Processes, Proceedings of the 12th International Scientific and Practical Conference, Rezekne, Latvia, 2019, Vol. 3, pp. 129 -133, DOI: 10.17770/etr2019vol3.4140.

[6] N. Kenarov, PIC mikrokontroleri – chast 2,Mlad konstruktor, Varna, 2006.

[7] Siegman, A.E., Lasers, Oxford University Press, University Science Books, Oxford, England, 1986.

[8] Yu. M. Klimkov, Prikladnaya lazernaya optika, Moskva, Mashinostroenie, 1985.

[9] D. Dichev, H. Koev, T. Bakalova and P. Louda, "A Gyro-Free System for Measuring the Parameters of Moving Objects", Measurement Science Review, Vol. 14, Issue 5,2014, pp. 263-269, DOI:10.2478/msr-2014-0036.

[10] Pencheva T., D. Pulov, B. Gyoch, M. Nenkov Design of CCD Optical System for Thermal IR Spectral Region. In pr. 29-th International Spring Seminar fn Electronics Technology, St. Marienthal, Germany, Verlag Dr. Markus A. Detert, 2006, pp. 413-418, DOI: 10.1109/ISSE.2006.365380.

[11] D. Shafer, "Laser beam steerer–expander", Applied Optics, Vol. 17, Issue 22, 1978, pp. 3584-3586, DOI: 10.1364/AO.17.003584

[12] M. Scaggs and G. Haas, "Optical alignment influenced aberrations in laser beam delivery systems and their correction", Proc. SPIE 9343, Laser Resonators, Microresonators, and Beam Control XVII, 93430T (March 3, 2015), DOI: 10.1117/12.2076630.

[13] G. Simonova and V. Maximov, „Collimation system design for multi-wavenlength Nd:Yag laser", Interexpo Geo – Siberia, Vol. 5, Issue 3, 2013, pp.63-67.

[14] G. Kohanenko, M. Makogon, Y. Ponomarev, O. Rinkov and G. Simonova, „Calculation of two-wavelength laser beam expander fluorescent lidar", Opticheski zhurnal, Vol. 4, Issue 79, 2012, pp. 28-32.

[15] M. Guo, G. Jin, J. Cai, W. Zhang and Z. Wei, "Study and design of beam expander with wide aperture", Proc. SPIE 9295, International Symposium on Optoelectronic Technology and Application 2014: Laser Materials Processing; and Micro/Nano Technologies, 92950T (December 18, 2014).

[16] Sidney A. Self, "Focusing of spherical Gaussian beams", Applied Optics, Vol. 22, Issue 5, 1983, pp. 658-661, DOI: 10.1364/AO.22.000658

[17] H. Sun, "Thin Lens Equation for a Real Laser Beam with Weak Lens Aperture Truncation", Optical Engineering, Vol. 37, No. 11, 1998, pp. 2903-2913, DOI: 10.1117/1.601877.

[18] D. L. Shealy, "Optical design of laser beam shaping systems," in International Optical Design Conference, 2002 OSA Technical Digest Series (Optical Society of America, 2002), paper IWA2, DOI: 10.1364/iodc.2002.iwa2

Environment. Technology. Resources. Rezekne, Latvia
Proceedings of the 13th International Scientific and Practical Conference. Volume 3, 291-295

Temperature Measurement with Photodiode in Different Operating Modes

Dimcho Pulov
Department of Mechanical and Precision Engineering
Technical University of Gabrovo
Gabrovo, Bulgaria
pulov@mail.bg

Tsanko Karadzhov
Department of Mechanical and Precision Engineering
Technical University of Gabrovo
Gabrovo, Bulgaria
karadjov_s@abv.bg

Abstract - A method for contactless temperature measurement with photodetectors in different operating modes has been developed. It is based on the periodic change of the spectral sensitivity of the photodiode depending on the applied reverse voltage. This is accomplished by switching the photodiode within one measurement from photovoltaic to photoconductive mode. For this purpose, the scheme of the respective electronic key has been developed.

Keywords - contactless measuring of temperature, IR diapason, photovoltaic and photoconductive mode, spectral ratio pyrometer .

I. INTRODUCTION

Temperature is one of the main parameters of most modern production technologies. For this reason, its measurement and control is essential for the correct implementation of the respective technological process. This can be done both by traditional contact methods and by applying non-contact optical methods. The two main ways in which the method of optical pyrometry can be realized: energy and spectral ratio, are described in [4], [7], [10], [12], [14], [16]. For its part, the pyrometers of the spectral ratio can be realized in three variants: with two photodetectors, light-dividing device and narrow-band optical filters; with one tandem photodetector and with a matrix photodetector. It has been shown that in the pyrometers of the spectral ratio the uncertainty can be reduced when measuring the temperature, which arises as a result of:

a) Different distance to the objects and their different shape;

b) Different temperature of the environment;

c) Presence of side background objects in the field of view of the device;

d) Presence of nearby high temperature sources and reflection of their radiation to the device;

e) Obscurity of the radiation coefficient of the objects and its dependence on the temperature and wavelength, i.e. $\varepsilon = f(\lambda, T)$.

All the mentioned pyrometers of the spectral ratio have a significant drawback. They correctly measure the temperature of only gray objects for which $\varepsilon = const$. If the objects are non-gray (selectively radiating), then for them the radiation coefficient will depend on the wavelength, i.e. $\varepsilon = f(\lambda)$. In this case, the ratio between the refractive indices in two narrow spectral ranges $\varepsilon_{\lambda 1} / \varepsilon_{\lambda 2}$ may change and lead to a measurement error. This error will be the greater the steeper the function $\varepsilon = f(\lambda)$ [1],[6]. For some metals it can reach up to 10%.

These disadvantages can be reduced with pyrometer with a single photodiode operating in series in different operating modes.

II. EXPOSITION

The goal of this publication is to develop a spectral ratio pyrometer using only one photodiode operating in two different modes to increase the accuracy and sensitivity of non-contact temperature measurement.

The set goal can be achieved by solving the following tasks:

- Development of a block functional scheme of the pyrometer;
- Development of a schematic electrical circuit diagram of the pyrometer;
- Development of the control program.

Online ISSN 2256-070X
https://doi.org/10.17770/etr2021vol3.6556

A. Essence of the method

It is known that the photodiode can operate in two modes: photovoltaic and photoconductive. There is no external power supply in photovoltaic mode and the photodiode generates photo-EMF. The maximum voltage sensitivity in this mode is

$$S_{U\max} = R_0\left[\frac{S_i I_s}{S_i \Phi_{\max} + I_s}\right] \qquad (1)$$

where: S_i - sensitivity by current; $\Phi_{\max}$ - falling optical flux; I_s - sum of the reverse drift currents of the non-core carriers; R_0 - resistance of $p-n$ junction.

Here

$$R_0 = {kT}/{eI_s}$$

where: e - electron charge; k - Boltzmann's constant; T - temperature of $p-n$ junction.

At room temperature ${kT}/{e} = 0.025V$ and expression (1) is as follows:

$$S_{U\max} = 0.025\left[\frac{S_i}{S_i \Phi_{\max} + I_s}\right]$$

In the photoconductive mode, a reverse voltage supply is connected in series with the photodiode. In this case, a reverse current flows through the photodiode, which is proportional to the optical flux falling on it. The voltage sensitivity in photoconductive mode is defined as

$$S_U = \frac{dU_n}{d\Phi} = S_i R_n$$

where: U_n - voltage drop across the electrical load; Φ - falling optical flux; R_n - load resistance.

Therefore, the voltage sensitivity can be increased if the load resistance increases. In order for the photodiode to operate in linear mode, the maximum load resistance $R_{n\max}$ must be related to the falling optical flux by the expression

$$R_{n\max} = \frac{U_p}{I_\Phi + I_s} = \frac{U_p}{S_i \Phi + I_s}$$

where: U_p is the supply voltage; I_Φ is the photocurrent of non-core carriers (current in the dark).

Then the maximum voltage sensitivity in photoconductive mode is

$$S_{u\max} = \frac{S_i U_p}{S_i \Phi + I_s} \qquad (2)$$

From expressions (1) and (2) the ratio between the sensitivities of the photodiode in photoconductive mode $S_{u\max FC}$ and in photovoltaic mode $S_{u\max FV}$ can be determined

$$\frac{S_{u\max FC}}{S_{u\max FV}} = \frac{U_p}{{kT}/{e}}$$

It is clear that the maximum sensitivity in photoconductive mode is higher than in photovoltaic mode.

Graphs of the spectral sensitivity of the *Hamamatsu S2386* photodiode $S_{FC}(\lambda)$ in photoconductive mode and $S_{FV}(\lambda)$ in photovoltaic mode are shown in Fig.1.

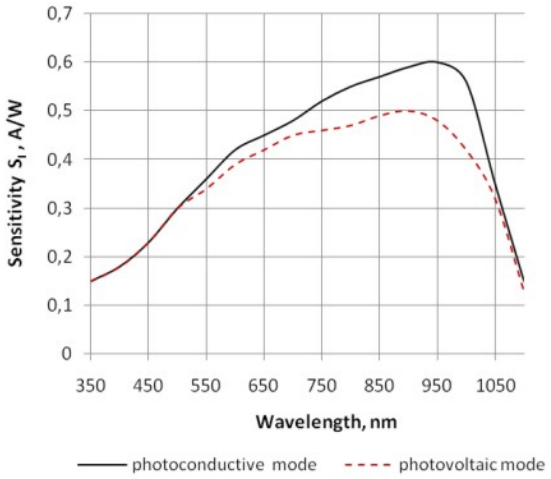

Fig. 1. Spectral sensitivity of the Hamamatsu S2386 photodiode in photoconductive and photovoltaic mode

The spectral sensitivity of the photodiode depends mainly on the properties of the semiconductor material from which it is made [8], [17]. As the reverse voltage increases (switching from photovoltaic to photoconductive mode) the volume charge, the potential barrier height and the $p-n$ junction width increase. All this leads to an increase in the collection coefficient of non-core charge carriers. As a consequence, there is an increase in the maximum of the spectral sensitivity of the photodiode and its displacement in the long-wavelength region [9], [16]. These properties of the photodiode can be used in a pyrometer in order to simplify its design and increase the accuracy and sensitivity of pyrometric measurements [11], [13].

The proposed method consists in the use of one photodiode and in the sequential switching within one measurement of its modes from photovoltaic to photoconductive, whereby its sensitivity and, consequently, the photocurrent flowing through it will be successively changed. In goal to minimize the

methodological error, the operating spectral range will be relatively wide.

The electric current at the output of the photodiode is determined by the expression

$$I(T) = A\int_{\Delta\lambda} M(\lambda,T)S(\lambda)d\lambda \qquad (3)$$

where: $M(\lambda,T)$ - the spectral exitance of the studied object; $S(\lambda)$ - the spectral sensitivity of the photodiode; $\Delta\lambda$ the operating spectral range of the pyrometer; A - coefficient depending on the parameters of the lens, the photodiode and the distance between them.

According to the proposed method, the output signal of the pyrometer K_I will be the ratio of the individual signals received in the two modes of operation of the photodiode

$$K_I(T) = \frac{I_{FC}}{I_{FV}} \qquad (4)$$

where: I_{FC} - photocurrent in photoconductive mode;

I_{FV} - photocurrent in photovoltaic mode.

The pyrometer is graduated according to a reference blackbody radiation source (bb). In this case, according to (3) and (4) it can be written

$$K_I(T) = \frac{\int_{\Delta\lambda_{FC}} M_{bb}(\lambda,T)S_{FD}(\lambda)d\lambda}{\int_{\Delta\lambda_{FV}} M_{bb}(\lambda,T)S_{FV}(\lambda)d\lambda} \qquad (5)$$

where: $M_{bb}(\lambda,T)$ - spectral exitance of the reference.

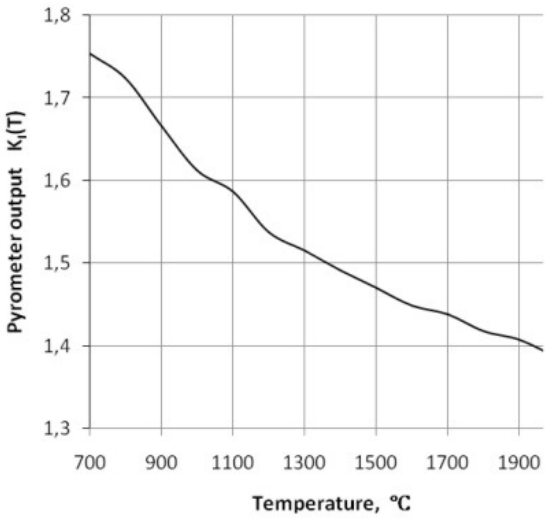

Fig. 2. The dependence $K_I(T)$

According to expression (5) the dependence $K_I(T)$ is drawn, which is shown in Fig. 2.

The total error in the pyrometer of the spectral ratio is determined by the instrumental error, the error of calibration of the pyrometer on a black body, the presence of parasitic reflections and the methodological error caused by the uncertainty of the emission coefficient. The methodological error has the greatest influence. It is shown in [2], [3], [5], [15] that when using wide spectral ranges and near the maxima of the spectral sensitivity of the two photodetectors, the methodological error decreases to 3.5%. The instrumental error is comparable to that of spectral ratio pyrometers using two photodetectors and narrow spectral ranges, as well as tandem and matrix photodetectors.

B. Block functional diagram of the pyrometer

The block functional scheme of the pyrometer is shown in Fig. 3. The lens forms an image of the object under study on the photodiode (*Hamamatsu S2386*). A light filter is situated between the lens and the photodiode that absorbs the radiation in the visible range of the spectrum. The function of the light filter is to eliminate the influence of visible light on the measurement. *FEL070* was selected as a filter from the *Thorlabs* catalog. This is a long-wave cut-off filter that transmits radiation with a wavelength of $\lambda > 750$ nm. The scheme works in two cycles. In the first cycle, the electronic switch S, according to the instructions from the microcontroller, switches the anode of the photodiode to ground. In this case, the photodiode operates in photovoltaic mode. The output current from the photodiode is converted into voltage by an operational measuring amplifier OA. The voltage from the output of the amplifier is converted into digital form by a 10-bit ADC of the microcontroller and stored.

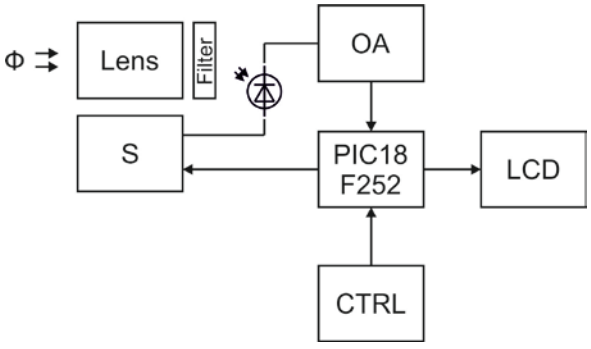

Fig. 3. Block chart of an optoelectronic device for measuring the power of laser radiation

In the second cycle, the electronic switch under the instruction of the microcontroller supplies a negative voltage of $-14V$ to the anode of the photodiode. Then the photodiode operates in photoconductive mode. The output current from the photodiode is similarly converted to voltage, then digitally and stored. After the end of the second cycle, the microcontroller calculates the ratio of the output signals of the photodiode in the two operating

modes. The information from the measured temperature is visualized on a two-line liquid alphanumeric indicator.

C. Schematic electrical circuit diagram

Fig. 4 shows the schematic electrical circuit of the device. An 8-bit PIC18F252 microcontroller with a built-in 10-bit ADC was used to control the operation of the entire device. The controller has a sufficient number of input-output ports, memory for measurement data and program memory, where the control program can be located. The threshold voltages that determine the measuring range are from 0 V to 5 V. The number of digital levels in this range is 210 or 1024 levels. The step of increasing the voltage is determined by the formula:

$$\Delta U = \frac{U_{CC}}{2^{10}} = \frac{5}{1024} = 4.88mV \qquad (6)$$

he voltage from the operational amplifier is fed to the analog input RA2 / AN2. Two consecutive voltage measurements are made at this input and the photodiode is switched synchronously from photovoltaic mode to photoconductive mode via digital output RB7.

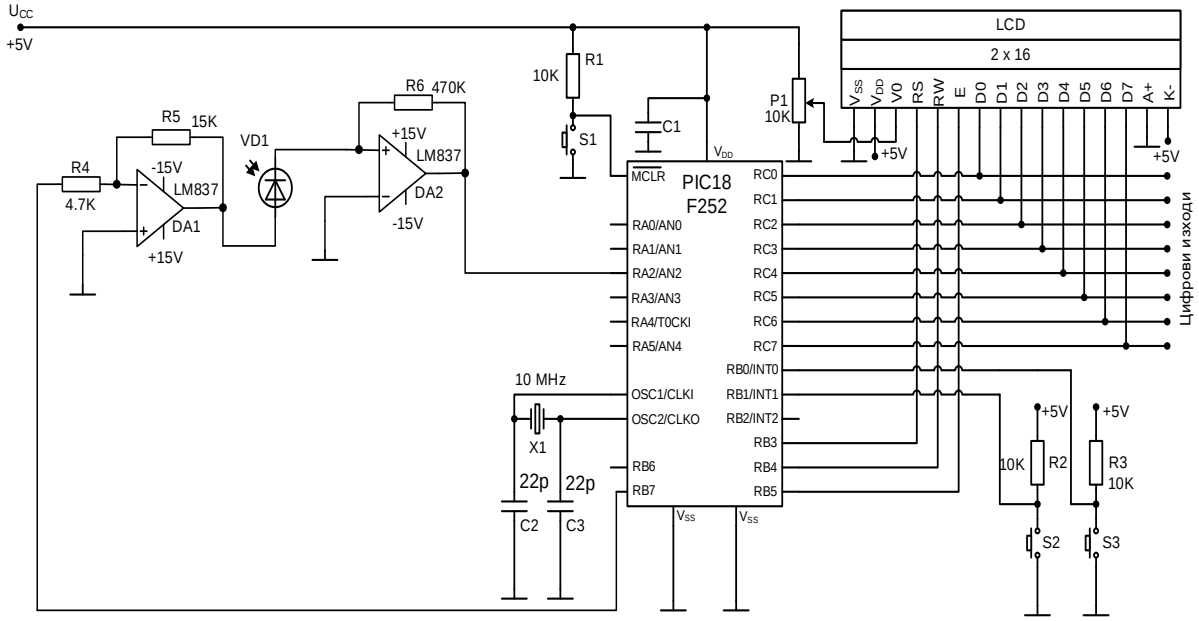

Fig. 4. Schematic electrical circuit diagram of the device

D. Description of the control program

First, the controller is initialized, constants and variables are defined and corresponding cells from the data memory are reserved for them. The next stage of the block chart is related to determining the I/O ports to be used. Digital inputs, analog inputs and digital outputs are determined. PIC18F252 has 4 internal module timers. Only Timer 0 is used. It sets time lags in the program which are used to synchronize the operation of the microcontroller and the alphanumeric LCD. Next, an initialization of the display is performed. The master program is a continuous loop, which stops only when the voltage measurement from the ADC (analog-to-digital converter) has been completed. The processing of the result of each measurement takes place in a subroutine, which starts when an ADC interrupt occurs. At the beginning of the subroutine an analog input for the measurement is selected. The result of the previous measurement is then processed, which includes – hardware multiplication of the measurement value by a preset constant. The ratio U_1/U_2 between the voltages measured in the two modes is determined. The result is converted from hexadecimal to binary-decimal code. The second stage of the subroutine is related to outputting the measurement results on an LCD display. First, the output addresses are defined, it means - to determine in which position to display each digit from the result, including the decimal points. The values of the calculations are then displayed. Finally, a subsequent measurement is started in the subroutine and then returning to the master program takes place.

Connecting to the microcontroller and controlling the LCD display.

The display used is a two-line, alphanumeric, liquid crystal display, with 20 characters per line. It is a smart display with its own control scheme – LCD driver hd44780. The display has a total of 16 ports to enable power supply and connection to an external microcontroller. For controlling the LCD module a control bus is used comprising RS, R/W, E ports which are correspondingly connected to microcontroller ports RB3, RB4, RB5 initialized as digital outputs. The data bus of this type of display consists of 8 ports. The microcontroller communicates with the LCD module by means of the data bus. In this case a mode is selected for this communication to take place using 4-bit interface. The DB0, DB1, DB2, DB3, DB4, DB5, DB6, DB7 display ports are initialized as inputs and correspondingly connected to the

microcontroller's RD0, RD1, RD2, RD3, RD4, RD5, RD6, RD7 ports which are initialized as outputs. At the beginning of the program, initialization of the display takes place, which selects the following:

a) 8-bit interface;

b) two-line mode;

c) character format 5x8 dots;

d) incrementing the address counter by one unit when in read/record mode.

III. CONCLUSION

A two-spectrum pyrometer using only one photodiode has been developed. The device can be used to measure temperature in a wide range from $700°C$ to $2000°C$. The spectral ratio is obtained by switching the photodiode from photovoltaic mode to photoconductive mode. The device operates in two wide spectral ranges and the corresponding two maxima of the spectral sensitivity of the photodetector are close. The use of the proposed scheme leads to an increase in the accuracy and sensitivity of the measurements.

REFERENCES

[1] A. G. Senkov, V. A. Firago, „Optimizaciya harakteristik pirometrov spektralnogo otnosheniya", Vestn. BGU, Vol. 1, no. 3, 2008, pp. 38-44.

[2] A. G. Senkov and V. A. Firago, „Reduction of methodological errors in determining the temperature of metals by two-color pyrometers", Journal of Engineering Physics and Thermophysics, Vol. 79, 2006, pp. 768-772.

[3] A. V. Frunze, „Metodicheskie pogreshnosti pirometrov I sposobi ih minimizacii", Metrologiya, Vol. 7, 2012, pp.25–38.

[4] A. V. Frunze, „A numerical method of determining the spectral-ratio temperature", Measurement Techniques, Vol. 53, 2010, pp. 664-667.

[5] A.V. Yakovlev, „Osobennosti primeneniya shirokopolosnih priemnikov izlucheniya v pirometrah spektralnogo otnosheniya", Avtometriya., Vol. 4, 2004, pp. 44-49.

[6] D. Dichev, I. Zhelezarov, R. Dicheva, D. Diakov, H. Nikolova and G. Cvetanov, „Algorithm for estimation and correction of dynamic errors", 30th International Scientific Symposium Metrology and Metrology Assurance. MMA 2020; Sozopol; Bulgaria, 2020, DOI: 10.1109/MMA49863.2020.9254261.

[7] M.S. Jadin and S. Taib, „Two-Color Pyrometer for Process Temperature Measurement During Machining", Journal of lightwave technology, Vol. 34, no. 4, 2016, pp. 1380-1386:

DOI: 10.1109/JLT.2015.2513158 .

[8] K. Chrzanowski, Non-Contact Thermometry. Measurement Errors, SPIE Polish Chapter, Warsaw, 2001.

[9] L. Lazov, N. Angelov, E. Teirumnieks and Erika Teirumnieka, Preliminary Numerical Analysis for the Role of Speed on to Laser Technological Processes, Proceedings of the 12th International Scientific and Practical Conference, Rezekne Latvia, , Vol. 3, 2019, pp. 137- 142, DOI: 10.17770/etr2019vol3.4154.

[10] Ts. Karadzhov, D. Pulov and N. Angelov, „Contactless measuring of temperature with differential photo receiver", in 12th International Scientific and Practical Conference on Environment. Technology. Resources, Rezekne Academy of Technologies, Vol. 3, 2019, pp. 101-104 , DOI: 10.17770/etr2019vol3.4132.

[11] D. Dichev, H. Koev, T. Bakalova and P. Louda, „A Model of the Dynamic Error as a Measurement Result of Instruments Defining the Parameters of Moving Objects", Measurement Science Review, Vol. 14, Issue 4, 2014, pp. 183-189, DOI: 10.2478/msr-2014-0025.

[12] A.N. Magunov, „Spektralnaya pirometriya: osobennosti, preimushchestva, ogranicheniya", Fotonika, Vol. 1, 2012, pp. 40-45.

[13] T. Fu, J. Liu, M. Duan and A. Zong, „Temperature measurements using multicolor pyrometry in thermal radiation heating environments", Review of Scientific Instruments, Vol. 85, Issue 4, 044901, 2014, DOI: 10.1063/1.4870252.

[14] D. Ya. Svet, Opticheskie metodi izmereniya istinnih temperatur, Moskva, Nauka, 1982.

[15] A. Araujo, Multi-spectral pyrometry - a review, „Measurement Science and Technology", Vol. 28, Issue 8, 082002, 2017, DOI: 10.1088/1361-6501/aa7b4b.

[16] D. B. Ponomarev and V. A. Zakharenko, Silicon photodiode as the two-color detector, Journal of Physics: Conference Series , Vol. 643, Issue 1, 2015, DOI: 10.1088/1742-6596/643/1/012030.

[17] G. G. Ischanin and V. P. Chelibanov, Priemniki opticheskogo izlucheniya, Sankt Peterburg, Lan, 2014.

Environment. Technology. Resources. Rezekne, Latvia
Proceedings of the 13th International Scientific and Practical Conference. Volume 3, 296-299

Reduction of the Stress Concentration Factor of Prismatic Specimens Through the Use of Topological Optimization

Raycho Raychev
Faculty of Mechanical Engineering
Technical University of Sofia, Branch Plovdiv
Plovdiv, Bulgaria
rpraichev@tu-plovdiv.bg

Ivanka Delova
Faculty of Mechanical Engineering
Technical University of Sofia, Branch Plovdiv
Plovdiv, Bulgaria
prosto_vanq89@abv.bg

***Abstract* - The article presents studies related to the reduction of stress concentration acting on prismatic specimen subject to axial loading. Using ANSYS software, a topological optimization was performed which aims to reduce the stresses in the endangered areas. The aim of identification of the geometric parameters accomplished after the completion of topological optimization of the objective function is to minimize the stresses in the engaged areas. An analysis performed were to show the influence of stresses acting on the fatigue limit during different cycles. The results of the study were present in a graphical form.**

Keywords - stress concentration, ANSYS, axial loading, topological optimization.

I. INTRODUCTION

This article presents the results of simulations related to the study of stress concentration in prismatic specimens subjected to axial loading.

A number of scientific papers are devoted to research related to the reduction of stresses in local areas by specific details.

Studies related to the reduction of the stress concentration coefficient in rectangular plates are presented in [1]. Plates with a main central notch in two variants were studied: with the presence of additional notches and without them. The results of the experiment show that the presence of additional notches located at a certain distance from the main notch reduces the stress concentration factor by more than 30%.

Examination of a rectangular plate with the presence of a central notch with a square and triangular shape is presented in [2]. The main purpose is to determine the influence of the various parameters of the specific notches, such as the direction of loading and the orientation of the notches, on the stress distribution and SCF in the perforated plates. The study was performed using specialized ANSYS software. The presented results show that the stress concentration factor can be significantly reduced by using a suitable shape and orientation of the central notches.

Reducing the concentration of stresses through the introduction of a new approach is the subject of [3]. This approach is called Reliever Topological Material Elimination (RTME) and involves the removal of material from test specimens. Topological optimization was used to determine the best areas for material removal. To evaluate the effectiveness of the method, an analysis was performed using specialized software. The obtained results show that the RTME approach reduces the stress concentration by 35.5% and reduces by about 28% the initial volume of the studied specimen.

An approach for optimizing the shape of the studied specimens is also presented in [4]. It is based on the Level Set Method and the X-FEM method, compiling between shape optimization and topological optimization. The application of the described approach is illustrated by minimizing the stress concentration in a 2D mechanical structure.

Minimization of the peak tangential stresses around the notch boundary in a uniaxially or biaxially loaded plate is the main goal in [5]. The optimization method used is based on iterative finite element analysis. The Fortran 90 software was used to perform the optimization task. The efficiency of the proposed multi-peak method was

Online ISSN 2256-070X
https://doi.org/10.17770/etr2021vol3.6536

demonstrated by 2D and 3D numerical examples, some of which include significant geometric constraints.

A significant number of studies of perforated plates with optimized notch shapes have been performed. Analysis of the results shows that the optimal notch shapes lead to a significant reduction in peak stress for all regions around the notch boundary, compared to typical suboptimal round notches.

Reducing the stress concentration by obtaining shoulder fillet with a variable radius is described in [6]. Two approaches are used: The first approach is called the local curvature method (LCM). It is based on the results of stress analysis in stepped test specimens with a constant radius, with a change in the local curvature as a function of the local surface tension. The second approach involves the use of specialized modeFrontier software to perform a systematic search for possible design solutions of shoulder fillets radius, using multiple finite element models.

The main purpose of this article is to reduce the stress concentration in prismatic specimens subjected to axial loading with the help of specialized software.

II. MATERIALS AND METHODS

The objects of study are a rectangular plate with symmetrically arranged semicircular notches and stepped flat specimen with shoulder fillets. The samples are subjected to axial loading performed with the help of specialized ANSYS software.

To reduce the stress concentrations, the built-in ANSYS module "Topology Optimization" was used, which simulates the removal of material from the studied objects. In this way, along with reducing the mass of the samples, the stresses in the endangered areas are reduced.

The objects of the study are presented in schematic form in Fig. 1.

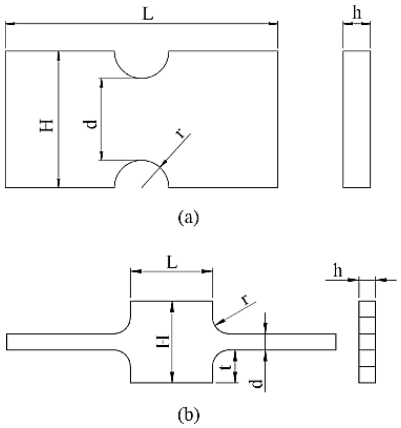

Fig. 1. Objects of study: (a) Rectangular plate with symmetrically arranged semicircular notches, (b) Stepped flat specimen with shoulder fillets.

The geometric dimensions of the tested specimens are given in Table I and Table II.

TABLE I.

Geometric dimensions of a plate with symmetrical semicircular notches.				
H, mm	***L, mm***	***h, mm***	***d, mm***	***r, mm***
50	100	10	40	5
			30	10
			20	15
			10	20

TABLE II.

Geometric dimensions of stepped flat specimen with shoulder fillets.					
H, mm	***L, mm***	***h, mm***	***t, mm***	***d, mm***	***r, mm***
50	50	10	20	10	1,5
					2,5
					6
					10

With the help of the static load module in ANSYS, an axial force was applied to the tested specimens, as a result of which the maximum values of the stresses in the endangered areas were obtained. The results of the static analysis were used to perform the software topological optimization.

In order to identify the geometrical parameters of the taken material after the optimization, the OptiSLang additional module was used, and the minimization of the stresses in the endangered areas was indicated as a target function.

III. RESULTS AND DISCUSSION

Table III and Table IV present the results of the static analysis at different ratios of the geometric parameters in the models.

TABLE III.

Plate with symmetrical semicircular notches.					
d, mm	***Axial Force***	***σ max***	***σ***	***Ktg-sim***	***Ktg-theory***
	P, N	***MPa***	***MPa***	-	-
40	50000	315,46	100	3,155	3,08
30		318,29	100	3,183	3,1
20		358,38	100	3,584	3,52
10		581,93	100	5,819	5,78

TABLE IV.

Stepped flat specimen with shoulder fillets.					
r, mm	***Axial Force***	***σ max***	***σ nom***	***Kt-sim***	***Kt-theory***
	P, N	***MPa***	***MPa***	-	-
1,5	10000	220,4	100	2,204	2,386
2,5		183,8		1,838	2,038
6		144,3		1,443	1,562
10		138,2		1,382	1,35

Comparisons between the theoretical coefficients of stress concentration and those obtained with the simulation

data for the two specimens are presented in a graphical form in Fig. 2 and Fig. 3.

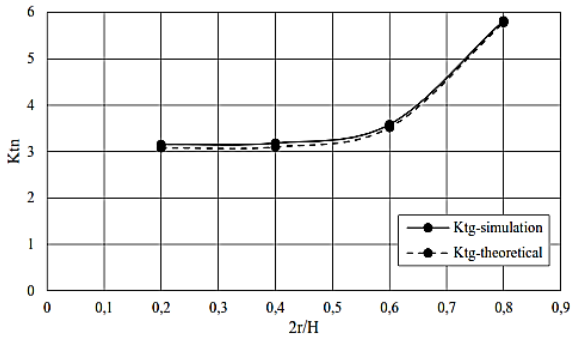

Fig. 2. Comparisons between stress concentration coefficients at plate with symmetrical semicircular notches.

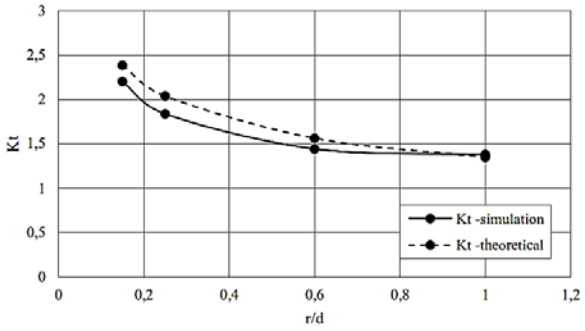

Fig. 3. Comparisons between stress concentration coefficients at Stepped flat specimen with shoulder fillets.

The theoretical coefficients are calculated according to (1) and (2) which are presented in the specialized literature [7].

For the rectangular plate with semicircular notches:

$$K_{tn} = \frac{\sigma_{max}}{\sigma}; \quad \sigma = \frac{P}{h.H} \qquad (1)$$

Where P is the applied axial force, and h and H are geometrical parameters of the specimen.

For stepped flat specimen with shoulder fillets:

$$K_t = C_1 + C_2\left(\frac{2t}{H}\right) + C_3\left(\frac{2t}{H}\right)^2 + C_4\left(\frac{2t}{H}\right)^3; \quad (2)$$

Where t and H are geometrical parameters of the specimen, and C_1, C_2, C_3 and C_4 are defined by (3):

$$C_1 = 1{,}020 + 1{,}009\sqrt{t/r} - 0{,}048t/r;$$

$$C_2 = -0{,}065 - 0{,}165\sqrt{t/r} - 0{,}007t/r; \qquad (3)$$

$$C_3 = -3{,}459 + 1{,}266\sqrt{t/r} - 0{,}016t/r;$$

$$C_4 = 3{,}505 - 2{,}109\sqrt{t/r} + 0{,}069t/r.$$

The topological optimization was performed with a given reduction of the mass of the studied specimens by 10%, 20% and 30%, respectively.

The specimens after the topological optimization are presented in graphical form in Fig. 4 and Fig. 5.

Fig. 4. Visualization of the rectangular plate after topological optimization.

Fig. 5. Visualization of the stepped flat specimen with shoulder fillets after topological optimization.

With the help of the additional specialized optimization module OptiSLang, the geometric parameters of the reduced material from the specimens have been identified, and the set target function is to minimize the stresses in the endangered areas.

The stress values obtained after the optimization for the studied cases are presented in Table V and Table VI.

TABLE V.

Stress values obtained after the optimization for rectangular plate.			
r	***σ nom -10%***	***σ nom -20%***	***σ nom -30%***
mm	***MPa***	***MPa***	***MPa***
5	250,112	300,809	346,7
10	272,703	296,655	388,727
15	357,314	352,018	360,351
20	568,111	568,423	575,822

TABLE VI.

Stress values obtained after the optimization for Stepped flat specimen with shoulder fillets.			
r	***σ nom -10%***	***σ nom -20%***	***σ nom -30%***
mm	***MPa***	***MPa***	***MPa***
1,5	181,523	172,512	172,571
2,5	165,308	161,639	159,412
6	132,12	129,931	130,214
10	119,005	118,727	121,054

Fig. 6 and Fig. 7 shows the graphs of the stress concentration coefficient as a function of the geometric parameters of the studied specimens.

The analysis of the results shows that with the topological optimization of the rectangular plate, the reduction of the mass up to 20% can reduce the stresses in the endangered areas by more than 20%.

In the topological optimization of stepped flat specimen with shoulder fillets, the stresses in the endangered areas in the considered cases decrease by more than 15%.

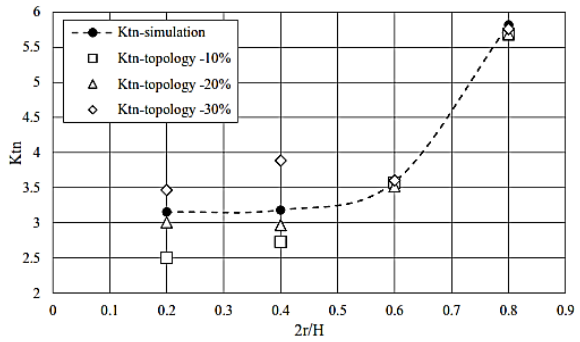

Fig. 6. Stress concentration coefficients after optimization for rectangular plate.

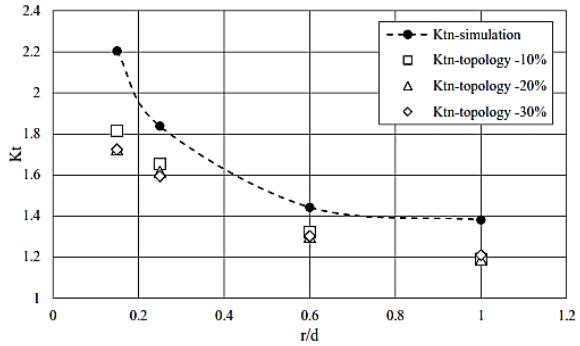

Fig. 7. Stress concentration coefficients after optimization for stepped flat specimen with shoulder fillets.

IV. Conclusions

The object of the present work is to reduce the stress concentration in the tested specimens with the help of specialized software. The application of the modules "topological optimization" and "OptiSlang" in the ANSYS software proves to be a suitable method for realization of the set tasks and achievement of optimal solutions.

The results obtained from the simulations can be used as a basis for future experimental studies.

Acknowledgements

The authors would like to thank the Research and Development Sector at the Technical University of Sofia for the financial support.

References

[1] A. Wankar, H. Mishra and J. Bayas, “Experimental Investigation of Reduction in SCF of Rectangular plate with central circular hole by Providing Relief Holes”, International Research Journal of Engineering and Technology (IRJET), Volume: 03 Issue: 061 June-2016.

[2] S. Sayyad and J. Shitole, "Exploration of the stress concentration in metallic plates with extraordinary cutout and bluntness", International Journal of Advanced Technology in Engineering and Science, Vol. No.5, Issue No. 05, May 2017.

[3] S. Karimi and J. Fesharaki, "Using Topology Optimization to Reduce Stress Concentration Factor in a Plate with a Hole", Journal of Stress Analysis Vol. 3, No. 2, Autumn — Winter 2018-19.

[4] L. Miegroet and P. Duysinx, "Stress Concentration Minimization of 2D filets using X-FEM and Level Set Description", Structural and Multidisciplinary Optimization volume 33, pages425–438(2007).

[5] W. Waldman and M. Heller, “Shape optimisation of holes for multi-peak stress minimisation”, Australian Journal of Mechanical Engineering, Volume 3, 2006 - Issue 1, https://doi.org/10.1080/14484846.2006.11464495

[6] D. Taylor, A. Kelly, M. Toso and L. Susrne, "The Variable Radius Notch: Two New Methods for Reducing Stress Concentration", Engineering Failure Analysis, Volume 18, Issue 3, April 2011, Pages 1009-1017, https://doi.org/10.1016/j.engfailanal.2010.12.012

[7] W. Pilkey, D. Pilkey and Z. Bi, "Peterson's Stress Concentration Factors, 4th Edition", ISBN: 978-1-119-53252-1, Wiley, January 2020.

Environment. Technology. Resources. Rezekne, Latvia
Proceedings of the 13th International Scientific and Practical Conference. Volume 3, 300-303

Methods for Reducing the Stress Concentration in Cylindrical Specimens, at Axial Loading

Raycho Raychev
Faculty of Mechanical Engineering
Technical University of Sofia, Branch Plovdiv
Plovdiv, Bulgaria
rpraichev@tu-plovdiv.bg

Ivanka Delova
Faculty of Mechanical Engineering
Technical University of Sofia, Branch Plovdiv
Plovdiv, Bulgaria
prosto_vanq89@abv.bg

Abstract **- The article presents specialized software methods for reducing stress concentration. Objects of study are cylindrical test specimens subjected to axial loading. Notching with different shapes and sizes on the specimens were formed to reduce the stresses in the endangered areas. The geometric parameters of notches identified through the specialized built-in modules to the ANSYS software. An analysis performed were to show the influence of stresses acting on the fatigue limit during different cycles. The results of the study were present in a graphical form.**

Keywords - stress concentration, ANSYS, axial loading, notch.

I. INTRODUCTION

Stress concentrations are one of the main problems that arise in the construction of parts in mechanical engineering. Increasing stresses in local areas can lead to loss of performance or destruction of components. This is one of the main reasons why the optimization of the details in mechanical engineering is related to the reduction of the stress concentration and the increase of the fatigue limit.

The reduction of stress concentration is the subject of a number of specialized literature sources.

An optimization approach for stress reduction in stepped specimens subjected to axial loads is proposed in [1]. The purpose of optimization is to minimize the maximum value of stresses in the main shoulder fillet, thus increasing the fatigue limit. The objects of study are two stepped details: the first with the presence of only a basic shoulder fillet, and the second with the presence of a basic shoulder fillet and an additional cylindrical notch. The main approach presented by the authors consists in defining geometric parameters to be optimized to achieve a minimum value of the objective function. Specialized software MATLAB and ANSYS were used for performing the optimization.

Elaboration of an additional cylindrical channel in the danger zones in order to reduce the stresses in a specific steel part is presented in [2]. The stress values are obtained by the finite element method using the specialized MARC/MENTAT software. The results show that due to the additional channel, the equivalent stresses decrease by about 10%.

Determining the best shape of shoulder fillet for stepped shafts and plates so that the maximum equivalent stress has the lowest possible value is a key goal in [3]. The optimization task is achieved with the help of a stochastic global search algorithm called "direct search simulated annealing". The optimized shape of the shoulder fillet is obtained with the help of spline curves passing through certain key points.

The analysis of the obtained results shows that the applied "direct search simulated annealing" method not only reduces the stress values, but also the optimized shoulder fillet are located on a smaller area.

A study of the stress concentration at a stepped shaft subjected to an axial load is described in [4]. Two types of shafts are considered: a stepped shaft with shoulder fillet of the foot and a shaft with shoulder fillet and a conical part of the foot. A simulation was realized with the help of the specialized ANSYS software. The analysis of the obtained results shows that:

- The coefficient of stress concentration at the step shaft is 30% higher than the coefficient known from the specialized literature.

- The stress concentration factor for a stepped shaft with a conical part is lower than that of a stepped shaft without a conical part by 5-10%.

Online ISSN 2256-070X
https://doi.org/10.17770/etr2021vol3.6535

An approach to stress reduction in stepped shafts is presented in [5]. It is based on the methods CAO (Computer Aided Optimization) and FEM, which are used to optimize the geometric parameters, with the main shoulder fillet located between the steps of the shafts. Different variants of optimized shoulder fillet are proposed, in which the stress concentration is significantly lower compared to the shoulder fillets before optimization.

The main goal of the present work is to reduce the stress concentration in cylindrical test specimens subjected to axial loading with the help of the specialized ANSYS software.

II. MATERIALS AND METHODS

Objects of study are a cylindrical part with a centrally located U-shaped notch and a two-stage cylindrical part with a shoulder fillet. Both specimens are subjected to axial loading.

Schemes of the examined specimens are presented in Fig. 1, and the values of their geometrical parameters are given in Table I and Table II.

The simulations are realized with the help of the static module to the specialized ANSYS software. Initially, the specimens are subjected to axial loading and the values of the maximum stresses at different geometric ratios of the input parameters are determined.

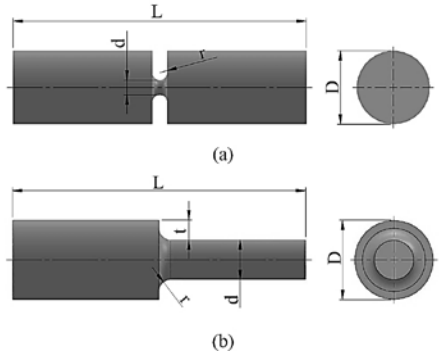

Fig. 1. Objects of study: (a) U-shaped specimen, (b) Specimen with shoulder fillet.

TABLE I.

Geometric dimensions of the specimen with a U-shaped notch.			
D, mm	***r, mm***	***L, mm***	***d, mm***
50	0,5	200	5
			15
			25
			35
			45

TABLE II.

Geometric dimensions of the specimen with the presence of shoulder fillet.				
D, mm	***d, mm***	***L, mm***	***t, mm***	***r, mm***
54	27	200	13.5	2,7
				4,05
				5,4
				6,75
				8,1

The coefficients of stress concentration are determined with the obtained results from the simulation. These coefficients are compared with those existing in the specialized literature [6]. In order to reduce the stresses in the endangered areas, additional notches with specific shapes and sizes were made on the specimens. With the help of the built-in ANSYS module OptiSLang, the geometrical parameters of the additional notches were identified, and a target function was set to minimize the maximum values of the stresses in the endangered areas.

With the help of the specialized module ANSYS nCodeDesignLife the influence of the additional notches on the fatigue limit in the examined samples was reported.

The stress concentration coefficients for both specimens are determined according to (1):

$$K_{tn} = \frac{\sigma_{max}}{\sigma_{nom}}; \quad \sigma_{nom} = \frac{4P}{\pi d^2} \tag{1}$$

Where *P* is the axial force applied to the specimen.

III. RESULTS AND DISCUSSION

Fig. 2 shows the specific geometric shapes of the additional notches used in the simulations of the cylindrical specimen with a central U-notch.

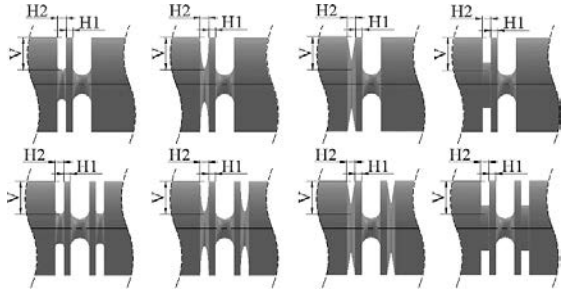

Fig. 2. Geometric shapes of the notches in the cylindrical specimen with a central U-notch.

Table III present the obtained values for the stresses and the concentration coefficient after the simulations, for different geometrical parameters d.

Table IV presents the values of the geometric parameters of the additional notches obtained after the optimization with OptiSLang, the maximum stresses at these parameters, as well as the stress concentration coefficient.

TABLE III.

Results from the simulation of a cylindrical specimen with a U-shaped notch.				
Parameter	***Axial force***	***σ nom***	***σ max***	***Ktn***
d, mm	***P, N***	***MPa***	***MPa***	**-**
5	2000	101,859	272,34	2,673
15		11,317	49,592	4,381
25		4,0743	23,538	5,777
35		2,078	13,269	6,383
45		1,257	6,4164	5,102

TABLE IV.

Additional notches	H1, mm	H2, mm	V1, mm	σ max, MPa	Ktn -
d=5 mm					
U-notch	2,459	1,250	21,013	192,987	1,895
V-notch	1,622	2,222	20,988	237,063	2,327
Prismatic notch	4,636	1,873	15,249	243,613	2,392
Elliptical notch	2,471	1,471	18,485	200,065	1,964
Double-sided U-notch	3,426	1,452	18,620	180,924	1,776
Double-sided V-notch	2	2	15	241,069	2,367
Double-sided Prismatic notch	0,859	0,851	16,312	242,990	2,386
Double-sided Elliptical notch	4,018	4,305	19,591	205,433	2,017
d=15 mm					
U-notch	2,579	1,694	14,878	39,795	3,516
V-notch	3,274	2,087	11,087	46,535	4,112
Prismatic notch	1,461	1,809	17,572	34,879	3,082
Elliptical notch	3,870	0,731	9,972	39,113	3,456
Double-sided U-notch	2,825	0,500	11,838	39,690	3,507
Double-sided V-notch	2,015	1,983	15,085	38,002	3,358
Double-sided Prismatic notch	1,526	2,292	10,553	41,946	3,706
Double-sided Elliptical notch	1,441	4,714	9,500	37,414	3,306
d=25 mm					
U-notch	1,023	4,195	13,461	12,233	3,003
V-notch	1,705	2,232	8,321	21,514	5,281
Prismatic notch	2,484	1,844	12,381	15,069	3,699
Elliptical notch	4,979	4,439	12,398	15,848	3,890
Double-sided U-notch	1,070	4,998	12,982	9,801	2,406
Double-sided V-notch	3,013	3,709	11,021	15,535	3,813
Double-sided Prismatic notch	1,930	2,941	11,473	13,574	3,332
Double-sided Elliptical notch	3,241	4,059	3,545	16,128	3,959
d=35 mm					
U-notch	3,521	3,726	8,514	7,360	3,540
V-notch	3,770	2,858	6,402	10,968	5,276
Prismatic notch	1,839	1,421	7,501	8,738	4,203
Elliptical notch	2,930	2,720	5,945	9,674	4,653
Double-sided U-notch	3,848	5,000	7,781	5,314	2,556
Double-sided V-notch	3,254	2,756	5,730	9,189	4,420
Double-sided Prismatic notch	1,176	3,404	6,567	7,338	3,529
Double-sided Elliptical notch	2,014	4,877	7,455	7,260	3,492
d=45 mm					
U-notch	1,491	2,211	2,823	4,145	3,295
V-notch	3,293	1,878	1,506	5,653	4,494
Prismatic notch	1,532	3,285	2,420	4,443	3,532
Elliptical notch	1,436	3,577	3,086	3,918	3,115
Double-sided U-notch	1,762	4,675	2,653	2,973	2,363
Double-sided V-notch	2,864	2,626	1,265	4,937	3,925
Double-sided Prismatic notch	0,860	3,244	1,837	3,803	3,023
Double-sided Elliptical notch	1,686	3,405	2,841	3,640	2,893

Fig. 3 presents the stress concentration coefficients for all studied cases, as a function of the geometric ratio d / D.

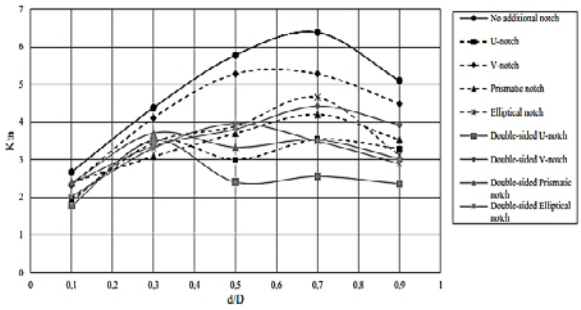

Fig. 3. Stress concentration coefficients for all studied cases, as a function of the geometric ratio d / D.

The obtained results show that the presence of additional notches significantly reduces the stresses in the endangered areas. The most significant influence in the present study is exerted by the double sided U-notch. With it, the stress concentration factor decreases by more than 30% compared to the results obtained without the presence of additional notches.

Table V presents the results for the maximum stresses and the stress concentration coefficient obtained in the simulation of the cylindrical stepped specimen, at different radius of fillet of the step.

TABLE V.

Results of the simulation of a cylindrical specimen with shoulder fillet.				
Parameter r, mm	***Axial force P, N***	***σ nom MPa***	***σ max MPa***	***Ktn*** -
2,7	100000	174,656	361,4	2,069
4,05			323,22	1,851
5,4			298,33	1,708
6,75			276,58	1,584
8,1			262,92	1,505

In Fig. 4 shows the notch shapes used in the simulation of the stepped cylindrical specimen.

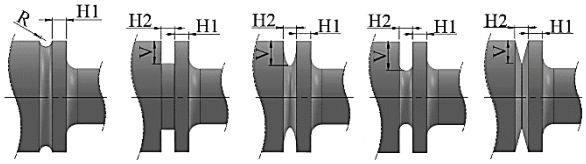

Fig. 4. Geometric parameters and shapes of the notches used in the simulation of the stepped specimen.

Table VI presents the values of the geometrical parameters of the notches, the maximum values of the stresses in the endangered areas, as well as the stress concentration coefficient obtained after the optimization with OptiSLang.

TABLE VI.

Additional notches	H1, mm	H2, mm	V1, mm	σ max, MPa	Ktn -
r=2,7 mm					
U-notch	7.166	3.242	10.471	310.743	1.779
V-notch	8.667	1.425	5.366	355.476	2.035
Prismatic notch	9.885	4.334	7.283	340.392	1.949
Elliptical notch	8.197	2.271	6.028	344.039	1.970
Semicircular notch	4.018	R=1.520 mm		351.458	2.012
r=4,05 mm					
U-notch	8.273	2.033	9.134	304.926	1.746
V-notch	7.234	3.586	1.161	317.822	1.820
Prismatic notch	7.803	3.696	4.451	318.712	1.825
Elliptical notch	6.007	4.542	9.140	306.172	1.753
Semicircular notch	9.939	R=9.987mm		303.824	1.740
r=5,4 mm					
U-notch	6.522	4.278	10.155	277.760	1.590
V-notch	6.779	2.655	0.977	293.532	1.681
Prismatic notch	5.863	4.897	6.061	291.457	1.669
Elliptical notch	6.886	4.209	7.947	288.098	1.650
Semicircular notch	7.434	R=9.999mm		282.777	1.619
r=6,75 mm					
U-notch	6.666	3.565	9.207	267.454	1.531
V-notch	5.830	0.777	0.500	273.844	1.568
Prismatic notch	4.521	1.652	5.893	274.309	1.571
Elliptical notch	8.967	4.704	6.965	272.547	1.560
Semicircular notch	2.853	R=9.908mm		265.375	1.519
r=8,1 mm					
U-notch	6.165	4.562	9.367	254.801	1.459
V-notch	4.350	1.151	5.123	260.696	1.493
Prismatic notch	6.135	1.976	3.389	260.875	1.494
Elliptical notch	1.144	1.709	5.418	261.017	1.494
Semicircular notch	5.802	R=10 mm		255.498	1.463

In Fig. 5 the stress concentration coefficients are presented in a graphical form as a function of the geometric ratio r / d.

The analysis shows that the best results are achieved in the presence of an additional U-shaped notch. With it, the stress concentration coefficients decrease by more than 10%.

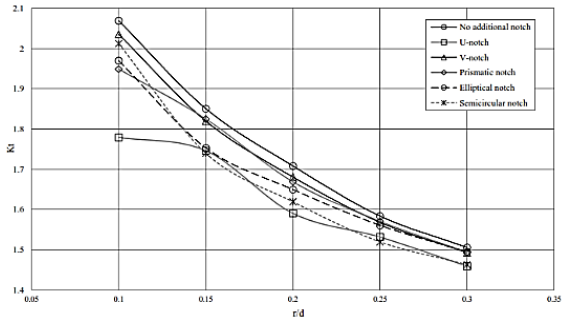

Fig. 5. Stress concentration coefficients for all studied cases, as a function of the geometric ratio r / d.

IV. Conclusions

The aim of the present study is to determine the influence of the additional notches on the stress concentration in the examined specimens with the help of specialized software. The results of the performed simulations show that with a certain shape, geometric dimensions and location on the studied specimen, the stresses in the endangered areas can be significantly reduced.

The obtained results can be used as a starting point for forthcoming experimental studies.

Acknowledgements

The authors would like to thank the Research and Development Sector at the Technical University of Sofia for the financial support.

References

[1] J. M González-Mendoza., S. Alcántara-Montes., J. Silva-Lomelí., C. Cruz-Alejo and A. Ocampo-Ramírez, “Size optimization of shoulder filleted shafts with relief grooves for improving their fatigue life”, Ingenlería e InvestIgaclón vol. 37 №3, december - 2017 (85-91),
http://dx.doi.org/10.15446/ing.investig.v37n3.57957

[2] Y Otsuka, H. Baron and Y. Mutoh, "Design Optimization of Stress Relief Grooves in Lever Guide of Pressure Vessel for Food Processing", Open Journal of Safety Science and Technology, 2012, 2, 1-7.
http://dx.doi.org/10.4236/ojsst.2012.21001

[3] F. Sonmez “Optimal shape design of shoulder fillets for flat and round bars under various loadings”, IMechE Vol. 223 Part C: J. Mechanical Engineering Science, 2009.
https://doi.org/10.1243/09544062JMES1457

[4] V. Prasad, B Ram B, K. Krishna, T Reddy and S Kumar, “Stress Concentration Factors For Shouldered Shaft With Fillet And Taper Loaded In Tension”, International Journal Of Scientific & Technology Research, volume 9, issue 04, April 2020.

[5] C. Mattheck, M. Scherrer, K. Bethge and L. Tesari, "Shape Optimization: An Analytical Approach", WIT Transactions on the Built Environment, Volume 80, 2005.

[6] W. Pilkey, D. Pilkey and Z. Bi, "Peterson's Stress Concentration Factors, 4th Edition", ISBN: 978-1-119-53252-1, Wiley, January 2020.

Environment. Technology. Resources. Rezekne, Latvia
Proceedings of the 13th International Scientific and Practical Conference. Volume 3, 304-309

Studies of the Possibilities to use Ozone for the Grain Storage

Adolfs Rucins
Latvia University of Life Sciences and Technologies, Ulbroka Research center Ulbroka, Latvia
adolfs.rucins@llu.lv

Evita Straumite
Latvia University of Life Sciences and Technologies, Faculty of Food Technology Jelgava, Latvia
evita.straumite@llu.lv

Dainis Viesturs
Latvia University of Life Sciences and Technologies, Ulbroka Research center Ulbroka, Latvia
viesturs_uzc@apollo.lv

Alberts Kristins
University of Latvia, Institute of Solid State Physics Riga, Latvia
kristin@latnet.lv

Abstract **- In this study was impact of ozone treatment efficiency of wheat quality (physical-chemical and microbiological parameters, chemical composition and germination rate) during storage analysed. Ozone is a powerful oxidizer, used in processing the agricultural products, including inactivation of pathogens and microorganisms.**

Investigations in the grain storage by using ozone were performed under farm conditions during two grain storage stages. The first stage – August 2019 – February 2020 and the second stage August 2020 – January 2021. In both stages after harvesting winter wheat yield was 6 t ha^{-1}. Winter wheat was ventilated and then stored for about five months in two identical 20 m^3 tanks, with an initial grain layer height of 5.1 m and moisture content the first stage of about 14% and the second stage of about 11% and initial grain mass 17.4 t.

At the beginning of the storage period the grain in both tanks was ventilated for 8 hours - in one grain storage tank with the outdoor air, in the other with an ozone supply of 28 mg $(m^3)^{-1}$ in the ventilation air. The grain ventilation and storage process was monitored with a specially designed sensor system; the additional parameters of the process (the grain moisture content, temperature, the ozone concentration) were periodically controlled with hand tools. There were analysed changes of the grain parameters during the storage periods in the ozone-supplied tank and in the tank without ozone treatment.

The microbiological contamination during storage did not exceed the allowed level; however it was lower in the ozone treated wheat grain than in the ozone untreated grain. The ozone treatment did not affect the grain quality parameters. The grain germination rate for 3 and 5 days of the ozone treated grain was about 20% higher than that of the untreated grain. During storage, microbiological contamination did not exceed the permissible level, but ozone treated grains were lower than those of untreated, grain quality indicators were not affected by ozone treatment, germination of ozone treated grains was about 20% higher than untreated, baking properties were not affected by ozone treatment. The treatment of grain with ozone makes stored grain more expensive approximately 5.00 EUR per ton, due to additional technical equipment required to ensure the ozone treatment process. One can conclude from the attained results that processing the restored grain under the conditions mentioned reduces the grain microbiological contamination; it does not affect the grain quality parameters and baking properties; it slightly improves the grain germination rate and has no impact upon the shell of the grain.

Keywords – wheat storage, ozone, microbiological safety

I. INTRODUCTION

Technologies are becoming increasingly topical in agriculture that do not have a harmful impact upon the environment. This also applies to the traditional and conservative grain growing. Since the middle of the 20th century investigations have started of the impact of ozone upon grain – that ozone can replace weed control and grain pickling chemicals, as well as improve the quality of the grain during drying and storage [1].

Online ISSN 2256-070X
https://doi.org/10.17770/etr2021vol3.6519

The main factors that have negative impact upon the storage quality of grain are the presence of pathogens and microorganisms that can form toxins which are harmful to human and animal health [2]. Also Reed, 2006 [3] notes that grain spoilage is mainly caused by moulds. In study of Sauer et al., 1992 [4] are analyzed the effects of various mould species upon the grain. The European Commission has worked out recommendations [5] that set maximum levels for toxins produced by microorganisms in cereals and cereal products. One way to control the growth of moulds and thus reduce the formation of toxins is to regulate the temperature and moisture content of the grain through active ventilation [2]. Several authors recommend adding ozone to the active ventilation air to control development of different microorganisms producing toxins more effectively. In experiments from Avdeeva et al., 2019 [6] made under the laboratory conditions to reduce toxins, there was used an ozone dose of 370 g s / m^3 of air with a sample treatment time of 12 hours. In experiment of Sandhu et al., 2012 [7] with the treatment of the wheat flour and the wheat starch with the ozone gas (1500 mg / kg at a rate of 2.5 L/ min) for 45 minutes and 30 minutes, respectively, it was revealed that the treatment with ozone had a positive effect upon the wheat flour properties. From the analysis made by other authors [8] who have treated the wheat grain and the wheat flour with ozone one and are concluded that ozone has a great potential for the improvement of the functionality of the grain products simultaneously ensuring food safety. In his turn author [9], looking extensively at the studies of other authors, has found that the most frequently used ozone doses in the fumigation experiments are 30 – 50 ppm, and the treatment time is 5 – 3 days, respectively. Under such conditions ozone is an effective fumigant for decreasing of mycotoxin amount, and microbial inactivation with minimal or no impact upon the grain quality. By active ventilation of initially 22.3% of wet grain to 14.0% moisture with a mixture of ozone and air at an O_3 concentration of 700 ppm, in study [10] has found a reduction in microbiological contamination up to 3 times. The author [11] has studied the treatment of grain with ozone at a concentration of 8 – 10 mg m^3 of air and the duration of the treatment in the 36 hour. She has found that such a treatment considerably reduces the amount of microorganisms in the grain.

All the authors note the ability of ozone to reduce the impact of microorganisms and thus the effect of toxins upon the grain; however most studies have been performed with small amounts of grain under laboratory conditions. In our opinion the treatment of grain with the addition of ozone into air for ventilation in large–volume grain storage tanks and the effect of such treatment upon the pathogenic microorganisms during the storage of grain for several months has been insufficiently studied.

The aim of the research is to determine whether active ventilation of grain with an initial moisture content of 14% in high–volume grain storage tanks with an ozone additive of 28 mg $(m^3)^{-1}$ and a long–term storage in these tanks reduces the amount of microorganisms compared to grain storing non–treated with the ozone in an identical tank.

II. Materials and methods

A. Grain storage tanks and equipment

For the experiments the wheat grain with the same humidity content were stored in two identical storage tanks. The investigations in the grain storage by using ozone were performed 2019 and 2020 after harvesting. The winter wheat yield was 6 t. and the storage time was approximately the five month. At the beginning of storage, during ventilation of the ozone produced by the generator in one tank (ozone tank – OT), was connected to the ventilation air taken from the outside, the other (reference tank – RT) was ventilated with the outdoor air. The height of the tanks was 5.6 m; the wheat grain for the experiments was loaded up to 5.1 m level; the approximate grain weight (mass) in each tank was 17.4 t; the grain moisture was the first stage of about 14% and the second stage of about 11.2%; the duration of ventilation before the long–term storage was 8 hours – in the ozone tank (OT) – with an ozone treatment and in the reference tank (RT) – with the outdoor air. In the centre of each tank there is a suspension for fixing the sensor system, installing the boxes with sensors after every metre. The structure and operating principles of the sensor system are described by Kleperis et al., 2019 [1].

Ozone for the experiments was produced by two generators, model OPV–100.03 (made by "ZhemchuzhinaRusi", RU), with a total capacity of 200 g O_3 h^{-1} and the installed capacity of 2 kW. To ensure a constant flow of ozone, both ozone generators were equipped with a filter to purify the ambient air. Ozone was fed into the fan air supply pipe. Next to each grain storage tank there were installed fans, connected to the grain discharge opening at the bottom of the grain storage tank with a polypropylene 0.35 m diameter pipe, the capacity of the fans being 7000 m^3 h^{-1}, their speed 2800 revolutions min^{-1} and the engine power 4.0 kW.

In parallel with the measurements of the sensor system, the ozone concentration was periodically monitored with a hand–held instrument QL – 800 – O_3 (Manufacturer QLOZONE, China), the measurement range of which is from 0 to 100 ppm with a resolution of 0.01 ppm. The accuracy of the instrument is 1%, which is equal to the minimum ozone concentration reading of 0.01 ppm. The ozone conversion, measured by volume in the air, is 1 ppm of ozone = 2.14 mg O_3 / m^3.

In parallel with the measurements of the sensor system, the grain moisture was periodically monitored with a hand tool Wile 66 (FarmComp Oy, Finland), the measurement ranges of the humidity range being 8 – 35% for grain, 6 – 25% for the oil plants, the measuring accuracy +/– 0.5% for the whole grain.

B. Sensor system for monitoring grain storage

The sensor system is designed to record the air humidity in the grain internal space, the temperature and ozone concentration in five levels, and to transmit the recorded data to a computer, where these parameters can be read online or viewed remotely.

The sensor system (see Fig. 1) is formed of five sets of sensors in each grain storage tank (OT and RT tank), and of separate outdoor air temperature and humidity sensors, as well as the data storage and transmission modules (one module for each grain storage tank), which includes a microcontroller with memory for data storage, power supply and data transmission – the reception module E–32 with an antenna. The sensor system is connected to a computer via a USB converter, connected to it, and an E–32 transceiver module with an antenna.

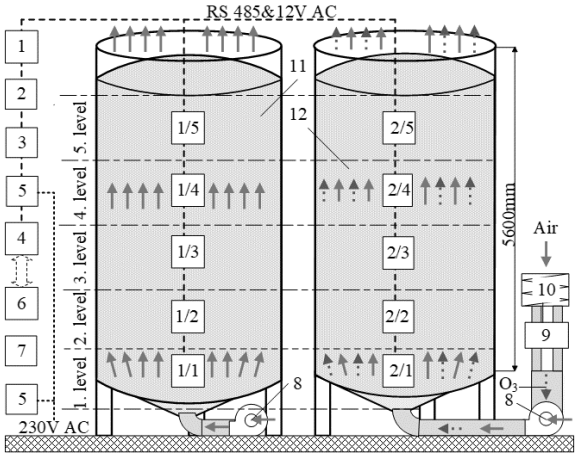

Fig. 1. A layout diagram of the grain storage equipment and sensors. 1. The outdoor humidity sensor, RH%; 2. The outdoor temperaturesensor, T°C; 3. The microcontroller; 4., 6. The transceiver E32; 5. The source of power; 7. The computer interface; 8.The fan; 9. The ozone generator; 10. Air filter; 11. The reference tank (RT); 12. The grain storage tank with the ozone supply (OT); 1/1 – 1/5 Sensors, T°C, RH %; 2/1 – 2/5 Sensors, T°C, RH %, O_3, ppm.

The microcontroller and the connected sensors communicate via the RS485 communication channel with a MODBUS RTU data exchange protocol [1]. The transceiver module E–32 is used for data transfer between the controller and the computer. The E–32 series modules are UART wireless modules, based on the SEMTECH SX1276 / SX1278 RF chip, using a LoRa transmission technology for the data exchange [12].

The user program of the grain storage process monitoring system works with a database and allows to see the changes of the measurements of the selected sensors in real time or in a certain time interval (in a table and a diagram display). The user program allows one to select the measurement display of a specific parameter (humidity, temperature, the ozone concentration) in different layers of the grain storage tank in the selected time period (real time or historical data during the selected time interval).

During the harvesting season, the sensor system was used to control the active ventilation and ozone treatment process of the grain [12], but during long–term storage – to periodically control the temperature and humidity of the stored grain in the inter–grain space.

C. Analysis of the wheat grain quality

Determination of the amount of mesophilic aerobic and anaerobic bacteria (TPC) was determined according to LVS EN 4833: 2003. For analysis of the moisture content, water activity and microbiological analysis there were used approximately 100 g ground wheat grains. All the parameters were analysed for the wheat grain samples, taken from each storage tank (without ozone and with ozone treatment).

The moisture content of the analysed wheat grain was determined according AACC Method 44–15.02, in the oven Memmert ULM 500 GmbH Memmert, Germany). The water activity was determined using the LabSwift–aw devise (AG Novasina, Switzerland).

The gluten, starch and protein content was determined using (Grain Analyzer Infratec™ 1241, Denmark). For analysis there were used approximately 500 g of the whole wheat grain.

Wheat grain germination capacity (after 3 days) and rate (after 5 days) was determined. The 100 wheat grain was placed in the Petri dish with filterpaper, pour 4 ml of water and place in a dark place at the room temperature (22 ± 2°C).

III. Results and Discussion

The grain storage research was performed in two stages – 22.08.2019. – 03.02.2020. and 12.08.2020. – 24.01.2021. On the first day of grain storage both tanks were ventilated for 8 hours, in the ozone tank (OT) – with an ozone supply of 28 mg $(m^3)^{-1}$ in the ventilation air; in the reference tank (RT) – with the outdoor air. This was followed by storage for the indicated periods of time (approximately five months), with the sensor system periodically monitoring the storage modes. At the first and the second stages of the research the grain samples for the assessment of their biological properties and quality at the beginning and at the end of storage were taken at tank levels 1/1 and 2/1 (see Fig. 1).

In the studies on the use of ozone in the treatment of cereals and their products, all the authors believe that the use of ozone essentially reduces the development of microorganisms [2, 4, 6, etc.]. This thesis is also confirmed by our study. The total amount of microorganisms in the grain was already below the allowed 10×5 CFU g^{-1} at the beginning of storage; in both storage periods it was considerably reduced for the ozone treated grain, as compared to the storage of the ozone non–treated grain.

The development of microorganisms is essentially influenced by the grain moisture and the water activity. The water activity reflects the activity of the free water in the food product; for dry products the water activity may be 0.4 – 0.6. The summary of the water activity of the wheat grain at the beginning and the end of storage is shown in Figure 2. As the moisture content of the grain slightly changes during storage due to external conditions, this also affects the water activity of the grain. For the

non–treated grain with the ozone the water activity increases slightly, but for the ozone treated grain it decreases; however the changes are insignificant. On the whole, one can concluded that ozone treatment does not affect ($p>0.05$) the water activity of the wheat grain.

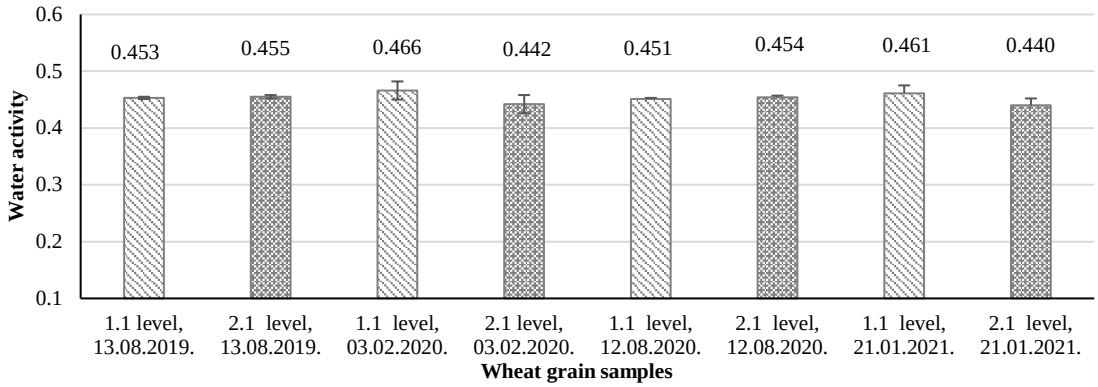

Fig. 2. The water activity of the wheat grain.
1.1 level – ozone non–treated and 2.1 level – ozone treated grain at the bottom of the tank.

In order to assess the baking properties of ozone treated wheat grain, it is important to compare the quality of the ozone treated and the ozone non–treated grain, which is characterised by the moisture of the grain, the protein the starch and the gluten content, as well as the fall figure.

In order the wheat grain to be suitable for bread baking, its moisture content is allowed up to 14%, the protein content – not less than 12.5%, the minimum gluten content – 28%, the falling number – not less than 220 s. The quality parameters of the stored wheat grain are summarized in Table I.

TABLE I.

Quality of the grain before and after the grain storage					
Sample No.	**Moisture, %**	**Protein, g 100 g^{-1}**	**Starch, g 100 g^{-1}**	**Gluten, %**	**Falling number, s**
Level 1.1, 13.08.19.	13.9	16.4	63.6	35.5	306
Level 1.1, 03.02.20.	14.2	16.0	65.2	35.5	297
Level 2.1, 13.08.19.	14.0	16.3	63.9	36.3	325
Level 2.1, 03.02.20.	14.4	16.1	64.4	35.3	229
Level 1.1, 12.08.20.	11.2	16.2	64.8	35.5	300
Level 1.1, 24.01.21.	12.8	16.0	64.4	35.6	287
Level 2.1, 12.08.20.	11.1	16.5	64.7	36.0	310
Level 2.1, 24.01.21.	13.0	16.0	64.6	36.1	290

1.1 level –ozone non–treated and 2.1 level – ozone treated grain at the bottom of the tank.

According to the data obtained in the study (Table I), it can be concluded that ozone does not significantly affect the quality of wheat grains during storage. The falling number of wheat grain increases slightly during storage, but this is not significant changes. As no significant changes in the quality of wheat grain were found, then didn't show any significant differences in the quality of wheat bread. Therefore, it can be concluded that did not significantly affect the baking properties of the wheat grain.

Researchers have differing views on the effects of ozone on the wheat germination capacity and germination rate. Tiwari et al., 2010, [9] treating the wheat grain for 3 – 5 days with an ozone concentration of 50 ppm, have noticed a slight decrease in the germination capacity. Also [8] considers that high ozone doses and long treatments can reduce the grain germination capacity. The authors [7] believe that the ozone treatment does not affect the germination capacity. These authors have performed experiments under laboratory conditions with small amounts of grain [6], on the other hand, regard that the use of ozone treated seeds increases the yield by 10 – 25%, although without indicating the ozone concentration. The results of the germination rate for and germination capacity analyses after long–term storage of the grain are shown in Table II.

TABLE II.

The germination rate and germination capacity of the analysed grain		
Sample No.	**Number of the germinated grain, %**	
	Germination rate	**Germination capacity**
Level 1.1, 13.08.2019.	25	48
Level 1.1, 03.02.2020.	37	56
Level 2.1, 13.08.2019.	38	75
Level 2.1, 03.02.2020.	77	97
Level 1.1, 30.08.2020.	80	90
Level 1.1, 24.01.2021.	73	75
Level 2.1,12.08.2020.	81	81
Level 2.1, 24.01.2021.	97	100

1.1 level – ozone non–treated and 2.1 level – ozone treated grain at the bottom of the tank.

The results of our experiments are not convincing either. For the ozone non–treated grain (Level 1.1), at the first stage of the experiments, after about five months of storage, the germination capacity and the germination rate have increased but at the second stage they have decreased. On the other hand, for the ozone treated grain, the

germination capacity and the germination rate after storage have increased by about 20% at both stages of the experiments. It is possible that the results, different from other studies [8, 9], can be explained by about a three times lower ozone concentration and a shorter treatment time.

To study the grain morphology, two series of research were performed under the ECLIPSE L150 optical microscope (Nikon). There were analyzed the outer appearance and the cross–sectional view of the grain obtained by an optical microscope.

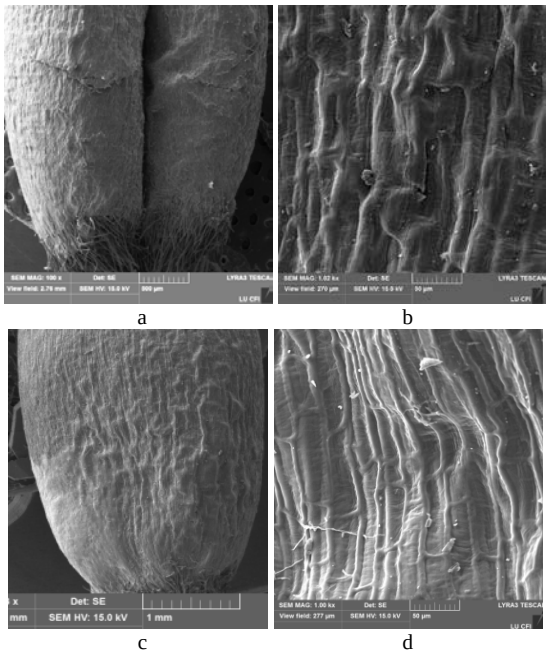

Fig. 3. The morphology of the wheat grain after storage

Due to the corrugated and wavy surface, an image in good magnification could be obtained during the analysis of the outer appearance of the grain [only] from separate surface areas. Figure 3 (a; b – 1.1 level, ozone non–treated and c; d – 2.1 level, ozone treated grain) shows typical examples of the four grain. One can draw a conclusion from the performed study that, within the limits of variations of the surface relief, which is characteristic for the samples, no visually detected differences between the ozone treated and the ozone non–treated grain were observed. All the four images of the grain were obtained at the same magnification. The main focus is turned at the grain seed coat. The grain seed coat is clearly visible in the samples examined; no shell peeling or other essential differences between the ozonized and ozone non–treated grain shell were observed. A similar result has been found in the study by [13].

A conclusion follows from the morphological examination of the grain that the grain stored under the impact of the ozone treatment with a concentration of 28 mg $(m^3)^{-1}$ no damage or destruction was made to the grain seed coat, ensuring at the same time the limitation of microbiological contamination.

IV. Conclusions

The treatment of the grain, stored with ozone at a concentration of 28 mg $(m^3)^{-1}$ for 8 hours, demonstrated the efficiency of ozone concerning limitation of the microbiological contamination without affecting the quality of the stored grain.

The study of the grain quality parameters and the baking properties showed that they are not essentially affected by ozone treatment under the conditions used in the study.

The germination capacity and the germination rate of the ozone treated grain at both stages of the experiments increased after storage by about 20%.

As the morphological examination of the grain shows, the treatment of ozone with a concentration of 28 mg $(m^3)^{-1}$ did not damage the grain shell, while ensuring the limitation of microbiological contamination.

The sensor systems, developed and installed in the grain storage tanks, provided an opportunity to monitor the grain storage on a computer, both on the farm and from the distance. Particularly important in the production conditions was the ability to control the temperature and humidity of the grain in the inter–grain space in the grain storage tanks in layers during grain storage.

Acknowledgments

The financial support of Rural Support Service Project No l8–00–A01620–000003 "Technology development of grain drying with active ventilation using ozone" is greatly acknowledged. The authors thank Dr.sc.ing. Aivars Cesnieks and Ing. Sandris Cesnieks, representatives of the farm “Mazkalnini”, Tervetes region, Tervete district, Latvia for the support and active cooperation.

References

[1] Kleperis J., Kristins A., Veinbergs J. et .al. “Applicataion of Ozone in Grain Drying: Autonomous Sensor System Construction and Pecularities.” Proceedings of the 9th International Scientific Conference Rural Development 2019, 34–39.

[2] Campabadal, Carlos A., "Ozonation Systems as a Non–Chemical Alternative for Stored Grain Protection" (2013). Open Access Dissertations. 170. https://docs.lib.purdue.edu/open_access_dissertations/170

[3] Reed C. R. 2006. Managing Stored Grain to Preserve Quality and Value. St. Paul, MN: American Association of Cereal Chemists.

[4] Sauer D. B., Meronuck R. A., Christensen C. M. 1992. Microflora. In Storage of Cereal Grains and their Products.313–340. 4th Ed. D. B. Sauer. Ed. St. Paul, MN: American Association of Cereal Chemists.

[5] Komisijas Ieteikums2013/165/ES (2013. gada 27. marts) par T–2 un HT–2 toksīnu klātbūtni labībā un graudaugu produktos. (OV L 91, 3.4.2013., 12.–15.lpp.)) (Recommendation of the Commission of 2013/165/ES (27.03.2013) on the presence of toxins in the grain and cereal products (OV L91, 3.4.2013., pp. 12.–15.)) (In Latvian)

[6] Avdeeva, V., Zorina, E., Bezgina, J., & Kolosova, O. (2019). Ozone effects on toxicity of wheat grain and grain mixtures. Engineering for Rural Development, 17, 764–767. https://DOI: 10.22616/ERDev2019.18.N081

[7] Sandhu, H. P. S., Manthey, F. A., & Simsek, S. (2012). Ozone gas affects physical and chemical properties of wheat (Triticum

aestivum L.) starch. Carbohydrate Polymers, 87(2), 1261–1268. https://doi.org/10.1016/j.carbpol.2011.09.003

[8] Zhu, F. (2018). Effect of ozone treatment on the quality of grain products. Food Chemistry, 264(May), 358–366. https://doi.org/10.1016/j.foodchem.2018.05.047

[9] Tiwari, B. K., Brennan, C. S., Curran, T., Gallagher, E., Cullen, P. J., & Donnell, C. P. O. (2010). Application of ozone in grain processing. Journal of Cereal Science, 51(3), 248–255. https://doi.org/10.1016/j.jcs.2010.01.007

[10] Raila A., Lugauskas A., Steponavičius D., Railienė M., Steponavičienė A., Zvicevičius E. 2006. Application of ozone for reduction of mycological infection in wheat grain. Annals of Agricultural and Environmental Medicine, Vol. 13 (2), pp. 287–294.

[11] Троцкая Т.П. Электроактивирование процессов сушки растительных материалов. Автореферат диссертации доктора технических наук. 32с., Москва, ГАУ, 1998. Electroactivation of drying processes of plant materials. Abstract of the dissertation of a doctor of technical sciences. 32 pages, Moscow, GAU, 1998 (In Russian).

[12] Rucins A., Viesturs D., Kristins A., Bruveris J. 2020. "Investigations in Intensification of Grain Drying by Active Ventilation Applying Ozone." Engineering for Rural Development 19: 231–37. https://doi.org/10.22616/ERDev.2020.19.TF057.

[13] Savi G.D., Piacentini K.C., Bittencourt K.O., Scussel V.M. Ozone treatment efficiency on *Fusarium graminearum* and deoxynivalenol degradation and its effects on whole wheat grains (*Triticum aestivum* L.) quality and germination. Journal of Stored Products Research, 59 (2014), pp. 245–253.

Environment. Technology. Resources. Rezekne, Latvia
Proceedings of the 13th International Scientific and Practical Conference. Volume 3, 310-313

3D Modeling, Simulation and Analysis of Anti-Vibration Boring Bar

Sabi Sabev
Technical University - Sofia, Plovdiv Branch
Plovdiv, Bulgaria
sabi_sabev@tu-plovdiv.bg

Plamen Kasabov
Technical University - Sofia, Plovdiv Branch
Plovdiv, Bulgaria
kasabov_p@abv.bg

***Abstract* - This study presents the capabilities of the engineering dynamic analysis according to the Finite Elements Method (FEM), demonstrated on a 3D virtual prototype of a part "Anti-vibration boring bar" for lathe. The analysis is performed with help of CAE system Ansys. The modal frequencies are determined which are necessary for optimizing the constructive parameters of the product during the design stage.**

Keywords - boring bar, FEM, modal frequencies, virtual prototype.

I. INTRODUCTION

In practice in the production of parts with deep holes (e.g., deep > 5xD) usually select a boring process to achieve the desired dimensional accuracy when dealing with cases of large holes as an alternative approach to the conventional drilling and surface finishing.

Finished surface quality and dimensional accuracy of high-precision mechanical parts produced by machining processes are greatly affected by the static and dynamic behaviour of the machining system. Inadequate cutting parameters or machining system compliance may give rise to undesired vibration arising during the cutting process, which is degrade quality for surface finish and dimensional accuracy. The long work in conditions of vibrations of a boring bar may cause premature tool wear or tool breakage, and damage to machine tool elements such as tooling system or spindle bearings. It is desired to increase the dynamic stiffness of the boring bar by improving its damping properties. The damping is increased either actively [2], [3] or passively [4].

There have been many theoretical investigations regarding stable and unstable operating ranges for various cutting conditions. These works typically rely on constructing models and varying one parameter (cutting speed, width of cut, etc.) at a time in order to generate stability lobe diagrams showing regions of stable and unstable cutting [6].

Virtual engineering includes a wide range of engineering activities such as: analysis, simulations, optimizations, etc., related to both the design process (CAD) and the production process (CAM). Engineering analysis is a key element in making a 3D model.

One of the most common operations performed by CAE systems on a 3D prototype is Finite Element Analysis (FEA). This method is used as a universal tool for calculations and analysis of the behaviour of mechanical systems in power, heat and others. loads [1].

The main thing for this method is that the continuous elastic structure of the structure is divided into a finite number of small, discrete elements. They are: linear, planar or spatial, with a simple geometric shape, connected to each other at nodal points located along their boundaries. The displacements of these nodal points under the influence of loads applied in them are unknown variables in a system of equations, the solution of which represents the behaviour of the whole structure. In the stress analysis of the problem, these equations are for the static equilibrium of the nodes. The most commonly used two-dimensional finite elements are triangular or quadrangular. The two-dimensional finite elements are used in solving a two-dimensional stress (strain) state.

Modal analysis is used to find out the natural frequencies and mode shapes of a structure. The natural frequencies and mode shapes are extremely significant factor in the design of a structure for dynamic loading conditions. They are also compulsory for a spectrum study or transient study. [5]

Online ISSN 2256-070X
https://doi.org/10.17770/etr2021vol3.6560

Typically, the type of chatter encountered in turning is of the regenerative type. There has been a great body of work performed on chatter in the last 60 years. Chatter was purported as the result of a negative damping effect. [6]

Both passive damping and active damping methods have been applied to reduce the dynamic response for the bar structure. A passive damping method will be introduced to reduce the structural vibration and dynamic response of the bar in this paper. The constrained layer damping composite bar is a typical passive damping structure which offers an easier and cheaper approach to solve the problem of structural detrimental vibrations. The polyurethane as a viscoelastic material of the damping layer improved the damping property, and the hard metal as a high stiffness material of the constrained layer increased the damping property and compensated the static stiffness. Compared with the bar without the constrained layer damping structure, the damping ratio of the C-P-H composite bar was increased by 400% and the static stiffness lost 12%.

A study of the literature on the subject found that most of the natural frequencies of vibration and vibrations during the operation of the bar are in the sound range up to 5 kHz. [6-10].

Based on the above, the purpose of the study is: Analyzing the impact of the damping system on the natural frequencies of anti-vibration boring bar on a lathe in an environment of Ansys CAE system.

II. Materials and Methods

To achieve this goal, a Factorial Desing 2-level was made in Minitab. The number of factors is 3. The three factors used are: Weight of the damping elements (X1), the amount of dampering oil (X2) and the diameter of the O-rings (X3). The following restrictions are provided for these factors:

$$80 \leq X1 \leq 20 \quad (1)$$

$$5 \leq X2 \leq 10 \quad (2)$$

$$2 \leq X3 \leq 5 \quad (3)$$

On the basis of the claimed limitations to the factors in the programming environment is generated a table of 8 experiments (Table.1).

Table.1 Experiments planning

Design Table			
Run	X1	X2	X3
1	+	-	-
2	+	-	+
3	+	+	+
4	-	+	+
5	-	-	+
6	+	+	-
7	-	-	-
8	-	+	-

After experiment planning was made, 3D models of 8 types of boring bar base were designed in SolidWorks environments (Fig.1). For each of them a modal analysis with the CAE Ansys will be performed.

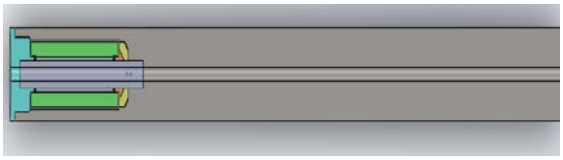

Fig. 1. Section view of boring bar -X1=80 X2=5 X3=2

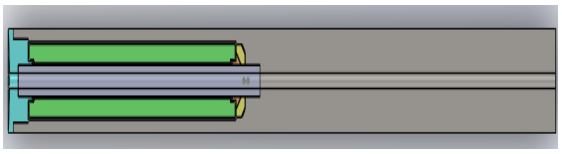

Fig. 2. Section view of boring bar - X1=200 X2=5 X3=2

III. Method of Analysis

The methodology of the model analysis covers the following events:

- ✓ Preparation of the 3D model of virtual prototype with CAD Protect;
- ✓ Defining the prototype material constants: Young's modulus (elastic module) - E ; density of the material - ρ ; Poisson's ratio - μ ;
- ✓ Generation of the discretionary calculation model, based on the finite element method;
- ✓ Defining of the restrictive (border) conditions;
- ✓ Selecting the parameters of the numerical results of the modal analysis;
- ✓ Processing of the results - graphically and tabularly.

The following figure represents the boring bar mesh.

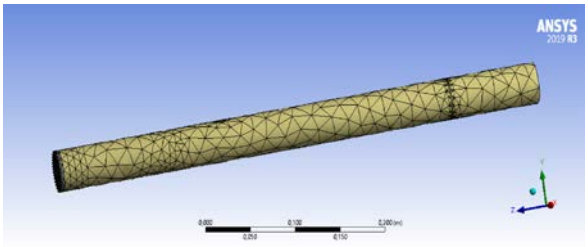

Fig. 3.Mesh

Figure 4 presents the fixe restrain.

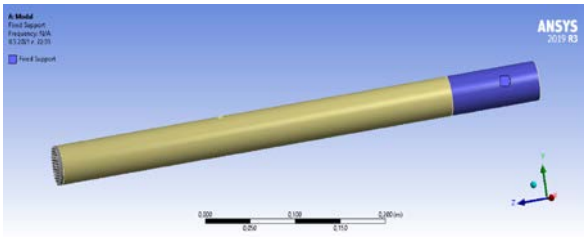

Fig. 4.Fixed restrain

IV. Results and Discussion

After the modal analysis has been performed, the natural frequencies were determined for each pattern. The obtained experimental results for the modal frequencies are presented in Table 2.

Table 2 Natural Frequencies

Run	X1 [mm]	X2 [mm]	X3 [mm]	*y [Hz]*
1	80	5	2	501
2	200	5	2	860
3	80	10	2	274
4	200	10	2	536
5	80	5	5	390
6	200	5	5	878
7	80	10	5	274
8	200	10	5	520

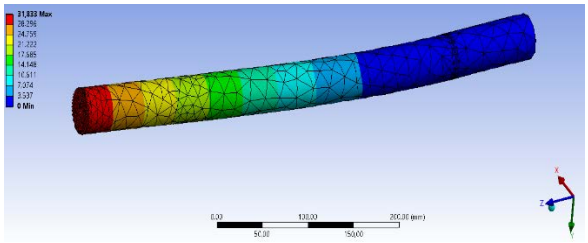

Fig. 5. Mode shape at 501 Hz

The mathematical and statistical processing is made with the MINITAB 17. The regression equation is shown as follow:

$$y = 253 + 4{,}942\,X1 - 11{,}7\,X2 - \\ - 9{,}08\,X3 - 0{,}2825\,X1 * X2 \qquad (4)$$

Table 3 Coefficients

erm	Coef	SE Coef	95% CI	T-Value	P-Value	VIF
Const	253	120	(-129; 636)	2,11	0,126	
X1	4,942	0,758	(2,529; 7,354)	6,52	0,007	10,00
X2	-11,7	14,6	(-58,2; 34,8)	-0,80	0,482	6,44
X3	-9,08	9,59	(-39,60; 21,43)	-0,95	0,413	1,00
X1*X2	-0,2825	0,0959	(-0,5877; 0,0227)	-2,95	0,060	15,44

Table 4 Model Summary

S	R-sq	R-sq(adj)	PRESS	R-sq(pred)	AICc	BIC
40,6832	98,70%	96,96%	35309,3	90,75%	170,15	86,63

Table 5 Analysis of Variance

Source	DF	Seq SS	Contribution	Adj SS	Adj MS	F-Value	P-Value
Regression	4	376681	98,70%	376681	94170	56,90	0,004
X1	1	229503	60,13%	70330	70330	42,49	0,007
X2	1	131328	34,41%	1062	1062	0,64	0,482
X3	1	1485	0,39%	1485	1485	0,90	0,413
X1*X2	1	14365	3,76%	14365	14365	8,68	0,060
Error	3	4965	1,30%	4965	1655		
Total	7	381647	100,00%				

F - value of the Fischer' distribution used to verify the significance of the coefficient of a multiple correlation;

P - Multiple correlation coefficient. The multiple correlation coefficient is insignificant if $P > \alpha(\alpha = 0.05)$;

The analysis of the residuals does not show disruption of the prerequisites for the regression analysis. On Fig. 6 it can be seen that all residuals are within the range ± 2. Therefore, a conclusion can be made that there are no errors.

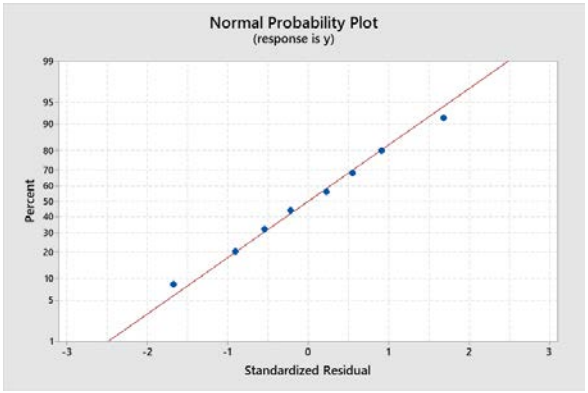

Fig. 6. Standardized Residual

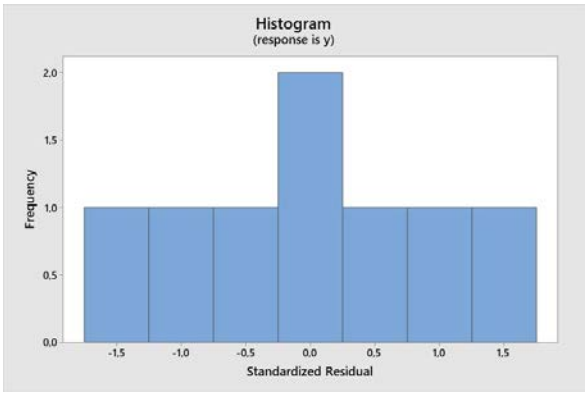

Fig. 7. Standardized Residual

Based on the regression model, the design of the anti-vibration bar was optimized. A minimum natural frequency was chosen for the optimization goal.

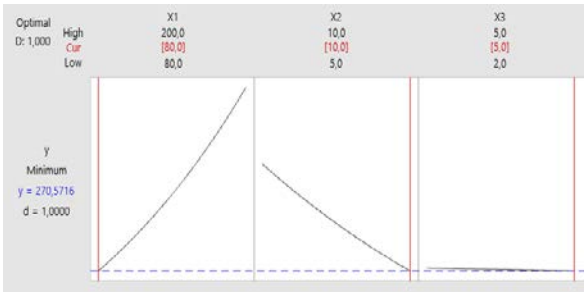

Fig. 8. Factorial Plots

V. CONCLUSIONS

The results of this work are summarized as follows:

- Theoretical and methodological presentation of the stages for conducting the analysis was performed through CAE systems for engineering calculations, simulations and analysis of details of an anti-vibration bar.
- A virtual prototype of an anti-vibration bar has been generated on SolidWorks CAD system.
- A dynamic simulation analysis has been performed using the finite element method (FEM) of an anti-vibration boring bar.
- Quantitative values were obtained for the natural frequencies of the model.

The optimization results show that the amount of damping oil and the length of the damping element have the most significant influence on the natural frequencies.

As it can be seen from Fig. № 8, by increasing the damping oil, the natural frequencies of the rod decrease, and conversely, by increasing the length of the damping element, the frequency increases.

Acknowledgments: The authors would like to thank the Research and Development Sector at the Technical University of Sofia for the financial support.

REFERENCES

[1] Zlatanov, Z. C., Ruschev, D. T., Raychev, R. P., Tashev, I. I., Determination natural frequency of beam with boundary element method , pp. 23-26, 2011, Bulgaria, ISBN ISSN1311-9192.

[2] Atsushi M, Minetaka M, Iwao Y, Vibration suppression of boring bar by piezoelectric actuators and LR circuit, 2014 Ann CIRP Manuf Technol 1243:619–642 https://doi.org/10.1016/j.cirp.2014.03.132

[3] Lu XD, Chen F, Altintas Y, Magnetic actuator for active damping of boring bars, 2014, Ann CIRP Manuf Technol 1238:771–774 https://doi.org/10.1016/j.cirp.2014.03.127

[4] R. Vinayaravi, D.Kumaresan, K.Jayaraj, A.K.Asraff , R.Muthukumar, Experimental investigation and theoretical modelling of an impact damper, Journal of Sound and Vibration Volume 332, Issue 5, 4 March 2013, Pages 1324-1334 https://doi.org/10.1016/j.jsv.2012.10.032

[5] Singaravelu Chockalingam, Ramabalan S., Govindan K., Chatter control and stability analysis in cantilever boring bar using FEA methods, MaterialsToday: Proceedings Volume 33, Part 7, 2020, Pages 2577-2580 https://doi.org/10.1016/j.matpr.2019.12.166

[6] Adam.A. Cardi, H.A. Firpi, M.T. Bement, S.Y. Liang, Workpiece dynamic analysis and prediction during chatter of turning process, Mech. Syst. Signal Process., 22 (2008), pp. 1481-1494 https://doi.org/10.1016/j.ymssp.2007.11.026

[7] Mohit Law, Pulkit Gupta, Suparno Mukhopadhyay, Modal analysis of machine tools using visual vibrometry and output-only methods, CIRP Annals, Volume 69, Issue 1, 2020, Pages 357-360 https://doi.org/10.1016/j.cirp.2020.04.043

[8] Mohsen Fallah, Behnam Moetakef-Imani, Ali Hosseini, Mostafa Ebrahimi, Boring Bar Chatter Control using Feedback Filtered-x Normalized Least Mean Square Algorithm, IFAC-Papers On Line, Volume 52, Issue 10, 2019, Pages 358-363. https://doi.org/10.1016/j.ifacol.2019.10.057

[9] Yang Bu, Zhanqiang Liu, Reduction of dynamic response of a bar using constrained layer damping composite structure, September 2018 Journal of Physics Conference Series 1074(1):012009 https://iopscience.iop.org/article/10.1088/1742-6596/1074/1/012009

[10] Tatiana Smirnova, Henrik Akesson ,Lars Hakansson, Modeling of an Active Boring Bar, December 2007

[11] Sentyakov, Kirill; Peterka, Jozef; Smirnov, Vitalii; Bozek, Pavol; Sviatskii, Vladislav. 2020. "Modeling of Boring Mandrel Working Process with Vibration Damper" Materials 13, no. 8: 1931. https://doi.org/10.3390/ma13081931

Environment. Technology. Resources. Rezekne, Latvia
Proceedings of the 13th International Scientific and Practical Conference. Volume 3, 314-318

The Effect of Feed Rate and Cutting Speed to Surface Roughness During Hole Boring of Aluminum with Anti-Vibration Boring Bar

Sabi Sabev
Technical University - Sofia, Plovdiv Branch
Plovdiv, Bulgaria
sabi_sabev@tu-plovdiv.bg

Plamen Kasabov
Technical University - Sofia, Plovdiv Branch
Plovdiv, Bulgaria
kasabov_p@abv.bg

Abstract **- this study is focusing on the experimental investigation of the effects of cutting parameters on surface roughness during hole boring of 8062 aluminums with anti-vibration boring bar on lathe. Several experiments were conducted with different cutting conditions. Based on the results and using "Minitab 19" software, a mathematic model was made to predict the surface quality in connection with different cutting conditions. Finally, an experiment analysis was carried out to verify the analytical results.**

Keywords - anti-vibration, boring bar, DOE, lathe

I. INTRODUCTION

In the production of details, surface quality is very important in quality determination. Good surface coating not only provides quality but also reduces production costs. Surface coating is important in terms of tolerances, reduces the assembly time and avoids the need for secondary work, thus reducing working time and leads to a general cost reduction. In addition, the high-quality surface is significant to improve the strength of fatigue, resistance to corrosion and creep life [3].

Literature is very rich in terms of turning operation owing to its importance in metal cutting. The three important process parameters in this research are speed, feed rate and depth of cut. Surface roughness of a turned work piece is dependent on these process parameters and also on tool geometry: nose radius, rake angle, side cutting edge angle and cutting edge. It also depends on the several other exogenous factors such as: work piece and tool material combination and their mechanical properties, quality and type of the machine tool used, auxiliary tooling, lubricant used and vibrations between the work piece, machine tool and cutting tool [4-7]

Throughout the world, machinists have to deal with the presence of problematic vibrations on a daily basis. Most recently, the design and development of anti-vibration tools, otherwise known as tuned or damped tools, has been applied to the boring bar.

Choosing the appropriate nose radius of the insert is also a vitally important consideration. A lower nose radius is recommended as this configuration significantly reduces the cutting forces, due to the lower contact between the insert and work piece, which helps to limit and reduce vibration. A greater nose radius creates much larger radial and tangential cutting forces that can produce increase the roughen Ra and unwelcome vibrations.

In order to get good surface quality, it is necessary to use optimization technique to find optimal machining parameters. This paper investigates the effect of machining parameters on the quality of surface finish. Used is design of experiment (DOE) method. Analyses the considerable influence of each experimental parameter using statistical analysis of variance (ANOVA), and after all determine the optimal parameters combination to yield the best machining condition. The machining parameters involved in this experiment are cutting speed, feed rate, and depth of cut. The main objective is to find the combination of machining parameters to achieve low surface roughness during end milling. [7]

Online ISSN 2256-070X
https://doi.org/10.17770/etr2021vol3.6537

II. MATERIALS AND METHODS

For the purpose of the experiments we use ISCAR AVC-D32-SVLCR-16T boring bar (Fig.1). The boring head that we use is ISCAR AVC-D32-SVLCR-16T (Fig.2), equipped with VCGT 160402-AS inserts with a 7° positive flank, very positive rake angle and sharp cutting edge for machining aluminum. . The nose radius of the inserts is 0.2mm (Fig.3).

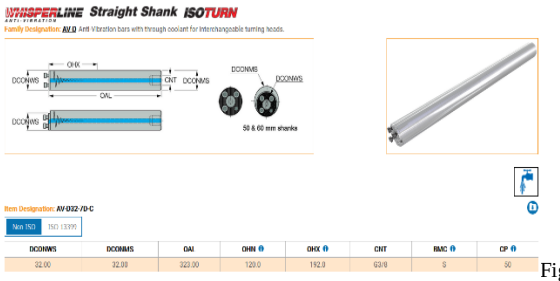

Fig.1

Boring bar specification

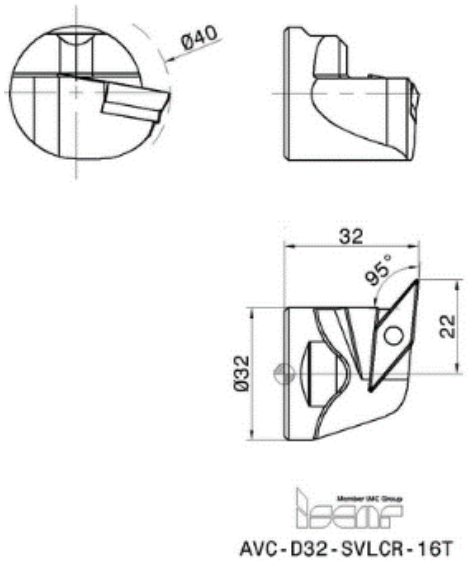

Fig.2 Boring head

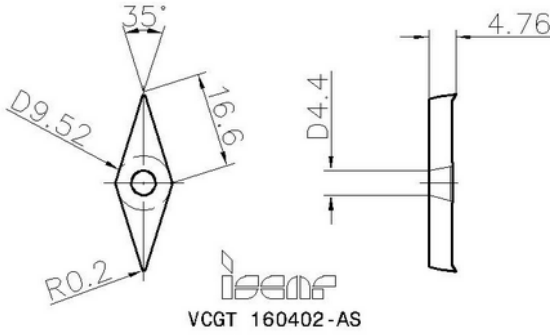

Fig. 3. Inserts VCGT 160402-AS

The machine that we use is DMG MORI CLX 400 with the following specification (Table.1):

TABLE.1 MACHINE SPECIFICATION

Max. work piece length with a tailstock (can be machined)	800 mm
Max. chuck size	315 mm
Max spindle motor speed	4,000 rpm
Drive power rating (100% DC)	17 kW
Max. bar capacity diameter	80 mm

The boring bar is held on the machine by VDI40 AV-D32-JHP holder. The specification of tool holder is as follows(Fig.4):

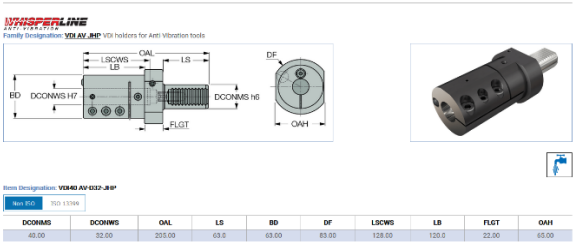

Fig4 Tool holder specification

As a result of the literary survey on the experiments topic [8] the following conclusion has to be made- the cutting depth has the smallest effect on the surface finish. The value of the effect varies between 1%-3%. The theoretical value for the surface finish proves that.

Based on the theoretical dependence (1) and (2) [1] the theoretical values for the surface finish using insert with nose radius 0.2mm, are calculated. The results are as follow(Table.2).

$$R_t = r - \sqrt{r^2 - f^2/4} \qquad (1)$$

$$R_a = \frac{Rt}{4} \qquad (2)$$

TABLE.2 THE THEORETICAL VALUE FOR THE SURFACE FINISH

Feed rate mm/rev	**Rt**	**Ra**
0,05	1,569	0,392
0,07	3,086	0,772
0,08	4,041	1,010
0,10	6,351	1,588
0,12	9,212	2,303
0,15	14,595	3,649
0,16	16,697	4,174
0,18	21,394	5,349
0,20	26,795	6,699

A modal analysis was performed. On the basis of it were determined 5 modes for the experiments. Three trails were made for each mode to minimize the errors. That means that the total number of the experiments is 15.

The chosen work material is AL8062-T. The dimensions of the work piece are: diameter Φ80mm, length L-50mm and size of the boring hole Φ45mm Fig.3.

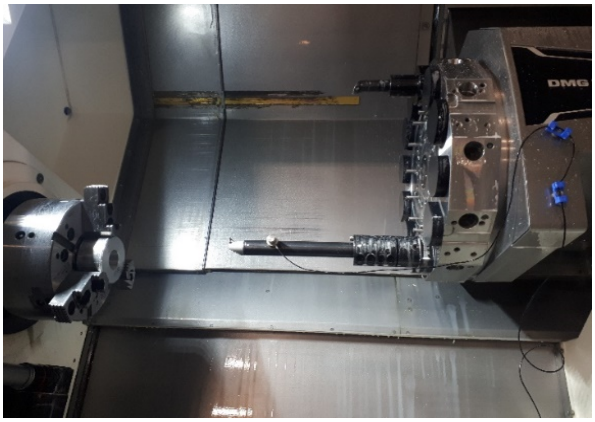

Fig. 5 Scheme of the experimental installation.

III. Results and discussion,

After processing the experimental samples, the roughness of the treated surfaces was measured with a roughness tester Tesa Rugosurf 20 (shown in Fig.6). This device is a compact roughness measuring instrument for mobile use. The maximum measuring range of Tesa Rugosurf 20 is Z axis: 400 µm and X axis: 16 mm.

Fig.6 Scheme of the experimental installation for taking data on the roughness of the treated surface

The Table.3 shows the experiment results.

TABLE.3 Roughness measurement data

N	Feed	Speed	Ra
1	0,200	430	5,534
2	0,200	300	5,151
3	0,050	300	0,310
4	0,050	430	0,232
5	0,125	365	1,930
6	0,200	430	5,371
7	0,200	300	5,134
8	0,050	300	0,306
9	0,050	430	0,249
10	0,125	365	1,824
11	0,200	430	5,542
12	0,200	300	5,358
13	0,050	300	0,346
14	0,050	430	0,230
15	0,125	365	1,890

Using the equation (3) and the value of the theoretical and experimental roughness we find the difference between them. The results are shown in tab.4

$$Error = \frac{Rat - Rae}{Rat} x\ 100\ \% \qquad (3)$$

, where

Rat- theoretical roughness;

Rae - experimental roughness.

TABJE.4 Error between theoretical and experimental roughness

№	Feed mm/rev	Experimental Ra	Theoretically Ra	Error [%]
1	0,200	5,482	6,669	17,794
3	0,050	0,321	0,392	18,197
5	0,120	1,881	2,303	18,309

The mathematical and statistical processing was made with the software product MINITAB 19. For the mathematical description of the target function *Ra.*

The data in Table 3 is processed and the following regression model was obtained:

$$Ra = 0{,}053 - 9{,}27F + 0{,}0007S + 172{,}3\ FF \qquad (4)$$

TABLE.5 COEFFICIENTS

TERM	COEF	SE COEF	T-VALUE	P-VALUE	VIF
CONSTANT	0,053	0,247	0,21	0,835	
F	-9,27	3,34	-2,77	0,018	56,56
S	0,000709	0,000513	1,38	0,194	1,00
F*F	172,3	13,3	13,00	0,000	56,56

TABLE .6 MODEL SUMMARY

S	R-SQ	R-SQ(ADJ)	R-SQ(PRED)
0,115507	99,82%	99,77%	99,67%

TABLE 7ANALYSIS OF VARIANCE

SOURCE	DF	ADJ SS	ADJ MS	F-VALUE	P-VALUE
REGRESSION	3	79,3781	26,4594	1983,18	0,000
F	1	0,1025	0,1025	7,68	0,018
S	1	0,0255	0,0255	1,91	0,194
F*F	1	2,2531	2,2531	168,88	0,000
ERROR	11	0,1468	0,0133		
LACK-OF-FIT	1	0,0928	0,0928	17,17	0,002
PURE ERROR	10	0,0540	0,0054		
TOTAL	14	79,5249			

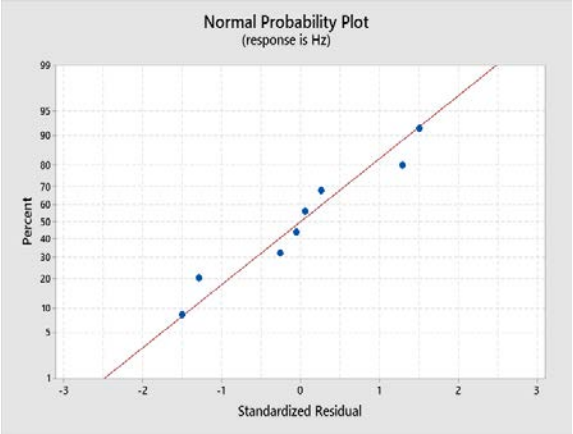

Fig.7. Standardized Residual

The analysis of the residuals was made by means of the charts of the standardized residuals, Fig.7.

The analysis of the residuals does not show disruption of the prerequisites for the regression analysis. Fig. 5 shows that all residuals are within the range ± 2. Therefore, a conclusion can be made that there are no gross errors.

It was performed optimization of the parameters. Criterion of optimization was Ra= 0.8. The results are presented in Tablets 8-11 and Fig.8

TABLE 8. PARAMETERS

RESPONSE	GOAL	LOWER	TARGET	UPPER	WEIGHT	IMPORTANCE
RA	TARGET	0,23	0,8	5,542	1	1

TABLE 9 VARIABLE RANGES

VARIABLE	VALUES
F	(0,05; 0,2)
S	300

TABLE 10 SOLUTION

SOLUTION	F	S	RA FIT	COMPOSITE DESIRABILITY
1	0,0887592	300	0,800000	1,00000

TABLE.11 MULTIPLE RESPONSE PREDICTION

VARIABLE	SETTING
F	0,0887592
S	300

RESPONSE	FIT	SE FIT	95% CI	95% PI
RA	0,8000	0,0636	(0,6600; 0,9400)	(0,5098; 1,0902)

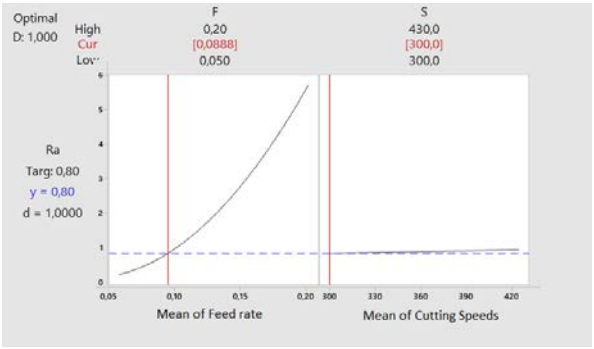

Fig.8 Predicted Value

Fig. 9 shows graphical presentation of the influence of cutting parameters on the roughness

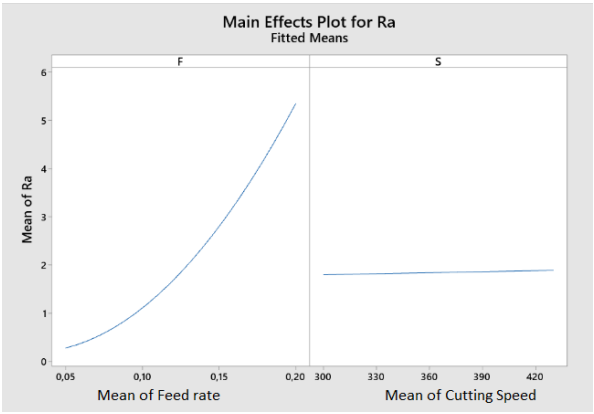

Fig.9 Factorial Plots for Ra

IV. CONCLUSIONS

- From the performed analysis it has been experimentally proven that the greatest influence on the roughness of the treated surface has the feeding;

- The difference between the theoretical and the experimental roughness values is approximately 18%.

- A check of the predicted value of the obtained regression model was performed, which proves the reliability of the model.

- Come to the fact that the experimental roughness is lower than the theoretical one, we can say that the anti-vibration bar has excellent dynamic stability in the studied power range.

Acknowledgments: The authors would like to thank the Research and Development Sector at the Technical University of Sofia for the financial support

REFERENCES

[1] David J. Whitehouse, Surfaces and Their Measurement. Book 2002 https://doi.org/10.1016/B978-1-903996-01-0.X5000-2

[2] Zurita-HurtadoO. J., Di Graci-TiralongoV. C., & Capace-AguirreM. C. (2017). Effect of surface hardness and roughness produced by turning on the torsion mechanical properties of annealed AISI 1020 steel. Revista Facultad De Ingeniería Universidad De Antioquia, (84), 55-59. https://doi.org/10.17533/udea.redin.n84a07

[3] Kumar NS, Shetty A, Shetty A, Ananth K, Shetty H (2012) Effect of spindle speed and feed rate on surface roughness of Carbon Steels in CNC turning. Procedia Engineering 38: 691-697. https://doi.org/10.1016/j.proeng.2012.06.087

[4] J.D. ThieleandS.N. Melkote,"Effect of cutting edge geometry and work-piece hardness on surface generation in the finish hard turning of AISI 52100 steel,"Journal of MaterialsProcessing Technology, vol. 94, 1999, pp. 216-226.

[5] W.Chen, "Cutting forces and surface finish when machining mediumhardness steel using CBN tools," International Journal of Machine Tools Manufacturing, vol. 40, 2000, pp. 455-466.

[6] S.M. Darwish,"Theimpact of the tool material and the cutting parameters on surface roughness of supermet 718 nickel superalloy," Journal of Materials Processing Technology,Vol. 97, 2000, pp. 10-18.

[7] Samya Dahbi, Haj El Moussami, Latifa Ezzine. Optimization of turning parameters for surface rough-ness. Xème Conférence Internationale: Conception et Production Intégrées, Dec 2015, Tanger. https://hal.archives-ouvertes.fr/hal-01260818

[8] M. Nurhaniza, M. K. A. M. Ariffin, F. Mustapha, B. T. H. T. Baharudin, "Analyzing the Effect of Machining Parameters Setting to the Surface Roughness during End Milling of CFRP-Aluminium Composite Laminates", International Journal of Manufacturing Engineering, vol. 2016, Article ID 4680380, 9 pages, 2016. https://doi.org/10.1155/2016/4680380

[9] C. Rao, D. Rao, P. Srihari Influence of cutting parameters on cutting force and surface finish in turning operation Procedia Eng., 64 (2013), pp. 1405 1415 https://doi.org/10.1016/j.proeng.2013.09.222

Environment. Technology. Resources. Rezekne, Latvia
Proceedings of the 13th International Scientific and Practical Conference. Volume 3, 319-323

Research of Human Hand Movements Repeatability Using Robotic System

Paulius Sakalys
Vilniaus Kolegija University of Applied Sciences
Vilnius, Lithuania
p.sakalys@eif.viko.lt

Loreta Savulioniene
Vilniaus Kolegija University of Applied Sciences
Vilnius, Lithuania
l.savulioniene@eif.viko.lt

Dainius Savulionis
Vilniaus Kolegija University of Applied Sciences
Vilnius, Lithuania
d.savulionis@eif.viko.lt

Abstract **- The aim of the research is to determine and evaluate the repeatability of the robotic system by repeating the movements of the human hand, to identify the displacement using digital infrared projection equipment, skeletal methods and depth cameras. The article reviews and selects possible skeletal methods, motion recognition algorithms, reviews and substantiates the physical equipment selected for the technical stage of the experiment. The plan of experimental research stages, research stand, systematized research results, conclusions and usability suggestions are described.**

Keywords - robotic system, skeletal methods, IR projection, depth camera.

I. INTRODUCTION

There are many areas of activity where a sequence of interactions between a human and a robot could be implemented - a collaborative effort that requires training the robot or robotic system to observe, record, and accurately reproduce the movements of the human body.

The aim of this study is to investigate the accuracy of the robotic system control method based on skeletal methods and machine learning algorithms to determine the repeatability indices of the robotic system manipulator using digital optical means of human body motion recognition. The article reviews the most commonly used skeletal methods, the principles of operation of digital optical human body motion recognition devices, the methodology of their interconnection, and presents the results, conclusions and suggestions of the first tests of real robotic manipulator packaging.

II. LITERATURE REVIEW

Structured recognition of human movement is necessary for robotics movement control training. It is appropriate to use the skeletal method to identify the main human kinematic motion points. In order to select the most appropriate skeletal method, it is necessary to define the concept of skeleton and the issues related to the creation of a skeletal model.

Skeletal separation is important in a variety of fields: medical image processing, visualization, navigation, virtual endoscopy, computer graphics. Some authors often refer to the skeleton as the medial axis [4]. Set of maximum circles a maximum circle is one that is not completely drawn on any other circle within the surface o of the object in question [11] in three-dimensional space, instead of circles, maximum balls are drawn:

$$S_r = \{y \in R_3, d(x,y) < r\}, \qquad (1)$$

where r is the radius of the sphere (or circle in the case of two dimensions); x O∈ is the central point when 3 O R ⊂; d (x, y) - distance between x and y points in three-dimensional space. Without any additional operations, the central axis becomes the central surface in three-dimensional space [1]. It can be argued that the skeleton is a subset of the central surface [9] [10]. By reviewing the relevant sources of information, two main types of skeletons can be distinguished:

Geometric skeleton - depicts the center of the object. The image does not always have to be one point wide (Fig. 1 a). Often the geometric skeleton is called the central axis [3], so the geometric skeleton does not necessarily have to be one pixel wide, but it always corresponds to the center of the object.

Online ISSN 2256-070X
https://doi.org/10.17770/etr2021vol3.6591

Skeleton of curves - a set of connected central lines is called a skeleton of curves (Fig. 1 b). The number of skeletal branches does not necessarily coincide with the branches of the skeletal object, so not every curved skeleton is at the same time a topological skeleton. The skeleton of the curves is one-dimensional everywhere except for the branching points, because the one-dimensional centerlines intersect at those points.

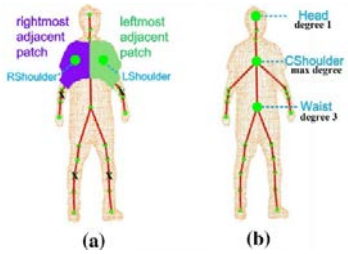

Fig. 1. The main types of skeletons [15]

Many skeletal extraction (skeletal) algorithms have been developed. Algorithms that implement skeletonization can be divided into the following groups [11]:

Iterative thinning. The main principle of this group of algorithms is the identification and destruction of simple points. Deleting a simple point does not affect the topology of the object. All iterative thinning algorithms operate in discrete space. Thinning iterations are performed until no simple points remain in the object. The main problem with this group of algorithms is limb clipping or uneven reconstruction, so additional conditions are introduced to preserve them. Also, the resulting skeleton is not always geometric, it is centered [8].

The distance field is formed when each point of the object is assigned a distance value to the nearest point of the surface. After calculating the distance field, an attempt is made to pave the way through the points where the distance to the boundaries of the object is the maximum. It is these points that correspond to the skeleton of the object [10]. The aggregation of points is performed using a gradient search or graph theory (searching for the shortest path between the selected maximum). The main advantage of these algorithms is that the distance field is quickly calculated.

Geometric methods are most commonly used in cases where the surface of an object is represented using a set of scattered points [2] or a grid of surfaces. These points are used to construct the Voronoi diagram, that is, to create the Voronoi cells. Each wall of a Voronean cell is equidistant from the vertices or points of the grid that constructs it (Fig. 2). The inner edges of Voronoi can be used to approximate the geometric skeleton. The main advantage of these algorithms is speed, because to determine a simple point it is enough to examine the position of its 3 × 3 adjacent points [9]. Additional transformation steps are required to isolate the one-dimensional skeleton.

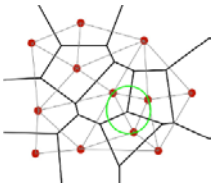

Fig. 2. Example of Voronoy's cell [7]

When creating a skeleton based on points in three-dimensional space, the change of human movement describing the coordinates using digitization means must take into account the calculation speed of the chosen skeletal method [13]. The fastest in terms of calculations is the latter described geometric method.

III. Methodology

The description of the research methodology is divided into four components: description of the research object (Part a), explanation of the principle of forming a digital skeleton of a moving object (human) (Part b), robotic system motion repetition training algorithm analyzes (Part c):

a. The object of the study is a robotic system (Fig. 3) - a robotic system printed by a 3D printer is identified with the human body, having two robotic arms with nine kinematic degrees of freedom - manipulators, and a head representing a two degrees of freedom robotic mechanism equipped with environmental video surveillance equipment. Servo drives are used for motion motors. The initial repeatability tests presented in the article will be performed with the right-hand movements of the model.

Fig. 3. Robotic system

b. The principle of digital skeleton formation of a moving object (human): The Kinect multi-infrared projection camera (Fig. 4 a) is used for the study. The device consists of a standard RGB VGA camera, a depth camera, an infrared projector, an array of microphones and a controller.

For the specified cameras and infrared projector, the device forms a three-dimensional image field in which it distinguishes moving points (Fig. 4 a):

1. The depth camera sensor illuminates the real space and determines the distances specified for each pixel of the image based on the reflections of the infrared point projections [14].

2. The software that combines the depth camera results and the RGB camera image creates a map of the depth pixel projections of each object in front of the camera, and creates RGB textures based on the location corresponding

to the RGB pixels. All information is generated in real time at a rate of 30 times per second.

3. The processed data is sent to the middleware on the receiving computer.

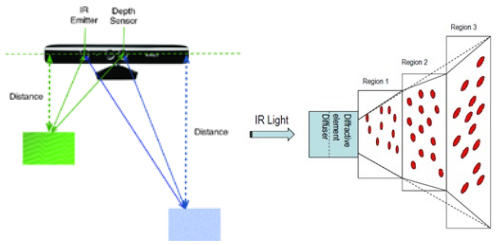

(a) **(b)**

Fig. 4. Kinect Multi-Infrared Projection Camera and Formation of Three-Dimensional Image Field Points by Infrared (Stitilis, 2014)

The first version of the Kinect used for the study returns the joint positions with a three-dimensional vector. The OpenNI library (for access to the cameras) used on the receiving computer provides a function that returns the position of the joint in the orientation matrix (Fig. 5):

```
public float getJointOrientationSkeleton(int userId, int joint, PMatrix3D jointOrientation) {
  float[] mat = new float[9];

  float ret = getJointOrientationSkeleton(userId, joint, mat);

  jointOrientation.set(mat[0], mat[1], mat[2], 0,
                       mat[3], mat[4], mat[5], 0,
                       mat[6], mat[7], mat[8], 0,
                       0,      0,      0,      1);

  return ret;
}
```

Fig. 5. An OpenNI library function that outputs a position orientation matrix

After the calculations, the value of the returned matrix changes only in the first 3 rows. Therefore, we can reduce the size of this matrix to 3x3. Using Euler's characteristics for a given 3x3 matrix (Fig. 6):

$$R = \begin{bmatrix} r_{11} & r_{12} & r_{13} \\ r_{21} & r_{22} & r_{23} \\ r_{31} & r_{32} & r_{33} \end{bmatrix}$$

Fig. 6. Transformed orientation coordinate matrix

The steering angles at the three coordinate points are calculated using formulas 1-3:

$$\theta_x = \operatorname{atan2}(r_{32,} r_{33}), \quad (2)$$

$$\theta_y = \operatorname{atan2}(-r_{31,} \sqrt{r_{32}^2 + r_{33}^2}), \quad (3)$$

$$\theta_z = \operatorname{atan2}(r_{21,} r_{11}), \quad (4)$$

The coordinates of the obtained moving points are linked to each other to form a skeleton.

c. Robot system motion repetition training algorithm: positions of the obtained skeleton coordinate points - gestures are stored every 30 milliseconds in the control program, giving access rights to call them. Robot system training algorithm (Fig. 7).

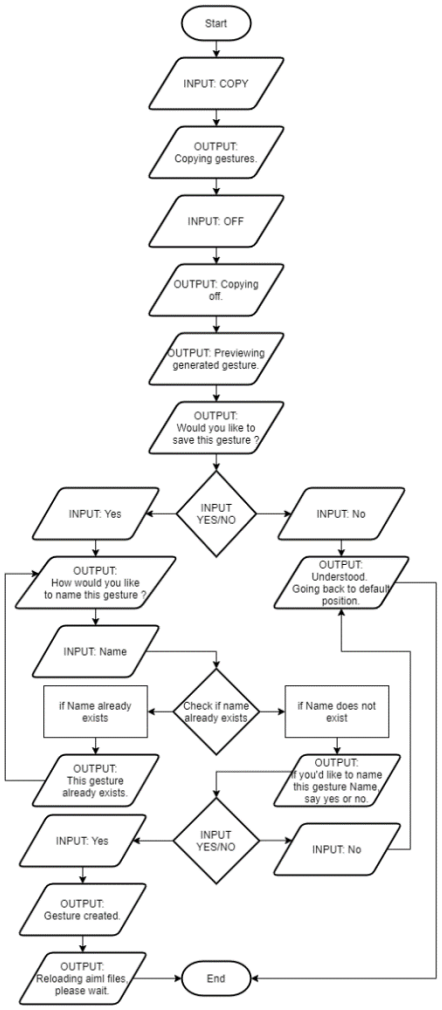

Fig. 7. Robotic system training algorithm

The sequence of the motion capture function of the Kinect camera is shown in the activity diagram. When using this feature, the client makes a "Copy" request in the command input field or with voice commands. This request starts the repetition of the robot's movements with the Kinect camera. As already mentioned, the positions of the robot servo motors are saved in a new file called "positions" during the entire repetition of the movements. The customer can stop repeating the robot's movements at any time by sending the command "Off". When this is done, the robot repeats the movements again this time taking the positions of the servo drives from the generated file. The user is then asked if they want to save this gesture. For the gesture to be saved successfully, it needs to be given a name. The name must be unique because it is used in two places. The first place is to generate a Python script. This name is used to identify the script file. Also, in order to call the generated method, one of the AIML type files needs to be edited. The AIML interpreter is used to call this function during program operation.

AIML is a recursive language based on XML [6], which allows to parse natural language text input so that it

corresponds to the response that a robotic system can send (Fig. 8).

```
<?xml version="1.0" encoding="UTF-8"?>
<aiml>
    <category>
        <pattern>HELLO WORLD</pattern>
        <template>Hello to you too!</template>
    </category>
</aiml>
```

Fig. 8. Example of AIML code structure

The first "<aiml>" tag indicates the beginning and end of the AIML document. The <category> tag defines the unit of knowledge in the robot database. The number of these tags in AIML-type files is often large, so they simply separate each unique query content, of which we have only one in example 8. Thus the robotic system is trained to identify, record and reproduce the movement of the human body.

IV. Research Results

The test procedure of the performed study is shown in Fig. 9. The training part of the robotic system is performed first: the fixed image is scleted, the motion is recognized, the point matrix is interpreted and obtained and converted into a coordinate motion point matrix of the kinematic connection servo drives, which is saved in the form of an AIML file and stored in a database. Part of the next study: the motion matrix is called from the database, the servo drives create a displacement of the manipulator axes (the manipulator has a built-in writing device with which it must reach the initial reference point memorized during the training part). When the system reaches a possible reference point, it returns to its original servo drive coordinates, the deviation data is recorded, the motion matrix is recalled from the database, and the test is repeated (20 times).

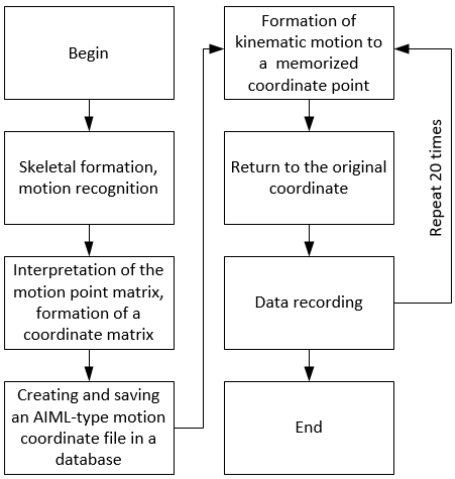

Fig. 9. Test Flow Chart

Data for all twenty test deviations are shown in Fig. 10 of the diagram.

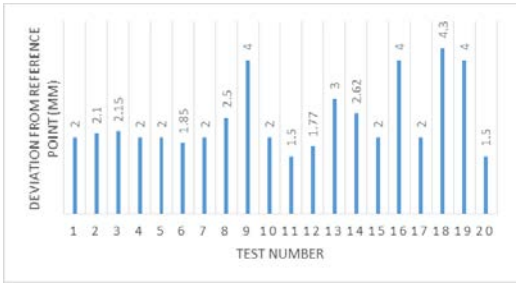

Fig. 10. Deviation from the Reference Point Diagram

V. Conclusions

The study developed a primary methodology that combines skeletal methods, machine learning algorithms and digital optical equipment to identify human body motion by creating a coordinate system and storing it in a robotic system database with the ability to retrieve servo drive motion displacement for manipulator freedom.

1. After reviewing the most suitable skeletalization methods available, the fastest geometric skeletalization method in terms of calculation was selected;

2. Kinect digital optical infrared projector used to isolate the human body from the environment;

3. OpenNI library was used for three-dimensional vector processing, algorithm for calculation, setup, recording and calling of motion angles was developed using AIML software interpreter;

4. Tests with a robotic right-hand manipulator (hand) containing a writing instrument to reach the reference point during the tests have a minimum deviation of 1.5 mm, a maximum of 4.3 mm and a mean deviation of 2.46 mm from the fixed starting point of the training point;

The description of the performed research methodology and the obtained research results can be used in areas where synergistic interaction of human and robotic system synchronous movements is possible: performing dynamic, time-varying functions that do not operate according to a predetermined sequence of actions. The results of the study also have a wide range of applications in the training process: researching the properties of machine training, the development of robotics, control systems for robotic systems and algorithms.

References

[1] Carmelo, M., Acutis, A., Carrabba, M., Criscenti, G., Vozzi, G. (2016). Nanobiomaterials in Soft Tissue Engineering: Applications of Nanobiomaterials. Volume 5. Machine design for multimaterial processing, 111-140. DOI: https://doi.org/10.1016/B978-0-323-42865-1.00005-2

[2] Chaminade, T., & Cheng, G. (2019). Journal of Physiology-Paris. Volume 103. Social cognitive neuroscience and humanoid robotics, 286-295. DOI: https://doi.org/10.1016/j.jphysparis.2009.08.011

[3] Davies, E.R. (2017). Computer Vision. London: AcademicPress.

[4] Jin, D., Chen, C., Hoffman, E.A., Saha, P.K. (2017) Skeletonization: Theory, Methods and Applications. Curve skeletonization using minimum-cost path, 151-180. DOI: https://doi.org/10.1016/B978-0-08-101291-8.00007-9

[5] Kar, A. (2011). *Skeletal Tracking using Microsoft Kinect.* Kanpur

[6] Nava, A., Brena, R., Garrido, L. (2014). Recognizing Activities Using a Kinect Skeleton Tracking and Hidden Markov Models. *13th Mexican International Conference on Artificial Intelligence (MICAI)*, DOI: https://ieeexplore.ieee.org/document/7222846.

[7] N.D. *Example of Voronoy's cell*. Retrieved from: https://stackoverflow.com/questions/42047077/voronoi-site-points-from-delaunay-triangulation

[8] Palionyte, A (2011). *Discretization of Continuum Structures via Image Algebra Methods*. Vilnius: Vilnius Gediminas Technical University.

[9] Paulinas, M., & Rokicki, J. (2008). Panasios formos pavirsiu, centrines asies radimo ir filtravimo metodika. *Biomedical Engineering*, 209-212.

[10] Rokicki, J. (2010). Skeletavimo metodu apzvalga. *Science - Future of Lithuania, Vol. 2 (No. 1)*, 19-22.

[11] Saha, P.K., Borgefors, G., Baja, G.S. (2017). Skeletonization: Theory, Methods and Applications. *Skeletonization and its applications – a review*, 3-42. DOI: https://doi.org/10.1016/B978-0-08-101291-8.00002-X

[12] Stitilis, R. (2014). *Kinect Controlled Computer Game*. Siauliai: Siauliai University

[13] Vassilevski, Y., Olshanskii, M., Simakov, S., Kolobov A., Dailov, A. (2020) Personalized Computational Hemodynamics: Models, Methods, and Applications for Vascular Surgery and Antitumor Therapy. *Computational hemodynamics in vascular surgery, 189-215. DOI: https://doi.org/10.1016/B978-0-12-815653-7.00009-9*

[14] Palagyi, K. (n.d.) *Skeletonization*. Retrieved from: http://www.inf.u-szeged.hu/~palagyi/skel/skel.html

[15] Yong, Z., Fei, T., Shaofan, W., *3D human body skeleton extraction from consecutive surfaces using a spatial–temporal consistency model*. Retrieved from: https://link.springer.com/article/10.1007/s00371-020-01851-3

Environment. Technology. Resources. Rezekne, Latvia
Proceedings of the 13th International Scientific and Practical Conference. Volume 3, 324-329

Selection of a Transportation Option for the Procurement of Goods for Own Needs, in Order to Increase the Efficiency of Operational Planning

Silviya Salapateva
Faculty of Mechanical Engineering
Technical University of Sofia, Plovdiv branch
Plovdiv, Bulgaria
sisisal@tu-plovdiv.bg

Maria Chulkova
Faculty of Mechanical Engineering
Technical University of Sofia, Plovdiv branch
Plovdiv, Bulgaria
mkaniks@yahoo.com

***Abstract* - The competitiveness of each product mostly depends on its price, which includes transport costs from the place of its production to the place of its consumption. Sometimes these costs can be comparable the cost of production. Due to the high transport costs, the competitiveness of the manufactured products decreases, not only on the domestic but also on the foreign market. Substantial part of the freight transport nationwide is carried out by trucks owned by the manufacturing companies. They transport goods needed for their production needs with their own transport and at their own expense. At the same time, the operational planning of such shipments has been insufficiently studied, in which a large number of factors of technological and organizational nature must be taken into account. Operational planning has a significant potential for reducing transportation costs. The article considers the possibility to increase the efficiency of own-account transport at the stage of operational planning.**

Keywords* - *road transport, efficiency criterion, operational planning, cargo for own needs, pendulum route.

I. INTRODUCTION

Research by scientists [1, 2 ,3, 4 and other] proves that modern practice of operation of motor vehicles on routes in urban conditions has many features, which determines the need to apply a systematic approach in their study. The presence of system properties in the operation of vehicles on urban routes requires a systematic solution to the problem and separately for each level of complexity, starting with the simplest system. Professor Nikolin's scientific concept for the development of the theory of road freight transport was adopted as a basis. The concept envisages the application of a systematic approach, according to which the vehicle can't work in isolation and the result of its work is influenced by many factors: other vehicles, the method of preforming loading and unloading operations and others.

The practice and theory of road freight transport over the last 30 years shows that the existing methods for increasing the efficiency of freight transport are in most cases applied to public transport. The transport of goods for own needs of enterprises, which are characterized by certain features are not well reflected in modern scientific approaches. In addition, an analysis of research shows that the operational planning of such shipments, which must take into account a large number of factors of a technological and organizational nature, has not been well studied.

The purpose of the study in this article is to analyze the possibilities for increasing the efficiency of freight transport for own needs of enterprises with one vehicle by improving operational planning.

II. MATERIALS AND METHODS

In practice, when transporting goods for the company's own needs with one vehicle, the following types of routes are performed: pendulum without the use of reverse mileage; pendulum with full use of reverse mileage; pendulum with incomplete use of reverse mileage; pendulum with full use of the reverse mileage, but with a different load utilization factor; circular;

Online ISSN 2256-070X
https://doi.org/10.17770/etr2021vol3.6626

delivery; collection and collection-delivery routes. The article discusses the different types of pendulum routes.

The minimum level of complexity of the organization of road freight transport corresponds to the operation of one vehicle in operational mode, then the planned volume of transport over a specific distance doesn't exceed the possible transport work per unit of rolling stock for one workday.

Since one vehicle is used for the transport of goods on each of the listed routes, the compatibility of the goods during transport (transport uniformity of the cargo) is taken into account when compiling more complex routes.

The study considers a topographic method for routing, which consists in the development and application of more complex routes than the pendulum with no use of reverse mileage [2]. When applying a route for a vehicle with a certain load capacity, the following factors are taken into account: transport characteristics of the load, the method of loading and unloading activities, allowable axle load, size restrictions and the need to meet the planned volume of transport per working day. Alternatives for solving the task of choosing a vehicle are considered its ownership (own or rented at an hourly rate) and its load capacity. The minimum cost of transporting goods for a workday is accepted as a criterion for choosing a vehicle. [5] Based on the characteristics of the load and the type of loading platform of the vehicle, the manner and duration of the loading and unloading activities is determined. [6] The duration of operation of the vehicle is limited to one shift, which corresponds to modern practice.

As a criterion for the efficiency of the transport of goods for own needs of the manufacturing companies is accepted the difference in the costs of transport of goods with its own vehicle and for the transport of same volume of goods with rented one.

The method of chain substitutions has been adopted as a method of analysis, as it has become the most widespread in road transport. In this method, all factors, except one, are provisionally considered constant, and one is variable.

The factors that influence the increase of the efficiency of the transportations are the distance over which the goods are transported on the listed routes in urban conditions. The distance at which transport can be performed in urban conditions for our country is 80 km, and the step of changing the distance is assumed to be 1 km. It is known from the theory of road freight transport that the distance at which the goods are transported depends on the productivity of the vehicle, expressed in tons (t) and ton-kilometers (tkm), which was reported in the study.

When performing the calculations for determining the indicators of the transport activity, the widely known and tested mathematical models for determining the technical-operational indicators for the operation of the rolling stock on the respective routes were used.

III. Result and Discussion

A. Pendulum route without reverse mileage (mileage utilization factor β = 0,5)

The task is to transport goods on pendulum route without the use of reverse mileage (reverse mileage without load), where the vehicle must perform one course for one cycle, i.e. $Z_o = 1$. In this case, the own rolling stock performs first zero mileage $L_{н1}$, loading T, mileage with cargo $L_{т1}$, unloading P, second zero mileage $L_{н2}$ (Fig.1).

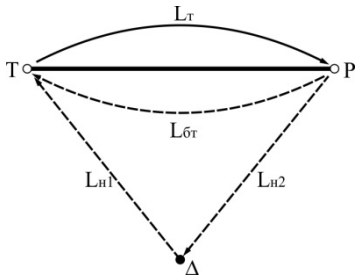

Fig. 1. Pendulum route scheme with no reverse mileage.

The solution of the problem is made with the following initial data: vehicle with load capacity $q_н$=3 t, one-way cargo flow, first class loads γ_c = 1, one-shift operation, urban operating conditions, the quantity and parameters of the load are known in advance and don't change, mechanized loading and unloading. The numerical values of the output data at a distance equal to the mileage with load $L_т$ = 1 km are presented in Table 1.

TABLE 1
OUTPUT DATA AT LT = 1 KM

Indicator	Value
Number of requests	1
Load class	1
Load capacity of the vehicle, q, t	3
Volume of cargo, Q, t	3
Coefficient of static load capacity utilization, γ_c	1
First zero mileage, $L_{н1}$, km	1
Second zero mileage, $L_{н2}$, km	1
Mileage utilization factor, $\beta_к$	0,5
Average technical speed, $V_т$, km/h	25
Loading and unloading time, $t_{т-р}$, h	0,425

The determination of the technical-operational indicators during operation of own rolling stock is made according to the following formulas:

- Time to complete a course:

$$t_k = \frac{L_т}{V_т} + t_{т-р}, \text{ h}; \quad (1)$$

- Performed transport work:

$$P = Q \cdot L_т, \text{ tkm}; \quad (2)$$

- Total mileage of the vehicle for one course:

…….. $L_{общ} = L_{н1} + L_т + L_{н2}$, km; (3)

- Actual operating time:

$$T_{нф} = \frac{L_{общ}}{V_т} + t_{т-р}, \text{ h.} \quad (4)$$

The results of the calculations are presented in Table 2.

TABLE 2
TECHNICAL AND OPERATIONAL INDICATORS FOR OPERATION OF A VEHICLE AT $L_т$ = 1 KM, β = 0,5

Indicator	Value
Own transport	
Time for one course, $t_к$, h	0,5
Transport work, P, tkm	3,0
Total mileage, $L_{общ}$, km	3,0
Actual operating time, $T_{нф}$,h	0,55
Rented transport	
Time for one course, $t_к$, h	0,5
Transport work, P, tkm	3,0
Total mileage, $L_{общ}$, km	1,0
Actual operating time, $T_{нф}$,h	0,5

The total cost (P, BGN) for transportation of goods for own needs on a pendulum route without using the return mileage for one course at $L_т$ = 1 km is ≈ 10,00 BGN. A company that provides car rental offers the following tariffs: for vehicle with a load capacity q = 3 t - 40 BGN per course within 2 hours. Every next hour is paid 20 BGN, and every 15 minutes – 5 BGN.

Table 3 presents some of the results obtained. They show that when transporting goods at a distance L = 1, 2, …, 23 km the criterio for efficiency C_e for the use of rented rolling stock doesn't increase,which is indicative of the fact that in this range it is more profitable to use own rolling stock.

TABLE 3
Expenses for transportation of goods with own and rented rolling stock with equal load capacity. (q = 3 t) при Z_o = 1

L, km	Q, t	Freight transpotation costs		C_e, BGN.
		Own transport	*Rented transport*	
1	3	12,5	40	-
2	3	13,75	40	-
3	3	15	40	-
…	…	…	…	…
22	3	38,75	40	-
23	3	40	40	-
24	3	41,25	40	1,25
25	3	42,5	40	2,5
…	…	…	…	
78	3	108,75	75	33,75
79	3	110	75	35
80	3	111,25	75	36,25

On the basis of regression analysis with the help of MS EXCEL a functional dependence of the criterion for efficiency C_e in transportation of goods for own needs from distance $L_т$ is obtained (Fig.2). This dependence is a third degree polynomial, which is:

$$C_e = 0{,}0003L^3 - 0{,}0533L^2 + 3{,}0302L - 56{,}432. \quad (5)$$

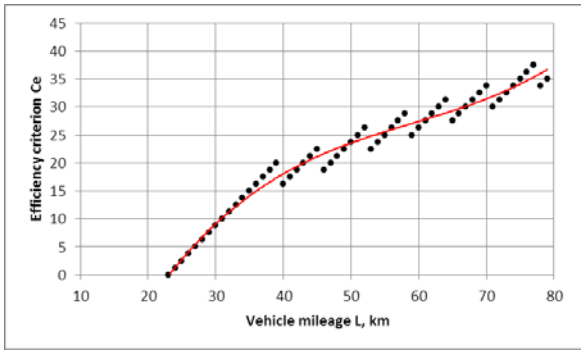

Fig. 2. Dependence of $C_e = f(L)$ at $L_т$ = 24, 25, …, 80 km

The coefficient of determination of equation (5) is R^2 = 0,9801,which shows that it well describes the studied process. The standart error of the approximation is 2,51%, which allows us to claim that the regression dependence for the influence of the distance L = 24, 25, 26 …, 80 km on the efficiency criterion C_e on a pendulum route without using the reverse mileage Z_o = 1 adequatly describes the studied process.

B. Pendulum route with full use of reverse mileage (mileage utilization factor β = 1)

The task is to transport goods on pendulum route with full use of reverse mileage, where it can be performed one cycle Z_o = 1. In this case the own rolling stock performs first zero mileage $L_{н1}$, first loading T_1, first mileage with cargo $L_{т1}$, first unloading P_1, second loading T_2, second mileage with cargo $L_{т2}$, second unloading P_2, first zero mileage $L_{н1}$ (Fig.3). The output is similar, i.e. $L = L_т = 1$.

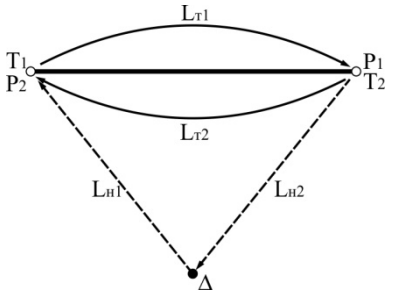

Fig. 3. Pendulum route scheme with full use of reverse mileage.

Determining the technical-operational indicators on a pendulum route using the reverse mileage is made according the following formulas:

$$L_м = L_{т1} + L_{т2}, \text{ km;} \quad (6)$$

- Time to make one cycle:

$$t_o = \frac{L_м}{V_т} + t_{т-р1} + t_{т-р2}, \text{ h;} \quad (7)$$

- Total mileage of the vehicle:

$$L_{общ} = L_{н1} + L_м + L_{н1}, \text{ km;} \quad (8)$$

- Actual operating time:

$$T_{нф} = \frac{L_{общ}}{V_т} + t_{т-р1} + t_{т-р2}, \text{ h.} \quad (9)$$

The results of the calculations are presented in Table 3.

TABLE 3
TECHNICAL AND OPERATIONAL INDICATORS FOR OPERATION OF A VEHICLE AT $L_т$ = 2 KM, β = 1,0

Indicator	Value
Own transport	
Time for one cycle t_o, h	0,93
Quantity of transported goods Q, t	6
Transport work, P, tkm	6
Total mileage $L_{общ}$, km	4
Actual operating time $T_н$, h	1,01
Rented transport	
Time for one cycle t_o, h	0,93
Quantity of transported goods Q, t	6
Transport work, P, tkm	6
Total mileage $L_{общ}$, km	2
Actual operating time $T_н$, h	0,93

The influence of the distance on the efficiency criterion C_e for a pendulum route with full use of the mileage at one cycle was studied in an analogous was. When transporting goods at a distance L = 1, 2, …, 11 km the criterio for efficiency C_e for the use of rented rolling stock doesn't increase, which is indicative of the fact that in this range it is more profitable to use own rolling stock.

According to the results of the research the functional dependence of the criterion for efficiency C_e on the distance L at L = $L_{т1}$ has been established, the equation is:

$$C_e = 0,8972L - 7,9888. \quad (10)$$

Figure 4 shows graphically the regression dependence of C_e in the range from 12 to 80 km.

The coefficient of determination of equation (10) is R^2 = 0,9933, which shows that it well describes the studied process. The standard error of the approximation is 1,49%, which allows to claim that the regression dependence for the influence of the distance L = 12 – 80 km on the efficiency criterion C_e when transporting goods on a pendulum route with full use of the mileage at Z_o = 1 adequately describes the researched process.

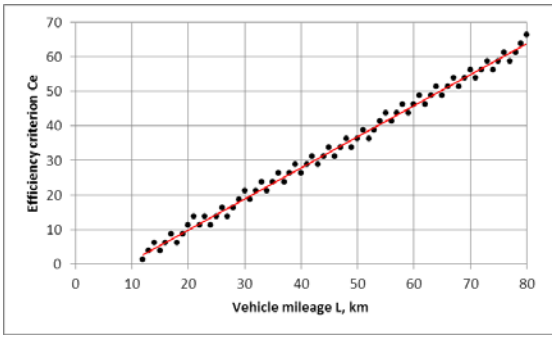

Fig. 4. Dependence of C_e = f(L) at $L_т$ = 12, 17, …, 80 km

C. Pendulum route with incomplete use of reverse mileage (mileage utilization factor β = 0,75)

The task is to transport goods on pendulum route with incomplete use of reverse mileage, where it can be performed one cycle Z_o = 1. In this case the own rolling stock performs zero mileage $L_{н1}$, first loading T_1, first mileage with cargo $L_{т1}$, first unloading P_1, second loading T_2, second mileage with cargo $L_{т2}$, second unloading P_2, zero mileage $L_{н3}$ (Fig.5).

The initial data (except $L_{т2}$ = 0,5, $L_{н1}$ = 1 km) and the calculation of the technical performance indicators are the same as the pendulum route with full use of the reverse mileage. The results of the calculations are presented in Table 4.

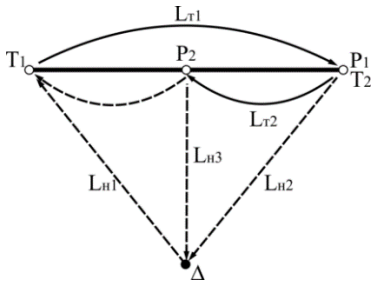

Fig. 5. Pendulum route scheme with incomplete use of reverse mileage.

TABLE 4
TECHNICAL AND OPERATIONAL INDICATORS FOR OPERATION OF A VEHICLE AT $L_т$ = 1,5 KM, β = 0,75

Indicator	Value
Own transport	
Time for one cycle t_o, h	0,91
Quantity of transported goods Q, t	6
Transport work, P, tkm	4,5
Total mileage $L_{общ}$, km	4
Actual operating time $T_н$, h	1,01
Rented transport	
Time for one cycle t_o, h	0,91
Quantity of transported goods Q, t	6
Transport work, P, tkm	4,5
Total mileage $L_{общ}$, km	1,5
Actual operating time $T_н$, h	0,91

The study of the influence of the distance on the criterion for efficiency on a pendulum route with incomplete use of the reverse mileage at $Z_o = 1$ was done in the same way as in previous pendulum routes. When transporting goods at a distance L = 1, 2, …, 12 km the efficiency criterion C_e from the use of hired rolling stock doesn't increase, which is indicative of the fact that in this range it is more profitable to use own rolling stock.

According to the results of the research the functional dependence of the criterion for efficiency C_e on the distance L at $L = L_{т1}$ has been established, the equation is:

$$C_e = 1{,}3275L - 8{,}3498. \quad (11)$$

Figure 6 shows graphically the regression dependence of the efficiency criterion C_e on the distance at $L = L_{т1}$ in the range from 13 to 80 km.

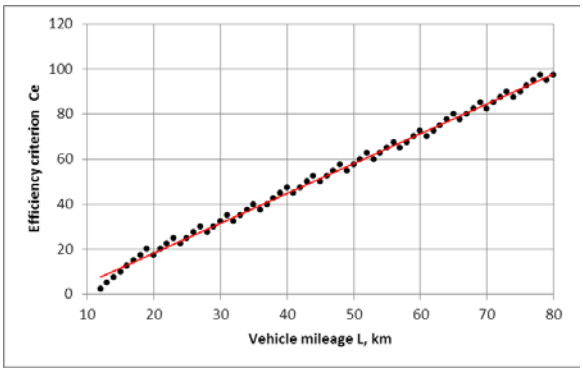

Fig. 5. Dependence of $C_e = f(L)$ at $L_т = 13, 14, …, 80$ km

The coefficient of determination of equation (11) is $R^2 = 0{,}9959$, which shows that it well describes the studied process. The standard error of the approximation is 1,72%, which allows to claim that the regression dependence for the influence of the distance L = 13 – 80 km on the efficiency criterion C_e when transporting goods on a pendulum route with incomplete use of the mileage at $Z_o = 1$ adequately describes the researched process.

D. Pendulum route with full use of reverse mileage, but with a different load utilization factor (mileage utilization factor $\beta = 1{,}00$, $\gamma_1 \neq \gamma_2$)

The task is to transport goods on pendulum route with full use of reverse mileage, but with a different load utilization factor $\gamma_1 \neq \gamma_2$, where it can be performed one cycle $Z_o = 1$. In this case the own rolling stock performs zero mileage $L_{н1}$, first loading T_1, first mileage with cargo $L_{т1}$, first unloading P_1, second loading T_2, second mileage with cargo $L_{т2}$, second unloading P_2, zero mileage $L_{н1}$ (Fig.3).

The output data are the same as for the previous routes, except for $Q_2 = 2$ t. In this route $\gamma_1 \neq \gamma_2$, from which follows $t_{т\text{-}р1} \neq t_{т\text{-}р2}$. The results of the calculations are presented in Table 5.

TABLE 5
TECHNICAL AND OPERATIONAL INDICATORS FOR OPERATION OF A VEHICLE AT $L_т = 2$ KM, $\beta = 1$, $\gamma_1 \neq \gamma_2$

Indicator	Value
Own transport	
Time for one cycle t_o, h	0,80
Quantity of transported goods Q, t	5
Transport work, P, tkm	5
Total mileage $L_{общ}$, km	4
Actual operating time $T_н$, h	0,88
Rented transport	
Time for one cycle t_o, h	0,80
Quantity of transported goods Q, t	5
Transport work, P, tkm	5
Total mileage $L_{общ}$, km	2
Actual operating time $T_н$, h	0,80

The study of the influence of the distance on the criterion for efficiency on a pendulum route with full use of the reverse mileage, but with a different load utilization factor at $Z_o = 1$ was done in the same way as in previous pendulum routes. When transporting goods at a distance L = 1, 2, …, 11 km the efficiency criterion C_e from the use of hired rolling stock doesn't increase, which is indicative of the fact that in this range it is more profitable to use own rolling stock.

According to the results of the research the functional linear dependence of the criterion for efficiency C_e on the distance L has been established, the equation is:

$$C_e = 0{,}903L - 4{,}4001. \quad (12)$$

Figure 7 shows graphically the regression dependence of the efficiency criterion C_e on the distance L in the range from 12 to 80 km.

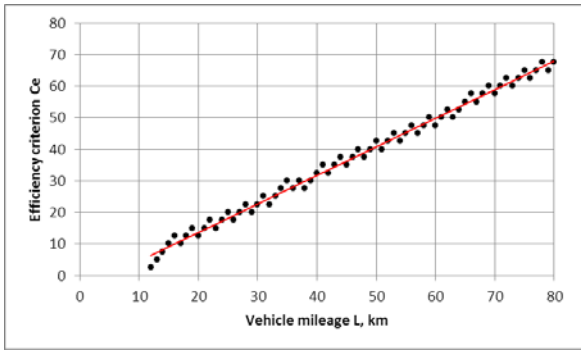

Fig. 5. Dependence of $C_e = f(L)$ at $L_т = 12, 13, …, 80$ km

The coefficient of determination of equation (12) is $R^2 = 0{,}9928$, which shows that it well describes the studied process. The standard error of the approximation is 1,71%, which allows to claim that the regression dependence for the influence of the distance L = 12 – 80 km on the efficiency criterion C_e when transporting goods on a pendulum route with full use of the reverse mileage, but with a different load utilization factor at $Z_o = 1$ adequately describes the researched process.

IV. CONCLUSIONS

The influence of the distance on the criterion for efficiency in the transport of goods for own needs on pendulum routes of any kind – with no use of reverse mileage, with full use of reverse mileage, with incomplete use of reverse mileage and full use of reverse mileage, but with a different load utilization factor is revealed. Upcoming studies are expected to reveal the influence of distance and volume of transportation on the criterion of efficiency, both for the routes discussed in the article and for circular, delivery, collection and collection-delivery routes.

The dependence of the efficiency criterion on the distance of the transportation is described by linear equations and polynomials of different degree. Checking the quality of the equations shows that with 95% confidence they adequately describe the studied process.

The proposed dependencies for the transport of goods for own needs in urban conditions can help to correctly determine the costs that correspond to the interests of the main production.

The results were obtained under a project funded by the research grant at TU – Sofia - contract 202ПД0026 – 24 – Improvement of the plan for transport of goods by road.

REFERENCES

[1] V. Nikolin, Transport process and optimizatipon of its elements, Publisher “Transport”, Moscow, 1990, pp. 90-91.
[2] V. Nikolin, “Freight road transport”, monograph, Publisher „Variant-Siberia“, Omsk, 2004, pp. 480-485.
[3] V. Nikolin, “Scientific bases for improving the theory of road freight transport”, dissertation, Moscow, 2000.
[4] A. Gorev, Freight road transport, Publishing Center „Academy “,Moscow, 2008, pp. 288-290.
[5] M. Mirgorodsky, “Selection of rolling stock for transport of goods in small batches in urban conditions”, monograph, KAN Polygraphic Center, Omsk, 2012, pp. 139-141.
[6] S. Sapundjiev and P. Stefanova, Road transports of goods (530 questions), Investpress Printing House, Sofia, 2017, pp. 22-25.

Environment. Technology. Resources. Rezekne, Latvia
Proceedings of the 13th International Scientific and Practical Conference. Volume 3, 330-335

Modeling the Operation of a Galvanic Bath with Electric Heaters and Optimizing its Design Based on Numerical Simulation

Alexander Samarkin
Institute of Medicine and Biology
Pskov State University
Pskov, Russia
Alexsamarkinru@gmail.com

Sergey Dmitriev
Institute of Engineering Sciences
Pskov State University
Pskov, Russia
dmitrievsi55@gmail.com

Alexander Dementyev
Institute of Engineering Sciences
Pskov State University
Pskov, Russia
damix01@yandex.ru

Evegeniya Evgenyeva
Institute of Engineering Sciences
Pskov State University
Pskov, Russia
zhen_sheny@mail.ru

Elena Samarkina
Institute of Engineering Sciences
Pskov State University
Pskov, Russia
ElenaSPsk@gmail.com

A model of the processes in a galvanic bath during heating is based on the finite element method. The processes of heating the air chamber and directly the reagent solution are simulated. Based on the constructed model, an automatic control system for heating elements is being developed, which provides a sufficient heating rate, a stable temperature and protects the heating elements from burnout. An application program has been created that allows performing the calculations without studying complex modeling systems.

Keywords - automated controls, computed fluid dynamics, finite element analysis.

I. INTRODUCTION

Formulation of the problem. The enterprises of the region are interested in using medium-sized galvanic bathtubs (width - 800 mm, length - 1000-1400 mm, bath height - 400 mm) to apply resistant coatings. During the process, it is necessary to maintain the temperature of the solution 35-500C, which involves heating the solution.

The most popular is the design with a bathtub, under which electric heating elements (heating elements) are in a thermally insulated compartment [1]. The length of the working part of the heating element (about 700 mm) determines the maximum width of the bathtub. The length of the bath is determined by the number of heating elements and the distance between them. Features of production do not allow to change the distance between the axes of the heating elements.

During operating the bathtubs, several negative phenomena are observed associated with increased failure of the heating elements during the initial heating of the bath solution (during operation, the temperature of the solution is maintained by a separate control system). It was established experimentally that the heating element burns out when its working surface is heated above a certain temperature, which is T_{kr} = 820 °C for the most common heating element in production and works in such conditions for over 15 minutes. Used in manufacturing heaters are precision alloys with high electrical resistance [2]. These include alloys based on chromium and nickel (chromium-nickel), iron, chromium, and aluminum (chromium-aluminum). The grades and properties of these alloys are considered in GOST 10994-74 “Precision alloys. Stamps." [3] Representatives of chromium-nickel alloys are nichrome of the grades Cr20Ni80, Cr20Ni80-H (950-1200 ° C), Cr15Ni60, Cr15Ni60-H (900-1125 ° C), iron-chromium-aluminum alloys - fechral of the grades Cr23Al5Ti (950-1400 ° C), Cr27Al5Ti (950-1350 ° C), Cr23Al5 (950-1200 ° C), Cr15Al5 (750-1000 ° C). In the modern market, fechral is cheaper than nichrome at least 3-5 times at the price of a kilogram of the semi-finished products. This is because the cost of nickel, which is the basic element of nichrome, is an order of magnitude higher than the cost of iron - the basis of fechral.

Online ISSN 2256-070X
https://doi.org/10.17770/etr2021vol3.6581

The task is to increase the resistance of the heating element by optimizing the algorithm for primary heating of the bath solution [4].

II. Materials and Methods

Ways and methods of solving. Possible ways are:

1. Placement of heaters in contact with the galvanic solution.
2. Changing the structural implementation of the bottom of the bath by fins, blackening of surfaces to improve heat dissipation and achieve temperature equilibrium below the point T_{kr}.
3. Connection of a control system capable of connecting the heaters discretely or changing its operating temperature continuously.

The first option is impossible since the galvanic solution has high chemical activity. There are also sanitary and technological requirements for the complete tightness of the bath.

Changing the design of the bath is also difficult, as it entails a change in the process and significant costs.

The control system is inexpensive to implement, allows you to implement both fairly complex logic when implemented on industrial controllers and integrate the product into an automated quality control system or remote control, and is simple [5].

Control System can be implemented:

1. With discrete control of the turn-on time parameter of the heating element without temperature feedback.
2. With discrete control of the turn-on time parameter of the heating element with temperature feedback.
3. With continuous power control of the heating element (from 0% - off, up to 100% - turned on at full power).

The first option involves turning on / off the heaters according to a predetermined algorithm. It is relatively simple to implement, but it does not allow to control the actual operating conditions of the heaters.

Option 2 involves the installation of a temperature sensor with a direct or indirect measurement method, and it is difficult to directly measure the temperature of the heater with a sensor.

The third option is relatively complex and potentially the most flexible, however, the power consumption is controlled either by a switching power supply, which is difficult with a heater power of about 5 kW, or by a parasitic load, which reduces the efficiency of the installation.

Thus, we choose for further implementation of a system with discrete heater control and temperature feedback.

Feedback must control the process. The controlled parameter is the surface temperature of the heating element, however, its direct measurement is difficult, so we measure the temperature in an indirect way, namely through the air temperature in the heating zone.

To implement this control method, it is proposed to simulate heating the bath by numerical methods, using the model of the bath and the heater by the finite element method [6].

Process simulation. Bath heating and cooling

Since all bath cross-sections from the viewpoint of temperature distribution and fluid flow can be considered the same, we restrict ourselves to a two-dimensional statement of the problem.

To build the simplest model, we estimate the time of heating the solution in the bath from a temperature of 200C to a working temperature of 500C. A comparison of the calculation results of this model with practice will allow us to evaluate its adequacy. Below is a sketch of the cross-section of the bath and the grid of finite elements.

a)

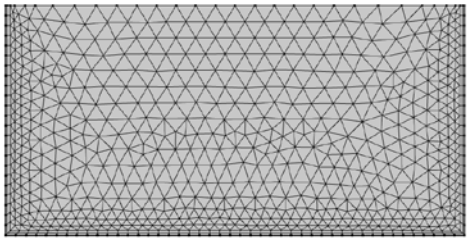

b)

Fig. 1. Galvanic bath cross-section sketch (dimension in mm) with finite-element 2d mesh.

Suppose that the upper plane and side walls undergo natural convection into the air with an ambient temperature of 200C. Heating is carried out by supplying heat to the lower plane of the drawing (Fig. 1).

Technical documentation (https://polymernagrev.ru/catalog/elektricheskie-teny/bloki-tenov/) for the used heaters gives: maximum diameter $d_{max} = 18\,mm$, length $l = 700\,mm$, specific power - $p_{ud} = 15\frac{W}{cm^2}$, whence the power of the 1st tube $P_1 = p_{ud}\,\pi\,d_{max}\,l = 5900\,W$

Since $k = 8$ heaters are used for the size understudy, they are located at an equal distance from each other, and taking into account that air heating losses are (for

reference) $\mu = 30\%$, we obtain the net heating power $P = (1-\mu)\, k\, P_1 = 33kW$.

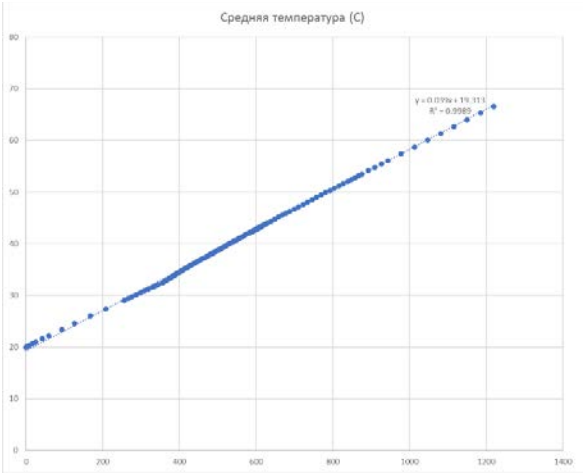

Fig. 2. Modeling the heating process using various mathematical models of heating a plating bath: Low-Re $k-\varepsilon$ model.

Several numerical models describe the flow of a fluid due to a change in its density under the influence of temperature. The most used are the model with the laminar and turbulent flow (having several formulations) (See results at Fig. 2) [7]. The laminar model might consider the effects of mixing, and the turbulent model becomes ineffective at low flow rates, however, turbulent models are necessary to describe the flows arising from mixing of hot and cold fluids, and the behaviour of media in the layers near the walls [8].

Bath heating with an electric heater

To increase the productivity of calculations, we use the assumption stated above that all bath sections are characterized by the same picture of heat transfer processes, which include the transfer of thermal energy and the turbulent flow of air and a galvanic solution. This allows us to pose the problem in a two-dimensional formulation.

Divide the flat section of the bath into departments above the heaters. Because we are interested in the process of heating, we can neglect the processes of flow near the walls and consider all such departments to be the same. It is also obvious that the left and right halves of each department are symmetrical both geometrically and from the viewpoint of the processes in them, which gives us reason to consider further only this half (see Fig. 3).

The presented geometry can be easily parameterized to obtain a generalized solution. The main parameters determining the geometry will be the width of the section, the height of the air chamber and the bath, the diameter of the heater, its position (height) in the air chamber, the power taken from the unit area of the outer surface of the heater, and the width of the bath. Parameter names are given under the rules for naming variables in the Java programming language and further they are used as variables of the developed specialized software (see Table 1).

TABLE 1 MODEL PARAMETERS

Parameter	Designation	Value	Units	Note
Bath width	len1	700	[mm]	According specs
Heater diameter	diam1	18	[mm]	According specs
Heater center offset	dy1	20	[mm]	According technical drawing
Section Width	b1	100	[mm]	
Air Compartment Height	h1	120	[mm]	
Bath height	h2	400	[mm]	
Heater specific power	pwr1	15	[W/cm^2]	According specs
Loss ratio	kp	0.3	-	
Useful specific	pwr2	(1-kp)*pwr1	[W/cm^2]	
Heater power	Tmax1	950	[degC] ^{0}C	
Maximum permissible	Tmin1	300	[degC] ^{0}C	

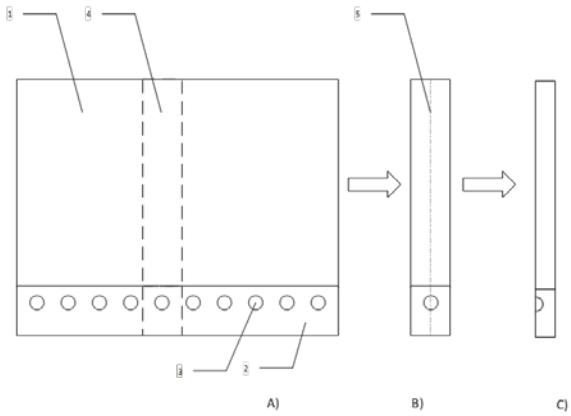

Fig. 3. Simplification of a galvanic bath model A) - flat cross-section (1 - bath, 2 - air chamber, 3 - heater, 4 - repeated section), B) - symmetric repeated section (5 - axis of symmetry), C) - half of a repeated section/

Continuous heater heating model

In the simplest case, when the heater is turned on on its outer surface with a certain time delay (this delay is necessary to obtain a convergent solution and is modeled as a ramp function - rise with saturation from the time it was turned on and is used later for all power turns on).

Thus, the specific power per unit area $P_{ud}(t)$ as a function of the turn-on time t is: $P_{ud} = P_0 ramp\,(t)$, where P_0 is the useful specific power of the heater pwr2 (Table 1), and the function $ramp\,(t)$ is defined as:

$$ramp(t) = \begin{cases} 0, t \le 0 \\ kt, t > 0 \\ 1, kt \ge 1 \end{cases}.$$

In the simulation, besides the Low-Re k-ε model, a normal-quality mesh with default settings is used,

excluding the number of wall layers increased to 5, a fragment of which is shown in Fig. 4, with the temperature and velocity distribution diagram.

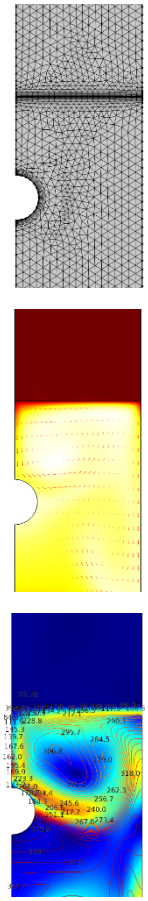

a)

b)

c)

Fig. 4. a) - mesh of finite elements, b) - temperature distribution diagram, arrows - velocity field vector, c) - velocity distribution diagram, with contours as isotherms

The simulation results in terms of heating time agree with the experiment and the previous model of bath heating (about 14 minutes for heating to 50°C). Then everywhere we take the total bath heating time $T_{all} = 15\ min$.

To control the temperature of the heater, the wall of the bathtub and the galvanic solution, the model includes domain and averaging sensors (domain probe and boundary probe, respectively) that integrate the temperature and guarantee smooth first and second time derivatives (this converges the solution), the plot of the readings of which is presented below.

A heating model with periodic timer activation

Since the approximate heating time is 15 minutes, as a first approximation, a decision was made to apply power by cycling the heater on and off. The cycle time is 6 minutes, of which 4 minutes the heater works.

Graphs of sensor readings and separately the average bath temperature is presented below at Fig. 5.

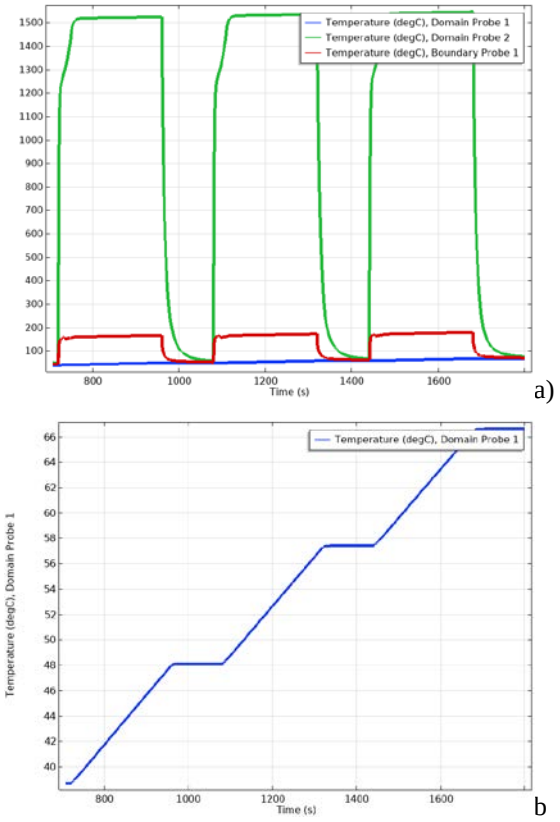

Fig. 5. Simulation of bath heating during periodic switching on of the heater a) - graphs of the temperature of the heater (green line), the bottom surface of the bath (red), solution (blue), b) - the average temperature of the galvanic solution

Note that for modeling on-off processes, it is necessary to use not only the traditional finite element model but also supplement it with a discrete state model. The specific way to implement such a system can be different, for example, ANSYS Fluent, in this case, involves writing custom functions () in C ++.

In a system like Comsol [7], there are more convenient tools a discrete state mechanism and explicit events. See below for more details. Figure 6

Explicit events occur at the onset of sometime and control state variables. The model uses a single ONOFF variable that takes the values 1 (on) and 0 (off). Events are formulated in such a way that at the beginning of the cycle the variable is set to 1, and after 4 minutes of operation, it is set to 0 until the end of the 6-minute cycle, after which everything repeats.

To turn on to operating temperature three switch-on is required, the solution overheating to 66 degrees, and the heater operates at extreme temperatures of 80% of the turn-on time, about 3 minutes per cycle, which is considered acceptable (the continuous operation is allowed up to 15 minutes, see the introduction to the article).

The heating model with the control of the upper and lower limit of the heater temperature.

More effective, although more complex, is the implementation of the heating process with feedback on the temperature of the heater (see [9] about theory). Here, the model uses implicit (implicit) event management. An element of control over the temperature of the heater is introduced into the model in indicator states (see indicator of states at Fig. 6).

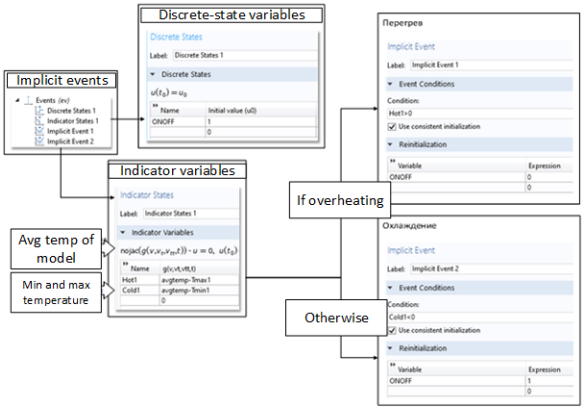

Fig. 6. Heater control using implicit events

The indicated indicator receives the average temperature of the heater through the integral operator and compares it with two parameters - the maximum upper and lower temperatures of the heater, set as parameters. Thus, a feedback effect is achieved, however, the values of the temperature boundaries require adjustment. The upper limit is determined from the condition of resistance of the heater. The lower limit is reached after turning off the power and, thus, its value determines the time the heater is turned off. Let, as a first approximation, the values of the parameters according to Table 2.

TABLE 2 CYCLE PARAMETERS (1-ST ATTEMPT)

Parameter	
Tmax = 950	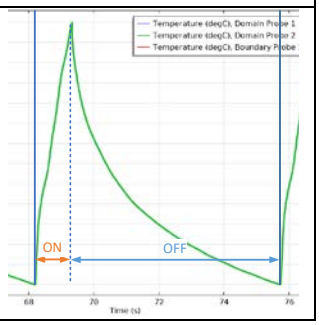
Tmin = 300	
Cycle time Tc = 6.1 sec	
On time Ton = 1 sec	
Duty Cycle S = 0.163	
Heating time with a continuously running heater (for reference) Tall = 15 min	

Since the duty cycle is 16.3%, the bath heating time will be $T = \frac{T_{all}}{S} = 91.5\ min.$

We take the temperature of inclusion 60^0C (Table 3).

TABLE 2 CYCLE PARAMETERS (ADJUSTED)

Parameter
Tmax = 950
Tmin = 600
Cycle time Tц = 2,8 сек
On time Ton = 0,75 сек
Duty Cycle S = 0.27
Heating time with a continuously running heater (for reference) Tall = 15 min

Since the duty cycle this time is 26.9%, the bath heating time will be $T = \frac{T_{all}}{S} = 56\ min.$

Thus, by adjusting the lower limit for turning on the heater, it was possible, due to a production-acceptable increase in the heating time of the bathtub, to ensure guaranteed operation of the heater in the modes recommended for heating elements.

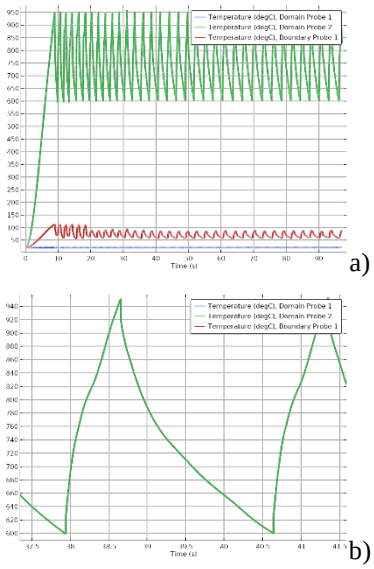

Fig. 7. Temperature diagram by on-off cycle with adjusted parameters (according Table 3), where a) – full-time diagramm, b) – one-cycled diagram.

III. RESULTS AND DISCUSSION

Generalized model

Due to the need to manufacture bathtubs for special orders, an application based on the presented calculations has been developed. The interface of the application presented below (see Fig. 8).

By changing the parameters, it is possible to change both the geometry of the section and the parameters of the heater and the control modes over the heating process (through the maximum and minimum temperatures).

Thus, as a result of the work, it was possible to calculate a complex problem, including the calculation of heat transfer and turbulent mixing of liquid and gas in interacting domains.

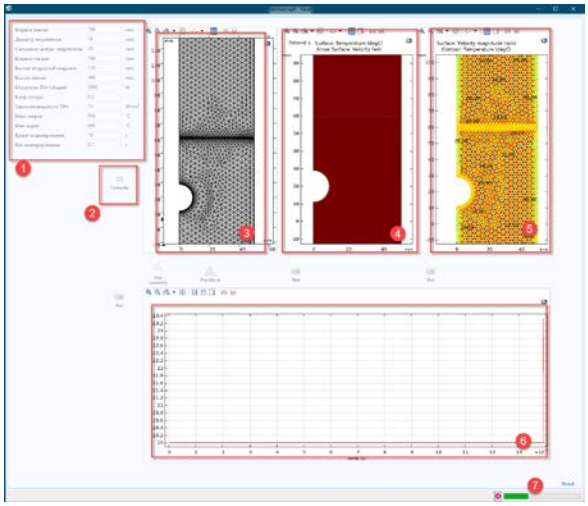

Fig. 8. Application interface, 1 - area for setting parameters, 2 - button for sending a task for calculation, 3 - area for display constructing geometry or a mesh of finite elements, 4 - temperature plot in the heating zone (dynamically rebuilds during the calculation), 5 - speed diagram in the heating zone (based on the calculation results), 6 - average domain temperatures (dynamically rebuilds).

IV. Conclusions

Numerical modeling tools allow you to solve very complex problems, and thanks to the possibility of creating "digital doubles", it is possible to reduce the production test time to a minimum, which drastically reduces the cost of modernization and implementation of new products.

Under consideration, it was possible to implement such operating modes of fechral heating elements that realize their advantages and level their disadvantages. It was possible to reduce the cost of purchased electrodes by 2–3 times while maintaining high product quality.

V. Acknowledgments

The work was performed on the provided trial version of the COMSOL Multiphysics program (https://www.comsol.ru/).

VI. References

[1] M. Hejfec, V. Borodavko, V. Ivashko, and S. Klimenko, Obrabotka i uprochnenie poverhnostej pri izgotovlenii i vosstanovlenii detalej: LitRes, 2021. [Online]. Available: https://books.google.ru/books?id=DFsVEAAAQBAJ

[2] ELEKTRONAGREVATELI TRUBCHATYE, 13268-88, GOSUDARSTVENNYJ STANDART SOYUZA SSR, M., 01/01/90.

[3] SPLAVY PRECIZIONNYE, 10994-74, MEZHGOSUDARSTVENNYJ STANDART, M., 01/01/75.

[4] V. Sheleg, K. avtorov, and M. Kane, Tekhnologiya mashinostroeniya. Kursovoe proektirovanie: LitRes, 2017. [Online]. Available: https://books.google.ru/books?id=TI0QDQAAQBAJ

[5] V. YAkuhin, Vysokotekhnologichnye metody metalloobrabotki. Uchebnik: Izd-vo MGIU, 2011. [Online]. Available: https://books.google.ru/books?id=sdZbma80B9oC

[6] P. D. Bates, S. N. Lane, and R. I. Ferguson, Computational fluid dynamics: Applications in environmental hydraulics. Hoboken, NJ: J. Wiley, 2010. [Online]. Available: http://search.ebscohost.com/login.aspx?direct=true&scope=site&db=nlebk&db=nlabk&AN=138344

[7] M. Tabatabaian, COMSOL for engineers. Dulles, VA: Mercury Learning and Information, 2014. [Online]. Available: http://search.ebscohost.com/login.aspx?direct=true&scope=site&db=nlebk&AN=1809110

[8] R. W. Pryor, Multiphysics modeling using COMSOL5 and MATLAB. Dulles: Mercury Learning and Information, 2016.

[9] N. V. Sahinidis, “Mixed-integer nonlinear programming 2018,” Optim Eng, vol. 20, no. 2, pp. 301–306, 2019, doi: 10.1007/s11081-019-09438-1.

Environment. Technology. Resources. Rezekne, Latvia
Proceedings of the 13th International Scientific and Practical Conference. Volume 3, 336-342

Side Slip of Wheels with Low and Ultra-low Profile Tires of a Personal Car negotiating a Turn

Stiliyana Taneva
Department of Transport and Aircraft Equipment and Technologies
Technical University of Sofia, Plovdiv Branch
Plovdiv, Bulgaria
email s.taneva@tu-plovdiv.bg

Krasimir Ambarev
Department of Transport and Aircraft Equipment and Technologies
Technical University of Sofia, Plovdiv Branch
Plovdiv, Bulgaria
email kambarev@tu-plovdiv.bg

***Abstract* - This article studies the influence of the speed of a car with low and ultra-low profile tires, 14″ and 16″, negotiating a turn through an interactive software system developed by us in the MATLAB environment. The changes of the normal and lateral loads of the wheels are obtained and the characteristics of the side slip angle (known as side slip) of the pneumatic tires are determined. Taking into account the side slip of the wheels, the software determines the center of the turn. The characteristics for the normal and lateral loads and of the side slip of the wheels for both types of tires are given. The influence of the tire profile on the handling characteristics is analysed. Recommendations are proposed for a personal car's motion in a turn with both types of tires.**

Keywords - speed, side slip, load, turn, car, low and ultra-low profile tires.

I. INTRODUCTION

The curvilinear motion of a vehicle is primarily associated with its stability and handling, and different models have been developed [1, 2, 3, 4, 5, 8, 9]. In a car's motion in a turn, a side slip of tires occurs under the action of lateral forces, which depends on various design and exploitation factors. In the developed models of a car's motion in a turn, the side slip is determined by a number of analytical models using experimental studies of tires [1, 2, 3, 4, 5, 7, 8, 9, 11, 12]. The most commonly used is the "Magic formula" by H. B. Pacejka [3, 7, 11], which describes the behaviour of the pneumatic tire in a steady motion, but the formula has a large number of coefficients and their determination is sometimes associated with significant errors. Existing research does not always take into account the influence of the forward speed and the average angle of the steered wheels on the side slip for current values of the loads for low and ultra-low profile tires when driving a car in a turn.

The aim of this research is to study the influence of the forward speed of a car with low and ultra-low profile tires 14" and 16" in a turn, taking into account the redistribution of normal (vertical) load, and its effect on the characteristics of the side slip of the wheel tires. For this study the MATLAB environment interactive software system is developed.

II. DETERMINING TIRE SIDE SLIP OF A CAR'S MOTION IN A TURN

For the side slip of the tires of four wheels of a car negotiating a turn (Fig. 1) the following equations are used [6]:

- for the front axle

$$\delta_{1v} = \theta_v^{'} - arctg\frac{R_\delta tg\left(\theta_{sr} - \delta_1\right)}{R_\delta - \frac{B_1}{2}},$$
$$\delta_{1vn} = \theta_{vn}^{'} - arctg\frac{R_\delta tg\left(\theta_{sr} - \delta_1\right)}{R_\delta + \frac{B_1}{2}} \quad (1)$$

- for the rear axle

Online ISSN 2256-070X
https://doi.org/10.17770/etr2021vol3.6630

$$\delta_{2v} = arctg\frac{tg\delta_2}{1-\frac{B_2}{2R_\delta}}, \qquad \delta_{2vn} = arctg\frac{tg\delta_2}{1+\frac{B_2}{2R_\delta}} \quad (2)$$

where B_1, B_2 are respectively the track widths of the front and rear axles of the car; $\delta_{1v}, \delta_{1vn}$ are the tire slip angles, respectively of the inner and outer front wheel; $\delta_{2v}, \delta_{2vn}$ are the tire slip angles, respectively of the inner and outer rear wheel; θ_v, θ_{vn} are the angles of rotation of the inner and outer wheel about the steering axis which is assumed to be equal to the steer angle of the inner and outer wheel in the ground plane $\theta_v^{'}$, $\theta_{vn}^{''}$; R_δ is the turning radius.

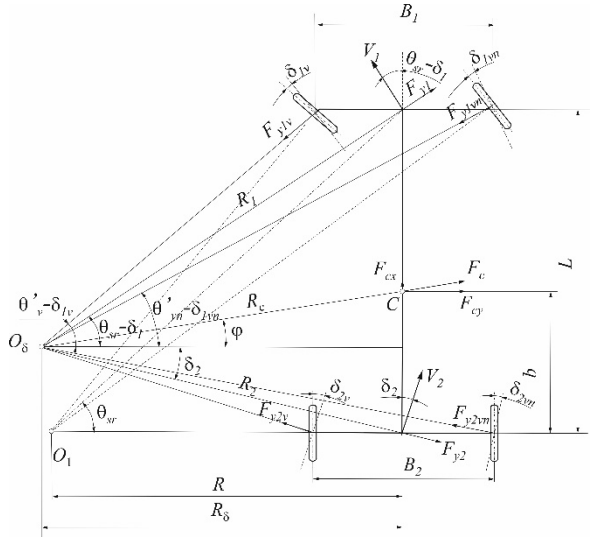

Fig. 1. Scheme of the side slip of tires of a car negotiating a turn [6].

To obtain the characteristics of the side slip of a car's tires, in [6] we propose these nonlinear dependencies

$$F_{yi} = k_t k_r \frac{arctg\left[\pi k_{\delta 0i}\delta_i / \left(2\varphi_{yi}F_{zi}\right)\right]}{\pi / \left(2\varphi_{yi}F_{zi}\right)} \quad (3)$$

$$F_{yi} = k_t k_r \frac{arctg\left[\pi k_{\delta 0i}\left(\delta_i - 0,026\right) / \left(2\varphi_{yi}F_{zi}\right)\right]}{\pi\left(\delta_i - 0,026\right) / \left(2\varphi_{yi}F_{zi}\right)}\delta_i, \quad (4)$$

where k_t is the coefficient of the tire profile; k_r is the coefficient of the rim dimensions; F_{zi} is the load on the i^{th} wheel in N; $k_{\delta 0i}$ is the cornering stiffness of the tires of the i^{th} wheel; φ_{yi} - the coefficient of lateral grip of i^{th} wheel.

The coefficients used above take into account the change in the tire profile and the normal load, and are explained in detail in [10].

Taking into account the basic parameters of the car, the normal, lateral and longitudinal reactions (forces) of the wheels in a car's motion in a turn can be defined by taking into account their grip with the road surface.

Normal reactions on the car's wheels are determined by taking into account the redistribution of the normal load between the front and rear axles. The outer wheels are additionally loaded, while the inner wheels are unloaded. For the normal loads of the inner and outer wheels, based on Fig. 1, the following equations apply [6]:

- for the front axle

$$F_{z1v} = \frac{G.b}{2L} + A\frac{\cos^2\delta_2}{R_\delta^2} - A\frac{\sin 2\delta_2}{2.b.R_\delta} - B\frac{\cos^2\delta_2}{R_\delta},$$

$$F_{z1vn} = \frac{G.b}{2L} + A\frac{\cos^2\delta_2}{R_\delta^2} - A\frac{\sin 2\delta_2}{2.b.R_\delta} + B\frac{\cos^2\delta_2}{R_\delta} \quad (5)$$

- for the rear axle

$$F_{z2v} = \frac{G\left(L-b\right)}{2L} - A\frac{\cos^2\delta_2}{R_\delta^2} + A\frac{\sin 2\delta_2}{2bR_\delta} - C\frac{\cos^2\delta_2}{R_\delta},$$

$$F_{z2vn} = \frac{G\left(L-b\right)}{2L} - A\frac{\cos^2\delta_2}{R_\delta^2} + A\frac{\sin 2\delta_2}{2bR_\delta} + C\frac{\cos^2\delta_2}{R_\delta} \quad (6)$$

and coefficients A, B and C are determined according to [6].

On Fig. 1, for the inner and outer wheel lateral forces, the following equations apply:

- for the front axle

$$F_{y1v} = F_{y1}\frac{\sin\left[\left(\theta_{sr} - \theta_{vn}^{'}\right) + \left(\delta_{1vn} - \delta_1\right)\right]}{\sin\left[\left(\theta_v^{'} - \theta_{vn}^{'}\right) + \left(\delta_{1vn} - \delta_{1v}\right)\right]},$$

$$F_{y1vn} = F_{y1}\frac{\sin\left[\left(\theta_v^{'} - \theta_{sr}\right) + \left(\delta_1 - \delta_{1v}\right)\right]}{\sin\left[\left(\theta_v^{'} - \theta_{vn}^{'}\right) + \left(\delta_{1vn} - \delta_{1v}\right)\right]} \quad (7)$$

- for the rear axle

$$F_{y2v} = F_{y2}\frac{\sin(\delta_{2v} - \delta_2)}{\sin[(\delta_2 - \delta_{2vn}) + (\delta_{2v} - \delta_2)]},$$

$$F_{y2vn} = F_{y2}\frac{\sin(\delta_2 - \delta_{2vn})}{\sin[(\delta_2 - \delta_{2vn}) + (\delta_{2v} - \delta_2)]} \quad (8)$$

where F_{y1} and F_{y2} are the total lateral forces acting on the front and rear axle, and they are defined by the centrifugal force and transforming trigonometric equations for the vector triangles of forces [6].

An iterative method with the system proposed in [6] is used to determine the center of the turn, the reactions of the road surface on the wheels, and the slip angles of a car's motion in a settled turn with low and ultra-low profile tires. The side slip of wheels at a different car's forward speeds is also defined.

Initially, the minimum steer angles of the steered wheels $\left(\theta_v^{'}, \theta_{vn}^{'}\right)$ are set and the average slip angle of the steered wheels is calculated. For each value of θ_{sr} and at different speed of the car, the side slip of the front δ_1 and rear axle δ_2 is defined by specifying the centre of the turn O_δ (Fig. 1) iteratively.

With the equations proposed in [6,10] and the K.Enke Method further developed by us [6] the non-linear characteristics of the side slip of the wheels $F_{yi} = f\left(\delta_i\right)$ for the corresponding normal load on each wheel are defined for the front and rear axle. The characteristics of the side slip are derived while defining the cornering stiffness by the averaged experimental curves defined by us in [10] for: the referred length of contact patch $a_{pr}^{"}$, angular stiffness $c_\omega^{"}$ and coefficient of lateral grip $\varphi_y^{"}$ for low and ultra-low profile tires with rim dimensions from 13" to 16" . The cornering stiffness is calculated by the equation $k_{\delta 0i} = 2c_\omega^{"} / a_{pr}^{"}$, and the coefficient of lateral grip - $\varphi_{yi} = k_{\varphi y}^{"}\varphi_y$ [10].

In this research lateral forces are defined by the Enke Method, but this can be also done by the equations (7) and (8).

The study is carried out according to the flowchart in Fig. 2. The full version of the software algorithm is presented in [6].

Fig. 2. Software flowchart.

III. Results and Discussion

The object of study was a Honda Civic Aerodeck personal car with the parameters given in table 1, with two tire dimensions, respectively 185/60R14 and 205/40R16. The second tire dimensions are proposed by the car manufacturer as an alternative, while preserving the rolling radius of wheels. According to Table 1, the rolling radius $r_k \approx 0,285\ m$.

Table 1 Car and tire characteristics.

Parameter, [unit]	Designation	Value
Car		
Total mass [kg]	m	1665
Front axle track width [m]	B_1	1,475
Rear axle track width [m]	B_2	1,475
Wheelbase [m]	L	2,62
Maximum inner steer angle [^{0}]	θ_v	36
Maximum outer steer angle [^{0}]	θ_{vn}	30
Distance between rear axle and the center of gravity (figure 1) [m]	b	1,286
Height of the center of gravity [m]	h	0,50
Maximum speed [km/h]	V	191
Tires		
Dimensions 185/60R14		
Width [mm]	B_t	185
Height [mm]	H_t	111
Rim diameter [mm]	d_r	355,6
Dimensions 205/40R16		
Width [mm]	B_t	205
Height [mm]	H_t	82
Rim diameter [mm]	d_r	406,4
Air pressure [MPa]	p_a	0,25

3.1. Results for the side slip, the lateral and normal load on the wheels and the car's turning radius with the two tire dimensions at forward speed of 20, 50 and 110 km/h

- for forward speed of 20 km/h

Fig. 3 shows the variation of the side slip of the front and rear axle with average steer angle in the plane of the road surface, and Fig. 4 - the variation of the side slip of the inner and outer wheels of the front and rear axle with average steer angle in the plane of the road surface, for the respective speed.

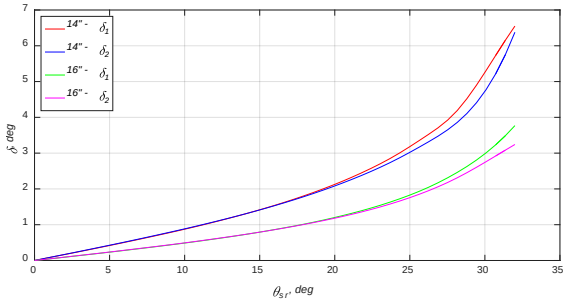

Fig. 3. Characteristics of the side slip of the front and rear axles.

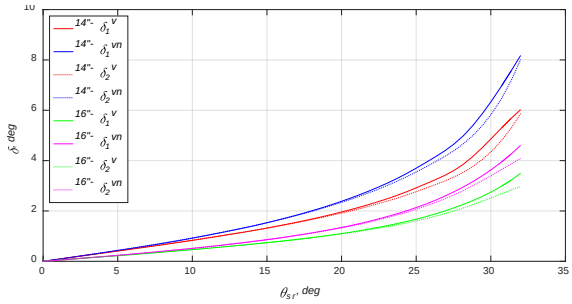

Fig. 4. Characteristics of the side slip of the tires.

Fig. 5 and Fig. 6 show the variation of the lateral and normal loads with average steer angle respectively and Fig. 7 - the variation in the turning radius with average steer angle.

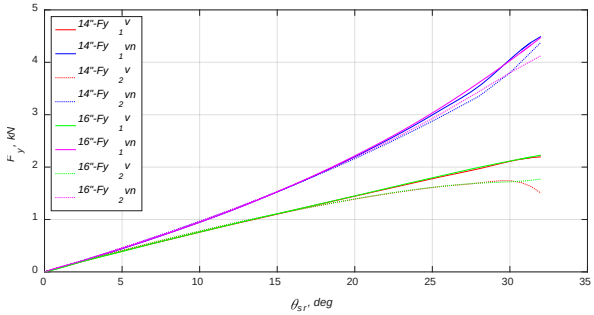

Fig. 5. The lateral loads of the wheels.

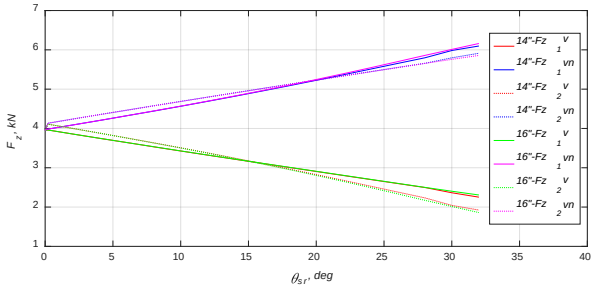

Fig. 6. The normal loads of the wheels.

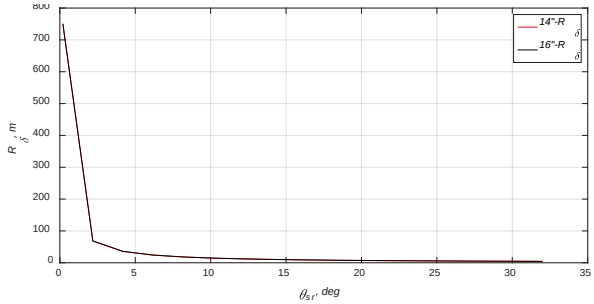

Fig. 7. The turning radius.

- for forward speed of 50 km/h

Fig. 8 presents the side slip of the front and rear axles and Fig. 9 shows the side slip of the four wheels of the car. Fig. 10 and Fig. 11, respectively, present the lateral and normal loads on the wheels, and Fig. 12 – the turning radius.

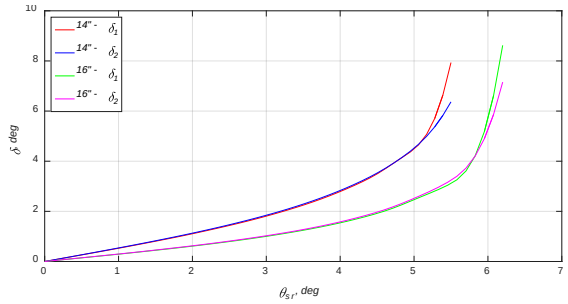

Fig. 8. Characteristics of the side slip of the front and rear axles.

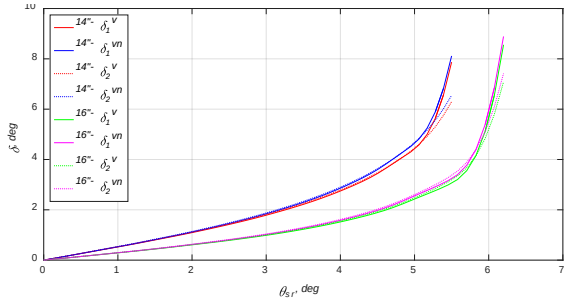

Fig. 9. Characteristics of the side slip of the tires.

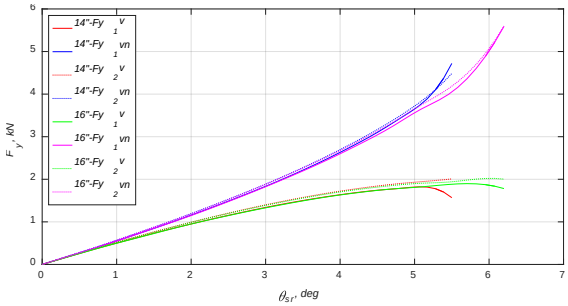

Fig. 10. The lateral loads of the wheels.

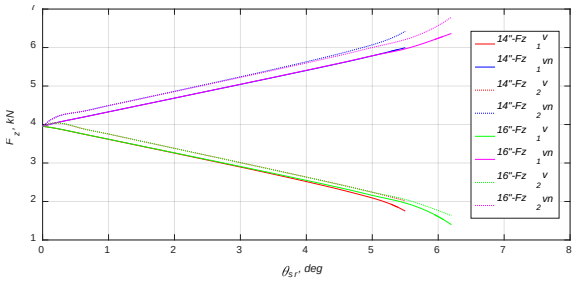

Fig. 11. The normal loads of the wheels.

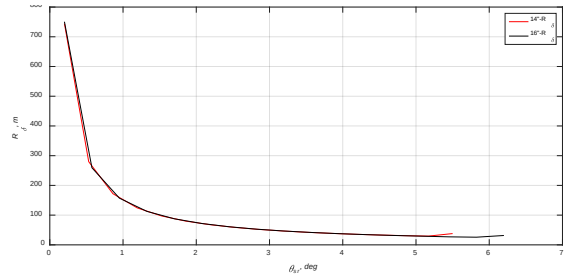

Fig. 12. The turning radius.

- for forward speed of 110 km/h

Fig. 13 presents the side slip of the front and rear axles and Fig. 14 shows the side slip of the four wheels of the car. Fig. 15 and Fig. 16, respectively, present the lateral and normal loads on the wheels, and Fig. 17 – the turning radius.

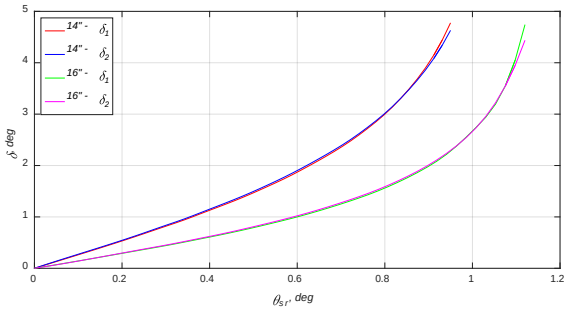

Fig. 13. Characteristics of the side slip of the front and rear axles.

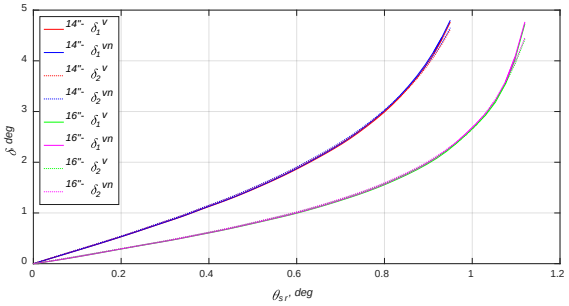

Fig. 14. Characteristics of the side slip of the tires.

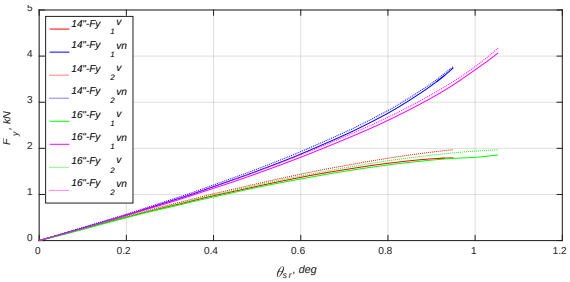

Fig. 15. The lateral loads of the wheels.

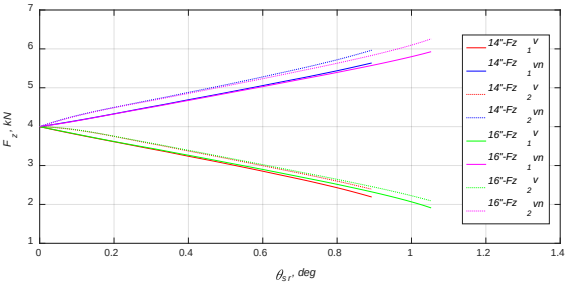

Fig. 16. The normal loads of the wheels.

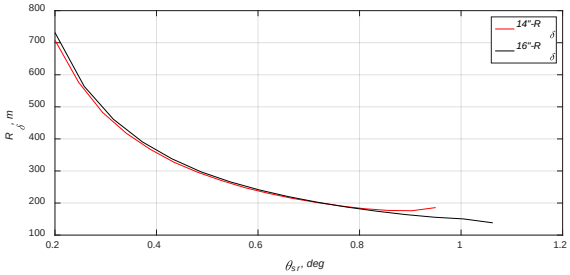

Fig. 17. The turning radius.

The analysis of the figures (from Fig. 3 to Fig. 17) shows that the car with ultra-low profile tires with dimensions 205/40R16 has a significantly lower value of side slip and also has a tendency to understeer $\delta_1 > \delta_2$. The outer wheels have greater side slip with regard to the turn, which is due to the change in their side slip characteristics due to the increased load. The lateral and normal loads on the inner wheels decrease and at a certain speed, the car loses stability and handling. When the speed increases, the turning radius decreases as the steer angle is changed. For the ultra-low profile tires, the steer angle increases.

3.2. Three-dimensional graphs of the variation in the side slip for the entire range of the car's forward speed

The study presented above is for stepwise change of speed of a car's motion in a turn (20, 50 and 110 km/h), which gives very good results for side slip, but three-dimensional graphics provide a clearer idea for the entire range of speed variation $\delta = f(\theta_{sr}, V)$.

The side slip of the two axles and of the tires for the entire range of the car's speed from 0 to 191 km/h, for both tire dimensions, is presented on Fig. 18 and Fig. 19.

Fig. 18*a* and Fig. 18*b* present the side slip of the front axle and Fig. 18*c* and Fig. 18*d* - of the rear axle for the two tire dimensions.

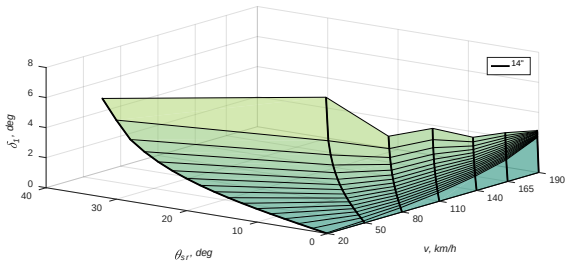

a) Tire "185/60 R14"

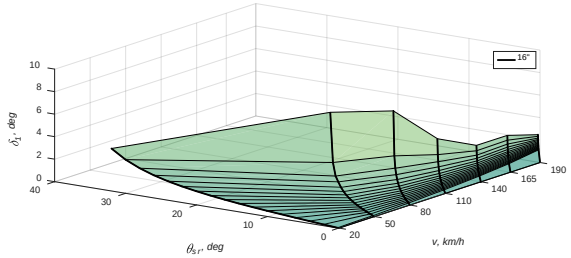

b) Tire “205/40 R16”

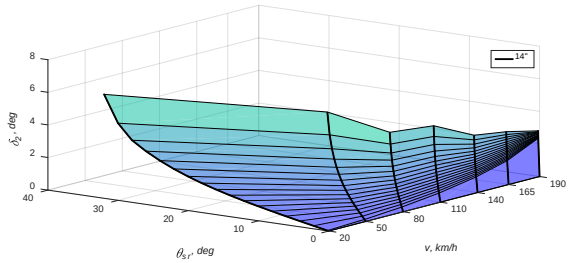

c) Tire “185/60 R14”

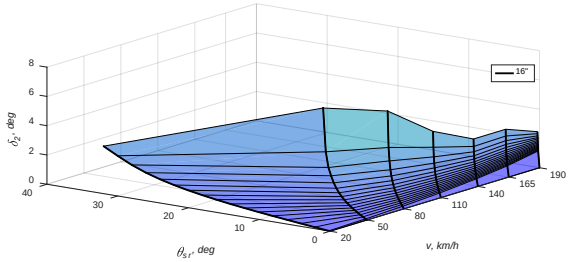

d) Tire “205/40 R16”

Fig. 18. Influence of the average angle of the steered wheels and the forward speed on the side slip.

Fig. 19*a* and Fig. 19*b* present the side slip of the most loaded front outer wheel for the two tire dimensions.

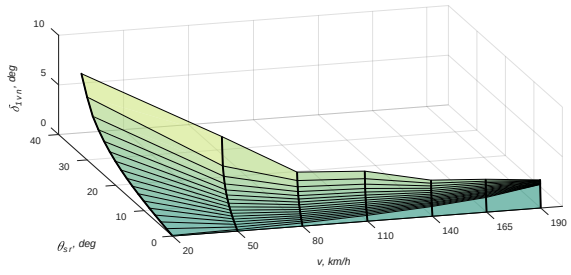

a) Tire “185/60 R14”

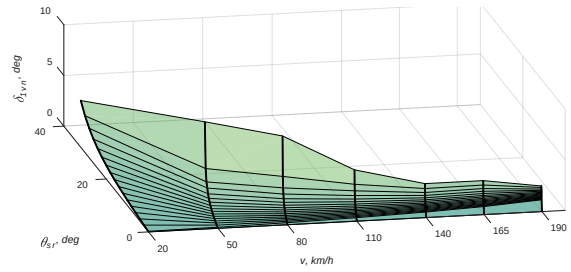

b) Tire “205/40 R16”

Fig. 19. Influence of the average angle of the steered wheels and the forward speed on the side slip.

The analysis of the data presented at the three-dimensional graphs gives a clear idea of the change of the wheels’ side slip, and the data in 3.1 for the different speeds agrees completely. On the basis of the presented three-dimensional graphs, the side slip of the car’s motion at all speeds can be analyzed.

IV. Conclusions

The study allows to make the follow conclusions:

- The proposed interactive software system in the MATLAB environment using the advanced Enke Method allows the determination of the lateral forces by the changing characteristics of the side slip of tires at constant values of the normal loads.

- As the turning radius decreases, the grip of the inner wheels decreases.

- The handling and stability of personal car during a turn at high speeds shall be improved by replacing low-profile tires with alternative ultra-low profile tires permitted by the vehicle design when motion on asphalt or concrete road, while preserving the rolling radius of the wheels.

- The three-dimensional graphics show that as the forward speed and the average steer angle increase the side slip of the tires decreases.

Acknowledgments

This work was supported by the European Regional Development Fund within the OP “Science and Education for Smart Growth 2014-2020”, Project Competence Centre “Smart Mechatronic, Eco-And Energy Saving Systems And Technologies”, № BG05M2OP001-1.002-0023.

REFERENCES

[1] D. A. Antonov, Theory of stability of vehicle motion, Moscow, Mechanical Engineering, 1978

[2] A.S. Litvinov, Handling and stability of the vehicle, Moscow, Mechanical Engineering, 1971.

[3] H. B. Pacejka, Tyre and Vehicle Dynamics, Second edition, Amsterdam, Boston, Heidelberg, London, New York, Oxford, Paris, San Diego, San Francisco, Singapore, Sydney, Tokyo, ISBN -13: 980-0-7506-6918-4, 2006.

[4] G. Rill, Road vehicle dynamics: Fundamental and Modeling, Taylor & Francis Group, LLC, ISBN – 13: 978-1-4398-9744-7, 2012.

[5] J. Y. Wong, Theory of ground vehicles, Third edition, New York, ISBN 0-471-35461-9, 2001.

[6] S. Taneva, K. Ambarev, D. Katsov, Interactive system for study of car’s movement with low and ultra-low profile tires in a turn, Proceedings of the 12th International Scientific and Practical Conference, Environment. Technology. Resources. Rezekne, Latvia, pp. 224-228, 2019.

[7] E. Bakker, L. Nyborn, H. Pacejka, Tyre Modelling for Use in Vehicle Dynamics Studies, SAE International Journal, Paper № 870421, Vol. 2, pp. 190-204, 1987.

[8] D. A. Katsov, D. A. Hlebarski, Dynamics of the turn of wheel vehicle with account of the deformations of the tires and the influence of the suspension, International Journal of Computational and Numerical Analysis and Applications, Vol. 6, No. 2, pp.97-106, 2004.

[9] D. A. Katsov, D. A. Hlebarski, Kinematics of the turn of wheel vehicle with account of the deformations of the tires and the

influence of the suspension, International Journal of Computational and Numerical Analysis and Applications, Vol. 25, No. 2, pp. 203-214, 2005.

[10] D. Katsov, S. Taneva, Investigation of the lateral slip and grip of low and superlow profile tires of cars, Journal of Machine Building and Machine Science, Varna, Bulgaria, Year. X, No. 2, Vol. 24, pp. 39-45, 2015.

[11] H. Pacejka, E. Bakker, The Magic Formula Tyre Model, International Journal of Vehicle Mechanics and Mobility, Suppl. Vehicle System Dynamics, Vol. 21, pp. 1-18, 1992.

[12] L. Palkovics, M. El-Gingy, Neural Network Representation of Tyre Characteristics: The Neuro-Tyre, International Journal of Vehicle Design, Vol.14, pp. 563-591, 1993.

Environment. Technology. Resources. Rezekne, Latvia
Proceedingsofthe 13th InternationalScientificandPractical Conference. Volume 3, 343-347

Increase of Indicators of Vehicles' Smooth Running by Internal Suspension of Wheels

Vladimir Timofeev
Institute of Engineering Sciences
Pskov State University
Pskov, Russia
timofeev1097@yandex.ru

Alexander Enaev
Institute of Engineering Sciences
Pskov State University
Pskov, Russia
enaa53@mail.ru

Anna Dmitrieva
Institute of Engineering Sciences
Pskov State University
Pskov, Russia
anna-listratova@rambler.ru

Evgeny Seleznev
Institute of Engineering Sciences
Pskov State University
Pskov, Russia
evgeniys84@yandex.ru

Tatyana Klets
Institute of Humanities and Linguistic Communications
Pskov State University
Pskov, Russia
kte63@yandex.ru

***Abstract* - The article discusses the relevance of increasing the smoothness of the movement of vehicles, and also substantiates the feasibility of using internal suspension of wheels in conjunction with a suspension and as an independent system.**

Keywords - inelastic resistance coefficient, normal stiffness coefficient, the smoothness of vehicles' course, the wheel with internal springing.

I. INTRODUCTION

The operational properties of the vehicle characterize the performance of transport and special works. These properties determine the vehicle's adaptability to operating conditions, efficiency and ease of use. Improving performance is a priority in automotive design.

Smooth running is an important performance property. It largely affects the average speed, fuel consumption, ride comfort, safety of the transported cargo and the health of the driver and passengers from the impact of road irregularities. With an improvement in the smoothness of the course, an increase in the overhaul mileage of vehicles is observed.

When a car moves on an uneven road, not only vibrations of the body occur, but also vibrations of different frequencies caused by the interaction of the wheels with the supporting surface, the peculiarities of the operation of individual suspension elements, as well as aerodynamic forces. All this, in addition to the above-described consequences, leads to the occurrence of mechanical stresses in the suspension and the occurrence of noise both inside the car and outside, which in turn leads to noise pollution of the environment.

Various factors influence the ride smoothness: the type of suspension, the use of certain elastic and damping devices, the elasticity of pneumatic tires, and others.

Obviously, the problem of improving the ride quality indicators is urgent. In this regard, continuous improvement is carried out not only for individual parts of vehicles, but also for equipment for testing them in various conditions, innovative solutions and non-standard approaches to design are applied.

The vibration system of a car is a complex multi-mass system that includes sprung and unsprung masses. The first ones rely on the elastic element of the car suspension and perform low-frequency vibrations (1 ... 1.5 Hz), the second ones - have contact with the road surface and vibrate with high frequencies (5.8 ... 12 Hz). The car makes free vibrations when driving on a flat road after passing an obstacle. In fact, such vibrations are damped by the friction in the suspension and the resistance of the damping devices.

Suspension and pneumatic tires of the vehicle are responsible for reducing vibration load and elastic seats for drivers and passengers.

Online ISSN 2256-070X
https://doi.org/10.17770/etr2021vol3.6592

The use of pneumatic tires improves the ride comfort due to their elasticity, smoothing and absorption capacity. Tires have a radial stiffness 6-12 times that of an elastic suspension element. They, along with the suspension, are involved in reducing the dynamic effects of road irregularities.

II. APPLICATION OF WHEELS WITH INNER SPRINGS ON THE AUTOMOTIVE TRANSPORT

An innovative solution was the creation of wheels with internal suspension, the elastic element of which is located between the wheel hub and the rim of the disc. Due to their compact size, the best indicators of absorption of the dynamic effects of road irregularities, the use of such structures is advisable on vehicles with a suspension installed or instead of a suspension. In the first case, there is an improvement in the smoothness of the movement, in the second, a simplification of the design and, as a result, an increase in reliability and a decrease in the cost of the product.

At Pskov State University, an experimental model of a wheel with internal suspension was created [1] Patent No. 2524269.

Studies of the smooth running of a vehicle equipped with such wheels have shown the effectiveness of their use. The wheel was installed on a car trailer instead of the standard suspension. At the same time, it was possible to maintain the values of the maximum vertical acceleration of the body without using the suspension. However, in the course of experiments, it turned out that the elastic element of the wheel is susceptible to lateral withdrawal. As a result of the action of the lateral force, the disc rim is displaced relative to the hub. As a result, the occurrence of vibrations in the horizontal plane is observed, which negatively affects the handling and safety of the vehicle (Fig. 1).

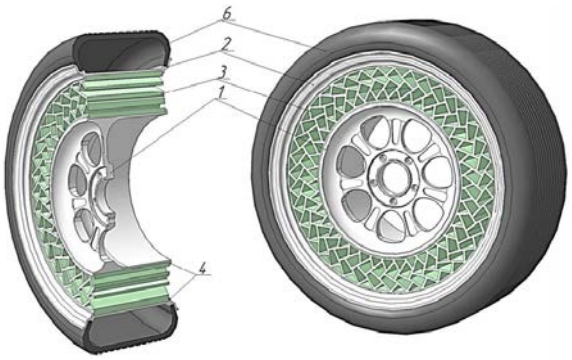

Fig. 1. Wheel with internal suspension. Patent No. 2524269

As a result of the analysis of the advantages and disadvantages of the wheel [1], a wheel with internal suspension was developed [2] Patent No. 2729851, the design of which is shown in Fig. 2. The wheel with internal suspension consists of separately made hubs with thrust plates 1 and a rim 2 connected by an elastic element 3 made of polymer material in the form of a closed ring of trapezoidal cross-section with end perforation. The rim of the disc, due to its trapezoidal shape, serves as an internal stop, partially preventing axial displacement of the hubs. The hubs with thrust plates are bolted together. Polymeric elastic element 3 is connected to the hub and rim by adhesion. The rim 2 has a pneumatic tire 4.

The thrust plates serve to limit the axial movements of the hub 1 relative to the rim 2 and prevent oscillations in the horizontal plane. The thrust plates are installed at an angle that provides a portion of the horizontal force that causes the longitudinal displacement of the rim 2 relative to the hub, redistribution to the wheel axle, and thereby reducing the action of this force. This reduces the amount of longitudinal movement that will take place within the elastic deformation of the polymer material of the elastic element 3 located between the stop plates. The internal suspension parameters are calculated for a specific vehicle. Achieving the best smoothness of the ride is due to the coordination of the properties of the elastic element with the parameters of the vehicle.

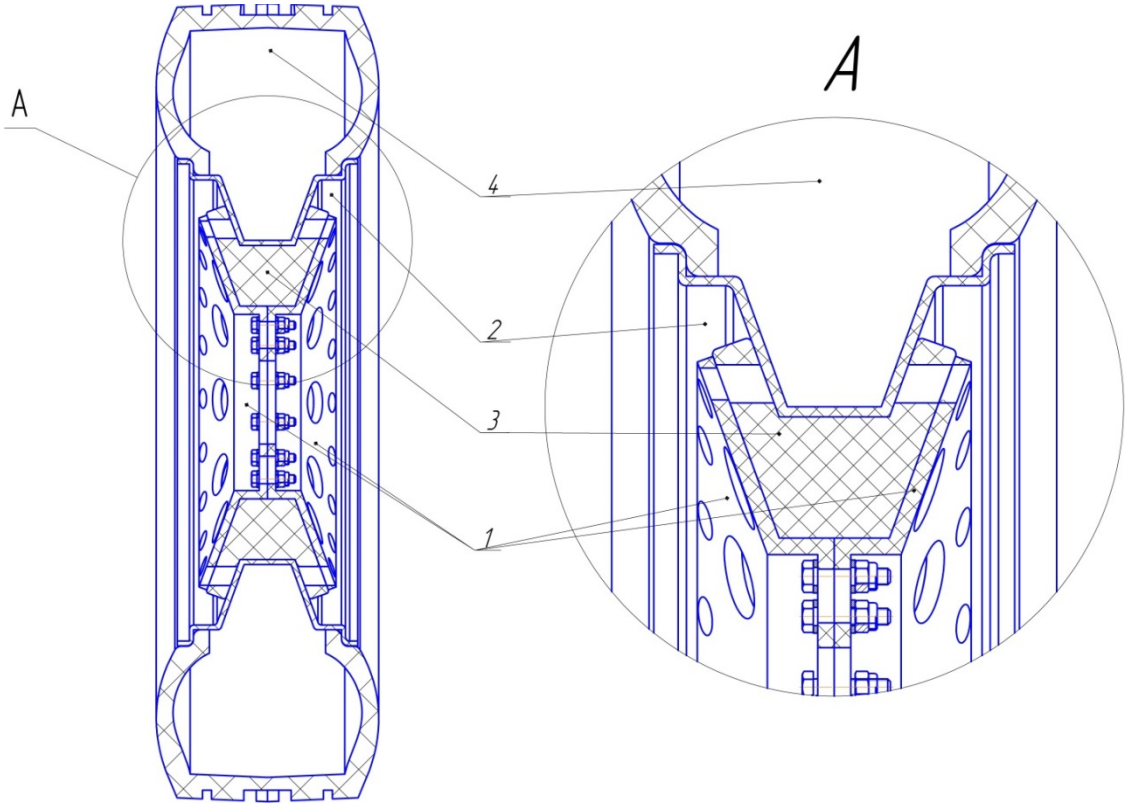

Fig. 2. Wheel with internal suspension. Patent No. 2729851.

With a decrease in the angle of inclination of the thrust plates, the normal load on the plates from the side of the action of centrifugal force decreases. The required amount of horizontal deformation of the elastic element is achieved.

Design requirements for an internally sprung wheel include:

- increasing the smoothness of the ride while maintaining controllability and stability of the vehicle by limiting the lateral movement of the wheel rim relative to the hub;

- reducing the load on the vehicle components due to the deformation of the elastic element.

The technical result is achieved by the fact that the elastic element is made of a polymeric material in the form of a closed ring with end perforation and is partially located between the thrust plates of the wheel hub and the rim of the disk. The thrust plates are angled to reduce the horizontal force. The amount of possible movement of the rim relative to the hub is determined by the end deformation of the polymer material located between the thrust plates. Improvement of the smoothness indicators is provided due to the possibility of deformation of the polymer elastic element.

Due to its trapezoidal shape, the rim of the disc acts as an internal thrust bearing. It should be borne in mind that the wheel is a complex elastic system consisting of several elements. The thrust plates are parallel and spaced from the inner rim bearing surface. The distance is determined by the angle of inclination of the thrust plates. The angle of inclination of the plates to the horizon ranges from 30 ° to 90 °.

The elastic and damping properties of the wheel can vary depending on the end perforation and the geometry of the elastic element. It is also proposed to adjust the stiffness of the wheel by using materials with different properties. So, for the production of an elastic element, it is possible to select urethane elastomers of different hardness. This makes it possible to match the internal suspension properties and vehicle-specific characteristics to achieve the best ride quality.

III. THEORETICAL MODEL OF VIBRATIONS OF A VEHICLE EQUIPPED WITH INNER SPRING WHEELS

A diagram of an oscillating system equivalent to a suspension with a wheel containing internal suspension is shown in Fig. 3.

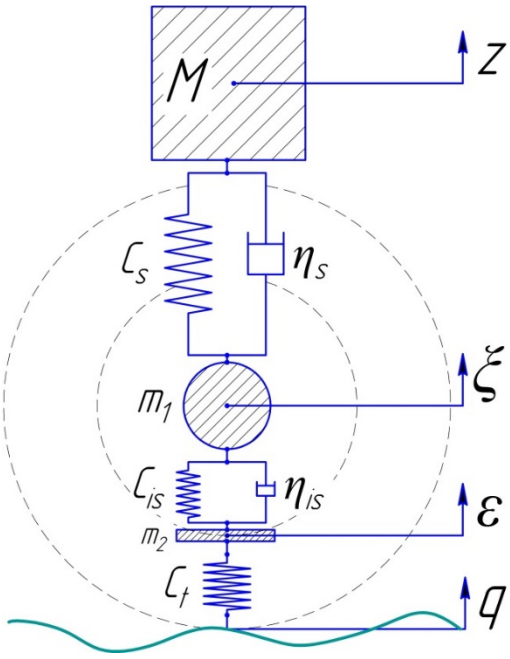

Fig. 3. Oscillation system equivalent to a suspension with an internally cushioned wheel.

When drawing up this scheme, the images and designations generally accepted in the theory of ride and cushioning are preserved:

M - sprung mass, kg

m_1 - the first unsprung mass, kg

m_2 - the second unsprung mass, kg

z - vertical movement of the sprung mass, kg

ξ - vertical movement of the first unsprung mass, m

ε - vertical movement of the second unsprung mass, m

C_S- normal stiffness of the elastic suspension element, N/m

C_{is} - normal stiffness of the elastic element of the inner suspension, N/m

C_t- normal tire stiffness, N/m

η_s- suspension inelastic resistance coefficient, N*s/m

η_{is} - coefficient of inelastic resistance of internal suspension, N*s/m

In this case:

$M\ddot{z}$ – sprung mass inertia, N

$c_s(z-\xi)$ – suspension elastic force, N

$\eta_s(\dot{z}-\dot{\xi})$ – inelastic suspension force, N

$m_1\ddot{\xi}$ – inertia force of the first unsprung mass, N

$c_{is}(\xi-\varepsilon)$ – internal suspension force, N

$\eta_{is}(\dot{\xi}-\dot{\varepsilon})$ – internal suspension inelastic resistance force, N

$m_2\ddot{\varepsilon}$ – inertia force of the second unsprung mass, N

$c_t(\varepsilon-q)$ – tire elastic force, N

Thus, the oscillations of the system can be represented as:

$$\begin{cases} M\ddot{z}+c_s(z-\xi)+\eta_s(\dot{z}-\dot{\xi})=0; \\ m_1\ddot{\xi}+c_{is}(\xi-\varepsilon)+\eta_{is}(\dot{\xi}-\dot{\varepsilon})— \\ \quad -c_s(z-\xi)-\eta_s(\dot{z}-\dot{\xi})=0; \\ m_2\ddot{\varepsilon}+c_t(\varepsilon-q)-c_{is}(\xi-\varepsilon)- \\ \quad —\eta_{is}(\dot{\xi}-\dot{\varepsilon})=0. \end{cases} \quad (1)$$

Dividing the left and right sides of the equations of system (1) by M, m_1 and m_2 respectively we get:

$$\begin{cases} \ddot{z}+\frac{c_s}{M}(z-\xi)+\frac{\eta_s}{M}(\dot{z}-\dot{\xi})=0; \\ \ddot{\xi}+\frac{c_{is}}{m_1}(\xi-\varepsilon)+\frac{\eta_{is}}{m_1}(\dot{\xi}-\dot{\varepsilon})— \\ -\frac{c_s}{m_1}(z-\xi)-\frac{\eta_s}{m_1}(\dot{z}-\dot{\xi})=0; \\ \ddot{\varepsilon}+\frac{c_t}{m_2}(\varepsilon-q)-\frac{c_{is}}{m_2}(\xi-\varepsilon)- \\ \quad —\frac{\eta_{is}}{m_2}(\dot{\xi}-\dot{\varepsilon})=0. \end{cases} \quad (2)$$

Taking into account the well-known designations

$$\frac{c_s}{M}=\Omega^2;$$

$$\frac{c_{is}}{m_1}=\omega_1^2;$$

$$\frac{c_{is}}{m_2}=\omega_2^2;$$

$$\frac{\eta_s}{M}=2k;$$

$$\frac{\eta_{is}}{m_1}=2k_1.$$

Introducing the notation

$$\frac{m_1}{M}=\mu_1;$$

$$\frac{m_1}{M}=\mu_2.$$

we get:

$$\frac{c_s}{m_1}=\frac{c_s}{\mu_1 M}=\frac{\Omega^2}{\mu_1};$$

$$\frac{\eta_s}{m_1}=\frac{\eta_s}{\mu_1 M}=\frac{2k}{\mu_1};$$

$$\frac{c_{is}}{m_2}=\frac{c_{is}}{\mu_2 m_1}=\frac{\omega_1^2}{\mu_2};$$

$$\frac{\eta_{is}}{m_2}=\frac{\eta_{is}}{\mu_2 m_1}=\frac{2k_1}{\mu_2}.$$

Then equations (2), taking into account the adopted designations, take the form:

$$\begin{cases} \ddot{z} + \Omega^2(z-\xi) + 2k\left(\dot{z} - \dot{\xi}\right) = 0; \\ \ddot{\xi} + \omega_1^2(\xi - \varepsilon) + 2k_1\left(\dot{\xi} - \dot{\varepsilon}\right) — \\ -\frac{\Omega^2}{\mu_1}(z-\xi) - \frac{2k_1}{\mu_2}\left(\dot{z} - \dot{\xi}\right) = 0; \\ \ddot{\varepsilon} + \omega_2^2(\varepsilon - q) - \frac{\omega_1^2}{\mu_2}(\xi - \varepsilon) - \\ — \frac{2k_1}{\mu_2}\left(\dot{\xi} - \dot{\varepsilon}\right) = 0. \end{cases} \quad (3)$$

or

$$\begin{cases} \ddot{z} + 2k\dot{z} + \Omega^2 z - 2k\dot{\xi} - \Omega^2\xi = 0; \\ \ddot{\xi} + 2\left(k_1 + \frac{k}{\mu_1}\right)\dot{\xi} + (\omega_1^2 + \frac{\Omega^2}{\mu_1})\xi - \\ -2k_1\dot{\varepsilon} - \omega_1^2\varepsilon - \frac{2k}{\mu_1}\dot{z} - \frac{\Omega^2}{\mu_1}z = 0; \\ \ddot{\varepsilon} + \frac{2k_1}{\mu_2}\dot{\varepsilon} + \left(\omega_2^2 + \frac{\omega_1^2}{\mu_2}\right)\varepsilon - \frac{2k_1}{\mu_2}\dot{\xi} - \\ -\frac{\omega_1^2}{\mu_2}\xi = \omega_2^2 q. \end{cases} \quad (4)$$

The proposed mathematical model (4) will allow at the design stage to determine, by the minimum value of the vertical displacements of the sprung masses, the optimal parameters characterizing the elastic and damping properties of the internal suspension.

IV. CONCLUSIONS

Thus, due to the use of the described product, it is assumed that the material consumption of the production of vehicles will be reduced, as a result of the exclusion of the suspension from the design. When using wheels with internal suspension in conjunction with the suspension, it is assumed that the dynamic effects on the vehicle parts and the road surface will be reduced. This will have a positive effect on the service life of both the vehicle and the road network.

REFERENCES

[1] A. A. Enaev and S. B. Manfanovsky, "Wheel with internal suspension No. 20121262213/11," Patent No. 2,524,269, Russian Federation, IPC B60B 9/26. Declared June 22, 2012; Publ. Dec. 27, 2013, Bul. No. 21.

[2] A. A. Enaev, V. S. Timofeev, and P. N. Maltsev, "Wheel with internal suspension. No. 2019133497", Patent No. 2729851 Russian Federation, IPC B60B 9/26. Declared October 21, 2019, Publ. August 12, 2020, Bul. No. 23.

[3] A. A. Enaev, "Fundamentals of the theory of vehicle vibrations during braking and its applications." M.: Mashinostroenie, 2002, 341 p.

[4] S. B. Manfanovsky, "Improving the smoothness of the movement of transport and transport-technological machines by internal suspension of wheels," PhD thesis, Pskov, 2019.

Environment. Technology. Resources. Rezekne, Latvia
Proceedings of the 13th International Scientific and Practical Conference. Volume 3, 348-356

Heat Source for TIG Welding Modelling

Manahil Tongov
Faculty of Idustrial Technology
Technical University of Sofia
Center of Welding
Institute of Metal Science, Equipment
and Technologies with Hydro-
and Aerodynamics Centre "Acad. A. Balevski"
Bulgarian Academy of Sciences
Sofia, Bulgaria
tongov@tu-sofia.bg

***Abstract* - A new model of heat source applicable to TIG welding is proposed. The model uses three calibration parameters - efficiency, effective heating spot radius and heat source concentration factor. Based on the experimental results, the model was calibrated and the results obtained for the form of penetration were compared with the experimental ones**

Keywords* - *TIG welding, modelling; heat source; calibrating parameters; calibrating methods; experimental results.

I. INTRODUCTION

One of the tasks that need to be solved within computer welding mechanics is thermal. Based on the obtained solution, such basic characteristics of the technological process are determined as: cooling time from 800[^{0}C] to 500[^{0}C] $t_{8/5}$; residence time of the metal above certain critical temperatures; obtained structures in the heat affected zone; determining the expected hardness in the joint area; the influence of the preheating temperature, determining the optimal one, etc. In addition, the solution of the thermal problem is the basis of the analysis of the obtained temporary and residual stresses, deformations and distortions in the welded structure. TIG welding is a widely used method in the welding of high-alloy corrosion-resistant steels. One of the steps that needs to be implemented in the simulation modelling of the process is the calibration of the heat source model. The ISO / TS 18166 standard makes it possible to do this by welding specimens and experimentally determining the shape and dimensions of the melting zone. The mathematical model uses calibration parameters, which are determined in such way that the shape and dimensions of the melting zone calculated by solving the model correspond as much as possible to the experimentally obtained results. The welding mode parameters, geometric dimensions of the samples and thermal properties of the basic and additional materials cannot be used as calibrating parameters. This means that the calibration parameters in practice refer to the heat source and heat dissipation from the welded specimens. There are different heat sources models published (table 1) – surface [1 ÷ 9], volume [10 ÷ 21], by combination of both types and those in which the modelling of the welding arc and the heating of the sample is calculated together [22 ÷ 25]. In TIG welding, the shape of the weld is usually obtained without inflection (Fig. 1a), but in some modes and mainly depending on the arc pressure, it is possible to obtain a curve with an inflection point (Fig. 1b).

II. HEATH SOURCE

In this study a new heat source is proposed, which is suitable for welds without inflection and also a method for its calibration. The heat flux is represented by the superposition of two normally distributed heat sources:

$$q(r) = q_{eff}\,\frac{A}{2}\left[\frac{1}{\sigma\sqrt{2\pi}}\exp\left(-\frac{(r-r_0)^2}{2\sigma^2}\right)+\right. \qquad (1)$$
$$\left.+\frac{1}{\sigma\sqrt{2\pi}}\exp\left(-\frac{(r+r_0)^2}{2\sigma^2}\right)\right] = q_{eff}\,Af(r)$$

where q_{eff} is the effective heat output, f(r) is a heat flux distribution function and A is a norming multiplier to be determined by the condition

Online ISSN 2256-070X
https://doi.org/10.17770/etr2021vol3.6601

$$\int_0^{\infty} Af(r)2\pi r dr = 1$$

The final result for the norming multiplier is obtained after solving the last equation:

$$A = \frac{1}{\sigma\sqrt{2\pi}\exp\left(-\frac{r_0^2}{2\sigma^2}\right) + \pi r_0 erf\left(\frac{r_0}{\sigma\sqrt{2}}\right)} \qquad (2)$$

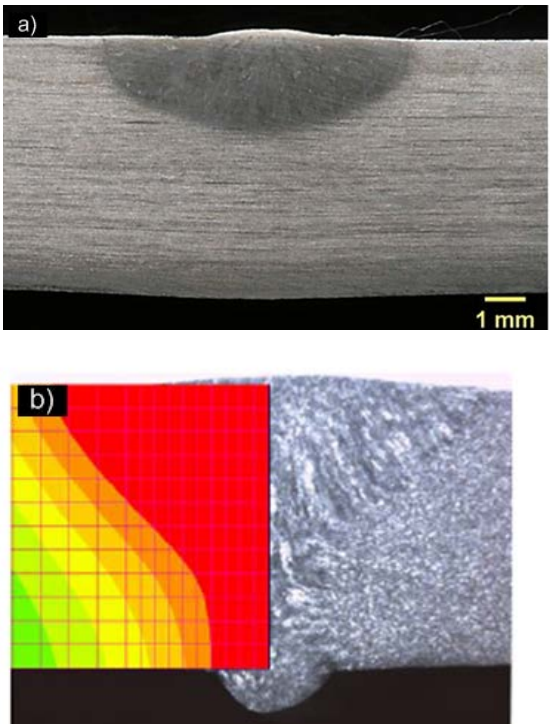

Fig.1. Two possible forms of penetration in TIG welding: seam shape without inflection point [26] – (a); weld shape with inflection [16] – (b).

For the use of the heat source it is convenient to define the effective heating radius r_{arc} and coefficient of deviation of the heat source from a normally distributed circular heat source $\alpha_{arc} = r_0/r_{arc}$ - distribution coefficient. These two parameters, as well as the efficiency, are determined by calibrating the thermal model in relation to the experimental results in the specific case of realization of the welding process. They determine q_{eff} and. $\sigma = 3.r_{arc}$. At such selected ratios $r_0/\sigma = \alpha_{arc}/3$. The influence of the coefficient α_{arc} on the heat flow distribution is shown in Fig.2.

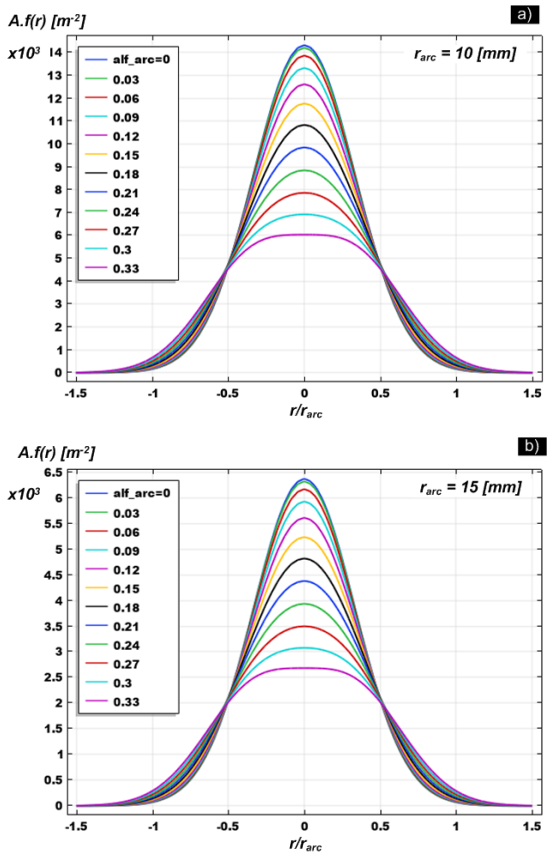

Fig.2. Influence of the heat source distribution coefficient on the heat flux density.

III. METHODOLOGY FOR THE THERMAL MODEL CALIBRATION

The calibration of the thermal model is performed by comparing experimental and simulation results. The simulation model must have calibration parameters to be determined on the basis of this comparison. The material characteristics, the geometry of the specimens and the parameters of the welding mode cannot be used as such. Usually the calibration parameters refer to the heat source. In this case, these are the efficiency (η), the effective radius of the heating spot (r_{arc}), and the distribution coefficient (α_{arc}). The comparison of the experimental and numerical results can be performed on the basis of experimentally recorded temperature cycles at several points of the welded specimens or the shape of the penetration determined by metallographic analysis. In the considered example the second variant is used. Beads with the welding mode of interest are performed on a plate with a thickness equal to the thickness of the welded parts in the structure and from the same material from which the structure is made with dimensions sufficient to reach a quasi-stationary process (Fig.3). The depth of penetration (h_p) and the width of the weld (b_w) are determined by making metallographic macrosection from the area of the established quasi-stationary process.

TABLE I. HEAT SOURCES.

Heat flux equation in the heat source coordinate system, [W/m²]	Calibrating parameters	Welding process	Source
$q(r)=\frac{\eta UI}{\pi r_H^2}\exp\left(-\frac{r^2}{r_H^2}\right)$	$\eta=0.65$ r_H [1)]	TIG	[1]
$q(r)=\frac{\eta UI}{2\pi\sigma^2}\exp\left(-\frac{r^2}{2\sigma^2}\right)$	$\eta=0.7$ $\sigma=0.5;1;2;3;4[mm]$	TIG	[2]
$q(r)=q_m\exp\left(-Cr^2\right)$	$q_m;C$ [1)]	MAG	[3]
$q(r)=\frac{3\eta UI}{\pi r_a^2}\exp\left(-\frac{r^2}{r_a^2}\right)$	$\eta=0.9$ r_a [1)]	MIG	[4]
$q(r)=\frac{\eta UI}{2\pi R_N^2}\exp\left(-\frac{r^2}{2R_N^2}\right)$	$\eta=0.85$ $R_N=1.2[mm]$	TIG	[6]
$q(r)=k\frac{\eta UI}{2\pi R_N^2}\exp\left(-\frac{3r^2}{R_N^2}\right)$	$\eta=0.7$ - determined by comparison $R_N=f(b_W)$ - determined as: 6.6[mm]	GMAW	[7]
$q(\xi,y,z)=\begin{cases}\frac{6r_fQ}{a_{hf}b_h\pi}\exp\left(-3\left(\frac{\xi^2}{a_{hf}^2}+\frac{y^2}{b_h^2}\right)\right)\\ \frac{6r_bQ}{a_{hb}b_h\pi}\exp\left(-3\left(\frac{\xi^2}{a_{hb}^2}+\frac{y^2}{b_h^2}\right)\right)\end{cases}$	$Q=\eta IU$ $r_f=\frac{a_{hf}}{a_{hf}+a_{hb}}\quad r_b=\frac{a_{hb}}{a_{hf}+a_{hb}}$ $\eta=0.656\quad a_{hf}=2.43[mm]$ $a_{hb}=6.96[mm]\quad b_h=2.96[mm]$ Parameters are determined by optimization task using records from thermocouples	GMAW	[8]
2 heat sources one above the other	Parameters not specified.	TIG	[9]
$q=\begin{cases}\frac{6\sqrt{3}\eta UIf_f}{\pi\sqrt{\pi}a_f bc}\exp\left(-3\left(\frac{x^2}{a_f^2}+\frac{y^2}{b^2}+\frac{z^2}{c^2}\right)\right)\\ \frac{6\sqrt{3}\eta UIf_r}{\pi\sqrt{\pi}a_r bc}\exp\left(-3\left(\frac{x^2}{a_r^2}+\frac{y^2}{b^2}+\frac{z^2}{c^2}\right)\right)\end{cases}$	Goldak's model with parameters $f_f, f_r, a_f, a_r, b, c,$ It is not shown how the parameters are determined.	TIG	[10] ÷ [12], [15], [18]
		TIG and MIG	[13], [14]
		SAW	17
	The parameters are set expertly in proportions	TIG	16
	No values specified	TIG	19
		TIG and MIG	20
	[1)]	MIG	21

[1)] the determination method and values aren't specified

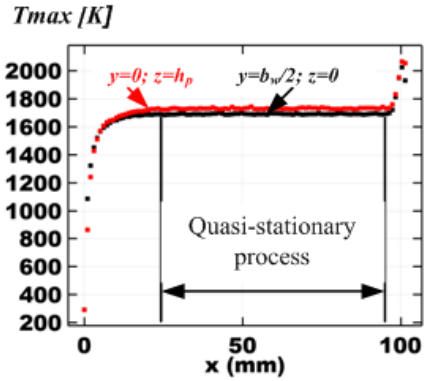

Fig.3. Maximum temperature reached for two lines parallel to the weld axis

A mathematical model is being developed to describe the realized welding process using the same geometry, material characteristics and welding mode. A simulation model is being realized, which solves the thermal task, and at the last moment of time for which the solution is performed, the heat source is in the zone of the quasi-stationary state. In the geometry of the model, two (or more) straight lines (l_1 and l_2) are drawn, parallel to the axis of the weld (Fig.4). One of these lines (l_1) is located in the upper plane of the welded specimens and is at a distance $b_w/2$ from the weld axis (passes through the point representing the width of the weld). The second line (l_2) is at a distance h_p from the upper surface of the welded specimens (in the direction of the depth of penetration) in a plane passing through the weld axis and perpendicular to the upper surface of the welded specimens - passes through the point determining the depth of penetration. The

temperature change along these two lines at the last moment of solving the task is shown in Fig.5. For this two lines the maximum of the temperatures for this moment are determined - T_{1max} and T_{2max}. The calibration parameters are found by solving an optimization problem with the following objective function (T_S is the solidus temperature):

$$\Phi(\eta,\alpha_{arc},r_{arc})=\left(\frac{T_{1\max}-T_S}{T_S}\right)^2+\left(\frac{T_{2\max}-T_S}{T_S}\right)^2\Rightarrow\min \quad (3)$$

or

$$\Phi(\eta,\alpha_{arc},r_{arc})=\max\left(\left|\frac{T_{1\max}-T_S}{T_S}\right|,\left|\frac{T_{2\max}-T_S}{T_S}\right|\right)\Rightarrow\min \quad (4)$$

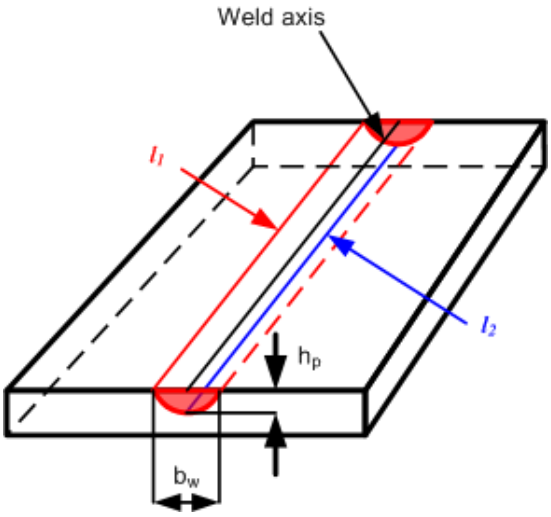

Fig.4. Lines passing through the points representing the width of the weld and the depth of penetration.

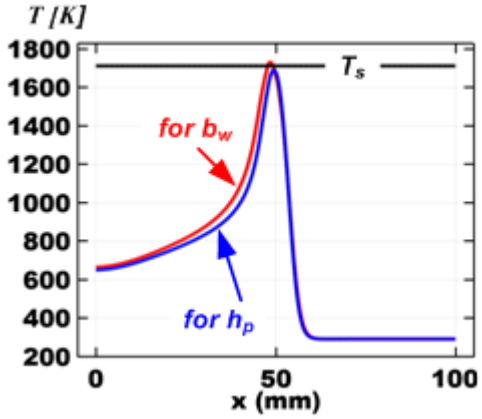

Fig.5. Temperature on the lines passing through the control points.

IV. Experimental results.

To verify the operability of the proposed heat source and methodology for calibration of the heat model, experiments were performed by TIG welding of steel AISI 304. The chemical composition of the base metal is given in Table 2. The size of the samples is 6x100x100[mm]. The welding modes used and the obtained seam dimensions aregiven in Table 3. Fig. 6 shows one of the measured depths of penetration and the width of the seam [29]. For mode №5, three of the measurements used to obtain averaged results are shown.

TABLE II. Chemical composition of base metal [26].

alloying element	***C***	***Mn***	***Si***	***Cr***
concentration [wt.%]	≤ 0.08	≤ 2.0	≤ 0.75	18÷20
alloying element	***Ni***	***S***	***P***	***N (ppm)***
concentration [wt.%]	8÷10.5	≤ 0.030	≤ 0.035	≤ 1100

TABLE III. Welding modes and weld dimensions.

No of mode	**I_w**	**U_a**	**V_w**	**b_w**	**h_p**
	[A]	**[V]**	**[cm/min]**	**[mm]**	
1	180	14.9	30	7.609	1.44
2	180	14.9	12	11.518	3.112
3	80	10.6	30	2.801	0.438
4	80	10.6	12	4.025	1.006
5	130	12.7	21	6.536	1.082

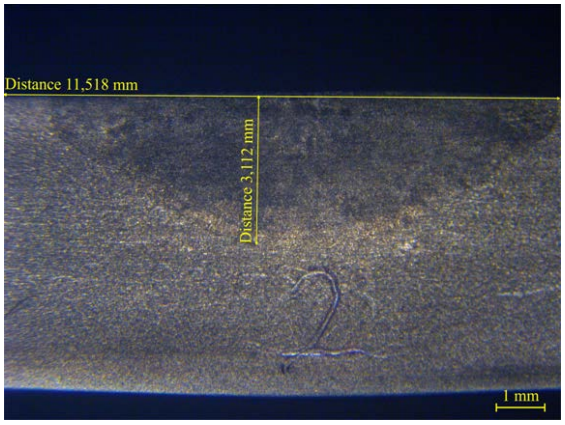

Fig.6. Measurement of the depth of penetration and the width of the weld – mode No 2

V. Task formulation, results and analysis.

The geometry of the considered example is shown in Fig.7. The welding process starts from point A and the arc moves along the weld line to point B. As an initial condition, a temperature of 20^0C is set (the ambient temperature). The heat dissipation is realized through all surfaces of the welded plates, taking into account convective and radiative heat exchange with the environment. The heat flux as a result of convective heat transfer is calculated according to Newton's law, and the radiative heat dissipation according to Stefan-Boltzmann's law. The heat source is in accordance with the described

model. The properties of the material are set as function depending on the temperature [27, 28]. The latent heat of fusion is set to - 260 [J / g].

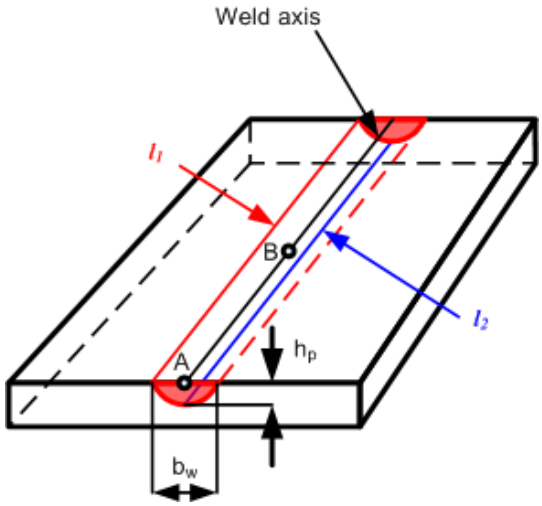

Fig. 7. Scheme of the process.

The optimization task is solved in two steps. In the first, the Monte Carlo method is applied and the objective function (4) is used. The obtained results, sorted by the value of the objective function are shown in Table 3. The points in the vicinity of which the best results were subsequently obtained are marked in red.

TABLE IV. MONTE CARLO OPTIMIZATION RESULTS (THE 10 BEST RESULTS ARE SHOWN).

η	α_{arc}	r_{arc}, [m]	Objective
Mode No 1			
0.62676	**0.139**	**0.0075832**	**5.46E-04**
0.6094	0.13694	0.0073976	5.72E-04
0.62289	0.28289	0.0071283	0.0010461
0.61545	0.23455	0.0066467	0.0015075
0.57382	0.21983	0.0072608	0.0018074
0.62579	0.22084	0.0068466	0.0019563
0.59112	0.15505	0.0068379	0.0025963
0.56749	0.03058	0.0076471	0.0030009
0.6433	0.12597	0.0077456	0.0034908
0.5398	0.27738	0.0059873	0.0039021
Mode No 2			
0.677227	**0.172152**	**0.010408**	**1.93E-05**
0.677551	0.227982	0.01017	1.66E-04
0.673553	0.032447	0.011367	2.86E-04
0.676452	0.063054	0.01104	2.93E-04
0.673522	0.12447	0.010174	3.35E-04
0.668108	0.045558	0.01194	3.47E-04
0.663445	0.039103	0.010712	5.68E-04
0.662133	0.169945	0.010963	6.36E-04
0.69563	0.148558	0.010328	6.91E-04
0.664232	0.201248	0.01089	8.66E-04

η	α_{arc}	r_{arc}, [m]	Objective
Mode No 3			
0.50787	0.16785	0.0028655	0.018412
0.52683	0.24217	0.002547	0.034804
0.60598	0.27434	0.0026486	0.074806
0.62347	0.20201	0.0029766	0.083158
0.65912	**0.24004**	**0.0029185**	**0.095695**
0.56873	0.079754	0.0029584	0.10973
0.5627	0.22405	0.0024966	0.11367
0.53239	0.24011	0.0022298	0.13301
0.69648	0.24806	0.0028376	0.15896
0.57409	0.22704	0.0023784	0.16116
Mode No 4			
0.60604	0.024693	0.0039079	0.00019048
0.57302	0.29392	0.0025921	0.00041417
0.60379	0.18183	0.003491	0.0005629
0.60144	**0.045476**	**0.0034605**	**0.0012541**
0.57667	0.16285	0.0036141	0.0019396
0.553	0.1964	0.0028921	0.002158
0.56408	0.11388	0.0037442	0.0027833
0.58814	0.15727	0.0029328	0.0028145
0.54868	0.11754	0.0036368	0.0036115
0.6	0.15	0.003	0.0041204
Mode No 5			
0.69837	0.27549	0.0058725	0.002596
0.64512	0.13544	0.0064706	0.002700
0.65704	0.25307	0.0069043	0.003926
0.62645	0.13075	0.0063511	0.004416
0.63179	**0.28696**	**0.0063072**	**0.004522**
0.61746	0.10342	0.0069153	0.005871
0.63154	0.25310	0.0067578	0.006330
0.59855	0.21107	0.0057579	0.006370
0.60833	0.17786	0.0066699	0.007518
0.59348	0.01467	0.0068286	0.009056

Within the second step of the optimization process in the vicinity of the five points with the best result from the first one optimization was performed using the objective function (3). One such result is shown in Table 5. As final results for the value of the calibration parameters are accepted those in which within the second step of the optimization process the lowest values of the objective function are reached (Table 6). The obtained solutions are illustrated in Fig.8. Comparing the data from Table 3 and Table 6, it can be said that for the considered cases the effective radius of the arc is approximately equal to the experimentally obtained width of the weld.

TABLE V. SEQUENCE OF THE OPTIMIZATION PROCESS.

No	η	α_{arc}	r_{arc}, [m]	Objective
1	0.60000	0.05000	0.00346	0.0018896
2	0.60000	0.06200	0.00346	0.0012531
3	0.60000	0.06680	0.00346	0.0010112
4	0.60000	0.06680	0.00386	3.85E-04
5	0.60000	0.06200	0.00386	4.78E-04
6	0.62832	0.06680	0.00386	0.0022941
7	0.57168	0.06680	0.00386	0.0026606
8	0.60000	0.06872	0.00386	3.97E-04
9	0.60000	0.06488	0.00386	3.72E-04
10	0.60000	0.06296	0.00386	3.64E-04
11	0.60000	0.05912	0.00386	3.43E-04
12	0.60000	0.05144	0.00386	3.14E-04
13	0.60000	0.03608	0.00386	3.21E-04
14	0.60000	0.06680	0.00386	3.85E-04

TABLE V – conti nued

No	η	α_{arc}	r_{arc}, [m]	Objective
15	0.60000	0.05758	0.00386	3.29E-04
16	0.60000	0.04530	0.00386	2.55E-04
17	0.60000	0.03915	0.00386	3.35E-04
18	0.60000	0.04530	0.00335	0.0027515

19	0.63625	0.04530	0.00386	0.0054476
20	0.56375	0.04530	0.00386	0.0034804
21	0.60000	0.04775	0.00386	2.63E-04
22	0.60000	0.04284	0.00386	2.47E-04
23	0.60000	0.04038	0.00386	3.43E-04
24	0.60000	0.04284	0.00365	7.23E-05
25	0.60000	0.04284	0.00345	0.0012105
26	0.63625	0.04284	0.00365	0.0086474
27	0.56375	0.04284	0.00365	0.0019852
28	0.60000	0.04530	0.00365	4.25E-05
29	0.60000	0.04775	0.00365	5.85E-05
30	0.60000	0.04530	0.00386	2.55E-04
31	0.60000	0.04530	0.00345	0.0012202
32	0.63625	0.04530	0.00365	0.0081506
33	0.56375	0.04530	0.00365	0.0019982
34	0.57046	0.04530	0.00368	0.0014195
35	0.58818	0.04530	0.00366	1.79E-04
36	0.59527	0.04530	0.00366	1.21E-05
37	0.59745	0.04530	0.00366	2.17E-07
38	0.61195	0.04530	0.00366	8.00E-04
39	0.58295	0.04530	0.00366	4.92E-04
40	0.59745	0.04628	0.00366	5.31E-07
41	0.59745	0.04431	0.00366	7.89E-08
42	0.59745	0.04333	0.00366	3.15E-08
43	0.59745	0.04136	0.00366	4.50E-07
44	0.59745	0.04333	0.00382	3.02E-04
45	0.59745	0.04333	0.00349	4.27E-04
46	0.62645	0.04333	0.00366	0.00359
47	0.56845	0.04333	0.00366	0.0017057
48	0.59745	0.04530	0.00366	2.17E-07
49	0.59684	0.04333	0.00366	3.24E-06
50	0.59721	0.04333	0.00366	1.38E-05
51	0.59740	0.04333	0.00366	4.80E-06
52	0.60905	0.04333	0.00366	4.61E-04
53	0.58585	0.04333	0.00366	3.18E-04
54	0.59745	0.04412	0.00366	5.87E-08
55	0.59745	0.04254	0.00366	1.55E-07
56	0.59745	0.04333	0.00372	1.95E-05
57	0.59745	0.04333	0.00359	1.16E-04
58	0.60209	0.04333	0.00366	5.93E-05
59	0.59281	0.04333	0.00366	5.05E-05
60	0.59745	0.04333	0.00366	3.15E-08

TABLE VI. RESULTS OF THE OPTIMIZATION PROCESS.

No of mode	**η**	**α_{arc}**	**r_{arc}, [mm]**	**Objective**
1	0.61848	0.16669	7.58	7.53E-08
2	0.68373	0.18469	10.41	1.39E-07
3	0.53322	0.26737	2.9766	1.25E-05
4	0.59745	0.04333	3.6567	3.15E-08
5	0.67603	0.2969	5.8135	6.29E-05

In order to check whether the solutions obtained in the described way adequately represent the temperature field, the numerical results are compared with the experimental ones. Fig. 9÷12 shows a comparison for the first 4 modes. Fig. 13 shows the comparison of the calculated result with the experimental ones for three of the welds produced with mode 5. From these figures it can be seen that the form of penetration predicted by the model coincides well with the experimentally obtained one.

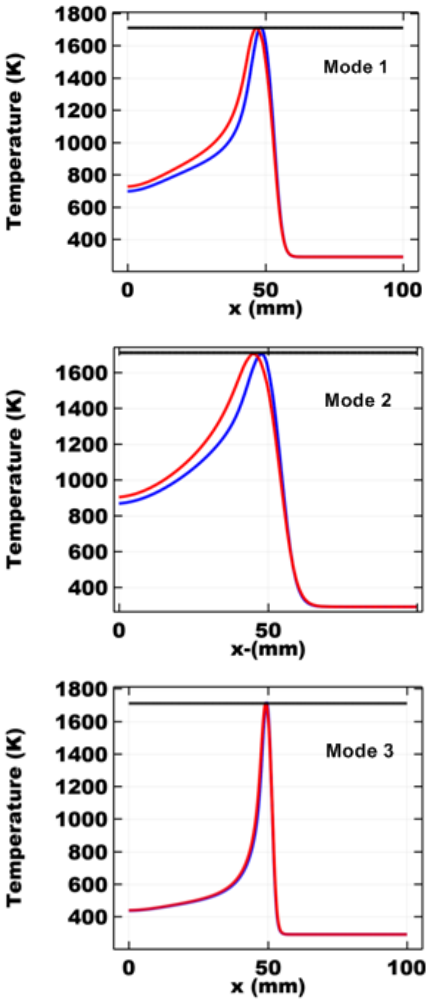

Fig.8. Solidus temperature (black) and temperature along the control lines - l1 (blue) and l2 (red) at the last moment for which the calculation was performed.

VI. CONCLUTIONS.

A new model of the heat source suitable for TIG welding is proposed. As calibration parameters used by the model are: efficiency, the effective radius of heating of the product from the arc and the coefficient accounting the heat source concentration. In the framework of the conducted researches it was established that the effective radius of the arc is approximately equal to the obtained width of the bead. A method of model calibration based on solving an optimization problem has been developed. The form of penetration predicted by the model was compared with experimental results and was shown to have a good match.

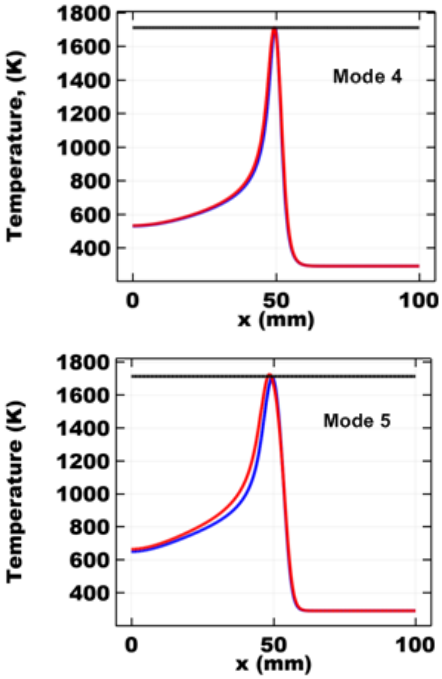

Fig.8. – continued

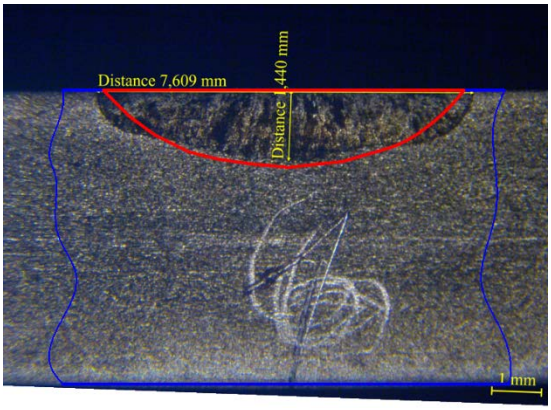

Fig.9. Comparison of the obtained results for mode No1

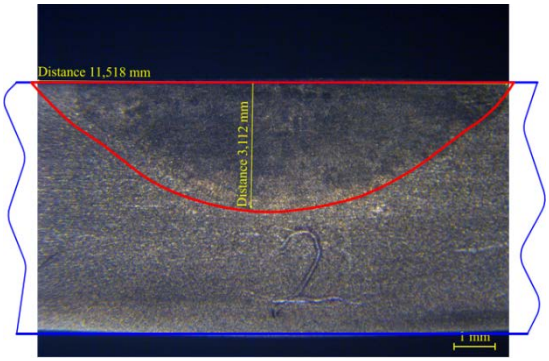

Fig.10. Comparison of the obtained results for mode No2

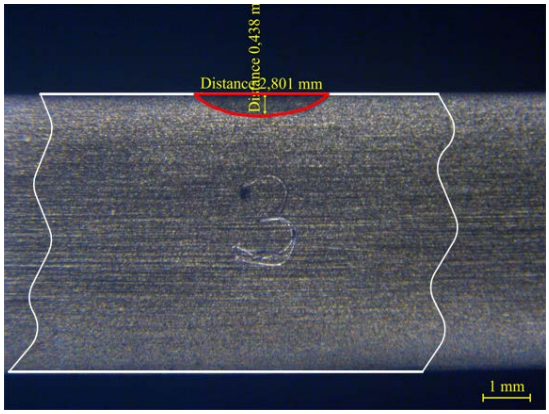

Fig.11. Comparison of the obtained results for mode No3

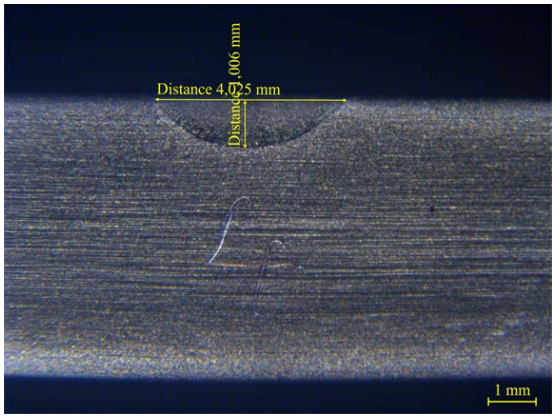

Fig.12. Comparison of the obtained results for mode No4

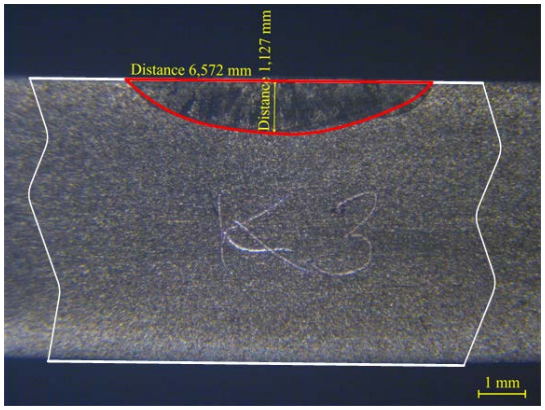

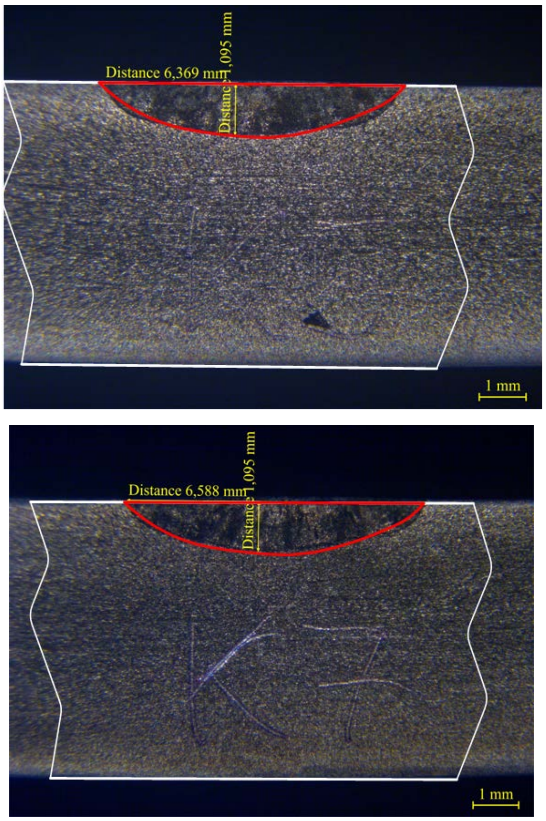

Fig.13. Comparison of the obtained results for mode No5

REFERENCES

[1] Huang Pengfei, Li Yan , Lu Yangyang and Lu Zhenyang, Numerical simulation of the temperaturbe filed in fixed-TIG welding pool, 2011 International Conference on Modeling, Simulation and Control, IPCSIT vol.10 (2011) © (2011) IACSIT Press, Singapore

[2] De Freitas Teixeira, P. R., De Araújo, D. B., & Da Cunha, L. A. B. (2014). Study of the gaussian distribution heat source model applied to numerical thermal simulations of tig welding processes. Ciencia y Engenharia/ Science and Engineering Journal, 23(1), 115-122. doi:10.14393/19834071.2014.26140

[3] LIU, H. and NIU, L., 2015. Finite element simulation research on medium plate multi-pass welding temperature field. The Open Mechanical Engineering Journal, 2015, Volume 9, pp.786-790

[4] ISMAIL, M.I.S. and AFIEQ, W.M.A., 2016. Thermal analysis on a weld joint of aluminium alloy in gas metal arc welding. *Advances in Production Engineering and Management*, Volume 11 | Number 1 | March 2016 | pp 29–37, ISSN1854-6250

[5] ZHANG, M., ZHOU, Y., HUANG, C., CHU, Q., ZHANG, W. and LI, J., 2018. Simulation of temperature distribution and microstructure evolution in the molten pool of GTAW Ti-6Al-4V alloy. Materials 2018, 11(11), 2288; https://doi.org/10.3390/ma11112288

[6] Wróbel, J., & Kulawik, A. (2019). Prediction of the superficial heat source parameters for TIG heating process using FEM and ANN modeling. *Entropy, 21*(10) doi:10.3390/e21100954

[7] YAMANE, S., YAMAZAKI, T., KANETA, T., NAKAJIMA, T. and YAMAMOTO, H., 2011. Experiment and numerical simulation in temperature distribution and welding distortion in GMA welding. *Yosetsu Gakkai Ronbunshu/Quarterly Journal of the Japan Welding Society*, **29**(3), (2011) pp. 31s-34s., https://doi.org/10.2207/qjjws.29.31s

[8] BJELIĆ, M.B., KOVANDA, K., KOLARIK, L., VUKIĆEVIĆ, M.N. and RADIČEVIĆ, B.S., 2016. Numerical modeling of two-dimensional heat-transfer and temperature-based calibration using simulated annealing optimization method: Application to gas metal arc welding. *Thermal Science*, **20**(2), pp. 655-665, doi:10.2298/TSCI150415127B

[9] Alexandre Campos Bezerra, Domingos Alves Rade and Américo Scotti, FINITE ELEMENT SIMULATION OF TIG WELDING: THERMAL ANALYSIS, 18th International Congress of Mechanical Engineering, November 6-11, 2005, Ouro Preto, MG, Proceedings of COBEM 2005

[10] M. Afzaal Malik, M. Ejaz Qureshi and Naeem Ullah Dar, Numerical Simulation of Arc Welding Investigation of various Process and Heat Source Parameters, MED UET Taxila (2007), pp 127÷142

[11] Pablo Batista Guimarães et all, OBTAINING TEMPERATURE FIELDS AS A FUNCTION OF EFFICIENCY IN TIG WELDING BY NUMERICAL MODELING, 21st Brazilian Congress of Mechanical Engineering October 24-28, 2011, Natal, RN, Brazil, Proceedings of COBEM 2011, DOI: http://dx.doi.org/10.5380/reterm.v10i1-2.61952

[12] Djarot B. Darmadi, Validating the accuracy of heat source model via temperature histories and temperature field in bead-on-plate welding, International Journal of Engineering & Technology October 2011 IJENS Vol: 11 No: 05

[13] DA NÓBREGA, J., SILVA, D., ARAÚJO, B., DE MELO, R., MACIEL, T., SILVA, A. and DOS SANTOS, N., 2014. Numerical evaluation of multipass welding temperature field in API 5L X80 steel welded joints. *International Journal of Multiphysics*, **8**(3), pp. 337-348.

[14] PAMNANI, R., VASUDEVAN, M., JAYAKUMAR, T., VASANTHARAJA, P. and GANESH, K.C., 2016. Numerical simulation and experimental validation of arc welding of DMR-249A steel. *Defence Technology*, Volume 12, Issue 4, August 2016, Pages 305-315, https://doi.org/10.1016/j.dt.2016.01.012

[15] Piekarska, W., & Rek, K. (2017). Numerical analysis and experimental research on deformation of flat made of TIG welded 0H18N9 steel. Paper presented at the *Procedia Engineering*, , *177* 182-187. doi:10.1016/j.proeng.2017.02.217 Retrieved from www.scopus.com

[16] Rui-ying Li, Chunyu Chen, Dawei Zhao and Chunmei Wu, Determination and Application of Double Ellipsoid Heat Source Model, International Conference on Material Science, Energy and Environmental Engineering (MSEEE 2017), Advances in Engineering Research, volume 125, pp. 267÷270, https://doi.org/10.2991/mseee-17.2017.49

[17] YAN, C., JIANG, H., WU, L., KAN, C. and YU, W., 2018. Numerical simulation of temperature field in multiple-wire submerged arc welding of X80 pipeline steel, *IOP Conference Series: Earth and Environmental Science 108 022048*, 2018

[18] P.Ferro, F. Berto, F. Bonollo and R.Montanari, Experimental and numerical analysis of TIG-dressing applied to a steel weldment, Procedia Structural Integrity Volume 9, 2018, Pages 64-70, https://doi.org/10.1016/j.prostr.2018.06.012

[19] Huang, H., Yin, X., Feng, Z., & Ma, N. (2019). Finite element analysis and in-situ measurement of out-of-plane distortion in thin plate TIG welding. *Materials, 12*(1) doi:10.3390/ma12010141

[20] Matuszewski, M. (2019). Modeling of 3D temperature field in butt welded joint of 6060 alloy sheets using the ANSYS program. Paper presented at the *IOP Conference Series: Materials Science and Engineering, , 659*(1) doi:10.1088/1757-899X/659/1/012034

[21] ZUO, S., WANG, Z., WANG, D., DU, B., CHENG, P., YANG, Y., ZHANG, P. and LANG, N., 2020. Numerical simulation and experimental research on temperature distribution of fillet welds. *Materials* ***2020****, 13(5), 1222; https://doi.org/10.3390/ma13051222*

[22] A.MOARREFZADEH and M.A.SADEGHI, Numerical Simulation of Thermal Profile By Gas Tungsten Arc Welding Process in Copper, WSEAS TRANSACTIONS on HEAT and MASS TRANSFER, Issue 3, Volume 5, July 2010, ISSN: 1790-504

[23] SAADLAOUI, Y., FEULVARCH, É., DELACHE, A., LEBLOND, J.-. and BERGHEAU, J.-., 2018. A new strategy for

the numerical modeling of a weld pool. *Comptes Rendus - Mecanique*, Volume 346, Issue 11, November 2018, Pages 999-1017, https://doi.org/10.1016/j.crme.2018.08.007.

[24] FLINT, T.F. and SMITH, M.C., 2019. HEDSATS: High energy density semi-analytical thermal solutions. *SoftwareX*, Volume 10, July–December 2019, 100243, https://doi.org/10.1016/j.softx.2019.100243

[25] Karim Agrebi, Asma Belhadj and Mahmoud Bouhafs, THREE-DIMENSIONAL NUMERICAL SIMULATION OF A GAS TUNGSTEN ARC WELDING PROCESS, IJTech 2019, International Journal of Technology 10(4) pp. 689-699, ISSN 2086-9614, DOI: https://dx.doi.org/10.14716/ijtech.v10i4.1849

[26] https://www.acerinox.com/en/productos/stainless-steel-grade/EN-1.4301---AISI-304-00001/

[27] (http://asm.matweb.com/search/SpecificMaterial.asp?bassnum=MQ304A)

[28] https://www.researchgate.net/figure/a-Thermal-conductivity-kT-as-a-function-of-temperature-for-SS-304-40-b-Specific_fig2_318688478

[29] Manahil Tongov, Rayna Dimitrova and Konstantin Konstantinov, Bead formation research in TIG welding of AISI 304 steel, 9-TH INTERNATIONAL SCIENTIFIC CONFERENCE "ENGINEERING, TECHNOLOGIES AND SYSTEMS", TECHSYS 2020, 14-16 May, Plovdiv, Bulgaria, IOP Conf. Series: Materials Science and Engineering 878 (2020) 012054, doi:10.1088/1757-899X/878/1/012054

Acknowledgments:
This work was made possible by a project KP-06-N37/31, funded by the NSF.

Environment. Technology. Resources. Rezekne, Latvia
Proceedings of the 13th International Scientific and Practical Conference. Volume 3, 357-362

Investigation of GMAW by Simulation Modelling

Manahil Tongov
Faculty of Idustrial Technology
Technical University of Sofia
Center of Welding
Institute of Metal Science, Equipment
and Technologies with Hydro-
and Aerodynamics Centre "Acad. A. Balevski"
Bulgarian Academy of Sciences
Sofia, Bulgaria
tongov@tu-sofia.bg

***Abstract* - The thermal and deformation cycle during welding is directly reflected on the formation of the welded joint and the imperfections that can occur in any specific case. The simulation modelling of the heating and cooling processes makes it possible to determine the temporary and residual stresses in the welded joint. When solving the thermal and deformation tasks, it is essential to use data on the characteristics of the material in the entire temperature range in which the studied processes take place. At the same time, these data are often not available. In order to be able to use simulation solutions in practice, the standard EN ISO 18166 provides for calibration of thermal and deformation models before they are applied to the welded structure. In this study, the calibration of a thermal model applicable to MIG / MAG welding is considered. The heat source is superficial and axisymmetric. The calibration parameters are efficiency, effective radius of the heat source and coefficient determining the deviation from the normal central Gaussian distribution. Experimental data on the bead shape were used for the calibration process. The obtained simulation results for the temperature field are compared with the experimental ones. Sensitivity analysis of the solution with respect to the material characteristics was performed.**

Keywords - GMAW; modelling; heat source; calibrating parameters; calibrating methods; sensitivity analysis.

I. INTRODUCTION

The bead formation during GMAW continues to be studied by different authors. Usually they investigate the welding process in different conditions, the used basic and auxiliary materials and protective media [1 ÷ 7], [18]. In parallel, different methods are used to model thermal processes [8 ÷ 17]. As a result of the combination of the two approaches, conditions are created for predicting the temperature cycles and the development of the deformation processes during welding. In addition, solving the temperature problem makes it possible to trace the structural changes in the HAZ. For this purpose, the cooling time from 800 to 500[^{0}C] is normally used. Different heat source models are used in solving the heat problem. The ISO / TS 18166 standard requires that the heat source used be calibrated before it is applied to the specific welded structure. The model calibration procedure involves adjusting the parameters of the model in such a way that the obtained calculated results practically coincide with the experimentally measured ones. The comparison of the experimental and calculated results can be performed on the shape and dimensions of the melting zone and / or temperature cycles at points of the welded joint. The specimens used to carry out the experimental tests must be of the same material and of the same thickness as the welded structure. During the experiment, the same welding mode parameters (arc current and voltage, and welding speed, heating temperature, etc.) should be used as in the actual design. The process modeling must be performed with the dimensions and material of the welded plates both during the experiment and with the same welding mode. As data on the thermal properties of the material are often not available in the entire range of interest, the standard requires an sensitivity analysis of the solution to the input data. Within this study, a heat source model is proposed, applicable for GMAW

Online ISSN 2256-070X
https://doi.org/10.17770/etr2021vol3.6608

with no inflection in penetration profile when the goal is analysis of the processes in the HAZ.

II. HEAT SOURCE

The proposed heat source is surface axisymmetric and is described by the equation:

$$q(r) = q_{eff}\ \frac{A}{2}\left[\frac{1}{\sigma\sqrt{2\pi}}\exp\left(-\frac{(r-r_0)^2}{2\sigma^2}\right)+ \right. \\ \left. +\frac{1}{\sigma\sqrt{2\pi}}\exp\left(-\frac{(r+r_0)^2}{2\sigma^2}\right)\right] = q_{eff}\,Af(r) \quad (1)$$

Here $q_{eff} = \eta I_w U_a$ is the effective heat output determined by the efficiency, the magnitude of the welding current and the arc voltage; f(r) is a heat flux distribution function and A is a norming multiplier to be determined by the condition $\int_0^\infty Af(r)2\pi r dr = 1$. To solve the heat problem, the effective heating radius r_{arc} and the coefficient of deviation of the heat source from a Gaussian heat source $\alpha_{arc} = r_0 / r_{arc}$ are used. The efficiency and the specified parameters are calibrated with respect to the heat source. They express q_{eff} , $r_0 = \alpha_{arc}.r_{arc}$ and $\sigma = 3.r_{arc}$.

The calibration of the thermal model is performed by solving an optimization problem with respect to the obtained experimental results. As a result of the experiment, the width of the seam and the depth of the penetration are known. Simulation modeling of the welding process is performed, and the length of the seam must be sufficient to reach a quasi-stationary process. Based on the obtained solution, the temperatures at the points corresponding to the depth of penetration and the width of the seam - T1max and T2max. Thouse temperatures are determined by finding the maximum values along lines parallel to the weld axis and passing through the corresponding point of the seam cross section. Here it should be borne in mind that these two quantities are located in different sections perpendicular to the axis of the seam. As a target function in solving the optimization problem can be used

$$\Phi(\eta, \alpha_{arc}, r_{arc}) = \left(\frac{T_{1\max} - T_S}{T_S}\right)^2 + \\ + \left(\frac{T_{2\max} - T_S}{T_S}\right)^2 \Rightarrow \min \quad (2)$$

or

$$\Phi(\eta, \alpha_{arc}, r_{arc}) = \\ = \max\left(\left|\frac{T_{1\max} - T_S}{T_S}\right|, \left|\frac{T_{2\max} - T_S}{T_S}\right|\right) \Rightarrow \min \quad (3)$$

As a result of solving the optimization problem, the calibration parameters are determined - the efficiency (η), the effective radius of the heating spot (r_{arc}), and the distribution coefficient (α_{arc}). Since the functions of the form (2) and (3) are usually multi-extreme, the optimization problem itself is solved in two steps. In the first step, the Monte Carlo method and equation (3) are used. The obtained solutions are sorted by the value of the objective function. Within the second step, the five solutions with the best result from the first step are used as the starting point of the optimization process. The coordinate method and equation (2) are used. The final solution is the one that has the smallest value of the objective function within the second step of solving the optimization problem.

The experimental results used to calibrate the model were taken from [18]. The chemical composition of the base and filler metal is shown in Table 1. The size of the samples is 20x20x100 [mm]. Mode No. 3 is considered, in which welding speed S = 50 [cm/min]; arc voltage U = 25 [V]; welding current I = 210 [A] and shielding gas is 80% Ar + 20% CO2. The results obtained are a penetration depth of 1.75 [mm] and a seam width of 10.3 [mm]. The characteristic feature of this welding mode is that an initial process of formation of an inflection point in the penetration profile is observed.

TABLE I. CHEMICAL COMPOSITION OF THE BASE AND FILLER MATERIALS USED [18].

alloying element	**quantity, wt%**		**alloying element**	**quantity, wt%**	
	base metal	***filler metal***		***base metal***	***filler metal***
C	0.01÷0.03	0.1	Cu	0.1	
Si	0.08÷0.1	0.5	Mo		0.2
Mn	0.2	1.1	S	0.03	0.03
Cr	0.1	0.5	P	0.04	0.03
Ni	0.1	0.5			

III. RESULTS AND ANALYSIS

When solving the problem within the first step of the optimization process, a result was obtained, which is partially shown in Table 2. The results obtained by the second step of solving the optimization problem are shown in Table 3. Figure 1 shows the changes of the temperatures along the control lines at the last moment of the calculation to determine the calibration parameters.

The maximum width of the weld pool is at x = 47.2 [mm] (Fig. 2). Along the seam axis, the liquid phase is in the range from 38.75 to 53.5 [mm] (Fig. 3). The length of the weld pool is 14.75 [mm]. To determine the shape of the weld, isotherms are constructed in planes perpendicular to the axis of the seam within the range of the weld pool (Fig. 4). The shell of these curves is the shape of the penetration. It is compared with the experimental results (Fig. 5).

TABLE II. SORTED RESULTS AFTER THE FIRST STEP OF SOLVING THE OPTIMIZATION TASK.

No	**η**	**α_{arc}**	**r_{arc}, [mm]**	**Objective**
1	0,8193517	0,20913114	9,51173436	0,01235520
2	0,7976760	0,25520187	8,52934354	0,02154287
3	0,8379909	0,24528641	9,57802056	0,03259657
4	0,8096316	0,28211004	9,09826960	0,03995324
5	0,7530350	0,29744560	8,34357737	0,04594332
6	0,7943647	0,26286507	7,78115176	0,05681203

7	0,8040391	0,27428205	7,51426740	0,07803883
8	0,7155430	0,25551316	8,67656483	0,08982455
9	0,8470320	0,06620380	9,7889645	0,09321748
10	0,8364268	0,03385723	9,64293343	0,10103100

TABLE III. RESULTS OF THE SECOND STEP OF CALIBRATION OF THE HEAT SOURCE MODEL..

No of start point	η	α_{arc}	r_{arc}, [mm]	Objective
1	0,81935	0,21393	9,5117	1,09E-006
2	0,7978	0,27797	8,512	1,04E-006
3	0,81422	0,20457	9,578	6,67E-007
4	0,82587	0,23711	9,0983	4,88E-006
5	0,80707	0,28622	8,3436	1,06E-005

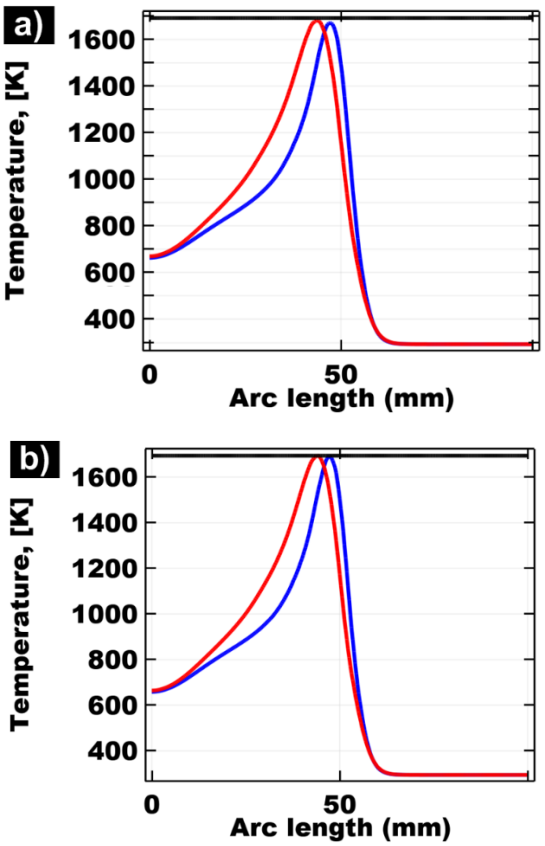

Fig.1. Results of solving the optimization problem: after the first step of the optimization process (a) and after the second step at starting point No. 3 (b).

It can be seen that in terms of the depth of penetration and the width of the bead, the model describes the well-obtained experimental shape. At the same time, the calculated form of penetration deviates from the experimentally obtained one. This confirms the fact that for seams with inflection in the form of penetration it is more appropriate to use models of heat sources combining surface and bulk heat source. An extreme example in this regard is electron beam welding [19].

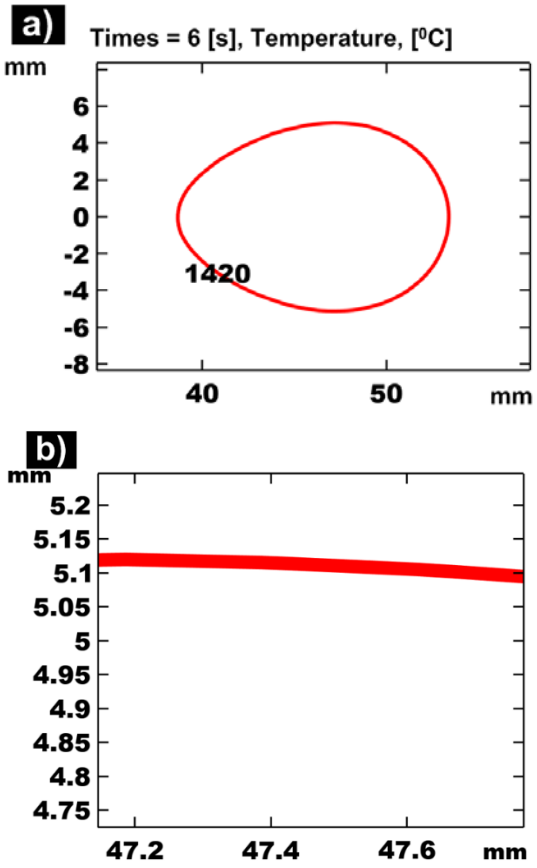

Fig.2. Determination of the maximum width of the seam by the isotherm of the solidus on the upper surface of the welded specimen

To check the sensitivity of the solution with respect to the thermal properties of the base metal, the temperature cycles obtained from two solutions were compared (Fig. 6). The first of them has temperature-dependent material characteristics (Fig. 7 ÷ Fig. 9), and the second is with constant values of the thermal properties: thermal conductivity λ = 36 [W / (m.K)]; specific heat capacity at constant pressure Cp = 660 [J / (kg.K)]; density ρ = 7740 [kg / m3]. The considered temperature cycles are shown in Fig. 10 and Fig. 11, respectively.

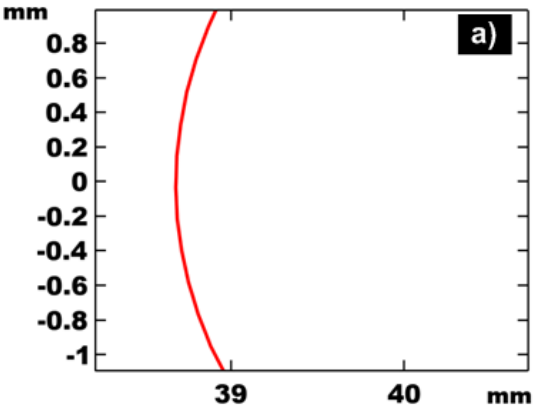

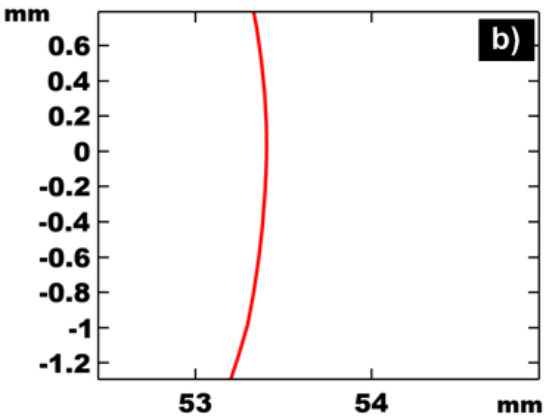

Fig.3. Determination of the length of the weld pool - crystallizing front of the weld pool (a) and melting front (b).

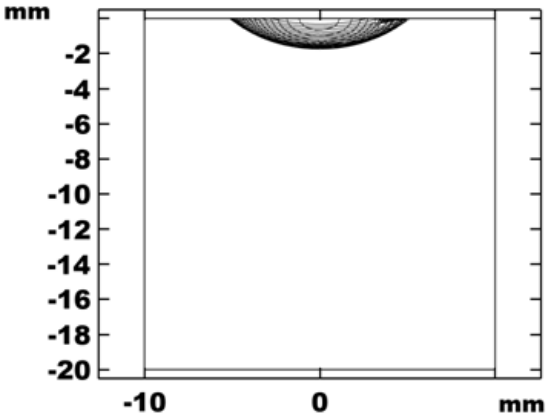

Fig.4. Isotherms in planes perpendicular to the seam axis for the solidus temperature in the weld pool range.

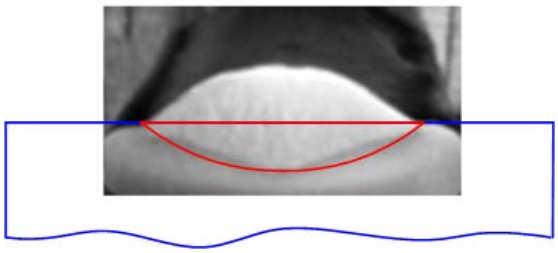

Fig.5. Comparison of the experimental and calculated form of the penetration.

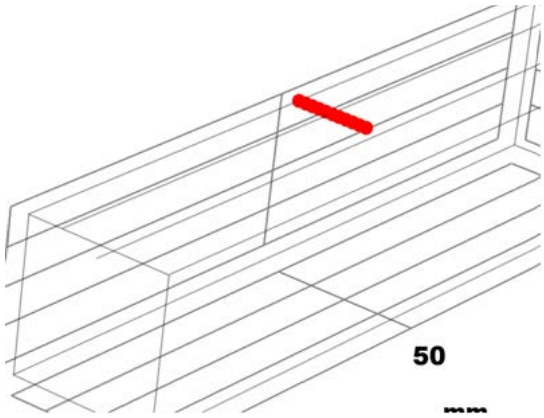

Fig.6. Control points for sensitivity analysis.

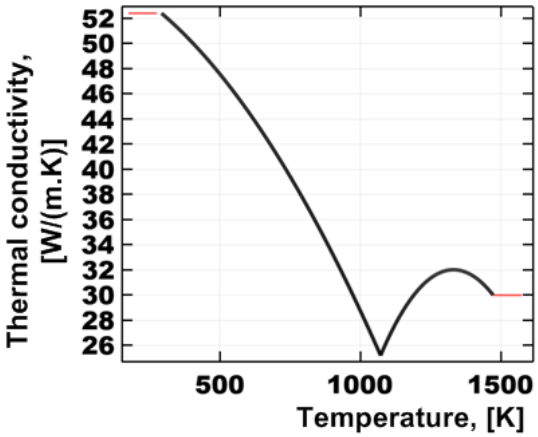

Fig.7. Base material properties – thermal conductivity.

Fig. 12 shows the square of the relative error. It can be seen that $\delta \le 0.095$. The RMS error is calculated as

$$\varepsilon = \frac{1}{N}\sqrt{\sum_{i=1}^{N}\left(1-\frac{T_{2i}}{T_i}\right)^2} \qquad (4)$$

Here N is the number of time points for which the comparison is performed, and i is the sequence number of that moment. We must emphasize that the comparison should not be made for the entire period of the welding process, but only for the time interval in which the temperature change of interest takes place. The obtained results are given in table 4 and visualized in fig.13.

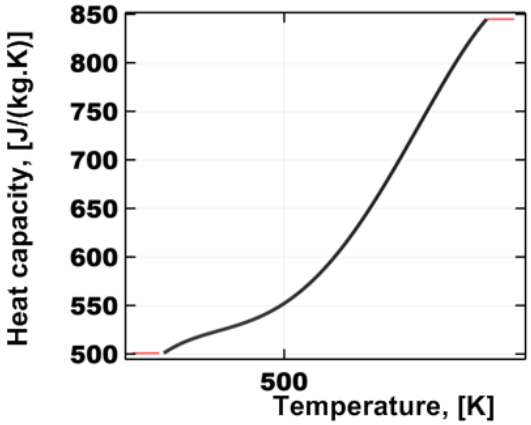

Fig.8. Base material properties – heat capacity at constant pressure.

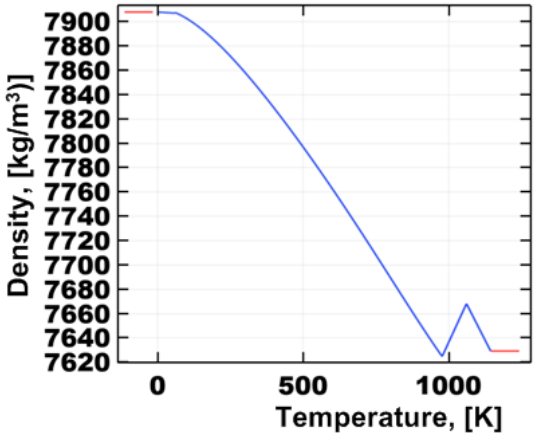

Fig.9. Base material properties – density.

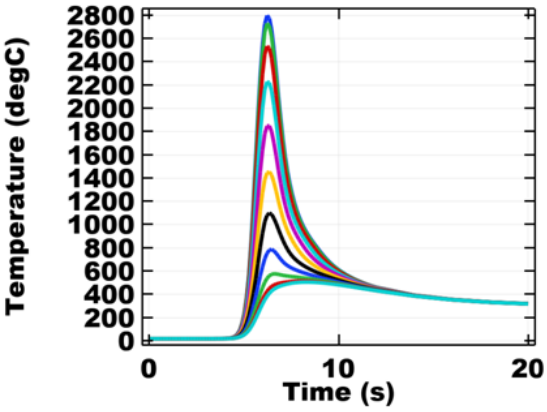

Fig.10. Temperature cycles taking into account the temperature dependence of the thermal properties.

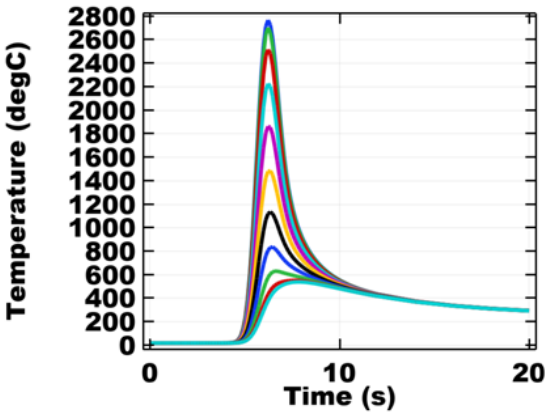

Fig.11. Temperature cycles at constant values of thermal properties.

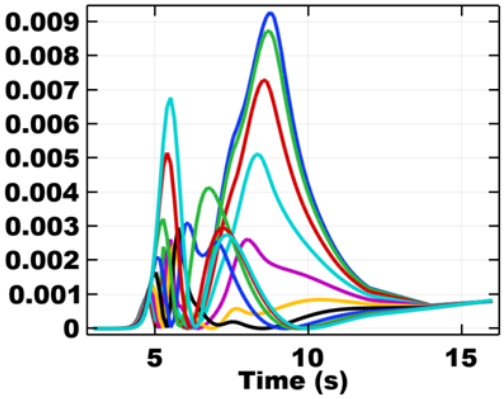

Fig.12. Changes in the square of the relative error over time for different points on the sample surface.

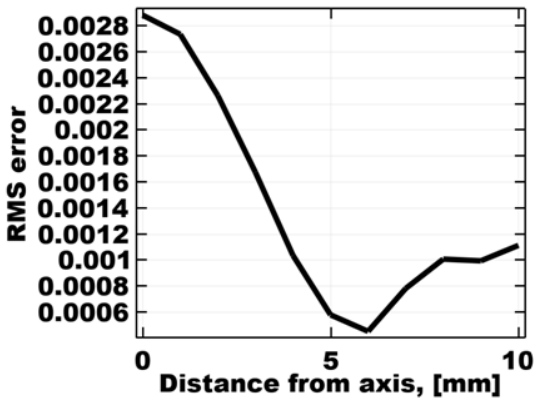

Fig.13. RMS error depending on the distance to the seam axis.

IV. CONCLUTIONS.

A new heat source model for GMAW has been proposed. It is shown that the heat source can be calibrated for the conditions of MIG / MAG welding. An analysis of the sensitivity of the heat transfer model to the thermal properties of the base metal was performed. The maximum value of the error obtained when using constant values of

the material characteristics is 9.5%. The root mean square error in this case is not more than 0.28%. The model describes very well the weld in terms of its width and depth, but when an inflection point is formed in penetration profile, the deviation can become significant - in this case a heat source model should be used, taking into account the processes in the key-hole.

TABLE IV. RMS ERROR DEPENDING ON THE DISTANCE TO THE SEAM AXIS.

y, [mm]	ε	y, [mm]	ε
0	2.88E-03	6	4.53E-04
1	2.74E-03	7	7.83E-04
2	2.27E-03	8	1.01E-03
3	1.68E-03	9	9.95E-04
4	1.04E-03	10	1.11E-03
5	5.80E-04		

REFERENCES

[1] do Nascimento, A.S., de Menezes Jr., L.C., Vilarinho, L.O., Effect of waveform and shielding gas on melting rate and bead geometry for MIG/MAG-PV [Efeito do formato de onda e gás de proteção sobre a taxa de fusão e geometria do cordão na soldagem MIG/MAG-PV], (2012) Soldagem e Inspecao, 17 (1), pp. 40-48, **ISSN:** 01049224, DOI: 10.1590/S0104-92242012000100007.

[2] Katayama, T., Tashiro, S., Tanaka, M., Improvement of bead formation of plasma MIG welding in pure argon atmosphere, (2011) Yosetsu Gakkai Ronbunshu/Quarterly Journal of the Japan Welding Society, 29 (3), pp. 39s-42s, **ISSN:** 02884771, DOI: 10.2207/qjjws.29.39s.

[3] Tong, H., Ueyama, T., Ushio, M., Study on phenomena of wire melting and bead formation in AC pulsed MIG welding, (2004) Yosetsu Gakkai Ronbunshu/Quarterly Journal of the Japan Welding Society, 22 (3), pp. 389-397, **ISSN:** 02884771, DOI: 10.2207/qjjws.22.389.

[4] Yamamoto, H., Harada, S., Ueyama, T., Ogawa, S., Development of Low Frequency Pulsed MIG Welding Process for Al and its alloy Study on Low Frequency Pulsed MIG Welding Process (Report 1), (1992) QUARTERLY JOURNAL OF THE JAPAN WELDING SOCIETY, 10 (2), pp. 233-238, **ISSN:** 02884771, DOI: 10.2207/qjjws.10.233.

[5] Maruo, H., Hirata, Y., Noda, Y., Effects of Welding Current Waveform on Metal Transfer and Bead Formation in Pulsed MIG Welding–Study on Pulsed Arc Welding (Report 1)–(1984) QUARTERLY JOURNAL OF THE JAPAN WELDING SOCIETY, 2 (1), pp. 12-18. ISSN: 02884771, DOI:10.2207/qjjws.2.12

[6] Ando, K., Nishikawa, J., Inoue, M., Phenomena of the Molten Pool at High Current and High Speed Mig Welding, (1971) JOURNAL OF THE JAPAN WELDING SOCIETY, 40 (4), pp. 307-311, **ISSN:** 00214787, DOI: 10.2207/qjjws1943.40.307

[7] Toshiyasu, F., Yoshihiko, S., Shiro, T., Effects of nitrogen, oxygen and hydrogen gases added to argon gas on mig-welding of aluminum alloys, (1968) Journal of Japan Institute of Light Metals, 18 (12), pp. 609-616, **ISSN:** 04515994, DOI: 10.2464/jilm.18.609

[8] Zuo, S., Wang, Z., Wang, D., Du, B., Cheng, P., Yang, Y., Zhang, P., Lang, N.,Numerical simulation and experimental research on temperature distribution of fillet welds, (2020) Materials, 13 (5), art. no. 1222, ISSN: 19961944, DOI: 10.3390/ma13051222

[9] Bai, Q., Ma, Y., Xing, S., Chen, Z., Kang, X., Prediction of the temperature distribution and microstructure in the HAZ of sa508gr4 reactor pressure vessel steel, (2017) ISIJ International, 57 (5), pp. 875-882, ISSN: 09151559, DOI: 10.2355/isijinternational.ISIJINT-2016-321

[10] Pamnani, R., Vasudevan, M., Jayakumar, T., Vasantharaja, P., Ganesh, K.C., Numerical simulation and experimental validation of arc welding of DMR-249A steel, (2016) Defence Technology, 12 (4), pp. 305-315, ISSN: 22149147, DOI: 10.1016/j.dt.2016.01.012

[11] Ismail, M.I.S., Afieq, W.M.A., Thermal analysis on a weld joint of aluminium alloy in gas metal arc welding, (2016) Advances in Production Engineering and Management, 11 (1), pp. 15-28, ISSN: 18546250, DOI: 10.14743/apem2016.1.207

[12] Bjelić, M.B., Kovanda, K., Kolarik, L., Vukićević, M.N., Radičević, B.S., Numerical modeling of two-dimensional heat-transfer and temperature-based calibration using simulated annealing optimization method: Application to gas metal arc welding, (2016) Thermal Science, 20 (2), pp. 655-665, **ISSN:** 03549836, DOI: 10.2298/TSCI150415127B

[13] Liu, H., Niu, L., Finite element simulation research on medium plate multi-pass welding temperature field, (2015) Open Mechanical Engineering Journal, 9 (1), pp. 786-790, **ISSN:** 1874155X, DOI: 10.2174/1874155X01509010786

[14] Liskevych, O., Scotti, A., Determination of the gross heat input in arc welding, (2015) Journal of Materials Processing Technology, 225, pp. 139-150, **ISSN:** 09240136, DOI:10.1016/j.jmatprotec.2015.06.005

[15] Yoshihiro, T., Manabu, T., Numerical Simulation of heat source property with metal vapor behavior in GMA Welding, (2012) Yosetsu Gakkai Ronbunshu/Quarterly Journal of the Japan Welding Society, 30 (1), pp. 68-76, **ISSN:** 02884771, DOI: 10.2207/qjjws.30.68

[16] Lidam, R.N., Yupiter, H.P.M., Redza, M.R., Rahim, M.R., Sulaiman, M.S., Zakaria, M.Y., Thama, G., Abasa, S.K., Haruman, E., Chau, C.Y., Simulation study on multipassed welding distortion of combined joint types using thermo-elastic-plastic FEM, (2012) Journal of Engineering Research, 9 (2), pp. 1-16, **ISSN:** 17266009, DOI: 10.24200/tjer.vol9iss2pp1-16

[17] Yamane, S., Yamazaki, T., Kaneta, T., Nakajima, T., Yamamoto, H., Experiment and numerical simulation in temperature distribution and welding distortion in GMA welding, (2011) Yosetsu Gakkai Ronbunshu/Quarterly Journal of the Japan Welding Society, 29 (3), pp. 31s-34s, **ISSN:** 02884771, DOI: 10.2207/qjjws.29.31s

[18] Mathieu TERNER, Tsend-Ayush BAYARSAIKHAN, Hyun-Uk HONG and Je-Hyun LEE Influence of Gas Metal Arc Welding Parameters on the Bead Properties in Automatic Cladding, Journal of Welding and Joining Volume 35 Issue 1 pp.16-25 (2017) ISSN: 2466-2232, Online ISSN: 2466-2100, https://doi.org/10.5781/JWJ.2017.35.1.16

[19] Peter Petrov, Manahil Tongov, Numerical modelling of heat source during electron beam welding, Vacuum 171 (2020) 108991, ISSN: 0042-207X, https://doi.org/10.1016/j.vacuum.2019.108991

Acknowledgments:
This work was made possible by a project KP-06-N37/31, funded by the NSF.

Environment. Technology. Resources. Rezekne, Latvia
Proceedings of the 13th International Scientific and Practical Conference. Volume 3, 363-367

Impact of the High-Speed Flow of Powder Particles on the Structure of Polymer Materials and Metal-Polymer Composites

Yulia Usherenko
Scientific Laboratory of Powder Materials
Riga Technical University
Riga, Latvia
osher_yu@mail.ru

Viktors Mironovs
Scientific Laboratory of Powder Materials
Riga Technical University
Riga, Latvia
viktors.mironovs@gmail.com

Leonids Pakrastins
Institute of Structural Engineering and Reconstruction
Riga Technical University
Riga, Latvia
Leonids.Pakrastins@rtu.lv

***Abstract* - The problem of protecting spacecraft from cosmic dust has recently come to the fore. There is still no enough data on the complex effect of short-term high-energy, dynamic loading on materials, including polymer materials and multilayer polymer-metal composites. The use of dynamic alloying in the super-deep penetration (SDP) mode by high-speed flows of powder particles allows assessing the effect on the material under dynamic action. Previous studies on steel and aluminum samples have shown a significant effect of high-speed flows of powder particles on the structure and properties of materials. As a result of a study of samples made of aliphatic polyurethane with steel reinforcement elements, it was found that there are traces of the penetration of high-speed particles into both metal and polymer layers. However, the number of flow elements detected in the polymeric part is significantly less than the number of elements in the metal reinforcing part. Thus, it is possible to assume that or the polymer material is a more effective barrier to the high-speed flow compared to the metal, or the "self-healing" effect is observed.**

Keywords* - *cosmic dust, super-deep penetration, composites, powders, polymers, dynamic alloying

I. INTRODUCTION

The collision velocities of spacecraft with high-speed bodies and objects included in space debris range from ~ 0.1 km·s^{-1} (lunar dust) to 70 km·s^{-1} (meteoric bodies) km·s^{-1}[1]. At such collision velocities, intense energy release occurs in a limited volume of matter, accompanied by the formation of shock waves with subsequent mechanical destruction, melting, evaporation, and thermal ionization of the resulting vapors. Solid particles with transverse dimensions less than 1 mm can be considered as a factor constantly affecting spacecraft, characterized by their flux density [2].

Previous studies on steel and aluminum samples have shown a significant effect of high-speed flows of powder particles on the structure and properties of materials. [3-5].

The problem of protecting spacecraft from cosmic dust has recently come to the fore [6,7]. Thick-walled metal shells do not provide reliable protection for control systems. The bulky multilayer compositions are assumed to provide adequate protection when piercing protective shells with cosmic dust. However, there is still no enough data on the complex effect of short-term high-energy, dynamic loading on polymer materials and multilayer polymer-metal composites.

There is currently a wide variety of polymeric materials used as structural, thermal, and electrical insulating materials. The main advantages of polymers are high elasticity, low density, impact strength, specific electrical properties, high resistance to the effects of various active media, and the possibility of obtaining them with a given set of mechanical and physical properties. However, the number of calculated and experimental results on the study of dynamic loading of solid and porous polymer composites samples is minimal. Polymer composites are widely used in the aerospace industry, as safety and lightweight are essential factors. Polymer composites are used to manufacture small and large aircraft, including commercial, civil and military aircraft. The expanded use of polymer composites over metals in the aerospace sector is due to their high specific strength and stiffness combined with low density, resulting in weight savings. The benefits of weight reduction include reduced fuel consumption and

Online ISSN 2256-070X
https://doi.org/10.17770/etr2021vol3.6627

emissions and increased speed, range, and maneuverability of aircraft [8-10].

For this reason, the development, testing, and implementation of a new generation of composite materials requires advanced studies. Currently, the aerospace industry needs to develop fundamentally new composite materials and tools for their diagnostics, which have a set of unique functional qualities and performance properties [11].

The use of dynamic alloying in the super-deep penetration (SDP) mode by high-speed flows of powder particles will allow assessing the effect on the material under dynamic action. Super-deep penetration (SDP) is a complex physical phenomenon, when in a split-second flow of powder particles with a fraction less than 100 microns, accelerated to speeds of 700-3000 ms^{-1}, penetrates the solid metal body at depth in tens, hundreds mm. Simultaneously, the high and ultra-high pressure (0.2-20 GPa), intensive deformation, local heating, and friction is occurred [3-5,12].

II. Materials and Methods

An aliphatic polyurethane plastic with a low viscosity was chosen as a model material. The density of the model material is 1.07 g/cm^3, the tensile strength is 21.8 MPa, and the hardness is 72 HSD. Polyurethanes are the most valuable and widely produced polymers in the industry. Polyurethanes contain a urethane group - NH-C(O)O-. They are characterized by the high modulus of elasticity, wear resistance, viscous coefficient of friction, vibration resistance, weather resistance, and resistance to oil and gasoline. Products made of polyurethane can be used when the temperature drops to -60…-70°C. Polyurethane fibers are low hygroscopic and have high chemical resistance. They are used for the manufacture of insulation, filter, and parachute fabrics. Today more than 3 million tons of polyurethane materials are processed every year. The promising nature of polyurethanes for the modern industry is since their properties substantially complement the possibilities of using other elastomers, rubbers, rubbers, etc. [13,14]. In terms of their structural and technological capabilities, polyurethanes are the most versatile polymer material. They find applications in aerospace, automotive, marine, railroad industries [15,16].

Dynamic alloying in SDP mode was carried out in the following conditions [12]: ballistic explosive accelerator, average particles speed 1000 ms^{-1}, exposure time - 400 microseconds, the material of samples: aliphatic polyurethane, quality structural carbon steel 10 (0.07-0.14% C, interstate standard GOST 1050-2013, DIN C10), the material of powder particles (strikers) – SiC powder (70%), 63- 70 microns, Al powder (30%), 10-70 microns.

The study of surface morphology and elemental composition was carried out on a certified high-resolution scanning electron microscope “Mira 3” “Tescan” with an X-ray spectral microscope analyzer from “Oxford Instruments Analytical”. The error of the method, in this case, is 3 - 5 relative %.

The microscope is equipped with detectors for secondary electrons (SE) and backscattered electrons (BSE), which allow the examination of samples in two modes. When taking samples in the secondary electron (SE) mode, a contrast in the image is created by the reflection of the electron beam from the sample surface. In the case of examination with a backscattered electron (BSE) detector, the contrast in the picture is created by the difference in the “averaged” atomic numbers. The type of detector used and other parameters are indicated on the information line at the bottom of each frame.

III. Results and Discussion

As a result of a series of tests, it was found that experimental polymer samples (Fig. 1) and cast in metal tubes made of steel 10 (multilayer composites) (Fig. 2) withstand a dynamic load of 600-1000 $m \cdot s^{-1}$ without significant macro fracture.

The metal-reinforced multilayer composite option was considered. For the simulation, an aliphatic polyurethane plastic molded into steel 10 steel tubes with a sealed bottom was used. Dynamic processing was carried out from the side of the metal bottom. Of particular interest was the polymer-metal contact zone.

The use of samples placed in a metal tube made it possible to record the shock wave’s propagation together with the outer metal shell. The pulsation of the initial metal cylinder along the samples’ length is realized and, accordingly, a change in the diameter of the polyurethane sample in the cross-section along the axis (Fig. 2).

Fig 1. Experimental samples of polyurethane material before and after dynamic processing

Fig. 2. Specimens made of polyurethane in a metal tube made of steel 10 after dynamic impact in the SDP mode.

Investigating the processed samples' structure made it possible to establish the superdeep penetration (SDP) process implementation. The channel elements in the steel shell were detected in the sample's metallic part (Fig. 3,4).

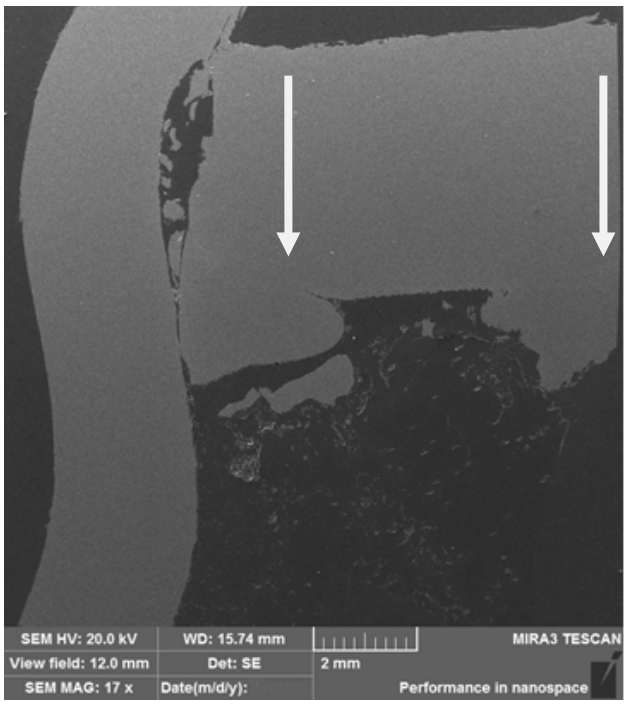

Fig. 3. Structure of the metal-polymer contact zone. The arrows show the direction of motion of the shock wave.

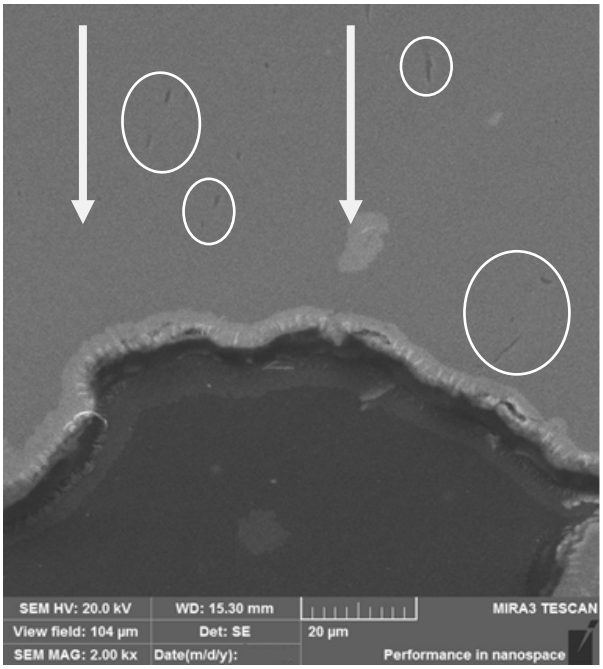

Fig. 4. Structure in the metal (top zone) -polymer (bottom zone) contact zone. The arrows show the direction of motion of the shock wave. Ovals indicate the flow residues (channel elements)

Microanalysis of the channel elements of the metal part of the protective barrier also confirmed the presence of powder flow residues in the channels (Fig. 5 and Table 1). In the material of the steel shell, a zonal drift of aluminum and silicon was recorded. At the same time, iron, sulfur, and manganese were found in local zones. It can be assumed that during the analysis of steels, sulfur and manganese are recorded instead of isotopes (for example, ^{55}Fe).

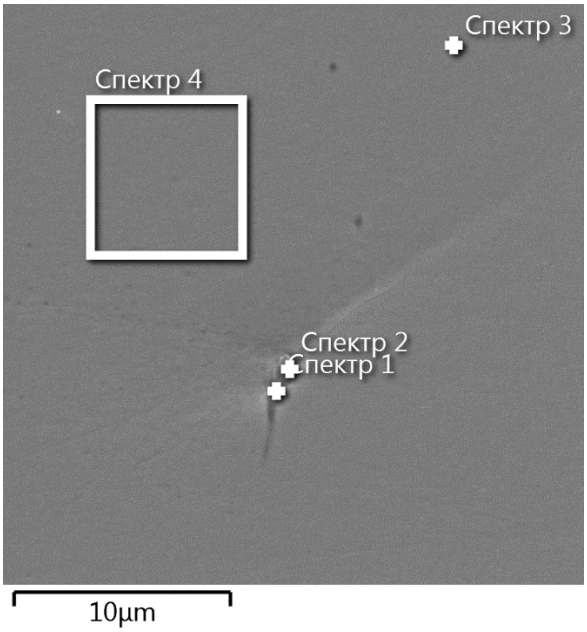

Fig. 5. Zone of microanalysis of the channel element (flow residue) of the steel part of the sample

TABLE 1 MICROANALYSIS OF THE CHANNEL ELEMENT OF THE STEEL PART OF THE SAMPLE

Spectrum number	Content of elements, %mass				
	Al	Si	S	Mn	Fe
1	1.57	0.22	17.50	32.48	48.23
2	22.03	0.00	7.89	13.39	56.69
3	0.00	0.31	8.79	15.46	75.43
4	0.00	0.42	0.00	0.61	98.97

The study of the polymer part structure showed the formation of the same structural element as in the metal part. Structural elements were identified with remnants of the powder flow material (Fig. 6) at a depth of 1-2 mm. It is confirmed by microanalysis results (Fig. 7 and Table 2). The proportion of aluminum in these zones was up to 75 mass. %, silicon 20-100 mass.%. Sulfur and iron are brought in by mass transfer from the steel shell.

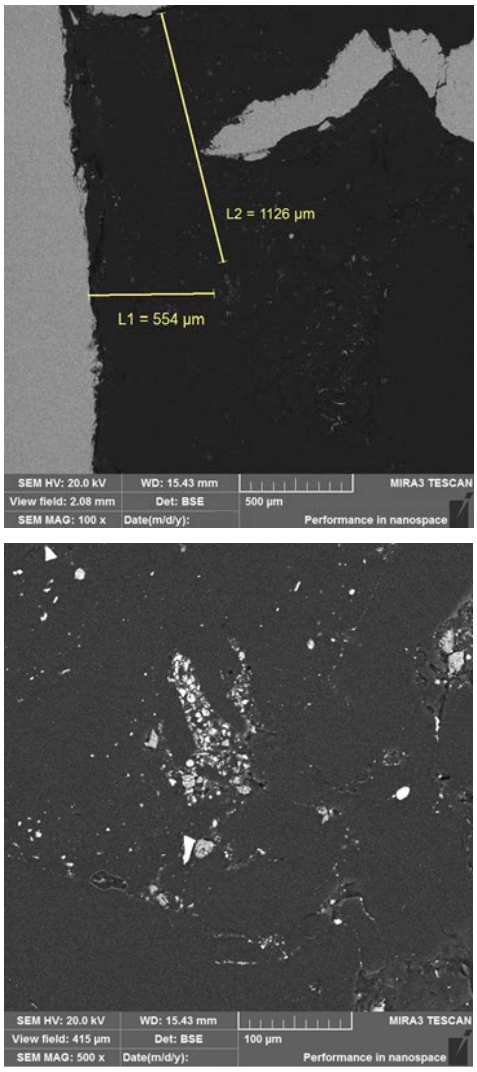

Fig. 6. The structural element of powder flow material residues in a polymer matrix.

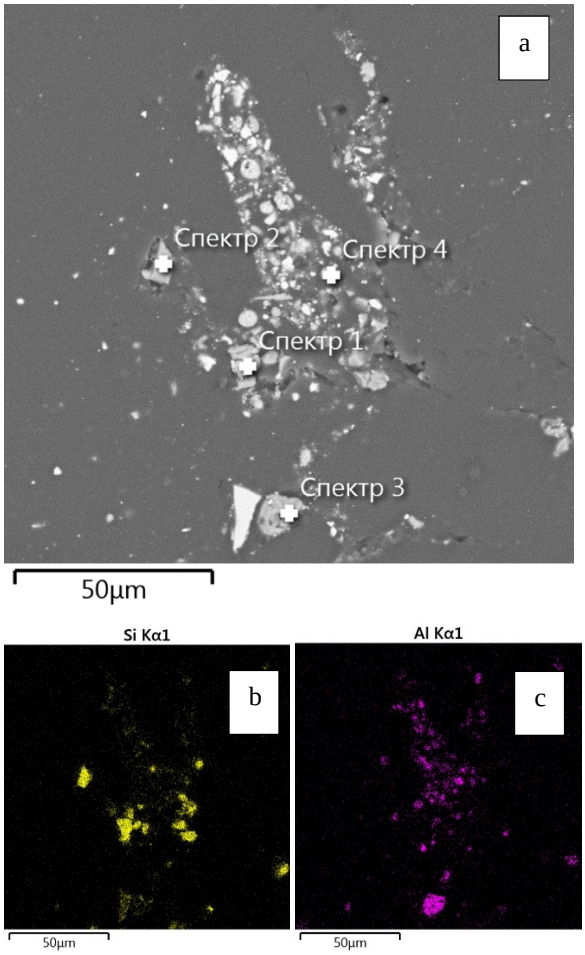

Fig. 7. Zone of microanalysis of a structural element from residues of powder flow material in a polymer matrix (a) and the distribution of traces of impactors from silicon carbide (b) and aluminum (c).

TABLE 2. MICROANALYSIS OF A STRUCTURAL ELEMENT FROM THE REMAINS OF THE POWDER FLOW MATERIAL IN A POLYMER MATRIX

Spectrum number	Content of elements, %mass				
	Al	Si	S	Mn	Fe
1	0.00	100.00	0.00	0.00	0.00
2	0.00	99.33	0.00	0.00	0.67
3	75.19	19.15	1.13	0.00	4.52
4	75.59	20.21	1.97	0.00	2.23

The study of the polymer part structure made it possible to establish the presence of remnants of the impactors of a high-speed powder flow. However, the number of flow elements detected in the polymeric part is significantly less than the number of elements in the metal reinforcing part (1 element in the polymeric part of the sample (fig. 6) versus a dozen of elements in the metal part (fig. 3,4). It can be assumed that the polymer part turned out to be a more effective material for decelerating high-speed particles in comparison with the metal one. Further studies, including the use of other types of polymeric materials, are of interest to refine this effect

IV. CONCLUSIONS

As a result of a series of studies of samples made of aliphatic polyurethane with steel reinforcement elements, it was found that there are traces of the penetration of high-speed particles into both metal and polymer layers.

However, the number of flow elements detected in the polymeric part is significantly less than the number of elements in the metal reinforcing part.

Thus, it is possible to assume that or the polymer material is a more effective barrier to the high-speed flow compared to the metal, or the "self-healing" effect is observed. Further research using other types of polymer materials is advisable.

V. ACKNOWLEDGEMENTS

This work has been supported by the European Regional Development Fund within the Activity 1.1.1.2 "Post-doctoral Research Aid" of the Specific Aid Objective 1.1.1 "To increase the research and innovative capacity of scientific institutions of Latvia and the ability to attract external financing, investing in human resources and infrastructure" of the Operational Programme "Growth and Employment" (No. 1.1.1.2/VIAA/2/18/335).

REFERENCES

[1] A. Belous, V. Saladukha, and S. Shvedau, "*High velocity microparticles in space: influence mechanisms and mitigating effects of electromagnetic irradiation*", Springer, 2019.

[2] John M.C. Plane, "Cosmic Dust in the Earth's Atmosphere", *Chemical Society Reviews*, vol. 41, no.19, pp. 6507-6518, 2012.

[3] Y. Usherenko, S. Usherenko, and J. Yazdani, "High-energy method of transformation of casting metals and alloys to the composite materials", *Key Engineering Materials*, vol. 721, pp. 290–294, 2016.

[4] Y.Usherenko, V. Mironovs, and S. Usherenko, "Analysis of the effects of dynamic alloying on the structure of aluminium and its alloys", *Solid State Phenomena*, vol. 320, pp. 8-13,2021.

[5] Y. Usherenko, V. Mironovs, S. Usherenko, O. Reut, and V. Lapkovskis, "Properties of aluminium and its alloys under the effect of dynamic alloying", *IOP Conference Series: Materials Science and Engineering*, to be published.

[6] A. Fletcher and S. Close, "Particle-in-Cell Simulations of an RF Emission Mechanism Associated with Hypervelocity Impact Plasmas", *Physics of Plasmas*, vol. 24, no.5, pp. 053102-1-7, 2017.

[7] A. Nuttall and S. Close, "A thermodynamic analysis of hypervelocity impacts on metals", *International Journal of Impact Engineering*, vol. 144, pp. 103645, 2020.

[8] R. Wang, S. Zheng, and Y. Zheng, "*Polymer Matrix Composites and Technology*", Woodhead Publishing, 2011.

[9] M.K.Gupta and R.K. Srivastava, "Mechanical properties of hybrid fibers-reinforced polymer composite: A review", *Polymer-Plastics Technology and Engineering*, vol. 55, pp. 626–642, 2016.

[10] M. R. Kessler, "Polymer matrix composites: A perspective for a special issue of polymer reviews", *Polymer Reviews*, vol.52, no. 3, pp. 229-233, 2012.

[11] V.Ya Velichko and P.R. Chirkov,"Analysis of the prospects for the use of composite materials in the production of modern aircraft", *Actual problems of aviation and cosmonautics*, vol. 2, pp. 458-460, 2017 (In Russian) Я.В.Величко, and П.Р.Чирков, "Анализ перспектив применения композиционных материалов при производстве современных летательных аппаратов", *Актуальные проблемы авиации и космонавтики*, vol. 2, no. 13, pp. 458-460, 2017.

[12] V. Lapkovskis, S. Usherenko, Y. Usherenko, V. Mironovs, and V. Gluschenkov, "Powder particle flow acceleration methods for simulation of interaction with materials used in spacecrafts", *Agronomy Research*, vol.17, no.6, pp. 2445–2454, 2019.

[13] M. Szycher, "*Szycher's handbook of polyurethanes*", CRC press, 1999.

[14] D. A. Jesson and J. F Watts, "The interface and interphase in polymer matrix composites: Effect on mechanical properties and methods for identification", *Polymer Reviews*, vol.52, no. 3, pp. 321-354, 2012.

[15] V. Jothi, A. Y.Adesina, M.M. Rahman, A. M. Kumar, and J.N. Ram, "Improved Adhesion and Corrosion Resistant Performance of Polyurethane Coatings on Anodized Mg Alloy for Aerospace Applications", *Journal of Materials Engineering and Performance*, vol.29, no. 4, pp. 2586-2596, 2020.

[16] Jie Liu, Zhao Li, Lunwu Zhang, Jian Hou, Zhonghai Lu, Peiqing Zhang, Bin Wang, and Nan Jin, "Degradation behavior and mechanism of polyurethane coating for aerospace application under atmospheric conditions in South China Sea", *Progress in Organic Coatings*, vol. 136 pp.105310, 2019.

Environment. Technology. Resources. Rezekne, Latvia
Proceedings of the 13th International Scientific and Practical Conference. Volume 3, 368-371

Gas Distribution System for Optimization of the Technological Process of Coating in an Unbalanced Magnetron Sputtering Installation

Ivan Uzunov
Central Laboratory of Applied Physics, Bulgarian Academy of Sciences
Plovdiv, Bulgaria
vanlu@mail.bg

Angel Lengerov
Technical University - Sofia, Plovdiv Branch
Plovdiv, Bulgaria
anlen@tu-plovdiv.bg

Abstract **- The paper proposes a new design solution for regulating the distribution of the working gases in the vacuum chamber of the installation (UDP -850/4) for unbalanced magnetron sputtering, which will improve the mode and quality of application of multilayer nano-coatings. Constructive documentation for manufacturing a gas distribution system has been prepared, as well as instructions for assembly to the vacuum chamber.**

Keywords optimization, distribution, gas, vacuum chamber, magnetron sputtering

I. INTRODUCTION

The technological coating process in an unbalanced magnetron sputtering installation (UDP - 850/4) is a well-known modern method for depositing thin layers on substrates (details) in order to improve their performance [8, 9, 10]. This is a vacuum technology (nanotechnology), based mainly on physical processes. The processes take place in a vacuum environment, under conditions of artificially and purposefully created argon plasma.

Vacuum deposition methods, whether physical or chemical, have some significant advantages, such as high level of purity, very good adhesion to the substrate, good uniformity and density of the layers, small residual stresses and microdefects in the structure, possibility for deposition of ultra-thin layers, very good possibilities for controlling the thickness, structure, mechanical stresses and other parameters of the layers, all of these leading to high quality of the obtained coatings [3,9,10].

The ion-plasma method includes diode and magnetron sputtering. The principle of operation in magnetron sputtering is shown in fig. 1 [5,6].

In magnetron sputtering, ionized argon fires at the target, releasing atoms, which, in turn, form layers on the substrate. The electrons and the argon ions form a plasma close to the target, due to the magnetic field. As a result of the magnetic action, the electrons move in a spiral along the magnetic field lines.

An important advantage of magnetron sputtering systems is the high speed of coating application, as well as the possibility for obtaining thin layers of uniform thickness on substrates with a considerable area.

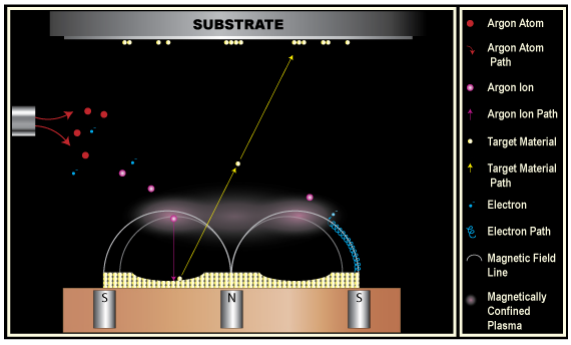

Fig.1. Magnetron sputtering [6]

Studies show that the main interrelated parameters, determining the rate of sputtering of the targets, are the discharge voltage, the discharge current, the induction of the magnetic field near the cathode surface, and the working gas pressure [5,6]. In these systems the inert gas argon is usually used in the role of a working gas.

Online ISSN 2256-070X
https://doi.org/10.17770/etr2021vol3.6525

Both the working gas argon (Ar) and the active gas are supplied to the vacuum space by pipelines. It is known that the size of the inlet and outlet openings of the pipeline, as well as the passability (the design features) of the individual elements of the vacuum gas system have a significant influence on the movement of the gas [1, 2, 4, 7].

In the considered vacuum chamber - part of the installation UDP - 850/4 - a vertical gas pipe with 4 or 6 openings is used, through which the working gases *Ar* and, in this case N_2, pass, to be used in processes of applying coatings by means of unbalanced magnetron sputtering. - Fig. 2.

The pipe is located between the third (on the right side of the heater) and the fourth target. This is a T-shaped tubular structure (pipe 6,3x4), in which the short, transversely welded pipe, serves for connection (inlet) to the gas supply system of the installation and, through the openings of the vertical pipe (ø 1), blocked at both its ends by a stopper - bolt - DIN 912 M5 x 8 ... 8N, the gases enter the working space.

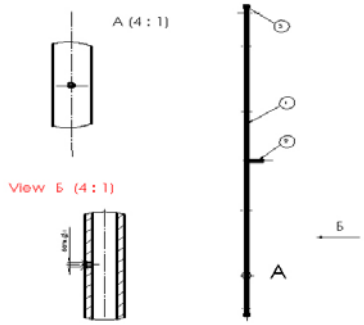

Fig. 2. Operating gas distribution system (gas line)
1 - vertical gas distribution pipe; 2 - transverse connection pipe; 3 - stopper - 2 pcs - bolt – DIN 912 M5 x 8

II. METHODOLOGY

The chamber uses different types of targets - Ti, Cr and Al. Each material has a different sputtering rate and forms stoichiometric nitride compounds using different amounts of nitrogen. Accordingly, the moment of occurrence of poisoning (deposition of harmful - nitride layers on the target material) of the targets is related to different amounts of nitrogen. On the other hand, in a vacuum environment, the movement of gases is inert and their distribution is non-uniform. Therefore, it is necessary to build an individual line for supplying each target in the chamber with working gases, with an option to change the number of openings depending on whether the given material needs less or more nitrogen.

The present work aims at designing and preparation of constructive documentation for building a new gas line, consisting of several parts and allowing the working gases used in the vacuum chamber (Fig. 3) to reach each of the targets – the 2nd, 3rd and 4th - in regulated amounts.

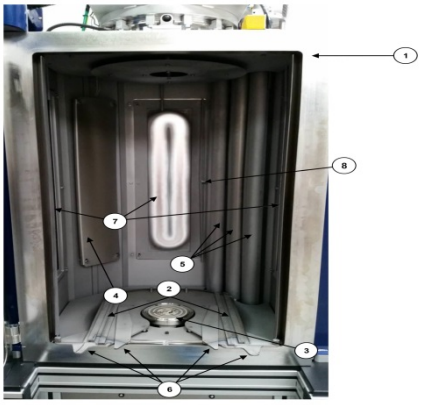

Fig.3. Vacuum chamber of a vacuum coating installation - (UDP - 850/4): 1 – Vacuum chamber; 2 - guides when moving the carousel; 3 - main carousel drive; 4 - heater (flat, infrared); 5 – thermocouples; 6 – locking lever system; 7 - 2nd, 3rd and 4th targets (from left to right); 8 – operating gas line

The realization of this aim is achieved by solving the following tasks:

1. The first section of the gas line must measure up to the current gas pipe on which stoppers can be placed.
2. A second section must be added to this main section. The second section must be a continuation of the first one and go in the base of the chamber, outside the carousel and under the heater.
3. The gas distribution system should consist of two separate outlet openings with stoppers, acting as additional connections for target 2 and target 4, respectively.

2.1. Design brief

The following main design parameters of the system are set:

- the gas pipeline part of the structure to be made of stainless steel pipes 1.4541, pipe 6.3x1;
- the distance (indentation) of the gas distribution pipes from the walls of the vacuum chamber to be 20mm - a safe distance from the carousel, ensuring also compactness of the structure in the interior of the chamber. The gas supply pipes to the targets to be located diametrically along a sector line of known length, defined by the position of the end gas supply elements of the system for the 2nd and 4th target;
- the distance (height of placing) of the connecting (the horizontal sectoral) distribution pipe from the bottom of the vacuum chamber to be - h = 40, mm;
- the height of the structure from the bottom of the chamber to the top of the gas distribution pipe to measure up to the height of the target frames - 920, mm;
- the openings for supplying the gas through the replaceable gas supply pipes - ø1, mm;
- reliable fixing of the structure during its building-up into the vacuum installation to be provided;
- all overall dimensions to comply with IT14.

The division of the gas line into sections allows for the inclusion or exclusion of a particular section, depending on the configuration of the targets and the used materials.

2.2. Design and construction of a gas distribution system for modification of the unbalanced magnetron sputtering installation (UDP - 850/4)

In accordance with the set tasks and the technical brief, a gas distribution system is designed and constructed, shown in Fig. 4, and aiming chiefly to regulate the gas supply inside the working space of the installation in specific places and specific quantities.

The positions of the end gas supply pipes (5) through which the gas enters the working space, are determined with the help of the main sections of the gas distribution system. They are welded to each other and form a monolithic structure (Fig. 4a). The supporting elements - heels (6) - are rigidly fixed to the monolithic structure, and with the help of them the structure is positioned (fixed) in the chamber (Fig. 4b). The construction of the heels complies with the requirements concerning the vacuum technologies, as well as with their function.

Through the inlet opening (13) the working gases enter the vertical pipe from section 1 (purple). The points of the positions A and B, from where the gas flow enters the two horizontal sections 2 (blue) and 3 (blue), are determined so that the lengths of the lines along which the gases pass through the pipes of the system until they reach the outlet (end) cross-sections of the three vertical parts of the sections (2 and 3 - blue), are equal. The idea in this case is to achieve a certain uniformity of the nature of movement of the gas flow by equating to some extent the resistance that the gas overcomes by passing along the length of the gas distribution system.

Section (3) is constructed as a part of an arc. It is located horizontally to the bottom of the chamber and goes under the heater. This position is determined by attaching it to the bearing heels in especially designed for the purpose grooves. The vertical pipes (4), serving as an extension of the pipeline, are welded at the end of the section and are respectively located at the 2nd and 3rd target.

Section (2) has a kidney-shaped form (bypasses the nests of the thermocouples). The gases, passing through it, are redirected through position B.

It is also horizontally placed, along section (3) and below its level. It is welded to the bearing heels through especially made openings (channels) and occupies a minimum distance (~3mm) from the bottom of the vacuum chamber. A vertical pipe (4) is welded at the end of the section, serving as a continuation of the pipeline from the gas distribution system and located at the 4th target.

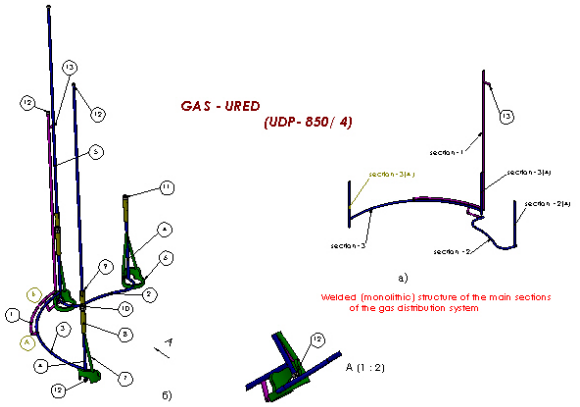

Fig. 4. Gas distribution system for modification of the installation for application of vacuum coatings - (UDP - 850/4):
1 - supply system - part of the gas distribution system
2 - section 2 - provides gas access to target 4
3 - section 3 - provides gas access to targets 2 and 3
4 - vertical tubes (branches) for fixing the gas supply pipes
5 - gas supply pipes at the respective targets
6 - heels (bearing supporting elements of the structure)
7 - braids - reinforcing elements of the structure
8 - lower connection sleeve
9 - upper connection sleeve
10 - fixing nut and counter-nuts Hexagon Hut ISO 4033 -M8 -W - N
11 - stopper - bolt – ISO4762 M8 x 12...12N
12 - stopper - bolt – DIN 912 M5 x 8...8N
13 - tube (branch) for connection to the gas system of the installation (UDP - 850/4)

The three vertical branches (positioning pipes 4) of the monolithic structure are located diametrically (at equal distances) inside the chamber and are shifted at a certain angle to the gas supply (central) pipe at the 3rd target. The gas distribution replaceable pipes (5) are attached to them by means of especially designed sleeves (8 and 9) and with the help of a threaded connection M8. Depending both on the number and on the location of the drilled holes of ø1mm on them, the amount of gas supplied to the chamber at the respective position is determined. In order to avoid "poisoning" of the targets, it is necessary to orient the position of the gas distribution pipes with the help of the fixing nuts (10) in order that the openings point diametrically toward the interior of the vacuum chamber.

With the help of this gas distribution system it is possible to supply gas separately and independently to each of the selected positions when applying vacuum coatings under the conditions of magnetron (unbalanced) sputtering. If necessary, by means of a stopper (11), the access of gas through a certain position can be blocked, as shown for the position at the 4th target.

The structure is designed to be built-in (fixed) and operate outside the scope of operation of both the carousel and of all moving elements in the structure of the installation (UDP - 850/4) in the vacuum chamber.

III. CONCLUSIONS

1. A new design solution for regulating the distribution of the working gases in the vacuum chamber of the

installation UDP-850/4 for unbalanced magnetron sputtering has been proposed. It will improve the mode and quality of application of multilayer nanocoatings.

2. Constructive documentation for producing the described gas distribution system and instructions for its assembly and installation to the vacuum chamber have been prepared.
3. Based on the technological parameters of the vacuum chamber operating mode and the results of its tests, it is possible to optimize the technological process of applying thin coatings (nanocoatings). This will speed up and optimize the research processes, related to their operational characteristic.

REFERENCES

[1] Kanev, V., G. Grigorov, High Vacuum, ed. "Technology" 1965.

[2] Mirchev, S., "Fundamentals of vacuum technology", PU "Paisii Hilendarski" - Plovdiv 1986.

[3] White AV, Karpenko GD, Myshkin NK Structure and methods of formation of wear-resistant surface layers, Moscow, Mechanical Engineering, 1991 (In Russian).

[4] Nikitin MM, Vacuum spraying technology and equipment, M, Metallurgiya, 1992 (In Russian).

[5] Danilin BS, Syrchin VK, Magnetron sputtering systems, M, Radio and communication, 1982 (In Russian).

[6] Kuzmichev AI, Magnetron sputtering systems", Kiev, Avers, 2008 (In Russian).

[7] Frolova ES, VG Minaycheva, Vacuum equipment "Handbook", Moscow , Mechanical Engineering, 1985 (In Russian).

[8] Mischev, G., Einfluss der Reibung auf das dynamische Verhalten der geradlinig bewegten Maschinensysteme. 13th International Colloquium Tribology, January 15-17, 2002 Stuttgart/Ostfildern, Germany, ISBN 3-924813-48-5, vol. II, s. 867-873.

[9] Mischev. G., Reibung in geradlinig bewegten Maschinensystemen (Führungen von Werkzeugmaschinen). Fast Print Books, 2020, ISBN:978-619-236-163-1.

[10] Rupetsov, V. , S. Dishliev, G. Mishev, F. Franek, M. Premauer, L. Kolakleva, Research of tribological parameters of multilayer coating Ti/TiN/CrN-ml deposited on 1.2343 steel. BCC, Vol.52, Issue 3, 2020. DOI: 10.34049/bcc.52.3.5236.

Environment. Technology. Resources. Rezekne, Latvia
Proceedings of the 13th International Scientific and Practical Conference. Volume 3, 372-377

Research of Power Generator Prototype Development and Integration into Autonomous Robotic Systems

1st Matutis Vaidotas
Faculty of Electronics and Informatics
Vilniaus Kolegija University of Applied Sciences
Vilnius, Lithuania
v.matutis@eif.viko.lt

2nd Savulioniene Loreta
Faculty of Electronics and Informatics
Vilniaus Kolegija University of Applied Sciences
Vilnius, Lithuania
l.savulioniene@eif.viko.lt

3rd Sakalys Paulius
Faculty of Electronics and Informatics
Vilniaus Kolegija University of Applied Sciences
Vilnius, Lithuania
p.sakalys@eif.viko.lt

4th Cesnauskas Simonas
Faculty of Electronics and Informatics
Vilniaus Kolegija University of Applied Sciences
Vilnius, Lithuania
s.cesnauskas@eif.viko.lt

Abstract **- The aim of the research is to perform experimental research based on patented technology to study the efficiency and applicability of it in the power supply circuits of autonomous robotic systems. Ensuring longer autonomous operation of the robotic system, was chosen electric car as the object of practical application at this stage of investigations to improve a process generation, utilization and regeneration of electricity. The article reviews the difficulties of technologies and aspects of their practical application. Described research methodology and a stand of investigations. Presented the results and conclusions of the performed simulation tests and practical measurements of the prototype electrodynamic parameters.**

Keywords - robotic system, electricity generator, regeneration, electric car.

I. INTRODUCTION

Members of the team - both teachers and students – are united by the idea to explore opportunities of creation of a generator for autonomic robotic systems. One of such systems accessible for research and not too complicated in the beginning can be an electric car. This system is partly autonomic in the aspect of its control; however, its electric circuit is fully autonomic.

The base of this research is a patented [8] idea (the Patent No. LT-6714B; the Application No. 2019-065). The patented invention was created upon striving to increase the distance covered by an electric car after a single charging its battery at a stationary charging station. The goal of the invention is use of a mobile electric power generator based on an environmentally friendly technology in combination with wind power (both kinetic and potential energy of air mass formed on movement of the car) that is equipped with a compensatory mechanism of a simple design (in principle, it is a component of an electric car involved in charging the battery during the car's movement). The mock-up of a wind turbine is presented in Fig.1 below.

Analyzing of analogous ideas shows that a majority of them do not achieve the efficiency required for practical application, because the losses exceed the expected level on a certain stage (phase) and the possible efficiency becomes negative (that means losses). So, the team agreed to analyze each phase and to carry out practical measurements on a test stand for searching the best efficiency for each of this phase; if possible, computer modelling media shall be applied or created for up-and-coming studies.

Online ISSN 2256-070X
https://doi.org/10.17770/etr2021vol3.6594

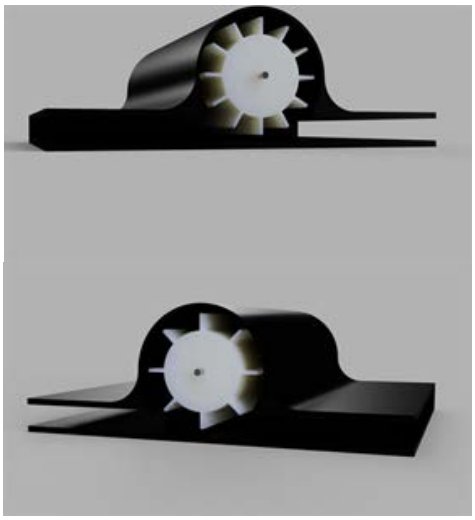

Fig. 1. Wind turbine model view.

To achieve the efficiency of a generator for electric cars that can provide a practical benefit, an integrated approach (Matutis, 2008) [7] is required, because it involves mechanics, electromechanics, electronics and some other areas of practical physics. On movement of an electric car, transformation of air flow around it into electric power required for charging the accumulator is one of the possible versions. Use of air flow power is analyzed in studies related to practical application of wind power systems where it is tried to use kinetic energy of air flow to the maximum possible extent. It was decided to carry out a practical analysis of this aspect in the first phase. The key problem of the said phase was a need to establish the number of wings of a chosen wind turbine that would ensure the best efficiency. The chosen geometric design of the turbine (Fig.1) is the simplest and is sensitive to environmental impact to the minimum extent. The design of the wings is simple as well; however, it ensures positive efficiency (in mechanical aspect) because of the relevant ratio of force levers.

However, the most interesting and uncertain factor remains use of air flow efficiency depending on the number of turbine wings. Such a formulation of the run of the study enabled starting to create a laboratory stand upon applying the available means and involving students in the works. It was planned to print a majority of details for the mock-up by 3D printers – these works were useful for developing skills of the students in design and manufacture, improved their figurative thinking and their abilities to convey it. In addition, they included modelling, programming and practical manufacturing educative activities. The short involvement of students in the project was highly beneficial both for them and for the total process of education at the College.

While talking about the consequences of a long-term involvement in such a project and the benefit provided, it should be remembered that the essence of the study was integrated approach, i.e. complexity. In this multi-phase study, almost each phase was related to a new area, such as mechanics, electromechanics, electronics and so on. In addition, each of the said areas was bound with other ones, so maintenance of the positive efficiency on transfer from one phase to another required to understand the interaction of the said areas and their integrity and to take them into consideration. In the process of education, this predetermines the general mastering of the conception of the surrounding world's integrity that is very important for our young generation to survive in the period tormented by crises and to create the future for themselves and their children...

Talking about the methodology of the study, the most effective and simple (in the aspect related to the design of the stand) way to find an answer to the put question would probably be measuring the behavior of the turbine at constant air flow and variable number of turbine wings. For the said purpose, a large number of rotors of different configurations (with different numbers of wings) (Fig.1) shall be made using the available 3D printers. Upon taking into account later aspects of practical application, it would be purposeful to measure two parameters – the starting point when the turbine starts its movement (rotation) and the torque developed by the rotating turbine in its internal cavity. Measurements of the torque can be carried out on gradual increasing the load and observing the turbine rotational speed. Such a curve was drawn at the constant air flow (that remains the same on any changes of the turbine rotor's configuration or in absence of them) and describes a turbine with a certain number of wings. If we suppose that varying the number of wings causes changes of the turbine characteristics, these measurements will enable entering the relevant data to the programmed computer simulator and providing more detailed clarification of the results of practical measurements through their abstraction.

The opportunity of involvement in discussions on the run of the said study, designing of the stand, carrying out the measurements, presentation & analysis of the results, their transfer to the simulation medium, summarizing the results and presenting the conclusions provides to students of our Faculty a totality of practical skills required in the future professional activities of electronic engineers

II. THE REVIEW OF THE THEORETICAL FRAMEWORK

While speaking about wind power engineering, the wind power potential is usually analyzed; however, not the total power of moving air flow is technologically transferred into the power useful for the consumer.

In this analysis, wind is described as horizontal movement of air mass that is caused by the temperature difference on the surface of the Earth, because the Sun does not warm the surface of the Earth and the air of the atmosphere to the same extent. Cold air is heavier – in the atmosphere, it moves downward, thus forming high pressure zones. Warm air is easier, and it moves upwards in the atmosphere, thus forming low pressure zones. Air

moves from a high-pressure zone to a low-pressure zone until the pressures become the same. Although wind is identified a renewable source of energy, it (because of its origin) is a phenomenon formed by the solar radiation. On analyzing the vertical section of the atmosphere, winds are divided to geostrophic winds and surface winds (Kytra, 2006) [6]. A geostrophic wind is formed on the height over 1 km; a wind formed on a lower height is a surface wind. In a layer of a surface wind, a zone of wind with the height up to 100 m may be found, because movement of air masses in the said zone is strongly affected by the roughness of the surface, i.e. inequalities of the surface of the Earth, buildings, plantations et cetera. It is natural that obstacles reduce the speed of the wind, so a higher speed of wind is observed in open territories, over oceans and seas. Close to obstacles, the windward and downwind zones are observed; they express themselves by the wind turbulence and its speed decrease.

The speed v is the key characteristic usable in wind power engineering analysis. According to the theory of classical mechanics, kinetic energy E of air flow (air mass) movement (Augulis, Jotautis & Rutkuniene, 2012) [1], shall be expressed as follows:

$$E = \frac{1}{2}mv^2; \qquad (1)$$

here: v – the wind speed, m/s;
m – the air mass, kg.

The air mass moving through the wind wheel can be expressed as follows (Boyle, 2012) [5]:

$$m = \rho V = \rho A l = \rho A v t \qquad (2)$$

here: ρ – air density, kg/m³;
V – air volume, m³;
A – area, m²;
l – length, m;
v – wind speed, m/s;
t – time, s.

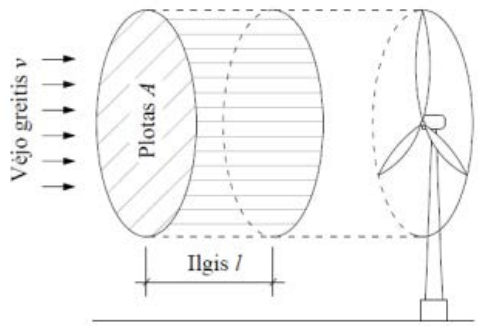

Fig. 2. The scheme of the air mass moving through the wind wheel (Boyle, 2012).

So, the formula (1) may be expressed as follows (Mukund, 2006) [9]

$$E = \frac{1}{2}mv^2 = \frac{1}{2}(\rho A v t)v^2 = \frac{1}{2}\rho A t v^3. \qquad (3)$$

Power P of air mass or air flow shall be expressed as power change per time unit (Mukund, 2006) [9]:

$$P = \frac{E}{t} = \frac{\frac{1}{2}\rho A t v^3}{t} = \frac{1}{2}\rho A v^3. \qquad (4)$$

We can see from the formula (3) that the maximum theoretical power of wind stream directly depends on the third degree of the value of the wind speed, so the wind speed is a key parameter usable for establishing techno-economical characteristics of wind.

The primary technological equipment that contacts with the air flow is the wind wheel. The power Pm_in, i. e. the power obtained from the air flow per time unit, can be calculated according to the formula (1) upon taking into account that power obtained by the wind wheel from the air flow depends on the difference between the wind speed before the wind wheel (v) and the wind speed behind the wind wheel (v0) (Mukund, 2006) [9]:

$$P_{m\_in} = \frac{1}{2}\frac{m}{t}\left(v^2 - v_0^2\right) = \frac{1}{2}G\left(v^2 - v_0^2\right); \qquad (5)$$

here: v – the wind speed before the wind wheel, m/s;
v0 – the wind speed behind the wind wheel, m/s;
G – the mass air flow, kg/s.

According to the formula (2), the mass air flow G may be expressed as an arithmetical average of the wind speed before the wind wheel and the wind speed behind the wind wheel (Mukund, 2006) [9]:

$$G = \rho A \frac{v + v_0}{2}; \qquad (6)$$

then:

$$P_{m\_in} = \frac{1}{2}\left(\rho A \frac{v + v_0}{2}\right)\cdot\left(v^2 - v_0^2\right) = \frac{1}{2}\rho A v^3 \frac{\left(1 + \frac{v_0}{v}\right)\cdot\left(1 - \left(\frac{v_0}{v}\right)^2\right)}{2}. \qquad (7)$$

The last member in the formula (7) singles out the ratio between the wind speed before the wind wheel and the wind speed behind the wind wheel, thus describing the property of the wind wheel to adopt useful kinetic wind energy, and this non-dimensional value is referred to as the

efficiency of the wind wheel, or the wind wheel's power factor cp:

$$c_p = \frac{\left(1+\frac{v_0}{v}\right)\cdot\left(1-\left(\frac{v_0}{v}\right)^2\right)}{2}; \quad (8)$$

then:

$$P_{m\_in} = \frac{1}{2}\rho A v^3 c_p. \quad (9)$$

The maximum power factor cp of an ideal wind wheel equals to 0.593 and takes place when the wind speed behind the wind wheel is suspended upon the ratio 2/3, as compared to the wind speed before the wind wheel. This law was formulated and proved by German scientist Albert Betz in 1919. A.Betz published the results of his study in 1920 in the paper „Das Maximum der theoretisch möglichen Ausnützung des Windes durch Windmotoren" („The theoretical limit of power of a wind turbine using the wind energy to the maximum extent") (Betz, 1920) [4], and since the said time, A. Betz's law has not been replaced or altered or proved otherwise A. Betz's law describes the maximum power transformation of a certain operating point; however, on operation of a wind turbine, other losses appear as well too.

Designs of wind wheels can be various; their technical propertied and the ones related to wind power transformation differ as well.

III. The Methodology of the Research

As it was mentioned above, designs of wind wheels vary, and our team had chosen one of them - the version of a turbine (Fig. 1). As a stand for tests, we can use an elementary analogue of a wind tunnel. The wind flow is generated by a fan; on its way, a prototype of a turbine is placed; in addition, one air flow meter is placed before the turbine and the second air flow meter – at the air flow output. As it was mentioned earlier, we measure two parameters: the starting point when the turbine starts moving (rotating) and the torque developed by the rotating turbine in its internal cavity. Torque measurements can be carried out on a gradual increasing the load and observing the rotational speed of the turbine. Such a curve drawn for a constant air flow (that remains the same after a change of the turbine rotor configuration) would describe a turbine with a certain number of wings. For this purpose, we print rotors of different configurations (with different numbers of wings) and then carry out the measurements at a constant air flow upon varying the number of turbine wings.

The practical measurements seem to be simple; however, the restrictions applicable both to the process of studies and the practical training prevented us at present from presentation of the collected data and their analysis. So, it was decided to present not only the computer simulation of the wind tunnel, but also some observations and measurements from the primary assembled model.

The simulations used Autodesk® CFD 7 [Autodesk CFD, 2021] [3] software to turn a 3D CAD workstation into a fully interactive liquid and gas test bench, thermal test rig, or wind tunnel. 3D layouts become interactive, at no cost to prototypes, revealing critical engineering information that is difficult to obtain through physical testing. Change the design of the model and we will see the same change in Autodesk® CFD right away. This software has been used in combination with Autodesk Fusion 360 6 [Autodesk Fusion, 2021] [2], which is 3D and 2D modeling software with a fairly user-friendly environment that allows you to use it comfortably without much challenge. It is a powerful program that allows you to create complex and large-scale layouts. Thanks to Fusion 360's ability to import layouts of required materials directly from the manufacturer's catalogs, it is possible to save time by designing less significant components (bolts, nuts, profiles, etc.) and use that time to implement the basic layout. Also, the ability to simulate moving parts of the device (albeit limited) allows for a better understanding of the performance, durability of the final layout, and the anticipation and improvement of potential engineering mismatches.

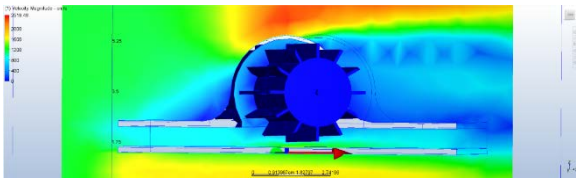

Fig. 3. The turbine in the wind tunnel simulation.

The initial situation of the wind tunnel is presented in Fig.3 above. The chosen design of the wind turbine appeared to be not very effective. As one can see from the image of the simulation, a very weak air flow moves through the turbine wings and our goal is to achieve the maximum possible efficiency. The colored scale in the left part of the Figure indicates the intensity of the air flow in colors. The colored distribution presented in the Figure shows where air flows are most intensive. So, it can be presumed that an improvement of the design of the turbine body upon preserving the existing chosen geometry of the turbine is required.

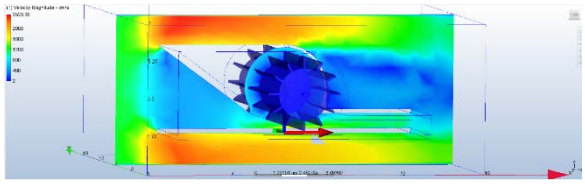

Fig. 4. The corrected turbine in the wind tunnel simulation.

It was decided to broaden the air inlet and to repeat a simulation once more. The repeated simulation is presented in Fig.4 above; it can be seen, that now, the

intensity of the air flow through the wings grows considerably.

Based on the highlights observed in these simulations, a study model was printed on 3D printers, the incision of which is shown in Fig. 5

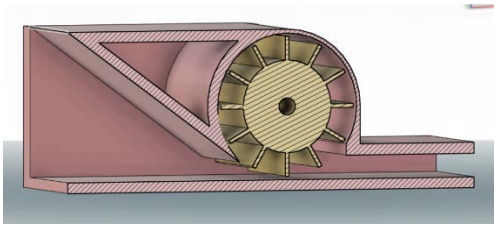

Fig. 5. The incision of model.

With 3D printers, all the necessary parts of the model were printed. In Fig. 6 we see a pictures of the work process.

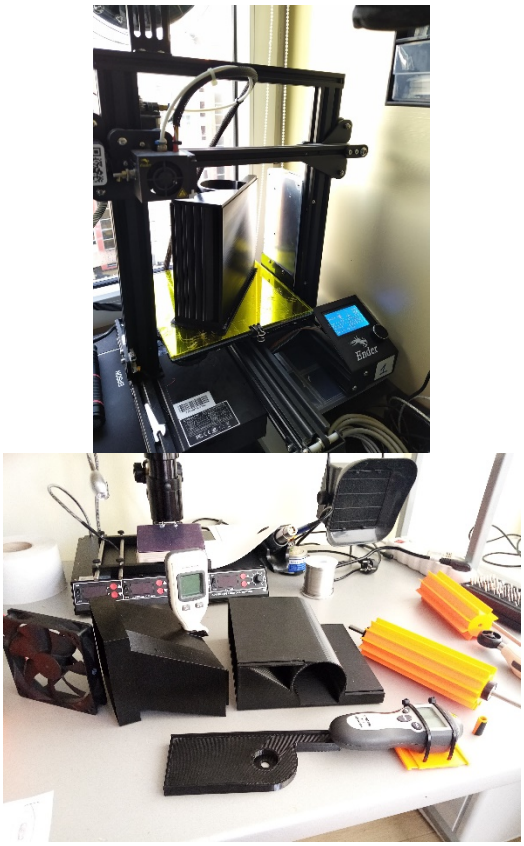

Fig. 6. Model printing process.

We see the finally assembled model in Fig. 7

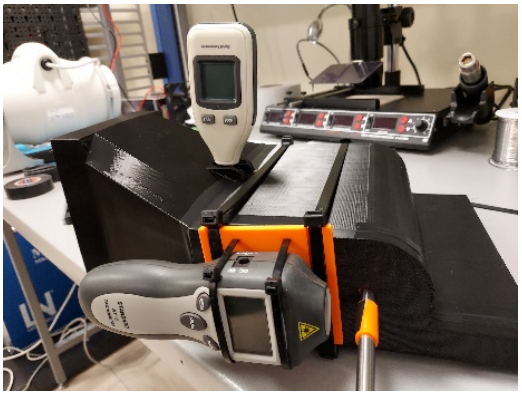

Fig. 7. The model was collected and prepared for research.

We plan step by step to identify coherently the maximum efficiency on each phase of the study and – after integrated coordination and summation of all phases – we hope to obtain a practically applicable electric generator for electric cars that enables to increase the distance coverable by a car after a single charging its battery at a stationary charging station. As it was mentioned earlier, an electric car may be considered a certain autonomic robotic system, so in a broader sense it is the first step towards creation of a generator for autonomic robotic systems.

In such a way, the methodology of the study, applicable methods and the strategy of the run of the experimental research chosen by our team can be defined. The scope of the experiments will be expanded in the future.

IV. THE RESULTS OF THE STUDY AND THE CONCLUSIONS

The result of this first phase of the study is an obvious improvement of the turbine body upon applying the results of computer simulation.

As for the first results of the practical tests, in the beginning the workshop failed to move the impellers with the planned fans and the air flow generated by them. When the impeller was still able to move, the required air flow was about 100 km / h (we used a compressor), the impeller rotation speed was recorded at about 1100 rpm; however, very high damping because after stopping the air flow in one revolution, the speed dropped to 200 rpm and stopped completely. Meanwhile, the speed of the outgoing air flow when the impeller was rotating was only 20 km / h. Initially planned fans for airflow generation were significantly weaker. The computer fan (originally intended) generated an air flow of only about 7 km / h, while the exhaust fan that was still available generated an air flow of up to 20 km / h. However, this was not enough for the first attempts.

A new generation of polymer bearings was used in the model, which should ensure a sufficiently low resistance. However, as experiments have shown, the resistance is quite high. Such a damping factor even surprised. Of course, this could also be influenced by the

geometrical inaccuracies and unforeseen deformations of the printed plastic parts of the layout. Here we will have to work on centering the model impeller and compensating for unexpected deformations.

The scope of the experiments will be expanded. Preliminary measurement results and observations have been performed, create preconditions for further improvement of the model and preparation for the planned measurements. We regret the incomplete scope of the experiments and apologize to colleagues for this, but this was due to circumstances beyond our control.

Initial tests have been carried out, and this is a great achievement, despite the fact that the results for this minute have not lived up to expectations - and most importantly, we now have a clear starting point. Also, the geometry of the air flow inlet was chosen in the model at the initial stage only half the height of the wing, which also limited the flexibility of the research. The team proposes to further improve the model - to make an adjustable supply air flow valve so that we can dynamically change the area of attack on the turbine blades. Such an improvement will allow the construction of a more promising model, which will allow more flexibility in planning further research and measurements.

These are very important technical achievements.

In summary, must be underlined:

- The very important social role of this phase in the training process is that the youth starts taking an interest in research activities and practical application of technological solutions important for the total community that guide towards environmental conservation and protection as well as care about each other. It will help our new generation, in addition to developing the sense of social responsibility and understanding, to observe and adopt the inevitability of integrity. In the higher education process, integration of such studies is undoubtedly a very useful and promising tool.
- Technically, several more steps have been taken to achieve the best possible efficiency, which encourages the team to be even more focused and concentrated on the improvement and development of the model. It is also a very important piece of work for the environment around us, as the desired result is an environmentally friendly device, ecologically clean and using renewable energy resources.

REFERENCES

[1] Augulis, L., Jotautis, A., & Ruktuniene, D. (2012). *Fizika: mechanika, termodinamika, elektromagnetizmas: mokomoji knyga*. Kaunas: Technologija. DOI: https://www.ebooks.ktu.lt/eb/656/fizika_mechanika_termodinamika_elektromagnetizmas/.

[2] Autodesk (2021). *Autodesk fusion abilities.* Retrieved from https://academy.autodesk.com/getting-started-fusion-360#:~:text=Fusion%20360%20helps%20students%20and,turn%20your%20ideas%20into%20reality

[3] Autodesk (2021). *What is Autodesk CFD.* Retrieved from https://www.autodesk.com/products/cfd/overview#:~:text=Autodesk%20CFD%20is%20a%20computational,into%20fluid%20flow%20design%20performance.

[4] Betz, A. (1920) Das Maximum der theoretisch möglichen Ausnützung des Windes durch Windmotoren. Zeitschrift für das gesamte Turbinenwesen, 26, 307-309. (In German)

[5] Boyle, G. (2012). *Renewable energy: power for a sustainable future*. Oxford: Oxford University Press.

[6] Kytra, S. (2006). Atsinaujinantys energijos saltiniai: vadovėlis aukstosioms mokykloms. Kaunas: Technologija

[7] Matutis, V. (2008). Political idea and national security. *Vadybos šiuolaikinės tendencijos = Modern tendencies of management : mokslo darbų rinkinys*, 219. ISSN: 978-9955-423-69-0. DOI: www.lka.lt/download/1393/vadyba_makstutis.pdf

[8] Matutis, V. & Matutis, M. (2020). Generator for electric cars. Vilnius: Official Bulletin of the State Patent Bureau of the Republic of Lithuania, 28. ISSN: 2029-2309, Patent No.: LT-6714. https://vpb.lrv.lt/uploads/vpb/documents/files/VPB-OB-Nr06-2020-03-25-1d.pdf

[9] Mukund, R.P. (2006). Wind and solar power systems: design, analysis, and operation. Boca Raton: Taylor & Francis.

Environment. Technology. Resources. Rezekne, Latvia
Proceedings of the 13th International Scientific and Practical Conference. Volume 3, 378-381

Development of the Optimal Design of Manual Garden Fork with the Ability to Quickly Clean the Working Surface

Ivan Voiku
Department of Business management
and innovation management
Pskov State University
Pskov, Russia
voiku-ivan@yandex.ru

Abstract **- Manual garden tools help a lot with different types of work with soil: digging, removing roots and weeds, harvesting root crops and bulbs, and much more would be much more difficult if it were not for the forks. This tool has a wide range of features. There are many varieties of this tool differing in shapes and sizes: manure, harvesting, hay, flower, pointed, fork-shovel, telescopic, digging, ball-pointed. A common problem for all manual garden forks is clogging of the tines. This reduces the productivity of those who use them. Attempts are constantly being made to solve the problem of quick cleaning of the tines of manual garden forks. Many technical solutions to this problem are patented and are actively used in practice. The employee of the FSBEI of Higher Education "Pskov State University" has developed a manual self-cleaning fork. The design of the manual self-cleaning fork consists of a handle and a frame with many elongated spaced tines, which is fixed at one end of the handle, as well as a cleaning plate that is fixed to the movable handle, and a spring located on top of the handle inside the movable handle. The movable handle has lateral longitudinal grooves. The movable handle provides movement of the cleaning plate relative to the handle, and, consequently, compression and releasing of the spring. The overall dimensions of the proposed device are accepted according to the existing standards for such structures. The principle of operation of the proposed device: during the operation of the fork, the cleaning plate is pressed against the frame by spring force. Cleaning of the tines is made by a cleaning plate, which is moved along the tines. To do this, the user withdraws the movable handle, overcoming the resistance of the spring. By doing so, the frame passes through the longitudinal grooves and serves as one guide for the movable handle, and the handle serves as the second guide. The fork returns to its original state by releasing the spring after the user releases the movable handle. The main technical result of the proposed device is an increase in the operational characteristics of the fork, reduction in the time and effort spent on cleaning of the tines.**

Keywords - cleaning of tines, gardening, manual fork, manual labor.

I. INTRODUCTION

"Gardening" is defined as the activity of working in a garden, growing and taking care of plants, and keeping the garden attractive. [1] Gardening is a popular activity and a pastime in many countries and cultures. In the UK for example, it is estimated that 49% of the adult population takes part in gardening activities and that there are 24 million domestic (home) gardens in the UK; the country with a population of 66 million people. Similarly, in the USA, it is estimated that 78% of home-owners take part in gardening on a regular basis [1].

Despite the ongoing automation of modern production processes, manual labor continues to be necessary due to its flexibility and ease of deployment [3]. That is why, unlike large-scale agricultural activities, gardening involves manual labor, and, consequently, the use of manual agricultural tools.

The manual garden tools help a lot with different types of work with soil: digging, removing roots and weeds, harvesting root crops and bulbs, and much more would be much more difficult if it were not for the forks. This tool has a wide range of features.

There are many varieties of this tool, differing in shapes and sizes: manure, harvesting, hay, flower, pointed, fork-shovel, telescopic, digging, ball-pointed.

Online ISSN 2256-070X
https://doi.org/10.17770/etr2021vol3.6617

The fertilization process is one of the stages that is very important for improving the quality and quantity of the crop. Manual forks are tools required for these agricultural operations. Their design is primarily developed for male workers taking their anthropometric body dimensions and strength parameters [4]. However, frequent use of manual forks even by men leads not only to a decrease in labor productivity, but also to health problems.

For example, in one study on tools for extracting components of the maize root system, an unscientific assessment of labor requirements estimates the productivity of using heavy garden forks at 28,6 roots/hour per person. While the use of tractor tools increases this figure to 92,4 roots/hour [5].

It's all about the common problem for all manual garden forks – clogging of the tines. This reduces the productivity of those who use them.

In recent years, many national governments and various stakeholders in the food value chain have purposefully introduced and used agricultural mechanization (AMT) technologies to stimulate agricultural production. With the advancement of technology, most Research and Development Institutes and Higher Educational Institutions (HEIs) involved in the agricultural sector of the country have been focusing on innovative technologies [2].

To facilitate tiresome work of cleaning of the tines of a manual fork, reduce corresponding health issues and increase labor productivity, the development of an ergonomic manual tool – manual self-cleaning fork – is in demand.

II. MATERIALS AND METHODS

There is a self-cleaning rake [Patent for invention US5713193 from 22.08.1996 “Self-cleaning rake” by Guinn Allen Y and Stapley Linda D (US)], consisting of a handle, a grip, a spring release button and two sets of tines [6]. The handle is made of fiberglass and consists of two telescoping pieces. One of the pieces is larger in diameter, and the other piece is slidably retained within it. The smaller handle piece is provided with a cleaning bar to which one set of tines are attached, and the cleaning bar further has a plurality of aligned apertures through which a second set of tines extend. The second set of tines are attached to the first handle piece, and reciprocable movement of the handle pieces relative to each other results in the cleaning bar and its attached tines moving in a manner which effects a removal of debris from both sets of tines.

The disadvantage of this device is that having two sets of tines leads to the removal of only large debris, and does not allow for full self-cleaning. In addition, a second set of tines significantly increase the weight of the device, reduce the effective area of the tines.

There is a device [Patent for invention US3884023(A) from 20.05.1975 “Self-cleaning rake” Robinson Melvin P (US)], which have tines with downwardly turned or depending front ends and is provided with a cleaning element slidably movable over the tines [7]. The cleaning element surrounds the tines and is pivotally connected to a bracket, which is in turn secured to a rod displaceable along the handle of the broom by means of a hand actautor. The cleaning element is designed to move along downwardly turned or depending front ends of the tines due to the pivotal connection to the bracket. The cleaning element also compresses the tines when it is moved downwardly over the tines.

The disadvantage of this device is that there is no return mechanism. In addition, cleaning of the tines involves compressing them, which in the case of heavy clogging can lead to deformation of the tines. The bracket located on top of the tines reduces the possibility of using this device in a confined space.

There is a self-cleaning rake [Patent for invention US4776158(A) from 11.10.1988 “Self-cleaning leaf rake” Baum Wendell E (US)], including an elongated handle and a frame with spaced tines, which is fixed at one end of the handle [8]. On the tines of the device there is a plate that is moved along the entire length of the tines by a push rod mounted on the handle. A spring clip holds the plate in the raised position and can be released by a guide element on the handle engaging the push rod.

The disadvantage of this device is the presence of a protruding push rod on the handle, as well as the lack of a return mechanism. To return the plate to its original state, the user must pause the process of using the device, must change the pose and position of the hands. The cleaning plate is moved by a push rod attached to the handle. The length of the handle, the lack of additional fasteners and items for stabilizing the position of the cleaning plate in case of severe clogging of the tines can lead to a device failure.

The closest to the claimed device is a self-cleaning rake [Patent for invention US2015257335 from 21.11.2014 “Self-cleaning rake” Riggs Christina and Riggs Donald (US)], which includes a hollow shaft and a frame with many elongated closely spaced tines, which is fixed at one end of the shaft [9]. Inside the shaft is a rod, at one end of which a cleaning plate is fixed, installed with the possibility of sliding along the tines. There is a grip on the outside of the shaft that is functionally connected to the rod. The handle allows you to move the cleaning plate along the tines. The rod is spring-loaded in such a way as to automatically return the cleaning plate to the frame.

The disadvantage of this device is low maintainability due to the location of the spring inside the hollow handle. Also, the use of a hollow shaft complicates the design and limits the list of materials for its manufacture. In addition, the location of the spring in the upper part of the handle increases material costs and reduces the usability due to the disruption of the user's familiar balance of the tool. In addition, this device cannot be created by upgrading the user's existing tools. In addition, to clean the tines the user must pause the process of using the device, change the pose and position of the hands.

III. Results and Discussion

The employee of the FSBEI of Higher Education "Pskov State University" has developed a manual self-cleaning fork [10].

The technical task solved by the claimed utility device is to increase maintainability, reduce material costs, increase usability, use standard materials, and ensure the possibility of upgrading existing tools.

The technical task is achieved by the fact that this manual self-cleaning fork consists of a handle and a frame with many elongated spaced tines, which is fixed at one end of the handle, a cleaning plate with many spaced holes in which the tines are located, a spring, a movable handle. The cleaning plate is fixed to the movable handle which has lateral longitudinal grooves, while the spring is located on top of the handle inside the movable handle.

The technical essence of the proposed device "Manual self-cleaning fork" is explained on Fig. 1 and Fig. 2.

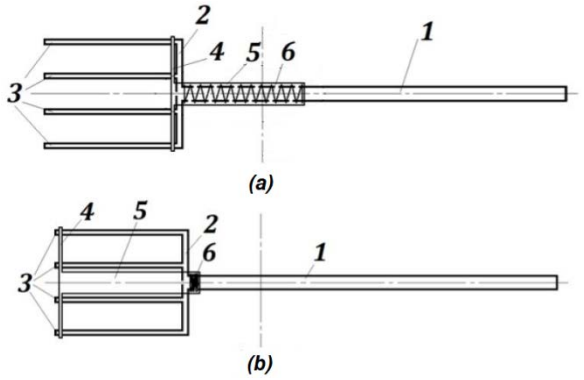

Fig. 1. Plan view of the manual self-cleaning fork (starting position (a) and working position (b)).

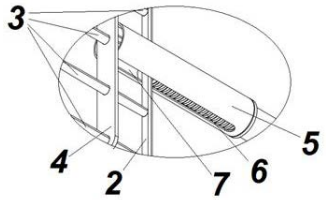

Fig. 2. Sketch of the movable handle of the self-cleaning fork as viewed from the teeth.

Essentially, the design of this manual self-cleaning fork consists of a handle 1 and a frame 2 with many elongated spaced tines 3, which is fixed at one end of the handle 1, as well as a cleaning plate 4, which is fixed to the movable handle 5, and a spring 6 located on top of the handle 1 inside the movable handle 5. The movable handle 5 has lateral longitudinal grooves 7.

The movable handle 5 provides the movement of the cleaning plate 4 relative to the handle 1, and, consequently, the compression and releasing of the spring 6. The overall dimensions of the proposed device are accepted according to the existing standards for such structures.

The principle of operation of the proposed device: during the operation of the fork, the cleaning plate 4 is pressed against the frame 2 by spring force 6. Cleaning of the tines 3 is performed by the cleaning plate 4, which is moved along the tines 3. To do this, the user withdraws the movable handle 4, overcoming the resistance of the spring 6. By doing so, the frame 2 passes through the longitudinal grooves 7 and serves as one guide for the movable handle 5, and the handle 1 serves as the second guide. The fork returns to its original state by releasing the spring 6 after the user releases the movable handle 5.

In the course of the experimental design work, the author of the device modeled two versions of mock-up samples (Fig. 3 and Fig. 4).

Fig. 3. Sketches of a mock-up sample of the manual self-cleaning fork (version 1).

Fig. 4. Sketches of a mock-up sample of the manual self-cleaning fork (version 2).

Each of these versions differs in the direction of distribution of the user's force on the cleaning plate: above a plane of the tines (version 1) and below this plane (version 2). The results of the evaluation of the comparative effectiveness of the use of the design solutions will be presented based on the test results.

In general, the technical result of the claimed utility device is an increase in the operational characteristics of the self-cleaning fork, reduction in the time and effort spent on cleaning of the tines.

IV. Conclusions

Gardening is a popular activity and a pastime in many countries and cultures.

Despite the ongoing automation of modern production processes, manual labor continues to be necessary due to its flexibility and ease of deployment.

Manual garden tools help a lot with different types of work with soil: digging, removing roots and weeds, harvesting root crops and bulbs, and much more would be much more difficult if it were not for the forks.

A common problem for all manual garden forks is clogging of the tines. This leads to a decrease in the productivity of those who use them.

In the course of the research work, patented scientific and technical developments aimed at solving the problem of quick cleaning of the tines of forks, rakes and other similar devices were identified. They all have their advantages and disadvantages.

The employee of the FSBEI of Higher Education “Pskov State University” has developed a manual self-cleaning fork.

Essentially, the design of the manual self-cleaning fork consists of the handle having at one end the frame with many elongated spaced tines, as well as the cleaning plate, which is fixed to the movable handle, and the spring located on top of the handle inside the movable handle. The movable handle has lateral longitudinal grooves. The movable handle provides the movement of the cleaning plate relative to the handle, and, consequently, compression and releasing of the spring.

The principle of operation of the proposed device is simple: cleaning of the tines is performed by the cleaning plate which is moved along the tines. To do this, the user withdraws the movable handle, overcoming the resistance of the spring. The fork returns to its original state by releasing the spring after the user releases the movable handle.

In the course of the experimental design work, the author of the device modeled several versions of the mock-up samples. In general, the technical result of the claimed device is an increase in the operational characteristics of the self-cleaning fork, reduction in the time and effort spent on cleaning the tines. The manual self-cleaning fork allows a gardener to clean the fork’s tines from clogging with a single movement of the hand.

REFERENCES

[1] L. Chalmin-Pui, A. Griffiths, J. Roe, T. Heaton, and R. Cameron, "Why garden? – Attitudes and the perceived health benefits of home gardening," Cities, vol. 112, p. 103+, May 2021. [Online]. Available: ScienceDirect, https://www.sciencedirect.com/ [Accessed February 10, 2021] , https://doi.org/10.1016/j.cities.2021.103118

[2] R. M. Amongo, E. Quilloy, M. A. Ranches, M. V. Larona, and M. Madlangbayan, "Development of an electric hand tractor (e-Tractor) for agricultural operations," IOP Conference Series: Earth and Environmental Science, vol. 542, p. 012+, 2020. [Abstract]. Available: https://doi.org/10.1088/1755-1315/542/1/012027

[3] C. Löffler, C. Nickel, C. Sobel, D. Dzibela, J. Braat, B. Gruhler, P. Woller, N. Witt, and C. Mutschler, Automated Quality Assurance for Hand-Held Tools via Embedded Classification and AutoML, 2021. [Abstract]. Available: Springer link, https://link.springer.com/, https://doi.org/10.1007/978-3-030-67670-4_33

[4] S. Chitraputhira Pillai and P. Surya, Drudgery Reduction Through Use of Hand Held Fertilizer Applicator, 2020.

[5] T. Praiswater, B. Hibbard, B. Barry, L. Darrah, and V. Smith, "An Implement for Dislodging Maize Roots from the Soil for Corn Rootworm (Coleoptera: Chrysomelidae) Damage Evaluations," Journal of the Kansas Entomological Society, vol. 70, pp. 335-338, 1997.

[6] A. Y. Guinn and L. D. Stapley, "Self-cleaning rake," U. S. Patent 5,713,193, August 22, 1996.

[7] M. P. Robinson, "Self-cleaning rake," U. S. Patent 3,884,023(A), May 20, 1975.

[8] W. E. Baum, "Self-cleaning leaf rake," U. S. Patent 4,776,158(A), October 11, 1988.

[9] C. Riggs and D. Riggs, "Self-cleaning rake," U. S. Patent 2,015,257,335, November 21, 2014.

[10] I. Voiku, "Manual self-cleaning fork," R. U. Patent 199,181 U1, February 10, 2020.

Environment. Technology. Resources. Rezekne, Latvia
Proceedings of the 13th International Scientific and Practical Conference. Volume 3, 382-386

On the Turbulence in a Viscous Heat-Conducting Gas

Sergey Voronkov
Institute of Engineering Sciences
Pskov State University
Pskov, Russia
vorss60@yandex.ru

Pavel Safronov
Institute of Engineering Sciences
Pskov State University
Pskov, Russia
safisfppi@list.ru

Alexander Dementiev
Institute of Engineering Sciences
Pskov State University
Pskov, Russia
damix01@yandex.ru

Olga Frolova
Institute of Engineering Sciences
Pskov State University
Pskov, Russia
_backof2@mail.ru

Tatiana Bugaeva
Institute of Engineering Sciences
Pskov State University
Pskov, Russia
tanya.bugaeva.69@mail.ru

***Abstract* – The problem of the emergence of turbulence is one of the unsolved problems of physics and technology of the 20th century. It is noted that in order to understand the emergence of turbulence in a viscous heat-conducting gas, it is necessary to take into account the compressibility of the medium. A definition of turbulence in a viscous heat-conducting gas is given, which is a cyclically repeating process of the emergence and decay of coherent vortex structures described by a vector wave equation. The decay of vortex structures is accompanied by an explosive, asymptotic increase in pressure pulsations, which triggers a new cycle of turbulence generation. The emergence and decay of coherent vortex structures in the boundary layer on a plate and in a round jet is considered.**

Key words – turbulence, viscous heat-conducting gas, coherent vortex structures, vector wave equation, boundary layer, round jet.

I. INTRODUCTION

The problem of the emergence of turbulence is one of the unsolved problems of physics and technology of the 20th century. Turbulent flow of liquid and gas is the main one for engineering equipment. Laminar modes are implemented extremely rarely, at low flow rates. Energetically, laminar regimes are more preferable, since the pressure losses in them are proportional to the first power of the flow rate, in contrast to the turbulent flow regime, where the pressure losses are proportional to the flow rate squared. It is traditionally believed [1] that the process of turbulence emergence can be considered in the approximation of the incompressibility of the medium, which greatly simplifies the mathematical formulation of the problem. But as shown in [2], the assumption that the medium is incompressible, which is valid for liquids, is unreasonably extrapolated to a viscous heat-conducting gas. The assumption about the incompressibility of the medium assumes that the divergence of the flow rate is zero $\mathrm{div}\boldsymbol{V} = 0$. In [2], as a result of a computational experiment, it was found that the divergence of velocity in a viscous heat-conducting gas at the leading edge of the plate undergoes a sharp jump with a negative sign and its value is $\mathrm{div}\boldsymbol{V} = -800$. This result casts doubt on the validity of the assumption about the incompressibility of the medium when turbulence emergences in a viscous heat-conducting gas. To understand the emergence of turbulence in a viscous heat-conducting gas, it is

Online ISSN 2256-070X
https://doi.org/10.17770/etr2021vol3.6527

necessary to take into account the compressibility of the medium.

II. TURBULENCE IN A VISCOUS HEAT-CONDUCTING GAS

Taking into account the compressibility of the medium and the dissipation of energy in a viscous heat-conducting gas during the emergence of turbulence made it possible to obtain a vector wave equation describing the emergence and decay of coherent vortex structures [3]

$$\frac{\partial^2 \boldsymbol{\omega}}{\partial t^2} = (a_s^2 + \frac{4}{3}(k-1)\nu \mathrm{div}\boldsymbol{V})\mathrm{grad}\mathrm{div}\boldsymbol{\omega}, \qquad (1)$$

where $\boldsymbol{\omega}$ — is the circular frequency of the vortex tube; a_s — is adiabatic and isentropic value of the speed of sound; $\boldsymbol{V}$ — is the vector of the pulsating gas velocity with projections u, v, w on the axis of the Cartesian coordinate system x, y, z respectively; ν — is coefficient of kinematic viscosity; k — is the adiabatic index; t — is time.

Coherent vortex structures emergences and decays during the transition to turbulence – Fig. 1

Fig. 1. Visualization of the process of emergence and decay of coherent vortex structures on a body of revolution. Figure from [4]. Quoted from [5]

The emergence and decay of coherent vortex structures occurs not only at the stage of transition, but also in a developed turbulent flow. The resulting equation (1) allows us to give the following definition of turbulence in a viscous heat-conducting gas [3]:

Turbulence in a viscous heat-conducting gas is a cyclically repeating process of the emergence and decay of coherent vortex structures described by a vector wave equation. The decay of vortex structures is accompanied by an explosive, asymptotic increase in pressure pulsation, which triggers a new cycle of turbulence generation.

An expression for the pressure pulsation arising during the decay of coherent vortex structures was obtained in [6]

$$\Delta p = 4\mu(k-1)\frac{\omega_0^2 t_0^2}{t_0 - t}, \qquad (2)$$

where ω_0 — is the circular frequency of the vortex tube before the beginning of decay, t_0 — is the total decay time of the vortex tube, μ — is the coefficient of dynamic viscosity.

Let us give a graph of the change in pressure pulsation that occurs during the decay of vortex structures – Fig. 2.

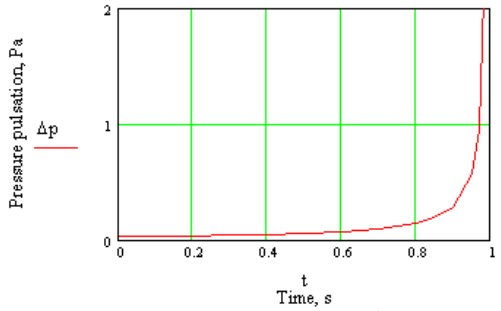

Fig. 2. Pressure pulsations calculated by the formula (2). When calculating it was taken: $\mu = 1{,}82 \cdot 10^{-5}\ \mathrm{Pa \cdot s}$; $k = 1{,}4$; $\omega_0 = 10\pi\ \mathrm{rad/s}$; $t_0 = 1\ \mathrm{s}$. Figure from [6]

Under the influence of pressure pulsation (2) at the place of the decay of coherent vortex structures, the formation of Emmons turbulent spots occurs - Fig. 3

Fig. 3. Emmons turbulent spot. Reynolds number $Re = 400000$. Visualization is carried out using smoke in the air, illuminated by a flash. Photo by R.E. Falco. Figure from [7]

Turbulent spots, propagating downstream, merge and form a developed turbulent flow.

III. COHERENT VORTEX STRUCTURES IN THE BOUNDARY LAER ON THE PLATE

Consider the emergence of vortex tubes in a natural transition on a plate – Fig. 4

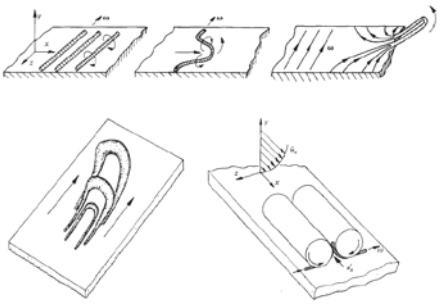

Fig. 4. The appearance of two-dimensional vortices and their decay into three-dimensional structures in a natural transition. Figure from [8]. Quoted from [9]

Circular frequency is related to speed circulation

$$\boldsymbol{\omega} = \frac{1}{2}\mathrm{rot}\boldsymbol{V}. \quad (3)$$

Considering that [10]

$$\mathrm{divrot}\boldsymbol{V} = 0, \quad (4)$$

Substituting (3) and (4) in (1), we obtain

$$\frac{\partial^2 \boldsymbol{\omega}}{\partial t^2} = 0. \quad (5)$$

We write the vector equation (5) in projections on the axes of the Cartesian coordinate system *x, y, z*

$$\frac{\partial^2 \omega_x}{\partial t^2} = 0, \quad (6)$$

$$\frac{\partial^2 \omega_y}{\partial t^2} = 0, \quad (7)$$

$$\frac{\partial^2 \omega_z}{\partial t^2} = 0. \quad (8)$$

The solutions to equations (6–8) will be written

$$\omega_x = C_1 t + C_2, \quad (9)$$

$$\omega_y = C_3 t + C_4, \quad (10)$$

$$\omega_z = C_5 t + C_6, \quad (11)$$

where $C_1, C_2, C_3, C_4, C_5, C_6$ — are constants.

In a natural transition, vortex tubes arise - two-dimensional vortices – Fig. 4, perpendicular to the main direction of flow. Consequently, constants C_1, C_2, C_3, C_4 will be equal to zero

$$C_1, C_2, C_3, C_4 = 0. \quad (12)$$

Let us consider a special case of the solution when the initial value of the circular frequency of the vortex tube does not depend on time and $C_5 = 0$.

Then the initial value of the vortex tube will be determined by a constant, which can be found as

$$C_6 = \frac{1}{2}\left(\frac{\partial v}{\partial x} - \frac{\partial u}{\partial y}\right), \quad (13)$$

that is, the initial value of the circular frequency of the vortex tube is determined by the derivatives of the pulsation components of the velocities *u* and *v*

$$\omega_z = \frac{1}{2}\left(\frac{\partial v}{\partial x} - \frac{\partial u}{\partial y}\right). \quad (14)$$

A further change in the circular frequency of the vortex tube ω_z is described by the vector wave equation (1). Let's write it in projections on the axes of the Cartesian coordinate system *x, y, z*

$$\frac{\partial^2 \omega_x}{\partial t^2} = \left(a_s^2 + \frac{4}{3}(k-1)\nu\mathrm{div}\boldsymbol{V}\right)\left[\frac{\partial^2 \omega_x}{\partial x^2} + \frac{\partial^2 \omega_y}{\partial y \partial x} + \frac{\partial^2 \omega_z}{\partial z \partial x}\right], \quad (15)$$

$$\frac{\partial^2 \omega_y}{\partial t^2} = \left(a_s^2 + \frac{4}{3}(k-1)\nu\mathrm{div}\boldsymbol{V}\right)\left[\frac{\partial^2 \omega_x}{\partial x \partial y} + \frac{\partial^2 \omega_y}{\partial y^2} + \frac{\partial^2 \omega_z}{\partial z \partial y}\right], \quad (16)$$

$$\frac{\partial^2 \omega_z}{\partial t^2} = \left(a_s^2 + \frac{4}{3}(k-1)\nu\mathrm{div}\boldsymbol{V}\right)\left[\frac{\partial^2 \omega_x}{\partial x \partial z} + \frac{\partial^2 \omega_y}{\partial y \partial z} + \frac{\partial^2 \omega_z}{\partial z^2}\right]. \quad (17)$$

An analysis of equations (15-17) shows that a vortex tube with circular frequency ω_z arising in the boundary layer will generate coherent vortex structures with frequencies ω_x and ω_y and will itself be deformed under the action of these vortex structures. Indeed, in equations (15) and (16), the spatial derivatives of frequency ω_z appeared on the right side, which will generate vortex tubes with frequencies ω_x and ω_y. Also, according to equation (17), the initially two-dimensional vortex tube and its circular frequency ω_z will deform and change, which is reflected in Fig. 4. Coherent vortex structures disintegrate and generate turbulent spots. The generation of turbulent spots occurs under the influence of pressure pulsations (2)

IV. COHERENT VORTEX STRUCTURES IN A ROUND JET

Let us consider the emergence and decay of coherent vortex structures in a round jet. During the natural transition in a round jet, ring vortices arise – vortex Kelvin – Helmholtz rings and streaky structures that are longitudinal vortices – Fig. 5.

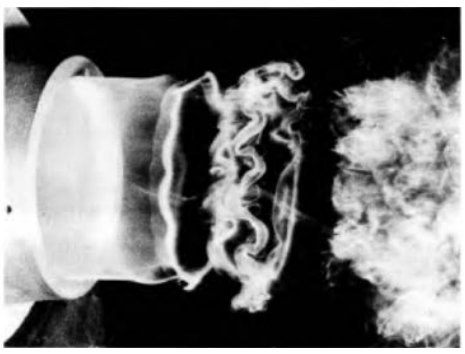

Fig. 5. Natural transition in a round jet. Photo by R. Wille, A. Michalke. Figure from [7]

Streaky structures, as noted in [11], appear in jets directly at the exit from flat and round nozzles.

It is more convenient to consider physical processes for a circular axisymmetric jet in cylindrical coordinates r, ε, z. The z axis is compatible with the jet axis. We write the vector equation (5) in projections on the axes of the cylindrical coordinate system

$$\frac{\partial^2 \omega_r}{\partial t^2} = 0, \quad (18)$$

$$\frac{\partial^2 \omega_\varepsilon}{\partial t^2} = 0, \quad (19)$$

$$\frac{\partial^2 \omega_z}{\partial t^2} = 0. \quad (20)$$

The solutions of equations (18–20) will be written

$$\omega_r = C_1 t + C_2, \quad (21)$$

$$\omega_\varepsilon = C_3 t + C_4, \quad (22)$$

$$\omega_z = C_5 t + C_6, \quad (23)$$

where $C_1, C_2, C_3, C_4, C_5, C_6$ — are constants.

In the natural transition of a round jet, ring vortices – ω_ε and streaky structures – longitudinal vortices – ω_z appear at the nozzle exit. Consequently, constants C_1, C_2 will be equal to zero

$$C_1, C_2 = 0. \quad (24)$$

Let us consider a particular case of solutions when the initial values of the circular frequencies of the vortex tubes do not depend on time and $C_3, C_5 = 0$. Then the initial values of the vortex tubes will be determined by constants C_4, C_6, which can be found as

$$C_4 = \frac{1}{2}\left(\frac{\partial V_r}{\partial z} - \frac{\partial V_z}{\partial r}\right), \quad (25)$$

$$C_6 = \frac{1}{2r}\left(\frac{\partial (rV_\varepsilon)}{\partial r} - \frac{\partial V_r}{\partial \varepsilon}\right), \quad (26)$$

where V_r, V_ε, V_z — are the projections of the pulsating gas velocities on the axis of the cylindrical coordinate system r, ε, z, respectively.

That is, the initial values of the circular frequencies of the vortex tubes are determined by the derivatives of the pulsation velocity components

$$\omega_\varepsilon = \frac{1}{2}\left(\frac{\partial V_r}{\partial z} - \frac{\partial V_z}{\partial r}\right), \quad (27)$$

$$\omega_z = \frac{1}{2r}\left(\frac{\partial (rV_\varepsilon)}{\partial r} - \frac{\partial V_r}{\partial \varepsilon}\right). \quad (28)$$

Further variation of the circular frequencies is described by the vector wave equation (1).

As noted in [11]: "An important aspect concerning streaky structures is their role in the process of turbulization of axisymmetric flows, for example, in a round jet. Such structures arise in jets directly at the exit from flat and round nozzles. When two-dimensional vortex rings of Kelvin – Helmholtz interact with streaky structures, their three-dimensional distortion occurs with the formation of characteristic azimuthal Λ – or Ω – shaped ejections (Fig. 6)."

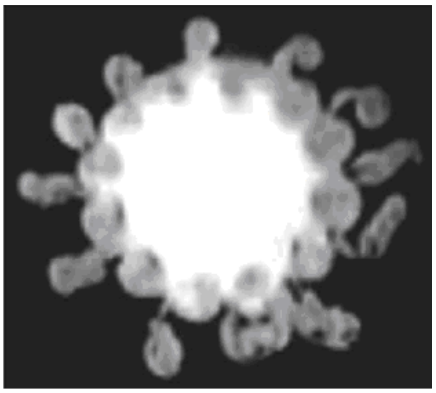

Fig. 6. Visualization of the cross-section of a round jet during the interaction of an ring vortex with streaky structures and the formation of azimuthal Λ – structures. Figure from [11]

The interaction of streaky structures with ring vortices leads to their decay with the formation of turbulent spots.

Coherent vortex structures appear in both laminar and turbulent jets.

In [12], the mechanism of the emergence and development of coherent vortex structures in laminar and turbulent round jets was investigated. The authors of [12] came to the following conclusions: "It has been shown that the mechanism of the emergence and development of coherent structures in laminar and turbulent jets is identical in general terms and is associated with the emergence and development of coherent structures such as Kelvin - Helmholtz ring vortices, streaky structures, and their interaction in both types of flow."

V. CONCLUSION

To understand the emergence of turbulence in a viscous heat-conducting gas, it is necessary to take into account the compressibility of the medium.

The presented vector wave equation for the circular frequency of a vortex tube describes the emergence and decay of coherent vortex structures in the boundary layer on a plate and in a round axisymmetric jet.

It is noted that coherent vortex structures are present not only at the transition stage, but also in the developed turbulent flow of a viscous gas.

It is shown that turbulence in a viscous heat-conducting gas is a cyclically repeating process of the emergence and decay of coherent vortex structures described by the vector wave equation $\frac{\partial^2 \boldsymbol{\omega}}{\partial t^2} = (a_s^2 + \frac{4}{3}(k-1)\nu \mathrm{div}\boldsymbol{V})\mathrm{graddiv}\boldsymbol{\omega}$. The decay of vortex structures is accompanied by an explosive, asymptotic increase in pressure pulsation $\Delta p = 4\mu(k-1)\frac{\omega_0^2 t_0^2}{t_0 - t}$, which triggers a new cycle of turbulence generation.

REFERENCES

[1] Schlichting G. Theory of the boundary layer. Moscow: Nauka, 1974, 712 p.

[2] Voronkov S. S. On the connection of Tollmin-Schlichting waves with acoustic waves. Scientific journal "Noise Theory and Practice", - access Mode. - URL: http://www.noisetp.com/ru/issues/journal-issues-archive/vol-6-no-4/, Volume 6 №4 (IV, 2020). Pp. 42-48.

[3] Voronkov S.S. On the emergence and decay of coherent vortex structures in a viscous gas. Electronic journal "Technical acoustics", http://www.ejta.org/2021 №1.

[4] Knapp C.F., Roache P.J. A combined visual and hot-wire, anemometerinvestigation of boundary layer transition. – AIAA J., 1968, v. 6, № 1, p. 29–36.

[5] Kachanov Y.S., Kozlov V.V., Levchenko V.Ya. Arising Turbulence in a Boundary Layer. Novosibirsk: Nauka, 151 pages, 1982.

[6] Voronkov S. S. On the mechanism of emergence turbulent Emmons spots. Electronic journal "Technical Acoustics", http://www.ejta.org/2020 №1.

[7] Van Dyke M. Album of fluid and gas flows. – M.: Mir. 1986. – 184 p.

[8] Davidson, P. A. Turbulence: an introduction for scientists and engineers. Oxford, UK: Oxford University Press, 2004. – 680 p.

[9] Garbaruk A.V. Transition to turbulence. Lecture 2. – S-P .: SPbSPU, 2019 . – 35 p. https://cfd.spbstu.ru/agarbaruk/turb_models/Term8_Lec02_transition.pdf

[10] Loitsyansky L.G. Mechanics of fluid and gas. Ed. 5th. – M.: Nauka, 1978. – 736 p.

[11] Boyko A.V., Gorev V.N., Kozlov V.V. Transition to turbulence in boundary layers: Success and prospects. NSU Bulletin. Series: Physics. 2006. Volume 1, Issue 2. P. 21-28.

[12] Kozlov G.V., Litvinenko Yu. A., Grek G.R., Sorokin A.M. On the mechanism of the emergence and development of coherent structures in laminar and turbulent round jets. NSU Bulletin. Series: Physics. 2008. Volume 3, Issue 1. P. 12-22.